EYEC Monograph

7th European Young Engineers Conference

April 23-25th 2018
Warsaw

Organizers:
Scientific Club of Chemical and Process Engineering
Faculty of Chemical and Process Engineering
Warsaw University of Technology
Foundation of Young Science

7th European Young Engineers Conference

www.eyec.ichip.pw.edu.pl

Edited by:
Bartosz Nowak, MSc Eng – Chief Editor
Piotr Cendrowski, BSc
Joanna Latocha, MSc Eng
Łukasz Werner, MSc Eng.
Patrycja Wierzba, MSc Eng.
Maria Zuzga, MSc Eng.

ISBN 978-83-936575-5-1

Printed in 100 copies

The authors are responsible for the content of the papers.
All papers reviewed by Scientific Committee.

Cover design: Antonina Krawczyk krawczyk.antonina@gmail.com

Cover photo of oiled aerogel from NCBiR project "Oil removal from gas and liquid streams thanks to filter media modified by aerogel"
LIDER/011/L-6/14/NCBR/2015

Published by:
Faculty of Chemical and Process Engineering
Warsaw University of Technology

Printed in Poland by:
Institute for Sustainable Technologies – National Research Institute
26-600 Radom, 6/10 Pułaskiego Street,
phone (+48) 48 36-442-41,fax (+48) 48 36-447-65
http://www.itee.radom.pl

Table of Content

Introduction

Since the very beginning of European Young Engineers Conference, since the first meeting of Students Scientific Club in 2011, we were wondering, how we can develop our work and how to provide a new, attractive and easy way to exchange knowledge and experience between young people. People who, like us, are passionate about creation, search for answers, create innovative solutions for current issues. In short – people of Science.

It may sound pompous, after all, there are many other conferences for young scientists, but we believe that thanks to EYEC's scope, friendly atmosphere and high level of presented research, it is the best way to start or continue your scientific career.

It is already 7th edition of EYEC and we still have not materialized half of our ideas. Every year we try to give you something new: interesting guest speakers, additional workshops or accompanying contests. It is also 5th time we give you our EYEC Monograph. In this book, you can find the most promising, important and reviewed papers of European Young Scientists. We hope, that this book you are holding right now, will be the first step in a great career of each and every of participants of our conference.

This year, with the article by Prof. Venken, we start a new section of our monograph – "From expert's perspective". We want it to be the first of regular articles, written by experienced scientists and covering or commenting vital issues.

We hope you will find the papers within this book highly interesting and important, as we do.

Organizing Committee
Editorial Team of EYEC Monograph

Scientific Committee

Prof. Eugeniusz Molga, PhD (WUT, Poland) – Chairman

Prof. Jerzy Bałdyga, PhD
(WUT, Poland)
Prof. Tomasz Ciach, PhD
(WUT, Poland)
Prof. Paweł Gierycz, PhD
(WUT, Poland)
Prof. Leon Gradoń, PhD
(WUT, Poland)
Prof. Marek Henczka, PhD
(WUT, Poland)
Prof. Łukasz Makowski, PhD
(WUT, Poland)
Prof. György Marosi, **PhD**
(BME, Hungary)
Prof. Arkadiusz Moskal, PhD
(WUT, Poland)
Prof. Masaki Nakahata, PhD
(Osaka University, Japan)
Prof. Wojciech Piątkiewicz, PhD
(ISTe-NRI, Poland)
Prof. Shinji Sakai, PhD
(Osaka University, Japan)
Prof. Tomasz Sosnowski, PhD
(WUT, Poland)
Prof. Andrzej Stankiewicz, PhD
(TUDelft, Netherlands)
Prof. Ilia Vorotyntsev, PhD
(NNSTU, Russia)
Bruno Bastos Sales, PhD
(Avans University, Netherlands)
Agata Bąk, PhD
(WUT, Poland)
Alessandro Benedetti, PhD
(Mareco CNR-IENI, Italy)
Marta Bojarska, PhD
(GVS, Italy)
Robert Cherbański, PhD
(WUT, Poland)
Katarzyna Dąbkowska, PhD
(WUT, Poland)
Julita Dworecka-Wójcik, PhD
(WUT, Poland)
Paweł Falkowski, PhD
(WUT, Poland)
Jakub Gac, PhD DSc
(WUT, Poland)
Oleksandr Ivashchuk, PhD
(LPNU, Ukraine
Anna Jackiewicz, PhD
(WUT, Poland)
Joanna Jankowska-Śliwińska, PhD
(IBB-PAS,Poland)
Magdalena Jasińska, PhD DSc
(WUT, Poland)
Naresh Kasoju, PhD
(IBME, UK)
Agnieszka Kierzkowska, PhD
(ETH, Switzerland)
Zoltan Kovacs, PhD
(SIU, Hungary)
Andrzej Krasiński, PhD
(WUT, Poland)
Jan Krzysztoforski, PhD
(WUT, Poland)
Piotr Machniewski, PhD
(WUT, Poland)
Łukasz Makowski, PhD
(WUT, Poland)

Artur Małolepszy, PhD
(WUT, Poland)
Marta Mazurkiewicz-Pawlicka, PhD
(WUT, Poland)
Marcin Odziomek, PhD
(WUT, Poland)
Wojciech Orciuch, PhD
(WUT, Poland)
Agata Penconek, PhD
(WUT, Poland)
Mariusz Pietrzak, PhD
(WUT, Poland)
Maciej Pilarek, PhD
(WUT, Poland)
Filip Sala, PhD
(WUT, Poland)
Marzena Sala-Tefelska, PhD
(WUT, Poland)
Paweł Sobieszuk, PhD
(WUT, Poland)
Iga Wasiak, PhD
(NanoVelos, Poland)

The Editorial Team of EYEC Monograph is extremely grateful for the effort and work of Scientific Committee put on the reviewing process of all the manuscripts published in this book. Right after authors, without Your work this book would not be created. Thank you.

Organizing Committee
Editorial Team of EYEC Monograph

Scientific Commission

Łukasz Makowski, PhD DSc

He graduated from the Faculty of Chemical and Process Engineering of the Warsaw University of Technology in 1997. In 2003 he has received a PhD degree in Chemical Engineering, PhD thesis was titled "Application of the closure hypothesis and CFD for description of complex chemical reactions in the systems with turbulent flow". In 2013 he has received DSc (habilitation) in Chemical Engineering titled „Effects of mixing in selected problems of product engineering processes". During of his work he was repeatedly manager or participant in many research grants funded by public resources for science or industry, for instance: State Committee for Scientific Research and National Science Centre as well as projects in 6th and 7th Framework Programme of the European Union, Bayer Technology Services GmbH, Unilever, CIECH Group Companies - ZACHEM, OLPP, Miejskie Przedsiębiorstwo Wodociągów i Kanalizacji w m.st. Warszawie, Cosmetic Packaging Factory Pollena S.A. He is co-author of 72 papers published in periodicals and conference materials.

His scientific current interests: investigation of effects of turbulent flow and turbulent mixing on the course of complex processes: chemical reactions and precipitations (including nanoparticles of MoS_2 precipitation) using large eddy simulations. The studies have used CFD codes and simulations results are verified by experimental data.

Alessandro Benedetti, PhD

Researcher in the MARECO CNR-ICMATE sea marine station, located in Bonassola (SP, Liguria, Mediterranean sea) also responsible for management of the CePAS-Bonassola office, a public structure by the Bonassola Municipality and CNR-ICMATE for the divulgation of sea environment peculiarities consisting in stormy waves formation and watching.

He received his PhD in Environmental Science from Università degli Studi di Milano. Dr Benedetti's research is currently related to surface and metals/alloys behavior in different and particular seawater environments. About surfaces, superhydrophobic layers are currently under investigation. About metallic materials,

traditional alloys are being studied along with non-traditional ones for particular seawater applications. Cathodic protection and testing of traditional vs. innovative paints are matter of interest too.

He is taking part in research projects related to oceanography and meteorology. The first, concerning the development of high resolution models for the description/forecast of meteomarine/shoreline dynamics, and, the monitoring of sea waves by accelerometric/seismologic techniques. The second, concerning the monitoring of rainfall events with high resolution-real time innovative techniques.
Beside a number of scientific papers he also published a book "Wave Watching – lo spettacolo delle mareggiate in Liguria" (S. Gallino, A. Benedetti, L. Onorato. Ed. Hoepli, 1st edition 2011, 2nd edition 2016).

Zoltan Kovács, PhD

Dr Kovács currently holds the position of associate professor at the Department of Food Engineering, Szent István University, Hungary. He received his MSc degree on Food Engineering in 2003 from the Szent István University. In 2008, he obtained his Ph.D. degree on Chemical Engineering from the Institute of Process Engineering at the Johannes Kepler Universitaet Linz, Austria. Prior to his current position, he had worked as a senior scientist for 5 years at the Institute of Bioprocess Engineering and Pharmaceutical Technology of the University of Applied Sciences Mittelhessen, Giessen, Germany. In 2013, he obtained the Marie Curie Career Integration Grant that allow him - after 10 years of international experience in abroad - to return in his home country and to establish his own research group. During his career, he has received distinctions from the European Membrane Society, the Association of German Engineers, and recently awarded the Bolyai Research Fellowship by the Hungarian Academy of Sciences. He has participated to and is responsible for many out-of-campus projects with industrial partners on bioprocess design and membrane technology development.

Ilya Vorotyntsev, PhD

Ilya Vorotyntsev received his M.S. and PhD degrees in Physical Chemistry from Lobachevsky University (Russia). He spent several years in industry working on the products launch of ultra-high purity gases for semiconductors industry. In 2005, he joined Russian flagship University - Nizhny Novgorod State Technical University n.a. R.E. Alekseev (NNSTU) to continue his teaching and research in the membrane area. In 2013, he became a Professor in NNSTU. His research activity covers material science, membrane gas separation, ionic liquids, hybrid and integrated process. In 2016, his research group was awarded «Green Chemistry for Live», sponsored by UNESCO's International Basic Sciences Program and PhosAgro in close cooperation with IUPAC. In 2017, he was elected as the first Chair of International Younger Chemists Network during the IUPAC General Assembly.

Marta Mazurkiewicz-Pawlicka, PhD

Dr Marta Mazurkiewicz-Pawlicka works at the Graphene Laboratory at the Faculty of Chemical and Process Engineering, Warsaw University of Technology. She finished her PhD in 2015 at the Faculty of Materials Science and Engineering, Warsaw University of Technology. Her thesis entitled "Preparation and characterization of palladium catalysts deposited on multi-walled carbon nanotubes for use in a direct formic acid fuel cell". She is a co-author of 27 publications in international journals mainly on the topic of carbon nanomaterials. Her research activity focuses on the preparation, modification and applications of different carbon nanomaterials (including carbon nanotubes, graphene oxide and carbon nanofibers) in alternative energy sources and polymer composites.

Marta Bojarska, PhD

She graduated from the Industrial Biotechnology at Faculty of Chemistry, Warsaw University of Technology in 2010. In March 2015, she received a PhD degree at Faculty of Chemical and Process Engineering, Warsaw University of Technology. During her PhD studies her work was awarded few times on international conferences by European Membrane Society. Dr Marta Bojarska did her two years postdoc training in group of Professor Mathias Ulbricht at Faculty of Chemistry at University of Duisburg-Essen. Since November 2017 she works as a senior researcher at GVS Filter Technology in Italy, where she is working on membrane development. She is a co-author of over 20 papers published in periodicals and conference materials. In 2015 she was granted a LIDER VI project from the National Centre for Research and Development. In 2017 she was recognized as one of the Ten Top Polish Talents by MIT Technology Review.

Her scientific interests are: membrane preparation, characterization of membrane properties, membrane modification via nanoparticles, photocatalysis, antibacterial properties, materials science.

Organizing Committee

Members of the Scientific Club of Chemical and Process Engineering
and Foundation of Young Science

Head of Committee
Nina Borzęcka, BSc

Magdalena Tomczak
Weronika Jaworska
Mieszko Boczkowski
Mateusz Bartczak
Robert Bitner
Paweł Antkowiak
Ewa Kamińska
Izabela Szczur, BSc
Olga Przybył
Radosław Krzosa
Agata Piros
Zuzanna Bojarska, BSc
Justyna Szczepańska
Hanna Nurczyńska
Kacper Siwek
Maksymilan Nowak, BSc
Joanna Kobek, BSc
Aleksandra Olszewska, BSc

Kinga Kalkowska
Krystian Jędrzejczak
Weronika Gołębiowska
Bartosz Nowak, MSc
Patrycja Wierzba, MSc
Łukasz Werner, MSc
Joanna Latocha, MSc
Maria Zuzga,MSc
Piotr Cendrowski, BSc
Kamila Bańkoska
Anna Dmowska, BSc
Karina Flasińska
Kinga Kurowska-Wilczyńska, PhD
Jacek Lewicki, PhD
Eliza Grzymkowska, BSc
Julia Bień, BSc
Grzegorz Tyl, MSc
Klaudia Jaworska

Special Guests

Prof. Mathias Ulbricht, PhD

Mathias Ulbricht is since 2001 a Full Professor for Industrial Chemistry at University Duisburg-Essen, Germany (www.uni-due.de/tech2chem).

He had studied chemistry at the Humboldt University in Berlin, Germany, and received his Ph.D. degree in organic chemistry in 1987. He had worked at Rensselear Polytechnic Institute, Troy, New York, USA, from 1992 to 1993. Based on various postdoctoral research projects, mostly with a small group based at Humboldt University, he had received his "Habilitation" from that University in 1997. From 1997 to 1999 he had worked at GKSS Research Centre in Teltow, Germany. In 1999 he had founded ELIPSA Inc. in Berlin and was CEO of this private company until 2003.

His research interests are in the field of functional polymeric as well as nanohybrid materials and have a focus on synthetic membranes and membrane-based technologies for water purification, bioseparation and energy conversion. He is in the editorial board of several international journals including "Journal of Membrane Science", "Polymer" and "Separation and Purification Technology" (all Elsevier). He has published more than 215 peer-reviewed scientific papers (current "Web of Science" h-index: 45), 14 book chapters and filed 30 patents (until now 19 issued).

Advanced polymer-based membranes with tailored barrier and surface properties

Membrane technologies have been established in a wide range of industrial applications; the most successful processes are nowadays realized in very large scale. Organic polymers are the dominating materials, and intense research and development is focused on innovations leading to advanced membranes with higher separation performance adapted to specific requirements of important applications [1].

In this presentation we will illustrate by recent examples from own research how the efficiency of membrane-based separations can be improved by developing membranes with higher intrinsic selectivity at high permeability, with high resistance to fouling and with added functionalities based on specific adsorptive, catalytic or stimuli-responsive properties. The focus will be on the integration of functional inorganic nanoparticles or polymeric nanolayers in polymer-based membranes (e.g. [2-8]). An interesting extension is the utilization of perforated ultrathin graphene monolayers in a novel type of polymer-based composite membrane to achieve advanced ultrafiltration performance [9].

Such generic innovations in membrane materials will contribute to more sustainable membrane processes for applications in water purification, bioseparation or medical therapies.

[1] M. Ulbricht, State-of-the-art and perspectives of organic materials for membrane preparation in Comprehensive Membrane Science and Engineering, 2nd Edition (Eds.: E. Drioli, L. Giorno, E. Fontananova), *Elsevier, ISBN: 9780444637758, 2017, Vol. 1, 85-119;* see also: https://doi.org/10.1016/B978-0-12-409547-2.12252-8

[2] M. Quilitzsch, R. Osmond, M. Krug, M. Heijnen, M. Ulbricht, Macro-initiator mediated surface selective functionalization of ultrafiltration membranes with anti-fouling hydrogel layers applicable to ready-to-use capillary membrane modules, *J. Membr. Sci.*, 2016, *518*, 328-337.

[3] J. Meyer, M. Ulbricht, "Poly(ethylene oxide)-block-poly(methyl methacrylate) diblock copolymers as functional additive for poly(vinylidene fluoride) ultrafiltration membranes with tailored separation performance", *J. Membr. Sci.* 2018, *545*, 301-311.

[4] X. Lin, B. Nguyen Quoc, M. Ulbricht, Magneto-responsive polyethersulfone-based iron oxide *cum* hydrogel mixed matrix composite membranes for switchable molecular sieving, *ACS Appl. Mater. Interf.* 2016, *8*, 29001-29014.

[5] Y. Tang, X. Lin, K. Ito, L. Hong, T. Ishizone, H. Yokoyama, M. Ulbricht, Tunable magneto-responsive mesoporous block copolymer membranes, *J. Membr. Sci.* 2017, *544*, 406-415.

[6] S. Schwark, W. Sun, J. Stute, D. Lütkemeyer, M. Ulbricht, B. Sellergren, Monoclonal antibody capture from cell culture supernatants using epitope imprinted macroporous membranes, *RSC Adv.* 2016, *6*, 53162-53169.

[7] D. Liu, M. Ulbricht, Highly selective protein adsorber via a two-step surface-initiated molecular imprinting utilizing a multi-functional polymeric scaffold on macroporous cellulose membrane, *RSC Adv.* 2017, *7*, 11012-11019.

[8] A. Wittmar, Q. Fu, M. Ulbricht, Photocatalytic and magnetic porous cellulose-based nanocomposite films prepared by a green method, *ACS Sustainable Chem. Eng.* 2017, *5*, 9858-9868.

[9] L. Madauß, J. Schumacher, M. Ghosh, O. Ochedowski, J. Meyer, H. Lebius, B. Band'Etat, M. E. Toimil-Molares, C. Trautmann, R. G. H. Lammertink, M. Ulbricht, M. Schleberger, Fabrication of nanoporous graphene/polymer composite membranes", *Nanoscale* 2017, *9*, 10487-10493.

Prof. Jörg Vienken, PhD

Jörg Vienken graduated in Chemical Engineering at the Technical University of Darmstadt and received a Doctoral Degree in Biophysics and Bioengineering from the Technical University of Aachen, both in Germany. He was then appointed the position of an Associate Professor at the Institute for Biotechnology of the University of Würzburg, Germany.

In 1985, he switched to the medical device industry and worked for 11 years at AKZO NOBEL Membrana in Wuppertal as Director for Clinical Research and Science Services, followed 1996 by a position as Vice President BioSciences in Fresenius Medical Care in Bad Homburg, Germany which he held until his retirement in 2013. From 2013 – 2015 he served as Board Member of Nephro-Solutions AG in Hamburg and is working since 2016 as a Freelance Advisor for the Medical Device Industry.

He has been awarded the "Emil-Bücherl-Award" for life-time achievement in the realm of Artificial Organs from the European Society for Artificial Organs (ESAO) and is a distinguished fellow of ERA-EDTA, the European Dialysis and Transplantation Association.

Jörg Vienken is Past President of the International Federation of Artificial Organs (IFAO, representing the umbrella organisation of the continental societies from Europe (ESAO), the USA (ASAIO) and Japan (JSAO)). He was a long lasting Board member of the European Society for Artificial Organs (ESAO) and served as its secretary treasurer between 1998 and 2006. He is also Past President of the Association of German Biotech Companies (VBU- DECHEMA).

Jörg Vienken still teaches Biomaterials and Artificial Organs at several German and European Universities and has published more than 300 scientific publications and book chapters as well as 8 books.

The new European Medical Device Regulation (MDR):Challenges and chances for young scientists

Marketing of medical devices requires successful approval procedures in all markets, where they should be sold. A series of healthcare scandals in past have cast doubt to the reliability of classical approval procedures and their supervision by both, healthcare authorities and *Notified Bodies*. Severe health problems in patients following malfunctioning or toxic medical devices, which bypassed regulatory prescriptions have motivated the EU Commission to abandon the former Medical Device Regulation (MDD) and replace it by the new Medical Device Regulation (MDR) in April 2017 [1]. This regulation became effective on May 25, 2017.

A regulation is a legal act of the European Union that becomes immediately enforceable as law in all member states simultaneously. Regulations can be distinguished from directives which, at least in principle, need to be transposed into national law. The newly established MDR regulations represent a series of strict rules related to all aspects of production, marketing, approval, post market surveillance and safety of medical devices. They impact both manufacturers and regulatory authorities, such as ***Notified Bodies***. A database called **EUDAMED**, which will be used by manufacturers to submit product specific details of their marketed devices, allows for a transparent information both for the public and the applicants on medical devices, their components, their expiry dates and specific application. A "Unique Device Identifyer (**UDI**)" has to be established, which provides a machine-readable tag for any medical device. Further, experienced laboratories for testing devices prior to approval or supervising clinical trials will be established.

Despite being based on a rather complex document (>170 pages), the new MDR also offers guidelines and advices for all partners of the medical device industry. New requirements for the guarantee of performance and safety of medical devices provide enormous chances and challenges for university graduates and start-up companies, given that they are engaged in device assessment, quality control and documentation.

Anne Ladegaard Skov, PhD

Dr Tech, Ph.D. Anne Ladegaard Skov is an associate professor of polymer science and engineering specialising in silicone elastomers at the Danish Polymer Centre, Department of Chemical Engineering, DTU. Her PhD project was performed at DTU with an external stay at Leeds University, UK. Subsequently, she held a research fellowship at Cambridge University, UK, before taking up a position as assistant professor at DTU. In 2010 she was promoted to associate professor and later promoted to head of the Danish Polymer Centre. She has worked with functionalisation and formulation of silicone elastomers with special focus on silicone elastomers utilised and optimised for dielectric elastomers. She is currently the president of the EuroEAP society which is a European society with the aim of promoting electroactive polymers.

She has published more than 100 articles and holds 8 patents within the field of dielectric elastomers and silicone-based materials. She has received numerous prizes for her research including the Statoil Prize and the Elastyren Prize as well as she holds the title of Dr Tech, the highest academic title in Denmark.

Dielectric elastomers – the human muscle wanna-bes

Dielectric elastomers basically consist of an elastomer with compliant electrodes which then comprise a stretchable capacitor. When an electrical field is applied to the electrodes, the film expands in area and compresses in thickness, i.e. it actuates. Due to the inherent softness of the utilized elastomers, dielectric elastomers resemble human muscles with respect to strength and capacity amongst others. Therefore dielectric elastomers were also originally nicknamed artificial muscles and were believed to take over as implants etc. However, the technology still – after almost 30 years of research – suffers from the need for relatively high voltages to create a significant actuation. Therefore the number of existing implants is limited to e.g. eyelid activators and shut-off devices for incontinence. Nevertheless dielectric elastomers hold great promise in many other areas where human muscle properties are sought. In contrast to common energy transducers dielectric elastomers are lightweight, soft and capable of large strains, and thereby their properties open up for completely new applications, such as thin and lightweight loudspeakers and light modulators.

In this talk the basic properties of dielectric elastomers will be discussed in context of some of the application areas where dielectric elastomers have shown great potential.

Marc Mueller, PhD

He graduated in 2011 with a Master degree in Biomedical Engineering at the Leibniz Universitaet Hannover, Germany. In December 2017, he received a PhD in Mechanical Engineering at the Faculty of Mechanical Engineering, Leibniz Universitaet Hannover, Gemany. He is working as a Post-Doc at the Institute for Multiphase Processes (Leibniz Universitaet Hannover). His research focuses on processing, characterisation and testing of polymeric materials for medical applications (e.g. cardiovascular implants). Since 2014, he is leading the research group "Interfacial processes", which is working in the fields of surface characterisation, biodegradation, flow visualisation and biocompatibility testing. Since he started working at the Institute for Multiphase Processes, he is responsible for the Master program in Biomedical Engineering at the Leibniz Universitaet Hannover, taking care for admissions, student advisory service and development of curricula.

Since 2016 he is one of the coordinators of the young researchers initiative of the European Society for Artificial Organs (yESAO), which brings together young researchers like engineers, scientists and clinicians, together with undergraduate, graduate and post-graduate students coming from different university laboratories, hospitals and companies.

Electrospinning of biodegradable implants

Electrospinning is a textile fabrication technique. It creates non-woven fibrous scaffolds made of polymeric fibers of various shapes. The size of electrospun fibers, which is in the range of nano- to micrometers, if beneficial for applications in Regenerative Medicine. It is possible to mimic the extracellular matrix native tissue by controlling the diameter in a defined range. This mimicry is important for the clinical success, since cell growth and infiltration depends on mechanotransduction and surface topography of the scaffold.

A common electrospinning-setup consists of a reservoir, a grounded collector and a high voltage-supply. The high voltage supply is connected to a nozzle and the collector. The polymeric solution is fed through the nozzle with a flow rate of a few milliliters per hour. With applying a voltage of several kilovolt to the polymeric solution, a charge separation is induced. If the force of the electric field overcomes the surface tension of the polymeric solution, a jet is accelerated out of the nozzle. On its way to the collector, the solvent evaporates and the fiber is elongated. Dry fibers are randomly deposited on the collector and create the scaffold. There are several parameters, which influence the process and by this the properties of the scaffold. Some of them are easy to control, like flow rate, voltage or nozzle to collector distance. Some of them, like the environmental parameters, require precise control techniques.

The morphology of the scaffold (e.g. fiber size, porosity) has a high impact on the mechanical properties as well as on the biocompatibility. There is a need to tailor the morphological parameters with regard to the specific application. The fiber diameter is a key parameter of an electrospun scaffold. For many polymeric solutions it can be adjusted by changing the concentration of the polymeric solution. This directly influences the viscosity and by this the size of the fiber. We could show that by increasing the concentration of a polymeric solution (polycaprolactone, PCL) from 100 to 200 mg/ml the fiber diameter increases with increasing concentration from 0.75 µm to 3.5 µm.

Based on the results of the fiber diameter measurements it is possible to calculate the specific surface of a scaffold. This value is important for studying wettability or cell attachment. In general, the specific surface increases with decreasing fiber size and can be adjusted by manipulating the fiber diameter.

The surface properties of biomaterials have a great influence on the biological interaction of scaffolds. This is mainly due to unsaturated bondings, which interact with the surrounding milieu. It is of high interest to determine surface properties like wettability or surface energy. A typical method to analyse these properties is to measure the contact angle between fluids and the surface. The captive bubble method is a specific method to measure contact angles of porous or rough materials.

Here, the sample is immersed in a fluid and a bubble or drop of immiscible fluid is placed at the lower surface of the sample. With the use of this method we could show, that scaffolds with small fiber diameters made of PCL resulted in higher contact angles to water compared to scaffolds with lager fibers sizes. This effect is based on the increase in specific surface with decreasing fiber size. The large specific surface of the hydrophobic polymer reduces the wettability with water. Measurements with additional fluids (e.g. ethylene glycol, glycerin, hexadecane) were performed to calculate the surface free energy of the scaffold. For scaffolds made of PCL an increase in fiber size led to an increase of surface free energy. It can be concluded that an increase in fiber diameter leads to an increase of the wettability of electrospun scaffolds. This allows for the improvement of mass transport (eg. nutrients) through the scaffolds and by this enhances cell infiltration.

Scaffolds for applications in the cardiovascular system have to withstand specific loading conditions at the implantation site. Here, circumferential and longitudinal stresses caused by the haemodynamic are of great importance. The compliance describes the ability of a blood vessel to increase its volume with increasing pressure. It can be analysed by increasing the pressure inside the scaffold and measuring the change in diameter. We could show that scaffolds with large fiber diameters show a significantly lower compliance than scaffolds with smaller fibers. Under uniaxial loading conditions in longitudinal direction (tensile test) scaffolds with larger fibers show significantly higher values for the force at break and strain at break than scaffolds with smaller fibers. Here, an increase in fiber size leads to a stiffer behavior of the tubular scaffolds.

The extracellular matrix of native tissues shows a multi-layered structure. Each layer has a specific microstructure with different fiber sizes (e.g. collagen) and fiber orientations. Modifications of the electrospinning process allow for the fabrication of multi-layered scaffolds with defined microstructures. The alignment of fibers can be realised by using a rotating drum collector with high rotating velocities. This forces the fibers to align parallel to the direction of rotation. For scaffolds made of PCL with small fibers sizes the alignment increases with increasing velocity, having a maximum at 8 m/s. With increasing fiber diameter, a higher velocity is needed to efficiently align the fibers.

Another method to align fibers is gap spinning. Here, two collectors are placed with a defined gap between each other. This forces the fiber to jump from one collector to the other. The resulting fiber mesh consists of nearly perfect aligned fibers. We automated this method with a custom-made device. The collectors are continuously moved towards a central collector and by this, deposit the fabricated fiber layer on the surface of the collector. This allows for the fabrication of multi-layered scaffolds with defined fiber orientation in each layer.

Another application, which requires specific scaffolds, is the regeneration of nervous tissue. The repair of a peripheral nerve is typically performed with a conduit, which guides the cell growth via an aligned, channel-like inner structure. This structure is protected by a shell, which is also used to attach the conduit to the nerve stumps via suturing. In addition, restoring the function of nervous tissue needs specific stimuli. The aim is to provide an active scaffold, fabricated of specific materials, which enhances the regeneration of the tissue. Our approach is to combine the method of electrospinning with directional solidification. We fabricated a porous core structure with longitudinal channels. This core is covered by electrospun fibers, fabricated of Polyvinylidene fluoride (PVDF). PVDF has piezoelectric properties. If the material is processed with appropriate parameters, it is possible to generate a voltage by applying mechanical stress to the structure. This voltage is thought to stimulate the cell growth of nervous tissue. Our results show, that with increasing polymer concentration and at constant loading conditions, the generated voltage increases from 15mV up to 80 mV. The electrospinning process has shown to be a suitable method for the fabrication active scaffolds and allows for modifying the piezoelectric properties of PVDF.

One additional feature in creating specific and functional tissue replacements is the use of pharmaceutical agents. The aim is to ensure a sustained release over a long period of time. In case of electrospinning, a suitable method is the use of a coaxial nozzle. This enables the processing of two different polymeric solutions at the same time and by this the fabrication of fibers with core/shell structures. Typically, a drug-loaded water-soluble solution is used for the core and water insoluble solution for the shell. The shell will act as a membrane and ensures a sustained release over time. We could show a biphasic release kinetic for coaxial-spun scaffolds loaded with acetylsalicylic acid or dipyridamole. About 35 % percent of the drug was released within the first 10 hours, followed by a sustained release with approx. 90 % release after 60 days.

The presented methods and data demonstrate, that electrospinning is a promising technique to fabricate tailor-made scaffolds for regenerative medicine.

Anna Jackiewicz-Zagórska, PhD

She graduated from the Faculty of Chemical and Process Engineering of the Warsaw University of Technology in 2004. Her master thesis was appreciated by the Award of the Ignacy Łukasiewicz Grant Fund of PGNiG S.A. for the best Master's thesis. In November 2010, she received a PhD degree and her Doctoral thesis entitled "Investigation into filtration of aerosol particles in inhomogeneous fibrous filters" was distinguished by the Faculty Council and by the jury awarding the Fiat grants. Dr Anna Jackiewicz-Zagórska has been employed by the Warsaw University of Technology as Assistant Professor since 2011. She is the supervisor of the filtration laboratory at the Department of Integrated Processes Engineering.

Dr Anna Jackiewicz-Zagórska is co-author of 57 papers published in periodicals and conference materials. She has presented her research results at 15 international and 11 national conferences. She received scholarships for distinguished Ph.D. students in the field of science and research and scholarship for young scientists awarded by the Centre for Advanced Studies, Warsaw University of Technology, and by the Marshal of the Mazowieckie province. In 2011, she was granted an individual Award of the Rector of the Warsaw University of Technology for scientific achievements. Her profile was presented at the exhibition entitled "Maria Skłodowska-Curie in the Service of Science Yesterday and Today" at the European Parliament in Brussels. Since 2012 Dr. Jackiewicz is the manager of the Leader III project from the National Centre for Research and Development. She was awarded first place in the project called “Internship as a success of a scientist”, intended to strengthen the cooperation between researchers and enterprises.

Her scientific interests: separation processes of gas-solid and -liquid particles, design of modern polymer-based filtering media, modeling of filtration process in fibrous filters, techniques for aerosol generation and detection.

Effective filtration using modern polymer-based materials

The issues of separation of abiotic and biotic particles from a continuous phase - gas or liquid - are a very important research area mainly for environmental protection, human health and technological reasons. The perfect tool used for this purpose are the polymer fibrous materials. Their range of applications is wide but is constantly expanded, i.e. purification of natural and shale gas from both solid and liquid contaminants, air cleaning in rooms and cars, purification of mine and drinking waters, purification of combustion air in modern high-pressure engines. New technological solutions replace old, requiring large apparatus, materials and energy expenditures. They direct filtration research to issues related to the development of modern filtration structures ensuring higher filtration efficiency, multifunctional properties, longer filter life and the removal of nanoparticles.

The concept of novel polymer filtration materials based on the melt-blown technology will be presented. The innovativeness of the developed structures is related to two aspects. The first of them is spatial heterogeneity (so-called gradient filters), which allows to extend their working time. The second one involves the use of composite fibers, which will affect the adhesion of the particles, and consequently the increase of filter efficiency, or give the filters additional properties. The functionalization will be carried out through two routes: during production process where various additives are added to the molten polymer and post-production modification in which additives are introduced into the surface of readily manufactured fibres.

From expert's perspective

The new European Medical Device Regulation (MDR): Challenges and chances for young scientists

*Jörg Vienken[1]
[1]Technical University Mittelhessen (THM), Gießen, Germany
e-mail: Vienken.usingen@gmail.com

Keywords: *Medical devices, healthcare scandals, European regulations, Notified Bodies, medical device classification*

ABSTRACT

Marketing of medical devices requires successful approval procedures in all markets, where they should be sold. A series of healthcare scandals in past have cast doubt to the reliability of classical approval procedures and their supervision by both, healthcare authorities and *Notified Bodies*. Severe health problems in patients following malfunctioning or toxic medical devices, which bypassed regulatory prescriptions have motivated the EU Commission to abandon the former Medical Device Regulation (MDD) and replace it by the new Medical Device Regulation (MDR) in April 2017 [1]. This regulation became effective on May 25, 2017.

A regulation is a legal act of the European Union that becomes immediately enforceable as law in all member states simultaneously. Regulations can be distinguished from directives which, at least in principle, need to be transposed into national law. The newly established MDR regulations represent a series of strict rules related to all aspects of production, marketing, approval, post market surveillance and safety of medical devices. They impact both manufacturers and regulatory authorities, such as ***Notified Bodies***. A database called **EUDAMED**, which will be used by manufacturers to submit product specific details of their marketed devices, allows for a transparent information both for the public and the applicants on medical devices, their components, their expiry dates and specific application. A "Unique Device Identifyer (**UDI**)" has to be established, which provides a machine-readable tag for any medical device. Further, experienced laboratories for testing devices prior to approval or supervising clinical trials will be established.

Despite being based on a rather complex document (>170 pages), the new MDR also offers guidelines and advices for all partners of the medical device industry. New requirements for the guarantee of performance and safety of medical devices provide enormous chances and challenges for university graduates and start-up companies, given that they are engaged in device assessment, quality control and documentation.

GENERAL OBSERVATIONS

Marketing of medical devices is only possible, if they have undergone an approval procedure during which their reliability in terms of both *in vitro* and *in vivo* performance and safety has been proven. This is not only valid for Europe, for which harmonized rules have now been established (Fig. 1). Countries like the United States, Japan and China, as well as the majority of worldwide healthcare markets, also require approval procedures for new devices. These procedures are generally supplemented by post market surveillance activities for already marketed products. The premise "*Better safe than sorry!*" imposes responsibilities and quality requirements for both manufacturers and healthcare authorities. It´s worth to note that medicinal products (pharmaceuticals) and medical devices are two different types of products. Consequently, their qualification for approval also follows different regulations.

In recent years, several adverse clinical events observed in specific patient cohorts have been attributed to the lack of quality of medical devices. Controversies arose about underlying causes. At first sight, it was often unclear, whether the selection of inappropriate polymers [2-4], the inadequate performance of clinical trials [5], or an unqualified packaging with an increased amount of extractables could be made responsible [6] for the observed adverse clinical events. During court hearings, scientists with dissenting opinions have often submitted their ratings based on individual observational studies. Interestingly, their analyses could support either side of the forensic parties. Consequently, not only the judge and healthcare authorities had difficulties to draw clear-cut conclusions, even the public was unable to decide in favour or disfavour of such an alleged malfunctioning product. That this observation refers to a long-lasting story, can be exemplarily mentioned by citing the ASAIO Journal from 1995. The authors Price & Gates wrote in their article about "Junk science in the courtroom" [7].

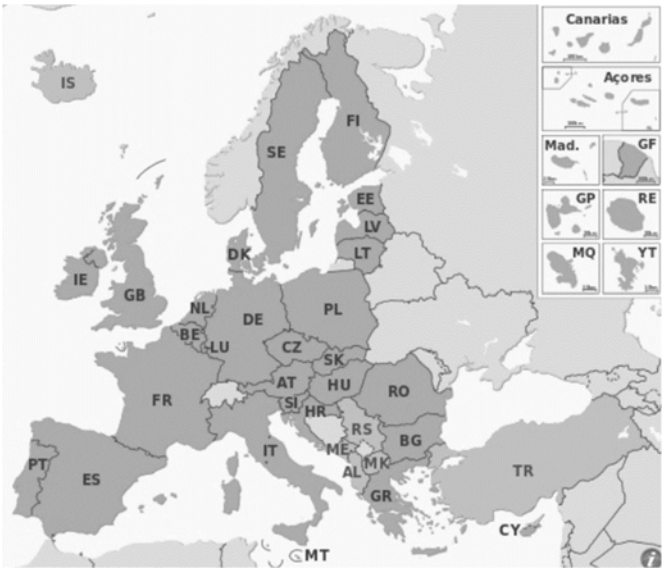

Fig. 1. The intention of the new European Medical Device Regulation is to harmonize its regulations in all European Member and Associated Member States. It is further meant to ensure high level of safety and health for patients and users. It became immediately enforceable as law on May 5, 2017.

Based on such and many other adverse clinical adverse events and in order to avoid further confusions, it is of no surprise, that the European Commission has started a new initiative. Already some years ago, the EU engaged a large number of scientists, manufacturers, avocats and legal authorities with the purpose to redesign its regulations for the approval of medical devices. After a rather long period of consultations and intense discussions, the new European Medical Device Regulation (MDR), has been published in the Official Journal of the European Union on May 5, 2017. This new MDR has been enforced as law in the EU and became effective on May 25, 2017 [1]. The EU MDR is replacing Medical Device Directive (MDD, Council Directive 93/42/EEC) and the Active Implantable Medical Device directive (AIMD, Council directive 90/385/EEC). *In vitro* Diagnostica undergo another new regulation, entitled "*In vitro* diagnostic medical device regulation (IVDR). The intend of the new requirements is respectable, as one of the key objectives of the new EU MDR is to ensure a high level of health and safety protection for EU citizens. Making clinical investigation and evaluation requirements more stringent is aimed at improving health and safety through transparency and traceability.

The new scheme of regulation is described in Fig 2.

Each new medical device, which is intended to be marketed in the European Union has to undergo this regulation starting with July 2017. In contrast, devices, which are already available on the market and bearing a CЄ-mark, profit from a three years transition period until July 2020.

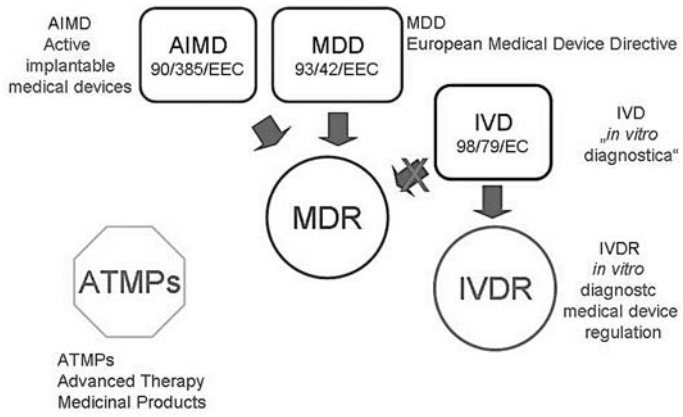

Fig. 2: Structure of the new Medical Device Regulation (MDR). It combines the regulation on active implantable medical devices (AIMD) and the scheme of the former European Medical Device Directive (MDD). *In vitro* diagnostics (IVDR) and Advanced Therapy Medicinal Products (ATMPs) are covered by separate regulations.

Starting with July 2020, all available medical devices have to be assessed under the new MDR rules. They need to receive an updated CЄ-mark for marketing. The time axis until May 2020 is extremely narrow, because companies marketing devices in the EU, have to set up again documentation on already existing medical devices until then. In addition, the documentation of general safety and performance requirements requires knowledgeable experts, both from the approval and the manufacturing point of view. Start-up companies are expected to suffer from this situation, because such experts are currently not part of their staff. They have to hire these experts either as new members of their personal or borrow them from consulting agencies. New documentation also includes clinical data, technical documentation and labelling, which have to be updated. It will, further, be necessary to revisit those device-related processes, that refer to quality assurance, risk management and post-market surveillance. The UK's Medicines and Healthcare Products Regulatory Agency (MHRA) has estimated that more than half a million different devices, which are currently CЄ-marked under the former Medical Device Directive (MDD), must transition to fully comply with the new MDR.

What is the intended general purpose of this new regulation? As stated in Paragraph 1, the new MDR will establish a robust, transparent predictable and sustainable regulatory framework for medical devices, which ensures a high level of safety and health whilst supporting innovation.

Paragraph 2 further elaborates on this statement by saying: The regulation "aims to ensure the smooth functioning of the European internal market, taking as a

base a high level of protection of health for patients and users, and taking into account the small- and medium sized enterprises, that are active in this sector. At the same time this Regulations sets high standards of quality and safety for medical devices in order to meet common safety concerns as regards such products!" [1].

It must, however, be stated that the new MDR does not apply to all types of medical devices. The following products are excluded, because they are covered under separate regulations:

a) *In vitro* diagnostics are covered by the new "*In vitro* diagnostics regulation (IVDR), EU 2017/746 from April 5, 2017 [8].
b) Advanced Therapy Medicinal Products (ATMPs).
   ATMPs also denominated "*combination products"* combine biomaterials and living tissue or cells (e.g., bioreactors) and are not considered to be Medical Devices due to their principal mode of action. ATMPs belong to a class of products which include gene-therapy, somatic cell therapy and tissue-engineering.
   „For such products, whatever the role of the (applied) medical device, the pharmacological, immunological or metabolic action of these cells or tissues should be considered to be the principal mode of action of the combination product and thus, they are qualified as medicinal products (pharmaceuticals) [9]. Such combination products are always regulated under this ATMP Regulation.". These special products which contain both, polymers/scaffolds and biological tissue/cells, called "Combination products", are covered by Regulation EC No 1394 /2007 [9].
c) Human blood, blood products, plasma or blood cells of human origin, or devices, which incorporate such blood products, plasma or cells, when placed on the market or put into service.
d) Cosmetic products are covered by Regulation EC No 1223/2009.
e) Transplants, tissues or cells of human origin or their derivatives are covered by directive 2004/23/EC or products containing or consisting of them.
   However, the new MDR does apply to devices manufactured utilizing derivatives of tissue or cells of human origin which are non-viable or are rendered non-viable (e.g. heart valves from pigs rendered non-viable by fixation with glutardialdehyde).
f) Food covered by Regulation EC No 178/2002

The new MDR comprises a document of 177 pages [1]. As an introduction, 101 paragraphs define the frame of the MDR, they are followed by 10 chapters (Fig. 3) and 17 Annexes. In the following, we will elaborate on some specific details of the 10 chapters. With the information included here young scientists may extract requirements for their possible future professional career.

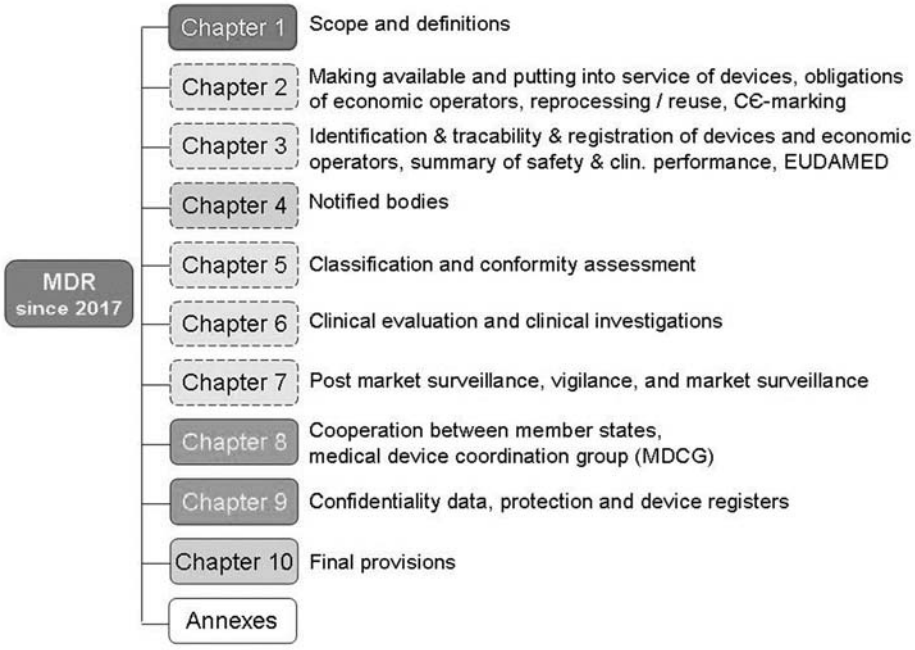

Fig. 3: In addition to 101 introductory paragraphs, 10 chapters of the new MDR describe in detail the requirements which are needed for future marketing of medical devices in the European Union. Dotted lines refer to those chapters, where young graduates might find job offers for new occupational positions.

Chapter 1 refers to definitions as to "What is a medical device and what are the rules for placing it for human use to market?"
According to this definition, a medical device is an instrument, apparatus, appliance, software, implant, reagent, material or other article intended by the manufacturer to be used, alone or in combination, for human beings for one or more of the following specific medical purposes: diagnosis, prevention, monitoring, prediction, prognosis, treatment or alleviation of disease, or compensation for an injury or disability.

Chapter 2 defines rules on how to put medical devices to the market. A medical device can only be marketed in the European Union, if it fully complies with the MDR. It must be duly supplied, properly installed, maintained and used in accordance with its intended purpose. Further, the device has to meet general safety and performance requirements related to its intended purpose. Demonstration of conformity (CE-mark) includes general safety and performance requirements which are based on clinical evaluations.
Manufacturers of medical devices are obliged to document, implement and maintain a system for risk management (Fig. 4) and have available one person responsible for

regulatory compliance with expertise in the field of medical devices. The EU MDR expects risk management and clinical evaluation to be interdependent processes. Clinical risks will have to be addressed in clinical investigations, evaluations and post market clinical follow-up.

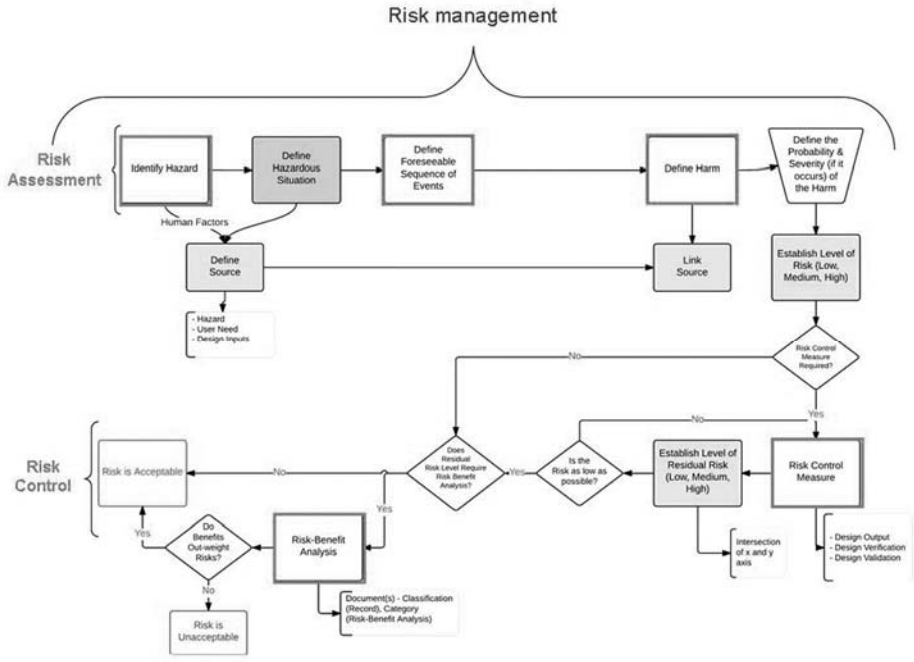

Fig. 4: Manufacturers of medical devices are obliged to document, implement and maintain a system for risk management and have available one person responsible for regulatory compliance with expertise in the field of medical devices.

The expertise of such an employee has to be demonstrated by the qualifications, such as diploma, certificate or other evidence of formal qualification, awarded on completion of a university degree in law, medicine pharmacy, engineering or another relevant scientific discipline. This person should have at least one year of professional experience in regulatory affairs or in quality management systems. Reprocessing of medical devices (re-use) is also covered by chapter 2 and says, that the reprocessor of a single use device is considered to have the role of a manufacturer with all related obligations.

Chapter 3 relates to the individual identification and traceability of medical devices. EUDAMED, the European database on medical devices will become a tool partly accessible by *Notified Bodies*, manufacturers and the public. Up to date, this database was an information repository exclusively accessible to national competent authorities and the European Commission. It had been used by European authorities for post

market surveillance. Under the new regulation, EUDAMED will integrate information regarding devices and the relevant economic operators, Notified Bodies, certificates, clinical investigations, vigilance and market surveillance. The web-based portal EUDAMED is expected to go live on March 25, 2020. An "Unique Device Identification system UDI" other than custom-made and investigational devices will also be made available to allow for the individual identification, labelling and traceability of medical devices.

Chapter 4 describes the role, obligations and responsibilities of *Notified Bodies*.
They have to make available all relevant documentation, including the manufacturers documentation to the authorities to allow it to conduct its assessment for conformity. The list of *Notified Bodies,* entitled NANDO (New Approach Notified and designated Organisations) with a registration number will facilitate the search for these institutions across Europe for manufacturers. NFs have also to establish lists of their standard fees for their conformity assessment activities and to make those lists publicly available.
Notified Bodies will be annually checked by the EU for fulfilling their tasks correctly, whilst the EU in conjunction with the newly established Medical Device Coordination Group (MDCG) may initiate an assessment of competence of individual NFs.

Chapter 5 refers to the classification (risk classes) and conformity assessment (CЄ-marking) of medical devices. The risk classes I, IIa, IIb, III take into account the intended purpose of the device and their inherent risk (for evaluation see also Fig. 4). Manufacturers have to undertake a conformity assessment, i.e. an analysis whether production and marketing of such products is well documented according to the manufacturers previewed conditions of safety, reliability and reproducibility, before placing a product on the market. These documents are also assessed by *Notified Bodies* prior to the provision of the CЄ-mark. If there might be a reasonable concern with regard to such a conformity assessment, the MDCG and the EU Commission may request scientific advice from expert panels in relation to the safety and performance of any device. Some classifications are currently under investigation and may change, such as implants (change from risk class IIb to III) and software (change from risk class I to IIa). Manufacturers of devices from the high-risk class III, other than custom-made or investigational devices, undergo a special conformity assessment which is specified in Annex IX of MDR.

Chapter 6 refers to clinical evaluation and investigation. Manufacturers have to plan, conduct and document its clinical product evaluation and confirm conformity according to general safety and performance requirements. For all class III and for

class IIb devices they may consult an expert panel prior to their clinical evaluation (see Annex XIV). The electronic UDI system will support these endeavours.
The clinical evaluation of a medical device must follow a defined and methodologically sound procedure, which is based on:
- a critical evaluation of the relevant scientific literature
  (all manuscripts independent of whether they are available as pdf-file or not)
- a critical evaluation of the results of other available clinical investigations
- a consideration of currently available alternative treatment options.

Such a clinical evaluation & documentation has to be updated throughout the life-cycle of a medical device, i.e. there is a need of a continuous check of state-of-the-art. Clinical investigations are subject of an authorisation by the EU Member State(s). There must be no objection of an ethics committee in relation to clinical investigations, an informed consent to be written which is dated and signed by the patient and the person performing the interview.

Chapter 7 refers post market surveillance and - vigilance. Manufacturers have to plan, establish, document, implement, maintain and update a post market surveillance system proportionate to the individual risk class and appropriate to the type of the medical device. This system is considered to become an integral part of the manufacturers quality management system. The post market surveillance activity of the manufacturer must be suited in such a way to actively and systematically gather, record and analyse relevant data on the quality, performance and safety of a device throughout its entire life cycle. In case of any adverse event, necessary conclusions have to be drawn and both, preventive and corrective actions to be determined, implemented and monitored. Manufacturers of class IIa, IIb and III devices have to prepare a *Periodic Safety Update Report* (**PSUR**) for each device.

Chapter 8 refers to the Cooperation between EU Member States, Medical Device Coordination Group (**MDCG**, see also above), other Expert Panels and Device Registers. Each EU Member State has to appoint to the MDCG one member and one alternate for a three-year term, each with expertise in the field of medical devices. The MDCG has the following tasks:
- to contribute to the assessment and supervision of applicant *Notified Bodies*
- to advise the Commission in matters concerning the coordination group of NBs
- to contribute to the development of guidance
  and harmonized implementation of MDR
- to contribute to the continuous monitoring of technical progress
- to contribute to the development of device standards

Further a set of *Expert Laboratories* has to be established following a consultation with the MDCG on the basis of their expertise in physico-chemical characterization, microbiology, biocompatibility, mechanical, electrical, electronic or non-clinical biological and toxicological testing of devices.
Expert laboratories have to certify the following criteria:

- have adequate and appropriately qualified staff with adequate knowledge and experience in the field of medical devices for which they are designated.
- possess the necessary equipment to carry out the tasks assigned to them.
- have the necessary knowledge of international standards and best practices
- have an appropriate administrative organization and structure
- ensure that their staff observe the confidentiality of information and data obtained.

Chapters 9 and 10 refer to the maintenance of confidentiality, IP protection and funding, where by chapter 10 refers to general conclusions which are beyond the scope of this short review.

CONCLUSION

The new MDR has been set to improve safety, quality, performance and traceability of medical devices in the EU. A first step will be the establishment of a European Medical Device Data Bank "EUDAMED", the introduction of a "Unique Device Identifyer (UDI) and the need to prepare a *Periodic Safety Update Report* (PSUR). These actions together with a continuous control and assessment of marketed medical devices impose increased responsibilities to manufacturers, Notified Bodies and Administrative Authorities. To support their activities, expert groups will be established, such as the *Medical Device Coordination Group* (MDCG) and *Expert Laboratories* will serve for product characterisation, as well as for supporting documentation of risk and conformity assessment. Further, as each manufacturer has to nominate a "Qualified Person" and a possible Deputy, opens a continuous need for qualified personal in the field of medical devices. Young and qualified graduates will, thus, profit from new job opportunities and occupational careers.

REFERENCES

[1] European Parliament & Council of European Union, Regulation (EU) 2017/745 of the European Parliament and the Council of 5 April 2017 on medical devices, amending Directive 2001/83/EC, Regulation (EC) no 178/2002 and Regulation (EC) No 1223/2009 and repealing Council Directive 90/385/EEC and 93/42/EEC,
Official J European Union, 2017, L117-L175

[2] Oulharj S., Pauchot J., Tropet Y., PIP breast implant removal: a study of 828 cases. J Plast Reconstr Aesthet Surg. 2014, 67:302-307

[3] Lee Y., Song S.E., Yoon E.S., Bae J.W., Jung S.P, Extensive silicone lymphadenopathy after breast implant insertion mimicking malignant lymphadenopathy. Ann Surg Treat Res, 2017 2017, 93:331-335.

[4] Klein D., Hadad E., Wiser I., Wolf O., Itzhaki Shapira O., Fucks S., Heller L., Poly implants prosthèse breast implants: A case series and review of the literature, Ann Plast Surg. 2018. 80:5-9

[5] Steffen J.E., Fassler E, Reardon K.J., Egilman D., Grave fraudulence in medical device research: a narrative review of the PIN seeding study for the Pinnacle hip system. Account Res, 2018, 25: 37–66

[6] Boven K., Stryker S., Knight J., Thomas A., van Regenmortel M., Kemeny D, Power D., Rossert J., The increased incidence of pure red cell aplasia with an Eprex formulation in uncoated rubber stopper syringes, Kidney Int, 2005, 67:2346–2353

[7] Price J. M., Gates G., „Junk Science" in the Courtroom: causes and effects. ASAIO J, 1995, 41:139-142.

[8] European Parliament & Council of European Union, Regulation (EU) 2017/746 of the European Parliament and the Council of 5 April 2017 on in vitro diagnostic medical devices and repealing Directive 98/79/EC and Commission Decision 2010/227/EU. Official J European Union, 2017, L175-L332

[9] European Parliament & Council of European Union, Regulation (EC) No 1394/2007 of the European Parliament and the Council of 13 November 2007 on advanced therapy medicinal products and amending Directive 2001/83/EC and Regulation EC No 726/2004
Official J European Union, 2007, L324/121

Monographic articles

Ceramic membrane foulingin ultrafiltration process of chicken egg white aqueous solution

*Borysiak Martyna, Gabruś Elżbieta
Faculty of Chemical Technology and Engineering, West Pomeranian University of Technology, Szczecin, POLAND
e-mail: borysiak.martyna@zut.edu.pl

Keywords*: ultrafiltration, ceramic membrane, chicken egg white, fouling, membrane transport resistance*

ABSTRACT

This paper presents an experimental study on chicken egg white solution ultrafiltration, where membrane fouling has been the main point of concern. Separation process has been performed with 150 kDa tubular ceramic TiO_2/Al_2O_3 membrane. The operating parameters have been set as follows: transmembrane pressure 105-310 kPa, cross-flow velocity 2.73-4.55 m/s, pH 5 and constant temperature of 293 K. Resistance-in-series model have been used to calculate total resistance and its components. The experimental data have been described with four pore blocking models (complete blocking, intermediate blocking, standard blocking and cake filtration). The results obtained show that the dominant fouling mechanism is represented by cake filtration model.

INTRODUCTION

Separation of macromolecular solutions (e.g. polysaccharides, proteins in water) is broadly realized through low pressure filtration processes. Among them we can distinguish microfiltration (MF) and ultrafiltration (UF). The driving force of these processes is transmembrane pressure. Micro- and ultrafiltration membranes are made from porous materials and separation is realized through sieve mechanism [1]. Microfiltration membranes are symmetric and their pore size is defined by diameter measured in micrometers, while ultrafiltration pores are asymmetric and their size is expressed with molecular weight in Daltons [1].

One of the main problems that occur in membrane processes is membrane fouling, which causes the decrease of permeate flux during filtration. There are several possible mechanisms that may be considered responsible for this phenomenon. Generally, when a solution containing macromolecules enters a membrane unit, the solvent and molecules smaller than the pores pass through, when the molecules equal and bigger than the pores size are stopped. Membrane pores can be blocked in several possible ways according to the appropriate models. The molecules can either block

the pore entrances, get adsorbed on pores surface, limit pores volume or form a cake layer [2, 3]. These mechanisms have been discussed in detail later in the paper.

One of the main areas where ceramic membranes are used is food processing industry. Separation of proteins, polysaccharides etc. from wine [4-6], wastewaters [7, 8], fruit and vegetable juices [9, 10], as well as bovine serum albumin [11-13] has been studied by many authors. Fractionation and purification of chicken egg white components (e.g. ovalbumin, lysozyme) from single and multiple protein solutions (protein in water, fresh chicken egg white, BSA/lysozyme binary solution etc.)has been successfully attempted with membranes made of polymeric materials [11, 14-19, 22], regenerated cellulose [19, 22] and inorganic materials [20].

The aims of this work are: estimating the resistances that occur during chicken egg white ultrafiltration, analysis of fouling mechanisms; identifying the dominant fouling mechanism in ultrafiltration of chicken egg white solution.

MATERIALS AND METHODS

Membrane system

The membrane unit consisted of feed tank, pump, membrane module, rotameter, tubular heat exchanger for stabilizing the temperature, permeate tank, scales and computer. Retentate stream was being recirculated back to the feed tank, while permeate stream was being collected in permeate tank placed on a scales linked to a computer. The scales' readings were saved in DasyLAB software with 15 seconds interval. Experimental setup with membrane unit is shown in Fig. 1.

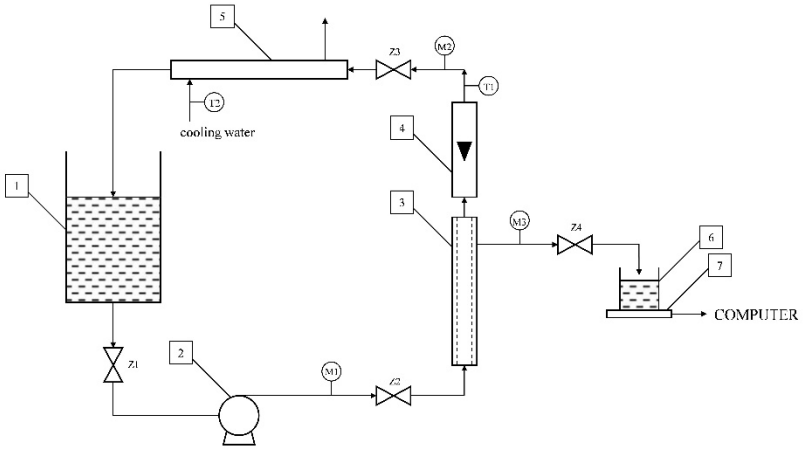

Fig. 1. Experimental setup with membrane unit; 1 – feed solution tank, 2 – pump, 3 – membrane unit, 4 – rotameter, 5 – tubular heat exchanger, 6 – permeate tank, 7 – scales linked to a computer

The experiments were conducted with 3-channel 150 kDa tubular ceramic TiO_2/Al_2O_3 membrane (Tami Industries, France), placed in stainless steel module. Complete characteristic parameters of the membrane have been enclosed in Tab. 1.

Severe fouling formed during ultrafiltration of proteins solutions ought to be removed chemically. Ceramic membranes, which are often used for protein separation, are more resistant to high temperatures and aggressive chemical environment than membranes made of polymeric materials, which is why this type has been chosen for research, despite the higher cost of production [21]. High temperatures resistance also allows steam sterilization, which combined with chemical cleaning regime, can be proven sufficient for biohazardous particles removal.

Tab. 1. Ceramic membrane parameters

Type	clover
Molecular weight cut-off	150 kDa
Separation area	0.009375 m^2
Length	0.25 m
Outer diameter	0.01 m
Single channel hydraulic diameter	0.0036 m
Max. temperature	<150°C
pH range	0-14
Destructive pressure	>9 MPa

Protein solution

The protein used for the experiments has been powdered chicken egg white purchased from Egg Factory "Ovopol" (Poland). Chicken egg white is not a single protein, but consists of a few proteins – the main one is ovalbumin (54-57% [22]) and its physical properties were taken into account. Concentration of solute in feed stream has been set to 0.2 g/L. Physical properties of this protein and its aqueous solution with the given concentration are enclosed in Tab. 2. As pH adjustment factors, 0.1 M NaOH and 0.1 M HCl have been used. Value of pH has been measured with MERA-ELMET N5122 universal pH-meter.

Tab. 2. Chicken egg white aqueous solution properties

molecular weight	45 kDa[22]
isoelectric point	4.5 [22]
concentration	0.2 g/L
diffusion coefficient	$1.18 \cdot 10^{-10}$ m^2/s [22]
density	1001 kg/m^3[23]
dynamic viscosity	$1.12 \cdot 10^{-3}$ Pas [23]
pH	5

Operating parameters of the test runs are enclosed in Tab. 3. All of the measurements have been carried out at temperature of 293 K. Every measurement lasted 80-100 minutes to acquire the pseudo steady-state flux. Each time directly after a single measurement, water permeation measurement was carried out. Then

a chemical cleaning process has been conducted to remove the protein particles remaining on the membrane surface. The cleaning regime consisted of rinsing the membrane system with: distilled water (10 minutes), ~1.7% NaOH solution (10 minutes), distilled water (5 minutes), 2% HNO_3 solution (5 minutes), distilled water (5 minutes), 2% HNO_3 solution (10 minutes), distilled water (10 minutes). After cleaning, water permeation measurements have been performed again. This procedure allowed to assess transport resistances through the membrane.

RESULTS AND DISCUSSION

The test results have been obtained in the form of permeation curves, permeate flux versus filtration time. Based on the experimental data, the transport resistances through the membrane has been determined using the resistance-in-series model and the results have been presented in Tab. 3. Afterwards, the pore blocking models were applied to identify membrane fouling mechanism during chicken egg white ultrafiltration.

Resistance-in-series model

This model is based on Darcy's law, which is an expression of relations between transmembrane pressure, permeate flux and the total hydraulic resistance [24]. Darcy's law has been presented as Eq. (1).

$$J_P = \frac{TMP}{\mu \cdot R_T} = \frac{TMP}{\mu \cdot \left(R_M + R_F + R_{RES}\right)} \tag{1}$$

In Eq. (1) $J_P(m^3/m^2s)$ is the permeate flux, *TMP (Pa)* is the transmembrane pressure, μ *(Pas)* is solution dynamic viscosity. The total hydraulic resistance R_T *(1/m)* is a sum of individual mass transport resistances that occur in membrane filtration, e.g. clean membrane resistance R_M, fouling resistance R_F and residual resistance R_{RES}. The results obtained from experimental data, calculated according to Eq. (1) are shown in Tab. 3. Additionally, the ratio of fouling resistance to total resistance has been calculated. Fouling resistance versus transmembrane pressure and cross-flow velocity is presented in Fig. 2.

The highest fouling resistance have been observed for u=2.73 m/s and TMP=205 kPa, and the lowest for u=4.55 m/s and TMP=110 kPa. The ratio of fouling resistance to total resistance is growing with the decrease of cross-flow velocity.

Tab. 3. Chicken egg white ultrafiltration mass transport resistances

u (m/s)	*TMP* (kPa)	R_T (1/m)	R_M (1/m)	R_F (1/m)	R_{RES} (1/m)	R_F/R_T (-)
2.73	105	8.34E+12	1.36E+12	6.57E+12	4.09E+11	0.788
	205	8.51E+12	1.16E+12	7.28E+12	7.84E+10	0.855
	305	7.60E+12	1.05E+12	6.44E+12	1.08E+11	0.848
3.64	107.5	4.66E+12	1.52E+12	2.94E+12	2.02E+11	0.631
	207.5	5.53E+12	1.11E+12	4.22E+12	2.01E+11	0.763
	307.5	4.77E+12	1.00E+12	3.59E+12	1.72E+11	0.754
4.55	110	2.32E+12	1.33E+12	6.47E+10	9.22E+11	0.279
	210	2.80E+12	1.10E+12	8.56E+11	8.42E+11	0.306
	310	3.11E+12	9.66E+11	1.88E+12	2.64E+11	0.604

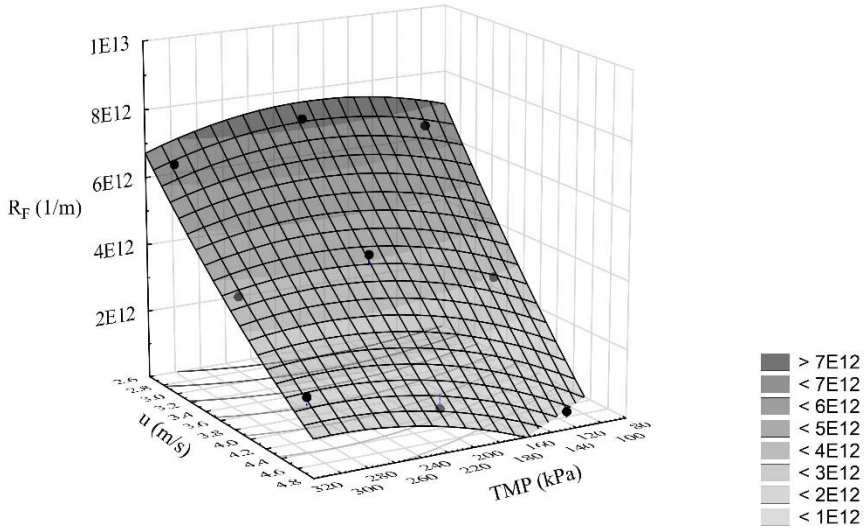

Fig. 2. Fouling resistance R_F versus cross-flow velocity *u* and transmembrane pressure *TMP* with 3D surface approximation

Pore blocking models

Four models of membrane pore blocking during dead-end filtration were developed by Hermia [2] and later adapted to cross-flow filtration by Field et al. [25]. The type of the adequate pore blocking model depends on the value of *n* parameter in general Eq. (2) [2].

$$\frac{d^2t}{dV^2} = K\left(\frac{dt}{dV}\right)^n \tag{2}$$

In Eq. (2) $V\ (m^3)$ is collected permeate volume, $t\ (s)$ is time of permeation, $n\ (-)$ is a specific parameter of pore blocking and K is a constant which unit depends on parameter n. For cross-flow filtration, Eq. (2) was modified into Eq. (3) [3, 25].

$$-\frac{dJ_P}{dt} = K(J_P - J_{Pss})J_P^{2-n} \tag{3}$$

where $J_{Pss}\ (m^3/(m^2s))$ is steady-state permeate flux.

Visual representations of the four models are shown in Fig. 3.

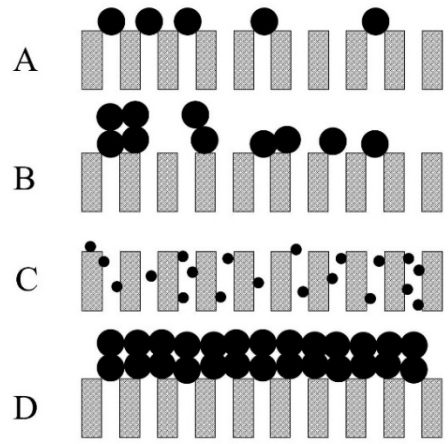

Fig. 3. Pore blocking models: A – complete pore blocking, B – intermediate pore blocking, C – standard pore blocking, D – cake filtration

Pore blocking models have been applied to experimental data using STATISTICA software. For complete and intermediate pore blocking models, cross-flow adaptations have been used. For standard pore blocking model and cake filtration model, classic dead-end filtration models have been used. To acquire the value of pore blocking models parameters K with respective indexes, nonlinear regression model has been used along with Gauss-Newton estimation method, where regression coefficient $R\ (-)$has been calculated. Additionally, average relative error $\delta\ (\%)$ (Eq. (4)) was estimated, and both parameters have been used for rating the quality fit of pore blocking model.

$$\delta = \frac{1}{N}\sum_{i=1}^{N}\left|\frac{J_{P\exp,i} - J_{Pcalc,i}}{J_{P\exp,i}}\right| \cdot 100 \tag{4}$$

In Eq. (4), $J_{Pexp,i}(m^3/(m^2s))$ is experimental permeate flux, $J_{Pcalc,i}(m^3/(m^2s))$ is calculated permeate flux and $N\ (-)$ is the number of runs.

- Complete blocking (n=2)

This model assumes that every particle that goes into the membrane module and reaches membrane surface blocks single pores' entrances completely. One

molecule can block only one pore, and another molecule will not settle on the previous one. Permeate flows only through unaffected pores. This type of blocking happens when the size of membrane pores is smaller than the size of molecules in the solution [3]. The Eq. for the permeate flux as a function of time is as follows:

$$J_P = J_0 \cdot e^{-K_b t} \tag{5}$$

where J_0 $(m^3/(m^2 s))$ stands for initial permeate flux and K_b (m^{-1}) is complete pore blocking parameter. This model was adapted for cross-flow filtration by adding a representation of molecules removal rate from the pore entrances [3].

$$J_P = J_{Pss} + (J_0 - J_{Pss}) e^{-K_b J_0 t} \tag{6}$$

Model parameters and results obtained for complete pore blocking model were presented in Tab. 4.

Tab. 4. Results obtained for complete pore blocking model

u (m/s)	TMP (kPa)	J_0 $(m^3/(m^2 s))$	J_{Pss} $(m^3/(m^2 s))$	K_b (m^{-1})	δ (%)	R (-)
2.73	105	1.41E-05	1.12E-05	18.88	6.46	0.741
	205	4.74E-05	2.15E-05	50.71	4.07	0.937
	305	4.93E-05	3.58E-05	6.19	2.65	0.954
3.64	107.5	2.68E-05	2.06E-05	17.25	4.85	0.865
	207.5	5.70E-05	3.35E-05	8.22	2.83	0.976
	307.5	8.62E-05	5.76E-05	7.10	1.58	0.983
4.55	110	7.18E-05	4.23E-05	4.47	4.87	0.923
	210	8.61E-05	6.71E-05	5.68	3.13	0.930
	310	1.35E-04	8.91E-05	3.50	2.29	0.977

Experimental data for cross-flow velocity 4.55 m/s and different transmembrane pressure values, along with appropriate complete pore blocking fit are visible in Fig. 4.

For complete pore blocking model, R coefficient is over 0.900 in most of the runs. Average relative error is below 5% in eight of nine runs. These values indicate that the model gives a good fit for experimental data, what is also shown in Fig. 4.

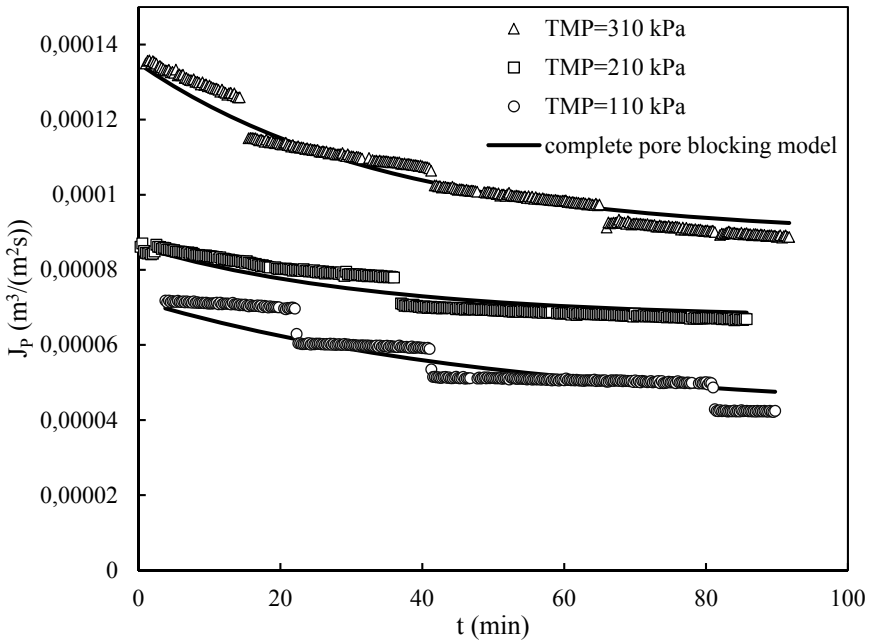

Fig. 4. Experimental data of $J_P=f(t)$ with fitted complete pore blocking model (u=4.55 m/s, TMP=110 kPa; 210 kPa; 310 kPa)

- Intermediate blocking (n=1)

This model assumes that pores are blocked by molecules, but in contrast to complete pore blocking model, other molecules can be deposited on top of the molecules originally blocking the pore entrances. Also, molecules do not necessarily have to block pores landing on membrane surface [3]. For dead-end filtration, intermediate blocking model is defined by Eq. (7).

$$J_P = \frac{1}{\frac{1}{J_0} + K_i t} \tag{7}$$

where K_i (m^{-1}) is intermediate pore blocking model parameter. Cross-flow adaptation of this model is as follows [3]:

$$J_P = \frac{J_0 J_{Pss} e^{K_i J_{Pss} t}}{J_{Pss} + J_0 \left(e^{K_i J_{Pss} t} - 1\right)} \tag{8}$$

The results of intermediate pore blocking model approximation are presented in Tab. 5 and Fig. 5.

Tab. 5. Results obtained for intermediate pore blocking model

u *(m/s)*	*TMP* *(kPa)*	J_0 $(m^3/(m^2s))$	J_{Pss} $(m^3/(m^2s))$	K_i (m^{-1})	δ *(%)*	*R* *(-)*
2.73	105	1.41E-05	1.12E-05	20.05	6.59	0.731
	205	4.74E-05	2.15E-05	67.59	3.12	0.951
	305	4.93E-05	3.58E-05	6.90	2.92	0.944
3.64	107.5	2.68E-05	2.06E-05	18.98	5.10	0.853
	207.5	5.70E-05	3.35E-05	9.98	3.53	0.964
	307.5	8.62E-05	5.76E-05	8.38	1.70	0.984
4.55	110	7.18E-05	4.23E-05	5.22	5.30	0.906
	210	8.61E-05	6.71E-05	6.25	3.35	0.920
	310	1.35E-04	8.91E-05	4.10	2.59	0.968

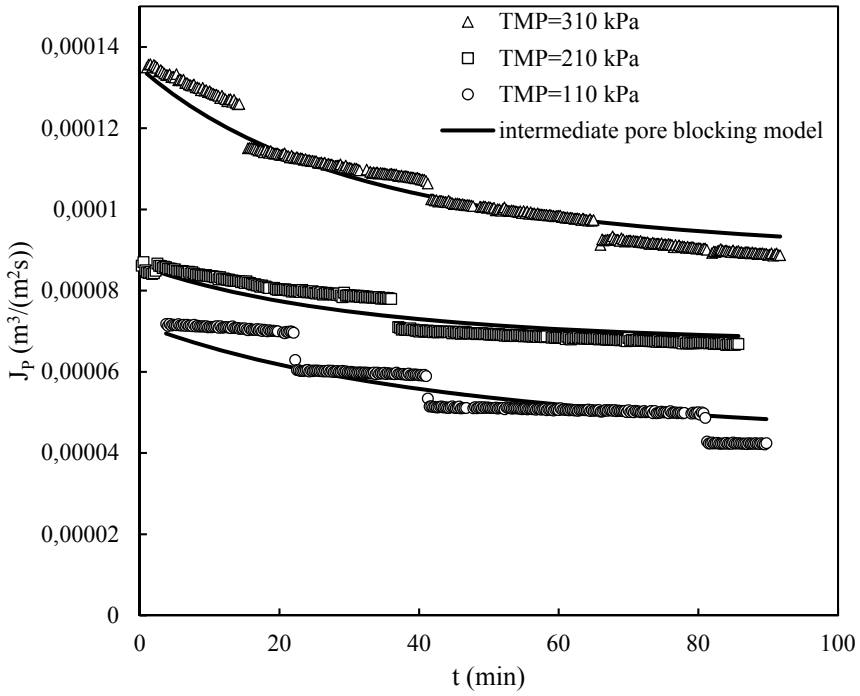

Fig. 5. Experimental data of $J_P=f(t)$ with fitted intermediate pore blocking model (u=4.55 m/s, TMP=110 kPa; 210 kPa; 310 kPa)

Analysis of the results obtained shows that intermediate pore blocking model gives also a good fit to the experimental data. Average relative error is over 5% in the runs where the transmembrane pressure has been in range of 105-110 kPa. Correlation coefficient is below 0.900 only in two runs (u=2.73 m/s, TMP=105 kPa; u=3.64 m/s, TMP=107.5 kPa). Comparing these results with the ones acquired with the use of complete pore blocking model, slightly better approximation was achieved.

Correlation coefficient is higher for complete pore blocking model in 7 of 9 runs, and the standard error is lower in all of the runs but one (u=2.73 m/s, TMP=205 kPa).

- Standard blocking (n=3/2)

Standard pore blocking model assumes that particles settle on pore walls, which causes a decrease in pore volume. Molecules can be either simply deposited on the walls, or adsorbed on their surface. Membrane pores volume is reduced proportionally to the amount of permeate volume [3]. The Eq. for standard blocking model in cross flow filtration is the same as in dead end filtration and presented below [3].

$$J_P = \frac{J_0}{(J_0 + J_0^{1/2} K_s t)^2} \tag{9}$$

In Eq. (9), $K_s(m^{-1/2}s^{-1/2})$is standard pore blocking model parameter.

Results achieved by applying standard pore blocking model to experimental data are enclosed in Tab. 6 and Fig. 6.

Tab. 6. Results obtained for standard pore blocking model

u *(m/s)*	*TMP* *(kPa)*	J_0 $(m^3/(m^2s))$	J_{Pss} $(m^3/(m^2s))$	K_s $(m^{-1/2}s^{-1/2})$	δ *(%)*	*R* *(-)*
2.73	105	1.41E-05	1.12E-05	1.37	96.11	0.000
	205	4.74E-05	2.15E-05	0.98	93.53	0.000
	305	4.93E-05	3.58E-05	0.74	96.50	0.000
3.64	107.5	2.68E-05	2.06E-05	4.39	99.67	0.000
	207.5	5.70E-05	3.35E-05	0.55	94.44	0.000
	307.5	8.62E-05	5.76E-05	2.55	99.02	0.000
4.55	110	7.18E-05	4.23E-05	0.32	91.92	0.000
	210	8.61E-05	6.71E-05	5.38	99.54	0.000
	310	1.35E-04	8.91E-05	0.94	98.00	0.000

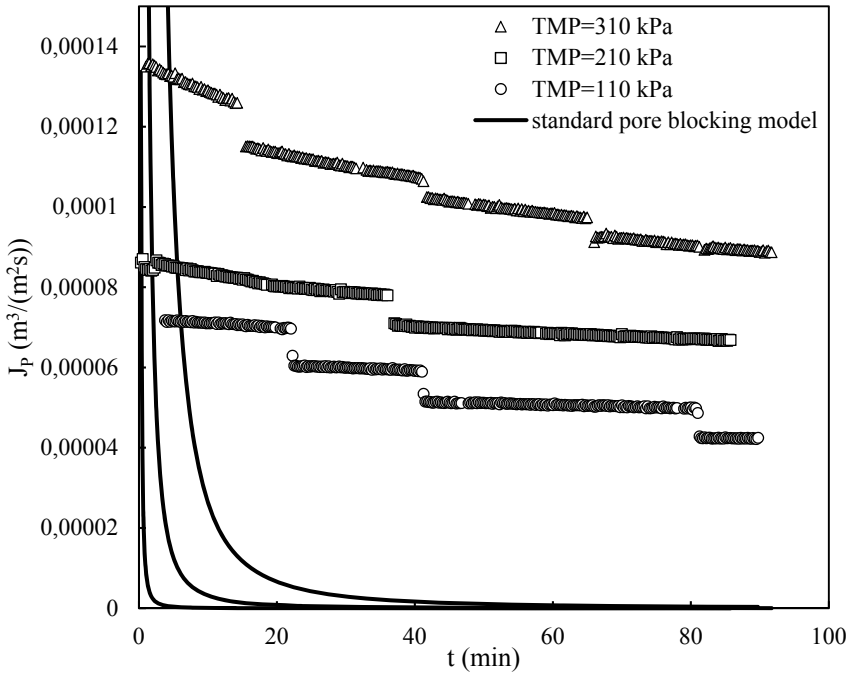

Fig. 6. Experimental data of $J_P=f(t)$ with fitted standard pore blocking model (u=4.55 m/s, TMP=110 kPa; 210 kPa; 310 kPa)

In case of standard pore blocking model, the correlation coefficient is equal to zero in every run and the average relative error is over 90% in all of the runs. Graphic representation of this model also shows that this model is not suitable for the experimental data achieved during ultrafiltration of chicken egg white.

- Cake filtration (n=0)

Molecules of solute bigger than pore entrance size aggregate and create a layer that blocks the flow completely. The cake layer gets thicker over time [3]. In dead-end filtration, cake filtration model is represented by Eq. (10) [3].

$$J_P = \frac{J_0}{\left(1 + 2K_c J_0^2 t\right)^{1/2}} \tag{10}$$

where $K_c(m^{-1})$ is cake filtration model parameter. In ultrafiltration process, cake filtration does not occur in the same way as in microfiltration. The particles are smaller and they do not enter the membrane pores, but form a gel layer over the membrane surface instead. For UF this model is called the gel layer formation and for cross-flow technique Eq. (11) was formed [3, 25].

$$t = \frac{1}{K_g J_{Pss}^{\ 2}} \ln\left[\left(\frac{J_P}{J_0}\frac{J_0 - J_{Pss}}{J_P - J_{Pss}}\right) - J_{Pss}\left(\frac{1}{J_P} - \frac{1}{J_0}\right)\right] \qquad (11)$$

Gel layer formation model presented in Eq. (11) resulted with no fitting at all, and for that reason the classic cake filtration model for dead-end process have been used. The results achieved by the use of this model are presented in Tab. 7.

Tab. 7. Results obtained for cake filtration model

u *(m/s)*	*TMP* *(kPa)*	J_0 $(m^3/(m^2s))$	J_{Pss} $(m^3/(m^2s))$	K_c (m^{-1})	δ *(%)*	*R* *(-)*
2.73	105	1.41E-05	1.12E-05	234850.45	5.55	0.788
	205	4.74E-05	2.15E-05	412417.05	12.10	0.581
	305	4.93E-05	3.58E-05	27949.31	1.48	0.984
3.64	107.5	2.68E-05	2.06E-05	108905.20	3.80	0.905
	207.5	5.70E-05	3.35E-05	55887.81	1.96	0.987
	307.5	8.62E-05	5.76E-05	19536.36	3.20	0.934
4.55	110	7.18E-05	4.23E-05	25640.75	4.70	0.931
	210	8.61E-05	6.71E-05	10124.25	2.17	0.960
	310	1.35E-04	8.91E-05	7180.30	1.62	0.987

In case of cake filtration model, correlation coefficient is below 0.900 in only two runs. Average relative error is over 5% also in two runs. Comparison of results achieved in complete pore blocking model and in cake filtration model has shown that cake filtration model has given a better fit than complete pore blocking model in most of the runs. Graphic representation of the obtained model fits have been presented in Fig. 7.

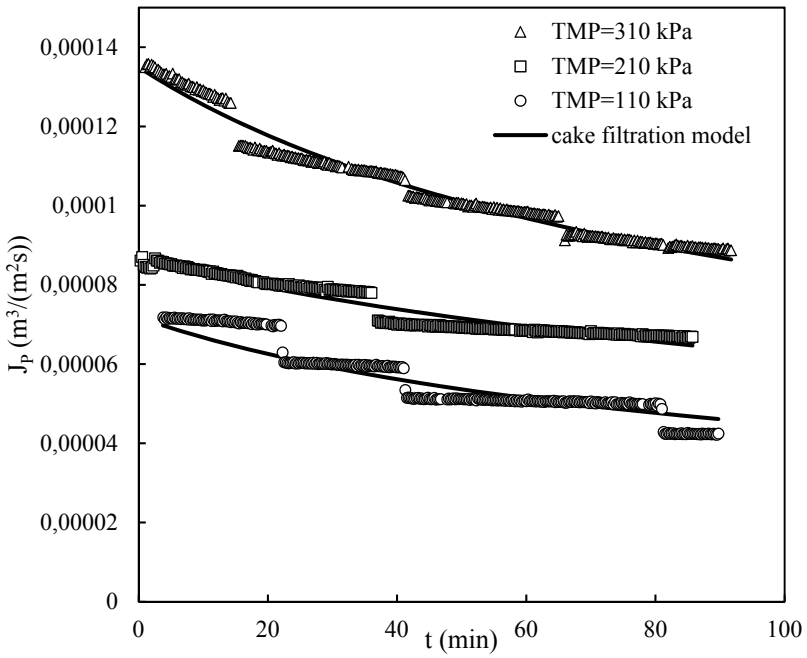

Fig. 7. Experimental data of $J_P=f(t)$ with fitted cake filtration model (u=4.55 m/s, TMP=110 kPa; 210 kPa; 310 kPa)

CONCLUSIONS

During ultrafiltration of chicken egg white solution, permeate flux decline in time has been observed. The reason for this phenomenon is membrane fouling – in general, particles of solute remaining on membrane surface. Fouling causes additional transport resistance in the filtration process. Total resistance and its components (fouling resistance, clean membrane resistance and residual resistance) were calculated using resistance-in-series model. The highest values of fouling resistance has been observed with the lowest value of cross-flow velocity (u=2.73 m/s). Maximum fouling resistance has been noted with the middle value of transmembrane pressure (u=2.73 m/s, TMP=205 kPa).The lowest values of fouling resistance has been achieved with the highest value of cross-flow velocity (u=4.55 m/s). Minimum fouling resistance has been noted with the lowest value of transmembrane pressure (u=4.55 m/s, TMP=110 kPa).

Particles can reside on the membrane surface in many different ways. Four pore blocking models (complete pore blocking model, intermediate pore blocking model, standard pore blocking model and cake filtration model) have been fitted to the experimental data and an identification of the fouling mechanism was attempted. The analysis of the achieved results indicate that in most of the runs, cake filtration model has resulted with the best fit to the experimental data, so this mechanism of pore blocking is the dominant one. Complete and intermediate pore

blocking models have also given a good fit to the experimental data, so it may imply that these pore blocking mechanism also occur in the process but not as intensively as cake filtration mechanism. Standard pore blocking has not given satisfying results, so it either is nonexistent or occurs in a very limited amount. The results obtained in the study indicate that the pore blocking mechanism in the process of chicken egg white protein ultrafiltration is a complex one.

REFERENCES

[1] Bodzek M., Bohdziewicz J., Konieczny K., Techniki membranowe w ochronie środowiska, *Wydawnictwo Politechniki Śląskiej*, 1997

[2] Hermia J., Blocking Filtration. Application to Non-Newtonian Fluids, in: A. Rushton (Ed.), *Mathematical Models and Design Methods in Solid-Liquid Separation*, Springer Netherlands, 1985, 83-89, DOI: 10.1007/978-94-009-5091-7_5

[3] Vincent Vela M.C., Álvarez Blanco S., Lora García J., Bergantiños Rodríguez E., Analysis of membrane pore blocking models adapted to crossflow ultrafiltration in the ultrafiltration of PEG, Chemical Engineering Journal, 2009, 149, 1, 232-241, DOI: 10.1016/j.cej.2008.10.027

[4] Li M., Zhao Y., Zhou S., Xing W., Clarification of raw rice wine by ceramic microfiltration membranes and membrane fouling analysis, *Desalination,* 2010, 256, 1, 166-173, DOI: 10.1016/j.desal.2010.01.018

[5] Rayess Y.E., Albasi C., Bacchin P., Taillandier P., Mietton-Peuchot M., Devatine A., Cross-flow microfiltration of wine: Effect of colloids on critical fouling conditions, *Journal of Membrane Science*,2011, 385-386, 177-186, DOI: 10.1016/j.memsci.2011.09.037

[6] Youravong W., Li Z., Laorko A., Influence of gas sparging on clarification of pineapple wine by microfiltration, *Journal of Food Engineering*,2010, 96, 3, 427-432, DOI: 10.1016/j.jfoodeng.2009.08.021

[7] Yin N., Zhong Z., Xing W., Ceramic membrane fouling and cleaning in ultrafiltration of desulfurization wastewater, *Desalination*,2013, 319, 92-98, DOI: 10.1016/j.desal.2013.03.028

[8] Agana B.A., Reeve D., Orbell J.D., Performance optimization of a 5nm TiO_2 ceramic membrane with respect to beverage production wastewater, *Desalination*,2013, 311, 162-172, DOI: 10.1016/j.desal.2012.11.027

[9] de Barros S.T.D., Andrade C.M.G., Mendes E.S., Peres L., Study of fouling mechanism in pineapple juice clarification by ultrafiltration, *Journal of Membrane Science*, 2003, 215, 1, 213-224, DOI: 10.1016/S0376-7388(02)00615-4

[10] Almandoz C., Pagliero C., Ochoa A., Marchese J., Corn syrup clarification by microfiltration with ceramic membranes, *Journal of Membrane Science*,

2010, 363, 1, 87-95, DOI: 10.1016/j.memsci.2010.07.017
[11] Muca R., Piątkowski W., Antos D., A shortcut method for evaluation of protein deposition onto the membrane surface in crossflow ultrafiltration, *Engineering in Life* Sciences, 2017, 17, 4, 370-381, DOI: 10.1002/elsc.201500159
[12] Prádanos P., Hernández A., Calvo J.I., Tejerina F., Mechanisms of protein fouling in cross-flow UF through an asymmetric inorganic membrane, *Journal of Membrane* Science, 1996, 114, 1, 115-126, DOI: 10.1016/0376-7388(95)00324-X
[13] Huisman I.H., Prádanos P., Hernández A., The effect of protein–protein and protein–membrane interactions on membrane fouling in ultrafiltration, *Journal of Membrane Science*, 2000, 179, 1, 79-90, DOI: 10.1016/S0376-7388(00)00501-9
[14] Tung K.-L., Hu C.-C., Li C.-L., Chuang C.-J., Investigating protein crossflow ultrafiltration mechanisms using interfacial phenomena, Journal of the Chinese Institute of Chemical Engineers, 2007, 38, 3-4, 303-311, DOI: 10.1016/j.jcice.2007.01.005
[15] Lu J., Wan Y., Cui Z., Strategy to separate lysozyme and ovalbumin from CEW using UF, Desalination, 2006, 200, 1-3, 477-479, DOI: 10.1016/j.desal.2006.03.402
[16] Jana S., Purkait M. K., Mohanty K., Clay supported polyvinyl acetate coated composite membrane by modified dip coating method: Application for the purification of lysozyme from chicken egg white, Journal of Membrane Science, 2011, 382, 1-2, 243-251, DOI: 10.1016/j.memsci.2011.08.011
[17] Ghosh R., Cui Z. F., Fractionation of BSA and lysozyme using ultrafiltration: effect of pH and membrane pretreatment, Journal of Membrane Science, 1998, 139, 1, 17-28, DOI: 10.1016/S0376-7388(97)00236-6
[18] Ehsani N., Parkkinen S., Nyström M., Fractionation of natural and model egg-white protein solutions with modified and unmodified polysulfone UF membranes, Journal of Membrane Science, 1997, 123, 1, 105-119, DOI: 10.1016/S0376-7388(96)00207-4
[19] Lu J., Wan Y., Cui Z., Fractionation of Lysozyme and Chicken Egg Albumin Using Ultrafiltration with 30-kDa Commercial Membranes, Industrial & Engineering Chemistry Research, 2005, 44, 20, 7610-7616, DOI: 10.1021/ie049042c
[20] Matsumoto Y., Ito N., Inui T., Characteristics of ovalbumin gel layer formed on ceramic microfiltration membranes, Journal of Chemical Engineering of Japan, 1996, 29, 6, 933-938, DOI: 10.1252/jcej.29.933
[21] Pabby A.K., Rizvi S.S.H., Requena A.M.S., Handbook of Membrane Separations: Chemical, Pharmaceutical, Food, and Biotechnological

Applications, Taylor & Francis, 2008
[22] Wan Y., Lu J., Cui Z., Separation of lysozyme from chicken egg white using ultrafiltration, *Separation and Purification Technology*, 2006, 48, 2, 133-142, DOI: 10.1016/j.seppur.2005.07.003
[23] Gabruś E., Wybrane metody adsorpcyjno-membranowe w inżynierii procesowej, *BEL Studio*, 2016
[24] Bader M.S.H., Veenstra J.N., Analysis of concentration polarization phenomenon in ultrafiltration under turbulent flow conditions, *Journal of Membrane Science*, 1996, 114, 2, 139-148, DOI: 10.1016/0376-7388(95)00136-0
[25] Field R.W., Wu D., Howell J.A., Gupta B.B., Critical flux concept for microfiltration fouling, *Journal of Membrane Science*, 1995, 100, 3, 259-272, DOI: 10.1016/0376-7388(94)00265-Z

Wettability of plasma-activated glass plates with deposited 3-bromopyruvic acid

*Michał Chodkowski[1], Magdalena Szaniawska[2], Anna Taraba[2]
[1]Department for the Modelling of Physico-Chemical Processes, Maria Curie-Sklodowska University, Lublin, POLAND
[2]Department of Interfacial Phenomena, Maria Curie-Sklodowska University, Lublin, POLAND
e-mail: michal@chodkowski.eu

***Keywords**: plasma, surface properties, 3-bromopyruvate, contact angle*

ABSTRACT

3-bromopyruvic acid ($C_3H_3BrO_3$, 3BrPA, 3-bromopyruvate) is the brominated derivative of pyruvic acid. There have been several reports of the use 3-bromopyruvate in the anticancer therapy. Surface properties of various materials can be modified using the plasma technique which nowadays is one of the most popular techniques. One of the consequences of this type of modification is a change in the material wettability. The aim of the study was a determination of surface properties of 3-bromopyruvic acid deposited on glass. The substrate was activated by air, nitrogen and argon plasma before deposition of 3BrPA. Contact angle measurements by the sessile droplet method were made in order to examine wettability of obtained surfaces. It was found that surface properties of substrates depending on the type of plasma. Wettability of surfaces was changed after plasma modifications.

INTRODUCTION

Contact angle

The measurements of contact angle are based on visual measurements of the wetting process occurring on the surface of a solid (or other liquid). It is defined as the angle (θ), which is formed at the three-phase contact point (*P*) between the surface of the wetted substrate and the tangent to the surface of the droplet (Fig. 1).

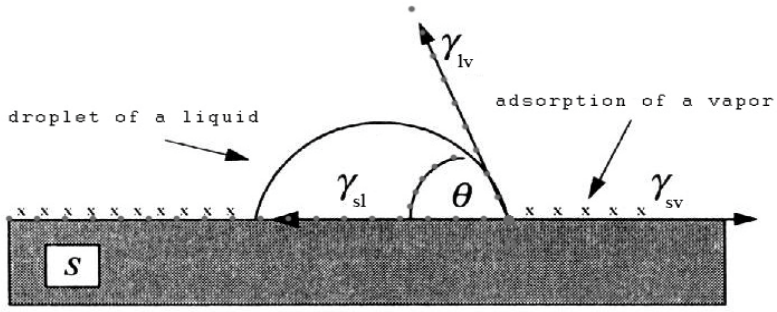

Fig. 1. Schematic representation of the principal of the contact angle measurement [1].

The contact angle depends on three parameters: the surface tension of the wetting liquid, the free surface energy of the wetted solid, the solid-liquid interfacial tension. The equation describing the balance of forces operating at the point of three-phase contact was proposed in 1805 by Thomas Young:

$$\gamma_{sv} - \gamma_{sl} - \gamma_{lv}\cos(\theta) = 0 \tag{1}$$

where: γ_{sv}– the free surface energy of the wetted surface being in equilibrium with the saturated vapor of the liquid, γ_{sl}– interfacial solid-liquid tension, γ_{lv}– the surface tension of the wetting liquid under saturated vapor conditions, θ– is the equilibrium contact angle.

It is also worth mentioning that the Young equation is fulfilled only in ideal systems. The value of the contact angle, which will be obtained in this case, is an equilibrium value. In real systems, due to the lack of saturated steam conditions and the phenomenon of liquid adhesion on the wetted surface, the Young equation does not allow to calculate the equilibrium value of the contact angle. For the above reasons, the modified Young equation is used in practice:

$$\gamma_s = \gamma_{sl} + \gamma_l\cos(\theta) \tag{2}$$

where: γ_s– the free surface energy of the wetted substrate measured under vacuum conditions, γ_l– surface tension of the wetting liquid.

The work of adhesion (spreading) can be calculated using the following equation:

$$W_{adh} = \gamma_s + \gamma_l - \gamma_{sl} = S \tag{3}$$

and it is equal to the spread factor S. Both of these parameters are a measure of the surface wettability. When $S>0$, the liquid completely wet the surface; when $S<0$, then partial wetting occurs.

By combining equations (2) and (3), we obtain the Young-Dupré equation, which make calculation of the wetting liquid adhesion possible, given only the contact angle and the surface tension of this liquid:

$$W_{adh} = \gamma_l(\cos(\theta) - 1) \tag{4}$$

The wetted body need not always be solid because a liquid having a lower surface tension can spill over the surface of the liquid having a higher surface tension; however, the opposite is not possible. Characteristics of wettability of solids with various liquids are very important for many industrial processes such as catalysis, flotation, protective coatings, lubrication, gluing and printing.

Contact angle hysteresis

The contact angle depends on the properties of the wetted surface such as roughness, irregularity, heterogeneity or the presence of other adsorbed components

on the surface [2]. In the case of drop movement across the surface, two different values of the contact angle can be measured: advancing contact angle (θ_{adv}) and receding contact angle (θ_{rec}). The values of advancing contact angle will be always bigger than the values of receding contact angle. This effect is called hysteresis of the contact angle.

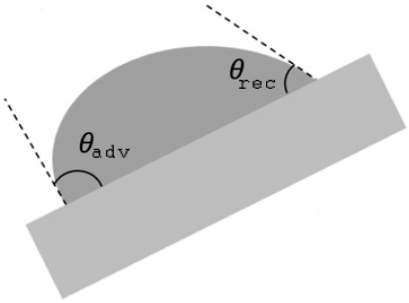

Fig. 2. Contact angle hysteresis when a drop of liquid moves.

Chibowski and Tadmor showed that the contact angle hysteresis occurs on each real surface [3] [4], and the equilateral contact angle is between the value of the advancing contact angle and the receding contact angle. The equation, which allows to calculate it, has been proposed by Tadmor [2]:

$$\theta_{eq} = \arccos\left(\frac{r_{rec}\cos\theta + r_{adv}\cos\theta_{adv}}{r_{rec} + r_{adv}}\right) \tag{5}$$

where the r_{adv} and r_{rec} are equal:

$$r_{adv} = \left(\frac{\sin^3\theta_{adv}}{2 - 3\cos\theta_{adv} + \cos^3\theta_{adv}}\right)^{1/3} \tag{6}$$

$$r_{rec} = \left(\frac{\sin^3\theta_{rec}}{2 - 3\cos\theta_{rec} + \cos^3\theta_{rec}}\right)^{1/3} \tag{7}$$

The contact angle hysteresis can be also observed during the reduction of the volume of a drop, which doesn`t move on a wetted surface.

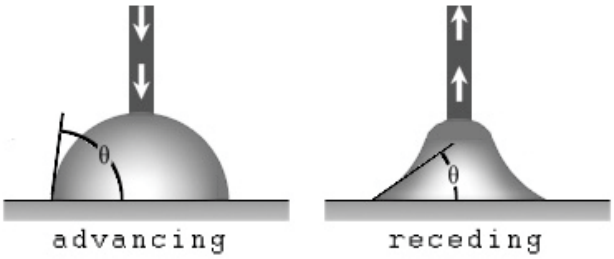

Fig. 3. Contact angle hysteresis when the volume of the drop is changed [5].

The occurrence of hysteresis of the contact angle can be explained by means of two groups of phenomena: dynamic and thermodynamics. Dynamic phenomena include liquid-surface interaction, particle rearrangement or liquid penetration into pores; they depend on the time of observation. Thermodynamic phenomena, on the other hand, are caused by inhomogeneity of the surface and give the possibility of finding drops in various metastable states to which different contact angles are assigned.

Contact angle measurements

The three main groups of measuring methods of the contact angle are:

- sessile drop technique,
- captive bubble method,
- Wilhelmy'splate method.

Wilhelmy'splate method based on a perpendicular immersion of the sample (usually in the form of a thin plate) in the measuring liquid and then its emersion. The sample is hung on the arm connected to the force measuring system. Having the given dimensions of the plate and its depth of immersion, as well as the density and surface tension of the tested liquid, you can calculate the advancing and receding contact angle.

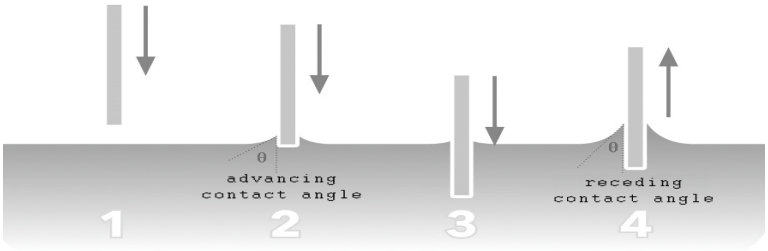

Fig. 4. Schematic representation of the contact angle measurement using the Wilhelmy's plate method [6].

The captive bubble method consists in immersing the test plate in the measuring liquid in such a way that its plane is perpendicular to the buoyancy force. Under the bottom plane of the plate, a bubble of air is introduced using a micro-syringe and its contact angle is determined by the bubble shape. The main disadvantage of the method is the lack of the possibility to test the hysteresis of the contact angle (the impossibility of measuring the advancing and receding contact angle), however, there is no error in the angle measurement caused by the forces of gravity.

The sessile (embedded) drop technique is most often used in laboratory practice. It is based on the analysis of the drop shape of the measuring liquid deposited

on the tested surface using a goniometer or, more and more often, using a computer program.

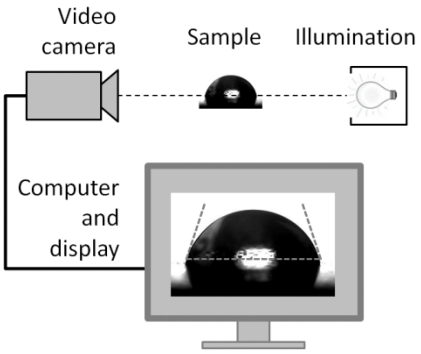

Fig. 5. Diagram of the measuring system for testing the contact angle with the sessile drop technique [7].

During the measurements, it is necessary to ensure the conditions in which the Young equation is best fulfilled:

- the highest homogeneity of the tested surface – it should be as homogeneous as possible and properly prepared (cleaned and degreased),
- the fixed temperature of measurement,
- conditions of saturated vapor of the tested liquid – preferred use of special measuring chambers,
- and as small droplets as possible – this minimizes the gravitational forces that cause spreading of the droplets,
- the shortest measurement time – eliminates the effects associated with evaporation of drops, as well as the action of gravitational forces.

Wetting phase transition

The temperature of the system is one of the factors determining the wetting process. With its increase, the contact angle decreases so that after exceeding a certain temperature T_w the surface is completely wetted. Then the phase transition of wetting takes place, and the liquid layer on the surface reaches the macroscopic thickness.

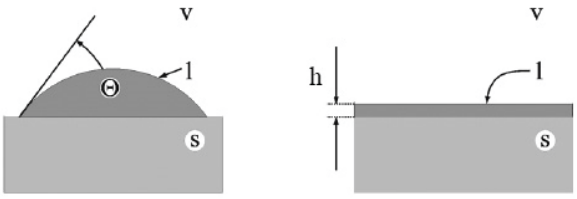

Fig. 6. Wetting transition.

The transition between the states shown in Figure 6 can be carried out in two ways – first or second order wetting phase transitionis possible. The tendency of the wetting phase transition can be determined by analyzing the dependence of course of cosine contact angle on temperature. The linear course of dependence near the wetting temperature determines the first order phase transition, otherwise, it will be the second order phase transition.

Plasma – the fourth state of matter

Plasma is often called the fourth state of matter, next to gas, liquid and solid. It is a separate state of matter resembling gas. However, it has definitely different physical and chemical properties. Plasma contains a significant portion of the particles that are electrically charged. Nevertheless, it is electrically neutral at the macroscopic scale. This is due to the anisotropic nature of the plasma [8].

The state of matter depends on the energy of binding which occurs between its particles. The change in the state of aggregation occurs as a result of heating the substance, i.e. providing kinetic energy to individual atoms. Supplying solid energy from the outside causes breaking of different types of bonds. This results in the transition from a solid state to a liquid state, then a gaseous state to a plasma state. The moment separating the gas and plasma state is the moment of changing the physical properties of the gas, including the appearance of electrical conductivity and the accompanying isolation. The natural occurrence of plasma in terrestrial conditions is relatively rare. The thick gas coating of the Earth's atmosphere absorbs a significant portion of the ionizing radiation. The Earth has, like other celestial bodies with a gas atmosphere, an external ionized (plasma) coating called the ionosphere. The only natural sources of plasma formation are the atmosphere discharges [9].

Plasma modification

Plasma modification involves the treatment of the top layer of existing material with plasma. The aim of this action is to obtain appropriate surface properties, such as surface energy, mechanical strength, durability, adhesion, friction, surface conductivity or biocompatibility [8]. During the modification, the surface undergoes purification, activation, etching, and coating. Very often plasma surface modification is the initial stage of various processes: printing, dyeing, gluing, laminating or metalizing. Plasma modification is a very complicated process, the mechanism of which has not been fully understood yet. The plasma structure of deposited layers is highly complex and depends on many parameters, such as reactor design, power level, frequency, substrate temperature, monomer structure, monomer pressure and monomer flow rate.

Plasma generators can operate at different plasma frequencies. Plasma frequency determines how the plasma ions behave. When plasma systems run

on a lower plasma frequency they create longer wavelengths which give ions a large amount of kinetic energy. With a lower plasma frequency, there is a higher ion density. This means there will be more plasma particles per unit of area. With a higher plasma frequency, there is a shorter wavelength which results in faster etching but it requires more energy to operate.

There are three frequencies most commonly used in plasma technology systems. They are respectively 40 kHz, 13.56 MHz, and 2.45 GHz. The 40 kHz plasma frequency is commonly used for plasma cleaning or desmearing; it can be used as well as for etching, but it takes longer time.

MATERIALS AND METHODS

The aim of the experiment was a determination of surface properties of 3-bromopyruvic acid (3BrPA) deposited on glass plates modified by plasma. Surface treatment was preceded by purification by rinsing with acetone. A low-temperature plasma generator from Diener Electronic was used to modify the tested surfaces. Samples were subjected to modification with plasma under vacuum conditions, generated by using of 40 kHz alternating current electrodes and 1000W power.

The substrates were activated by air, nitrogen and argon plasma during the 60s before deposition of 3-bromopyruvic acid. Layers of the acid on examined surfaces were obtained by deposition of 3% solution of the 3-bromopyruvate in water followed by evaporation. Diiodomethane and glycerol contact angle measurements by the sessile droplet method were made in order to examine wettability of obtained surfaces. Measurements were made using the *Digidrop*goniometer of the French company GBX for this purpose. The device has a thermostated, closed measuring chamber so that it is possible to carry out measurements in conditions of controlled temperature and humidity, as well as saturated steam produced by the use of a special attachment (also produced by the French company GBX).

The advancing and the receding contact angle of diiodomethane and glycerol were measured at 25°C as follows: 6µl droplet was settled on the examined surface and advancing contact angle was measured, then 2µl of tested liquid was sucked from the droplet into the syringe and receding contact angle was measured. Then the equilibrium contact angle was calculated using the Tadmor's approach [2] and surface free energy was calculated using the CAH (contact angle hysteresis) approach proposed by Chibowski[10, 11, 12, 13, 14].

Selection of the measuring liquids (diiodomethane and glycerol) was caused by the fact that they do not interact with the layer of the 3-bromopyruvic acid.

RESULTS AND DISCUSSION

Contact angle measurements

Modification of individual surfaces of various types with plasma resulted in diversification of the contact angle of diiodomethane and glycerol compared to the unmodified sample.

The equilibrium contact angle calculated from measurements with diiodomethane slightly decreased after plasma treatment, regardless of its type (Fig. 7). Such a small change can be explained by the fact of introducing polar groups into the modified surface; diiodomethane, as a non-polar liquid, interacts with the introduced groups to a small extent. The hysteresis of the contact angle is practically constant on each surface (Fig. 9 and 10). This indicates a similar degree of heterogeneity of each of them in terms of non-polar interactions with the measuring liquid.

In the case of the use of glycerol as a measuring liquid, the surface modification effect became much better. The equilibrium contact angle decreased; the smallest values were obtained in the case of surface treatment with air and nitrogen plasma (Fig. 10). This observation confirms the introduction to modified surfaces of polar groups; they interact more strongly with the polar measuring liquid (glycerol), which better wets the surface.

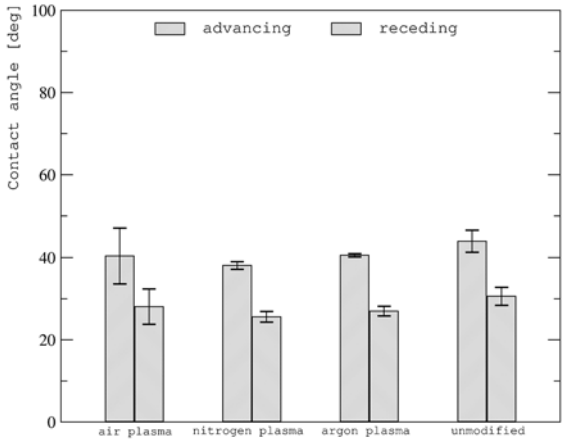

Fig. 7. Advancing and receding contact angles of diiodomethane on the glass plates.

Also noteworthy is the fact that there is a large relative error (significant error bars) for measuring of the surface wetness modified with air plasma. This effect is independent of the measuring liquid used. It can be explained by the fact that the air plasma is a mixture of different gases. During surface modification such an ionized mixture its structure becomes considerably heterogeneous. Thus, the value of the contact angle will strongly depend on the part of the surface on which the drop of the measuring liquid will be placed. Moreover, the measurements were done for samples after deposition of 3BrPA so it would be possible that the coating is less uniform.

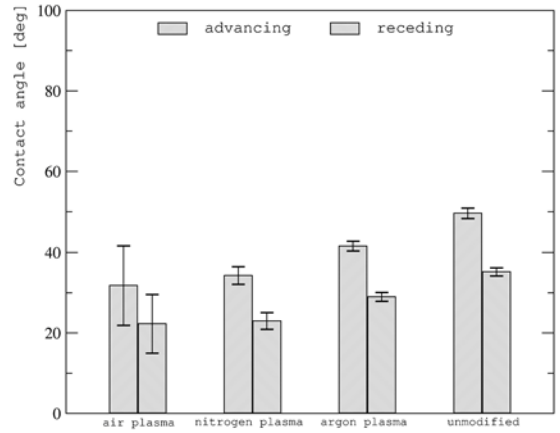

Fig. 8. Advancing and receding contact angles of glycerol on the glass plates.

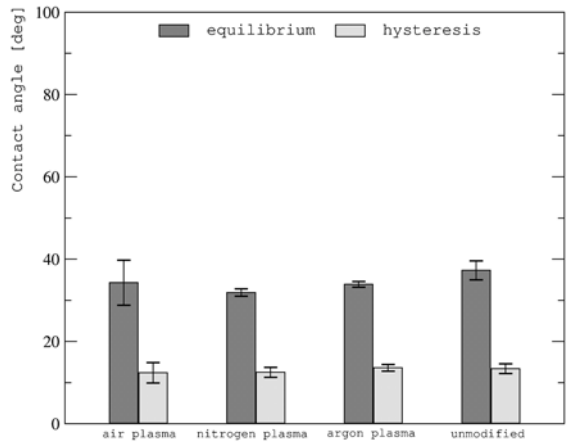

Fig. 9. Equilibrium contact angles of diiodomethane on each glass surfaces and hysteresis of the contact angle.

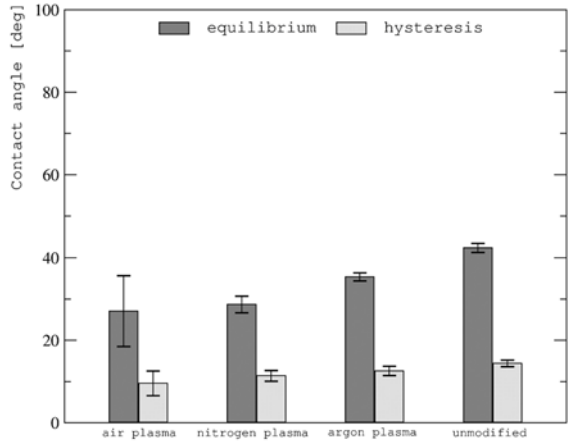

Fig. 10. Equilibrium contact angles of glycerol on each glass surfaces and hysteresis of the contact angle.

Surface free energy (CAH approach)

The value of free surface energy changed after the plasma modification. Slight changes, without a clear trend, can be observed in the case of the diiodomethane test. Taking into the consideration the results obtained with the use of glycerol, the surface modification increases free surface energy, regardless of the type of plasma used. The largest changes in surface properties can be observed after the modification of the plate with air and nitrogen plasma.

When carrying out the above analyzes, it should be borne in mind that the free surface energy calculated with the approach using the contact angle hysteresis depends partly on the physicochemical properties of the used measuring liquid. When comparing the values calculated for different surfaces, it should be remembered that these must be the results obtained with the help of identical measuring liquids. To avoid this inconvenience, one can calculate the average energy value using the contact angle hysteresis of several different liquids, e.g. water, formamide and diiodomethane. It should be remembered that using this approach to the calculation of free surface energy, you get an apparent energy value, some of which depends on the measuring liquid used.

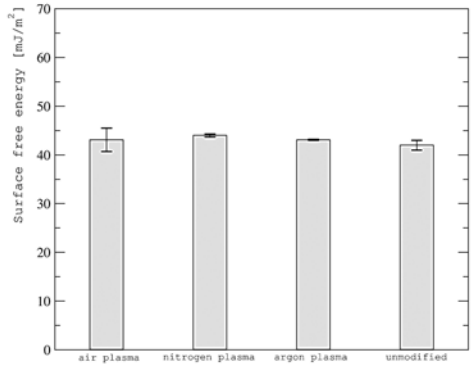

Fig. 11. The surface free energy of such glass surfaces measured by means of diiodomethane.

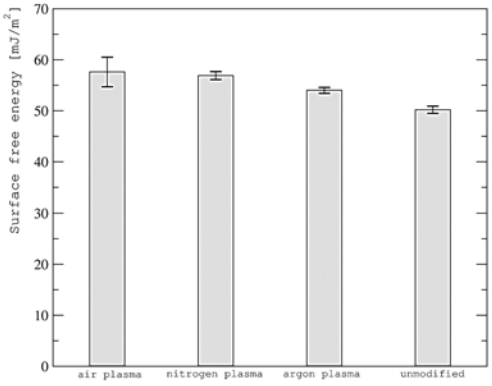

Fig. 12. The surface free energy of each glass surfaces measured with glycerol.

SUMMARY

Plasma modification is a very complicated process, the mechanism of which has not been fully understood yet. Plasma modification involves the treatment of the top layer of existing material with plasma. The aim of this action is to obtain appropriate surface properties, such as surface energy. The value of free surface energy was changed after the plasma modification. The largest changes in surface properties can be observed after the modification of the plate with air and nitrogen plasma

Modification of individual surfaces of various types with plasma resulted in diversification of the contact angle of diiodomethane and glycerol compared to the unmodified sample. The equilibrium contact angle calculated from measurements decreased after plasma treatment, regardless of its type.

REFERENCES

[1] http://dydaktyka.polsl.pl/rg5/slaczka/Rys_f_VI/F6_19.jpg
[2] R. Tadmor, Line energy and the relation between advancing, receding, and Young contact angles, *Langmuir* 20 (18): 7659–64 (2004).
[3] E. Chibowski, Surface free energy of sulfur - Revisited I. Yellow and orange samples solidified against glass surface, *Journal of Colloid and Interface Science* 319: 505 (2008).
[4] P.G.De Gennes, Wetting: statics and dynamics, *Reviews of Modern Physics* 57: 827–63 (1985).
[5] http://www.ramehart.com/images/ca4.jpg
[6] https://www.biolinscientific.com/hubfs/images/Biolin%20Scientific/Measurements/AT_AdvRecAngleWilhehmyPlate.jpg
[7] https://www.intechopen.com/source/html/48806/media/image6.png
[8] T. Homola, J. Matousek, B. Hergelova, M. Kormunda, L. Y.L. Wu, M. Cernak, Activation of poly(ethylene terephthalate) surfaces by atmospheric pressure plasma, *Polymer Degradation and Stability* 97 (11):2249-54 (2012).
[9] D. Stryczewska, Technologie plazmowe w energetyce i inżynierii środowiska, *Wydawnictwo Politechniki Lubelskiej* (2009).
[10] E. Chibowski, Surface free energy of a solid from contact angle hysteresis, *Advances in colloid and interface science* 103:149-72 (2003).
[11] H. Radelczuk, L. Hołysz, E. Chibowski, Comparison of the Lifshitz-van der Waals/acid base and contact angle hysteresis approaches to determination of the solid surface free energy, *Journal of Adhesion Science and Technology*16: 1547–68 (2002).

[12] E.Chibowski, Surface free energy and wettability of silyl layers on silicon determined from contact angle hysteresis, *Advances in colloid and interface science*113: 121-31(2005).
[13] E. Chibowski, Contact angle hysteresis due to a film present behind the drop, Contact Angle, *Wettability and Adhesion*2: 265−88(2002).
[14] E. Chibowski, On some relations between advancing, receding and Young's contact angles, *Advances in colloid and interface science*133: 51-9 (2007).

Effect of the plasma treatment on wettability and surface free energy of paper composites

*Michał Chodkowski[1], Magdalena Szaniawska[2], Anna Taraba[2]
[1]Department for the Modelling of Physico-Chemical Processes, Maria Curie-Sklodowska University, Lublin, POLAND
[2]Department of Interfacial Phenomena, Maria Curie-Sklodowska University, Lublin, POLAND
e-mail: michal@chodkowski.eu

Keywords*: composite material, plasma, surface properties, surface modification*

ABSTRACT

A composite material is made by combining two or more materials– often of different properties. The two materials work together to give the composite unique properties. Most composites are made of just two materials. The greatest advantage of modern composite materials is that they are both light and strong. Surface properties of composite materials can be modified for special applications. Nowadays a very popular method of surface modification is the plasma technique. One of the results of this type of modification is wettability change. It is alternative to traditional methods of surface modification (e.g. by chemical methods). The aim of the experiment was determination of surface properties of paper composite materials after plasma treatment. Contact angle measurements by the sessile droplet method were made in order to examine wettability changes. It was found that after plasma modification wettability and surface free energy of each surface were changed. The surfaces obtain more hydrophilic properties and an increase of surface free energy was observed.

INTRODUCTION

Wetting as a surface phenomenon

From observations and experiments it is well known that a drop of liquid placed on the surface of a solid or on the surface of a liquid immiscible with the test liquid can behave in two ways. In the first case, it can be observed that the droplet remains on the surface in a more or less spherical form; there is then non-wetting or partial wetting. In the second, extreme case, the test liquid spills over the surface, which can be observed in the form of a thin film; this is a case of complete wetting (see Figure 1).

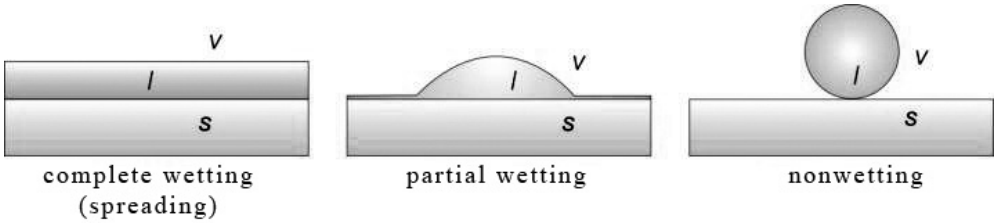

Fig.1. Possible conditions of wetting of the solid surface by a liquid.

The wettability of a given surface is closely related to its surface free energy and to the surface tension of the wetting liquid, as well as it is affected by the temperature of the system.

Surface tension and surface free energy

In the case of a solid, liquid or gas, the conformation of forces is slightly different for the atoms which are in the interface region or at the interface to that which are located in the depths of the phase. For this reason, they are in an asymmetrical, unbalanced field of forces.

In the case of liquids, the molecules interact with each other with intermolecular forces of different nature. These effects are called cohesion or cohesion forces, which cause the matter to remain in a certain state. The phenomenon of their occurrence is called cohesion. Unitary forces are very small, but in a system containing a large number of molecules, their sum can have high value. Due to the prevalence of these interactions, the orderly state is one in which each particle is adjacent to the largest possible number of other molecules. This configuration is possible to realize only in the depth of the phase volume; molecules located at the interface can only interact with neighboring molecules from their phase, whereas they do not occur from the neighboring phase of the cohesion force. In the absence of additional, external interactions, it causes that the liquid is striving to take such a shape that ensures the least amount of asymmetric molecules – forming the smallest possible boundary surface for the phase with a defined volume. The geometric block, which implements the above establishments is the sphere, because it has the smallest ratio of surface area to the volume, which gives the minimum surface energy for a given configuration. This is why freely falling drops of liquid - for example, rain - take on a shape similar to a spherical one.

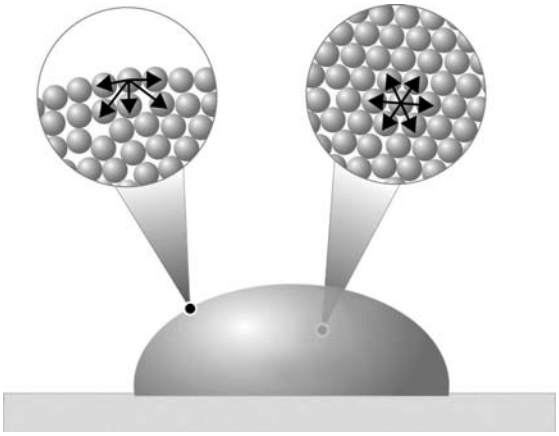

Fig. 2. Illustration of cohesion forces acting in a liquid drop.

The spontaneous trend to minimizing the surface of a liquid is shown by the existence of surface forces. These forces act tangentially to the surface of the liquid and cause the surface to behave like a resilient film; they are named as surface tension forces. The state of equilibrium of the atoms at the interface can be described using the concept of surface tension (σ) and surface free energy (γ, SFE).

The force acting along of the surface (commonly surface of a liquid), which is tangential to it and proportional to the length of the area, is called the surface tension force, *F*:

$$F = \sigma \times l \tag{1}$$

This force does not depend on the size of the surface, but it is proportional to the length of the surface edge (*l*) along which it works. It follows that the ratio of force to surface length is always constant:

$$\sigma = \frac{F}{l} = const \tag{2}$$

It is called the surface tension factor (typically also called only the surface tension), which can be defined as the surface tension force acting per unit of the surface length. The unit of surface tension isN/m:

$$\sigma = \frac{F}{l}\left[\frac{N}{m}\right] \tag{3}$$

Due to the relatively small values of usually acting forces, in practice derivative of these unit it is used: mN/m.

Let'sconsider a system, which consists of a liquid surface (e.g. a soap bubble), which is stretched on a thin wire frame with one movable inert edge (cross-bar). It is illustrated in the figure below (Fig.3).

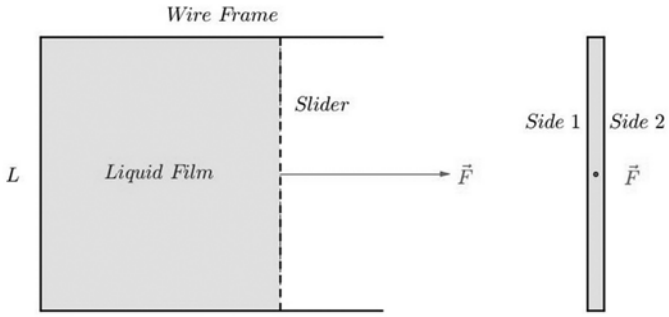

Fig. 3. Model illustrating the operation of surface tension forces.

Due to the surface tension forces, the film tends to shrink automatically, resulting in a reduction in surface area. The balancing force, *F*, which must be applied to the movable crossbar to maintain the unchanged liquid surface with respect to the length of the frame *l*, equals the value of the surface tension.

If we want to increase the surface of the film, additional work will be necessary. For this purpose, we need to apply the force *F* to the movable bar, which will cause the movement of the bare to the distance *dx*:

$$W = F \times dx \tag{4}$$

This will change the surface area *S* of the liquid to the length *dx*:

$$dS = dx \times l \tag{5}$$

The creation of a new liquid surface requires the extraction of additional molecules from the depth of the phase to its boundary surface. Such molecules, surrounded by neighbors to-date, with which they could interact symmetrically, are suddenly in an unbalanced field of forces, resulting from the lack of cohesion effects from the phase boundary. It causes their energy state to increase, because the work that was done during the surface increase is accumulated in the form of potential energy of interactions between molecules which create a new surface area.

The ratio of the work needed to create a unit interfacial surface area is constant:

$$\frac{W}{S} = \gamma = const \tag{6}$$

$$W = \gamma \times dS \tag{7}$$

Taking into account relation(5), we get finally:

$$W = \gamma \times l \times dx \tag{8}$$

The energy, which needs to be delivered to perform such work with respect to the surface area is referred as the potential energy of the surface or the surface free energy (γ, SFE) expressed in units:

$$[\gamma] = \left[\frac{J}{m^2}\right] \tag{9}$$

The following relationship can be obtained by using equations (4) and (5):

$$\frac{W}{S} = \frac{F \times dx}{l \times dx} = \frac{F}{l} \tag{10}$$

and by combining equations (2) and (6):

$$\gamma = \sigma \tag{11}$$

However, these quantities are not identical, because surface free energy is a scalar quantity and surface tension is a vectoral one. The actual relationship between them is described by the equation:

$$\sigma = \gamma + S\frac{d\gamma}{dS} \tag{12}$$

In the case of liquids, the atoms are spontaneously distributed in the equilibrium positions immediately after creating a new surface, hence:

$$\frac{d\gamma}{dS} = 0 \tag{13}$$

and for the change of a surface other than zero, the equation takes the form (11). Therefore, in the case of liquids, the most commonly used is the surface tension concept, and in the case of solids – surface free energy.

From the thermodynamic point of view, the surface tension is defined as the free enthalpy per unit area:

$$\gamma \equiv \left(\frac{\partial G}{\partial S}\right)_{T,p,n} \tag{14}$$

and surface free energy can be defined as the work necessary to transfer the molecule from the depth of the phase to its surface under isothermal conditions:

$$\gamma \equiv \left(\frac{\partial W}{\partial S}\right)_{T,V,n} \tag{15}$$

Macroscopically, this is the same as the work needed to create a new surface by removing a unitary surface from its depths.

Dependence of surface tension on the temperature and density of liquids

Liquid temperature largely determines its surface tension [1]. As the temperature rises, the surface tension decreases, and at the critical temperature σdrops to zero. There are several empirical formulas that allow finding the dependence of surface tension of clean liquids on temperature. In 1886, L. Eötvös reported a dependence that assumed approximately a linear decrease in surface tension as a function of temperature until a zero value was reached at critical temperature:

$$\gamma V_m^{2/3} = k_E(T_{ch} - T) \tag{16}$$

where: V_m– molar volume of the substance, k_E– Eötvös constant, T_{ch}– characteristic temperature, which is equal to the critical temperature.

It turned out that in practicebetter result are obtained from following formula:

$$\gamma V_m^{2/3} = k_E(T_{ch} - T - 6) \tag{17}$$

due to the lack of surface tension at a temperature 6℃ lower than the critical temperature [2]. In fact, the dependence of surface tension on temperature is scaled as follows [3]:

$$\gamma \sim \left(\frac{T - T_{ch}}{T_{ch}}\right)^{(d-1)\nu} \tag{18}$$

where: d – phase space dimensionality, ν – critical exponent of correlation length.

The relationship between surface tension and liquid density was proposed first by Baczyński [4]:

$$\sigma = c\left(\rho_c - \rho_p\right)^4 \tag{19}$$

where:ρ_c and ρ_p means the density of liquid and its saturated vapor at given temperature, respectively, and c is the constant independent of the temperature, but related to liquid properties.

Determination of the surface tension

There are various methods that allow to determine the surface tension, which are related to various phenomena observed as a result of its effects on the interface.

The selection of the optimal method depends on the properties of the tested liquid, the stability of its surface, and the conditions of measurement.

The most common are:

- methods based on the analysis of the shape of liquid droplets (so called drop shape),
- capillary methods,
- stalagmometric method (drop volume),
- method for removing the plate or ring (Wilhelmy plate od du Nouy ring),
- methods of maximum bubbles pressure.

Due to the practical subject matter of the work, only two methods will be described in more detail– with the widest practical use, and of historical importance (oldest one).

Ring detaching method

In laboratory practice, the ring-peel method is most often used due to the widespread availability of using automated tensiometers, adapted for testing the surface tension in this way. The measurement is based on the determination of the force, which is needed to detach the ring (usually made of platinum) from the surface of the tested liquid. In the initial phase, thanks to the surface tension forces, the liquid rises together with the ring; when the force that lifts the ring with the force of the surface tension is balanced, a ring is detaching the surface. The strength, needed for detachment is equal:

$$F = \sigma 4\pi r \tag{20}$$

where r is the radius of the measuring ring expressed in meters.

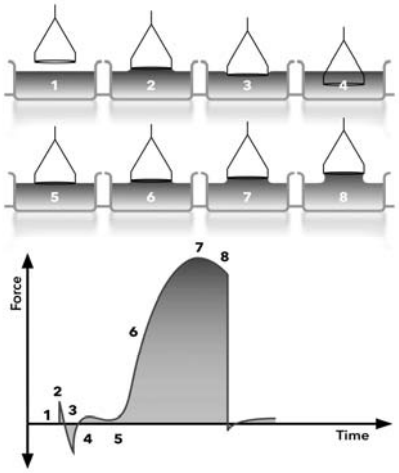

Fig. 4. The steps of the measuring liquid surface tension by ring detaching method.

Relation(20) is inaccurate and can cause measurement errors of up to 25%, thus requires the application of an amendment, which takes into account additional factors such as the radius of the wire forming the ring, the volume of raised liquid and the height of the ring above the liquid level. Therefore, Harkins and Jordan proposed an empirical correction factor [5]:

$$z = f\left(\frac{r_p}{V}, \frac{r_p}{r_d}, \frac{h^3}{V}\right) \tag{21}$$

where: r_d,r_p mean respectively the radius of the wire and the ring, h– the elevation of the ring above the surface of the liquid, V– volume of the raised liquid. Then equation (20) takes the form:

$$\sigma = \frac{Fz}{4\pi r} \tag{22}$$

Correction coefficient values are placed into tables [6], and the application of the formula with the correction gives the possibility of determining the surface tension using this method with high accuracy, in the order of 0.1 mN/m.

The capillary method

This is historically the oldest method, and at the same time the most accurate available thanks to the improvement from the experimental side in the 1970's and the well-known theory. It is based on the phenomenon of capillarity, or a spontaneous change in the level of liquid in the capillaries. The measurements are based on immersing a capillary in the test liquid of a not very large radius, the cross-section which must be round, this determines the formation of the semicircular meniscus of the liquid. For the liquid wetting the surface of the wall of the capillary, it can be observed the formation of a concave meniscus and the rise of its level in the capillary. It is caused by the surface force acting on the circumference of the capillary with radius r_k:

$$F_1 = 2\pi r_k \sigma \tag{23}$$

At the same time, this force is balanced by the weight of the liquid column in the capillary:

$$F_2 = \pi r_k^2 h_1 \rho g \tag{24}$$

where: h_1 is the height of the liquid column, ρ is the density of liquid, and *g*is the gravity. Combining equations (23) and (24) gives an expression for the surface tension of a liquid in a measurement system:

$$\sigma = \frac{r_k h_1 \rho g}{2} \tag{25}$$

In the situation, when the liquid does not wet the walls of the capillary, equation (23) takes the form:

$$F_1 = 2\pi r_k \sigma \cos(\theta) \tag{26}$$

where: cos(θ) is the cosine of the contact angle of the capillary wall; and the equation (24) can be written as follows:

$$\sigma = \frac{r_k h_1 \rho g}{2\cos(\theta)} \tag{27}$$

If the experimental system is built in such a way that the distance of the capillary from the walls of the vessel is small, additionally, the elevation of the liquid between the capillary and the edge of the vessel should also be considered.

The methods of determination of the surface free energy

There are many experimental methods to determine the value of surface free energy of a solid. These are indirect methods based, among others, on:

- measurement of dissolution heat on the tested surface,
- measurement of adsorption heat on the tested surface,
- measurement of gas and liquid adsorption on the tested surface,
- measurement of heat of wetting of the tested surface,
- measuring the contact angle of the tested surface by a drop of liquid.

The most commonly used method is the last one – based on the determination of surface free energy by measuring the contact angles of the liquid on the surface to be tested. Its popularity because of the simplicity of the testing (it does not require complicated apparatus) and many modifications (SFE determination by means of the Young equation, state equations, SFE division into independent components). The measurements of this value are very important issue, because research on the properties of the surface layer of different materials is the basis for assessing their characteristics.

One of the last known method, which is used to calculate surface free energy is Contact Angle Hysteresis (CAH) method. This approach was proposed by E. Chibowski from Maria Curie-Sklodowska University in Lublin (Poland) in 2003

[8, 9, 10, 11, 12].In opposite to other well-known methods (e.g. Fowke's or Owens and Wendt) it does not assume division the surface free energy for components. While the advancing contact angle of a probe liquid can be used for determination of the solid surface free energy and its components, so the receding contact angle also delivers very useful information about the solid surface energetic [8]. Using the contact angle hysteresis approach is suggested for evaluation of the solid surface free energy. It follows that only one test liquid can be used in order to estimate surface free energy. It is useful mostly in industry applications, when occurs the continuous necessity of controlling parameters of obtained surfaces. The energy is a function of the surface tension of a test liquid and contact angle hysteresis on examined surface, which depends on advancing and receding contact angle (both of the values are able to find by commonly used measurements methods):

$$\gamma_s = \frac{\sigma_l(1+cos\theta_a)^2}{(2+cos\theta_r+cos\theta_a)} \tag{28}$$

where γ_s is the surface free energy, σ_l is the surface tension of the test liquid, Θ_a and Θ_r are advancing and receding contact angle. It must be mentioned that the surface free energy calculated by using this approach partially depends on the physicochemical properties of the test liquid which was used. Comparing the values, which were calculated for different surfaces, it should be remembered that these must be results obtained with the use of identical test liquids. It is very convenient method among others for rapid estimation and comparison the surface free energies of various samples by using only one test liquid.

MATERIALS AND METHODS

The research involved fragments of a paper composite material used, among others, as a raw material for the production of cups for beverages, in form of rectangular plates of the size 2 cm x 6 cm. Surface treatment was preceded by rinsing with ethanol to purify the base surface. A low-temperature plasma generator from Diener Electronic was used to modify the tested surfaces. Samples were subjected to modification with air plasma under vacuum conditions, generated by using of 40 kHz alternating current electrodes and 1000 W power.

Immediately after the modification, measurements of the contact angles of water, formamide and diiodomethane were made using the *Digidrop* goniometer produced by GBX. The device was equipped with a thermostated, closed measuring chamber, thanks to which it is possible to carry out measurements in conditions of controlled temperature and humidity, as well as saturated steam produced by the use of a special attachment (additional part of the system purchased from GBX). Measurements of the contact angle were carried out on pure sections unmodified by plasma and on the plates treated with plasma for 10 and 30 seconds. In the case

where the water was used as theliquid, the conditions of the saturated vapor were provided during the measurement in the chamber.

Advancing and receding water contact angles were measured in order to determine wettability of each surface. Measurements were made using the sessile drop technique as follows: a 6 µl droplet was settled on the examined surface and the advancing contact angle was measured, then 2 µl of test liquid was sucked from the droplet into the syringe and the receding contact angle was measured in the temperature equal to 25°C. Then the equilibrium contact angle was calculated using the Tadmor's approach [7]and surface free energy was calculated using the CAH (contact angle hysteresis) method proposed by Chibowski.

RESULTS AND DISCUSSION

Contact angle measurements

Plasma surface modification caused visible changes in the contact angles of all three measuring liquids.

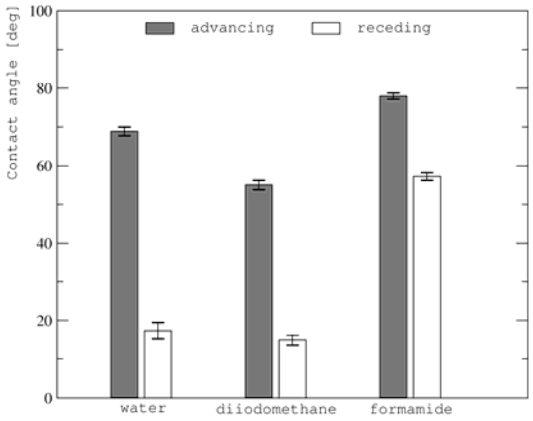

Fig. 5. Advancing and receding contact angles on the surface unmodified by plasma.

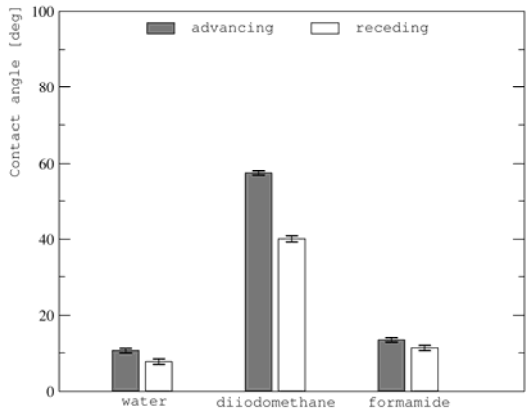

Fig. 6. Advancing and receding contact angles on a surface modified with plasma for 10s.

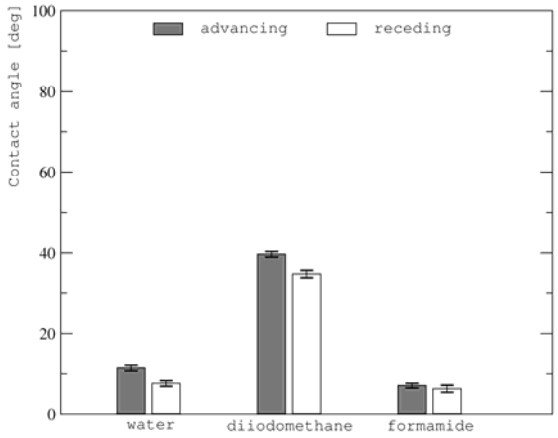

Fig. 7. Advancing and receding contact angles on a surface modified with plasma for 30s.

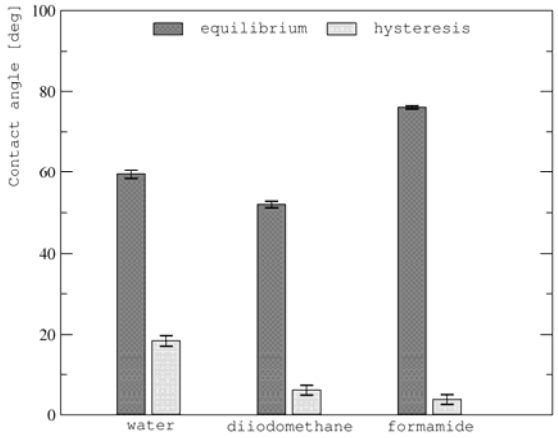

Fig. 8. Equilibrium contact angles and hysteresis on the surface unmodified by plasma.

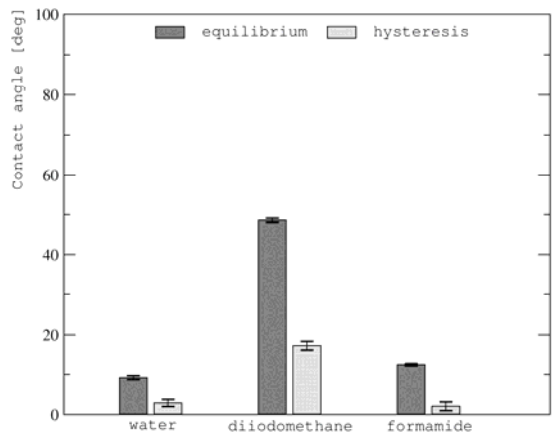

Fig. 9. Equilibrium contact angles and hysteresis on the surface modified with plasma for 10s.

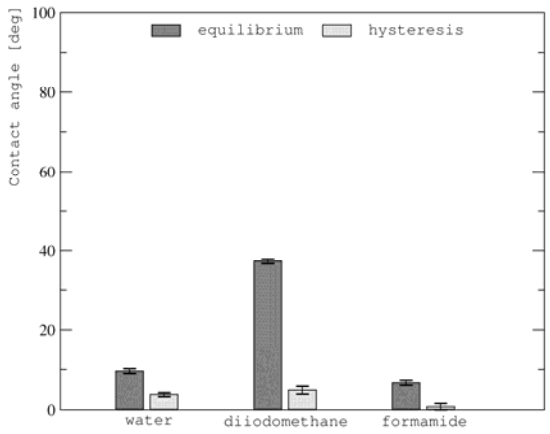

Fig. 10. Equilibrium contact angles and hysteresis on the plasma modified surface for 30s.

In the case of water, a significant decrease in the equilateral contact angle after surface modification with plasma for 10 seconds can be observed; however, a longer modification (over 30 seconds) didnot cause a significant change in surface wettability. After modification, the values of contact angle hysteresis also decreased.

In the case of diiodomethane, changes in surface wettability after a 10-second plasma modification are insignificant, however, after a 30-second exposure to the plasma, the contact angle has decreased by almost 10°. Hysteresis has also changed, but without a clear trend.

In the case of formamide, a 10-second plasma operation on the surface caused a significant decrease in the values of the contact angles; longer surface treatment causes a further decrease in the contact angle value. With increasing the modification time, the hysteresis valued decreases.

The contact angles of the tested liquidsdiffer before and after the plasma modification. The obtained results show that after applying the plasma treatment, the tested surfaces become more hydrophilic. The hydrophilicity effect of the surface increases after its modification with plasma, however, extending the duration of the plasma from 10 to 30 seconds does not have significantly effect on the wettability change (with water). During the operation of the air plasma, polar groups (mostly consisting oxygen atoms) are introduced onto the tested surface. The character of the surface changes, which can be observed by the improvement of its wettability after a 10second treatment. However, extending the time of surface modification, contrary to expectations, does not improve the wettabilityany further.

Surface free energy (CAH approach)

The values of surface free energy changed after the plasma modification. The values of energy obtained as a result of hysteresis calculations of the contact angle of water and formamide are increasing. The values, which were calculated based on the

hysteresis of the contact angle of diiodomethane increased only for 30 seconds of surface treatment with plasma. Differences in the calculated surface free energy value result from changes in the number and type of functional groups on individual surfaces as a result of plasma modification. It can be concluded that a longer time of plasma treatment than 10 seconds has no reasonable justification - the values of surface free energy do not differ significantly in the case of plasma modification lasting 10 and 30 seconds. Only in the case of diiodomethane, an increase in surface free energy can be observed after a 30-second treatment; this is due to the fact that the liquid is non-polar and confirms the hypothesis that the number of polar groups on the surface decreases after the plasma is too long.

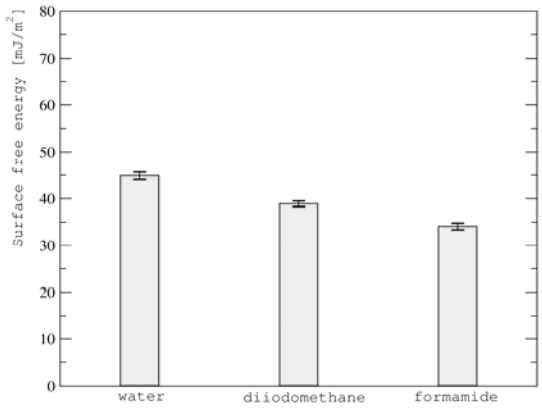

Fig. 11. Surface free energy of a sample unmodified by plasma.

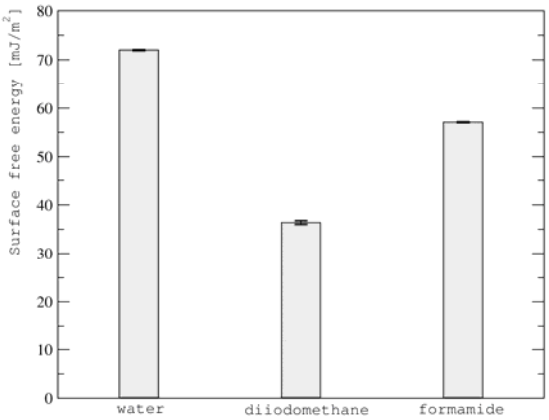

Fig. 12. Surface free energy of a sample modified with plasma for 10s.

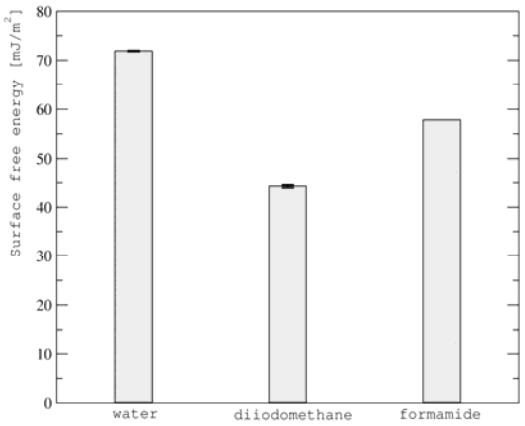

Fig. 13. Surface free energy of a sample modified with plasma for 30s.

It is extremely important that the surface free energy calculated by using the approach with the contact angle hysteresis partially depends on the physicochemical properties of the measured liquid used. Comparing the values, which were calculated for different surfaces, it should be remembered that these must be results obtained with the use of identical test liquids. To avoid this inconsistency, the values of average energy should be calculated using the contact angle hysteresis of several different liquids, e.g. water, formamide and diiodomethane. However, it should be remembered that using this approach to surface free energy, you will obtain the apparent energy value, which depends on used liquid.

REFERENCES

[1] J.G. Speight, *Lange's handbook of chemistry*, McGraw Hill, New York 2005.

[2] J.L. Shereshefsky, *Surface tension of saturated vapors and the equation of Eötvös*, The Journal of Chemical Physics 35(6): 1712-20 (1931).

[3] J.J. Binney, N.J. Dowrick, A.J. Fisher, M.E.J. Newman, *Zjawiska krytyczne. Wstęp do teorii grupy renormalizacji*, PWN, Warszawa 1998.

[4] Praca zbiorowa pod redakcją B. Kamińskiego, *Chemia fizyczna*, PWN, Warszawa 1980.

[5] W.D. Harkins, H.F. Jordan, *A method for the determination of surface and interfacial tension from the maximum pull on a ring*, Journal of the American Chemical Society 52.5: 1751-72 (1930).

[6] Norma ASTM D 1590: *Standard Test Method for surface tension of water*.

[7] R. Tadmor*, Line energy and the relation between advancing, receding, and Young contact angles*, Langmuir 20 (18): 7659–64 (2004).

[8] E. Chibowski, *Surface free energy of a solid from contact angle hysteresis,* Advances in colloid and interface science 103: 149-72 (2003).

[9] H. Radelczuk, L. Hołysz, E. Chibowski, *Comparison of the Lifshitz-van der Waals/acid base and contact angle hysteresis approaches to determination of the*

solid surface free energy, Journal of Adhesion Science and Technology 16: 1547–68 (2002).

[10] E. Chibowski, *Surface free energy and wettability of silyl layers on silicon determined from contact angle hysteresis*, Advances in colloid and interface science113: 121-31 (2005).

[11] E. Chibowski, *Contact angle hysteresis due to a film present behind the drop*, Contact Angle, Wettability and Adhesion 2: 265−88 (2002).

[12] E. Chibowski, *On some relations between advancing, receding and Young's contact angles*, Advances in colloid and interface science 133: 51-9 (2007).

Electrode materials used in bioelectrochemical systems

*Joanna Grudzień, Magdalena Jarosz, Kamil Kamiński, Grzegorz D. Sulka
Faculty of Chemistry, Department of Physical Chemistry and Electrochemistry, Jagiellonian University, Krakow, POLAND
e-mail: grudzien@chemia.uj.edu.pl

***Keywords**: bioelectrochemical systems, bioelectrodes, electroactive bacteria*

ABSTRACT

Nowadays, renewable energy sources are becoming increasingly important. One of the setups, which can produce green energy are bioelectrochemical systems (BESs). Among the factors that have an impact on current efficiency, electrode's material seems to be crucial. Generally, carbon-based, metallic-based and other materials are used. What is more, morphology and topography of electrodes have a significant effect on bacterial growth and current efficiency. Here, we present a short summary on the materials commonly used and factors that influence current efficiency in BESs.

BIOELECTROCHEMICAL SYSTEMS (BESs)

Nowadays, sustainable and renewable energy sources are intensively sought because of an increasing demand for energy which is connected with the dynamically growing populations. In addition, more and more attention is paid to the reduction of environmental pollution anddevelopment of the so-called "green chemistry" [1]. One type of the setups that can be utilized to produce green energy is bioelectrochemical systems (BESs).BESs are electrochemical systems in which specific groups of microorganisms such as bacteria, yeast or algae species are used [2-4]. Those organisms should be characterized by electrochemical activity and, therefore, are called exoelectrogens. When it comes to the configuration of such systems, microbes may either colonize the electrode surface or occur as a planktonic form in the electrolyte and thus contribute to the production of green energy [5]. Those microorganisms have an ability to convert energy stored in the chemical bond of organic compounds (e.g., pure glucose or complex mixture of organic matter) to electrical energy. BESs can be utilized in wastewater treatment [6], biofuel (hydrogen [7], ethanol [8], etc.) production or in sensing [9]. Considering the applicability of bioelectrochemical systems, two main types should be mentioned:(i) microbial fuel cells (MFCs) and (ii) microbial electrolysis cells (MECs).

Microbial fuel cells

The most intensively studied bioelectrochemical systems are microbial fuel cells [5, 10]. Generally, MFCs use microorganisms that occupy an anode to generate current. Most of the bacteria strains used in such systems are anaerobes which mean that they cannot live in the presence of oxygen. Therefore, anode have to be separated from cathode by using selective membrane (proton, cation or anion exchange membrane) or salt bridge, and these types of MFCs are called two-chambered systems [11]. However, if microbes are facultative anaerobes, they are able to respire in the oxygen-rich environment as well as in anaerobic conditions, single-chamber cell can be used [12].

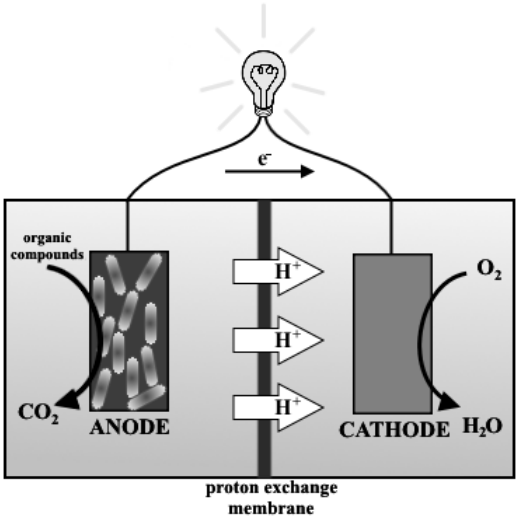

Fig. 1. Scheme presenting two chambered microbial fuel cell setup.

Processes that occur within the system are very complex and depend on various agents. However, the basic idea of what is happening inside the cell is common. Electroactive organisms that are located in the anode compartment oxidize organic compounds, e.g., acetate (equation 1) from the electrolyte to the carbon dioxide. Next, electrons obtained from the reactions are transported in the bacterial respiratory chain, then can be transferred to the surface of the electrode, and finally to the external circuit. At the same time, protons migrate through the membrane to the cathode compartment (Fig. 1).Then, electrons are transported to the cathode where they recombine with electron acceptors (usually with oxygen) and protons, and form water molecule (equation 2). In other words, electric current can be produced as a result of bacteria metabolism (equation 3) [13-14].

$$\text{Anode: } CH_3COOH + 2H_2O \rightarrow 2CO_2 + 8H^+ + 8e^- \quad (1)$$

$$\text{Cathode: } 2O_2 + 8H^+ + 8e^- \rightarrow 4H_2O \quad (2)$$

$$\text{Overall: } CH_3COOH + 2O_2 \rightarrow 2CO_2 + 2H_2O + \text{biomass} + \text{electricity} \quad (3)$$

It is worth noticing that only few bacteria species (for example *Shewanella* [15] or *Geobacter* spp. [16]) can transfer electrons directly to the surface of the electrode. Other species mediate electrons indirectly–by natural (organic compounds secreted by bacteria, like flavins) or artificial (for example dyes such as methylene blue) mediators. Electrons can also be transferred thanks to the substances which are present in the biofilm covering the electrode surface. It is a structure composed of organic and inorganic compounds produced by the microorganism, and in which such organism is embedded [5,17-19].

One of the most crucial aspects when MFCs are considered is working efficiency. It depends on numerous factors which can be divided into three main groups. In the first one there are biological parameters which mainly refer to the utilized bacteria species and their characteristics. For instance, it is essential if bacterial culture used in the system is pure or it is a mixture of different species. The second group consists of system design parameters that describe materials and components of the cell, as well as their arrangement. Finally, thermodynamic parameters play an important role, since pH and type of the electrolyte, applied potential and many others may influence the efficiency of the system. More detailed list of described above parameters is shown in table 1. [5].

Tab. 1. Parameters which influence current efficiency of MFCs [5].

Biological factors	**Thermodynamical factors**	**System design factors**
Inoculum source	External resistance	Electrode spacing
Type of bacteria (Gram-positive or Gram-negative)	Batch vs. flow system	Electrode properties (conductivity, porosity, hydrophilicity, etc.)
Single species or consortium	Redox potential	Electrodes surfaces
Biofilm growth rate	pH	Presence of membrane and type of membrane
Type of electron transfer	Temperature	Type of cathode
Ability to secretion of natural mediators	Ionic strength	
	Presence of oxygen	

ELECTRODEMATERIAL

When it comes to the constructing of the new MFC setup, the parameters mentioned above should be carefully considered and chosen. Among them, in the first step of research a selection of those which have the most significant and crucial impact on the current efficiency has to be made. One of them is electrode material, because it affects the biofilm formation (possibility of bacteria adhesion and their growth), electron transferand an open circuit potential of bioelectrodes. Moreover, electrodes used in MFCs or generally in BESs should meet some specific requirements like [2,20-22]:

- High electrical conductivity;
- Corrosion resistance;
- High mechanical strength;
- Developed surface area;
- Environmental friendliness;
- Low costs of production and use.

It must be taken into account that only some elements or those compound and alloys possess listed above features. Materials used in BES can be divided into three main groups: (i) carbon and its modifications, (ii) metals, and (iii) others (e.g., oxides or polymers).It is worth mentioning that anode and cathode materials can be the same or each electrode may be made from different material, which depends on various aspects. In case of anodes, the most important feature should be their biocompatibility towards bacteria strains that provides enhancement in biofilm development. On the other hand, cathodes should have good catalytic properties. Mainly for the oxygen reduction reactions (oxygen is the most commonly used electron acceptor). It is especially important because the reactions are relatively slow [2, 20-22]. They can occur via two ways: two- (equation 4) and four-electron (equations 5.1-5.2) pathways [23].

$$O_2 + 4H^+ + 4e^- \rightarrow 2H_2O \quad (4)$$

$$O_2 + 2H^+ + 2e^- \rightarrow H_2O_2 \quad (5.1)$$

$$H_2O_2 + 2H^+ + 2e^- \rightarrow 2H_2O \quad (5.2)$$

What should be highlighted is the fact that selection of suitable electrode material strictly depends on the type of microorganism. For example, some electroactive bacteria like *Geobacter* spp. can grow on gold surfaces [24], while other bacteria species cannot, since this metal may be lethal for them or may simply not be able to adhere to any metal surface.

Carbon electrodes

Electrodes commonly utilized in MFCs are made from carbon and graphite (paper, rods, cloth, brushes or fibers). In general, these materials have numerous advantages like biocompatibility, high electrical conductivity, low costs and high availability [20-21, 25-26]. However, there are also some drawbacks that significantly limit their use in bioelectrochemical systems. For instance, carbon rods possess low surface area which results in small current efficiencies. In contrary, carbon felt and paper have a comparatively high porosity which allows bacteria to easily penetrate substrates and effects insignificant increase in power output. What is worth noting is the fact that carbon paper is quite expensive; therefore it is used mostly on a laboratory scale. There are a lot of studies on high surface area carbon materials. Feng et al. [27] were examined carbon brushes that were connected to a titanium core which enhanced

electrode electric conductivity. However, costs of production also increased. In general, current conductivity of carbon anodes depends on their surface area in the following order: carbon felt > carbon foam > graphite [28]. One of the main disadvantages of carbon-based electrodes is their high background current that can mask current signals from the redox reaction that occurs thanks to the presence of electrochemically active bacteria. This undesirable phenomenon can be eliminated when glassy carbon electrodes are used and more universal current measurement can be done for the comparison of the electrodes [5].In order to further eliminate problems encountered with carbon electrodes, nanomaterials found applications in the field of bioengineering. Especially carbon nanotubes (CNTs) possess unique properties which can be useful in MFCs. These structures are known for their excellent electric conductivity, chemical stability, biocompatibility and high surface area [25, 29]. Utilizing CNTs as MFC electrodes was proved to give higher current efficiencies in comparison to the conventional carbon electrodes [30].

Furthermore, in order to enhance power output of bioelectrochemical setups, different modifications of carbon materials can be applied. It is especially important in the case ofcathodes. The aim of modifications is to improve their catalytic properties, because, as already mentioned, the oxygen reduction is a relatively slow reaction [31].Up to now, various types of modifications have been applied. First of all, carbon materials can be covered by platinum particles that are known for their excellent catalytic properties. Unfortunately, this approach is quite expensive. Next, doping method can be used where different dopants are used. Nitrogen is the most commonly utilized elements in this approach. N-doped carbon electrodes have significantly enhanced catalytic activity in comparison to Pt/C electrodes [32]. What is more, cathode surfaces can be modified by extra reactive groups (e.g., hydroxyl or carboxylic) by treating electrodes with strong bases, for instance potassium hydroxide, and strong acids like hydrochloric, nitric or phosphoric acids. Additionally, not only the chemistry of the electrode is changed but also the surface area is extended, which results in an increasing number of active centers. Thus, the reactivity of such electrodes is enhanced [2, 20, 25-26].

Metallic electrodes

Despite the fact that carbon materials possess a lot of advantages, they have about two to three magnitude higher electrical resistivity than metals. This feature has significant impact on the current efficiency of MFCs, because the higher the electrode resistance, the lower the actual power output. It is especially importantin the case of up-scale systems [38].That is why, the use of metallic electrodes for the needs of MFCs is being considered. It is worth noting that certain metals, e.g., silver and copper, can be toxic or lethal to the microorganisms. Both of those metals (even in relatively low concentrations) are known for their antibacterial and antifungal

properties [33]. When silver surface is oxidized, silver ions are highly reactive and can connect with bacterial cell walls or bacterial DNA and RNA, which then leads to the death of the microorganism [34]. A different mechanism is encountered when copper ions are released. They bind to bacteria proteins, e.g. from the respiratory chain, or with enzymes, altering their structure which causes changes in proper functioning of cells [35]. That is why, theuse of these metals is limited. For this reason, noble metals like gold and platinum found applications in MFC setups. However, their high cost causes that they may be used only in basic research. Especially, gold is being used as an excellent electrode for spectroscopic techniques applied to study mechanisms of the electron transfer [36]. Scaling up of such setups may be economically undesirable. Since platinum is one of the most applicable catalysts for oxygen reduction reactions, in order to minimize the costs of electrode synthesis, carbon-based or composite-based cathodes loaded with platinum can be used, as described in the previous paragraph. On the other hand, different platinum alloys with other metals like iron, cobalt or nickel also found applications in microbial fuel cells [26].What is more, there are studies in which pure metals (e.g., titanium [37], cobalt [38], nickel [38], etc.) were utilized. It is worth noting that stainless steel is widely applied because of its excellent mechanical and electrical properties and high resistance to corrosion processes [20, 26]. Stainless steel is a relativity inexpensive material in comparison to noble metals or other modified electrodes. However, the plain surface of stainless steel results in low current efficiency. That is why 3-dimentional foams were proposed which not only led to the increased power output, but also to the enhanced biofilm formation [39].

Others electrode materials

There are also some experiments in which utilizing electrodes different from the carbon or metallic are required. Indium tin oxide (ITO) is used mainly when optically transparent substrates are necessary [40].Furthermore, electrodes based on metal oxides can find applications in MFCs. For example, manganese dioxide was tested in such systems. However, manganese can easily change its oxidation states which may significantly worsen obtained current efficiencies. In order to overcome this issue, different types of synthesis method were proposed [26, 41].In addition, other metal oxides like lead [42], vanadium [43] or cobalt [44] oxides may be utilized. However, the possibility of using those electrodes in MFC is restricted, due to their toxic influence on microorganisms and environment caused by released ions. Next type of compounds used as electrodes are spinels, for instance, manganese-cobaltite spinel [45].

Another approach leading to obtaining effective electrode materials is the use of polymers that can either be used as a surfacecover or as a part of the composite material. Up to know, mainly conductive polymers like polyaniline [46] and

polypyrrole [47] were usedalongwith carbon nanotubes. As a result, higher current densities were registered in comparison to the conventionally used carbon/platinum electrodes.

In table 2,different anode materials which are commonly used in bioelectrochemical systems are shown along with their main advantages and drawbacks. Sometimes application of some electrodes is limited in view of their disadvantages [25].

Tab. 2. Comparison of widely used anode materials for bioelectrochemical applications [25].

Anode material	Advantages	Disadvantages
Stainless steel	High conductivity, relatively cheap, easilyaccessibile	Low surface area, low biocompatibility
Graphite rod	High conductivity and chemical stability, relatively cheap, easilyaccessibile	Difficulties in increasing the surface area
Graphite fiber brush	High specific area, feasible	Clogging
Carbon cloth	Large relative porosity	Relatively expensive
Carbon paper	Easy wire connection	Fragile
Carbon felt	Large surface area	High resistance

NANO, MICRO AND MACRO ELECTRODE'S ARCHITECTURE

As mentioned above, the choice of electrode material has significant influence on MFCs working efficiency. However, other features likeelectrode's morphology and surface chemistry should be considered in detail when designing bioelectrochemical systems [2,14, 21]. Both the morphology and surface chemistry have crucial impact on bacteria adhesion and biofilm formation, and finally on current efficiency of MFCs. There are three levels that should be mentioned in case of electrode's performance: nano, micro and macroscale. First of all, at the nanometric scale, interactions between particular bacterial cells and the electrode surface are the key issues. Some of the morphology features like surface charge, van der Waals forces, immobilized mediators, hydrophilicity and nanotopography (e.g., presence of ordered nanopatterns, nanoparticles), strongly affect cell-cell interactions. For example, most of the bacteria species prefer positively charged surfaces. Moving up to the micrometer scale, the biofilm formation and its growth strictly depend on the microtopogaphy and micromorphology. Therefore, it is extremely important that the electrode surface should be either two-dimensional (flat) or three-dimensional (with ordered nanostructures, fibers or microporous). In case of the three-dimensional materials features like porosity (pore size, shape)and roughness have an impact onbacteria attachment to the surface. In addition, other aspects like the diffusion within the biofilm, and between microorganisms and electrode surface, as well as the permeability of the bioanode should be considered. What is worth noticing is the fact

that sometimes bacteria do not colonize the whole available area. Thus, the obtained current densities are lower than theoretically predicted. Blanchet et al. [48] investigated 2D and 3D carbon materials and examined current efficiencies. The obtained results were similar for both systems, in spite of the differences in the surface area, proving that increasing the specific surface area not always results in the increased current. Finally, at macrometer scale, the architecture of the overall system like the electrode distance or electrode number (one or multi electrodes system) is crucial, especially in case of long term studies.

To sum up, the steps that have significant impact on working efficiencies of MFCs are presented in Fig.2 [2].

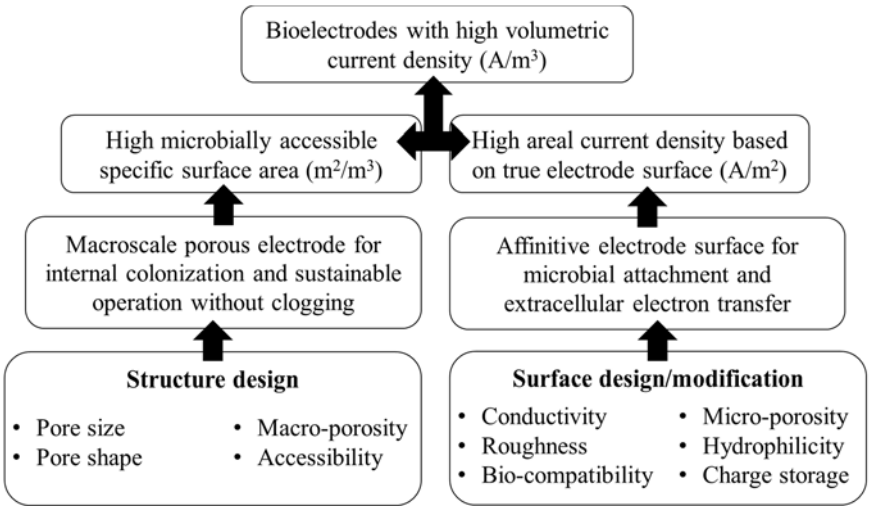

Fig. 2. Scheme representing the impact of the surface morphology and topography of electrodes on the overall working efficiencies of MFCs [2].

SUMMARY

Bioelectrochemical systems can be considered as the potential alternative energy sources. However, the possibility of using these setups for the energy generation depends on the obtaining relatively high current efficiencies. One of the most important factors that should be considered during optimizing working parameters of the MFCs is the choice of proper electrode material, because of its strong influence on the setup power output. Despite the fact that there are a lot of various electrode types, only some of them can be used in microbial fuel cell systems. An ideal electrode must be characterized by specific features like high surface area, mechanical strength, and good conductivity. What is more, when it comes to anodes, they have to be biocompatible since bacteria species interact with their surface. On the other hand, cathodes should possess high catalytic activity, especially when the oxygen reduction reaction is considered in most of the MFCs systems. Among the electrode materials used in the bioelectrochemical systems,

carbon-based materials, either pure or modified, are the most common. Despite their numerous advantages, they also have some significant drawbacks. That is why, metallic electrodes, like stainless steel are proposed for microbial fuel cells applications. What is more, noble metals can also beused. However, they can be applied only for some systems, depending on the utilized electroactive microorganisms. In some instances, carbon electrodes can be replaced by metal oxides or may be covered with polymeric layers. As shown above, not only electrode material is crucial for obtaining efficient currents. The morphology and topography of electrodes at nano, micro and macro levels also play a significant role. It is worth mentioning that high current efficiencies may be obtained when suitable electrode materials are used in combination with proper bacteria species. Therefore, the search of the most efficient system is still being conducted and a lot of challenges remain.

REFERENCES

[1] Anastat P.T., Warner J.C., Green Chemistry: Theory and Practice, *Oxford Univer. Press: New York*, 1998, 30.

[2] Xie X., CriddleC,. Cui Y., Design and fabrication of bioelectrodes for microbial bioelectrochemical systems, *Energy & Environmental Science*, 2015, 8, 3418 – 3441, DOI: 10.1039/C5EE01862E.

[3] Logan B.E., Rabaey K., Conversion of wastes into bioelectricity and chemicals by using microbial electrochemical technologies, *Science,* 2012, 337, 686 – 690, DOI: 10.1126/science.1217412.

[4] Schröder U., Harnisch F., Angenet L.T., Microbial electrochemistry and technology: terminology and classification, *Energy & Environmental Science*, 2015, 8, 513 – 519, DOI: 10.1039/C4EE03359K.

[5] Borole A.P., Reguera G., Ringeisen B., Wang., Feng Y., Kim B.H., Electroactive biofilms: Current status and future research needs, *Energy & Environmental Science*, 2011, 4, 4813 – 4834, DOI: 10.1039/c1ee02511b.

[6] Min, B., Logan, B.E., Continuous electricity generation from domestic wastewater and organic substrates in a flat plate microbial fuel cell, *Environmental Science & Technology*, 2004, 38, 5809-5814, DOI: 10.1021/es0491026.

[7] Huang, Y.X., Liu, X.W., Sun, X.F., Sheng, G.P., Zhang, Y.Y., Yan, G.M., Wang, S.G., Xu, A.W., Yu, H.Q., A new cathodicelectrode deposit with palladium nanoparticles for cost-effectivehydrogen production in a microbial electrolysis cell, *International Journal of Hydrogen Energy*, 2011, 36, 2773-2776, DOI: 10.1016/j.ijhydene.2010.11.114.

[8] Steinbusch KJ, Hamelers HV, Schaap JD, Kampman C, Buisman CJ., Bioelectrochemical ethanol production through mediated acetate reduction by

mixed cultures, *Environmental Science and Technology*, 2010, 44, 513-517, DOI: 10.1021/es902371e.

[9] Kim, B.H., Chang, I.S., Gil, G.C., Park, H.S., Kim, H.J., Novel BOD (biological oxygen demand) sensor using mediator-less microbial fuel cell, *Biotechnology Letters*, 2003, 25, 541-545, DOI: https://doi.org/10.1023/A:1022891231369.

[10] Babauta J., Renslow R., Lewandowski Z., Beyenal H., Electrochemically active biofilm: facts and fictions. A review, *Biofouling, The Jourlan of Bioadhesion and Biofilm Research*, 2012. 28, 789-812, DOI: https://doi.org/10.1080/08927014.2012.710324.

[11] Min B., Cheng S., Logan B.E., Electricity generation using membrane and salt bridge microbial fuel cells, *Water Research*, 2005, 39, 1675–1686, DOI: 10.1016/j.watres.2005.02.002.

[12] Liu H., Ramnarayanan R., Logan B.E., Production of electricity during wastewater treatment using a single chamber microbial fuel Cell, *Environmental Science & Technology*, 2004, 38, 2281–2285, DOI: 10.1021/es034923g.

[13] Sharma Y., Baikun L., The variation of power generation with organic substrates in single-chamber microbial fuel cells (SCMFCs), *Bioresource Technology*, 2010, 101, 1844–1850, DOI: 10.1016/j.biortech.2009.10.040.

[14] Kalathil S., Patil S.A., Pant D., , Chapter in the book: Microbial Fuel Cells: Electrode Materials, *Encyclopedia of Interfacial Chemistry: Surface Science and Electrochemistry,Elsevier*, 2017

[15] Okamato A., Nakamura R., Hashimoto K., In-vivo identification of direct electron transfer from *Shewanellaoneidensis* MR-1 to electrodes via outer-membrane OmcA–MtrCAB protein complexes, *Electrochimica Acta*, 56, 2011, 5526-2231, DOI: https://doi.org/10.1016/j.electacta.2011.03.076.

[16] Bond D.R., Holmes D.E., Tender L.M., Lovley D.R., Electrode-reducing microorganisms that harvest energy from marine sediments, *Science*, 2002, 295, 483–485, DOI: 10.1126/science.1066771.

[17] Marsili E., Baron D. B., Shikhare I. D., Coursolle D., Gralnick J. A., Bond D. R., Shewanella secretes flavins that mediate extracellular electron transfer, *Proceedings of the National Academy of Sciences,* 2008,105, 3968-3973, DOI: 10.1073/pnas.0710525105.

[18] Roller S.D., Bennetto H.P., Delaney G.M., Mason J.R., Stirling J.L., Thurston C.F., Electron-transfer coupling in microbial fuel cells: 1. comparison of redox-mediator reduction rates and respiratory rates of bacteria, *Journal of Chemical Technology and Biotechnology*, 1984, 34, 3-12, DOI: 10.1002/jctb.280340103.

[19] Srikanth S., Marsili E., Flickinger M.C., Bond D.R., Electrochemical characterization of Geobactersulfurreducens cells immobilized on graphite paper electrodes, *Biotechnology and Bioengineering*, 2008, 99, 1065-1073, DOI: 10.1002/bit.21671.

[20] Santoro C., Arbizzani C., Erable B., Microbial fuel cells: From fundamentals to applications. A review, *Journal of Power Sources*, 2017, 356, 225-244, DOI: http://dx.doi.org/10.1016/j.jpowsour.2017.03.109.

[21] Guo K., Prévoteau A., Patil S.A., Rabaey K., Engineering electrodes for microbial electrocatalysis, Current Opinion in Biotechnology, 2015, 33, 149-156, DOI: http://dx.doi.org/10.1016/j.copbio.2015.02.014.

[22] Rinaldi A., Mecheri B., Garavaglia V., Licoccia S., Di Nardo P., Traversa E., Engineering materials and biology to boost performance of microbial fuel cells: a critical review,*Energy Environmental Scicience*, 2008, 417-429, DOI: 10.1039/B806498A.

[23] Lim, D.H., Wilcox, J., Mechanisms of the oxygen reduction reaction on defective graphene-supported Pt nanoparticles from first-principles, *Journal of Physical Chemistry C*, 2012, 116, 3653-366,, DOI: 10.1021/jp210796e.

[24] Richter H., McCarthy K., Nevin K.P., Johnson J.P.,Rotello V.M., Lovley D.R., Electricity generation by Geobactersulfurreducens attached to gold electrodes, *Langmuir*, 2008, 24, 4376-4379, DOI: 10.1021/la703469y.

[25] Mustakeem, Electrode materials for microbial fuel cells: nanomaterial approach, *Materials for Renewable and Sustainable Energy*, 2015, 4, 22, DOI: 10.1007/s40243-015-0063-8.

[26] Yuan H., Hou Y., Abu-Reesh I.M., Chen J., He Z., Oxygen reduction reaction catalysts used in microbial fuel cells for energy-efficient wastewater treatment: a review, *Mateirals Horizons*, 2016, 3, 382-401, DOI: 10.1039/c6mh00093b.

[27] Feng Y., Yang Q., Wang X., Logan B.E., Treatment of carbon fiber brush anodes for improving power generation in air–cathode microbial fuel cells, Journal of Power Sources, 2010, 195, 1841-1844, DOI: https://doi.org/10.1016/j.jpowsour.2009.10.030.

[28] Chaudhuri S.K., Lovely D.R., Electricity generation by direct oxidation of glucose in mediatorless microbial fuel cells, Nature Biotechnology, 2003, 21, 1229–1232, DOI: 10.1038/nbt867.

[29] Iijima, S., Helical microtubules of graphitic carbon, *Nature,* 1991, 354, 56-58; DOI:10.1038/354056a0.

[30] Tsai, H.Y., Wu, C.C., Lee, C.Y., Shih, E.P., Microbial fuel cell performance of multiwall carbon nanotubes on carbon cloth as electrodes, *Journal Power Sources,* 2009, 194, 199-205, DOI: https://doi.org/10.1016/j.jpowsour.2009.05.018.

[31] Fan Y., Sharbrough E., Liu H., Quantification of the Internal Resistance Distribution of Microbial Fuel Cells, *Environmental Science & Technology*, 2008, 42, 8101-8107, DOI: 10.1021/es801229j.

[32] Watson V.J., Delgado C.N., Logan B.E., Improvement of activated carbons as oxygen reduction catalysts in neutral solutions by ammonia gas treatment and

their performance in microbial fuel cells, *Journal of Power Sources*, 2013, 242, 756-761, DOI: 10.1021/es401722j.

[33] Thota S., Crans D., Chapter in the book: Noble Metals Nanoparticles and Their Antimicrobial Properties, *Metal Nanoparticles: Synthesis and Applications in Pharmaceutical Sciences*, *Wiley-VCH Verlag GmbH & Co,* 2018.

[34] Rai Mahendra, Yadav A., Gade A., Silver nanoparticles as a new generation of antimicrobials, *Biotechnology Advances*, 2009, 27, 76-83, DOI: 10.1016/j.biotechadv.2008.09.002

[35] Thurman R.B., Gerba C.P., Bitton G., The molecular mechanisms of copper and silver ion disinfection of bacteria and viruses, *Critical Reviews in Environmental Control*, 1989, 18, 295-315, DOI: https://doi.org/10.1080/10643388909388351

[36] Busalmen J.P., Esteve-Nunez A., Berna A., Feliu J.M., ATR-SEIRAs characterization of surface redox processesin G. sulfurreducens, *Bioelectrochemistry*, 2010, 78, 25–29, DOI: 10.1016/j.bioelechem.2009.04.011

[37] Zhou X., Chen X., Li H., Xiong J., Li X., Li W., Surface oxygen-rich titanium as anode for high performance microbial fuel cell, *Electrochimica Acta*, 2016, 209, 582-590, DOI: https://doi.org/10.1016/j.electacta.2016.05.103.

[38] Baudler A., Schmidt I., Langer M., Greiner A., Schröder U., Does it have to be carbon? Metal anodes in microbial fuel cells and related bioelectrochemical systems. *Energy & Environmental Science*, 2015, 8, 2048-2055, DOI: 10.1039/c5ee00866b.

[39] Ketep S.F., Bergel A., Calmet A., Erable B., Stainless steel foam increases the current produced by microbial bioanodes in bioelectrochemical systems, *Energy & Environmental Science*, 2014, 7, 1633-1637, DOI: 10.1039/C3EE44114H.

[40] Jain A., Gazzola G., Panzera A., Zanoni M., Marsii E., Visible spectroelectrochemical characterization of Geobactersulfurreducens biofilms on optically transparent indium tin oxide electrode, *Electrochimica Acta*, 2011, 56, 10776–10785, DOI: https://doi.org/10.1016/j.electacta.2011.02.073

[41] Yuan H., Deng L., Tang J., Zhou S., Chen Y., Yuan Y., Facile Synthesis of MnO_2/Polypyrrole/MnO_2 Multiwalled Nanotubes as Advanced Electrocatalysts for the Oxygen Reduction Reaction, *ChemElectroChem*, 2015, 2, 1152-1158, DOI: 10.1002/celc.201500109.

[42] Morris J.M., Jin S., Wang J., Zhu C., Urynowicz M.A., Lead dioxide as an alternative catalyst to platinum in microbial fuel cells, *Electrochemistry Communications*, 2007, 9, 1730-1734, DOI: https://doi.org/10.1016/j.elecom.2007.03.028

[43] Ghoreishi K.B., Ghasemi M., Rahimnejad M., Yarmo M.A., Duad W.R.W., Asim N., ismail M., Development and application of vanadium oxide/polyaniline composite as a novel cathode catalyst in microbial fuel cell, *International Journal of Energy Research*, 2013, 38, 70-77, DOI: 10.1002/er.3082.

[44] Gong X., You S., Wang X., Zhang J., Gan J., Ren N., A novel stainless steel mesh/cobalt oxide hybrid electrode for efficient catalysis of oxygen reduction in a microbial fuel cell, *Biosensors and Bioelectronics*, 2014, 55, 237-241, DOI: https://doi.org/10.1016/j.bios.2013.12.015.

[45] Cheng F., Shen J., Peng B., Pan Y., Tao Z., Chen J., Rapid room-temperature synthesis of nanocrystalline spinels as oxygen reduction and evolution electrocatalysts, *Nature Chemistry*, 2011, 3, 79–84, DOI: 10.1038/nchem.931.

[46] Jiang Y., Xu Y., Yang Q., Chen Y., Zhu S., Shen S., Power generation using polyaniline/multi-walled carbon nanotubes as an alternative cathode catalyst in microbial fuel cells, *International Journal of Energy Research*, 2014, 38, 1416-1432, DOI: 10.1002/er.3155.

[47] Ghasemi M., Duad W.R.W., Hassan A.H.A., Jafary T., Rahimnejad M., Ahmad A., Yazdi M.H., Carbon nanotube/polypyrrole nanocomposite as a novel cathode catalyst and proper alternative for Pt in microbial fuel cell, *International Journal of Hydrogen Energy*, 2016, 41, 4872-4878, DOI: https://doi.org/10.1016/j.ijhydene.2015.09.011.

[48] Blanchet E., Erable B., Solan M., Bergel A., Two-dimensional carbon cloth and three-dimensional carbon felt perform similarly to form bioanode fed with food waste, *Electrochemistry Communications*, 2016, 66, 38-41, DOI: https://doi.org/10.1016/j.elecom.2016.02.017.

Experimental results and calibration of dynamic phase shift measurement system for liquid crystals application

*Aleksandra Kalbarczyk, Leszek R. Jaroszewicz
Faculty of Advanced Technologies and Chemistry, Military University of Technology, Warsaw, POLAND
e-mail: aleksandra.kalbarczyk@wat.edu.pl

***Keywords**: Young Interferometer, phase modulation, nematicliquid crystal*

Liquid crystal (LC) devices present strong potential application in dynamic modulation of optical signal. Depth of dynamic phase modulation of light propagating in LC depends on driving signal and mesomorphic properties of LC.

Interferometric setup based on Young experience for direct measurements and analysis of dynamic phase modulation in devices based on LC mixtures is presented in this work. LC cell was inserted in one arm of the interferometer. A dynamic shift of the interference pattern relates to the phase modulation controlled by LC placed in the reference path of the beam of the interferometer. For purpose of this work, the setup was calibrated by varying the distance between reference beam and probe beam. Experimental results for 5μm-thick nematic liquid crystal mixture (6CHBT) with a homogenous orientation are shown. Dynamic phase response of nematic LC is presented for three different waveforms applied to LC cell.

The work proposed Young's interferometer with possibility to control the distance between two point sources for dynamic phase change. The calibration process have been performed to optimize the interferometer. This method allows the examination of LC relaxation phenomena and provides information about the response time of molecular switching in LC.

The proposed device is low cost, has a simple control and high tunability. Our measurement method does not require complex mathematical algorithm to compute the phase shift. Interferometer calibration results show that a small distance between two beams is required. Fringe patterns show very high contrast.

INTRODUCTION

The superposition principle states that the displacement of any point due to the superposition of wave systems is equal to the sum of the displacements of the individual waves at that point. The superposition principle is a basis of the wave theory of the light. The consequence of this principle is observed as bright or dark fringes and their distribution called as fringe pattern. When a number of waves added together produce a maximum intensity of the resultant wave the bright fringes occur. When a number of waves added together produce a minimum intensity of the resultant wave the dark fringes can be observed.

The first interference experiment was performed by Thomas Young in 1802. Young experiment demonstrates the interference between waves from two similar slits illuminated by a single source of the light (double-slit Young's interferometer). In this work, the interferometer setup is based on the Young experiment and earlier systems realized at the Institute of Applied Physics at the Military University of Technology [1-3].

Interferometry is a popular method used in medical diagnostics due to its non-destructive property. The applications are wide for example imaging of microvascular blood flow [4], middle ear diagnosis [5] or serological diagnosis of infectious disease[6]. The literature [7-8] proposes interferometric measurement methods, based on comparing images obtained from a CCD camera. They use a single CCD camera, and phase is calculated at every single pixel to give a phase map. Methods based on comparison of fringe pattern photos are limited. Complicated algorithms are supported to give a value of phase shift at each pixel, which is calculated with help of neighboring pixels. In our system we also used a CCD camera, but it has been adapted only for the purposes of adjustment of the system and to check whether the proposed system is working properly. In works[9-10], Mach–Zender interferometer configuration have been used with single photodetector. A quadrant photodetector and similar technique was proposed in work [11] to measure the angular position of parallel laser beam with interferometric precision. In our system we proposed two channel photodetector in Young interferometer using He-Ne laser as a source of light. The measurement itself is relative to the measurement using a CCD camera, less time consuming and does not require the use of complex algorithms. This is a completely new tool for phase measurements adapted for liquid crystal materials.

MATERIALS AND METHODS

The idea for the construction of the measuring system was taken from work [3] and based on the measurement system with Fiber-optic phase demodulator based on spatial integration in Young fiber interferometer system [1-2]. The study has proven the possibility to demodulate the phase of an optical signal propagating in the fiber by integration of the spatial distribution of field intensity diffraction in the Fourier plane. Field diffraction arises from the interference of light beams outputted from two single-mode fibers. The signal from the one optical fiber is a reference signal, for which the difference in the phase to the second optical fiber is measured. This phase difference is affecting the transfer bands in the resulting interference. An example of the spatial distribution of the interference field from work [12] is shown in Fig.1.

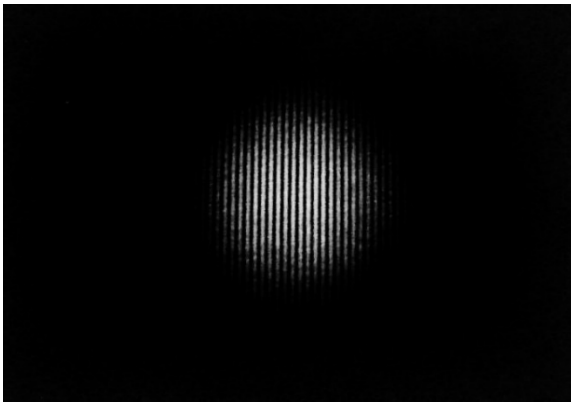

Fig. 3 Picture of fringes pattern [12].

Experimental system for measuring the phase difference of LC cells is sketched in Fig. 2 and Fig.3. The light source used in the system is a He-Ne laser (633 nm). The light from the laser passes through the polarizer (Pol_1) and is spatially filtered (*SF*) and collimated by lens (L_1). The light splits into two beams by the beam splitter (BS_1). The reference beam is reflected by a mirror (M_1) and a probe beam is reflected by a mirror (M_2). In both paths, telescopes consisting of two positive lenses were inserted to obtain a small diameter collimated beams. In order to adjust the equality of the diameter of the reference beam and the probe beam and a homogenous distribution, two small collimators with circular pinhole diameter (s = 400 μm) were situated after telescopes. We used a right angled gold coated prism to bend the light coming from the collimators by 90°. Thus, the reflected beams become parallel to each other.

The possibility to set the position of the prism enables us to change the distance between two beams (d). This feature is significantly important in the adjustment process and was used for the calibration of the system. Two rays passes through a Fourier Lens (L_2) are focused at a Fourier plane, where the interference pattern can be observed. The fringe pattern can be detected, only if both beams are focused at the same point. These adjustments are very complicated and require high manual skills and experience. In the system, photodetectors $PhoD_A$ and $PhoD_B$ with an active area of 2,5mm x 2,5mm are separated with a distance d (48μm). Photodetectors are situated exactly at the Fourier plane. In Fourier plane, the size of airy disc containing fringe pattern is determined by the wavelength, the source size s and the focal length f. The second beam splitter was inserted in the system in order to monitor the fringe pattern by a CCD camera. During the measurement liquid crystal cell is inserted in a probe beam and oriented parallel to the polarization of the light. If a specific temperature for measurement of the LC material is required, the cell is connected to temperature controller.

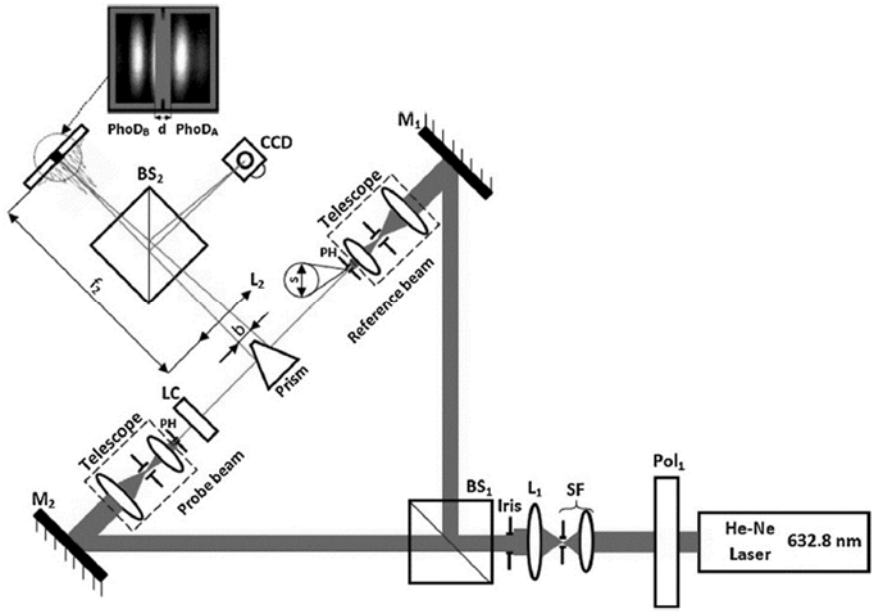

Fig. 2. The scheme of the interferometer setup. Light source: HeNe laser with λ = 633 nm; Pol1: linear polarizers; BS1 and BS2 beam splitters; M1 and M2: mirrors; PH: pinhole; LC: liquid crystal cell; L1, L2: lenses [3].

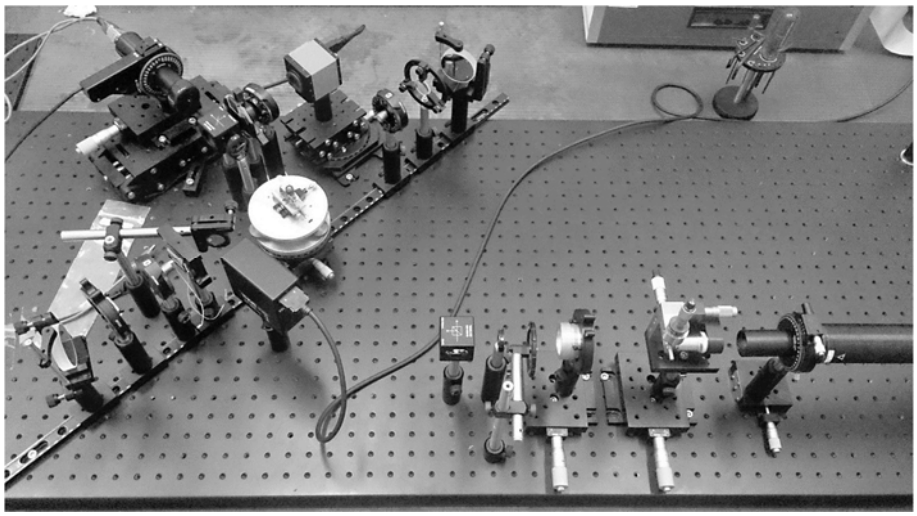

Fig. 3. The picture of the designed interferometer system.

RESULTS

The distance between two point sources and distance between two photodetectors significantly affects the performance of our setup. Due to the fact, that the distance between two photodetectors is fixed, the calibration process requires the adjustment of the distance between two rays, which is affected by the position of the

prism. If the position of the prism is changed, the intensities collected by photodetectors also change. Those intensities are collected in an acquisition card (DAC). LabVIEW software was prepared to record the data. In general, two intensities are added or substracted to each other:

$$Sum = I_A + I_B \quad (1)$$

$$Diff = I_A - I_B \quad (2)$$

In reference [1], the detected signals can be described as follows:

$$S_R = a_1 + a_2 cos\Delta\varphi - a_3 sin\Delta\varphi \quad (3)$$

$$S_L = a_1 + a_2 cos\Delta\varphi + a_3 sin\Delta\varphi \quad (4)$$

where S_L , S_R are the signal from the left detector and the right detector, respectively. Those signals depend on the combination of cosine and sine of the measured phase shift. Coefficients a_1, a_2, a_3 are constants depending on the wavelength, the distance between two beams, the focal length f and the size of the beam s can be calculated from [1]:

$$a_1 = const \int_{q/2}^{\infty} A^2(\rho) d\gamma_f dx_z \quad (5)$$

$$a_2 = const \int_{q/2}^{\infty} A^2(\rho)[2cos^2(\theta)\cos(4\pi bu)]dx = const \int_{-\infty}^{-q/2} A^2(\rho)[2cos^2(\theta)\cos(4\pi bu)]dx \quad (6)$$

$$a_3 = const \int_{q/2}^{\infty} A^2(\rho)[2cos^2(\theta)\sin(4\pi bu)]dx = -const \int_{-\infty}^{-q/2} A^2(\rho)[2cos^2(\theta)\sin(4\pi bu)]dx \quad (7)$$

Then, using the relationship describing the signals from the left and right side, the sum $Sum = (S_R + S_L)$ and the difference $Diff = (S_L - S_R)$ can be expressed:

$$Sum(\Delta\varphi) = 2a_1 + 2a_2 cos\Delta\varphi \quad (8)$$

$$Diff(\Delta\varphi) = 2a_3 sin\Delta\varphi \quad (9)$$

According to equations (8), (9) a_1 is the amplitude of the sum function, a_2 is the average value of the sum function and a_3 is the average value of the difference function. To determine the phase difference between the two beams we need to know the sum and the difference of the signal values of coefficients a_1, a_2, and a_3:

$$tg(\Delta\varphi) = \frac{\Delta S_{diff} * a_2}{a_3(\Delta S_{sum} - 2a_1)} \quad (10)$$

$$\Delta\varphi = arctg \frac{\Delta S_{diff} * a_2}{a_3(\Delta S_{sum} - 2a_1)} \quad (11)$$

The information about an error of the phase difference, induced by this system was analyzed and described in reference and has the following expression [1]:

$$\varepsilon = \frac{\rho - 1}{2} \sin(2\Delta\varphi) \quad (12)$$

where: $\rho = \frac{a_3}{a_2}$. According to equation (12), in case of $\rho = 1$the error is equal to zero. Those results indicate that $a_2 = a_3$ and the error is not dependent on the phase difference value.

For the calibration process, 5μm-thick nematic liquid crystal mixture (6CHBT) was fabricated with a homogenous orientation. The cell was inserted in one arm of the interferometer and aligned parallel to the polarization of the illuminating light. For the purpose of this part, three different waveforms were proposed. To find the situation of equality of $a_2 = a_3$, the distance between two beams b was varied. In Fig. 4, a modulated signal applied to LC is shown. For all cases the amplitude of AC pulses was fixed at 8V and off state time is equal to AC square signal. The phase fluctuation is detected during the alternating square waveform pulses. When the carried signal is removed molecules relax to their initial state. In the work, only selected measurements are implemented.

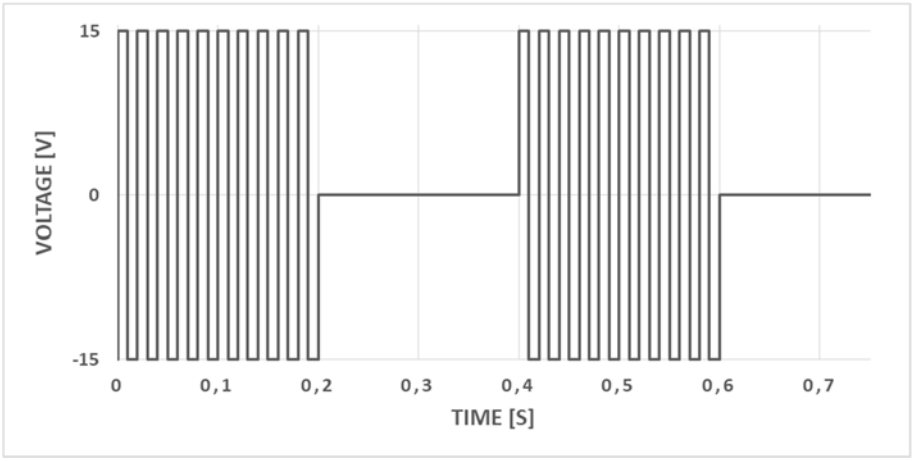

Fig. 4. The voltage pattern applied to LC device (1kHz AC voltage modulated by envelope (5kHz, 10kHz, 50kHz)).

The numbers (1-13) presented on Figures 7-10 correspond to the distance between two spots b. The higher number, the higher distance b.We have presented only selected measurements what is related to higher errors obtained for missing cases and visuality of results. The fringe pattern photos obtained for situation number 1 and 13 are shown in Fig. 5 and Fig. 6.

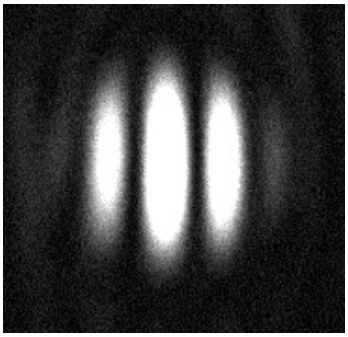

Fig. 5. The fringe pattern obtained for small distance between two beams b.

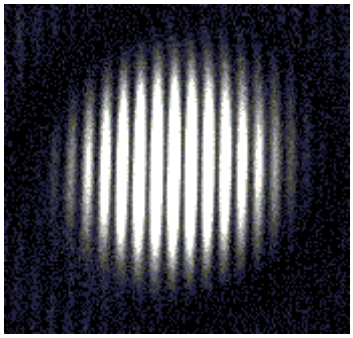

Fig. 6. The fringe pattern obtained for large distance between two beams b.

The equality of coefficients $a_2 = a_3$ can be noticed as the smoothness of the phase shift characteristics. From the dynamic phase measurements presented in Fig. 7, Fig. 8 and Fig. 9, it can be observed that first three situations are preferred.

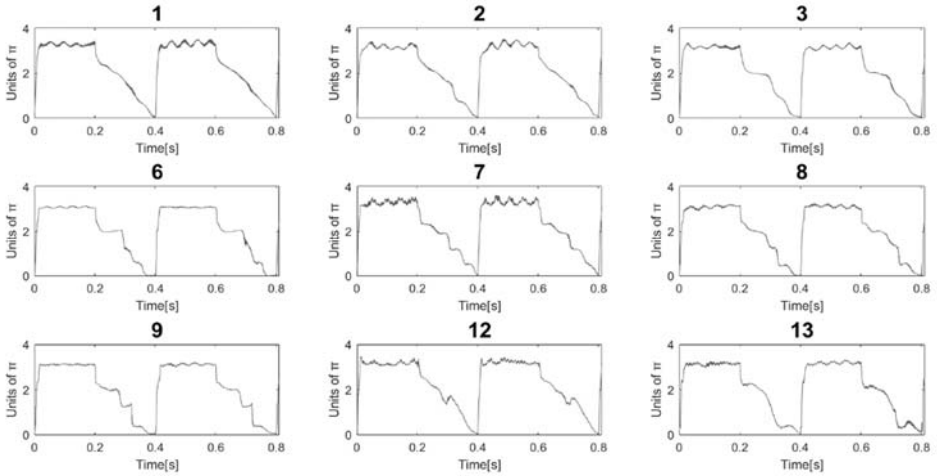

Fig. 7. Dynamic phase measurements at different values of the distance between two beams b. The voltage pattern applied to LC device was 1kHz AC Voltage modulated by 5kHz envelope.

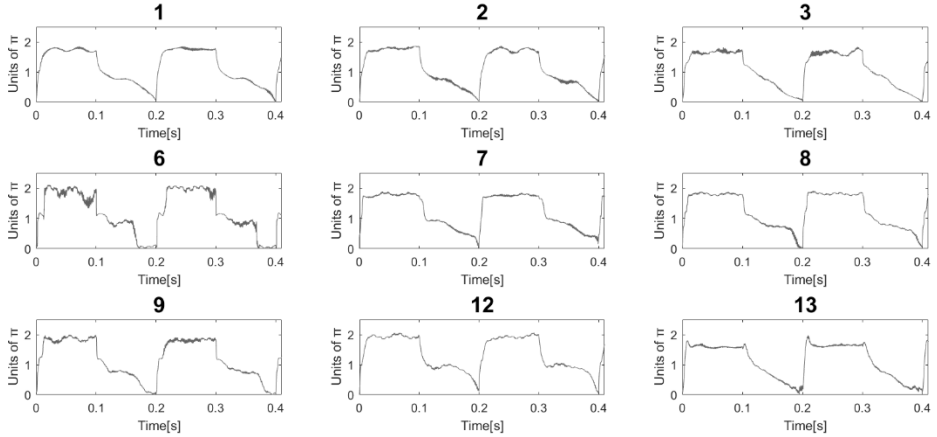

Fig. 8. Dynamic phase measurements at different values of the distance between two beams b. The voltage pattern applied to LC device was 1kHz AC Voltage modulated by 10kHz envelope.

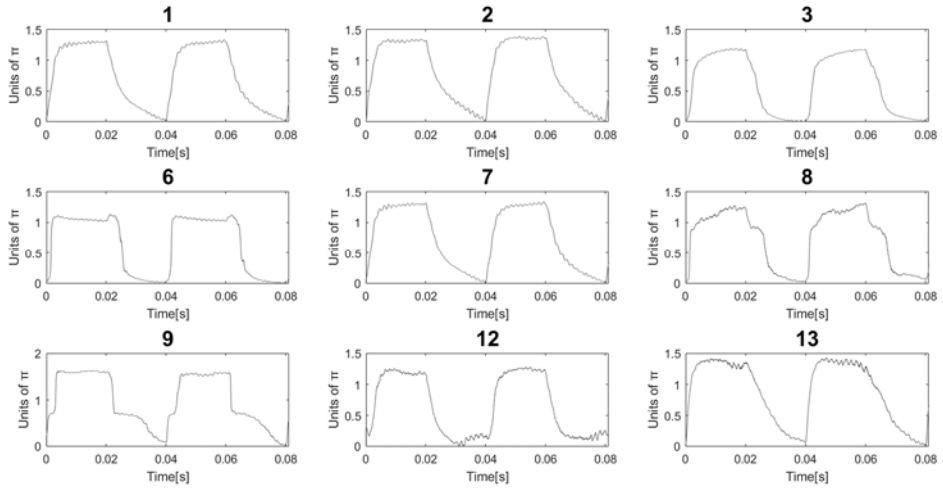

Fig.9. Dynamic phase measurements at different values of the distance between two beams b. The voltage pattern applied to LC device was 1kHz AC Voltage modulated by 50kHz envelope.

The fringe pattern optimized for the best position of the prism is shown in Fig. 5. Moreover, the investigation of the sum and difference as a function of phase was studied and values of a_2 and a_3 were calculated. In case of the example shown in Fig. 7, the part of the molecule switching (rising) in a range from 0 to 2π for the sum and difference signals was examined. The sum and difference plots are sketched in Fig. 10. The best results were obtained for the first situation sketched in Fig. 5. Calculated values of a_2 and a_3 are:

$$a_2 = 0{,}2840$$
$$a_3 = 0{,}2778$$

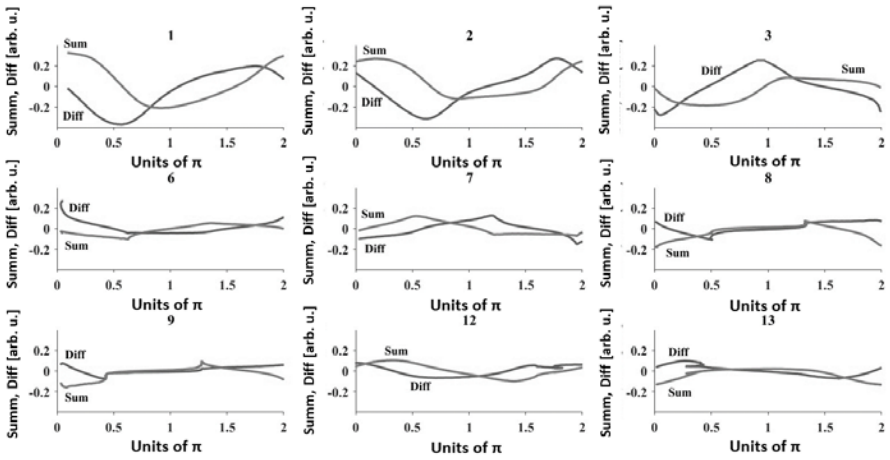

Fig. 10. Sum and Diff as a function of the phase difference (Δφ) at different values of the distance between two beams b.

The theoretical function of the sum and difference signals were calculated from (8), (9) and presented in Fig. 11. In this case, the absolute error for obtained values can by calculated from equation (12).

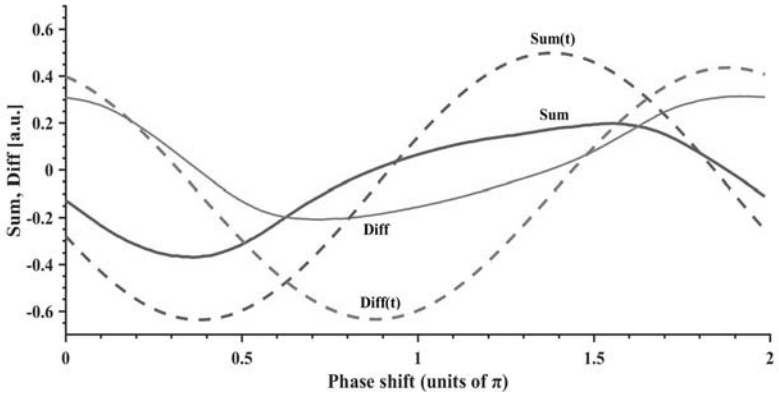

Fig. 11. Sum and Diff as a function of the phase difference (Δφ) obtained for the first situation. Sum(t) and Diff(t) are theoretical functions calculated from eq. (8) and (9).

CONCLUSION

Our setup provides a dynamic phase measurement in free space for LC cell using Young's interferometer. A dynamic shift of the interference pattern relates to the phase modulation controlled by LC placed in the reference path of the beam of the interferometer. The proposed device is low cost, has a simple control and high tunability. Our measurement method does not require complex mathematical algorithm to compute the phase shift.

The proposed interferometer could be implemented as a high-speed scanning fringe-pattern technology for precision measurement. The most difficult issues in the adjustment were the appropriate setting of collimators, because it required high accuracy, high manual skills and technical procedures to obtain a comparable values of the light intensity in both arms of the interferometer. The obtained fringe patterns show very high contrast.

Interferometer calibration results show that a small distance between two beams b is required. However, in the future it is planned to evaluate b value. The distance between two beams can be also calculated from the fringe pattern photo. To improve this setup in the future, the acquisition card should be changed, and the system could be adapted for a different software.

REFERENCES

[1] I. Merta, Z. Hołdyński, L. Jaroszewicz, Bicell-photodetector in the Fourier plane as a fiber optic homodyne phase demodulator: theoretical model and experimental results, *Applied Optics,* 52(19), 4468-4476, (2013).

[2] Z. Hołdyński, I. Merta, T. Nasiłowki, L. Jaroszewicz, Bi-cell homodyne phase demodulator - experimental results, *Proc. of SPIE*, vol. 8794, 87940G, (2013).

[3] N. Bennis, I. Merta, A. Kalbarczyk, Real time phase modulation measurements in liquid crystals, *Opto-Electronics Review*, 25,69–73,(2017)

[4] C. Magnain, A. Castel, T. Boucneau, M. Simonutti, I. Ferezou, A. Rancillac, T.Vitalis, J.A. Sahel, M. Paques, M. Atlan, Holographic laser Doppler imaging ofmicrovascular blood flow, *J. Opt. Soc. Am. A*, 31(12), 2723–2735, (2014).

[5] A. D. Drake, Laser interferometry applied to middle ear diagnosis, Proceedings of the fifth New England Bioengineering Conference, 225-228, (1977)

[6] A. Kussrow, C. S. Enders, A. R. Castro, D.L. Cox, R.C. Ballard, D.J. Bornhop, The potential of backscattering interferometry as in vitro clinical diagnostic tool for the serological diagnosis of infectious disease, Analyst, 135(7), 1535-1537, (2010)

[7] J. Burke, Application and optimization of the spatial phase shifting technique in digital speckle interferometry, Carl von Ossietzky University, Oldenburg, Germany, (2000).

[8] V. Bavigadda, A new versatile electronic speckle pattern interferometer for vibration measurements, Dublin Institute of Technology, Dublin, Ireland, 2008.

[9] Th. R. Clark and M. Dennis, Coherent optical phasemodulation Link, *IEEE Photon. Technol. Lett*. 19, 1206–1208 (2007).

[10] N. Fernandes, K. Gossner, and H. Krisch, Low power signal processing for demodulation of wide dynamic range of interferometric optical fibre sensor signals, *Proc. SPIE* 7653, 765328 (2010).

[11] P. Paolino and L. Bellon, Single beam interferometric angle Measurement, *Opt. Commun*. 280, 1–9 (2007).

[12] Z. Hołdyński, Modelowanie i badanie eksperymentalne światłowodowego demodulatora fazy z całkowaniem przestrzennym w płaszczyźnie Fouriera, Wojskowa Akademia Techniczna, Warszawa, 2010.

Investigation of liquid crystals with frequency controlled birefringence

*Aleksandra Kalbarczyk[1], Noureddine Bennis[1], Przemysław Kula[1], Leszek R. Jaroszewicz[1]
[1]Faculty of Advanced Technologies and Chemistry, Military University of technology, Warsaw, POLAND
e-mail: aleksandra.kalbarczyk@wat.edu.pl

***Keywords**: liquid crystal, dielectric relaxation, dielectric anisotropy, dynamic phase demodulation*

Due to the optical quality and high birefringence liquid crystals (LCs) are extensively used in electro-optical applications. In present work, the optical and phase behavior of a novel nematic liquid crystal (NLC) with frequency controlled birefringence and dual frequency liquid crystal (DFLC) have been investigated. A novel nematic mixture with frequency controlled birefringence is a composition of three different dielectrically positive families of rod-like molecules. The frequency dependence of parallel component of electric permittivity is different for each family. Instead of bistable DFLC, this mixture is dielectrically positive in the whole range of frequencies. In this work, the relationship of frequency modulation and amplitude modulation to the relaxation dynamics of LC is examined. Our material allows to create a multiple gray levels with a stabilized phase in frequency modulation, what makes this material of a special interest for optical and photonic applications.

INTRODUCTION

Liquid crystal (LC) materials are widely used in optical and photonic devices. The term "Liquid crystal" was firstly introduced by German physicist Otto Lehmann at the end of the last century. He was a follower of the work of the Austrian botanist Friedrich Reinitzer. Reinitzer discovered that the cholesterol benzoate after melting at 145°C passes into the turbid liquid, which when heated to 179°C, becomes clear and does not change at higher temperatures. With a polarizing microscope Lehmann observed that the turbid phase has optical anisotropy and called it mesomorph, which is characterized by the presence of LC. The temperature range of existence of the mesophase is different for different substances and ranges within a temperature range from -20°C to +250°C. Heating LC above the upper temperature limit of existence of the mesophase (T_{iso}) leads to another transition phase - the state of isotropic liquid.

Liquid crystal exhibits optical and dielectric anisotropy as crystal. LC director is easily reoriented while supplying a low voltage signal. Due to the optical quality and high birefringence they are extensively used in electro-optical applications. From application point of view, the critical issue of LC technology is slow response time.

To improve the switching time, low viscosity and high birefringence are required, however, it increases costs and causes technology problems. Another idea is to modify the liquid crystal mixture. For this purpose, polymer networks [1-3], carbon nanotubes [4], blue phases [5] or dual frequency liquid crystals (DFLC) [6] were proposed. This last option, deals with a problem of slow response the best, as for now. A DFLC consists of two types of compounds. One of them is positive and its dielectric anisotropy is positive at low frequencies of the applied electric field, but it decreases with higher frequencies to negative value. The second is negative and its dielectric anisotropy is negative and almost constant in a whole range of frequencies [7]. For this reason, the LC director can be reoriented by varying the frequency of the applied electric field, instead of the amplitude. In general, DFLC materials obtains higher viscosity than normal NLC mixtures. The main drawback of DFLC materials is high crossover frequency. Therefore, there are problems with high driving frequencies (>50 kHz), costs of the applied signal, strong heat dissipation and dielectric heating.

In this work a novel nematic liquid crystal (NLC) with frequency controlled birefringence is investigated. This material is a composition of three different families of rod-like LC. The novelty of this material is that all of the components are dielectrically positive. The frequency dependence of parallel component of electric permittivity, which is different for each component. Therefore, the dielectric anisotropy is dependent on frequency for one component, whereas for others is not. In such case the characteristic of the dielectric anisotropy has smooth changes in range of kHz frequencies. Instead of bistable DFLC, this mixture is positive in the whole range. Thus, the above-mentioned drawbacks for DFLC can be eliminated. The application of this mixture was proposed as low aberration fast switching micro lenses[8].

MATERIALS AND METHODS

Dual frequency liquid crystals

Dual frequency liquid crystals (DFLCs) are materials which $\varepsilon_{\parallel}$ is highly dependent on the frequency range of kHz up to MHz, while $\varepsilon_{\perp}$ is independent. DFLC mixture consists of two groups of compounds. One is dielectrically positive, but as applied frequency of a signal increases, the relaxation leads to decrease $\Delta\varepsilon$. The second compound has negative dielectric anisotropy in a wide range up to MHz frequencies. Thus, dual frequency liquid crystals are dielectrically positive at low frequencies and dielectrically negative at higher frequencies. The crossover frequency is a point where the dielectric anisotropy changes it sign. This group of materials was designed for fast response and high optical quality for laser beam steering. DFLC can be used in both homogeneous and homotopic cells. A homogenous cell requires a low frequency to reorient the director and a high frequency to relax the molecules to initial position. In a homeotropic alignment this situation is reversed. In general,

a homogenous cell has higher birefringence and dielectric anisotropy, while a homeotropic cells are characterized by better contrast between crossed polarizers. In applications homogenous alignment is used for phase modulation and a homeotropic cells are preferred for displays. In dual frequency liquid crystals rise and decay times of response on applied signals are connected with the voltage. The response time of the cell is faster, while a voltage applied is higher. Equations for rise and decay time for DFLC materials can be expessed as [9]:

$$\tau_{decay} = \frac{\tau_0}{\left(\frac{V_h}{V_{th,h}}\right)^2 + 1} \quad (1)$$

$$\tau_{rise} = \frac{\tau_0}{\left(\frac{V_l}{V_{th,l}}\right)^2 - 1} \quad (2)$$

where $\tau_o = \frac{\gamma_1 d^2}{K_{11}\pi^2}$, is free relaxation time of the director, V_h and V_l are voltages for turning-off and turning-on, respectively, $V_{th,h}V_{th,l}$ are three-shold voltages at high and low frequencies, d is the thickness of the cell and γ_1/K_{11} is the visco-elastic coefficient for the LC mixture. In general, DFLC materials obtains higher viscosity than normal NLC mixtures. The main disadvantage of DFLC materials is high crossover frequency. Therefore, there are problems with high driving frequencies (>50 kHz) and costs of the applied signal. Further, strong heat dissipation and dielectric heating are observed.

In this work properties of DFLC material has been investigated to compare the results with novel positive nematic frequency controlled material. The 5μm cell filled with DFLC mixture (1999A) was studied. The frequency dependence on $\varepsilon_{\parallel}$ and $\varepsilon_{\perp}$ is shown in Fig. 2. From results of dielectric measurements, a cross-over frequency is given as 7,41kHz. It determines positive and negative dielectric of the material.

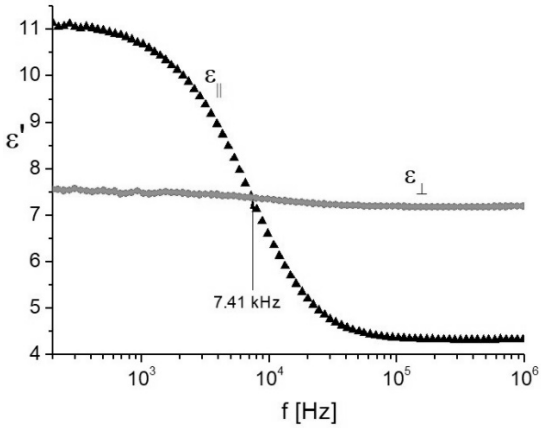

Fig. 1. Dispersion spectra for DFLC recorded for parallel and perpendicular orientations. The dielectric anisotropy changes its sign at 7,41 kHz.

Novel mixture with frequency controlled birefrigence (5005)

In this work, a novel kind of LC with frequency controlled birefringence is presented. All mixtures were prepared at Institute of Chemistry (WAT). Cells consist of a glass substrates, spacers determining cell thickness and ITO electrodes, which allows to apply driving signal. Cells were fabricated at Department of Physics and Crystals Technology (WAT). Cells of defined thicknesses were filled with the mixtures under study. Presented dielectric measurements were performed at Institute of Physics (UJ).

The LC nematic mixture under a code name (5005) is a composition of three different families with rod-like molecular shape. The effect of frequency is dependent on different values of parallel components of electric permittivity for component 1, 2 and 3. All those components are dielectrically positive or neutral nematics. The special composition of this three components enables the low voltage driving signal with variable modulation frequencies, which shows the unique properties of mixture (5005). The application for mixture (5005) was proposed as low aberration microlenses [8]. Dispersion spectra of this mixture is shown in Fig. 2. For this mixture $\Delta\varepsilon_{\parallel}$ and $\varepsilon_{\perp}$ are strongly decreasing with increasing frequency. At low frequency regime mixture (5005) exhibits a large $\Delta\varepsilon$ about 5.5.

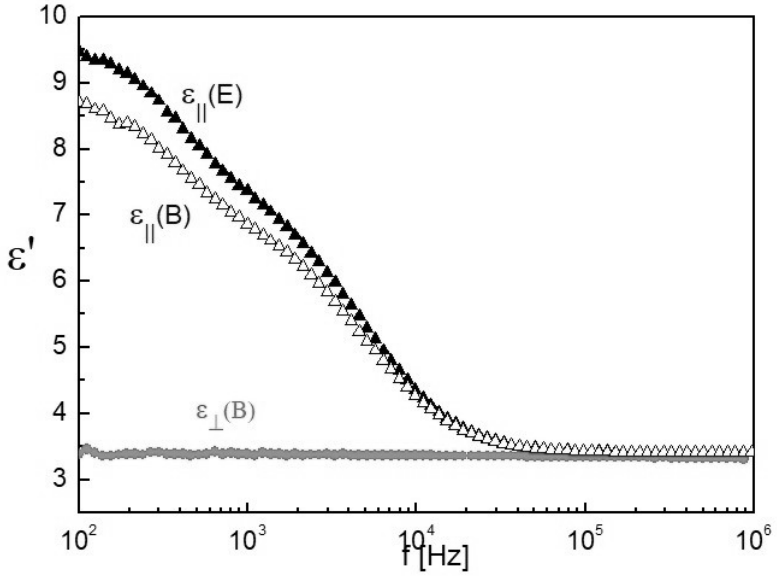

Fig. 2. Dispersion spectra for mixture (5005) recorded for parallel and perpendicular orientations.

As it was mentioned above mixture (5005) consists of three different groups of families, which are presented in Fig. 3.

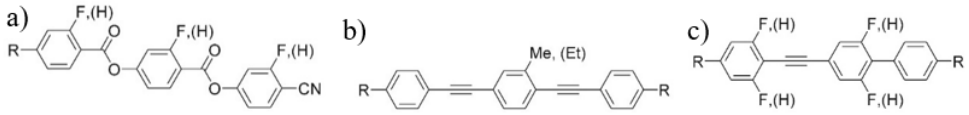

Fig. 3. Chemical structure of: a) compound 1, b) compound 2, 3) compound 3.

- Compound 1 is the fluorine substituted 4-[(4-cyanophenoxy)carbonyl]phenyl 4-alkylbenzoates (Fig. 10.a) with the phase transition to isotropic liquid (Iso) at 239.5°C. It is a dielectrically positive nematic material anisotropy. The dipole moment of polar groups is the principal molecular axis, therefore $\Delta\varepsilon$ is large and positive. A larger $\Delta\varepsilon$, helps to reduce the switching. However, he molecules in compound 1 are very large. The longer the molecule, the more viscous is the LC medium, hence the slower is a molecule rotation and lower its relaxation frequency.
- Component 2 is alkyl-alkyl bistolanes with the temperature of Iso at 127.1°C (Fig.10. b). This material is used in the mixture as a LC solvent medium. Compound 2 is a dielectrically neutral material. In Fig. 10 the dielectric dispersion and temperature dependence on $\Delta\varepsilon_{\parallel}$ and $\varepsilon_{\perp}$ are sketched. Its non polar liquid crystal compound, its dipole moment is very small, thus its $\Delta\varepsilon$ is expected to be small (around 0,6). For this compound $\Delta\varepsilon_{\parallel}$ and $\varepsilon_{\perp}$are almost constant and do not depend on the frequency of the electric field.
- Compound 3 is the fluorine substituted alkyl-alkyl phenyl-tolanes (Fig. 10.c) with phase transition to Iso at 152.9°C. It is a dielectrically positive nematic as compound 1 having dielectric anisotropy dependent in range of kHz frequencies.

The combination of component 1 and 3 leads to frequency controlled birefringence at exact range of frequency in mixture (5005). As result of this combination LC mixture (5005) is a positive nematic with frequency controlling at kHz range. In this work properties of all compounds were studied.

We traced the director dynamics by measuring the optical phase shift response as a function of modulation frequency of the applied electric field. The phase shift achieves its maximum value when the molecules have enough time to relax to their horizontal position and it decreases when modulation frequency increases. To measure dynamic phase response of LC cells we proposed interferometer setup based on Young experience, which is described in reference [10]. The scheme of our setup is shown in Fig. 4. For dynamic phase measurements the cells were situated in the probe beam path and oriented such as its optical axis parallel to the polarization of the incident light.

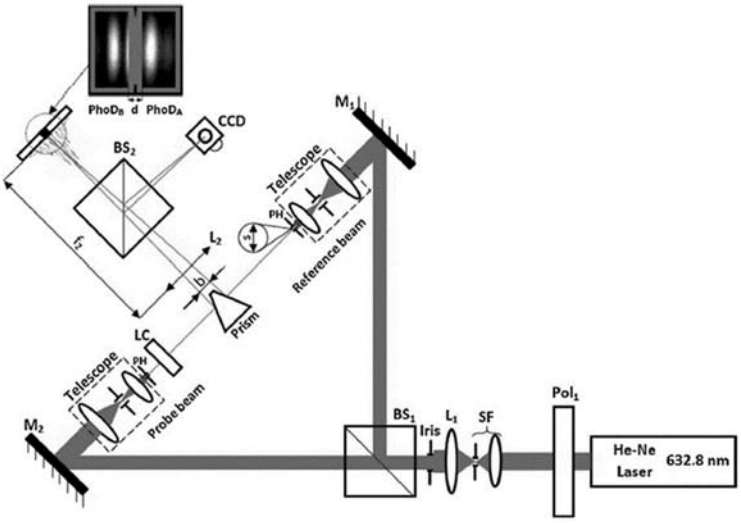

Fig. 4. The scheme of the interferometer setup. Light source: HeNe laser with λ = 633 nm; Pol1: linear polarizers; BS1 and BS2 beam splitters; M1 and M2: mirrors; PH: pinhole; LC: liquid crystal cell; L1, L2: lenses [10].

RESULTS

In this chapter, the dynamic phase measurements has been presented, when the frequency modulation and amplitude modulation of electric field were applied to the cells.The waveforms used for amplitude modulation and frequency modulation in the interferometer setup are sketched in Fig. 5 and Fig 6, respectively. In amplitude modulation measurements the step of the voltage value was 1V. For frequency modulation, waveform applied to LC modulator consists of 1 kHz square signal modulated by square envelope. The envelope modulation step was 2kHz. The work presents only selected results.

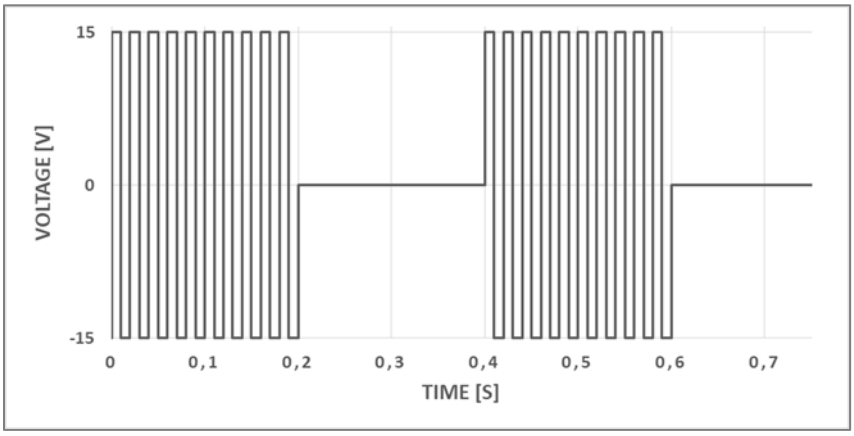

Fig. 5. The voltage pattern applied as amplitude modulation (1kHz AC voltage modulated by 5kHz envelope).

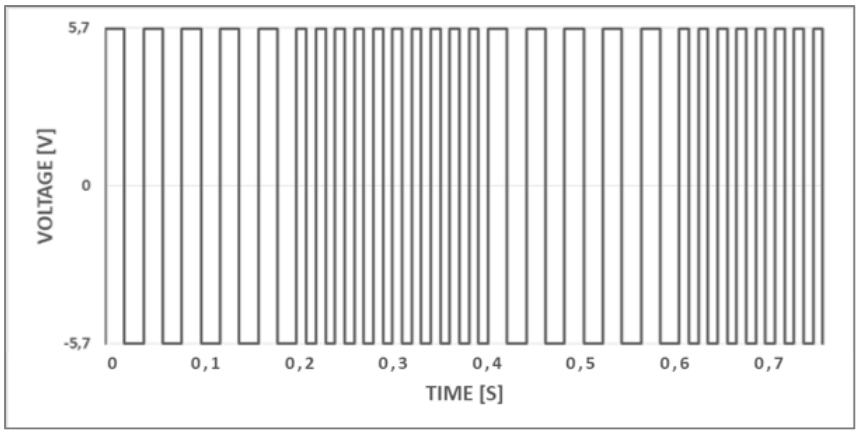

Fig. 6. Applied waveform as frequency modulation signal.

The response time in case of the dynamic phase measurement can be studied more precisely. The results of dynamic phase difference for the mixture(5005) with varying voltage value are presented in Fig. 7. Clear relationship between the voltage value and the rise and decay time is drawn. The rise time is strongly affected by the voltage level. When the voltage applied is small, the rise time is lower, and this relation is proportional. However, the fall time is not influenced by the voltage value. Its strongly dependent on the LC parameters such as elastic constant, viscosity and the cell thickness.

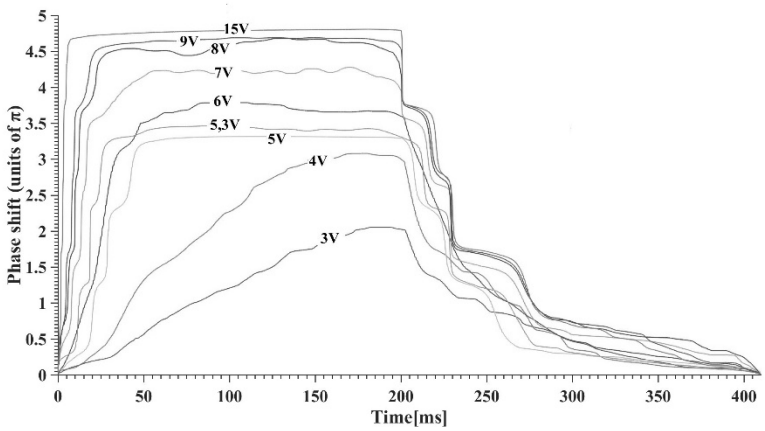

Fig. 7. Dynamic phase measurement response to amplitude modulation waveform for mixture (5005).

Dynamic phase measurement for frequency modulation of mixture (5005) in Fig.8, shows that the maximum modulation depth increase with increasing modulation frequency. In this graph a square waveform with 5,69V amplitude and an increasing frequency was used to modulate a phase of an input beam. As the

frequency of the signal changes, the phase of the carrier beam changes correspondingly. The maximum number of allowable phase levels could depend on the relationship of the carrier frequency and the envelope frequency to the relaxation dynamic of the LC. The dynamic phase measurement versus frequency modulation is shown in Fig. 9. Dotted line is linear approximation for obtained results. A linear characteristic cannot be realized due to the limitation of the acquisition card. In our system, the sample frequency is to small and the data for more complicated signals cannot be recorded.

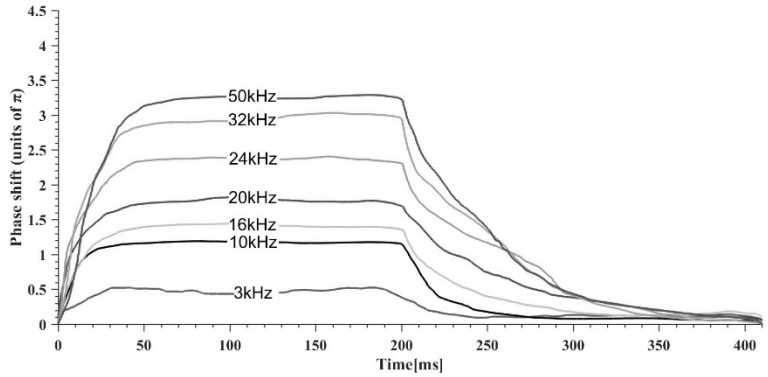

Fig. 8. Dynamic phase measurement for frequency modulation of mixture (5005).

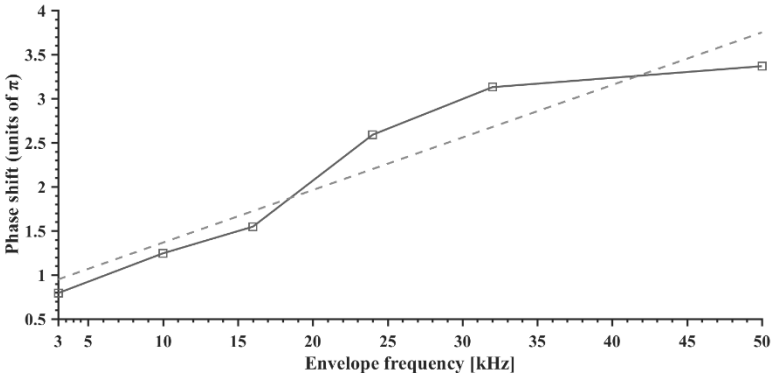

Fig. 9. Dynamic phase measurement for frequency modulation of mixture (5005). Dotted line is a trend line.

It is worth to emphasizing that the frequency phase modulation in mixture (5005) affects the presence of gray levels. This material allows to create a multiple levels with a stabilized phase what can be a huge benefit for the LC technology, especially LCDs. Slow relaxation time comes from large viscosity of the studied mixture in comparison with typical NLC, because of highly polar positive $\Delta\varepsilon$ of compound 1.

The effect of each component in the dynamic measurements was also investigated. In Fig. 10. we presented dynamic phase measurement response

to amplitude modulation waveform at fixed voltage 15V of mixture (5005), compound 1, compound 2, and compound 3.It can be noticed that compound 2 may cause a slow response time of mixture (5005). In Fig. 11 we presented dynamic phase measurement for frequency modulation with high frequency fixed at 50kHz of mixture (5005), compounds 1, and compound 3.The frequency modulation was only detected for compound 1 and compound 3. However, the modulation is relatively small and appears in small range of frequencies (>50kHz). From these results we are not able to define which of the components leads to the frequency modulation of mixture (5005) in the range of 3-50kHz.

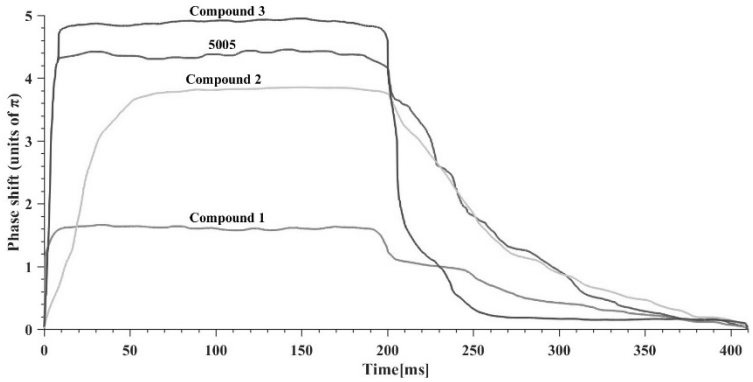

Fig. 10. Dynamic phase measurement response to amplitude modulation waveform at fixed voltage 15V of mixture (5005), compound 1, compound 2, and compound 3.

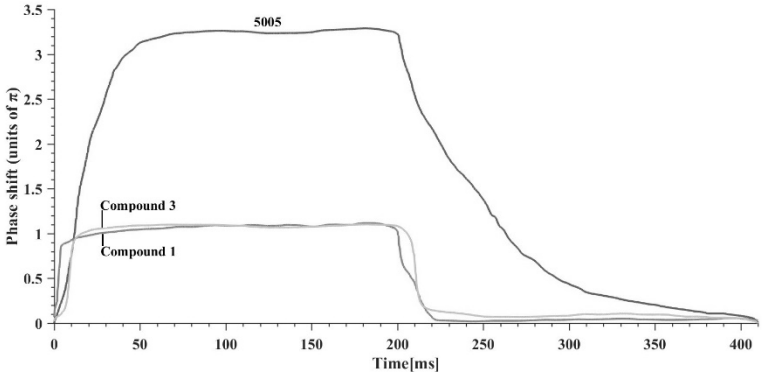

Fig. 11. Dynamic phase measurement for frequency modulation with high frequency fixed at 50kHz of mixture (5005), compounds 1, and compound 3.

For DFLC material, the results obtained from the dynamic phase measurements gives us more information about the behavior of this material. The measurements taken with the amplitude modulation shows different response in rise part and relaxation of the phase shift curve (Fig. 12). In comparison to mixture (5005),

DFLC molecules rise is delayed in respect of the carrier signal. As expected, the relaxation observed is definitely faster. However, the frequency modulation for DFLC material does not cause the existence of multiple levels (Fig. 13). In fig. 14 we presented the comparisation of obtained results for both materials. Dual frequency effect allows to obtain only 3 levels, with the intermediate state which is much slower, then the other two. Frequencies below 11kHz exhibits a response of 4kHz modulation, when frequencies above 11kHz exhibits a response of 50kHz modulation. The fast response is observed for these frequencies. This effected can be related with the sharpness of the dispersion spectra.

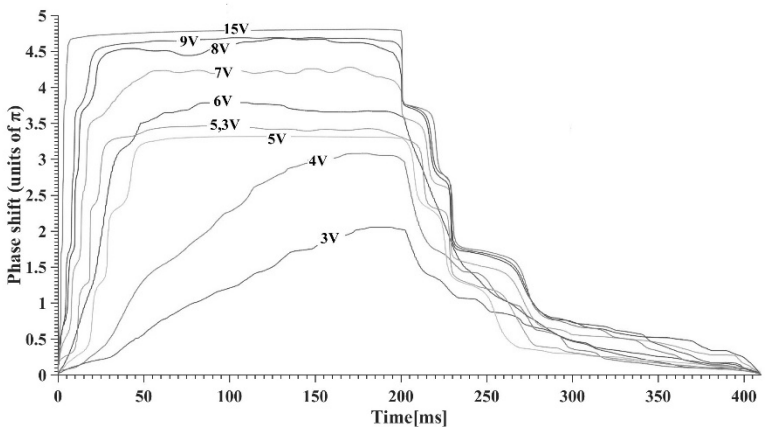

Fig. 12. Dynamic phase measurement for amplitude modulation of DFLC.

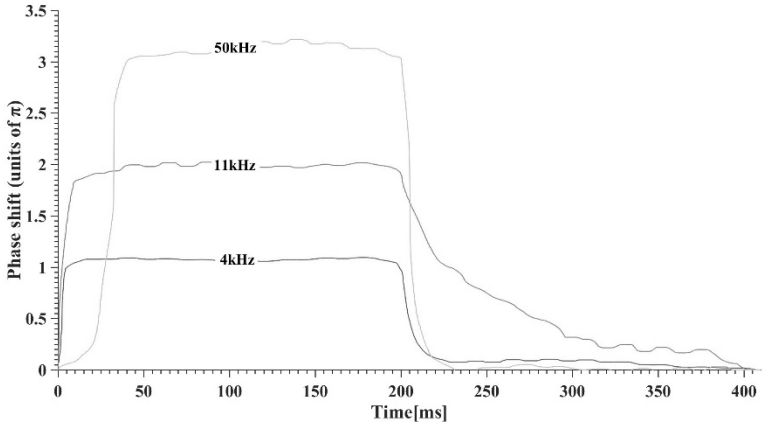

Fig. 13. Dynamic phase measurement for frequency modulation of DFLC.

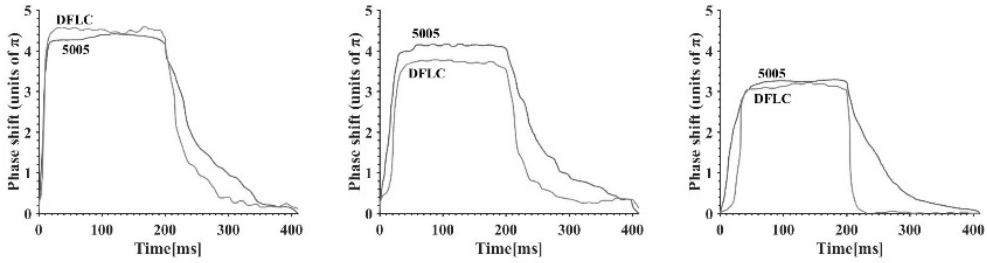

Fig. 14. From the left side; Dynamic phase measurement for amplitude modulation with voltage fixed at 15V of mixture (5005) and DFLC; Dynamic phase measurement for amplitude modulation with voltage fixed at 7V of mixture (5005) and DFLC; Dynamic phase measurement for frequency modulation with high frequency fixed at 50kHz of mixture (5005) and DFLC.

CONSLUSION

It has been proved that the relaxation mechanism and deep of phase modulation depend on amplitude modulation and frequency modulation. This is due to the different behavior of the LC molecules on the applied voltage and its nature. For frequency modulation the maximum modulation depth increase with increasing modulation frequency. As the frequency of the signal changes, the phase of the carrier beam changes correspondingly

The maximum number of allowable phase levels could depend to the relationship of the carrier frequency and the envelope frequency to the relaxation dynamic of the LC. For frequency modulation the response time of the cell is not affected as in amplitude modulation. To understand this problem, the Frederic-Leslie equation, which describe the response of the LC should be adapted for frequency. The frequency phase modulation in mixture (5005) affects the presence of gray levels. This material allows to create a multiple levels with a stabilized phase. For each frequency the rise and decay timer are comparable, what cannot be obtained in amplitude modulation. It can be a huge benefit for the LC technology, especially LCDs.

The impact of each component on the overall behavior of mixture (5005) was investigated. The first attempt to improve the response time was taken. In the future it is planned to replace compound 2 which strongly affects LC response.

In case of DFLC the presence of multiple grey levels is not observed. The parallel constant of the dielectric anisotropy is to sharp, thus, the frequency range is small. Moreover, the rise and decay time are strongly affected in case of frequency modulation. Each level has different characteristic. As for now, this phenomena cannot be explained.

In the future it is planned to measure the frequency phase modulation varying the amplitude value. To understand the frequency impact on rise and decay time, this phenomenon must be thoroughly investigated. As for now, this effect have not been widely studied and presented in the literature

REFERENCES

[1] H. Ren and S.-T. Wu, "Tunable electronic lens using a gradient polymer network liquid crystal" *Appl. Phys. Lett*. 82(1), 22–24, (2003).

[2] A. Kalbarczyk, "Temporal phase stabilization in Liquid Crystals using Polymer Stabilized Network", MUT, Warsaw, (2016).

[3] R.A.M Hikmet, J. Lub, Anisotropic Networsk and gels obtained by photo-polimerization in liquid crystalline state: synthesis and applications, Prog. Polym. Sci., 21,1165-1209, (1996).

[4] R.A.M Hikmet, J. Higgins, Fast switching anisotropic networks obtained by in situ photopolimerization of liquid crystal molecules, Liq. Cryst., 12(5), 831-845, (1992).

[5] H. Ren, Y.-H. Lin, and S.-T. Wu, "Adaptive lens using liquid crystal concentration redistribution" *Appl. Phys. Lett*.,88(19), 191116, (2006).

[6] R. Rajasekharan, Q. Dai, H. Butt, K. Won, T. D. Wilkinson, and G. A. J. Amaratunga, "*Optimization of nanotube electrode geometry in a liquid crystal media from wavefront aberrations*" Appl. Opt.,51(4), 422–428, (2012).

[7] I.-C. Khoo, S.-T. Wu, Optics and Nonlinear Optics of Liquid Crystals, *Appl. Phys. Lett.* 96(11), 113505, (2010).

[8]J. F. Algorri, N. Bennis, Low aberration and fast switching microlenses based on a novel liquid crystal mixture*, OPTICS EXPRESS,* 25(13), 14795-14808,(2017).

[9] Q. Song, Fast response dual frequency liquid crystal materials*,* PhD dissertation, Tsingua University, (2010).

[10] N. Bennis, I. Merta, A. Kalbarczyk, Real time phase modulation measurements in liquid crystals, *Opto-Electronics Review*, Vol. 25, 69–73, (2017).

Additive Manufacturing of stainless steel, advantages and disadvantages of the process – short review

*Magdalena Karpowicz
Department of Advanced Materials and Technologies, Military University of Technology, Warsaw, POLAND
e-mail: magdalena.karpowicz@wat.edu.pl

***Keywords**: Additive Manufacturing, Laser Engineered Net Shaping, stainless steel, corrosion resistant steel, austenitic steel*

ABSTRACT

The main part of this work is a comprehensive literature review, which clearly shows that the microstructure of stainless steels manufactured by additive technologies is fundamentally different from the microstructure of this steel manufactured in a conventional technique (such as: shaping process, plastic forming, powder metallurgy). Literature data also allowed to choose and characterization of a specific material for the experiment – austenitic stainless steel. The work describes stainless steels, paying attention to the fundamental property of them. In this work pointed to the extensive possibilities of using this type of material in today's economy. The collected literature review also allowed to the thorough characterization and division of additive manufacturing technologies. Steel elements were manufactured using Laser Engineered Net Shaping (LENS) technology. During the process, the speed of the working table (feed rate) and the thickness of a single layer were controlled. The constant parameters of the production process were laser power and powder output. After preliminary research results, it was found that thanks to the use of LENS technology, coherent samples of austenitic stainless steel can be produced. The microstructure of such manufactured steel is in agreement with literature data. In addition, it was noted that the parameters of the manufacturing process directly affect the microstructure (grain size) of the received samples.

INTRODUCTION

For several years, dynamic economic development has been continuously observed, especially in such industries as: construction, medicine, aviation, food, military or automobile. The effect of this phenomenon is the constantly increasing demand for modern, characterized by better properties, construction materials [1]. The most frequently used materials, that are the answer to economic problems, are all kinds of steels. These materials are characterized by a relatively low price compared to other construction materials and it is important that they can be recycled – which is a very big advantage in the current world [2]. The natural ecosystem of land surrounding us is getting more and more polluted year by year through various types

of industrial and commercial sewage, waste and chemical reagents. These pollutants cause a slow degradation of the environment in a direct way - which affects the length and quality of life of the constructed structures or buildings, as well as the work of various types of machinery and equipment in the acidified or corrosive environment. Therefore, since the 20th century, the trend of increasing the importance and use of stainless steels has been constantly observed [2, 3]. In this work, steel belonging to the group of corrosion resistance steel was used. This material is characterized by good mechanical properties, very high corrosion resistance and affordable price - thanks to these advantages, it has become a material that is very popular in the current economy. The dynamic development of medicine is also based on the use of this steel (implants, surgical instruments) [2, 3].There are many technologies for manufacturing this type of material. In addition to conventional manufacturing methods, there are other methods that enjoy great interest and efficiency [3]. There are, for example, additive technologies using a laser (SLM, SLS, DMLS or LENS). Thanks to the use of this type of manufacturing techniques, stainless steel elements with a complicated shape can be manufactured. Very often is that these elements characterized by better properties than those produced in a traditional way. During the manufacturing processes of this material, the process parameters such as: laser power, feed rate, powder feed speed and thickness of the applied layer, play a significant role. It is important to find a relation between the parameters of manufacture and the resulting phase composition and microstructure of the finished elements, because these factors then directly affect the mechanical properties and corrosion resistance. Precise selection of parameters allows the control of the properties of the manufactured elements [4]. Therefore, this relationship has become the reason for a large number of experiments and research, the aim of which is to analyze it thoroughly [2-4].

THEORETICAL BACKGROUND

Corrosion resistance steel

For the experiment, steel belonging to the group of corrosion resistance steel with austenitic structure was used. Corrosion resistance steel is a common name designating the entire family of special steel family that are not susceptible to rusting. The characteristic feature of these steels is the several times higher corrosion resistance compared to other steel types. Such high corrosion resistance is obtained through alloy additions in the form of chromium - about 13% of Cr (or 10.5% according to PN EN 10088 [5]). At this value of this alloy addition, there isa rapid change in the electrochemical potential (Fig. 1) [6].As a result, a tight and invisible oxide film is formed on the steel surface to prevent corrosion (passive layer). The film separates the material from the environment, thus protecting it against oxidation. In many different environments, the oxide layer, in places of damage, e.g. scratching

or bending, is characterized by the ability to surface regeneration. Corrosion resistance may increase with increasing Cr content in steel as well as the addition of other elements, e.g. nickel or molybdenum. Corrosion resistance is dependent not only on the chemical composition but also on the state of the steel surface and its phase composition, which can be obtained during various types of processing [6, 7] This is very well shown in the Scheffler chart (Figure 2), showing the phase composition of stainless steels, with respect to the equivalent content of chromium and nickel[2].

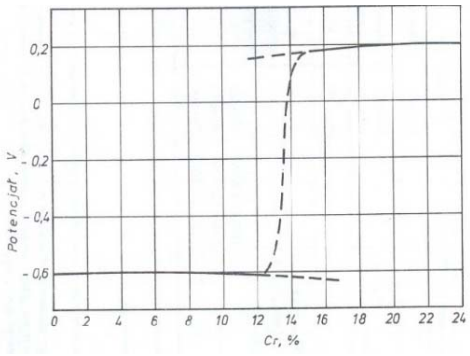

Fig. 4. Changing the electrochemical potential in steel depending on the chromium content [2].

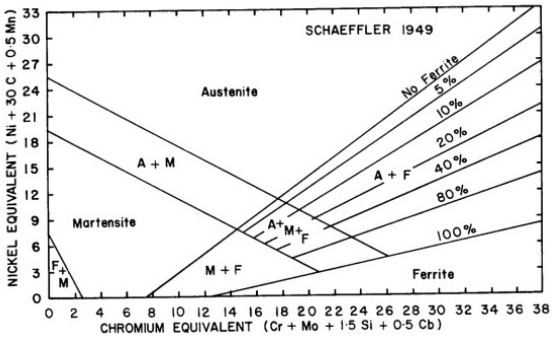

Fig. 5. Scheffler diagram [2].

Corrosion-resistant steels can be divided into: martensitic, austenitic, ferritic, ferritic-austenitic (two-phase: duplex steels). Austenitic steels steadily account for over 2/3 of all production of this type of material [7, 8]. Figure 3 shows the four most common types of microstructure of corrosion-resistant steel.

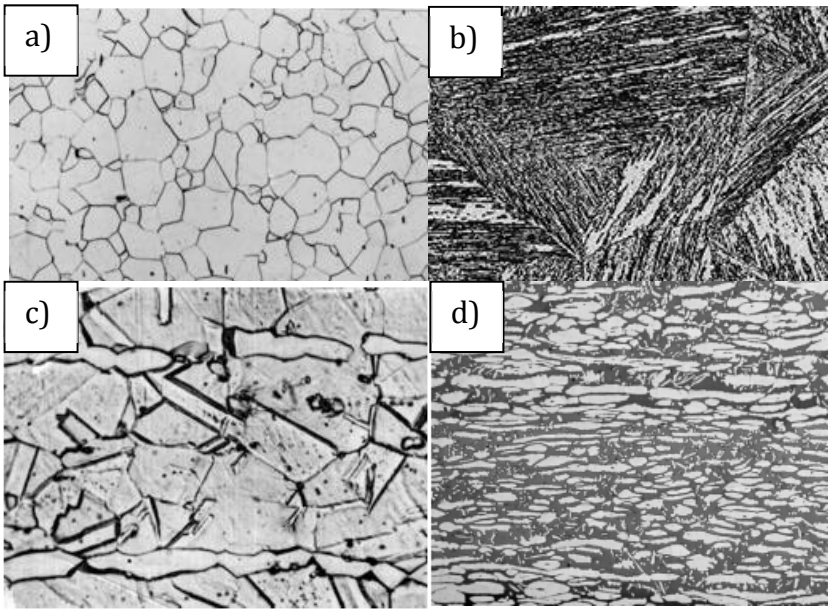

Fig. 6. Examples of microstructure of various steel types: a) ferritic steel No. 1.4510, b) martensitic steel No. 1.4013, c) austenitic steel No. 1.4301, d) austenitic-ferritic steel No. 1.4462 [7].

Austenitic stainless steel

Austenitic stainless steel - steel containing 16 - 25% of chromium with a sufficient amount of nickel and manganese, sometimes also with nitrogen, silicon, aluminum, titanium, niobium, and in some cases even with sulfur and selenium [2]. The high Ni content makes it possible to stabilize the austenitic structure from the solidus line to room temperature. In some cases ferrite may be found in these types of steels, and martensite in low temperatures, especially during deformation. The crystal structure, austenitic stainless steels are fcc - face-centered cubic. It results from the fact that these steels are paramagnetic - in low temperatures they do not become brittle and cannot be hardened[7, 8].Thanks to numerous advantages, austenitic steels are used in many branches of industry (Figure 4). The largest area of application are industrial applications as well as construction, kitchen fittings and the car industry. Currently, there is a great interest in this type of material also in medicine - as surgical tools and bone implants [8].

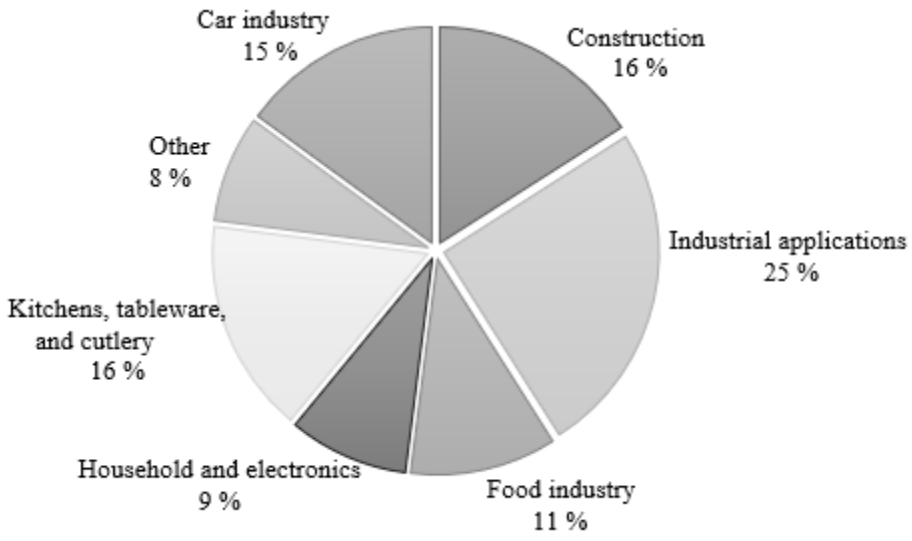

Fig. 7. Application of austenitic steels - based on [8].

Additive manufacturing processes

Currently, there are many methods of manufacturing stainless steels in the industry. The most well-known are conventional methods of production of this type of materials, such as shaping process, plastic forming, powder metallurgy. However, more and more often (especially at the turn of the last two decades) less conventional techniques appear - for example additive manufacturing. Thanks to these technologies, it is possible to produce elements with complex shapes, which cannot be obtained by traditional techniques or their production is highly expensive and long-lasting. These technologies are often more cost-effective than conventional techniques (especially in the case of unit production) due to the fact that the manufacturing process is much faster and the cooling time of the element is shorter. Additive manufacturing methods also enable the regeneration of damaged machine parts or structural components [9].

A lot of research has been carried out in the area of using additive manufacturing process for the production of steel elements. Currently, there are still innovative applications of these technologies. These techniques are classified in terms of the function of the manufactured product [10]:

- Rapid Prototyping - RP
- Rapid Manufacturing- RM

The theoretical and practical basics of these methods were developed already in the 80's of the last century. The basis for their operation is the production of a prototype or finished product based on a three-dimensional model. The previously designed block is built as a result of applying subsequent layers of material to the

product being formed. The RP and RM techniques are based on a different production methodology, however the overall mechanism of the whole process is the same. It is based on the basic steps that are implemented before the creation of new elements [11]. Figure 5 shows the individual steps of the entire RP and RM process, which are necessary to obtain the finished element.

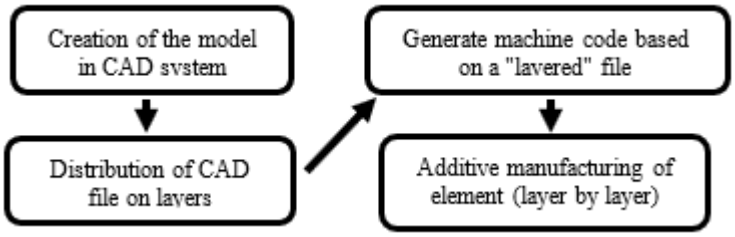

Fig. 8. Diagram of the ideas of RP and RM processes - based on [10].

The use of CAD software is the first stage of the rapid prototyping and manufacturing process. The 3D solid can be modeled in two ways. The first of these is the aforementioned CAD program, where the shapes of products are usually determined by means of surfaces and solids. The second way is a 3D scan. However, in both cases, the designated geometry must be in a neutral format. This allows further processing in RP and RM systems.The basic operation performed after the introduction and validation of the geometry to the RP and RM systems is the orientation of the obtained solid in the working space of the device. The next stage of additive production is the creation of auxiliary geometries that are necessary to keep the product in a fixed position during the process - supporting elements. This step is often omitted if there is no necessity or possibility (e.g. LENS) for supporting elements - the powdermay be a support. The last step is always to divide the model into layers. After completing all the above-mentioned activities, the physical creation of the object takes place [12].

There are currently many additive techniques in the industry. The fast growing economy is conducive to the development of newer, better and more efficient processes, thanks to which finished products or machine parts are produced very quickly. There is, however, a typical criterion for the division of these techniques: manufacturing processes using a laser beam and those that do not use it (Fig. 6) [13].

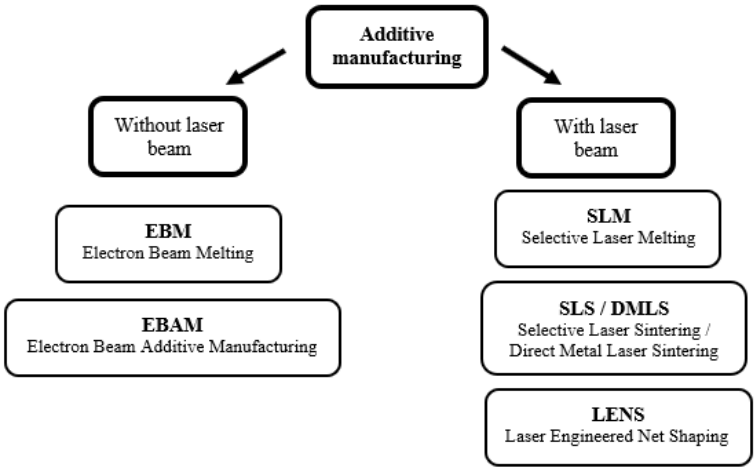

Fig. 9. The most commonly used techniques of additive manufacturing of steel elements – based on [13].

LENS technology

Laser Engineered Net Shaping (LENS) technology was used in this work. This technique is included in the group of methods: DMLS - Direct Metal Laser Deposition. The LENS technology was developed in 1990 in the USA. However, its importance and application has increased significantly.During the LENS process, elements are produced based on solid files that have been previously divided into layers. No kind of auxiliary engineering tools are required for the LENS process. Thanks to this technique is very competitive in relation to conventionally used technologies of steel production (casting, plastic processing and powder metallurgy) [14]. Figure 7 illustrates the operation diagram of the device using the LENS technique.

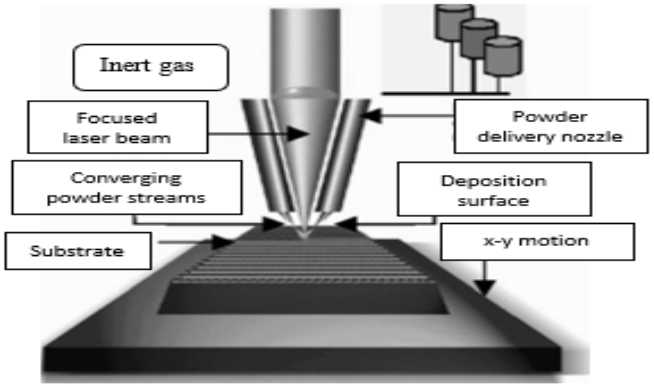

Fig. 10. The scheme of the device using LENS technology - based on [15].

The necessary element during the LENS process is the substrate. The chemical composition of the substrate must be close to the chemical composition of the manufactured element. The substrate is also a support for the final product. Currently machines using the LENS technique are equipped with a fiber laser with powers up to 3 kW.The LENS process consists in controlling the laser beam (towards the substrate) so that the focus of the delivered powder is located in the area of the focus of the incident laser beam.Through the intensive interaction of the laser beam, a pool of liquid metal is obtained. Powder is delivered to this point with four identical nozzles. This powder can be completely or partially melted during the process. Then in this state the powder in the form of "stitches" is applied to the manufactured product. The entire LENS process takes place in a chamber with an inert gas (usually argon) at a low oxygen content and water vapor [15].

The feedstock material is usually a metallic powder (but it can also be a ceramic, intermetallic or composite powder). The powder material has to meet several requirements: the average diameter of the powder particles must be in the range of 40 to 150 μm, and the shape of the powder should be spherical [16].

The advantages of LENS technology include:

• the ability to manufacture products from several different powders at the same time,
• high speed of cooling and solidification of the manufactured element (shortening the production time and obtaining a fine-grained structure),
• manufacturing gradient structures (controlling the thickness of a single layer and chemical composition),
• good (sometimes better than with conventionally manufactured elements) mechanical properties,
• regeneration of worn parts or machine parts [16].

The disadvantages of the LENS process are mainly:

• uncertainty of dimensions,
• low surface quality (high roughness) of manufactured products,
• the need to cut the element from the substrate,
• thermal and mechanical stresses in the element during and after manufacturing process [17].

ADDITIVE MANUFACTURING OF AUSTENITIC STAINLESS STEEL– SHORT REVIEW

Based on literature data, it was found that the austenitic stainless steel microstructure after additivemanufacturing process is substantially different from the microstructure of this steel after the production using conventional technologies. This is illustrated in figures 8. Additive manufacturing process in this case was multiple-

layer diode laser cladding [18].The difference in the microstructure results directly from the nature of the additive manufacturing process, which contributes to columnar crystallization. As a result of this phenomenon, the grains take the form of long columns or small cells, arranged in the so-called microstructure of “fish scales” or “snake skin”, which is definitely different from the commonly known austenite microstructure with different-axis grains and characteristic transformation twins. It is also known that their different microstructure will contribute to the occurrence of different mechanical and physicochemical properties[18, 19].

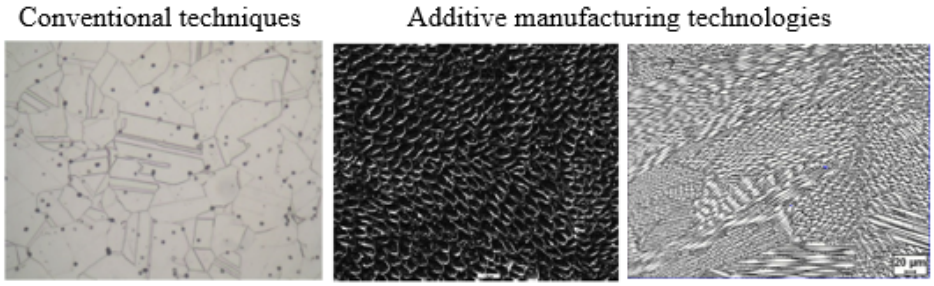

Fig. 11. The difference in the microstructure of austenitic stainless steel produced as a result of other manufacturing techniques [18, 19].

This phenomenon has been studied by many scientists. Researchers used various types of additive technologies, changed process parameters, shapes and sample dimensions, however, the end result always remained the same - a characteristic “fish scale / snake skin” microstructure.

LAM process of 316 stainless steel

In the paper[20] authorsdescribed the possibility of manufacturing elements from AISI316 stainless steel using Laser Additive Manufacturing (LAM) technique.316 steel(in terms of properties) is very similar to 316 L, with the exception that it has more carbon in its chemical composition. Thus, the reduced carbon content, in 316 Lsteel, protects it against intergranular corrosion in the heat affected zone [2]. During LAM process samples were produced with different laser power, feed rate and layer thicknesses (Tab. 1).

Tab. 3. Manufacturing parameters [20]**.**

No.	Laser Power [W]	Feed rate [mm/min]	Layer thickness [mm]
A	200	500	0,26
B	200	500	0,26
C	200	200	0,44
D	200	200	0,44
E	350	500	0,40
F	350	500	0,40

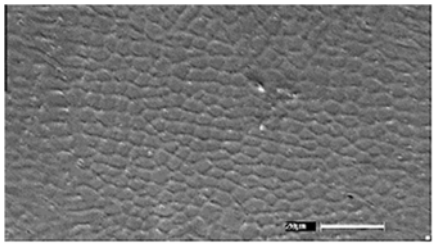

Fig. 12. Scanning electron microscopy of manufactured sample – B [20].

The microstructure of the obtained samples was analyzed on optical and scanning microscopy. Fig. 9. presents image from scanning electron microscopy. Observed microstructure (sample No. B) indicated that the solidification is either cellular or dendritic, with the cell size of about 4 μm. According to the authors of the publication, intercellular spaces in microstructure of samples (visible in the picture) should be the place where austenit-ferrite eutectics occur. However, the XRD analysis did not confirm the occurrence other than austenitic phases. The delta ferrite, which theoretically should be present in the samples - was not detected. This phenomenon may be due to the fact that austenite is strongly stabilized by nickel. The presence of ferrite is very unfavorable for steel because it impairs its corrosion resistance. Therefore, it is worth to noting that the authors of the paper have been able to produce samples free of delta ferrite.

Multiple layer laser cladding of 316 L stainless steel

Thanks to the multiple layer laser cladding technique, it is possible to manufacture prototypes of functional elements, various types of precision cutting tools obtained in low-series production and, similarly as in the case of LENS technology, it is possible to regeneration of damaged parts of machines or structures. Such technology was used in the experiment described in [21]. The aim of the experiment was to obtain two samples of 316L steel, differing in production parameters - laser pulsation (on and off). Laser power during process was constant: 450 W.

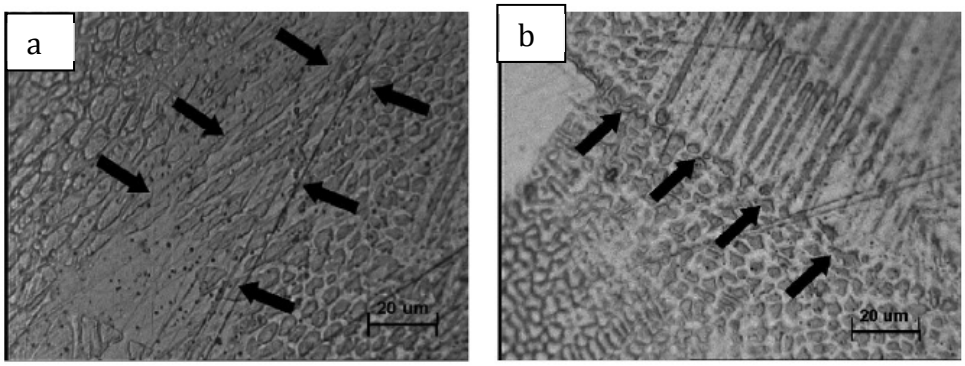

Fig. 13. Microstructure after manufacturing process, a) continuous wave, b) pulse.

The microstructure of the manufactured samples is shown in Figure 10. The images clearly show two types of grain arrangement: random and regular - cellular. The boundary between the two types of microstructure is marked with black arrows in the figure below. The difference in the order of grains results from the different rate of heat removal from the sample – different crystallization front. The grain size is also very diverse - the largest grains are near of the sample substrate. As expected, in the microstructure of samples there are targeted areas with the same orientation of grains - there are much more these areas in the sample produced using laser pulsation. The authors of the paper expected that the dark secretions visible in the pictures are places of delta ferrite, however, the XRD analysis showed that in both samples there is austenitic phase with minimal residues of the original ferrite delta. As can be seen with this method, it is also possible to create samples with a maximally minimized content of unwanted delta ferrite.

LENS process of 316 L stainless steel

As confirmed in the tests [22] thanks to the LENS technology it is possible to manufacture 316L steel, whose microstructure has a specific appearance of "fish scale" – Fig. 11. In this experiment sample was produced with constant parameters: Laser powder - 400 W, speed rate - 15 mm/s and layer thickness - 0.3 mm. With such parameters, a full dense cubic sample without structural defects was created. Dimensions of this sample was 20 mm x 20 mm x 20mm. The article also shows that in the phase structure of the manufactured element, in addition to austenite, there is also a delta ferrite, which is unwanted because it contributes to lowering the corrosion resistance.

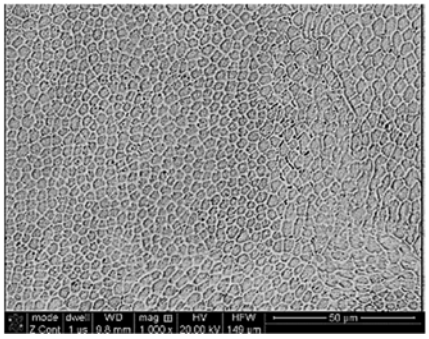

Fig. 14. Microstructure of 316 L steel after LENS process [22].

Therefore main assumption of this work and creating new experiment is to check how the change of process parameters and different size of the samples will affect the obtained microstructure and phase composition.

PRELIMINARYEXPERIMENT

Materials and methods

To the LENS process used an alloy powder of 316 L stainless steel, with a dimensional fraction that was within the required range (for technological reasons) of 40 μm to 150 μm. This fraction was obtained by 1 hour sieving on properly selected sieves. The granulometric analysis shows that 97% of powder is in the range of 44 μm

to 124 μm (Fig. 12).The shape of the powder particles was spherical - which was checked on the prepared metallographic sample (Fig. 13).

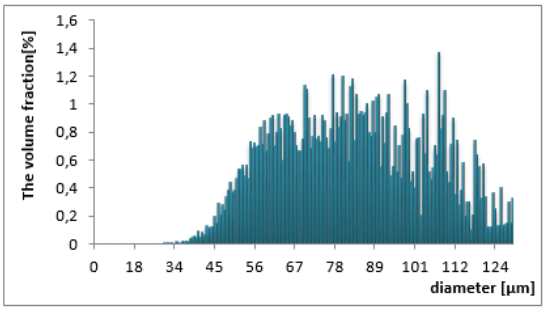

Fig. 16. Separated fraction of purchased powder.

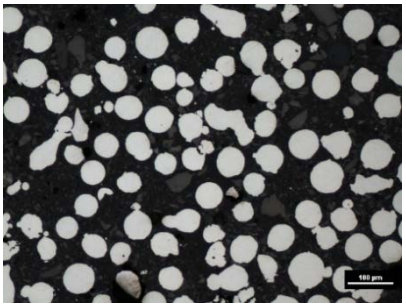

Fig. 15. Spherical shape of particles of purchased austenitic steel powder.

The LENS process was planned in such a way as to obtain several samples differing in production parameters. For this purpose, the speed of the manufacturing process and the thickness of a single layer were controlled. The speed was change in range of 6 mm/s to 20 mm/s and the thickness in range of 0,2 mm to 0,7 mm. The laser power and powder output for each sample was the same: 450 W and 8 g/min respectively. The shape and size of the samples were determined in the CAD program. The dimensions of samples were 52 mm x 80 mm x 12 mm - the samples were much larger than in [22], therefore the heat dissipation and powder crystallization was also different. After the end of the process, the samples were cut into smaller ones and subjected to the preparation (mounting, grinding, polishing and etching) to reveal the microstructure of the samples.

RESULTS AND DISCUSSION

Initial observation of the microstructure of the samples was performed on an optical microscope (Fig. 14). The taken pictures confirm that the microstructure of austenitic stainless steel, obtained thanks to the LENS process, is consistent with the literature data. Their characteristic appearance is due to the specificity of the manufacturing process, which is Laser Engineered Net Shaping which contributes to columnar grain crystallization. Small columnar and cell grains are present in the whole sample volume. Thanks to the special software of the optical microscope and the determined binary images of the microstructure, the average grain size of individual samples was calculated. After analyzing these results, it was found that the parameters of the LENS process essentially affect the manufactured microstructure - the average grain size decreases with the increase of the feed of the working table (speed rate) and reduction of the thickness of a single layer. The average grain size for the sample produced slowest with the largest thickness of a single layer is approx. 35 μm, and the sample produced fastest with the thinnest layer is approx. 26 μm. Preliminary tests also confirm the existence of only one phase in the sample

structure– austenite. The test was carried out using special magnet with high sensitivity. In the near future, very accurate tests will be carried out to confirm the obtained phase composition.

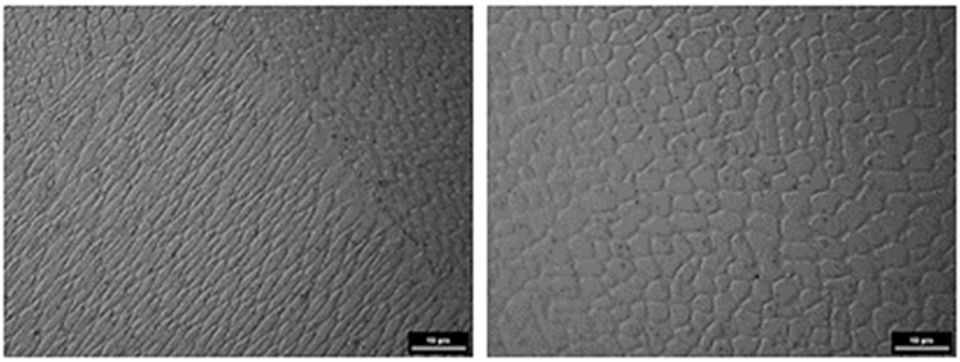

Fig. 17. Microstructure of LENS steel samples.

CONCLUSIONS

After thoroughly analyzing the test results, it was found that thanks to the Laser Engineered Net Shaping technology, it is possible to produce austenitic stainless steel, which microstructure is consistent with the literature data. Columnar and cellular grains - a microstructure known colloquially as "snake skin" or "fish scale". It was additionally shown that the applied parameters of the LENS process directly affect the average diameter of grains in the produced samples. Thanks to this technology, it is also possible to produce samples without the presence of unwanted delta ferrite.

The tests presented in this paper are preliminary tests for the next stage of the experiment, the main purpose of which will be to check the influence of the microstructure of the manufactured samples on the mechanical properties, corrosions resistanceand phase composition of this steel.

REFERENCES

[1] Bienaś J.,*Struktura i właściwości materiałów kompozytowych*, Politechnika Lubelska, Lublin, 2005.

[2] Dobrzański L.A.,*Metalowe materiały inżynierskie*, Wydawnictwo Naukowo Techniczne, Warszawa, 2004.

[3] Dobrzański L.A.,*Podstawy nauki o materiałach i metaloznawstwo*, Wydawnictwo Naukowo-Techniczne,Warszawa, 2006.

[4] Gibson I.,Rosen D.,Stucker B.,*Additive Manufacturing Technologies,* Springer-Verlag Gmbh, New York, 2015.

[5] Polski Komitet Normalizacyjny, *Stale odporne na korozję, część pierwsza - Gatunki stali odpornych na korozję"* PN-EN 10088-1:2007.

[6] Blicharski M., "*Inżynieria materiałowa - stal*, Wydawnictwo Naukowo-Techniczne, Warszawa, 2004.

[7] The European Stainless Steel Development Association, *Własności stali odpornych na korozję,*euro inox, Luksemburk, 2002.

[8] The European Stainless Steel Development Association, *Zastosowanie stali odpornych na korozję,* Materiały i zastosowanie, seria 7, Luksemburg, 2008.

[9] Łędzki A., Zieliński K., Klimczyk A., *Podstawytechnologi wytwarzania i przetwarzania*,Akademia Górniczo - Hutnicza, Kraków, 2010.

[10] Yan Y., Li S., Zhang R., Lin F.,*Rapid Prototyping and Manufacturing Technology:Principle Representative Technics Applications and Development Trends*,Tsinghua Science and Technology*, vol.* 14, 2009.

[11] Jain P., Kuthe A.M.,*Feasibility Study of manufacturing using rapid prototyping: FDM Approach,*Procedia Engineering, vol. 63, 4-11, 2013.

[12] Miecielica M., *Techniki szybkiego prototypowania - rapid prototyping,*Przegląd Mechaniczny, vol. 2, 39-45,2010.

[13] Jin G.Q., Li W.D., Gao L., *An adaptive process planning approach of rapid prototyping and manufacturing,*Robotics and Computer Integrated Manufacturing*, vol. 29,* 23-38, 2013.

[14] Santos E.C., Shiomia M., Osakada K., Laoui T., *Rapid manufacturing of metal components by laser forming,International Jurnal of Machine Tool & Manufacture,*vol. 46, 1459-1468, 2006.

[15] Xiong Y., Smugersky J.E., Ajdelsztajn L., Schoenung J.M.,*Fabrication of WC-Co cermets by laser engineered net shaping,* Materials Science and Engineering, vol. 493, 261-266, 2008.

[16] Lu Z. L., Li D.C, Lu B.H., Zang F., Zhu G.X., Pi G.,*The prediction of the building precision in the Laser Engineered Net Shaping process using advanced networks,*Optics and Lasers in Engineering *, vol. 48,* 519-525, 2010.

[17] Picas J.A., Xiong Y., Punset M., Akdelsztajn L., Forn A., Schoenung J.M., *Microstructure and wear resistance of WC-Coby three consolidation processing techniques*,International Journal of Refractory Metals & Hard Materials, vol. 27,344-349, 2009.

[18] Majumdar J.D., Pinkerton A., Liu Z., Manna I., Li L., *Mechanical and electrochemical properties of multiple-layer diode laser cladding of 316L stainless steel,*Applied Surface Science*,* 373-377, 2005.

[19] Lee W.S., Chen T.H., Lin C.F., Luo W.Z.,*Dynamic Mechanical Response of Biomedical 316L Stainless Steel as Function of Strain Rate and Temperature,* Bioinorganic Chemistry and Applications,2011.

[20] Fernandes de LimaM. S., Sankare S., *Microstructure and mechanical behavior of laser additive manufactured AISI 316 stainless steel stringers*, Materials and Design*,* vol. 55, 526-532, 2014.

[21] PinkertonA.J., LiL.,*The effect of laser pulse width on multiple-layer 316L steel clad microstrucure and surface finish,*Applied Surface Science, vol. 209, 411-416, 2003.

[22] Ziętala M., Durejko T., Polański M., Kunce I. and others, *The microstructure,mechanical properties and corrosion resistance of 316Lstainless steel fabricated using laser engineered net shaping*, Materials Science & Engineering A*,* vol. 677, 1-10, 2016.

The Sr doping influence on $K_{0,5}Bi_{0,5-x}Sr_xTiO_3$ electrochemical properties

*Małgorzata Dziubaniuk[1], Jan Wyrwa[1], Mieczysław Rękas[1], Kamila Kluczewska[2], Piotr Czaja[2], Jan Suchanicz[2]

[1]Faculty of Materials Science and Ceramics, AGH University of Science and Technology, Cracow, Poland

[2]Institute of Technology, Pedagogical University, Cracow, Poland

*e-mail: dziubaniuk@o2.pl

***Keywords**: ferroelectrics, potassium bismuth titanate, solid state synthesis, solid state ionics, electrochemical impedance spectroscopy*

ABSTRACT

The main aim of presented studies was determination of Sr doping impact on $K_{0,5}Bi_{0,5}TiO_3$ (KBT) electrical properties in different gas atmospheres of precisely controlled compositions. The first step consisted of materials synthesis by solid state route using analytically pure Bi_2O_3, TiO_2, K_2CO_3 and $SrCO_3$. According to SEM images KBT ceramics consist of round grains of about 250 nm in diameter. Besides the XRD peaks coming from main tetragonal phase, there are visible additional weak peaks from unclassified parasitic compounds. It was found out that the preparation conditions as well as the amount of used dopant influence on electrical specific conductivity of the specimens. Based on Arrhenius plots obtained from analysis of EIS spectra, mechanisms of reactions in materials with gaseous ammonia and hydrogen has been proposed. The results indicate on mixed ionic electronic conduction in KBT material at investigated temperatures range 473-773 K.

INTRODUCTION

$K_{0,5}Bi_{0,5}TiO_3$ (KBT) and $Na_{0,5}Bi_{0,5}TiO_3$ (NBT) are $A_{0,5}^{+}Bi_{0,5}^{3+}B^{4+}O_3$ type perovskites capable of working at elevated temperatures. The materials ferroelectric and piezoelectric properties exhibited in wide range of temperatures as well as high environmental and chemical stability makes them interesting candidates for applications in devices range from multilayer actuators to buzzers, diesel engine fuel injectors, sonar, ultrasound appliances and nanopositioners in scanning microscopes [1].

KBT at room temperature is a perovskite with a high tetragonality c/a of 1.02 and undergoes two phase transitions upon heating: tetragonal to pseudocubic at approximately 533 K and pseudocubic to complete cubic at approximately 683 K. KBT is generally regarded as a relaxor without long-range polar ordering showing broad dielectric peak with a frequency dependent dielectric maximum temperature (T_m) around 653 K [2-4].

NBT materials have been extensively studied, while research on KBT has rarely been reported due to difficulty to fabricate high density KBT ceramic. First of all secondary phases $K_2Ti_6O_{13}$ and $K_4Ti_3O_8$ can be form during the synthesis [5]. Secondly the materials shows narrow sintering temperature range. The preparation of dense sintered bodies is possible at high temperature of about 1273 K. However according to literature the melting process begins at 1343K [6]. Moreover compounds containing potassium and bismuth tend to be volatile which results in poor sinterability of the material. In order to obtain the KBT ceramic of improved properties different synthesis methods were widely investigated, such as mechano synthesis [7], sol–gel [8, 9],hydrothermal [8, 10] molten salt [11] or the polymerized complex method [12].

Up to now few research reports are available concerning KBT single phase dielectric [3, 10, 14-18] ferroelectric [16, 18, 19], piezoelectric [16] and pyroelectric properties [17], C-V and I-U characteristics [15] and AC and DC conductivity [19, 17]. One of the effective technique for investigation of electrical and electrochemical properties of oxide materials is Electrochemical Impedance Spectroscopy (EIS) performed in wide range of temperatures and in different gaseous atmospheres. Basing on EIS measurements it was stated that KBT is a mixed oxide-ion electronic conductor at temperatures above 873 K, whereas proton conduction occurs below 573K during exposition on wet atmosphere [20].

One of the possible way to modify the properties of the material besides by selection of synthesis method and preparation condition is by doping with metal ions. For example Sr^{2+} was reported as promising dopant for NBT [21]. Improvement of conduction in the material is caused by growth of oxide vacancies concentration according to the formula:

$$2SrO \leftrightarrow 2Sr_{Bi}' + 2O_O^x + 2V_o^{\cdot\cdot} \quad (1)$$

The main aim of presented research was determination of synthesis conditions as well as Sr ions addition impact on KBT electrochemical properties in different gaseous atmospheres by EIS method. In particular the reaction with ammonia and hydrogen occurring at three phase boundary (gas-metal-ceramic) were investigated as well as the reversibility of this processes.

MATERIALS AND METHODS

$K_{0,5}Bi_{0,5}TiO_3$ was synthesized by conventional solid state reaction method using powders of Bi_2O_3 (99,9%), TiO_2 (99.5%) and K_2CO_3 (anhydrous pure p.a.) in their stoichiometric ratio. After mixing with isopropanol and ball milling for 24h with 350 mph, the mixture was dried at 373 K for 24h. The obtained powder was pressed into pellets of a 13 mm diameter and 2 g weigh and calcinated at 1073 K for 2h. The product was crushed, grinded in agate mortal into powder and at this stage several pellets of 10 mm and 0.5 g weigh were formed. The specimen after sintering

at 1253 K for 1h was labeled as KBT1. The chosen temperature of sintering was the highest as possible as even slight sintering temperature increase leaded to melting of the material. The resting powder was formed into 13 mm diameter and 2 g weight and process of calcination was repeated at 1073 K for 2h. After preparing the final pellets of 10 mm in diameter in the same route as stated above it turned out that the maximal sintering temperature which do not lead to melting is higher than after single calcination. The specimens were sintered at 1313 K in 1h and labeled as KBT2.

$K_{0,5}Bi_{0,5-x}Sr_xTiO_3$ (x=0.1, 0.2) were prepared from the same reagents as stated above and $SrCO_3$ (98%) in the conditions the same as in case of KBT2. The specimen with 10% at. Sr is labeled as KBTSr10, and that with 20% at. Sr as KBTSr20.

Sintered pellets were examined by X-ray diffraction (XRD) method. The measurements were done in air at room temperature using CuK_α radiation (Philips X'Pert) within the 2Θ range 10-90° with the scan ratio 0.008°/s.

The surface morphology of sintered materials was observed using ultrahigh-resolution scanning electron microscope with field emission (FEG-Schottky emitter; Nova Nano-SEM 200, FEI Europe BV) cooperating with EDAX EDS analyzer.

The pellets were prepared for EIS measurements by covering on both sides with Ag paste provided by Pelco and firing at 1073 K for 5 minutes.

The EIS measurements were performed in controlled atmospheres using a frequency analyzer (Solartron model FRA 1260) coupled with Dielectric Interface (model 1296) in temperature range 473-773 K. Frequency range was 0.1 Hz -32MHz, the amplitude of sinusoidal voltage signal was 20 mV. The measurements were performed in the following atmospheres: synthetic air(series no 1 and 3 and 5), 3000 ppm NH_3 in argon (series no 2), 10% H_2 in argon (series no 4). The series no 3 and 5 in synthetic air were conducted in order to determine the reversibility of the material impedance response in H_2 and NH_3 rich atmospheres. The values of the resistances were derived using Zview software (version 2.2, Scribner Associates, Inc.).

RESULTS AND DISCUSSION

Spectra from XRD are presented in Fig. 1. All specimens are mainly composed of assumed $K_{0.5}Bi_{0.5}TiO_3$ tetragonal phase with P4mmm space group. However there are some extra peaks coming from secondary phases visible. The positions of additional peaks, marked by asterisks in Fig.1 and listed in table 1, are week in comparison to these coming from $BiFeO_3$ compound. Nevertheless the amount of parasitic products is not negligible. Despite the efforts to determine the originate of additional peaks, the secondary phases were not identified. The peaks do not coming from used in synthesis precursors nor from K_2TiO_6 or $K_4Ti_3O_8$ phases reported in literature. Moreover, the presence of additional peaks is not attribute to possible $SrTiO_3$ products in case of KBTSr10 and KBTSr20.

Basing on XRD spectra the lattice parameters were calculated and presented in table 1. In each case the determined lattice parameters are somehow higher that the theoretical values. The nominal ionic radius of K^+, Bi^{3+}, Sr^{2+} and Ti^{4+} are 138, 117, 118 and 60.5 pm, respectively. The addition of Sr dopant to KBT decrease the lattice constant, which contradict the assertion that Sr ions locates in Bi ions positions in lattice. The only possibility which correlate with experimentally obtained values is infix of Sr dopant ions in K^+ node positions. However the difference in valence of the above mentioned ions would result in excess of oxygen in KBT material in order to fulfill the neutral charge of the lattice.

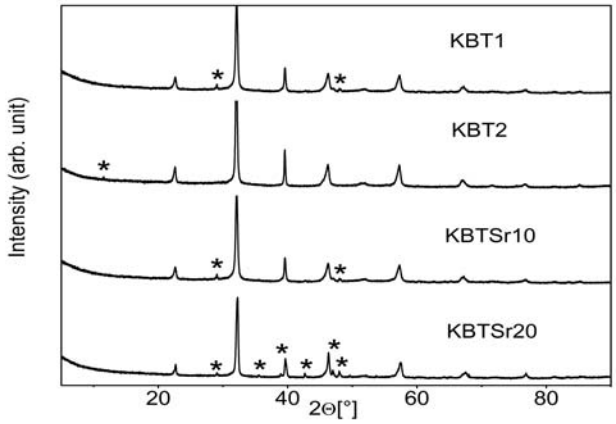

Fig. 1. XRD patterns for sintered bodies.

The measurement of elemental compositions were performed by EDS analyzer. The experimental results as well as the theoretical predictions are presented in Table 2. During calculation of theoretical content, it was assumed that the composition of the products are given by the formula $K_{0,5}Bi_{0,5-x}Sr_xTiO_3$ (x=0.0; 0.1; 0.2). Only peaks originating from assumed elements were revealed in experimental spectra, which provide the evidence for lack of unexpected contamination in materials.

Tab. 1. Data from XRD analysis.

	Specimen label			
	KBT1	KBT2	KBTSr10	KBTSr20
Experimental lattice constant [Å]	a=3.9295 c=3.9717	a=3.9306 c=3.9696	a=3.9284 c=3.9732	a=3.9199 c=3.9566
Theoretical lattice constant [Å]	a=3.9180 c=4.0130			
Undefined peak position [°]	29; 48	11.5	29; 48	29; 35.5; 42.5; 48

The EDS results are generally consistent with theoretical predictions, however the content of Sr in KBTSr10 is much lower, than it was assumed. The analysis shows significant deficiency in oxygen in every specimen. It revealed that the concentration of oxygen vacancies is high in KBT material and impact on its electrical properties.

Tab 2. Elemental composition analysis.

	Element content	Specimen label			
		KBT1	KBT2	KBTSr10	KBTSR20
Experimental	K [wt %]	9.26	9.12	8.87	7.98
	Sr [wt %]	0.00	0.00	0.58	8.39
	Bi [wt %]	51.56	52.50	56.49	44.38
	Ti [wt %]	24.39	22.89	24.81	25.09
	O [wt %]	14.79	15.50	9.25	14.17
Theoretical	K [wt %]	8.89	8.89	9.41	9.99
	Sr [wt %]	0.00	0.00	4.22	8.96
	Bi [wt %]	47.52	47.52	40.23	32.05
	Ti [wt %]	21.77	21.77	23.04	24.47
	O [wt %]	21.83	21.83	23.10	24.53

The exemplary images of KBT1 specimen microstructure studied by SEM technique are presented in Fig. 3. The investigated ceramic materials are comprised of well-developed round grains with clearly separated boundaries. Grains are of similar size about 250 nm in diameter and do not adhere tightly to each other. Rugged surface with some empty spaces is visible on the images.

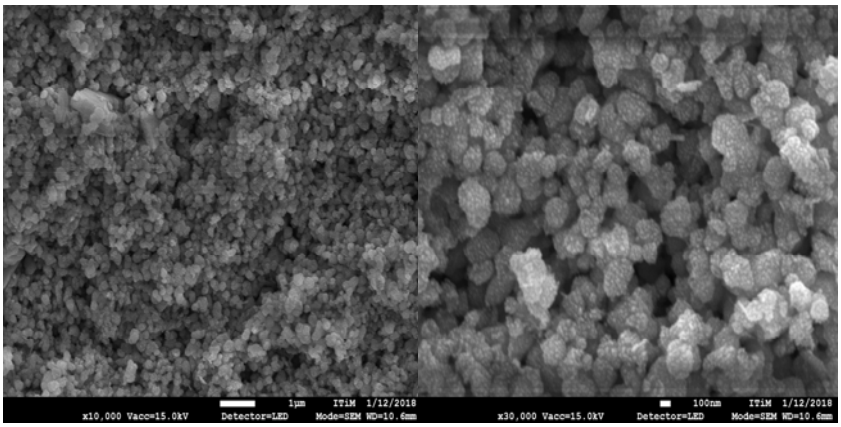

Fig. 2. SEM images for KBT1 sintered body.

The electrochemical properties were investigated by EIS spectra analysis realized by dedicated software. The exemplary sets of data obtained in 673 K in different atmospheres for KBT2 and KBT20Sr in Nyquist plane are presented in Fig. 3 and 4 respectively. The spectra are comprised of semicircle in high and medium frequencies and in some cases with short spur in low frequencies. The properties of the polycrystalline sintered ceramic are demonstrated by part of the spectrum in high and medium frequencies. The spur corresponds to behavior of a connection between ceramic and metallic electrode. The inset in Fig. 3 shows the spectra obtained in atmosphere rich in hydrogen. The exposition on gaseous hydrogen not only inducted drastic increase of conductivity but also caused the deformation of the semicircle shape of the spectra. It means that the reaction with material on the three phase boundary gas-metal-ceramic is effective and long lasting. The deformation of the spectra indicates that the reaction was still in progress during the measurement.

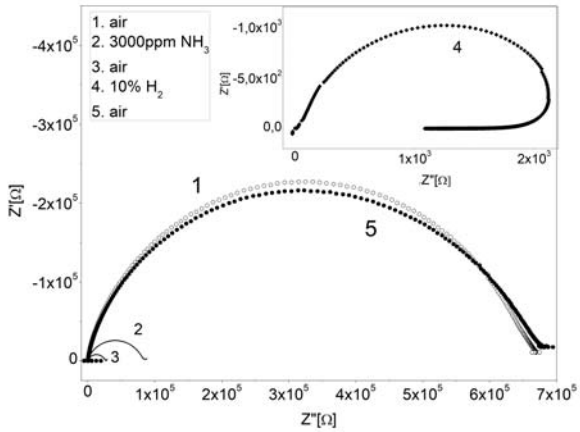

Fig. 3. Nyquist spectra of KBT2 at 673 K.

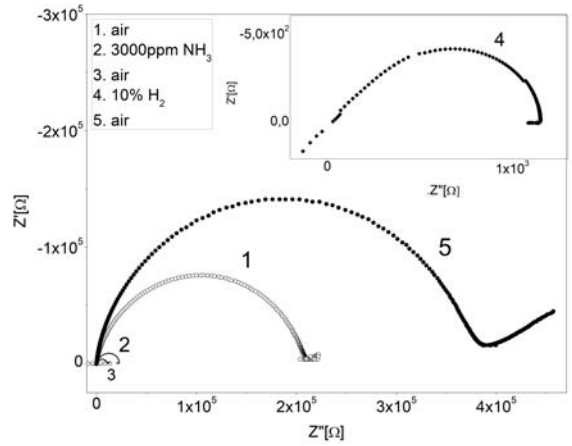

Fig. 4. Nyquist spectra of KBTSr20 in 673 K.

Fig. 5 and 6 contains the comparison of the spectra obtained in 673K for different specimens for first and last series in air respectively. Exposition for $NH_3$and H_2 containing atmosphere leads to significant permanent modification of electrical properties. For example during the first run the KBT2 was characterized by the lowest conductivity and KBT10Sr showed the lowest resistance. In case of the last series no. 5 performed in the same conditions KBT1 exhibited much higher conductivity than the rest specimens and the KBT20Sr was the most resistant. It means that the reactions with used reducing gases occurring in investigated materials are irreversible in regard to air.

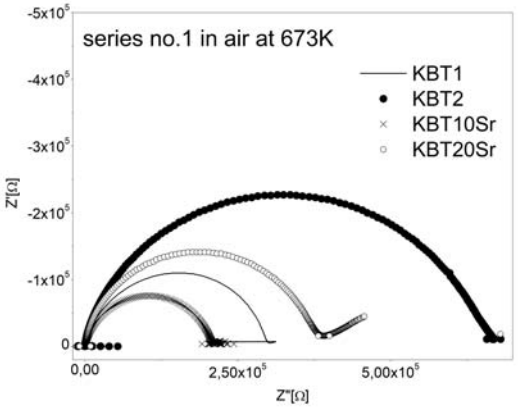

Fig. 5. Nyquist spectra in air series no. 1 at 673 K.

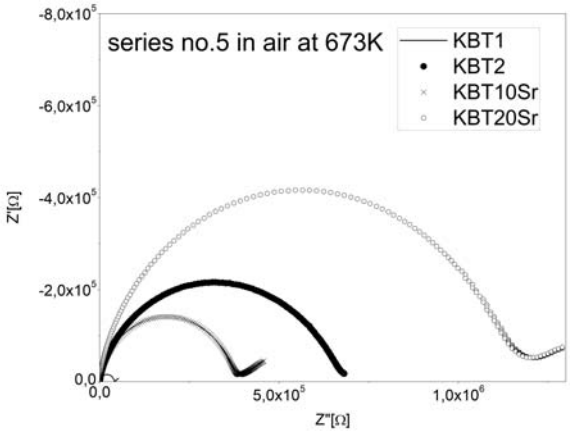

Fig. 6. Nyquist spectra in air series no. 5 at 673 K.

The specific conductivities were calculated using values of specimens resistance obtained by analysis of the spectra taking into account the pellets geometry. The collation of specific conductivities values obtained during series no 1 in air which can be consider as reference measurements of electrical conductivity before further modification of the materials, are presented in table 3. The orders of conductivity

values for different specimens are similar. The worst conducting properties shows material labeled as KBT2, while KBT1 is the best electrical conductor. It means that preparation conditions have direct effect on macroscopic electrical properties of the materials. Conductivities in specimen doped by 10% are somehow higher than that with 20%. It indicates that low content of doping agent improve electrical conductivity of KBT materials, which is consistent with equation (1).

Tab. 3. Specific conductivities obtained in 1 series in air from EIS spectra.

Temperature [K]	Specimen conduction [$\Omega^{-1}\cdot cm^{-1}$]			
	KBT1	KBT2	KBT10Sr	KBT20Sr
473	$2.27\cdot10^{-11}$	$5.16\cdot10^{-12}$	$1.87\cdot10^{-11}$	$1.78\cdot10^{-11}$
573	$2.92\cdot10^{-10}$	$4.30\cdot10^{-10}$	$4.87\cdot10^{-10}$	$2.38\cdot10^{-10}$
673	$2.67\cdot10^{-9}$	$1.22\cdot10^{-9}$	$3.78\cdot10^{-9}$	$2.35\cdot10^{-9}$
773	$2.72\cdot10^{-8}$	$1.01\cdot10^{-8}$	$2.29\cdot10^{-8}$	$1.70\cdot10^{-8}$

The final EIS results are presented in form of Arrhenius plots in Fig. 7-10. Some similarities in behavior of four investigated materials were stated based on analysis of the presented outcome. All the specimens shows conductivity growth in NH_3 rich atmosphere in comparison to that from first run in air. Basing on literature gaseous ammonia reacts with oxide ceramic resulting in increase of free electrons concentration in accordance with the equations [22]:

$$2NH_3+3O_O\rightarrow N_2+3H_2O+6e^-, \quad (2)$$

$$2NH_3+4O_O\rightarrow N_2O+3H_2O+8e^-, \quad (3)$$

$$2NH_3+5O_O\rightarrow 2NO+3H_2O+10e^-. \quad (4)$$

In consequence improved conductivity is observed. However the mentioned reactions would not explain the further conductivity growth during the 3th series in air in comparison to reference measurements in first series. On the other hand, there is possibility of free electrons and oxygen vacancies creation simultaneously during two-step process [22]:

$$2H_{ads}+O_O^x\rightarrow H_2O_{ads}+V_O^x\rightarrow H_2O_{ads}+V_O^{\bullet\bullet}+2e^-. \quad (5)$$

Such reaction with gaseous hydrogen leads to irreversible improvement of conductivity in hydrogen and oxygen rich atmospheres. Thus, the behavior of the material could be explained by analogous reaction with gaseous ammonia:

$$2NH_3+3O_O^x\rightarrow N_2+3H_2O_{ads}+3V_o^x\rightarrow N_2+3H_2O+3V_o^{\bullet\bullet}+6e^-. \quad (6)$$

It suggest that specimens exhibit mixed type ionic electronic conductivity and the risen concentration of oxygen vacancies and valence electrons cause permanent electrical conductivity improvement.

According to literature besides the reaction (5) the electrochemical process with gaseous hydrogen could run as follow [22-24]:

$$2H_2+O_{2ads}^- \rightarrow 2H_2O+e^-. \quad (7)$$

$$H_{(ads)}+O_{structural} \rightarrow (OH)_{ads}+V_O. \quad (8)$$

$$H_{(ads)} \rightarrow H_{ads}^{\bullet}+e^-. \quad (9)$$

Basing on obtained Arrhenius plots reactions with H_2 run differently at higher and lower temperatures. At higher temperatures significant growth of conductivity was observed. The last series performed in air leads to lowering of conductivity in comparison to 3 series in air. Such effect could be explained by reaction in which valence electrons are created accompanied with the oxygen vacancies recombination. In literature the reaction with water vapor has been postulated [25]:

$$2H_2O+O^{2-}+V_o^{n-} \rightarrow 2(OH)^-+ne^-. \quad (10)$$

Analogous reaction with hydrogen leading to similar macroscopic modification of electrical conduction would proceeds as followed:

$$H_2+2O^{2-}+V_o^{n-} \rightarrow 2(OH)^-+ne^-. \quad (11)$$

The improved conductivity in hydrogen is due to the risen concentration of valence electrons and increased resistance in the 3rd series arise from recombination of oxygen vacancies.

At lower temperatures the conductivity deteriorates in H_2 rich atmospheres. During the last series in air further decrease of conduction is observed. Such behavior could not be explained by equations given above. Reaction reported in literature between water vapor and oxygen vacancies, which would lead to similar effects is [22]:

$$2H_2O+V_o^{\bullet\bullet}+O_O^x \rightarrow 2(OH)_O^{\bullet}. \quad (12)$$

Thus postulated analogical reaction involving H_2 can be written:

$$H_2+V_o^{\bullet\bullet}+2O_O^x \rightarrow 2(OH)_O^{\bullet}. \quad (13)$$

Lowered concentration of oxygen vacancies results in conductivities values reduction.

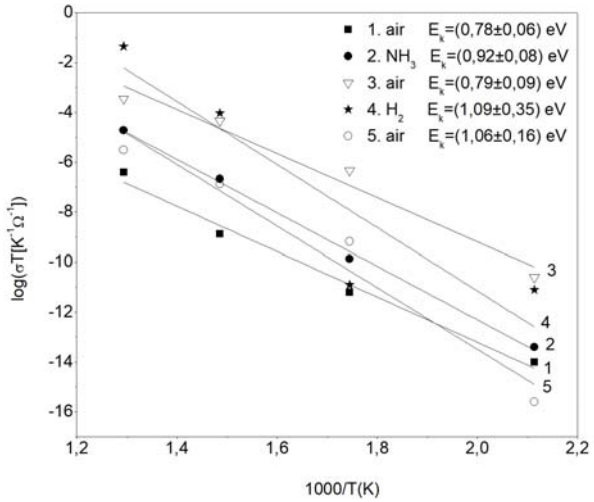

Fig. 7. Arrhenius plots for KBT1.

Additionally basing of Arrhenius plots, the linear regression analysis was performed and the energy of activation values were determined. The values about 1 eV indicate the intrinsic character of the conductivity. The lower values like in case of KBTSr10 in air and KBTSr20 in H_2 demonstrates the impact of extrinsic conduction on materials electrical properties. The higher values in case of KBT2 specimen in H_2 and KBT10Sr in H_2 may be due to partial reduction of oxide phases to metals. Values of energy of activation for KBTSr20 in air during 3rd and 5th series are not predicted by the theory and impossible to explained basing on the presented research. However it may be related to the possible reaction in secondary $SrTiO_3$ phase present in material. Some more detailed experiments should be conducted for elucidation of the observed phenomenon.

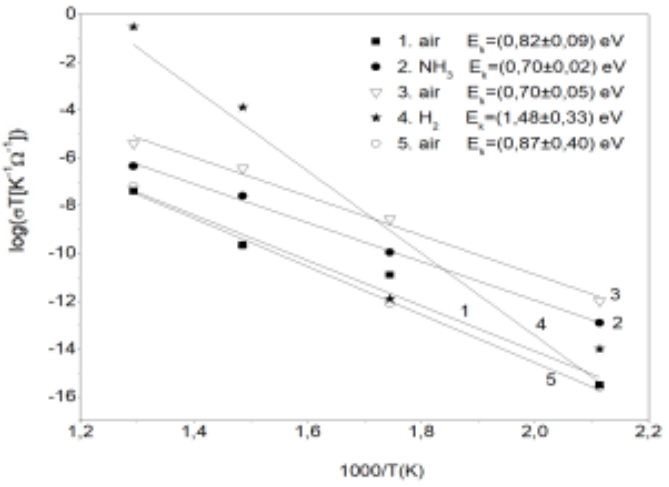

Fig. 8. Arrhenius plots for KBT2.

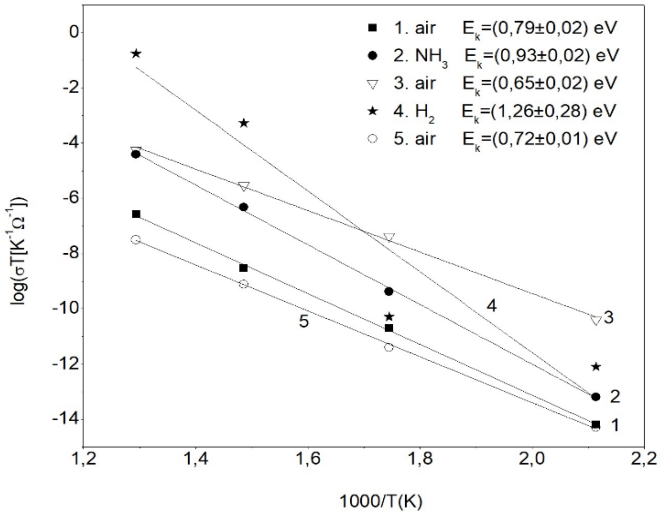

Fig. 9. Arrhenius plots for KBTSr10.

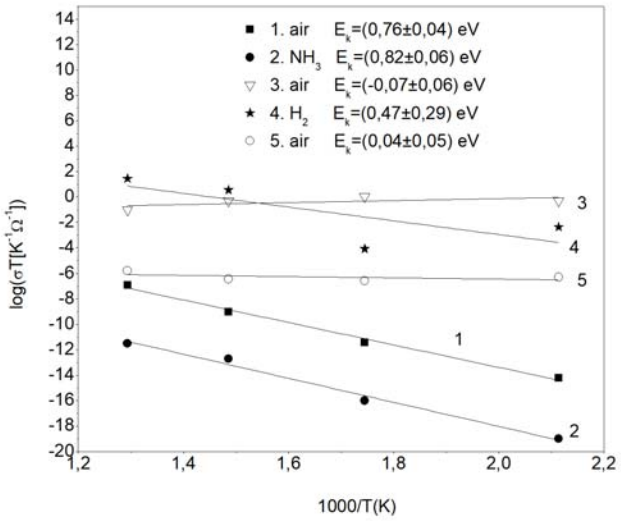

Fig. 10. Arrhenius plots for KBTSr20.

CONCLUSIONS

The mechanically stable sintered bodies of the nominal compositions $K_{0,5}Bi_{0,5-x}Sr_xTiO_3$ (x=0, 0.1 and 0.2) were prepared by mechanosynthesis route. It was found out that the double calcination improve the mechanical properties of the materials in comparison to use of single calcination process. In case of pure material and doped with 10%at Sr the main tetragonal phase was confirmed in specimen. However in all specimens small amounts of the parasitic unspecified phase were present in the material.

The investigated materials supported with silver electrodes reacted with gaseous ammonia and hydrogen in irreversible way which was demonstrated by electrical properties permanent modification. The mechanism of reaction was explained based on obtained Arrhenius plots. It was determined that the conduction in materials is mainly realized by oxygen vacancies and valence electrons.

ACKNOWLEDGMENTS

This work was supported by the National Science Centre of the Republic of Poland, under Grant No 2016/23/B/ST8/00163.

REFERENCES

[1] Aksel E., Jones J. L., Advances in Lead-Free Piezoelectric Materials for Sensors and Actuators, *Sensors,* 2010, 10, 1935-1954; DOI:10.3390/s1003019354

[2] Hou Y., Zhu M., Hou L., Liu J., Tang J., Wang H., and Hui Y., Synthesis and characterization of lead-free $K_{0.5}Bi_{0.5}TiO_3$ ferroelectrics by sol–gel technique,

Journal of Crystal Growth 2005, 273, 3-4, 500-503, DOI: https://doi.org/10.1016/j.jcrysgro.2004.09.055

[3] Hiruma Y., Aoyagi R., Nagata H., Takenaka T., Ferroelectric and Piezoelectric Properties of $(Bi_{1/2}K_{1/2})TiO_3$ Ceramics, *Japanese Journal of Applied Physics*, 2005, Part 1 44, 5040, DOI: https://doi.org/10.1143/JJAP.44.5040,

[4] Li Z., Wang C., Zhong W., Li J., Zhao M., Dielectric relaxor properties of $K_{0.5}Bi_{0.5}TiO_3$ ferroelectrics prepared by sol–gel method, *Journal of Applied Physics* 2003, 94, 2548 DOI: https://doi.org/10.1063/1.1592290

[5] König J., Spreitzer M., Jancar B., D. Suvorov, Samardzija Z., Popovic A., The thermal decomposition of $K_{0.5}Bi_{0.5}TiO_3$ ceramics, *Journal of the European Ceramic Society* 2009, 29, 1695–1701, DOI: https://doi.org/10.1016/j.jeurceramsoc.2008.10.002

[6] Baradarana S., Nasiri-Tabrizi B., Velayutham T.S., Basirun W.J., Sarhana A. A. D., Thermally induced crystallization of mechanically alloyed $Na_{0.5}Bi_{0.5}TiO_3$, *Ceramics International*, 2015, 41, 14157–14164 DOI: https://doi.org/10.1016/j.ceramint.2015.07.038

[7] Himura Y., Aojagi R., Nagata H. and Takenaka T., Ferroelectric and piezoelectric properties of $(Bi_{1/2}K_{1/2})TiO_3$ ceramics, *Japanese Journal of Applied Physics*, 2005, 44(7A), 5040–5044, DOI:

[8] Hou Y. D., Hou L., Huang S. Y., Zhu M. K., Wang H., Yan H., Comparative study of $K_{0.5}Bi_{0.5}TiO_3$ nanoparticles derived from sol–gel hydrothermal and sol–gel routes. *Solid State Communications*, 2006, 137, 658–661, DOI: https://doi.org/10.1016/j.ssc.2006.01.023

[9] Li Z. F., Wang C. L., Zhong W. L., Li J. C., Zhao M. L., Dielectric relaxor properties of $K_{0.5}Bi_{0.5}TiO_3$ ferroelectrics prepared by sol–gel method. 2003, *Journal of Applied Physics*, 2003, 94, 4, 2548–2552, DOI: https://doi.org/10.1063/1.1592290

[10] Hou L., Hou Y. D., Song X. M., Zhu M. K., Wang H., Yan H., Sol–gel-hydrothermal synthesis and sintering of $K_{0.5}Bi_{0.5}TiO_3$ nanowires, *Materials Research Bulletin*, 2006, 41, 1330–1336, DOI: https://doi.org/10.1016/j.materresbull.2005.12.010

[11] Yang J., Hou J., Wang C., Zhu M., Yan H., Relaxorbehavior of $K_{0.5}Bi_{0.5}TiO_3$ ceramics derived from molten salt synthesizes single-crystalline nanowires. *Applied Physics Letters*, 2007, 91, 023118, DOI: https://doi.org/10.1063/1.2754366.

[12] Wada T., Fukui A. and Matsuo Y., Preparation of $(K_{0.5}Bi_{0.5})TiO_3$ ceramics by polymerized complex method and their properties. *Japanese Journal of Applied Physics*, 2002, 41(11B), 7025–7028, DOI: http://iopscience.iop.org/article/10.1143/JJAP.41.7025/pdf

[13] Zhu M., Li L., Zheng m., Hou Y., Relaxor to ferroelectric crossover in KBT ceramics by prolonged annealing, J*ournal of Alloys and Compounds*, 2017, 703, 448-453, DOI:https://doi.org/10.1016/j.jallcom.2017.01.299

[14] Zhu M., Hou L., Hou∗Y., Liu J., Wang H., Yan H., Lead-free $(K_{0.5}Bi_{0.5})TiO_3$ powders and ceramics prepared by a sol–gel method, *Materials Chemistry and Physics*, 2006, 99, 329–332, DOI: https://doi.org/10.1016/j.matchemphys.2005.10.031

[15] Yang Ch.H., Wang Zh. ,Xu H.Y.,SunZh.H. ,Jiang F.Y. ,Han J.P. Zh. J.R. Preparation and main characteristics of lead-free $K_{0.5}Bi_{0.5}TiO_3$ ferroelectric thin films, *Journal of Crystal Growth*, 2004 262, 304–307, DOI: 10.1016/j.jcrysgro.2003.10.02

[16] König J., Suvorov D., Evolution of the electrical properties of $K_{0.5}Bi_{0.5}TiO_3$ as a result of prolonged sintering, *Journal of the European Ceramic Society*, 2015, 35, 2791–2799, DOI: 10.1016/j.jeurceramsoc.2015.04.003

[17] Vijaya Bhaskar Rao P., Ramana E.V. , Bhima Sankaram T., Electrical properties of $K_{0.5}Bi_{0.5}TiO_3$, *Journal of Alloys and Compounds* 2009, 467, 293–298, DOI: 10.1002/chin.200912007

[18] Guo J., Zhu M., Li L., Qing T., Wang C., Liu L., Zheng M., Hou Y.,Normal-relaxor ferroelectric modulation of a-site complex perovskite ferroelectric $(K_{1/2}Bi_{1/2})TiO_3$ by post-annealing, Journal of *Applied Physics*, 2017, 121, 014101, DOI: https://doi.org/10.1063/1.4973124

[19] Vijaya Bhaskar Rao P., Bhima Sankaram T., Impedance spectroscopy studies of $K_{0.5}Bi_{0.5}TiO_3$, *J Electroceram*, 2010, 25, 60–69, DOI: https://doi.org/10.1007/s10832-009-9589-4

[20] Li L., Li M., Reaney I. M., Sinclair, D. C., Mixed ionic-electronic conduction in K1/2Bi1/2TiO3, *J. Mater. Chem. C*, 2017, 5,6300-6310, DOI: 10.1039/c7tc01786c

[21] Dutkiewicz E.M., Suchanicz J., Bovtun V., Konieczny K., Czaja P., Kluczewska K., Handke B., Antonova M., Sternberg A., Raman spectra and anomalies of dielectric properties and thermal expansion of lead-free $(1-x)Na_{0.5}Bi_{0.5}TiO3\text{-}xSrTiO_3$ (x = 0, 0.08 and 0.1) ceramics, Phase Transitions, 89, 7-8, 823-828, DOI: 10.1080/01411594.2016.1182167

[22] Szczurek A., Pomiary lotnych związków organicznych rezystancyjnymi czujnikami gazów, Oficyna Wydawnicza Politechniki Wrocławskiej, Wrocław 2006, DOI http://www.dbc.wroc.pl/Content/2019/Szczurek.pdf

[23] Pohle R., Fleischer M., Meixner H., In situ infrared emission spectroscopic study of the adsorption of H_2O and hydrogen-containing gases

on Ga_2O_3 gas sensors, *Sens. Actuators B*, 2000, 68, 151–156. DOI: https://doi.org/10.1016/S0925-4005(00)00476-7

[24] Kohl D., Ochs Th., Geyer W., Fleischer M., Meixner H., Adsorption and decomposition of methane on gallium oxide films, *Sens. Actuators B*, 1999, 59, 140–145, DOI: 10.1016/S0925-4005(99)00211-7

[25] Yamazoe N., Fuchigami J., Kishikawa, T. Seiyama, Interactions of tin oxide surface with O_2, H_2O and H_2, *Surf. Sci*. 1979, 86, 335–344,*DOI*: 10.1016/0039-6028(79)90411-4.

Determination of oil sorption properties of fibrous media coated with aerogel particles

Juliusz Kondracki[1], *Patrycja Wierzba[1], Bartosz Nowak[1], Andrzej Krasiński[1], Marta Bojarska[1,2]

[1]Faculty of Chemical and Process Engineering, Warsaw University of Technology, Warsaw, POLAND

[2]GVS Filter Technology, Zola Predosa (Bologna), ITALY

*e-mail: patrycja.wierzba.dokt@pw.edu.pl

Keywords*: polypropylene fibrous media, hydrophobic organosilica aerogels, wettability, capillary rise test, emulsion separation*

ABSTRACT

The research is focused on polypropylene nonwoven media modified with aerogel particles. A capillary rise test was used to determine sorption properties of five different materials: untreatedpolypropylene nonwoven, three materialsmodified with aerogel and reference polypropylene exposed to modification conditions but without methyltrimethoxysilane precursor resulting inany aerogel particles deposited on its' surface. Pure polypropylene filterswerecoated with aerogel particles synthesized at volume ratios of precursor methyltrimethoxysilane (MTMS) to solvent (methyl alcohol): 1:20, 1:15 and 1:10. The influence of these modifications on sorption kinetics was studied for three pure oils: di-ethyl-hexyl-sebacate (DEHS), diesel fuel, and vegetable oil, as well as for their 10% vol. emulsions in water. Additionally, the static contact angles of water droplet on the porous media immersed in oil were determined, which can be considered as a measure of relative affinity of sorbent to each liquid.

INTRODUCTION

The separation of oil in water emulsionis carried outusing oil sorptive materials due to numerous of advantages. The use of sorbents is easy, relatively cheap and environmentally friendly when biodegradable materials are used. However, one of main advantages is treatment of oil spill areas with limited access, for example during oil tankers accidents or on sites of crude oil extraction [1].

Sorbents are materials which enable to adsorb of other substances on the surface and inside the pores. The binding mechanism is based on interaction between molecules of the substance that is being removed (e.g. oil) and the surface of adsorbent. In majority cases, the interactions have a physical character and relate to adhesion force that occurs on the entire surface of the porous material. The application of sorbents is an effective method for small amount of oil spills when oil forms thin layer on water surface. Sorbents enhance agglomeration of oil and

consequently reduce the area of spillage. In case of large spillage, mechanical barriers are used in order to reduce contaminated area and sorbents play only the role of support for mechanical methods. Sorption materials dedicated to above mentioned application are available in the form of mats, rolls, sleeves or pillows filled with adsorbent. The most common adsorbents are polymer based nonwovens (polypropylene, polyethylene, polyurethane, polystyrene) prepared by the melt-blow technique [2, 3]. They are able to adsorb wide range of synthetic and natural oils. Additionally, they are unsinkable which gives the possibility to easily remove them from the water environment after imbibition of oils. Adsorbents can also be used to remove oil contaminations from water streams in a various types of water purification systems [4]. Sorbents in the form of polymer cartridges, bag filters or canisters with activated carbon or zeolites are commercially available. Their main drawback is related to limited sorption capacity, which results in additional costdue to frequent regeneration or replacement of adsorption cartridges. Hence, they are usually used for relatively small amounts of oil or as the final stage of a "deep" purification process.

The quality and application of sorbents can be assessed on the basis of surface, structural and sorption properties of a porous material.

The sorption properties, such as sorption capacity and sorption selectivity should be possibly the highest corresponding to tested type of dispersion. Sorption materials characterized by high selectivity are able to adsorb only one kind or group of chemical compounds with simultaneous low affinity to other substances. The selectivity of sorbents depends on their chemical composition and structure, therefore by modification of these properties, a desired selectivity and sorption capacity can be obtained [5].

Taking into account the surface properties, the oil adsorbents used in water purification should be characterized by strong hydrophobic and oleophilic properties, which enable selective separation of oil from water. Therefore, the measurement of contact angles (CA) (for water droplets surrounded by oil)can be used to determine oil/water selectivity. From practical point of view the precise determination of CA for porous materials can be difficult due to non-uniform structure, therefore this method is recommended only for comparative analysisof porous materials.

In order to characterize sorption properties and wettability kinetic of porous structures, the widely used capillary rise method can be applied [6]. For materials of known geometry(described by pore sizes and fibers diameter distribution), the rate of oil imbibition provides information about the capillary pressure, which is the driving force for oil transport. In the case of single capillary the dynamics of this process is described by the modified Washburn equation (Eq. 1)[7]. The following assumptions were included to define presented equation: liquid flow inside the

capillary is laminar, liquid flow is stationary, no slip condition on the surface is assumed and the influence of hydrostatic pressure is neglected.

$$m^2 = C \cdot \frac{\rho^2 \cdot \sigma \cdot cos\theta}{\mu} \cdot t \quad (1)$$

In Eq. 1ρ, σ and μ denote liquid density, surface tension and dynamic viscosity, respectively. Parameters m and t stand for weight and time. Constant C describes geometrical parameters of the capillary and can be determined experimentally for liquid of known contact angle (usually perfectly wetting liquid is selected, i.e. $\theta = 0°$).According to the modified Washburn equation (Eq. 1) the weight square is linearly proportional to time [7]. This relationship is fulfilled only for the viscous flow regime in the capillary, when influence of hydrostatic pressure can be neglected. In order to describe results presented in section Results and Discussion, the Eq. 1 was simplified to the form:

$$m^2 = A \cdot t \quad (2)$$

and values of coefficient A were provided.

In presented work, the capillary rise test was used to determine sorption properties of five different materials: reference polypropylene nonwoven, three modifications with aerogel and untreated polypropylene material exposed to modification conditions but without presence of precursor.The influence of modifications on the sorption kinetics was studied for three pure oils: di-ethyl-hexyl-sebacate (DEHS), diesel fuel, and vegetable oil, as well as for their 10% vol. emulsions in water.

MATERIALS AND METHODS

Experimental setup

The experimental setupused for the capillary rise test was equipped with a laboratory balance (1) connected to a PC which enables transmission and storage of data (Figure 1). A glass Petri dish (2) placed on the balance was filled with the tested oil. The polypropylene nonwoven media (3) were cut to specific dimensions and placed manually above the glass Petri dish. A handwheel (4) enabled slow lowering of the tested material until it reached surface of the liquid. The recorded loss of mass, in Petri dish, with time indicated the amount of oil transported through the media due to the capillary rise.

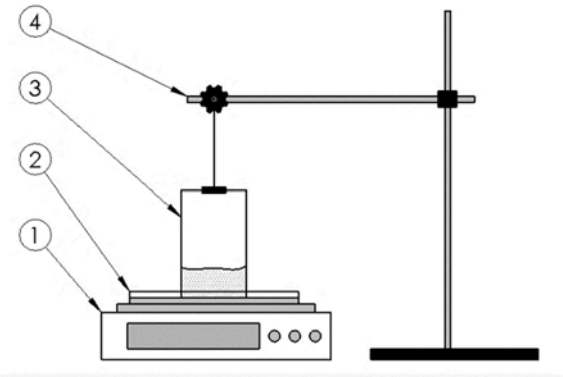

Fig. 1. Scheme of the experimental setup for capillary rise tests: 1- laboratory balance, 2- glass Petri dish, 3- tested material(in a form of square), 4- handwheel placed on the laboratory stand.

Characterization of fibrous media

Studied fibrous media were made of polypropylene using the melt-blow technique. This method is based on extrusion of molten polymer through a multichannel nozzle with a simultaneous elongation of polymer jets by a stream of hot air. Thin polymer streams solidify very fast forming fibers, which are collected on the receiver and form a mat. Operating parameters such us polymer flowrate, temperature, air flowrate and nozzle type, as well as method of fiber collection enable to obtain polymer media of different fiber diameters and porosities.

In this work polypropylene media with average diameter of fibers equal to 5.15±3.42 μm were investigated. In Figure 2 scanning electron microscopy images of reference polypropylene fibers are presented.

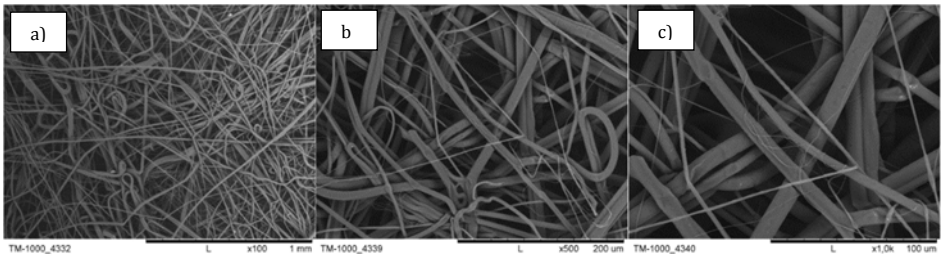

Fig. 2.SEM images of polypropylene fibers in magnification: a) 100x, b) 500x, c) 1000x.

To characterize the surface properties of materials, measurements of static contact angle (CA) for water droplet surrounded by oils were carried out. To this purposethe goniometer Dataphysics OCA 25 was used. Obtained contact anglesdefine the ability of the sorption material to repel water, prevent its accumulation on the surface, thus making the surface easily accessible for oil to be adsorbed.

Modification method

To enhance sorption properties of polypropylene materials, the fiber modification with aerogel spheres was applied[8].Aerogel synthesized from the methyltrimethoxysilane (MTMS) precursorwas chosen due toits hydrophobic, oleophilic and oil-sorptive properties [9]. Organosilica structure of aerogel was obtained in two-step sol-gel process. Firstly, hydrolysis reaction in presence of precursor, methanol and oxalic acid solution was carried out. Secondly, after 24 hours, condensation of silanols occurred as a result of slowly dosed ammonium hydroxide solution. Finally, reference polypropylene material was dipped into reactive solution and drying step in 50°C by 24 hourswas started. Drying procedure enabled transformation of alcogel solution into aerogel spheres. Application of different MTMS:methanol ratios (1:20, 1:15 and 1:10) with simultaneous maintainingthe same ratio of MTMS:oxalic acid:ammonium hydroxide (1:4:4) for all modifications allowed to obtain materials with different amount of aerogel deposited in the filters [10]. Amount of deposited aerogel increased in the following order 1:20, 1:15, 1:10. The SEM images of modified polypropylene fibers are shown in Figure 3.

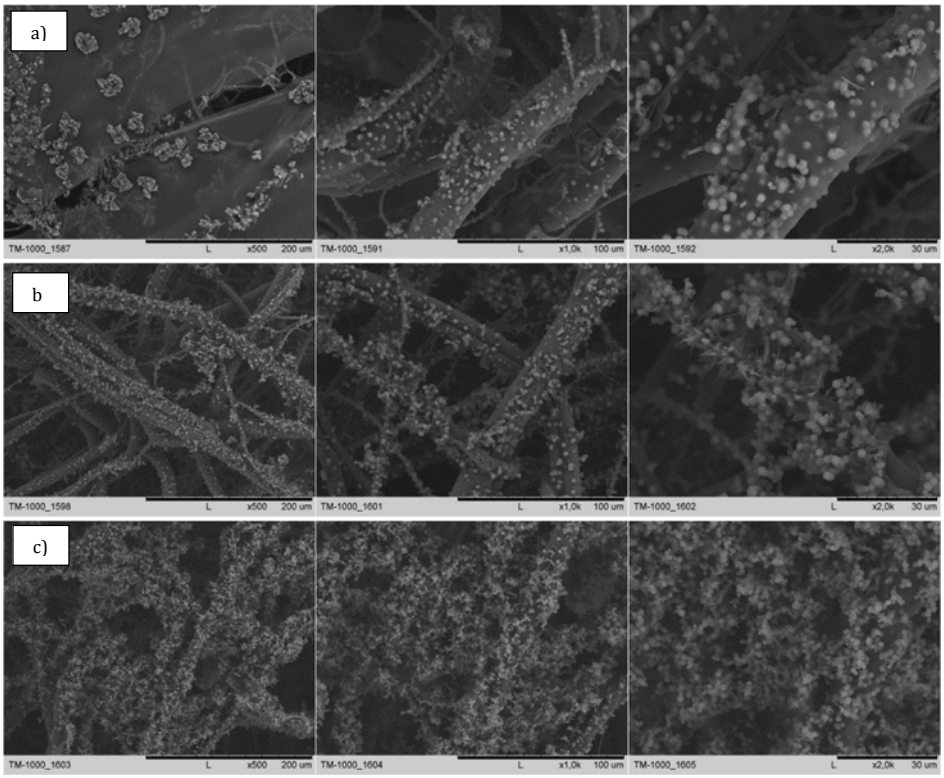

Fig. 3.SEM images of material modified with aerogel for MTMS:methanol ratios: a) 1:20, b) 1:15, c) 1:10. Magnification 500x, 1000x, 2000x (from left to right).

Additionally, reference polypropylene material was exposed to modification conditions but without precursor presence, therefore deposition of aerogel did not occur . In this way, the effect of temperature and solvent on the structure and properties of reference material was verified.

Characterization of oils and dispersions

Three pure oils: di-ethyl-hexyl-sebacate (DEHS), diesel fuel, and vegetable oil were usedas a test liquids. The properties such as density and viscosity for all liquids were determined experimentally using tensiometer EasyDyne (KRÜSS) and viscometer LVDV2 (BROOKFIELD), respectively. The results are listed in Table 1.

Tab. 1. Properties of oils used in experiments.

Type of oil	Density [kg/m^3]	Viscosity [Pa s]
Diesel fuel	823	0.0024
Di-ethyl-hexyl-sebacate (DEHS)	912	0.022
Vegetable oil	885	0.0653

Besides of pure oils, oil/water dispersions were also used in the capillary rise test. In order to produce 10%vol. oil/water emulsions the rotor-stator type homogenizer (Ultra Turrax T18) with the agitation time equal to 1 minute was used.The dispersions were stabilized by addition of surfactants: Tween 20 (0.25%wt. solution in water) and Span 80 (2%wt. solution in oils). Surfactants concentrations were determined experimentally in orderto obtain the highest stability of dispersions.The size distribution of oil dropletswas determined based onthe optical microphotographs method. The average droplet size of number distribution was equal to 5.19±2.56 μm for DEHS, 5.26±2.78 μm for diesel fuel and 5.75±4.54 μm for vegetable oil droplets.

RESULTS AND DISCUSSION

To simplify the description of results the following symbols for tested materials are used: PP reference for polypropylene material without modification, PP SC for polypropylene material exposed to synthesis conditions but without aerogel deposition. Additionally, abbreviationsPP 1:20, PP 1:15, PP 1:10 mean polypropylene materials modified with aerogel with precursor to solvent ratios equal to 1:20, 1:15 and 1:10, respectively.

Static contact angle

The results for measurements of static contact angle (CA) for water droplet surrounded by oils (DEHS, diesel fuel, and vegetable oil) are presented separately in Figures 4a-4c. The graphs show that tested materials exhibit hydrophobic properties regardless of the type of ambient oil. The obtained results in majority indicate values of the contact angle above 150° whichis commonly referred to superhydrophobic properties. The standard deviations for average value of CA are a consequence of porous and heterogeneous material soaked with oil. The massive amount of aerogel deposited on the filter surface caused the structure to float, therefore it was impossible to place the water droplet on the surface of immersed material for the measurement. For this reason, the results for polypropylene material PP 1:10 were not presented in graphs.

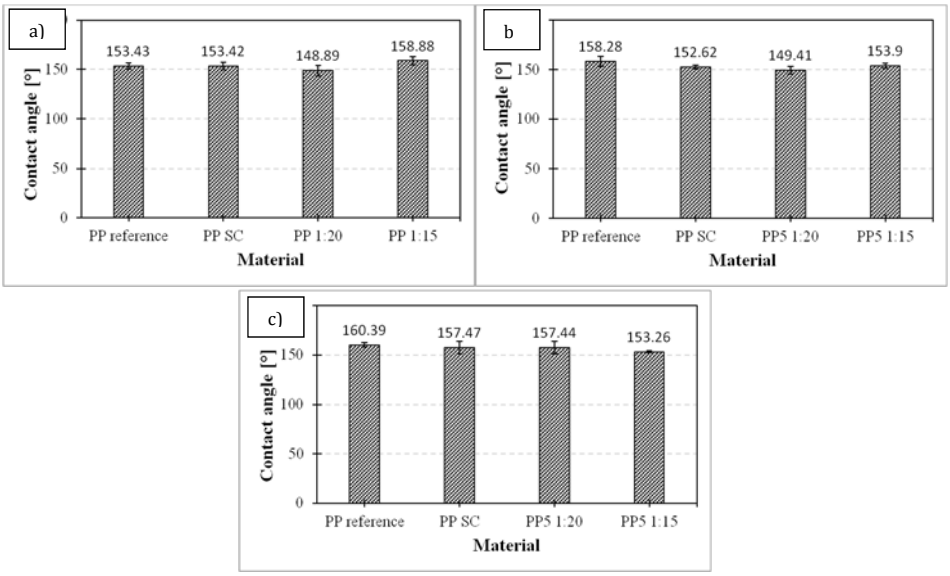

Fig. 4. The results of static contact angle for water droplet placed on tested materials in the surrounding of: a) DEHS, b) diesel fuel, c) vegetable oil.

Capillary rise tests

The results of capillary rise tests were shown in graphs of mass square versus time according to the modified Washburn equation (Eq. 2).Obtained results were presented separately for each oil and for their 10% vol. emulsions in water. All materials were tested in the same manner in order to compare the influence of modification on the sorption process. Additionally, graphs with linear curves determined for initial stage of sorption process for selected materials were also presented. The slope of experimental curves $m^2 = f(t)$(in the range where the linear dependence was observed)are presented in Figures 5-7 and 9-11. The slope coefficients account for sorption kinetics of oils in tested materials.

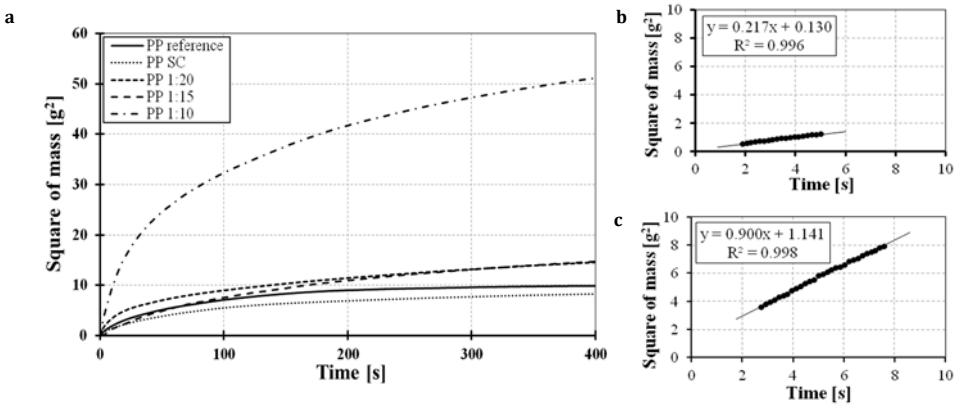

Fig. 5. a)Comparison ofsorption kinetics of DEHS by all tested materials. Initial step of DEHS sorption process by b) PP reference and c) PP 1:10.

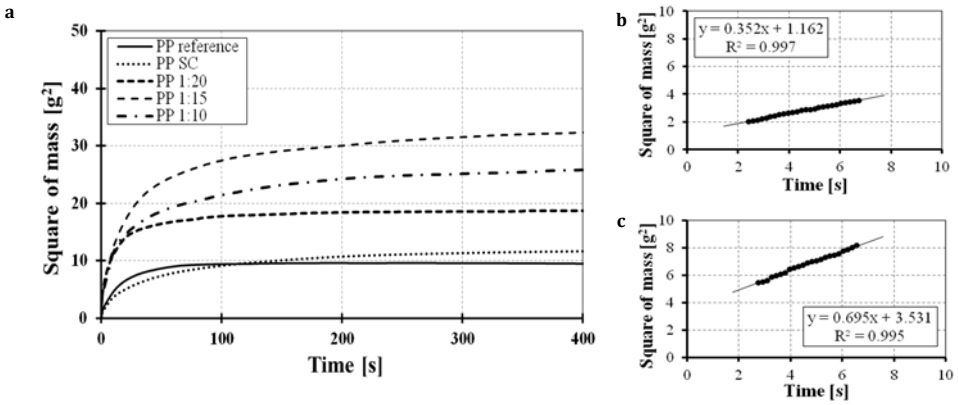

Fig. 6. a)Comparison ofsorption kinetics of diesel fuel by all tested materials. Initial step of diesel fuel sorption process by b) PP reference and c) PP 1:10.

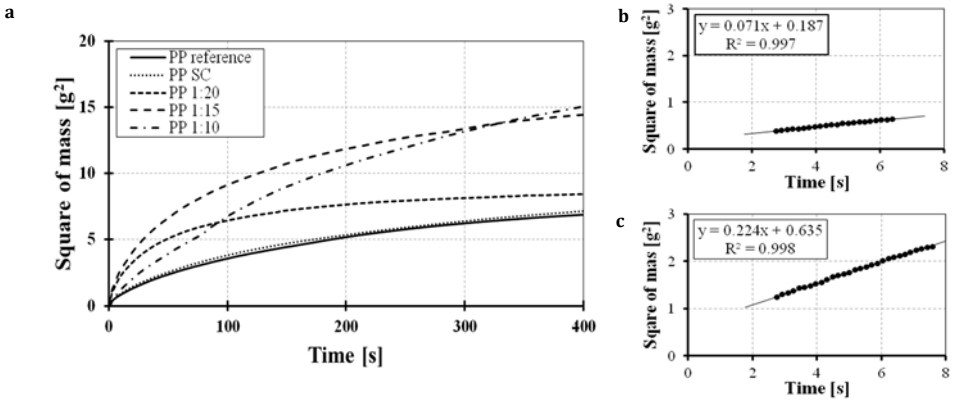

Fig. 7. a)Comparison ofsorption kinetics of vegetable oil by all tested materials. Initial step of vegetable oil sorption process by b) PP reference and c) PP 1:15.

On the basis of the presented graphs (Fig. 5-7) it can be concluded that modifications of polypropylene material with aerogel have a pronounced impact on oil sorption capacity and kinetics of the imbibition. Modified materials possess better sorption capacity than polypropylene reference material. Aerogel particles obtained at lower ratio of precursor (MTMS) to solvent (methanol) such as 1:15 and 1:10 enabled to obtain materials with the best sorption kinetics for all tested oils. The largest differences of sorption kinetics between tested materials were observed for diesel fuel (Fig. 6). In the case of DEHS sorption, the best results were obtained for PP 1:10 material (Fig. 5). Additionally, it is worth to note that PP reference and PP SC materials show similar sorption properties for all tested oils, which means that the treatment conditions do not affect the properties of original structure.

In order to show the influence of tested oils properties on sorption process, the results of imbibition PP reference and PP 1:10 materials by three oils are presented(Fig. 8).

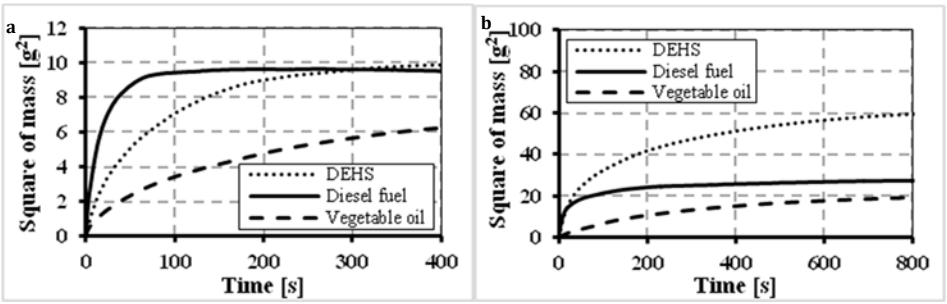

Fig. 8. Sorption kinetics of three oils: DEHS, diesel fuel, vegetable oil by a) PP reference and b) PP 1:10 materials.

The results presented in Figure 8 show that sorption kinetics of vegetable oil is the slowest for PP reference and PP 1:10 materials. In the case of other tested materials observed tendencies are similar, therefore detailed results are not presented. In the case of two other oils, e.g. DEHS and diesel fuel, it is difficult to determine which oil was sorbed better. However, it is clearly visible that sorption kinetics in the initial stage is much faster in the case of diesel fuel than DEHS. Additionally, the state of saturation of the material structure with oil was reached faster for diesel fuel. The obtained results are closely related to the viscosity and specific weight of tested oils. As it was presented in Tab. 1, oil viscosity increases successively for diesel fuel, DEHS and vegetable oil. Moreover, diesel fuel is characterized by lower specific weight than DEHS and vegetable oil.

The results of capillary rise tests for oils dispersed in water are presented in Figs.9-11.

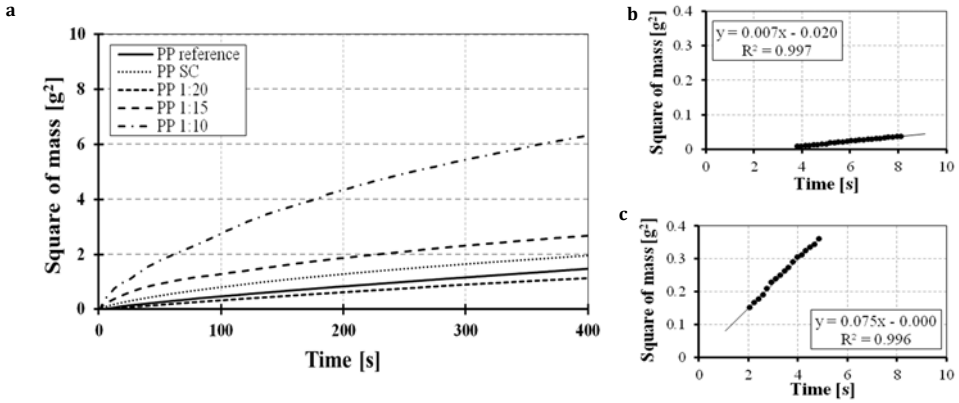

Fig. 9. a)Comparison ofsorption kinetics of DEHS from its' 10% vol. emulsion in water by all tested materials. Initial step of sorption process of DEHS from its' 10% vol. emulsion in water by b) PP reference and c) PP 1:10.

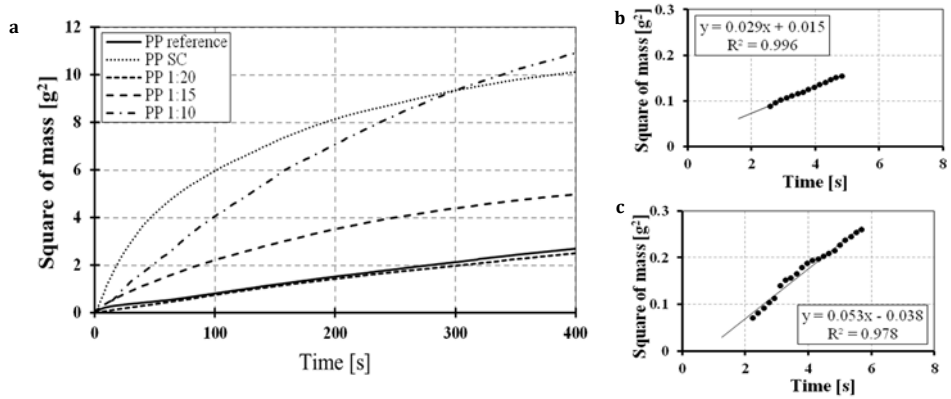

Fig. 10. a)Comparison ofsorption kinetics of diesel fuel from its' 10% vol. emulsion in water by all tested materials. Initial step of sorption process of diesel fuel from its' 10% vol. emulsion in water by b) PP reference and c) PP 1:10.

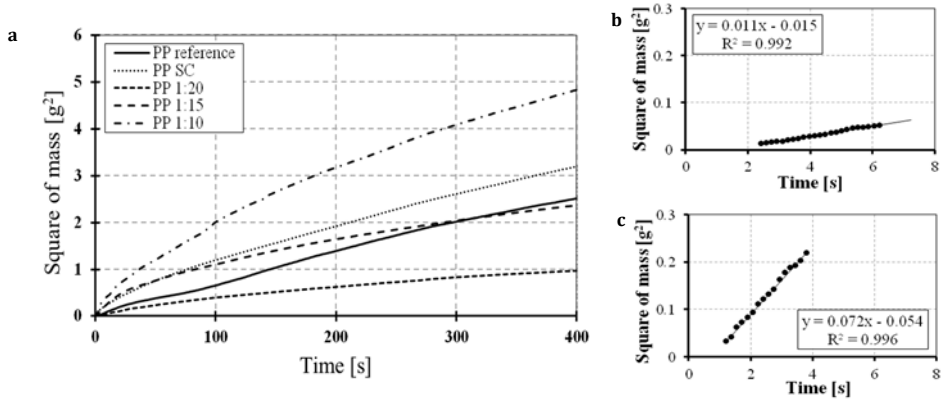

Fig. 11. a)Comparison ofsorption kinetics of vegetable oil from its' 10% vol. emulsion in water by all tested materials. Initial step of sorption process of vegetable oil from its' 10% vol. emulsion in water by b) PP5 reference and c) PP 1:10.

Based on the presented results (Figures 9-11), the significant increase of sorption properties of dispersed oils by PP 1:15 and PP 1:10 materials was noticed. On the other hand, PP 1:20 material shows similar or weaker sorptioncapacity than PP reference material. The surprising results were obtained for PP SC material. This can be explained by changed surface properties of the bottom part of the flat reference material from hydrophobic to more hydrophilic ones due to treatment in aerogel synthesis conditions. The specific deposits appeared on bottom layer of material, which adhered to glass dish during material treatment. Properties of PP SC were confirmed by analysis of spectra obtained by Fourier transformed infrared spectroscopy (FTIR), where thenew hydrophilic (e.g. –OH,–COOH) chemical bonds appeared only on the bottom surface of the material. Additionally, measurements of static contact angle for water droplets were carried out. Both described analysis of PP SC material properties confirm a low selectivity of material. Moreover, the imbibition of both oil and water was observed during the capillary rise test.

The influence of applied emulsions on sorption process by PP reference and PP 1:10 materialsis presented in Fig. 12.

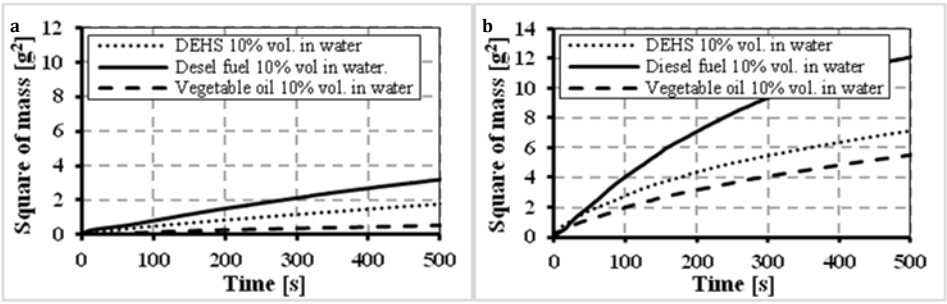

Fig. 12. Sorption kinetics of 10% vol. oil emulsions in water by:
a) PP reference and b) PP 1:10 materials.

The Figure 12 confirms that diesel fuel dispersed in water is adsorbed the most effectively by PP reference and PP 1:10 materials. The opposite tendency is observed for vegetable oil dispersed in water, i.e. the difference is not as significant when compared with DEHS dispersed in water. The other tested materials show similar tendencies, therefore detailed results were not presented.

To summarize, the averaged coefficients$A$ (Eq. 2) obtained for initial and linear stage of sorption process for all tested materials and liquids are presented in Table 2.

Tab. 2. Results of sorption kinetics.

	PP reference	PP SC	PP 1:20	PP 1:15	PP 1:10
Pure oils	**Averaged coefficient *A* [g²/s]**				
Diesel fuel	0.394±0.088	0.258±0.030	0.665±0.058	0.896±0.021	0.580±0.208
DEHS	0.251±0.057	0.139±0.032	0.262±0.027	0.509±0.178	0.585±0.334
Vegetable oil	0.075±0.007	0.087±0.008	0.202±0.020	0.243±0.021	0.171±0.053
Oil dispersions	**Averaged coefficient *A* [g²/s]**				
10% vol. Diesel fuel in water	0.030±0.002	0.114±0.007	0.008±0.002	0.043±0.004	0.058±0.015
10% vol. DEHS in water	0.007±0.000	0.015±0.003	0.006±0.001	0.040±0.013	0.071±0.011
10% vol. vegetable oil in water	0.011±0.002	0.027±0.010	0.008±0.004	0.034±0.009	0.043±0.010

As it was mentioned above, the results obtained for PP SC material during tests with aqueous dispersions refer to sorption of both oil and water, therefore they will not be taken into account in further considerations. However, the experimental data shown in Table 2 indicate some tendencies. In the case of pure oils, the averaged coefficient *A* decreases with increase of oil viscosity in order: diesel fuel, DEHS and vegetable oil.This tendency is not observed for tests performed for emulsions, however, significant influence of oil viscosity on sorption process is clearly visible. The results prove that modification of polypropylene nonwovens by aerogel improves material sorption properties. For tests performed for pure oils the best results demonstrate PP 1:15 and PP 1:10, while in the case of oil emulsions in water, the PP 1:10 materialshowsthe best sorption capacity and kinetics. For both cases, the values of coefficient*A* increase several times after applying the material modification. For PP 1:10 material used to DEHS sorption from the aqueous dispersion, the coefficient *A* was approximately ten times higherthan *A* coefficient obtained for PP reference sample. The PP 1:20material is characterized by medium sorption properties, probably because of not sufficient amount of aerogel deposited on its' surface.

CONCLUSIONS

The capillary rise test is a good method to assess and compare sorption kinetics of selected liquids by different materials. On the basis of obtained results, very strong influence of applied modificationon sorption kinetics was observed. Materials obtained by aerogel synthesis in volumetric ratio of precursor to solvent equal to 1:15 and 1:10 exhibit higher sorption capacity and faster sorption kinetics

than PP reference material in testsperformed for pure oils and their aqueous emulsions.

Moreover, the results obtained for studied oils characterised by different physicochemical properties show a pronounced influence of oil viscosity on sorption process. The imbibition of high viscous vegetable oil was very slow in comparison with fast transport of diesel fuel characterized by smaller viscosity (i.e. more than 27 times smaller than vegetable oil viscosity). This tendency observed in experiments comes directly from the modified Washburn equation where value of mass square versus time is inversely proportional to viscosity of the liquid.

The presented results provide significant contribution in research focused on materials modified by organosilica aerogels. The development of aerogel modified materials can lead to production of good sorbents, which are able to ensure more effective purification of water from oil impurities than original base materials, thus, reducing the environmental impact of oil spillages in water reservoirs.

ACKNOWLEDGEMENTS

This work was supported by NCBiR project "Oil removal from gas and liquid streams thanks to filter media modified by aerogel" LIDER/011/L-6/14/NCBR/2015

REFERENCES

[1] Al-Majed A.A., Adebayo A.R., Hossain M.E., A sustainable approach to controlling oil spills, *J. Envir. Manag.*, 2012, 113, 213-227, DOI: 10.1016/j.jenvman.2012.07.034

[2] Wei Q.F., Mather R.R., Fotheringham A.F., Yang R.D., Evaluation of polypropylene nonwoven oil sorbents in marine oil spill recovery, *Marine Poll. Bull.*, 2003, 46 (6), 780-783, DOI: 10.1016/S0025-326X(03)00042-0

[3] Lin J., Shang Y., Ding B., Yan J., Yu J., Al-Deyab S.S., Nanoporous polystyrene fibers for oil spill cleanup, *Marine Poll. Bull.*, 2012, 64 (2), 347-352, DOI: 10.1016/j.marpolbul.2011.11.002

[4] Ali I., New generation adsorbents for water treatment, *Chem. Rev.*, 2012, 112, 5073-5091, DOI: 10.1021/cr300133d

[5] Adebajo M.O., Frost R.L., Kloprogge J.T., Carmody O., Kokot S., Porous materials for oil spill cleanup: A review of synthesis and absorbing properties, *J. Porous Mater.*, 2003, 10, 159-170, DOI: 10.1023/A:1027484117065

[6] Dang-Vu T., Hupka J., Characterization of porous materials by capillary rise method, *Physicochemical Problems of Mineral Processing*, 2005, 39, 47-65

[7] Yang W., Chang Q., Wettability studies of filter media using capillary rise test, *Sep. Purif. Technol.*, 2008, 60, 335-340, DOI:10.1016/j.seppur.2007.04.009

[8] D., McLaughlin E., Pfefer R., Lin Y.S., Adsorption of oils from pure liquid and oil-water emulsion on hydrophobic silica aerogels, *Sep. Purif. Technol.*, 2012, 99, 28-35, DOI: 10.1016/j.seppur.2012.08.001

[9] Yun S., Luo H., Gao Y., Superhydrophobic silica aerogel microspheres from methyltrimethoxysilane: rapid synthesis via ambient pressure drying and excellent absorption properties, *RSC Adv.*, 2014, 4, 4535-4542, DOI:10.1039/C3RA46911E

[10] Rao A.V., Bhagat S. D., Hirashima H., Pajonk G. M., Synthesis of flexible silica aerogels using methyltrimethoxysilane (MTMS) precursor, *J.Coll. and Int. Sc.*, 2006, 300, 279-285, DOI: 10.1016/j.jcis.2006.03.044

Heat Transfer in Helical Coil Heat Exchanger: Parametric Study

* Krzysztof Kowalski, Dorota Downarowicz
Faculty of Chemical Technology and Engineering, West Pomeranian University of Technology, Szczecin, POLAND
e-mail: krzysztof.kowalski@zut.edu.pl

***Keywords**: helical coil, heat exchanger, condensation, Wilson method, laminar flow, pressure drop*

ABSTRACT

Helical coil heat exchangers are widely used in a variety of industry applications such as refrigeration systems, power generation, process plants and heat recovery. The purpose of this paper is to investigate the effect of Reynolds number and the operating temperature on the heat transfer performance and the pressure drop for laminar flow conditions. The experiments were performed in the following invariability range of operating parameters: air velocity 6.6 - 26.6 m/s, the coolant temperature 243 – 273 K. The data analysis showed, that the overall heat transfer coefficient and the pressure drop are increased with the increase of the gas flow rate.

INTRODUCTION

A helical coil heat exchanger consists of a cylindrical shell and a helical coiled tube with constant curvature ratio and coil pitch. It is widely applied in various industrial applications due to its simple and compact structure, large heat transfer area and high heat transfer rate [1]. This heat exchanger is one of the key devices in chemical, petroleum, refrigeration, food, power generation and nuclear industries as well as in air-conditioning and heat recovery systems. It can be used in sterilization, pasteurization, cryogenic, crystallization, separation (distillation) and reaction processes [2,3].

The flow and convective heat transfer in a helical coiled tube are more complex than in a straight tube, because it strongly depend on the behaviour of secondary flow which enhances the heat transfer rate and fluid mixing. This phenomenon is particularly distinct in the laminar flow regime [4,5].

In a straight tube, the velocity profile of laminar flow is parabolic because the viscous forces are larger than the inertial and are enough to suppress fluid fluctuations. When the fluid flows through a coiled tube, the main (primary) velocity profile is distorted due to the formation of a secondary flow induced by centrifugal forces [6]. This flow is produced in the plane perpendicular to the axial flow direction.

The flow in coiled tubes is governed by coil curvature ratio and the Reynolds number. The former parameter is defined as the ratio of coil to tube diameters, whereas

the other as the ratio of inertia to viscous forces [7]. The product of both dimensionless parameters is the Dean number, which is defined as the ratio of centrifugal to inertial forces. The inertial forces are negligible for low Dean numbers (De<20). They are balanced by the viscous forces in the intermediate Dean value range (20<De<40). In other cases, viscous forces are significant only in the boundary near the tube wall.

Pressure drop in helical coils at low values of Reynolds number are highly dependent on curvature ratio. As the values of flow rate increases, the effect of curvature ratio on the pressure drop decreases [8].

The helical coil heat exchangers can be applied to the separation of solvent vapours from gas stream in air purification plants. However, very few studies have addressed this issue to date. The knowledge of the heat transfer and flow characteristics is essential to design and optimization such devices [9,10]. In optimal conditions the heat transfer coefficient should be as high as possible with the lowest possible pressure drop.

The main objective of this study was to investigate the influence of gas flow rate and the operating temperature on the heat transfer performance and the pressure drop in the helical coil heat exchanger which was used as to cool vapour-air mixtures. Heat transfer coefficients were determined by the Wilson method and from Nusselt number correlations for laminar flow regime.

EXPERIMENTAL SETUP

Apparatus and materials

Fig. 1 shows a schematic diagram of the experimental set up.

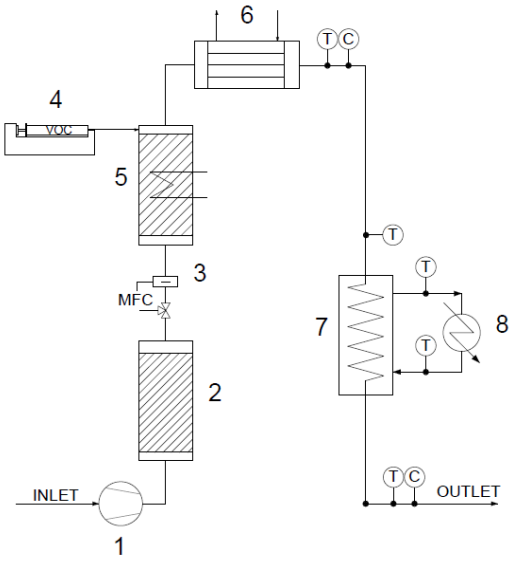

Fig. 1. Schematic diagram of experimental setup; 1 –compressor, 2 – desiccant dryers , 3 –flowmeter, 4 – VOC syringe pump, 5 – static mixer, 6 – water cooler, 7 – condenser, 8 - refrigerating circulator, T – PT100 sensor, C – sampling point.

The set-up consists of a gas preparation section, a helical coil heat exchanger, a refrigerated circulator (FP ME50, Julabo) and a data acquisition and a control system. The schematic diagram of the heat exchanger and its geometry parameters are shown in Fig.2 and Tab.1, respectively.

The construction of the heat exchanger is shown in Fig.2. The pure or 2-propanol (IPA)-laden air streams with specified concentrations ranging from 3.9 to 10.4 g/m^3 were used to the study. The experiments were performed in the following invariability range of operating parameters: air velocity 6.6 - 26.6 m/s and the coolant temperature 243 - 273K. The measurements were conducted at ambient laboratory temperature (297 - 301 K).

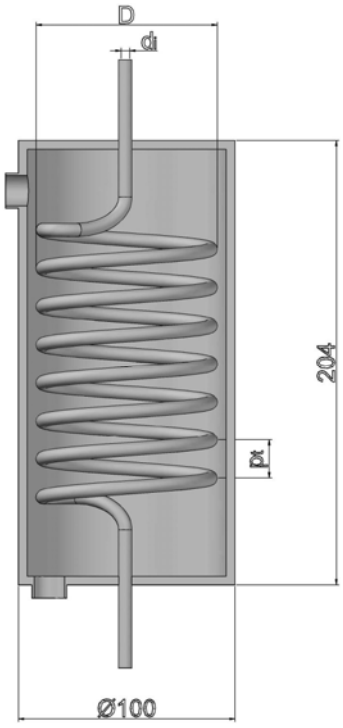

Fig. 2. Geometry of heat exchanger

Tab. 1. Geometry parameters of the heat exchanger

Parameters	Value
Inner diameter of coiled tube (d_i)	4 mm
Tube thickness	1 mm
Coil diameter (D)	74 mm
Tube lenght (L)	1700 mm
Coil pitch (p_t)	7.5 mm
Curvature ratio $\left(\delta = \frac{D}{d_i} \right)$	18.5

As can be seen from Fig.1, vapour-gas mixture was generated by mixing IPA with air in the gas preparation section. Compressed air was passed through desiccant dryers (Kaeser, DC 1.5 - 7.5) in order to minimize the effect of moisture during adsorption process. A static mixer with a syringe pump (model 100, KD Scientific, accuracy: ±1%) was used to generate a target vapor concentration in the air stream. The gas flow rate was measured by a mass flow controller (model GFC 47, Aalborg, accuracy: ±0.25%). The resulting gas mixture was passed through a cooper coil pipe in the heat exchanger. The pure or isopropanol (IPA)-laden air streams with specified concentrations ranging from 3.9 to 10.4 g/m^3 were used to the study. The IPA vapour concentration was measured using a gas chromatograph (SRI 8610C) with a flame ionization detector (FID). The cooling medium (methylsilicone oil) flowed outside the coil (inside the shell). Inlet and outlet temperatures of both working fluids were measured during the tests. The measurements were conducted until the steady-state was reached, indicated by a stable gas outlet temperature. The measurements were conducted at ambient laboratory temperature (297 - 301K). The experiments were performed in the following range of operating parameters: air flow rate 0.3 - 1.2 m^3/h and the coolant temperature 243 - 273K. LabView software was used in order to monitor and record the temperature data (measurement accuracy: ±0.15%).

Flow characteristics of helical coil heat exchanger

The Dean number is a characteristic parameter for flow in a helical tube, similarly like Reynolds number for flow in a straight pipe. The numbers are defined as:

$$De = Re \sqrt{\frac{d_i}{D}} \tag{1}$$

$$Re = \frac{4G}{\pi d_i \mu_f} \tag{2}$$

The Dean number characterizes the strength of secondary flow, which is perpendicular to the main flow direction (Fig. 3) and enhances fluid mixing. The centrifugal force exerted by a pipe curvature causes this phenomenon [5, 11, 12].

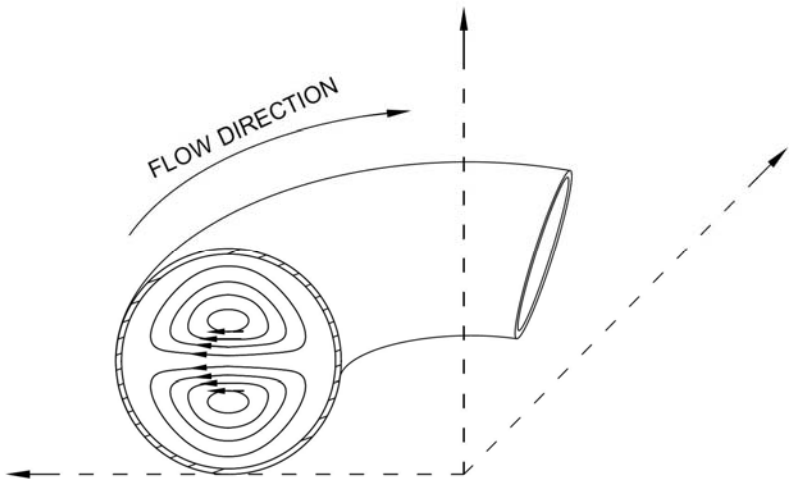

Fig. 3. The secondary flow pattern in a helical pipe.

In the investigated air flow range, the Re and De numbers were ranged from 1670 to 7500 and from 390 to 1750, respectively.

The critical Reynolds number (Re_{cr}) is defined as the maximal value of the Reynolds number for which the flow in a coil pipe is still laminar. The following empirical equations are commonly used to define of Re_{cr} in laminar flow region:

Ito equation [11]:

$$Re_{cr} = 2000\left[1 + 13.2\delta^{-0.6}\right] \text{ for } 5 \le \delta \le 2000, \tag{3}$$

where δ is a curvature ratio.

Srinivasan equation [11, 13]:

$$Re_{cr} = 2100\left[1 + 12\,\delta^{-0.5}\right] \text{ for } 7.5 \le \delta \le 100 \tag{4}$$

Cioncolini equation [11, 14]:

$$Re_{cr} = 30000\delta^{-0.47} \text{ for } 7 \le \delta \le 24 \tag{5}$$

Schmidt equation [8, 15]:

$$Re_{cr} = 2300\left[1 + 8.6\left(\frac{d_i}{D}\right)^{0.45}\right] \tag{6}$$

The estimated values of the Re_{cr} number are given in Tab. 2.

Tab. 2. Critical Reynolds values for air flow in the coil pipe

Authors	results
Ito	6585
Srinivasan	7959
Cioncolini	7613
Schmidt	7619

As Tab. 2 shows, the Re_{cr} number calculated from Ito's equation is slightly lower than from other equations. Whereas the value determined from Cionciolini equation agrees well with Schmidt's correlation. Both values are close to 7600 and are higher than the maximum Reynolds number for laminar flow in a straight pipe (Re=2100) by about 3.6 times. The Re_{cr} value is slightly larger than the upper limit of the test Re values thus all experiments were conducted in the laminar flow region.

The Wilson-plot technique

The heat released during the gas cooling can be determined from the following equations:

For single-phase IPA- air mixture [16]:

$$Q=\left(m_{AIR}C_{p,AIR}+m_{IPA}C_{p,IPA}\right)\left(T_{coil,out}-T_{coil,in}\right) \tag{7}$$

For air stream [17, 18]:

$$Q=m_{AIR}C_{p,AIR}\left(T_{coil,out}-T_{coil,in}\right) \tag{8}$$

The overall heat exchange coefficient is defined as [18, 19]:

$$U=\frac{Q}{A_o\cdot LMTD} \tag{9}$$

where: the log mean temperature difference (LMTD) in a counter flow heat exchanger can be expressed as [16, 18]:

$$LMTD=\frac{\left(T_{coil,out}-T_{shell,in}\right)-\left(T_{coil,in}-T_{shell,out}\right)}{\ln\left(\frac{T_{coil,out}-T_{shell,in}}{T_{coil,in}-T_{shell,out}}\right)} \tag{10}$$

The total thermal resistance is the reciprocal of the overall heat transfer coefficient referred to the outer pipe surface area (A_o). It can be defined as the sum of the convective resistances at the inner and outer sides of the coil pipe and of the wall conduction resistance [20, 21]:

$$\frac{1}{UA_o} = \frac{1}{\alpha_i A_i} + \frac{\ln\left(\frac{d_o}{d_i}\right)}{2\pi\lambda_{wall} L_{wall}} + \frac{1}{\alpha_o A_o} \tag{11}$$

In the coil heat exchanger, the coolant flow rate was constant while the gas stream velocity was varied. In this case, it can be assumed that the values of total thermal resistance depend on the change in the internal heat transfer coefficient, while the remaining thermal resistances are almost constant [23]. Therefore, the sum of the convective resistances of the outside coil tube and in the tube wall can expressed as [20, 22]:

$$C_1 = \frac{1}{\alpha_o} + \frac{A_o \ln\left(\frac{d_o}{d_i}\right)}{2\pi\lambda_{wall} L_{wall}} \tag{12}$$

The internal heat transfer coefficient (α_I) can be calculated by the following Nusselt number (Nu) correlation:

$$Nu = C Re^n Pr^{0.4} = \frac{\alpha_i d_i}{\lambda_i} \tag{13}$$

This general equation can be applied to laminar as well as turbulent forced convection. When the gas mixture properties are constant, then the convective coefficient inside the tube is proportional to the nth power of the fluid velocity [23]:

$$\alpha_i = C_2 w^n \tag{14}$$

Substituting, the Eqs. (12) and (14) into Eq. (11) results in [23]:

$$\frac{1}{U} = C_1 + \frac{C_3}{w^n} \tag{15}$$

In the Wilson technique, the plot 1/U versus $1/w^n$ should be linear for an assumed value of the n exponent. The C_2 and C_1 coefficients are the slope and y-intercept of the straight line graph. Both constants are determined with the last square fitting method. The obtained values of the best-fit parameters enable calculating external and internal convective coefficients for a given gas flow rate. As can be seen from Fig. 4, the experimental data are well represented by Eq. 15 for the assumed value of n=1.23. The fit quality is very good, as proven by the high values of the determination coefficients (R^2 >0.999)

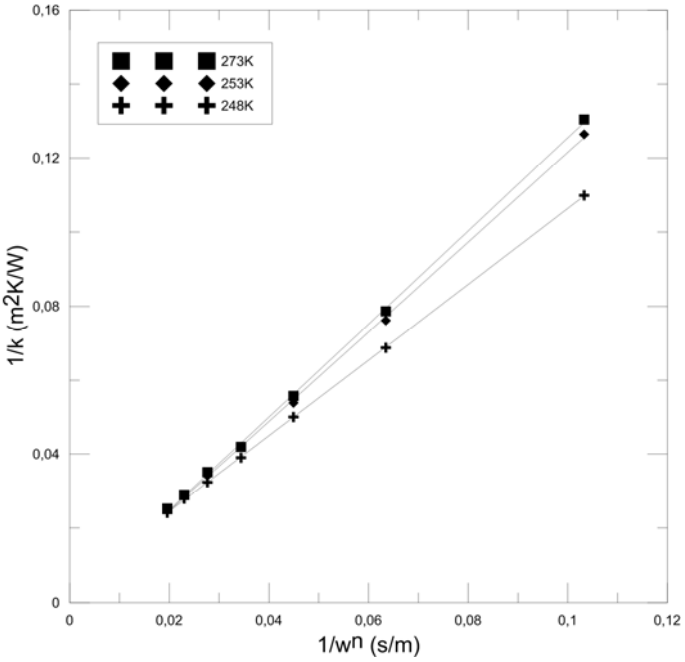

Fig. 4. The plot of inverse overall heat transfer coefficient versus inverse air velocity inside coil tube.

Effect of Re number on internal heat transfer coefficient was presented in Fig. 5.

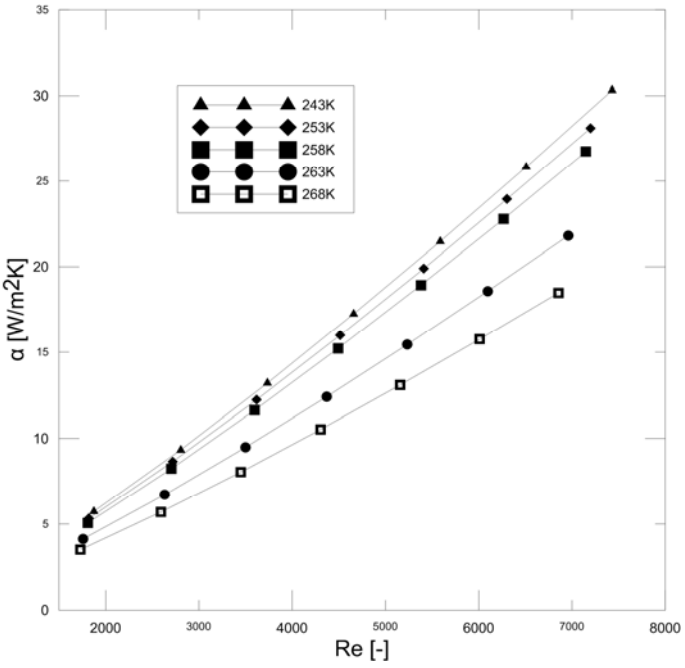

Fig. 5. The plot of inside heat transfer coefficient versus Reynolds number for air cooling.

Fig.5 shows that an increase in Reynolds numbers and a decrease in temperature affect an increase in the heat transfer coefficient values. In the laminar flow regime, due to the curvature of the coil tube, a centrifugal force is generated which produced a secondary flow. The decrease in temperature affects an increase in gas temperature difference in exchanger. Therefore, more heat is transferred to the cold medium. These results are in agreement with the finding reported by Ghias et al. [6]

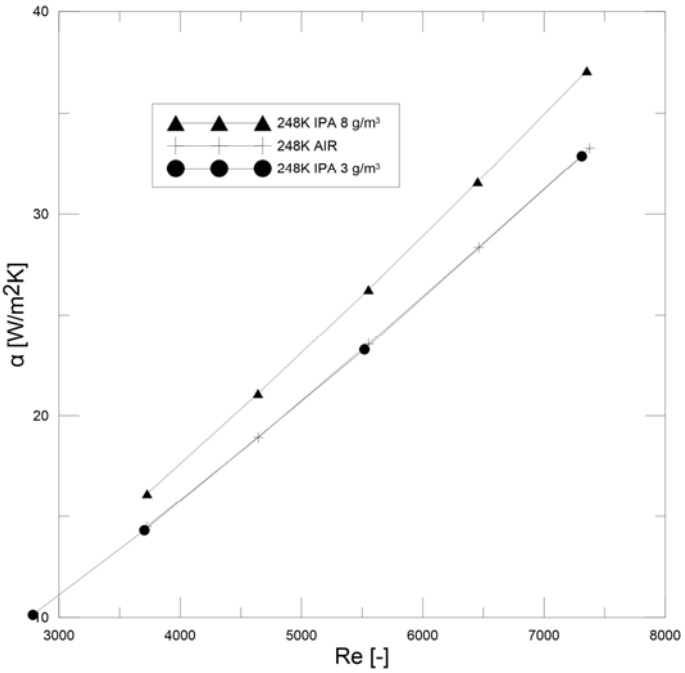

Fig. 6. Comparison between heat transfer coefficients for air and IPA-air mixture inside coil tube at 248K.

Fig. 6 shows that the effect of the Reynolds number was stronger than the change in the gas mixture composition. As can be seen, heat transfer coefficients for the IPA vapour concentration of 3 g/m^3 were very close to those for clean air and lower than for 8 g/m^3 by ca. 40%. This suggests that other additional phenomena may have occurred in the coil tube. Because of the complexity of this issue, further studies are necessary to fully elucidate this process.

RESULTS AND DISCUSSION

Nusselt number correlations

The Nusselt number values were calculated using the following equations:

Schmidt equation [15, 20]:

$$Nu = 3.65 + 0.08\left[1 + 0.8\left(\frac{d_i}{D}\right)^{0.9}\right] Re^{0.5+0.2903\left(\frac{d_i}{D}\right)^{0.194}} Pr^{\frac{1}{3}} \text{ for } 100<Re<Re_{cr} \quad (16)$$

Seban and Mclaughlin equation [11]:

$$Nu = 0.023 Re^{0.8} Pr^{0.4}\left[Re^{0.05}\left(\frac{d_i}{D}\right)^{0.1}\right] \text{ for } 5000<Re<100000 \quad (17)$$

Xin and Ebadian equation [11]:

$$Nu = 0.0019 Re^{0.92} Pr^{0.4}\left[1 + 3.455\left(\frac{d_i}{D}\right)^{0.1}\right] \quad (18)$$

when 5000<Re<100000

Naphon and Wongwises equation [9]:

$$Nu = \left(2.153 + 0.318 De^{0.643}\right) Pr^{0.177} \quad (19)$$

when 20<De<2000

Kalb and Seader equation [9]:

$$Nu = 0.836\, De^{0.5}\, Pr^{0.1} \text{ for } De \geq 80,\ 0.7<Pr<5 \quad (20)$$

Tab. 3. Calculated Nu number versus Re number at 273K

Authors	Re [-]						
	1708	2554	3400	4246	5090	5932	6776
	results						
Wilson	0.801	1.302	1.837	2.400	2.986	3.591	4.214
Xin and Ebadian	-	-	-	-	4.945	5.665	6.379
Seban and Mclaughlin	-	-	-	-	7.266	8.276	9.268
Schmidt	14.481	17.807	20.774	23.498	26.041	28.440	30.733
Naphon and Wongwises	16.204	20.389	24.095	27.480	30.625	33.581	36.398
Kalb/Seader	16.179	19.788	22.831	25.513	27.933	30.155	32.230

As Tab.3 shows, the convective heat transfer coefficients determined by Wilson's procedure are significantly lower than those calculated from empirical correlations. In the range of Re>5000, the equation of Xin and Ebadian is more suitable than that of others.

Pressure drop in helical coiled tube

The pressure drop of single-phase flow in a straight tube can be calculated from Darcy-Weisbach equation [24, 25]:

$$\Delta p = f_S \frac{L \cdot w^2 \cdot \rho}{2 d_i} \tag{21}$$

The friction factor (f_S) in smooth tubes depends on the Reynolds number.

$$f_S = 64/Re \quad \text{for } Re<2100 \tag{22}$$

$$f_S = 0.316/Re^{1/4} \quad \text{for } 3000<Re<100000 \tag{23}$$

The pressure drop in a coil tube can be calculated from Eq.(21) after replacing the friction factor f_S by Fanning (coil) friction factor f_C or the ratio of both friction factors (f_S/f_C). The following equations were used in the present analysis:

Shiragami [26]:

$$f_C = f_S 0.0040 \left[Re \left(\frac{1}{\delta} \right)^{0.2} \right]^{0.87} \quad \text{for } 1/\delta \le 0.0729 \tag{24}$$

Gnieliński et al. [24]:

$$f_C = \left(1.82 \log Re^{-1.64} \right)^{-2} \tag{25}$$

Ito [27]:

$$f_C = f_S \left(0.1033 \sqrt{De} \left[\left(1 + \frac{1.729}{De} \right)^{0.5} - \left(\frac{1.729}{De} \right)^{0.5} \right]^{-3} \right) \tag{26}$$

Manlapaz and Churchill [25] suggested a correlation valid in the wide range of Dean number:

$$f_C = f_S \left(1 + \left(1 + \frac{d_i}{3D} \right)^2 \frac{De}{88.33} \right)^{0.5} \quad \text{for } De < 40 \tag{27}$$

Mishra and Gupta [27]:

$$f_C = f_S \left(1 + 0.033 \left(\log_{10} He \right)^4 \right) \quad \text{for } 1<He<3000 \tag{28}$$

where: He is Helix number defined as

$$He = De \left[1 + \left(\frac{p_t}{2\pi D} \right)^2 \right]^{1/2} \tag{29}$$

Tab. 4 shows a comparison of the pressure drop values determined from Darcy-Weisbach equation with experimental data obtained for the same dimensions

of the pipe. The frication factors were predicted from Eqs. (22) and (26) that were developed for straight and coiled pipes, respectively. As can be seen, the values of the pressure drop are underestimated in comparison to experimental data (average relative errors were 329% and 176%, respectively). Therefore, it may be concluded that both equations are not appropriate to predict the pressure drop inside the coiled pipe in low Re number range.

Tab. 4. Pressure drops versus the Re number in the laminar flow regime (Re<2100)

Air flow [m^3/h]	Re [-]	Pressure drop [Pa]		
		Experimental	Straight pipe	Ito equation
0.03	157	238	42	50
0.04	220	289	58	75
0.06	315	400	83	117
0.08	409	442	108	163
0.09	472	489	125	197
0.10	535	595	142	232
0.12	630	650	167	288
0.13	693	716	183	328
0.15	787	787	208	389
0.16	850	920	225	432
0.18	945	957	250	499

As seen in Tab. 5, the Eqs. (26 - 28) provide good consistencies of frication factor values with those calculated with Blasius correlation. While the frication factors calculated from Eq. (24) is higher than from the Blasius equation and calculated from Eq. (25) is close to the Blasius equation. Based on the data analysis for Re <2100, it can be assumed that the Eqs. (26 - 28) give more reliable results than the Eqs. (24) and (25) and may be used to evaluate of pressure drops in the coiled tube in laminar regime.

Tab. 5. Friction factor values versus the Re number (Re>3000)

Air flow [m3/h]	Re [-]	Blasius (Eq.23)	Shirigami (Eq.24)	Gnieliński (Eq.25)	Ito (Eq.26)	Manlapaz/Churchill (Eq.27)	Mishra/ Gupta (Eq.28)
0.60	3334	0.041	0.034	0.044	0.063	0.059	0.063
0.75	4163	0.039	0.040	0.041	0.055	0.053	0.055
0.90	4992	0.038	0.045	0.038	0.050	0.048	0.050
1.05	5821	0.036	0.050	0.037	0.046	0.044	0.045
1.20	6649	0.035	0.054	0.035	0.043	0.041	0.042
		Approximation error					
		20%	31%	18%	12%	11%	11%

CONCLUSION

The data analysis revealed that the value of Reynolds number had a crucial impact on the heat transfer efficiency. The decrease in coolant temperature by 25 K resulted in increase of the heat transfer coefficients by ca. 10%. However, a threefold increase in the gas flow rate affected an increase in value by ca. 80%. This is due to the more efficient mixing of fluids induced by the centrifugal force in the coil tube.

Due to the lack of general correlations for whole geometrical and flow conditions, several empirical equations were selected to calculate the Nu number and the pressure drop inside the coiled pipe. A comparison between experimental and calculated results for the same Reynolds number showed that the predicted data were overestimated and prediction accuracy was dependent on the fluid flow conditions. Therefore, the usefulness of these equations for designing helical coil heat exchangers was very limited.

NOMENCLATURE

Letter symbols

A – coil area, [m^2]
C_1 – constant, [-]
C_2 – constant, [-]
Cp – heat capacity, [J/(kg K)]
D – coil dimension, [m]
De – Dean number, [-]
d – pipe dimension, [m]
f – friction factor, [-]
G – mass flow, [kg/s]
He – Helix number, [-]
h – heat transfer coefficient, [W/ (m^2 K)]
L – coil length, [m]
n – Wilson method coefficient, [-]
Nu – Nusselt number, [-]
Pr –Prandtl number, [-]
pt – coil pitch, [m]
R – total thermal resistance, [m^2 K/W]
Re – Reynolds number, [-]
Re_{cr} – critical Reynolds number, [-]
R – thermal resistance, [m^2 K/W]
T_1 – gas temperatures difference, [K]
U – overall heat transfer coefficient, [W/ (m^2 K)]
w – gas velocity, [m/s]

Greek symbols

α – heat transfer coefficient, [W/ (m^2 K)]
δ – curvature ratio, [-]
λ – thermal conductivity, [W/ (m K)]
μ – viscosity of gas, [Pa s]
ρ – density, [kg/m^3]

Subscripts

i – inside
o – outside
c – for curved tube
s – for straight tube

REFERENCES

[1] Pimenta T.A., Campos J.B.L.M, Friction losses of Newtonian and non-Newtonian fluids flowing in laminar regime in a helical coil, *Experimental Thermal and Fluid Science*, 2012, 36, 194–204, DOI: 10.1016/j.expthermflusci.2011.09.013

[2] Nada S.A., Eid E.I., Abd El Aziz G.B., Hassan H.A., Performance Enhancement of Shell and Helical Coil Water Coolers Using Different Geometric and Fins Conditions, *Heat Transfer Asian Research*, 2016, 45, 7, 631-647, DOI: 10.1002/htj.21180

[3] Pandey A.K., Mishra P.K., Srivastava K.K., Theoretical Study of Single Phase Heat Transfer in a Helically Coiled Tube of Small Diameter, *International Journal of Chemical Engineering and Applications*, 2015, 6, 6, 460-463, DOI: 10.7763/IJCEA.2015.V6.530

[4] Jayakumar J.S., Chapter: Helically Coiled Heat Exchangers, Heat Exchangers - Basics Design Applications, edited by Mitrovic J., *InTech*, 2012, 311-342, DOI: 10.5772/22242

[5] Ju H., Huang Z., Xu Y., Duan B., Yu Y., Hydraulic Performance of Small Bending Radius Helical Coil-Pipe, Journal of Nuclear Science and Technology, 2001, 38, 10, 826-831, DOI: 10.1080/18811248.2001.9715102

[6] Ghias A.S.A., Ananth S.V., Anand M.D., Devadhas G.G., Experimental Study of Thermal Performance of Coil in Shell Heat Exchanger, *Indian Journal of Science and Technology*, 2016, 9, 13, DOI: 10.17485/ijst/2016/v9i13/90571

[7] Pandey A.K., Mishra P.K., Srivastava K.K., Theoretical Study of Single Phase Heat Transfer in a Helically Coiled Tube of Small Diameter, *International Journal of Chemical Engineering and Applications*, 2015, 6, 6, 460-463, DOI: 10.7763/IJCEA.2015.V6.530

[8] Vashisth S., Kumar V., Nigam K.D.P., A Review on the Potential Applications of Curved Geometries in Process Industry, *Industrial & Engineering Chemistry Research*, 2008, 47, 10, 3291-3337, DOI: 10.1021/ie701760h

[9] Naphon P., Wongwises S., A review of flow and heat transfer characteristics in curved tubes, *Renewable and Sustainable Energy Reviews*, 2006, 10, 5, 463–490, DOI: 10.1016/j.rser.2004.09.014

[10] Alimoradi A., Study of thermal effectiveness and its relation with NTU in shell and helically coiled tube heat exchangers, *Case Studies in Thermal Engineering*, 2017, 9, 100–107, DOI: 10.1016/j.csite.2017.01.003

[11] Flórez-Orregoa D., Ariasa W., Lópeza D., Velásqueza H., Experimental and CFD study of a single phasecone-shaped helical coiled heat exchanger: an empirical correlation, *The 25th International Conference on Efficiency, Cost, Optimization, Simulation and Environmental Impact Of Energy Systems – Proceedings*, 2012, 26-29

[12] Kocatepe Y, Ahn H, Aydin C, Karacasu A, Experimental Investigation of a Heat Exchanger with a Helical Coil Made of Corrugated Tubes, *ULIBTK'09 17. National Congress of Heat Science and Technology*, 2009

[13] Srinivasan, P.S., Nandapurkar, S.S., Holland, F.A., Pressure Drop and Heat Transfer in Coils, *The Chemical Engineer*, 1968, 218, 113-119

[14] Cioncolini A.; Santini L., An experimental investigation regarding the laminar to turbulent flow transition in helically coiled pipes, *Experimental Thermal and Fluid Science*, 2006, 30, 4, 367-380, DOI: 10.1016/j.expthermflusci.2005.08.005

[15] Schmidt E.F., Wfirmeiibergang und Druckverlust in Rohrschlangen, *G'zemieJng Tech*., 1967, 39, 781–789

[16] Sapali S.N., Patil P.A., A New Experimental Technique to Determine Heat Transfer Coefficient and Pressure Drop in Smooth and Micro-Fin Tube, *Journal of Mechanical Engineering Research,* 2010, 2, 4, 71-84

[17] Uhía1 F.J., Campo A., Fernández-Seara J., Uncertainty analysis for experimental heat transfer data obtained by the Wilson plot method: Application to condensation on horizontal plain tubes, *Thermal Science*, 2013 , 17, 2, 471-487, DOI: 10.2298/TSCI110701136U

[18] Witchayanuwat W., Kheawhom S., Heat Transfer Coefficients for Particulate Airflow in Shell and Coiled Tube Heat Exchangers, *World International Journal of Chemical and Biological Engineering*, 2010, 3, 1, 7-11

[19] Pettersen J., Rieberer R., Munkejord S.T., Heat Transfer and Pressure Drop for Flow of Supercritical and Subcritical CO_2 in Microchannel Tubes, European Research Office of the U.S. Army, 2000

[20] Sobota T., Chapter: Experimental Prediction of Heat Transfer Correlations in Heat Exchangers, Developments in Heat Transfer, edited by Dos Santos Bernardes M.A., *InTech*, 2011, DOI: 10.5772/822

[21] Kumbhare B.P., Purandare P.S., Mali K.V., Experimental Analysis of Square and Circular Helical Coil for the Heat Recovery System, *International Journal of Engineering & Science Research*, 2, 5, 2012, 318-327, ISSN 2277-2685

[22] Yang R., Chiang F.P., An experimental heat transfer study for periodically varying-curvature curved-pipe, *International Journal of Heat and Mass Transfer*, 2002, 45, 15, 3199–3204, DOI: 10.1016/S0017-9310(02)00023-6

[23] Fernández-Seara J., Uhía F.J., Sieres J., Campo J., A general review of the Wilson plot method and its modifications to determine convection coefficients in heat exchange devices, *Applied Thermal Engineering*, 2007, 27, 17-18, 2745–2757, DOI: 10.1016/j.applthermaleng.2007.04.004

[24] Silva L.F., Marczak L.D.F., Möller S.V., Determination of the Local Heat Transfer Coefficient in pipes with Helical Turbulence Promoters through the Naphthalene Sublimation Technique, *Latin American Applied Research,* 2001, 31, 5, 495-500

[25] Urbanowicz-Górska A., Wojtkowiak J., Method of Heat and Fluid Flow Calculations of Vertical Helical Pipe Immersed in Cold Liquid of Constant Temperature. Part 1. Equations and Algorithm of the Method, *Ciepłownictwo , Ogrzewnictwo , Wentylacja*, 2012, 43, 7, 284-288

[26] Shiragami N., Inoue I., Chapter: Pressure Losses in Rectangular Bends, Encyclopedia of Fluid Mechanics: Flow phenomena and measurement, edited by Cheremisinoff N.P., *Gulf Publishing Company*, 1986, ISBN: 0872014924

[27] Gupta R., Wanchoo R.K., Jafar Ali T.R.M., Laminar Flow in Helical Coils: A Parametric Study, *Industrial & Engineering Chemistry Research*, 2011, 50, 2, 1150–1157, DOI: 10.1021/ie101752z

Synthesis of hydroxyapatite in continuous reactor: a review

*Joanna Latocha[1], Michał Wojasiński[1], Paweł Sobieszuk[1], Tomasz Ciach[1]
[1]Faculty of Chemical Process and Engineering, Warsaw University of Technology, Warsaw, POLAND
e-mail: Joanna.Latocha.dokt@pw.edu.pl

Keywords*: hydroxyapatite, synthesis in continuous reactor, continuous precipitation, microparticles, nanoparticles*

ABSTRACT

Because of excellent properties, similar to natural bone minerals, and variety of possible biomedical applications hydroxyapatite (HAp) is valuable compound among the calcium phosphate salts. A number of synthesis routes for producing HAp powders have been reported. Despite, it is important to develop new methods giving precise control over the reaction and having potential to scale-up. The main motivation for the current paper is a view of continuous synthesis methods toward medical application of produced hydroxyapatite, especially in the form of nanoparticles.

INTRODUCTION

Hydroxyapatite plays an important role as a regenerative material in a bioengineering. Synthetic HAp has been explored in tissue engineering applications as a material for hard tissue repair, regeneration or reconstruction [1]. Chemical and structural resemblance of synthetic HAp to human bone made hydroxyapatite commonly used as an additive in bone cements, scaffolds, orthopedic and dental implant coatings, and drug delivery applications[2]. Hydroxyapatite is the most thermodynamically stable compound in near-physiological conditions of temperature (37°C) and pH (7) form a group of calcium phosphates. Stoichiometric HAp:$Ca_{10}(PO_4)_6(OH)_2$ has Ca/P ratio equal to 1.67 (10/6) [3].

The human bone includes of approximately 70% of hydroxyapatite, which is the most of the inorganic part of the bone. Natural origin HAp is non-stoichiometric with a Ca/P ratio less than 1.67. It exhibits nanostructured crystals, low crystallinity, and needle-like morphology and is responsible for mechanical strength of bone. Low amounts of ions such as Mg^{2+}, K^{+}, F^{-}, Cl^{-}, CO_3^{2-} built into its structure play an important role in bone metabolism[4]. Natural nanohydroxyapatite (nHAp) belongs to B-type hydroxyapatite where some of PO_4^{3-} groups are replaced by carbonate groups. Among the types of hydroxyapatite, one can distinguish A-type substituted HAp, where hydroxide groups OH^{-} are replaced by CO_3^{2-} groups, and third type known as AB when both substitutions are allowed in the HAp structure. Hydroxyapatite in natural bone and teeth have a nanoscale structure while the most

of types of HAp synthesis lead to obtain microscale aggregates. In case of application of synthetic HAp, difference in scale between natural and synthetic material causes worse osteogenic and mechanical properties of bone implants. Nanosized particles have greater specific surface area and more uniform distribution than microparticles of HAp, thus it is crucial to design methods for synthesis of HAp in nanoscale form [5].

Hydroxyapatite as a biomaterial is biocompatible with hard tissue. It means, that HAp interacts with the human tissue without response of the immune system and has no toxic effect on biological system. What is more, HAp is well known from its outstanding properties like osteconductivity and osteoinductivity. It positively influences processes of bone regeneration. HAp interacts with the surrounding bone tissue and creates a direct bond with host living bone as a result of bone remodeling (formation of new bone tissue in damaged spot). Moreover, it possess high bioactivity and promotes the adhesion and the proliferation of bone cells [6].

Synthesis of hydroxyapatite in controlled way represents a challenge. Nucleation, growth companying with Ostwald ripening, and aggregation are three stages during particle formation [7]. There have been broad studies on the effects of changing process parameters such as temperature, pH, Ca/P ratio, initial solution concentration on particle properties even though the reaction kinetics is still unknown. The various preparation methods of HAp also have significant influence on its properties and result in different size distribution, morphology, purity, crystallinity, crystallites size and are directly related to HAp biological characteristics [8].

The type of hydroxyapatite application demands the particular size range. Therefore many batch or semi-batch techniques have been developed to industrial scale production, for example: mechanochemical [9], sol-gel [10], chemical precipitation [11], micro-emulsion [12], sonochemical [13], hydrothermal [14]. It is observed that precipitation method is the most promising and the most widely studied route due to low cost, simplicity and easy application in industrial production [15]. Despite this, batch methods provide only limited amounts of powder. Wide residence time and heterogeneous supersaturation in the reaction medium are also problems with these techniques. Even small changes in stoichiometry can affect the material properties leading to problems with further application. These difficulties are significant especially as the scale rises from laboratory to industrial production.

The concept of the synthesis of hydroxyapatite in continuous process has expanded the possibility to obtain hydroxyapatite with better control over the reaction conditions. Nevertheless, synthesis in continuous flow reactor is not common way to produce hydroxyapatite. The literature reports describe need to use special equipment, N_2 atmosphere inside the reactor or high process temperature, among others. Thus, these methods might be demanding and some of them could be restricted to laboratory scale. On the other hand, the approach based on continuous synthesis

in microreactor characterize high surface to volume ratio, short residence time, efficient mass transfer which promote more homogenous reaction conditions and thereby better monodispersity of resulting product. What is more, continuous production allows higher productivity. This article presents continuous synthesis methods of hydroxyapatite micro- and nanoparticles towards biomedical applications. We also pay attention to the economic aspects. In this context, HAp needs to be produced as nanoscale particles with high purity and narrow size distribution using low-cost equipment.

PREPARATION OF HAp IN CONTINUOUS REACTOR

Among the various HAp preparation methods, most of them consider batch or semi-batch synthesis. The aim of this review is to present and compare HAp synthesis routes in continuous systems. We also put an emphasis on possibility of scaling up of the presented procedures. The main advantages of these methods, over batch processes, are better control over the reaction and higher yield. On the other hand, presented methods are associated with a number of difficulties in reactor geometry, size distribution, crystallinity, stoichiometry and degree of particle agglomeration, which will be pointed out in a view of an economical obstacles.

Type of reactor and synthesis

Gomez-Morales et al. synthesized HAp by precipitation method in continuous system called Mixed Suspension Mixed Product Removal Reactor (MSMPR), maintaining temperature at 85°C and pH equal to 9 [16]. The aqueous solutions were prepared by dissolving $CaCl_2$ (or $Ca(NO_3)_2$) and K_2HPO_4 in distilled water with a Ca/P ratio 1.67. Thereafter, the starting solutions were pumped into reactor maintaining continuous flow of N_2 inside reactor to avoid the presence of atmospheric CO_2. Residence time (τ) equals to 30 or 60 minutes. Samples were collected at the output of the reactor. Post processing treatment involved filtration, washing with distilled water and drying in an oven. Authors point out, that described method accomplishes high production rate, up to 1.17 g/min, which increases with the rise in the concentration of reagents, and decreases when the residence time was longer. In short, this research was focused on the synthesis of pure HAp with stoichiometric Ca/P ratio under careful control of the pH and temperature.

Another production system is given in Figure 1. This type of reactor was described by Fujii et al. [17]. Researchers have used tube reactor (2 mm in inner diameter, 10 m in length) equipped with mixing unit containing T-shaped connector. To control reaction temperature the test system was placed in an incubator. Aqueous solutions of $Ca(NO_3)_2 \cdot 4H_2O$ and $(NH_4)_2HPO_4$ with flow rate 2ml/min each were pumped into the reactor. Residence time was about 8 min; pH was maintained at 6.4 or 9 and temperature ranged from 0 to 100°C. Collected products were filtered,

rinsed with distilled water and subjected to vacuum freeze-drying. Authors intended to control phase purity and morphology of resulting HAp particles.

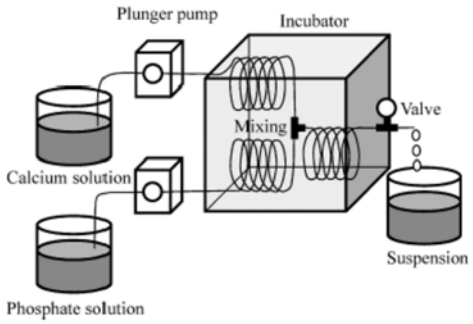

Fig. 1. Production of hydroxyapatite in tube reactor[17].

A successful approach to produce hydroxyapatite presented Lester et al. [18]. They created continuous hydrothermal rig to produce high quality powders. Figure 2 shows scheme of this reaction system. The aqueous solution of $(NH_4)_2HPO_4$ was superheated and pumped (20ml/min) into the nozzle reactor as a downflow. At the same time, the cold aqueous $Ca(NO_3)_2{\cdot}_4H_2O$ was used as the upflow and pumped (10ml/min) to form particles at the interface of two solutions. Temperature of the preheater varied between 200 and 400°C. The pressure was maintained at 240 bar and pH at 8 and 5 for $(NH_4)_2HPO_4$ and $Ca(NO_3)_2{\cdot}4H_2O$, respectively. Authors described the influence of altering parameters such as pH and temperature on morphology of produced particles.

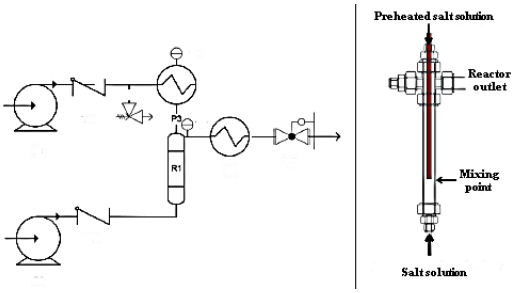

Fig. 2. Scheme of continuous hydrothermal synthesis (left) and hydrothermal rig (right)[19].

In turn, Anwar et al. have used a continuous plastic flow synthesis (CPFS) to obtain Zn substituted HAp[20]. They conducted reaction at pH 11 and at temperature of 70°C. Different weight percent (wt%) of Zn ions from 0 to 4wt% were used. Procedure involved preparing aqueous solution of $Ca(NO_3)_2{\cdot}4H_2O$ and $(NH_4)_2HPO_4$. Then, as prepared reagents were contacted into T-piece and passed through 8m long tube. Flow rates were tailored to give a total residence time

of 5 minutes. Then, obtained powders were filtered and washed. In the next step, powder was dried in an oven at 90°C for 12h. The aim of this process was a synthesis of modified hydroxyapatite with antibacterial activities.

Interesting way to produce hydroxyapatite particles is microporous tube-in-tube microchannel reactor (MTMCR) used by Yang et al.[21]. Scheme of this system is presented in Figure 3. The main part of the system are two coaxial tubes which form annular cross-sectional microchannel. In the inner tube consisted micropores that ensure dispersion of reagents. The width between inner and outer tube is 500μm. Aqueous solution of $Ca(NO_3)_2 \cdot 4H_2O$ as a continuous phase (outer tube) and $(NH_4)_2HPO_4$ as a dispersed phase (inner tube) were adjusted to pH 9.5 and pumped at room temperature. Produced HAp was carried forward to a Teflon autoclave and hydrothermally treated at 220°C for 4h. Then product was filtered, washed and dried at 80°C for 12h.

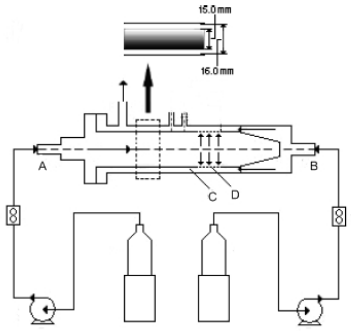

Fig. 3. Scheme of tube-in-tube microchannel reactor. A-inlet of inner tube; B-inlet of outer tube; C-microchannel; D-micropores[21].

Kandori et al. described microreactor system presented in some details in Figure 4 [22]. Reactants like aqueous solutions of $Ca(OH)_2$ and H_3PO_4were prepared. The temperature of the bath was modified in range of 20-70°C and flow rate varied from 5-75 ml/min. The ratio of Ca/P was determined to 1.67. Microreactor with 48 channels was used as a mixing part. Streams from all channels were merged at a center channel with diameter of 1 mm. Solutions of reactants flowed along channels and mixed into center channel. Authors conducted experiments with the increasing flow rate and temperature and investigated their influence on product properties.

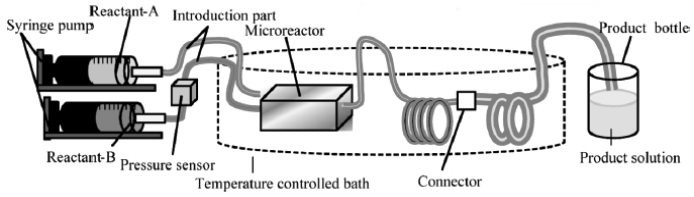

Fig. 4. Scheme of microsystem reactor [22].

Castro et al. reported the preparation of HAp in near-physiological conditions[23].They used ultrasonic tubular reactor inserted in an ultrasonic bath (Figure 5). Authors clearly define the meaning of the ultrasound application as a way to avoid clogging and to decrease level of particles aggregation. Single-phase flow (SPF, laminar) and gas-liquid flow (GLF, segmented) were used to compare monodispersity of synthesized HAp. Reactants contact in T-mixer (SPF) or cross-mixer (GLF) chamber, then flow through tubular reactor with inner diameter of 1.02mm. $Ca(OH)_2$ and H_3PO_4 aqueous solutions were used in Ca/P molar ratio 1.33. Different liquid flow rates (0.152-4ml/min) and gas flow rates (1.2-4ml/min) were experimented.

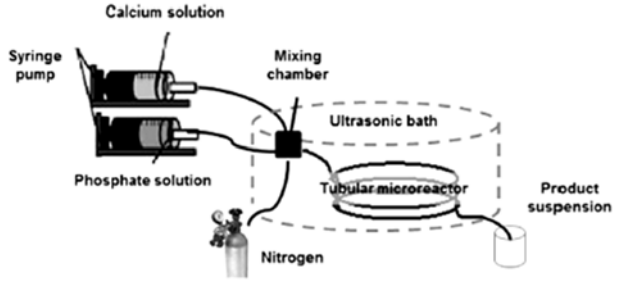

Fig. 5. Scheme of production HAp in ultrasonic tubular reactor [23].

Using the same reactants in the same conditions, Castro et al. carried out synthesis in a meso oscillatory flow reactor (meso-OFR) and in scaled-up meso-OFR (Figure 6) [24]. To obtain better production rate, scale-up reactor was employed. Scaled-up reactor is a series of eight connected vertical meso-OFRs. One meso-OFR contains glass jacked tube with 4.4mm in inner diameter and 35cm in length. It is equipped with smooth periodic cavities and baffles. Fluid moves from the walls to the center of the tube with intensity controlled by the oscillation frequency and amplitude. HAp precipitation was carried out, for both systems, with the same liquid flow rate 4.5 and 9ml/min (but different residence time, due to differences in reactors construction).

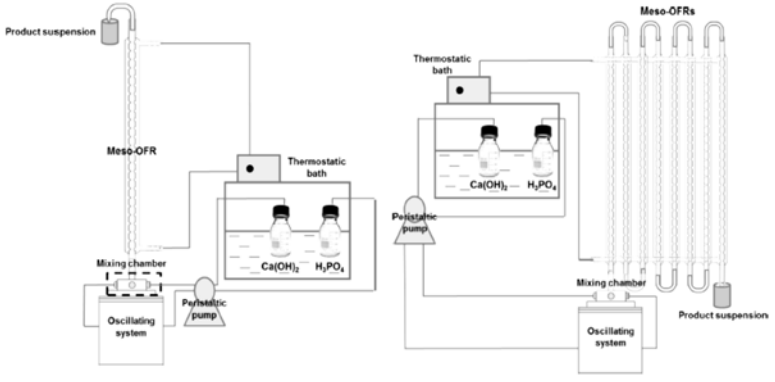

Fig. 6. Scheme of production HAp in meso-oscillatory reactor (meso-ORF) and in scaled-up meso-OFR [24].

Phase purity and chemical analysis

All research groups characterized obtained powders by X-ray diffraction (XRD) and Fourier transform infrared spectroscopy (FTIR) in order to determine the crystalline structure and chemical composition of the product. This kind of analysis is crucial to determine the type of calcium phosphate obtained in the synthesis based on crystalline structure (XRD) and to determine characteristic chemical groups or possible substitutions in the chemical composition of the product (FTIR). Gomez-Morales et al. indicated that suggested synthesis conditions allow to obtain pure hydroxyapatite without other calcium phosphates phase [16]. After 4 residence time, steady state with Ca/P ratio was equal or close to the stoichiometric value. Chemical analysis also confirmed presence of functional group characteristic for HAp structure. Despite N_2 atmosphere inside reactor some signals from carbonated group were observed. Different results present Fujii et al. [17]. They obtained powders prepared at pH 6.4 and temperature range from 0 to 60°C which contain two phases: dicalcium hydrogen phosphate dehydrate (DCPD) and octacalcium phosphate (OCP). What is more, OCP phase increases with higher temperature synthesis. Using temperature range 80-100°C caused arise only one phase - HAp. In contrast, under pH 9, no matter what synthesis temperature was used, only HAp with improved crystallinity was obtained. At pH 6.4 the Ca/P ratio was correlated with temperature. When the temperature rises, the Ca/P ratio is higher achieving 1.66 in 80°C.Results of Lester et al. showed that powder produced in various conditions of temperature and pH were identified as hydroxyapatite[18]. It should be pointed out here that using the continuous hydrothermal rig allow to produce doped HAp too. Hydroxyapatite can easily exchange ions, so Zn^{2+} can replace Ca^{2+} in HAp lattice. Analysis of structure indicated mixture of phases but hydroxyapatite was a main phase.In turn, Anwar et al. have reported that synthesized powders had good correlation with stoichiometric hydroxyapatite [20]. A slight change in unit cell lattice in comparison with HAp without Zn indicated that Zn substitution (replacement of Ca with Zn) is possible. Consequently, Ca/P ratio decreased by increasing Zn substitution. Samples collected in experiments in MTMCR by Yang et al. indicated obtainment of hydroxyapatite without any other phase present[21]. Kandori et al. obtained hydroxyapatite with low crystallinity what confirmed structural and chemical analyses[22]. Parameters of crystals lattice came close to the literature data. The Ca/P ratio was attributed between 1.57 to 1.64. In addition, HAp prepared by microreactor system contains CO_3^{2-} in crystal lattice. That indicates the presence of B-type HAp. In ultrasound tubular reactor Castro et al. received hydroxyapatite in SPF conditions and mixed hydroxyapatite, dicalcium phosphate dihydrate (DCPD), and β-tricalcium phosphate (β-TCP) using GLF[23]. Breadth of peaks of all powders differed from commercial HAp. Chemical analysis indicated that all tested samples had characteristic typical HAp structure. Due to presence of carbonated ions, some of them can be classified

as B-type hydroxyapatite. In experiment with meso-OFR and scaled-up meso-OFR all preparations powders were identified as single-phased. All peaks in XRD diffractograms matched with reference and commercial HAp, which suggested that pure HAp was obtained for all the samples prepared at varied conditions. What is more, all the conditions of the synthesis used in that experiment make possible to obtain carbonated Hap [24].

Size and Morphology

It is known that hydroxyapatite can occur in different morphology. The most common shapes are rod (or needle), sphere and sheet. Gomez-Morales et al. synthesized HAp and obtained aggregates of needle-like particles with average size 0.48-1.5 μm [16]. It was observed that size of particles increases with increasing residence time. Whereas average crystallite size was between 81 and 53nm. This difference in size could confirm mechanism of particle formation: nucleation-aggregation-agglomeration growth. In turn, Fujii et al. obtained the sheet-like particles with size larger than 200nm in conditions at pH 6.4 and temperature range 20-60°C [17]. In 80 and 100°C rod-like morphology appeared with particles size between 100nm and 200nm. In contrast, under pH 9 and temperature below 80°C the particles were heavily agglomerated with undefined shape. In temperature range 80-100°C particles were smaller than 100nm and seemed oval and spindle-shaped. Results of Lester et al. showed that particles produced in 200°C have sheet morphology with widths and lengths up to 2μm and thicknesses <80 nm [18]. By changing only pH from 8 to 10 of the downflow particles had rod morphology with 30-40nm in diameter and variable lengths. What is more, increasing reaction temperature to 350°C caused appearance of particles with tube morphology and inner diameter between 30-70nm. In case of changing other conditions, they observed mixed morphology, whereas HAp with Zn addition was sheet-shaped. Researchers from Anwar's group obtained the rod-like nHAp particles with an average crystals length 80±15 nm and width 12±5 nm, while nHAp with 2wt% Zn had about 70±10 nm in length and 12±5 nm in width [20]. Increasing the level of Zn substitution in particles caused decrease in size and appearance of semispherical morphology. Moreover, particles were very prone to aggregate. Size measurement showed that particles had 100-300 nm in diameter. Yang et al. indicated that at a high reactants flow rate of 1667 or 2500 ml/min, HAp had more homogenous rod-like morphology with smaller size and narrower size distribution in comparison to particles obtained at a lower flow rate (500 or 833 ml/min) [21]. On the other hand, the mean particle size increased with increasing the concentrations of $Ca(NO_3)_2$ and $(NH_4)_2HPO_4$ solutions. Kandori et al. synthesized rod-shaped nanoparticles in their microreactor system. Increasing both flow rate and temperature caused decrease in size while maintaining the same morphology of particles [22]. This can be explained by particles growth only along

the longest axis (c-axis). The smallest particles had 2 nm in width and 15 nm in length. Castro et al. also obtained particles with rod-like morphology but samples obtained under GLF seem to have more defined shape [23]. The size of their HAp particles was found to decrease with the increasing flow rate. What is more, when residence time of reaction mixture in the reactor decreases, tendency to aggregation of particles is more visible. In GLF configuration, applying a gas flow to the reactor generates segmented flow and creates small reacting entities. As a result, formation of aggregates in those small entities was reduced. Using meso oscillatory reactor with longer residence time resulted with not obvious morphology of particles. They seemed as rod-shaped and plate-shaped for the meso-OFR and the scaled-up meso-OFR, respectively. Regarding shorter residence time, obtained particles had more uniform morphology, mostly rod-shaped. Received powders possessed micro-size aggregates composed of nano-size particles. The mean size and the level of aggregation increase with increasing residence time. At the residence times $\tau = 0.4$ and 3.3 min, for the meso-OFR and the scaled-up meso-OFR, respectively, the mean size of particles was 77nm for both reactors [24].

DISCUSSION

Precipitation is the most frequently reported method of synthesis of HAp among all reports described above. It is not a wonder that this method is the most popular, because it exhibits advantages like simplicity, and low energy consumption, just to name the most important[14]. In addition, using microreactor as a tool to contact two streams gives a possibility to better control the reaction conditions. Despite small volume of a reactor, it is possible to obtain high throughput of product. By contrast, hydrothermal method, another described above and presented as possible continuous production method for HAp, requires high temperature and is energy-intensive. Comparison of these two methods, including cost-benefit analysis, indicates that precipitation, as a method of continuous synthesis of hydroxyapatite, would have the better potential to perform as large-scale industrial production of nanoparticles.

Transfer of the same reaction conditions from batch reactor to continuous does not ensure to receive comparable particles. However, some research groups carried out HAp synthesis in batch reactor in order to compare the product with the one synthesized in continuous reactors. In microreactor and batch reactor, Kandori et al. obtained the same rod-shaped morphology but particles from batch system have bigger size (2×15 – microreactor; 12×75-batch) [22]. Castro et al. manufactured HAp in meso-oscillatory reactor [24]. This process has been described both on a batch and continuous level [25]. They strongly suggest that particles have better crystallinity, smaller size, narrow size distribution in continuous synthesis, rather than in batch type. Similar conclusion can be drawn considering the ultrasound tubular reactor.

From the look of these review, described methods of continuous synthesis mainly lead to obtain rod-like, carbonated HAp. Despite the particles have similar features, it is not possible to compare them. Mentioned authors reported either size of crystallites or size of particles (particles size distribution), or both. Moreover, they used different measurement methods and post processing treatment. Solution of this problem with comparing products from different processes and produced by different groups may be conducting the measurement in accordance with, for instance, ISO Standard.

Based on abovementioned results, it can be seen that 'standard' synthesis condition to receive selected kind of particle (rod, tube, sphere) do not exist. However, one can distinguish that main variables in continuous systems affecting particles properties are geometry of reactor, pH, reactants concentration, flow rate, etc. It must be noticed that one of the major factor leading to change in structure of HAp is a pH. It is possible to control phase purity of the product through precise adjusting of pH. In acidic condition DCPA and DCPD (Ca/P=1) are likely to appear, while OCP (Ca/P=1.33) is more probable in neutral environment of synthesis. Whereas, TCP (Ca/P=1.5) and HAp (Ca/P=1.67) are stable in basic condition[26]. Another factor bringing changes in synthesized HAp is reactants concentration. Higher concentrations of solutions of starting materials led to a high supersaturation level. This causes very fast nucleation and growth processes, thereby affecting the generation of small particles. What is more, the enhancement of flow rate increases Reynolds number and improves mixing effectiveness. That also lead to faster nucleation and create a possibility to obtain small particles with uniform size distribution (Yang et al. [21]).

In order to improve properties of hydroxyapatite Lester et al. and Anwar et al. synthesized HAp with additions[18, 20]. Lester's research group investigated influence of HAp substituted with Zn on cells viability. Results of cell proliferation assay show that independently of HAp concentration in medium, no changes of proliferation were observed in 3 days after exposure on mouse embryonic cells (mESC). In turn, Anwar et al. conducted antibacterial testing using disc diffusion method on pure HAp and HAp substituted with Zn. Results demonstrate that Zn doped hydroxyapatite has greater antibacterial activity in comparison to pure HAp. Authors suggest that mechanism of antibacterial bioactivity is connected with the ability of Zn ions to create strong bonds with functional groups such as carboxylic, thiol, amine. These groups are presented in the cell membrane of bacteria. When the metal ions contact with cells it generates damage in cell membrane. Essential components of the cytoplasm leak out of the cell, thereby it leads to bacteria's death. Because of the complicated relationship between parameters, biological experiments are not primary research in design of HAp synthesis processes. Appropriate approach is general characteristic of HAp first. Then, choosing well-defined powder to use

in biological assays, and then, eventually, tailoring process parameters to change HAp powder properties.

Potential application and economical assessment

Majority of research groups have seen potential application of their HAp in bone regeneration, orthopedic implants or bioceramics. Besides potential application, equally important are economical aspects and possibility to scale-up of the systems to produce HAp in continuous way. Gomez-Morales et al. obtained stoichiometric HAp by precipitation method [16]. This kind of apatite, due to its biodegradability, is more desirable in production of dense HAp ceramic rather than Ca-deficient (nonstoichiometric) HAp. Production in MSMPR in conditions proposed by Gomez-Morales et al. allows to achieve good productivity. On the other hand, it requires relatively high temperature (85°C) and additional stream of N_2 what increases the overall cost of production of HAp. Fujii et al. in their type of the reactor can control crystalline phase and shape of particles depending on the range of initial temperature and pH [17]. Simple system and possibility to change conditions in simple way, allow to obtain wide range of products, thereby use them in different application. But in case of scaling-up of this process, it is important to control pH and temperature, which in terms of the latter may generate additional cost. Yang et al. achieved rod-like particles with small size (55-95 nm) [21]. Nano-sized HAp has better properties in bone regeneration and repairing damaged enamel surface. The main advantages of this method are cost-effectiveness and high quality of powder. However, this method employs complicated, and costly, tube-in-tube system, but would have ability to produce HAp in large scale, balancing the equipment cost. In turn, Castro et al. obtained rod-like, carbonated nHAp in near-physiological conditions [23]. This HAp mimics apatite present in human bone. Using their production systems (meso-OFR, ultrasonic tubular reactor) requires control of additional parameters like: gas flow and frequency of ultrasound in ultrasonic tubular reactor or oscillation amplitude and frequency in meso-OFR. What is interesting, scaled-up meso-OFR has similar amount of precipitate to single meso-OFR. Lester et al. synthesized nanotubes, which are less common in literature [18]. These particles have potential application in drug delivery systems and as a material for porous bone scaffolds. However, the main disadvantages of the method proposed by this group are high synthesis temperature (200-400°C) and pressure, what makes it not commercially viable way of HAp production.

Hydroxyapatite can easily exchange ions so substituted HAp gathered a great interest in research [27]. Bioactivity of HAp can be boosted by applying different level of Zn substitution, for instance. Undoubtedly advantage of this approach is a strong inhibition effect on the growth of many kinds of bacteria and fungi. Anwar

et al. synthesized Zn doped HAp [20]. Using this kind of HAp in biomaterials can reduce infection around the implants. The advantages of this production method are not only limited to their biological aspects. Production in CPFS system offers facile, rapid, one step synthesis route which is undoubtedly important for large scale production. Interesting application of HAp is protein adsorption. Kandori et al. have seen potential in use of synthesized HAp in blood purification therapy to remove pathogenic proteins from blood [22]. They obtain small particles with good adsorption properties but using the system that is reported to be complicated. The summary of discussed method and obtained particles with their potential application is presented in Table 1.

Tab.1. The summary of production systems, particles properties, methods of synthesis and potential applications of products.

Production system	Morphology	Synthesis method	Potential application	References
Mixed suspension mixed product removal (MSMPR)	needle	precipitation	bioceramics	[16]
Tubular reactor	sheet, rod	precipitation	bone regeneration, implants, bioceramics	[17]
Microporous tube-in-tube microchannel reactor (MTMCR)	rod	precipitation	enamel surface damage	[21]
Ultrasonic tubular microreactor	rod	precipitation	bone regeneration, implants, bioceramics	[23]
Meso oscillatory flow reactor (meso-OFR)	rod	precipitation	bone regeneration, implants, bioceramics	[24]
Continuous hydrothermal synthesis	nanotube	hydrothermal	drug carrier	[19]
Continuous plastic flow synthesis (CPFS)	rod, semispherical	precipitation	antibacterial activity	[20]
Microreactor with 48 microchannels	rod	precipitation	protein adsorption, blood purification therapy	[22]

CONCLUSION

Through the entire spectrum of synthesis methods for HAp, the most common is precipitation, mostly because of a possibility to scale-up in simple way. This method of synthesis of HAp mainly lead to receive rod-like, carbonated hydroxyapatite.

Moreover, wet chemical precipitation method has advantages over the other methods like low production cost, and simplicity. But when process becomes continuous, level of complication increases and systems could become a multi-faceted. Beyond control of pH and temperature it requires monitoring of extra parameters such as, for instance, gas flow or frequency (depending on the reported method). However, it enables to obtain smaller particles and to reduce aggregation problem of resulting particles. Preparation of HAp is connected with difficulties in controlling size, morphology, purity and degree of particle aggregation. In continuous flow systems all variable parameters are linked and it is difficult to change one without affecting the others. However, after proper optimization, either experimental or by modelling, the continuous flow processes can lead to well defined hydroxyapatite products, with properties suitable for application in biomedical filed. What is more, choosing the proper system and balancing the energy consumption with high productivity, the continuous production of hydroxyapatite can be a cost-effective process.

ABBREVIATIONS

β-TCP – β-tricalcium phosphate
CPFS – continuous plastic flow synthesis
DCPA – dicalcium phosphate anhydrate
DCPD –dicalcium phosphate dihydrate
FTIR – Fourier-transform infrared spectroscopy
GLF – gas-liquid flow
HAp – hydroxyapatite
meso-OFR – meso oscillatory flow reactor
MSMPR –mixed suspension mixed product removal
MTMCR –microporous tube-in-tube microchannel reactor
nHAp – nanohydroxyapatite
OCP – octacalcium phosphate
SPF –single-phase flow
XRD – X-ray diffraction

REFERENCES

[1] Suchanek W., Yoshimura M., Processing and properties of hydroxyapatite-based biomaterials for use as hard tissue replacement implants, *Journal of Material Research,* 1998, 13**,** 1**,** 94–117, DOI: 10.1557/JMR.1998.0015
[2] Chaudhury K., Kandasamy J., Kumar H. S., RoyChoudhury S., Regenerative nanomedicine: current perspectives and future directions, *International Journal of Nanomedicine,* 2014, 9**,** 1**,** 4153-4167, DOI: 10.2147/IJN.S45332.
[3] Uskoković V.,Uskoković D. P., Nanosized hydroxyapatite and other calcium phosphates: Chemistry of formation and application as drug and gene delivery

agents, *Journalof Biomedical Materials Research - Part B Applied Biomaterials,* 2011*,* 96 B, 1, 152–191, DOI:10.1002/jbm.b.31746

[4] Dorozhkin S. V., Nanodimensional and nanocrystalline apatites and other calcium orthophosphates in biomedical engineering, biology and medicine, *Materials,* 2009, 2**,** 4, 1975–2045, DOI: 10.3390/ma2041975

[5] Dorozhkin S. V., Nanosized and nanocrystalline calcium orthophosphates, *Acta Biomaterialia,* 2010, 2, 4, 1975-2045DOI:10.1016/j.actbio.2009.10.031

[6] Catros S., Guillemont F., Lebraud E., Chanseau C., Perez S.,Physico-chemical and biological properties of a nano-hydroxyapatite powder synthesized at room temperature, *Irbm,* 2010, 31, 4, 226–233, DOI:10.1016/j.irbm.2010.04.002

[7] Rodríguez-Clemente R., López-MacipeA., Gómez-Morales J., Torrent-Burgués J., Castaño V. M., Hydroxyapatite precipitation: A case of nucleation-aggregation-agglomeration-growth mechanism, *Journalof the European Ceramic Society,* 1998, 18, 9, 1351–1356, DOI: 10.1016/S0955-2219(98)00064-8

[8] Pham, T. T. T., Phuong N. T., Pham T. N., Dinh T. M. T., Impact of physical and chemical parameters on the hydroxyapatite nanopowder synthesized by chemical precipitation method, *Advances in Natural Sciences: Nanoscience and Nanotechnology,* 2013, 4, 3, 35014, DOI: 10.1088/2043-6262/4/3/035014

[9] Fahami A., Ebrahimi-Kahrizsangi R., Nasiri-Tabrizi B. Mechanochemical synthesis of hydroxyapatite/titanium nanocomposite, *Solid State Sciences,* 2011, 13**,** 1, 135–141, DOI: 10.1016/j.solidstatesciences.2010.10.026

[10] Kunjalukkal S. P., Balakrishnan A., Chu M. C., Jai C.,Sol-gel synthesis and characterization of hydroxyapatite nanorods, *Particuology,*2009, 7, 6, 466–470, DOI: 10.1016/j.partic.2009.06.008

[11] Wojasiński M., Duszyńska E., Ciach T., Lecithin-based wet chemical precipitation of hydroxyapatite nanoparticles, *Colloid Polymer Science* 2015, 293**,**5**,**1561–1568, DOI: 10.1007/s00396-015-3557-0

[12] Ponomareva N. I., Poprygina T. D., Karpov S. I., Lesovoi M. V., Agapov B. L., Microemulsion Method for Producing Hydroxyapatite, *Russian Journal of General Chemistry,* 2010, 80, 5, 1070–3632, DOI: 10.1134/S1070363210050063

[13] Cóta, L F., Licona K. P. M., Lunz J. N., Pereira L. C., Hydroxyapatite nanoparticles: Synthesis by sonochemical method and assessment of processing parameters via experimental design, *Materials Science Forum,* 2016, 869, 896–901, DOI:10.4028/www.scientific.net/MSF.869.896

[14] Sadat-Shojai M., Khorasani M. T., Dinpanah-Khoshdargi E., Jamshidi A., Synthesis methods for nanosized hydroxyapatite with diverse structures, *Acta Biomaterialia,* 2013*,* 9, 8, 7591–7621, DOI:10.1016/j.actbio.2013.04.012.

[15] Afshar A, Ghorbani M, Ehsani N, Saeri MR, S. C., Some important factors in the wet precipitation process of hydroxyapatite, *Materials and Design*, 2003,24, 3, 197–202, DOI: 10.1016/S0261-3069(03)00003-7

[16] Gomez-Morales j., Torrent-Burgues J., Boix T., Sainz J. F., Clemente R. R.,Precipitation of stoichiometric hydroxyapatite by a continuous method, *Crystal Research and Technology*, 2001, 36, 1, 15-26 DOI: 10.1002/1521-4079(200101)36:1<15::AID-CRAT15>3.0.CO;2-E.

[17] Fujii E., Kawabata K., Shirosaki Y., Hayakawa S., Osaka A., Fabrication of calcium phosphate nanoparticles in a continuous flow tube reactor, *Journal of Ceramic Society of Japan*, 2015, 123, 1435, 101-105, DOI:10.2109/jcersj2.123.101

[18] Lester E., Tang S. V. Y., Khlobystov A., Rose V. L., Buttery L. D., Roberts C. J., Producing nanotubes of biocompatible hydroxyapatite by continuous hydrothermal synthesis, *CrystEngComm,* 2013, 15, 17, 3256-3260, DOI:10.1039/c3ce26798a

[19] Lester E., Aksomaityte G., Li. J.,Gomez S.,Gonzalez-Gonzalez J., Poliakoff M.,Controlled continuous hydrothermal synthesis of cobalt oxide (Co3O4) nanoparticles, *Progress in Crystal Growth and Characterization of Materials*, 2012, 58, 1, 3-13, DOI:10.1016/j.pcrysgrow.2011.10.008

[20] Anwar A., Akbar S., Sadiqa A., Kazmi, M., Novel continuous flow synthesis, characterization and antibacterial studies of nanoscale zinc substituted hydroxyapatite bioceramics, *Inorganica Chimica Acta*, 2016, 453, 1, 16-22, DOI:10.1016/j.ica.2016.07.041

[21] Yang Q., Wang J. X., Shao L., Wang Q. A.,Guo F., Chen J., Gu. L., An Y. T.,High throughput methodology for continuous preparation of hydroxyapatite nanoparticles in a microporous tube-in-tube microchannel reactor, *Industrial & Engineering Chemistry Research,* 2010,49, 1, 140-147, DOI:10.1021/ie9005436

[22] Kandori K., Kuroda T., Togashi S., Katayama E. Preparation of calcium hydroxyapatite nanoparticles using microreactor and their characteristics of protein adsorption, *The Journal of Physical Chemistry B,* 2011, 115, 4, 653-659, DOI:10.1021/jp110441e

[23] Castro F., Kuhn S., Jensen K., Ferreira A., Rocha F. , Vicente A., Teixeira J. A., Process intensification and optimization for hydroxyapatite nanoparticles production, *Chemical Engineerig Science,* 2013, 100, 352-359, DOI:10.1016/j.ces.2013.01.002

[24] Castro F., Ferreira A., Rocha F., Vicente A., Teixeira, J. A. Continuous-flow precipitation of hydroxyapatite at 37 °c in a meso oscillatory flow reactor, *Industrial Engineering Chemistry Research,* 2013, 52, 29, 9816–9821, DOI: 10.1021/ie400710b

[25] Castro F., Ferreira A., Rocha F., Vicente A., Teixeira J. A., Precipitation of hydroxyapatite at 37 °C in a meso oscillatory flow reactor operated in batch at constant power density, *AIChE Journal*, 2013, 59, 12, 4483-4493, DOI:10.1002/aic.14193

[26] Vallet-Regí M., González-Calbet J. M., Calcium phosphates as substitution of bone tissues, *Progress in Solid State Chemistry,* 2004, 32**,**1–31, DOI:10.1016/j.progsolidstchem.2004.07.001

[27] Šupová, M. Substituted hydroxyapatites for biomedical applications: A review. *Ceramics International,* 2015, 41**,** 8, 9203–9231, DOI: 10.1016/j.ceramint.2015.03.316

Investigation of formation and characteristics of heterocoagulates in flotation processes with *Shadowgraphy*

*Björn Lewandowski[1,2], ChristinaNielsen[2], Georg Krekel[2], Mathias Ulbricht[1]
[1] Chair of Technical Chemistry II, University of Duisburg-Essen, Essen, DE
[2] Faculty of Chemistry, Niederrhein University of Applied Sciences, Krefeld, DE
e-mail: Bjoern.Lewandowski@hs-niederrhein.de

***Keywords**: Flotation, surface chemistry, high-speed imaging, Shadowgraphy, heterocoagulates*

ABSTRACT

Influence parameters on the flotation of model glass particles, such as volumetric gas flow rate, collector concentration and frother concentration were rigorously investigated using a design of experiment approach. Furthermore, the influence of wetting on flotation was analysed using silanes for hydrophobisation of the particle surface. It was found that hydrophobic particles were floated better than hydrophilic ones. The yield increased by a factor of approx. 2.5. Additionally, formed heterocoagulates were studied using *Shadowgraphy*. Different types of bubble-particle aggregates were observed and are presented in this work.

INTRODUCTION

The flotation process is, with approx. two billion metric tonnes floated crude ore per year, one of the most important processes for the enrichment of valuable minerals [1]. Many works on the investigation of flotation processes are available in literature. However, most of these deal with empirical optimisation of the process parameters [2]. The main goal is often to maximize the separation efficiency. Nevertheless, the process has not yet been fully understood, since modelling of mechanical processes is mainly based on empirical correlations. Optical methods, such as *Shadowgraphy* and *Particle Image Velocimetry* (PIV) could help to improve the understanding of the basic principles of flotation. However, an application of optical methods to multiphase flows is challenging due to the presence of different phases and the complex flow structures. The liquid in flotation cells contains typically a high solids loading so that laser or LED light cannot pass through the cell.

The flotation of glass particles has already beeninvestigated by *Ata and Jameson*[3], [4]. They analysed the formation as well as the behaviour of formed bubble clusters in a flotation cell with optical methods. They used dodecylamine solution as collector and 4-methyl-2-pentanol as frother.An effect of dodecylamine on the size of the bubble clusters was reported. At a high particle loading, large clusters were formed, while only small clusters and single bubble-single particle heterocoagulates were formed at low solids concentration.

MATERIALS AND METHODS

Rigorous flotation tests were carried out in a poly(methyl methacrylate) (PMMA) flotation cell in laboratory scale (V = 2 l)at a constant impeller speed of 700 revolutions per minute using approx. 2 g spherical soda-lime glass particles in the size range of 200-300 µm (supplier: Sigmund Lindner GmbH).A schematic drawing of the experimental set-up is given in Fig. 18.Ambient air is compressed by a screw compressor. The pipe pressure is approx. 5 bar. The volumetric gas flow rate was adjusted using a variable area flowmeter, whose outlet was connected to a porous frit to produce bubbles. A Rushton turbine was used as agitator. The agitator had three main tasks:

1. Suspending of solid particles.
2. Shearing of bubbles.
3. Increase of bubble-particle collision probability via induced turbulence.

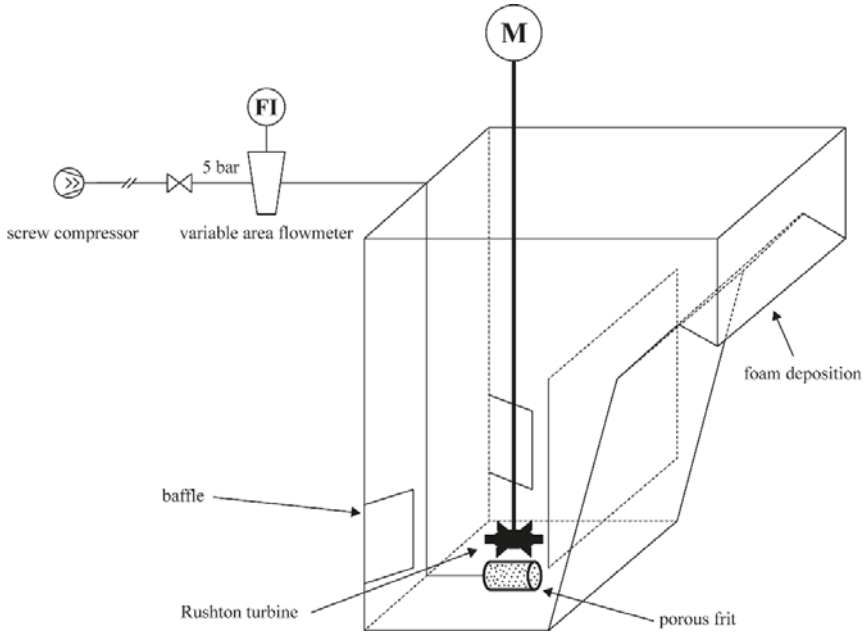

Fig. 18. Experimental set-up for flotation experiments

Baffles are included to prevent unwanted vortex formation. Additionally, the apparatus is divided into two sections by a vertical wall. On the left-hand side, high turbulence is induced through agitation and the bubbly flow. On the right-hand side, the flow is calmed so that stable foam formation is supported. Furthermore, particles which had floated by accident have time to settle back into the turbulent part of the apparatus. The foam is skimmed manually at the top right side of the apparatus with a wiper and collected in a beaker.

The experiments are stopped when no more foam accumulates. The collected foam is filtrated and washed several times with distilled water. Afterwards, the particles are dried to constant weight in an oven at 100 °C. The yield Y is calculated as the ratio of recovered to inserted mass of particles:

$$Y = \frac{m_{recovered}}{m_{inserted}} \quad (1)$$

Design of Experiments

A design of experiments (DoE) was conducted to find the optimum process parameters for the recovery of untreated glass particles. The collector and frother concentration as well as the volumetric gas flow rate were chosen as variables. Thus, a randomised 3^k plan was designed using Minitab©. As collector, hexadecylamine (HDA) solution was used and 4-methyl-2-pentanol (MIBC) was used as frother. The pH was adjusted using hydrochloric acid (HCl), so that a value of approx. 6 was present.In total, 31 experiments were carried out. The set parameters for the experiments are given in Tab. 4.

Tab. 4. Set points for the variables of the 3k DoE

Variable	Set point		
	Lower	Centred	Upper
$c_{Collector}$ in mg/g SiO_2	1.0	2.5	4.0
$c_{Frother}$ in ppmv	25.0	62.5	100.0
$\dot{V}_g$ in l/min	2.0	3.5	5.0

A graphical representation of the DoE is shown in Fig. 19. Only the corner points and the centre point of the DoE were investigated. Each experiment was carried out three times except for the centre point of the designed plan, which was determined nine times.

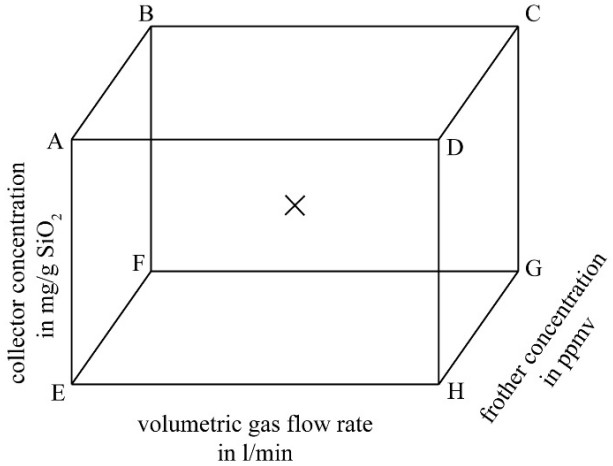

Fig. 19. Graphical representation of the 3k DoE (centre set point marked with an "X")

Modification of glass surfaces

The surface of the glass particles was selectively modified using different silane reagents to investigate the influence of wetting on particle recovery. As reagents ethyltriethoxysilane (ES) and 1H,1H,2H,2H-perfluorooctyltriethoxy-silane (PS) were used. The molecular structuresare given inFig. 20. The surface of the glass particles was first cleaned and activated using Caro's acid (three parts concentrated sulphuric acid and one part hydrogen peroxide) for 24 h. Afterwards, the acid was filtrated and the particles were cleaned with distilled water. The particles were then dried at 100 °C in an oven. Next, the particles were conditioned in 96 % ethanol for one day. The ethanol was extracted via filtration, the particles cleaned with distilled water and again dried in an oven at 100 °C. After this, the particles were put into fresh ethanol (96 %) and one volume percent of the silane was added to start the reaction. The reaction was conducted for 24 h. The glass particles were stirred during all of the procedure steps using a magnetic stirrer.

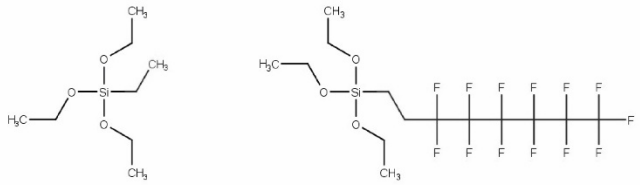

Fig. 20. Molecular structures of the silanes used for surface modification

Flotation of modified glass particles

For the flotation of the modified glass particles, no collector was used. The modified glass particles (2 g)were filled in the apparatus (see Fig. 18) and two litres of water were added. Afterwards, the optimum amount of frother and volumetric gas flow rate determined from the DoE were adjusted. The produced froth was collected in a beaker. The liquid was extracted via filtration and the particles were washed with distilled water. Afterwards, the particles were dried to constant weight in an oven at 100 °C.

Optical investigation using *Shadowgraphy*

The optical investigation of the formed bubble-particle heterocoagulates was conducted in a thin, transparent flotation column made of PMMA.A high-speed camera (type: Olympus iSpeed TR) recorded the rising heterocoagulates in 8 bit grayscale image sequences at a frame rate of 500 frames per second. The image resolution was 1280 x 1040 px with a field of view of approx. 50 x 40.6 mm.A LED backlight illumination (supplier: Dantec Dynamics) with 55,000 lux at continuous mode was used to illuminate the measurement area. Unmodified soda-lime glass

particles with a size of 53-63 µm (supplier: Sigmund Lindner GmbH) were floated using oleic acid as collector and calcium hydroxide as regulator at a pH of 8-9.

RESULTS AND DISCUSSION

Optimum process parameters

The yield for each set point given in Tab. 4 is represented in a cube diagram in Fig. 21. As can be seen, the highest yield (20.7 %) was observed at the top left corner of the cube at a volumetric gas flow rate of 2 l/min, a collector concentration of 4 mg/g SiO_2 and a frother concentration of 100 ppmv. The trend of the yield inside the cube diagram led to the assumption that a local maximum may be present on one of the cube edges. Thus, each of the four cube edges was investigated at least three times to check for a local maximum.

The additional experiments revealed that a local maximum exists on the cube edge BF (see Fig. 19 for nomenclature) with a yield of 26.7 %. Thus, the optimum process parameter in the investigated range are as follows:

- Volumetric gas flow rate: 2.0 l/min
- Collector concentration: 2.5 mg/g SiO_2
- Frother concentration : 100 ppmv

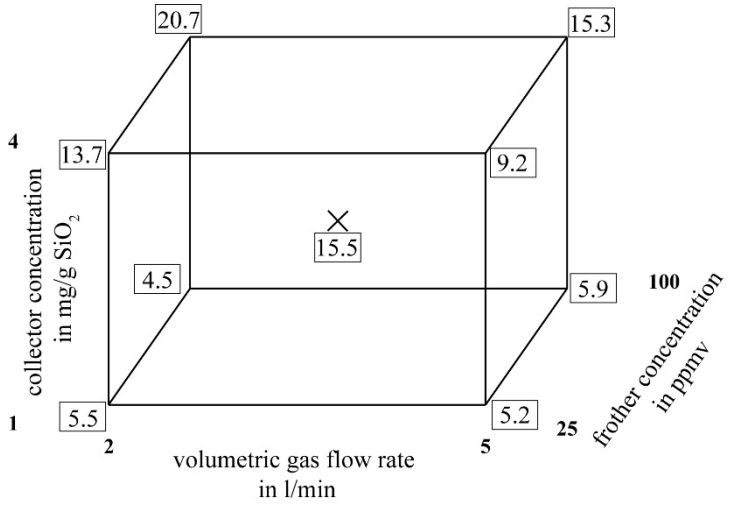

Fig. 21. Yield for the different set points of the DoE

The analysis of the standardised effects showed that except for $\dot{V}_g$and the binary interaction of $\dot{V}_g$ with $c_{Frother}$ all parameters are significant under the assumption of a significance level α of 0.01. The greatest effect on the yield had the collector concentration;. higher $c_{Collector}$resulted in a higher yield. Additionally, the effect of frother concentration was positive, which means that the yield increased with increasing frother concentration $c_{Frother}$.

Although the effect of the volumetric gas flow rate was not significant, an analysis of the main effects showed that the yield decreased with an increase of $\dot{V}_g$. The reason for this is the constant stirrer speed as stated in the materials and methods section. The produced bubbles became larger at constant stirrer speed with increasing $\dot{V}_g$. According to literature, the induction time, which is the contact time necessary for bubble-particle attachment, increases with increasing bubble size [5], [6]. This results in decrease of flotation probability. Thus, small bubbles should be used to increase collision and attachment probability of bubbles with particles[7].

Modification of glass surface

A coloured water drop on modified and unmodified glass particles is shown inFig. 22. The drop was coloured using bromothymol blue, which is an indicator. In acidic solutions it is orange while it turns blue in basic solutions.Firstly, it can clearly be seen that a drop contour forms on the modified particles, whereas a complete wetting of the particle surface occurs on unmodified particles.

Fig. 22. Coloured water dropon modified particles (left) and unmodified particles (right)

Secondly, a colour change is observed when comparing the liquid on the unmodified and modified particles. On the modified particles the water drop is orange while it turned blue on unmodified particles.The colour change can be attributed to a reaction with the glass surface, which took place. As stated in the material and methods section the used glass was soda-lime glass. This means that Na^+ and Ca^{2+} ions are present at the surface. These ions can be exchanged with protons in water. The resulting excess of OH^- ions charges the pH, which leads to a colour change of the indicator solution. On the modified particles the hydrophobic layer of the silane molecules prevents the wetting by and adsorption of water on the glass surface. Hence, no reaction with the surface occurs and no colour change is observed. A schematic visualisation of these two cases is given in Fig. 23.

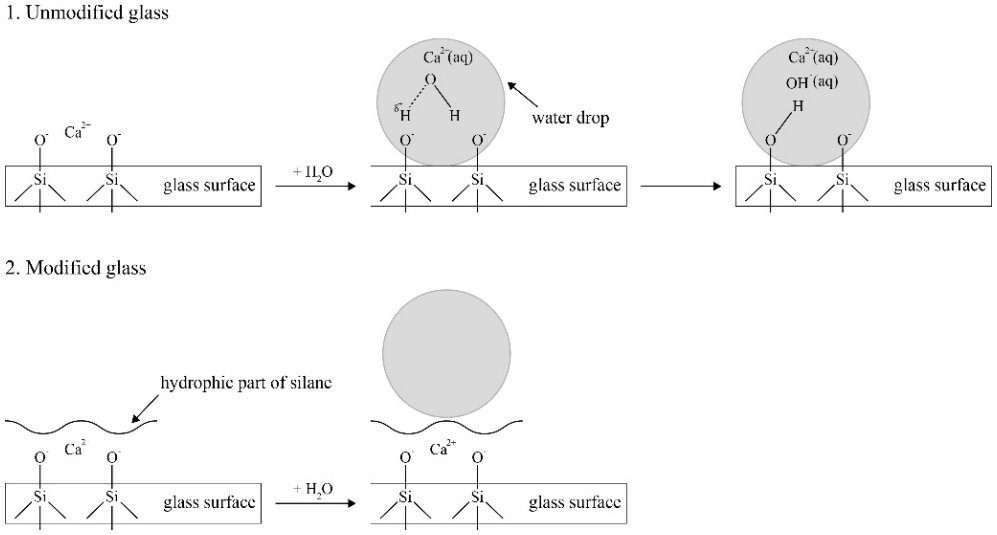

Fig. 23. Mechanism of water wetting and ion-exchange on unmodified glass surface (top) and water repulsion on hydrophobically modified glass surface (bottom)

Flotation of modified particles

The results for the flotation of ES and PS modified particles are given inTab. 5.For ES modified particles a yield of 77.0 % ± 16.0 % was achieved and for PS modified particles the yields was70.0 % ± 7.7 %. Thus, it can be concluded that there is no significant difference in the floatability of ES and PS modified particles.

Tab. 5. Resulting yields for modified particles

Silane	Yield in %
ES	77.0 ± 16.0
PS	70.0 ± 7.7

The yield for the flotation experiments with unmodified and modified particles are compared in Fig. 24. Hydrophobisingof the particles generally increased the yield of floated particles. Compared to unmodified particles, the yield was nearly 2.5 times higher. This proves the importance of hydrophobicity of particles for flotation. Due to the hydrophobic surface, air bubbles can easier attach to the particles and the stability of the formed heterocoagulates is improved.

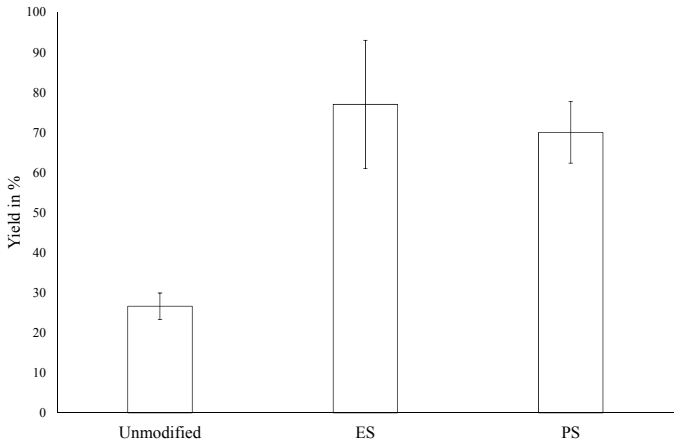

Fig. 24. Comparison of flotation yield for unmodified and modified glass particles

Form of heterocoagulates

Some exemplary structures of observed heterocoagulates are presented inFig. 25. The particles can be clearly identified at the bottom of the rising bubbles. Furthermore, the morphology of the observed bubbles was striking. Thebubble form was spherical, which is in consensus with literature for rising bubbles in solutions containing surface active reagents[11]-[13]. Several different types of heterocoagulates were observed ranging from one particle and one bubble (first image on the left in Fig. 25), to several bubbles and several particles (third image from the left in Fig. 25). According to *Ata and Jameson*, the particular form of formed heterocoagulates is referred to a low particle concentration [3].

The fourth image from the left in Fig. 25 shows a single bubble with a particle aggregate attached to the bottom of the bubble. The aggregation of the particles is favoured due to the interdependency of the adsorbed oleate molecules on the glass surface. Due to the negative charge of the glass surface [14], [15], positive charged calcium ions can function as bridge formers between glass particles and oleate molecules.The adsorbed calcium oleate molecules make the surface less hydrophilic and therefore formation of larger aggregates is facilitated.

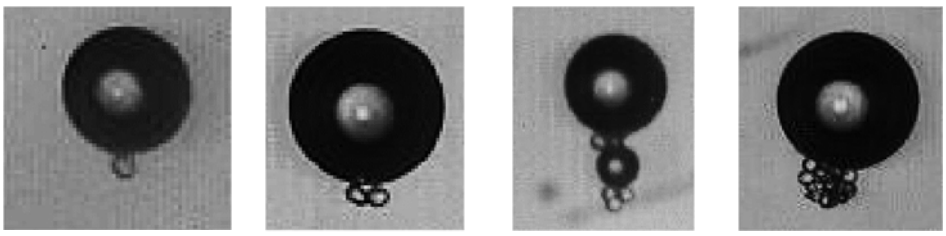

Fig. 25. Shadowgraphy images of formed heterocoagulates

CONCLUSIONS

A design of experiment (DoE) was conducted to find optimum process parameters for the flotation of glass particles. It was found that the collector concentration had the highest influence on the yield. The frother concentration had also a significant effect, while the volumetric gas flow rate had no significant effect. This was attributed to the constant stirrer speed,which led to an increasing bubble size.

Furthermore, glass particles were successfully hydrophobised using ethyltriethoxysilane (ES)or 1H,1H,2H,2H-perfluorooctyltriethoxysilane (PS). A collectorless flotation of these particles at the optimum process parameters found from the DoE resulted in a yield 2.5 times higher than with unmodified particles. Thus, the properties of the particle surface have a significant influence on the flotation result.

A comparison of the flotation results obtained with ES and PS modified particles showed no significant difference. The surface properties of the modified particles may have been too similar so that no difference in the flotation result was observed. In further studies, a rigorous characterisation of the surface shall help to get a better understanding of the influence of hydrophobicity on flotation.

NOMENCLATURE

c	Concentration	PMMA	Poly(methyl methacrylate)
DoE	Design of experiments	ppmv	Parts per million based on volumetric mixtures
ES	Ethyltriethoxysilane	PS	1H,1H,2H,2H-Perfluoro-octyltriethoxysilane
HCl	Hydrochloric acid	V	Volume
HDA	Hexadecylamine	$\dot{V}_g$	Volumetric gas flow rate
LED	Light-emitting diode	Y	Yield
m	Mass	α	Significance level
MIBC	4-Methyl-2-pentanol		

REFRENCES

[1] Mohanty, J. et al., *Role of Chemical Engineering in Processing of Minerals and Materials*, *Allied Publishers*, 2003

[2] Parekh, B., Miller, J., *Advances in flotation technology*, *Society for mining, metallurgy, and exploration*, 1999

[3] Ata, S., Jameson, G., *The formation of bubble clusters in flotation cells*, *International Journal of Mineral Processing*, 2005, 76, 123-139, DOI: 10.1016/j.minpro.2004.12.007

[4] Chen, Z., Ata, S., Jameson, G., *Behaviour of bubble clusters in a turbulent flotation cell*, *Powder technology*, 2015, 269, 337-344, DOI: 10.1016/j.powtec.2014.09.025

[5] Xing, Y. et al., *Recent experimental advances for understanding bubble-particle attachment in flotation*, *Advances in Colloid and Interface Science*, 2017, 246, 105-132, DOI: 10.1016/j.cis.2017.05.019
[6] Brabcová, Z. etal., *Bubble-particle collision interaction in flotation systems*, *Colloids and Surfaces A: Physicochemical and Engineering Aspects*, 2015, 473, 95-103, DOI: 10.1016/j.colsurfa.2014.11.040
[7] Shabazi, B., Rezai, B., Javad Koleini, S., *Bubble-particle collision and attachment probability on fine particles flotation*, *Chemical Engineering and Processing: Process Intensification*, 2010, 49, 622-627, DOI: 10.1016/j.cep.2010.04.009
[8] Ralston, J., Fornasiero, D., Hayes, R., *Bubble-particle attachment and detachment in flotation*, *International Journal of Mineral Processing*, 1999, 56, 133-164, DOI: 10.1016/S0301-7516(98)00046-5
[9] Carl Roth GmbH – Safety data sheet for ethanol, 2017
[10] VDI Gesellschaft, *VDI heat atlas*, *Spinger*, 2010
[11] Kracht, W., Finch, J., *Effect of frother on initial bubble shape and velocity*, *International Journal of Mineral Processing*, 2010, 94, 115-120, DOI: 10.1016/j.minpro.2010.01.003
[12] Li, Y., Zhu, T., Liu, Y., Tian, Y. Wang, H., *Effects of surfactant on bubble hydrodynamic behaviour under flotation-related conditions in wastewater*, *Water Science & Technology*, 2012, 65, 1060-1066, DOI: 10.2166/wst.2012.933
[13] Di Marco, P., Grassi, W., Memoli, G., *Experimental study on rising velocity of nitrogen bubbles in FC-72*, *International Journal of Thermal Sciences*, 2003, 42, 435-446, DOI: 10.1016/S1290-0729(02)00044-3
[14] Behrens, S., Grier, D., *The Charge of Glass and Silica Surfaces*, *The Journal of Chemical Physics*, 2001, 115, 6716-6721, DOI: 10.1063/1.1404988
[15] Gu, Y., Li, D., *The Zeta Potential of Glass Surface in Contact with Aqueous Solutions*, *Journal of Colloid and Interface Science*, 2000, 226, 328-339, DOI: 10.1006/jcis.2000.6827

Nanotechnological approach to bacterial cellulose/nanohydroxyapatite biocomposites fabrication for bone regeneration

Julia Rogowska-Tylman [1, 2], Nabanita Saha[3], Agnieszka Chodara[1, 2], Oyunchimeg Zandraa[3], Witold Łojkowski[1], Petr Sáha[3]

[1]Laboratory of Nanostructures, Institute of High Pressure Physics, Polish Academy of Sciences, Warsaw, POLAND

[2]Faculty of Materials Science and Engineering, Warsaw University of Technology, Warsaw, POLAND

[3]Centre of Polymeric Systems, University Institute, Tomas Bata University in Zlin, CZECH REPUBLIC

e-mail: juliaRT@labnano.pl / nabanita@utb.cz

Keywords*: bacterial cellulose, nanohydroxyapatite, biosynthesis, nanocomposites, bone regeneration*

ABSTRACT

In this study, authors proposed new route for fabrication of biocomposites by direct assimilation of synthetic nanohydroxyapatite (nHA) particles in the process of cellulose biosynthesis. During the process of cellulose excretion by bacteria, nHA particles are entrapped within the network of fibril structure of bacterial cellulose (BC), creating an unexpected structural composites morphology. nHA itself exhibit high affinity to natural human bone mineral phase. It was proved by authors that synthetic nHA material fabricated by microwave-assisted synthesis could successfully mimic the natural bone mineral. Thus, composites based on BC and synthetic nHA can serve as an alternative biomaterial for bone regeneration.

INTRODUCTION

The bacterial cellulose (BC) presents important properties as a result of several surface and macromolecular characteristics combination, such as good mechanical strength, water sorption capacity, porosity, stability and conformability [1,2,3]. Consequently, BC is one of the most prominent materials for biomedical utilization. It consists of a translucent and gelatinous film, formed by an interwoven indefinite-length cellulose microfibrils, distributed in random directions. BC is produced extracellularly by the Gram-negative bacterial cultures of *Gluconacetobacter*, *Acetobacte*r, *Agrobacterium*, *Achromobacter*, *Aerobacter*, *Sarcina*, *Azobacter, Rhizobium, Pseudomonas, Salmonella* and *Alcaligenes*. Among them, the most popular BC producer is the *Gluconacetobacter xylinus* strain [4,5]. Cellulose produced by bacteria is synthetized from several excretion sites located in the cytoplasmic membrane and being aligned parallel with the longitudinal axis of the bacterial cell. Bacteria produce 12-15 cellulose chains and extrude them into the

culture medium as fine fibrils with a lateral width of about 2 nm (supplementary fibrils) through small pores in the outer membrane. These fibers aggregate to form 4-6 nm thick structures, and the resulting microfibrils further aggregate to assemble into ribbons with a lateral width of 40-60 nm. During the biosynthesis, the polymer chains meshed by the micro- and macro-Brownian motions of the bacterial cells [6,7,8].

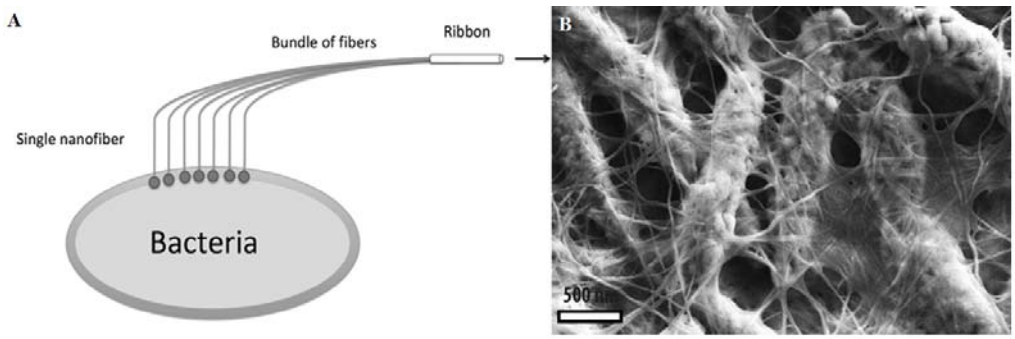

Fig. 1. A - Scheme of bacterium cellulose excretion, B - SEM image of bacterial cells surrounded by cellulose fibers

The ability to form homogeneous membrane fibrous structures under certain synthesis conditions lead to various applications of BC membranes. They are often suggested as base-materials for bone regrowth scaffolds [9]. From a physical and a medical perspective, it is necessary for the ideal bone scaffolds to have good biocompatibility and mechanical strength [10]. Studies on mechanical properties of BC showed that it had superior strength in wet state and was promising for use in tissue engineering materials. In vivo biocompatibility of BC was studied by implanting subcutaneously in various animal models and no signs of inflammation around the implants and fibrotic capsule were observed. The surface of native BC shows a non-satisfactory cell adhesion because cellulose is very inert material. The surfaces of future implant should promote the specific adsorption of proteins and subsequent cellular interaction [11,12]. Thus, many methods of BC modification to optimize the BC/cells interactions we proposed. These modifications aim to change the physical-chemical properties of BC, such as wettability, porosity and surface roughness. Hence, an overall entrapment or grafting with several bioactive and highly hydrophilic compounds with interest in tissue regeneration was reported. There were many trials of various particles incorporation to create composite matrices based on BC [13,14,15,16]. In our study, for this purpose nanohydroxyapatite (nHA) was used as a ceramic compound of the BC/nHA composite. Patients who suffered from trauma or bone diseases usually require biocompatible grafts to fill the gap in defect area and also enhance tissue regeneration. Autologous or allogenous bone transplantation carry a great risk of graft rejection, pathogen transmission and limits the scaffold material

to only certain shapes or sizes [17,18]. Hence, their replacement with a BC-based scaffold configures an interesting therapeutical choice. Moreover, it is well known that in BC culture glucose and fructose as the carbon source and acetic acid as the energy source can influence the morphology and yield of growth. Introduction of elements such as calcium, phosphorus (components of nHA structure) can also improve the effectiveness of the BC production [19,20,21].

MATERIALS AND METHODS

The inoculum for BC production was *Gluconacetobacter xylinus* (CCM 3611T) bacterial strain purchased from Czech Collection of Microorganisms, Masaryk University, Czech Republic. The components of media used in the experiments were as follows, Hestrin & Schramm (HS) medium for fermentation contained: 2% glucose (Sigma Aldrich, USA), 0.5% yeast extract (Himedia, India), 0.5% peptone (Himedia, India), 0.27% disodium phosphate (Penta, Czech Republic) and 0.15% citric acid from Penta (chemicals ratio of mass to volume %). Sodium hydroxide (NaOH) was purchased from Sigma Aldrich, USA. The starting materials for the nano-hydroxyapatite synthesis were: calcium hydroxide ($Ca(OH)_2$, Chempur, Poland) and orthophosphoric acid (H_3PO_4, 85 wt% solution, pure for analysis, Chempur, Poland). Milli-Q water was used throughout experiment and medium preparation for BC production. Double distilled water for hydroxyapatite synthesis was prepared in water purification system equipped with 0.22µm filter (HLP 20UV, Hydrolab, Poland).

Hydroxyapatite synthesis

The hydroxyapatite nanoparticles (nHAs) were synthesized via chemical precipitation method using calcium hydroxide and orthophosphoric acid (acid-base neutralization process)[22,23]. The starting materials were used in a molar ratio of Ca/P = 1.67. Phosphoric acid was added drop-wise to the water suspension of calcium hydroxide (Titrator, SI Analytics, Titronic universal, TZ3260, Germany). Hydroxyapatite was formed with the following reaction (Eq. 1.):

$$10Ca(OH)_2 + 6H_3PO_4 \rightarrow Ca_{10}(PO_4)_6(OH)_2\downarrow + 18H_2O \quad (1)$$

The precipitate was intensively mixed with a mechanical stirrer at ambient temperature. After the synthesis suspensions containing nHA precipitates were transferred to stainless steel containers. Liquid nitrogen was used to cool down the suspensions, followed by 72h of freeze-drying to obtain uniform nanopowders (freeze-dryer Lyovac GT-2, SRK Systemtechnik GmbH, Germany) equipped with pump (Trivac, Leybold GmbH, Germany)[24].

nHA X-ray diffraction (XRD) measurement

XRD patterns of nano-HAp powders were collected at room temperature on an X'Pert PRO, PANalytical diffractometer equipped with a copper anode (Cu Kα1) and an ultra-fast detector (PIXcel1 D). Samples were measured in the range 2θ = 10–100° with a step of 0.03°.

nHA density measurement

The density of nHA nanopowder was measured using a helium pycnometer (AccuPyc II 1340, Micromeritics) at 24 ± 2 °C, according to ISO 12154:2014 norm.

nHA specific surface area (SSA) measurement

Specific surface area of the obtained nHA nanopowder was measured by analysis of the BET isotherm method (Gemini 2360,Micromeritics) according to ISO 9277:2010 norm. The powders prior measurement were dried at 150 °C for 2 h in a constant flow of helium (FlowPrep 060, Micromeritics). The average diameter of the particles (d_{BET}) was calculated on the basis of SSA and density (Eq.2).

$$d_{BET}\ [\mathrm{nm}] \frac{6000}{SSA\left[\frac{m^2}{g}\right]\cdot\rho\left[\frac{g}{cm^3}\right]} \quad (2)$$

where d_{BET} is an the average particle diameter (from specific surface area measurement) and ρ is the density of the material.

BC biosynthesis

Hestrin-Schramm (HS) medium for the synthesis was prepared by mixing all components to obtain clear solution transferred in 100ml portions to separate glass bottles (DURAN® 250ml, Schott) and sterilized (by autoclaving in 121 °C for 15 min). After sterilization, 1% of absolute ethanol was added to bottles with the HS medium as an additional nutrient. *Gluconacetobacter xylinus* (CCM 3611T) inoculum for fermentation was cultivated in sterilized HS culture medium having pH 7.0. This medium was inoculated (with 2 days old bacterial culture in HS medium) and incubated at 30°C for 5 days.

BC/nHA composites fabrication

Nanohydroxyapatite (nHA) was incorporated to BC matrix directly during the biosynthesis of cellulose microfibrils by bacteria. 20 ml of sterilized HS medium solution containing 0.1, 0.5, 1.0 nHA (w/v%) was chosen for this study. These sterile HS medium with nanoparticles of aforementioned concentration was added drop-wise to 5 days old bacteria culture and kept again for 10 more days at 30 °C, in static condition in a temperature controlled incubator. Fig.2 shows the schematic view of nHA particles assimilation into the bacterial culture.

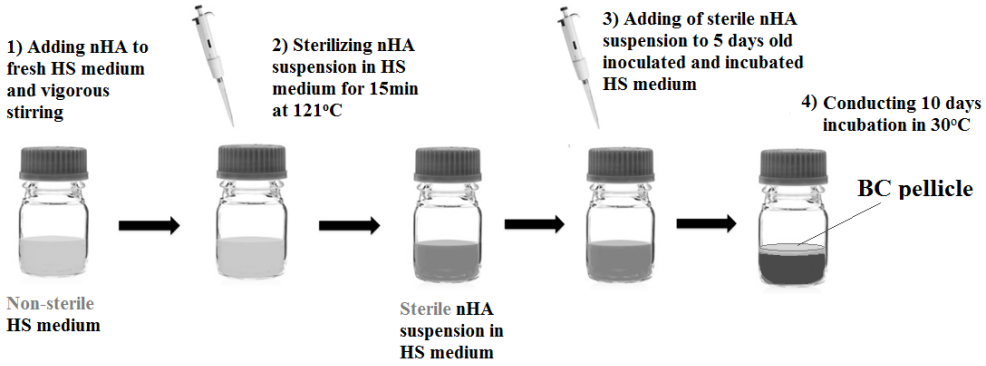

Fig. 2. Scheme of direct nanoparticles introduction into the fermentation medium

Purification of pellicles

The culture medium broth after fermentation was removed from bottles. Composite matrices were taken out from bottles and purified through immersion in 0.5M NaOH at 80°C for 30min to remove debris and microorganisms. After the alkali treatment the matrices were washed several times with distilled water until neutral pH was achieved.

Samples freeze-drying

BC/nHA composites prior further tests were pre-cooled in freezer at -20°C and freeze-dried for 24h at -110°C, 0.5hPa in CoolSafe 110-4 PRO device and stored in desiccator.

Morphology study

Freeze-dried samples were used for scanning electron microscopy imaging procedure. Flat surfaces of samples were mounted on a carbon tape and observed with accelerating voltage of 2-3kV. Morphologies of samples were studied with Field Emission Scanning Electron Microscope FE-SEM (Ultra Plus GEMINI, Carl Zeiss, Germany). Prior the observations on FE-SEM, samples were coated with carbon film of an average 10 nm thicknesses to produce conductive surfaces.

Weight measurement

Samples weight was measured after the introduction of nHA particles of different concentrations. Samples were collected in triplicates on a sieve and weighted at their wet state right after the incubation process and after the purification.

RESULTS

Hydroxyapatite nanopowders

Materials obtained during synthesis and post-processing (freeze-drying) were characterized with high homogeneity (Fig.3). X-ray diffraction patterns of the powders have shown similarities to the natural apatite chemical composition (Fig.4). Moreover, material characterize with high specific surface area of 258m^2/g, density of 2,84 g/cm^3, the calculated average particle of size 8 nm (+/-2nm) and high agglomeration level (Fig.3).

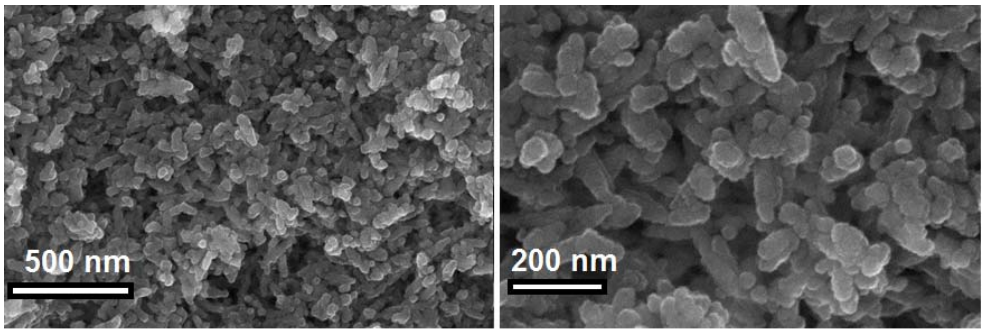

Fig. 3. SEM images of obtained hydroxyapatite nanopowder agglomerates

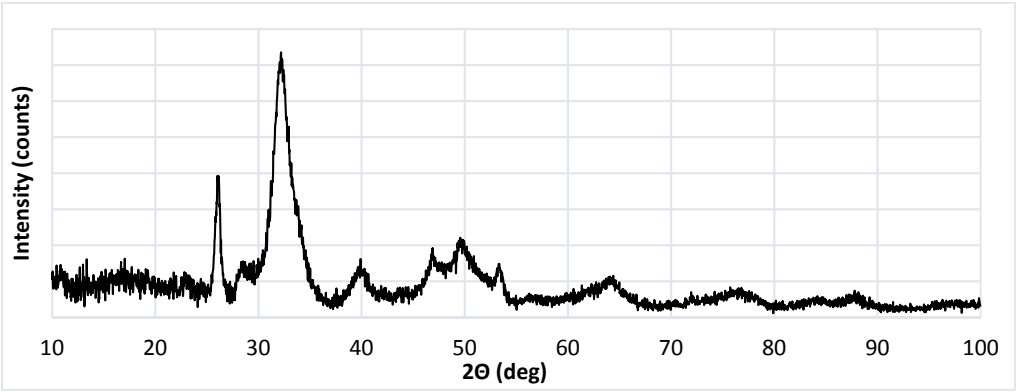

Fig. 4. X-Ray diffraction pattern of the nanohydroxyapatite powder after synthesis

BC/nHA composites

Visually, samples after process of cleaning were not damaged which proves good mechanical stability of bacterial cellulose. After freeze-drying SEM analysis revealed nanoparticles incorporated in the bacterial cellulose structure. Particles added to the medium during the fibers formation are trapped in between to form a composite materials. Microscopic examination of the fibrous structures showed the sizes of particles vary greatly, but most were in the range of 200–1000 nm (Fig.5). In case of composite with the lowest amount of particles (0.1% nHA) particles are nanometer size and distributed on the fibers directly. With the increase of introduced particles amount, micrometer size agglomerates were visible.

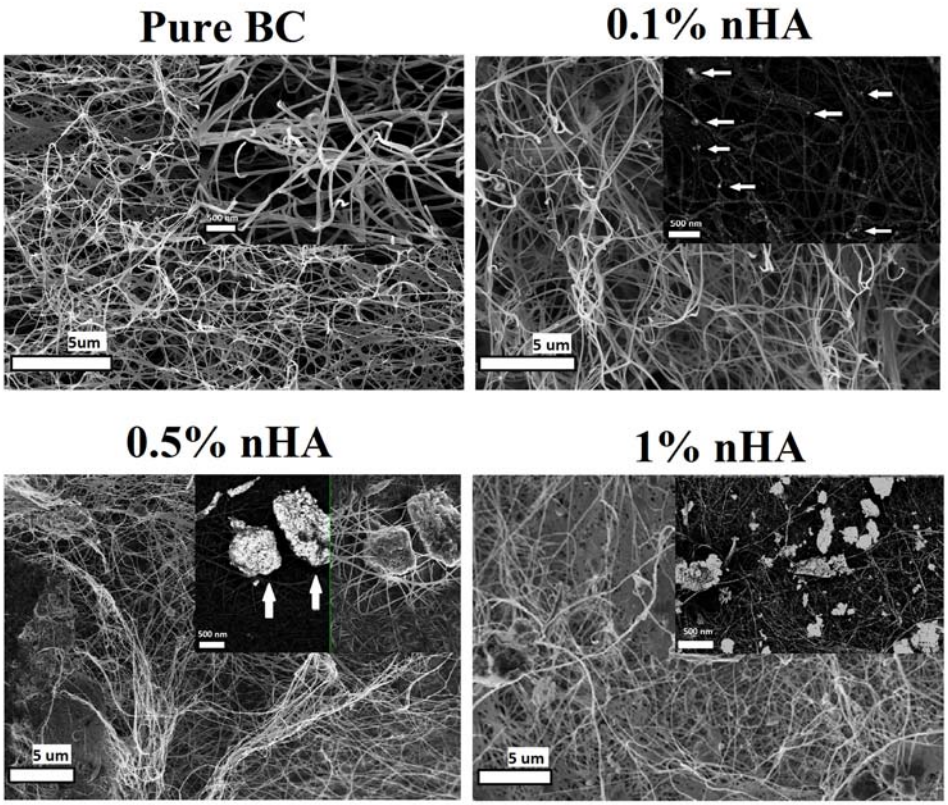

Fig. 5. SEM images of pure BC and BC/nHA composites containing 0.1, 0.5 and 1.0 % nHA, respectively

In samples containing 0.5% and 1% nHA particles agglomerates were visibly entangled in between fibers. One of the possible explanations for bigger particles presence in the composites after microorganisms' purification process is their strong attachment to the fibrous structure of BC. During Brownian motions of the bacterial cells, fibers in the presence of nHA are woven around the ceramic particles [19]. It

was observed that bigger ceramic agglomerates can sustain even the alkali treatment of cellulose purification in NaOH at 80°C.

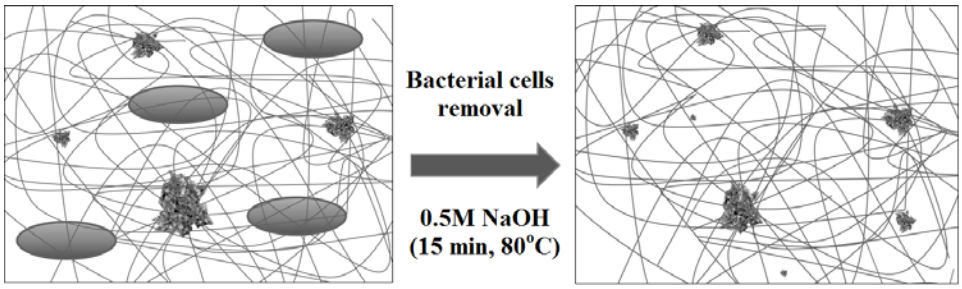

Fig. 6. Suggested mechanism of particles and agglomerates entrapment during biosynthesis of bacterial cellulose.

Influence of nHA on the BC synthesis

Medium rich in nutrients - containing yeast extract and peptone supports good BC production of *Gluconacetobacter* strains. Also introduction of source of elements such as calcium or phosphorus can improve the effectiveness of the BC production [25,26,27]. In our study, after the incubation of bacteria in HS medium with different nHA particles concentration, major improvement of membrane weight growth was seen (Fig.7,8).

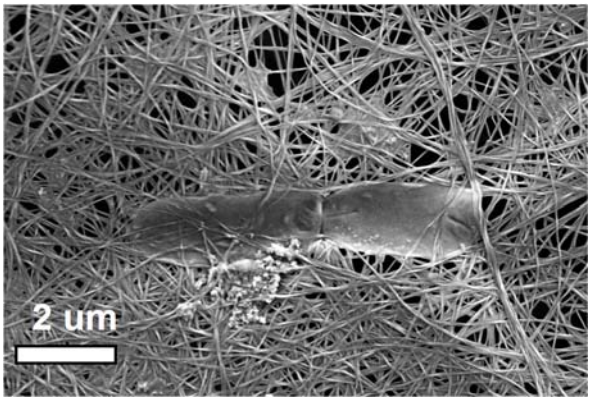

Fig. 7. SEM image of bacterial cell in vicinity of nHA agglomerate surrounded by cellulose fibers

The synthesis was very effective on BC production and the highest yield was obtained for 1.0 % nHA solution addition to inoculated HS medium (Fig.8).

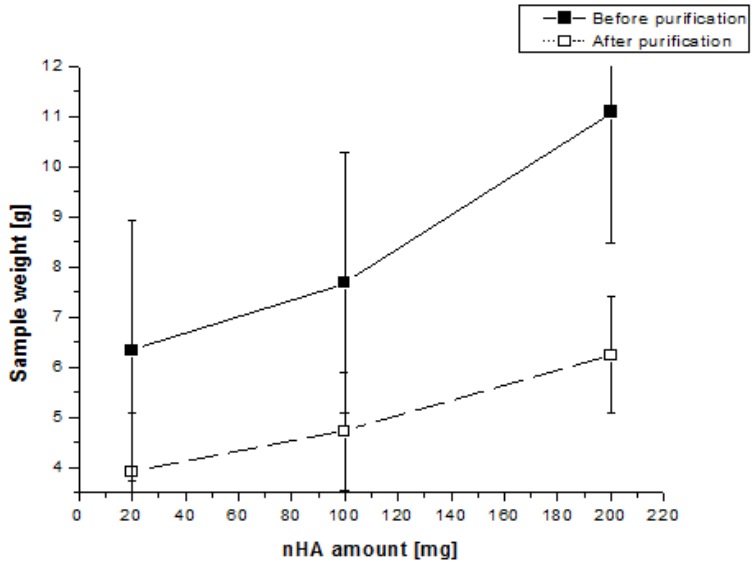

Fig. 8. Bacterial cellulose samples weight in a function of nHA amount added to fermentation culture medium

Purification process resulted in reduction of weight due to microorganisms removal. Nevertheless, the higher yields were visible in a function of simultaneous increase in amount of nHA. This clearly indicates the influence of calcium and phosphorus-rich culture medium on BC growth.

CONCLUSIONS

Nanocomposites of BC/nHA were fabricated by introducing the nHA particles into the bacteria culture medium during the formation of cellulose fibrils. For this purpose, HS medium was used in order to suspend the nHA and enable the stable fermentation. nHA particles were not toxic to the bacterial cells. Contrary, nHA increased the fibrils production by bacterial cells resulting in BC/nHA composites formation and increased weight yield during cellulose biosynthesis. After freeze-drying procedure all samples exhibited porous structure of randomly assembled nanofibers network with nHA particles and agglomerates entangled in between. The present study have shown unique possibilities of new biocomposites fabrication route with great potential in bone tissue regeneration.

ACKNOWLEDGEMENTS

This work is supported by the Ministry of Education, Youth and Sports of Czech Republic, Program NPU I(LO1504). The first author is thankful to COST Action MP1301 for providing financial support to avail the 7th STSM facilities of NEWGEN_MP 1301 (grant nr COST-STSM-MP1301-37776).

REFERENCES

[1] Tonouchi N., Tsuchida T., Yoshinaga F., Beppu T., Horinouchi S. ,Characterization of the biosynthetic pathway of cellulose from glucose and fructose in *Acetobacter xylinum*. *Bioscience, Biotechnology and Biochemistry,* 1996, 60, 8, 1377-1379, DOI: 10.1271/bbb.60.1377.

[2] Delmer P.D., Yehudit A. , Cellulose biosynthesis. *The Plant Cell*, 1995, 7, 7, 987-1000. DOI: 10.1105/tpc.7.7.987

[3] Ross P., Mayer R., Benziman M. Cellulose biosynthesis and function in bacteria. *Microbiol Rev*, 1991, 55, 1, 35-58.

[4] Chang A.L. , Tuckerman J.R., Gonzalez G., Mayer R. , Weinhouse H. , et al., Phosphodiesterase A1, a regulator of cellulose synthesis in Acetobacter xylinum, is a heme-based sensor. *Biochemistry*, 2001, 40, 12, 3420-3426. DOI: 10.1021/bi0100236.

[5] Haigler C.H., Weimer P.J. Biosynthesis and biodegradation of cellulose. Marcel Dekker, Inc. New York, USA, 1991, ISBN 9780824783877.

[6] Keshk S., Bacterial Cellulose Production and its Industrial Applications, *J Bioproces Biotechnique*, 2014, 4, 2 DOI: 10.4172/2155-9821.1000150.

[7] Mühlethaler K., The structure of bacterial cellulose, *Biochimica et Biophysica Acta*, 1949, 3, 527-535, DOI: 10.1016/0006-3002(49)90126-2.

[8] Embuscado M., Marks J., Bemiller J., Bacterial cellulose. Factors affecting the production of cellulose by Acetobacter xylinum. *Food Hydro*,1994, 8, 407-418.

[9] Zaborowska M., Bodin A., Bäckdahl H., Popp J., Goldstein A., et al. Microporous bacterial cellulose as a potential scaffold for bone regeneration. *Acta Biomaterialia*, 2010, 6, 2540-2547, DOI: 10.1016/j.actbio.2010.01.004.

[10] Finkemeier C.G. Bone-grafting and bone-graft substitutes. *Journal of Bone and Joint Surgery. American Volume*, 2002, 84, 3, 454-64, DOI: 10.2106/00004623-200203000-00020

[11] Keshk S., Nascent structure of microbial cellulose. 1999, *Ph.D. Thesis, Tokyo Metropolitan University.*

[12] Massari K.V., Marinho G.O. , Silva J.L. , Holgado L.A., Leão A.L. , Chaves M.R.M., Kinoshita A., Tissue reaction after subcutaneous implantation of a membrane composed of bacterial cellulose embedded with hydroxyapatite, *Dental, Oral and Craniofacial Research*, 2015, 2058-5314, DOI: 10.15761/DOCR.1000106.

[13] Yang J. , Liu X., Huang L. ,Sung D. , Antibacterial Properties of Novel Bacterial Cellulose Nanofiber Containing Silver Nanoparticles, *Chinese Journal of Chemical Engineering*, 2013, 21, 12, 1419-1424, DOI: 10.1016/S1004-9541(13)60636-9.

[14] C.J. Grande, F.G. Torres, C.M. Gomez, M.C. Bañó, Nanocomposites of bacterial cellulose/hydroxyapatite for biomedical applications., *Acta Biomaterialia*. 2009, (5), 1605-15, DOI: 10.1016/j.actbio.2009.01.022.

[15] Tsai Y.H., Yang Y.N., Ho Y.C. et al., Drug release and antioxidant/antibacterial activities of silymarin-zein nanoparticle/bacterial cellulose nanofiber composite films, *Carbohydrate Polymers*, 2018, 180, 15, 286-296, DOI: 10.1016/j.carbpol.2017.09.100.

[16] Kalia S., Dufresne A., Cherian B.M. et al., Cellulose-Based Bio- and Nanocomposites: A Review, *International Journal of Polymer Science*, 2011, 8, 1-35, DOI: 10.1155/2011/837875.

[17] Sakkas A. ,Wilde F. , Heufelder M. , Winter K. , Schramm A., Autogenous bone grafts in oral implantology—is it still a "gold standard"? A consecutive review of 279 patients with 456 clinical procedures, *Int J Implant Dent.* 2017, 3, 1, 23, DOI: 10.1186/s40729-017-0084-4

[18] Mellonig J.T., Autogenous and allogeneic bone grafts in periodontal therapy., *Crit Rev Oral Biol Med.* 1992,3, 4, 333-52, DOI: 10.1177/10454411920030040201.

[19] Shirai A., Takahashi M., Kaneko H., Nishimura S., Ogawa M., et al. Biosynthesis of novel polysaccharide by Acetobacter xylinum. *Int J Biol Macromol*, 1994, 16, 6, 297-300. DOI: 10.1016/0141-8130(94)90059-0.

[20] Chawla R. , Bajaj B. I. , S. A. Survase, R. S. Singhal, Microbial Cellulose: Fermentative Production and Applications, *Food Technol. Biotechnol.,* 2009, 2, 107–124.

[21] Krasteva P.V., Bernal-Bayard J., Travier L., Martin F. A., Kaminski P.A., Karimova G., Fronzes R., Ghigo J.M., Insights into the structure and assembly of a bacterial cellulose secretion system, *Nature Communications*, 2017, 8, 1, 2065, DOI: 10.1038/s41467-017-01523-2.

[22] Kuśnieruk S., Wojnarowicz J., Chodara A., Chudoba T., Gierlotka S., Łojkowski W., Influence of hydrothermal synthesis parameters on the properties of hydroxyapatite nanoparticles, *Beilstein Journal of Nanotechnology*,2016, 7 , 1586-1601. DOI: 10.3762/bjnano.7.153.

[23] Smoleń D., Chudoba T., Malka I., Kędzierska A., Łojkowski W., Święszkowski W., Kurzydłowski K.J., Kołodziejczyk-Mierzyńska M., Lewandowska-Szumiel M., Highly biocompatible, nanocrystalline hydroxyapatite synthesized in a solvothermal process driven by high energy density microwave radiation, *International Journal of Nanomedicine*, 2013, 8, 1–16. DOI: 10.2147/IJN.S39299.

[24] Smoleń D., Kędzierska A., Pietrzykowska E., Chudoba T., Łojkowski W. , Święszkowski W. Kurzydłowski K.J. , Polish Patent Application nr PL396906, Method for of producing nano-plates of synthetic hydroxyapatite

and nanopowder comprising a synthetic hydroxyapatite nano-plates. *Espacenet Database,* 13.05.2013.

[25] Krystynowicz A. Czaja W. , Wiktorowska-Jezierska A. , Gonçalves-Miśkiewicz M. Turkiewicz M., Bielecki S. , Factors affecting the yield and properties of bacterial cellulose, *Journal of Industrial Microbiology and Biotechnology,* 2002, 29, 4, 189–195, DOI: 10.1038/sj.jim.7000303.

[26] Mikkelsen D., Flanagan B.M., Dykes G.A., Gidley M.J., Influence of different carbon sources on bacterial cellulose production by Gluconacetobacter xylinus strain ATCC 53524, *Journal of Applied Microbiology*, 2009, 107, 2, 576-83, DOI: 10.1111/j.1365-2672.2009.04226.

[27] Fijałkowski K., Żywicka A. , Drozd A. , Kordas R. , Rakoczy M. , Effect of Gluconacetobacter xylinus cultivation conditions on the selected properties of bacterial cellulose, *Polish Journal of Chemical Technology*, 2016, 18, 4, 117-123, DOI: 10.1515/pjct-2016-0080.

Electrical Properties and Defect Structure of Vanadium Pentoxide Polycrystalline

*Krystyna Schneider[1],Kamila Kluczewska[2], Małgorzata Dziubaniuk[3], Jan Wyrwa[3]
[1]Faculty of Computer Science, Electronics and Telecommunications, AGH University of Science and Technology, Krakow, POLAND
[2]Institute of Physics, Pedagogical University, Krakow, POLAND
[3]Faculty of Materials Science and Ceramics, AGH University of Science and Technology, Krakow, POLAND
e-mail: kryschna@agh.edu.pl

Keywords*: vanadium pentoxide, electrochemical impedance spectroscopy, electrical conductivity, defect structure, metal-insulator transition*

ABSTRACT

Vanadium pentoxide (V_2O_5) was the subject of our studies. X-Ray Diffraction (XRD) and Scanning Electron Microscopy (SEM) were used for structural and phase characterization of investigated material. Electrical properties were determined by means of electrochemical impedance spectroscopy (EIS) as a function of temperature and oxygen activity. It was found that doesn't show metal-insulator transition (MIT) within entire phase stability of temperature and oxygen pressure. Electrical conductivity of the V_2O_5 results from the presence of singly ($V_O^{\bullet}$) and doubly ionized oxygen vacancies, ($V_O^{\bullet\bullet}$).

INTRODUCTION

Vanadium oxides are fascinating class of inorganic materials with outstanding physical and chemical properties. The investigations of these materials arecentred around phase transitions, in particular metal-insulator transitions (MIT) as a function of temperature which display peculiar structural, magnetic and electrical properties and which still pose open questions concerning their theoretical description [1-4].

From a chemical point of view, vanadium oxides are excellent heterogeneous catalysts used to manufacture of important chemical compounds and in the reduction of environmental pollutants [5, 6].

Vanadium is a transition metal element with the electronic configuration $[Ar]3d^34s^2$, what results in fact that this element in compounds can assume valence +2 (V^{2+} with electron configuration $[Ar]3d^3$), +3 (V^{3+} $[Ar]3d^2$): +4 ($V^{4+}[Ar]3d^1$) and +5 (V^{5+} [Ar]). There is a large variety of the vanadium oxide phases involving either single valence binary oxides in the form of VO, V_2O_3, VO_2, V_2O_5 or oxides with two different oxidation states of vanadium. Oxides containing two different vanadium ions can be classified toeither Magneli V_nO_{2n-1} [7] or WadsleyV_nO_{2n+1}[8] homogenous series (where n is an integral number).

Among vanadium oxide materials vanadium pentoxide occupies exceptional position due to the outstanding physical and chemical properties. The good chemical and thermal stability, excellent thermoelectric properties make a V_2O_5 promising material in oxide electronics. It is used in many technological applications, such as: electrical and optical switching devices [9, 10], in heterogeneous catalysis [6, 11], gas sensors [9, 12-14], temperature and pressure sensors [9, 15],super capacitors [16, 17], electrochromic devices [18, 19], energy storage devices [20-22], reversible cathode materials for Li batteries [23-27] and a thermo-resistive materials in thermal infrared detectors [28].

Despite of the basic and applied importance there are unresolved problems concerning of electrical properties of vanadium pentoxide, in particularly the MIT phenomenon [29, 30]. Pergament et al. [31] argued that the term metal-insulator transition in vanadium pentoxide is not quite correct. Furthermore, the precise mechanism of MIT in V_2O_5, if any, is still a matter of debate [30] and no theoretical understanding has been realized to predict the transition temperature

In the present work both structural (using XRD and SEM) and electrical properties (using EIS) of polycrystalline vanadium oxide have been studied.

EXPERIMENTAL

Sample preparation

The reagent V_2O_5, produced in Russia, distributed by POCh, Gliwice (Poland) was used to preparation of the specimens to structural and electrical studies. Chemical analysis and composition of the reagent is shown in Tab. 1.

The reagent was uniaxial pressed, under the pressure c.a. 50MPa, and sintered at 673 K in air atmosphere for 4hrs. Before performing the impedance measurements, Ag paste was applied as the electrode on two surfaces of the disc pellets (diameter ϕ =10.01 mm, thickness d=2.05 mm).

Tab. 1. Chemical composition of V_2O_5 reagent

V_2O_5 (main component	99.9 % min.
Impurities	
Si	0.003 % max
Fe	0.005 % max
P	0.002 % max
S	0.002 % max
As	0.001 % max
Na_2O+K_2O	0.010 % max

Structural and morphological characteristics

The phase composition of the samples was determined by XRD analysis using a Philips X'Pert Pro diffractometer within the range of diffraction angles, 2θ, from 20 to 100 deg with monochromated CuKα radiation. Crystallite sizes were determined from the X-ray broadening of the selected peaks by means of the Scherrer approach.

Microstructural observations with chemical analysis were carried out using scanning electron microscopy (SEM NOVA NANOSEM 200 FEI Europe Company) coupled with X-ray energy dispersive spectroscopy (EDAX company apparatus). For morphological observations, the samples were polished and subsequently thermally etched at 673K for 1 h.

Impedance measurements

The impedance measurements were performed by means of electrochemical impedance spectroscopy using a computer-controlled Solatron (FRA 1260 and dielectric interface 1294). The impedance spectra were analysed using the ZPLOT software package provided by Solatron. The measurements were performed within the 0.1 Hz ÷1 MHz frequency range. The amplitude of the sinusoidal voltage was 10 mV.

RESULTS AND DISCUSSION

Structural and microstructural characteristics

Fig. 1 presents the typical XRD patterns of the sample annealed at several temperatures in argon atmosphere. X-ray diffraction analysis of the samples revealed the presence of the V_2O_5 orthorhombic phase.

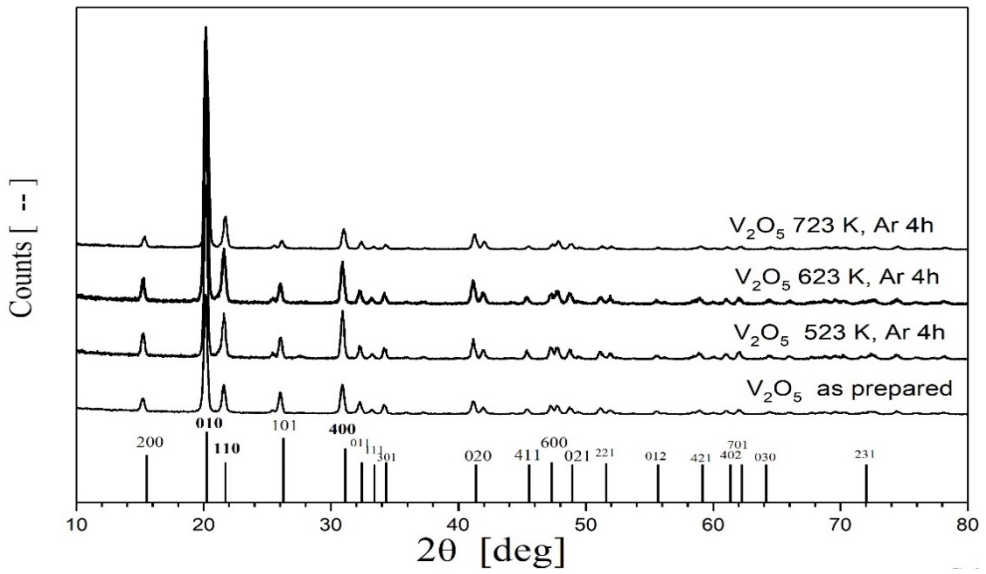

Fig. 1. X-ray diffraction patterns for V_2O_5 as prepared and sintered in argon at several temperatures.

Tab. 2. Results of XRD analysis

SAMPLE	Crystallo-graphic structure	Lattice parameter			d_{XRD} [nm]
		a [nm]	*b* [nm]	*c* [nm]	
As prepared	V_2O_5 Ortho-rhombic P_{nmm}	1.159±0.002	0.438±0.003	0.355±0.008	0.466±0.052
Ar 523 K, 4h		1.158±0.002	0.438±0.002	0.355±0.009	0.447±0.034
Ar, 623 K, 4h		1.158±0.001	0.438±0.003	0.354±0.007	0.490±0.037
Ar, 723 K, 4h		1.152±0.002	0.437±0.004	0.352±0.009	0.440±0.073
Ref. [21]		1.148	0.436	0.355	-
Ref. [22]		1.1519	0.4373	0.3564	-
Ref. [23]		1.1512	0.4368	0.3564	-
10% H_2/Ar, 723 K, 4h	V_2O_3 Rhombohedral R-3c	*a=b=c* [nm]		α [rad]	
		0.546±0.002		0.9477±0.0009	0.315±0.002
Ref. [21]		0.543		0.940	-

The determined lattice parameters well agree with that found in literature reports [21-23]. Presented XRD patterns were used for determination of the crystallite size. Crystallite size, d_{XRD}, was calculated according to Scherrer's method:

$$d_{\mathrm{XRD}} = \frac{0.9\lambda}{\Delta(2\theta)*\cos\theta} \qquad (1)$$

where λ= 0.154056 nm is X-ray used wavelength (CuK_α), $\Delta(2\theta)$ denotes the broadening of the XRD peak at half of its maximum intensity, and θ represents the Bragg diffraction angle. Parameter $d_{XRD}$was determined for 8 most intensive peaks. Determined values of d_{XRD} are collected in Tab.2. No effect of sintered temperature on obtained XRD results is observed.

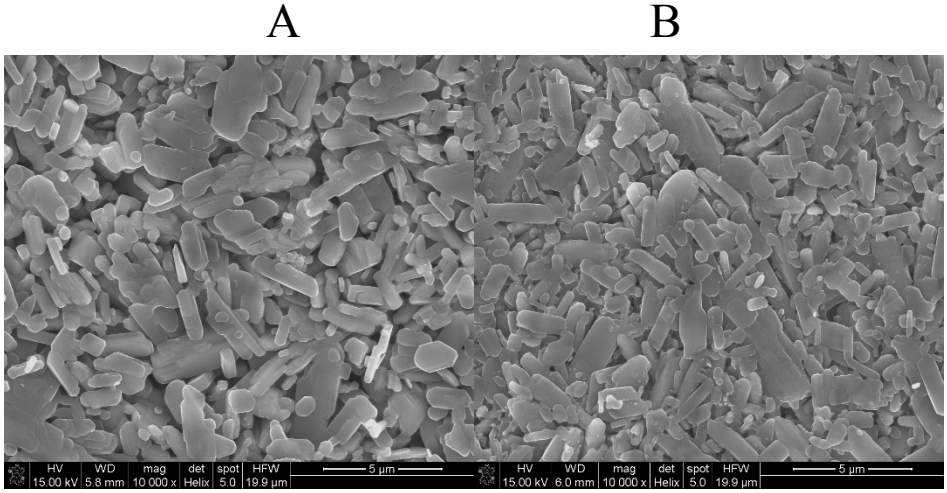

Fig.2. SEM images of samples: A-sintered at 573 K, 4hs in air; B- sintered at 573K in 10%H_2/Ar, 24 hrs. Magnification 3200.

Typical SEM micrographs of the samples sintered at 573 K in air –A and 10%H_2/Ar –B are presented in Fig. 2. A, B, respectively. As it can be seen, the samplesare poly-dispersed with elongated grains in shape. Determined mean grain sizes are listed in Tab. 3. The average EDX analysis carried out during SEM observations confirmed that the samples are composed of thesingle phase.

Tab. 3. Listed mean grain size.

Sample	Grain size	
	Length [μm]	Width [μm]
Sintered at 773 K in air, 4 hrs	2.4±0.9	1.0±0.4
Sintered at 773 K in 8% H_2/Ar, 24 hrs	2.2±0.5	0.8±0.2

Investigations on electrical properties of V_2O_5

Fig.3shows example of impedance spectra determined at different temperatures presented at complex plane Z" vs Z' (Nyquist plot).

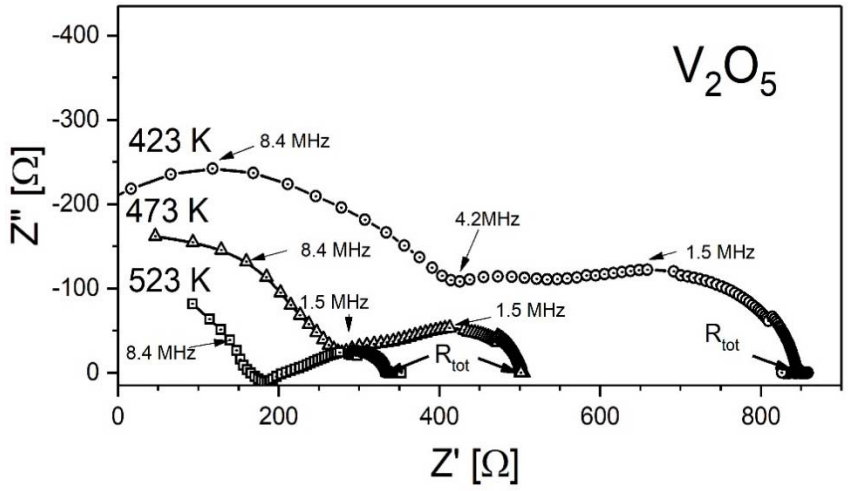

Fig. 3. Nyquist plots of the V_2O_5 obtained at several temperatures.

The separation of high frequency region corresponding to the bulk properties and an intermediate-frequency region corresponding to the grain boundary properties is difficult due to partial overlapping of both parts of the spectra. However, it is easy to determine of total resistivity R_{tot}.

Fig. 4 illustrates the Arrhenius of the electrical conductivity, σ, determined in air atmosphere. The experimental data fulfil the linear dependency, predicted by the equation:

$$\sigma = \sigma_o \exp\left[-\frac{E_{act}}{kT}\right] \quad (2)$$

where the σ_o parameter is independent of temperature, k - Boltzmann constant. The activation energy, E_{act}, of electrical conductivity determined from the slope of the straight-line was (0.255±0.009) eV. This value is much lower than half of the energy band gap, E_g, of V_2O_5 (E_g = 2.3 eV [24]) predicted to the intrinsic electrical conductivity.

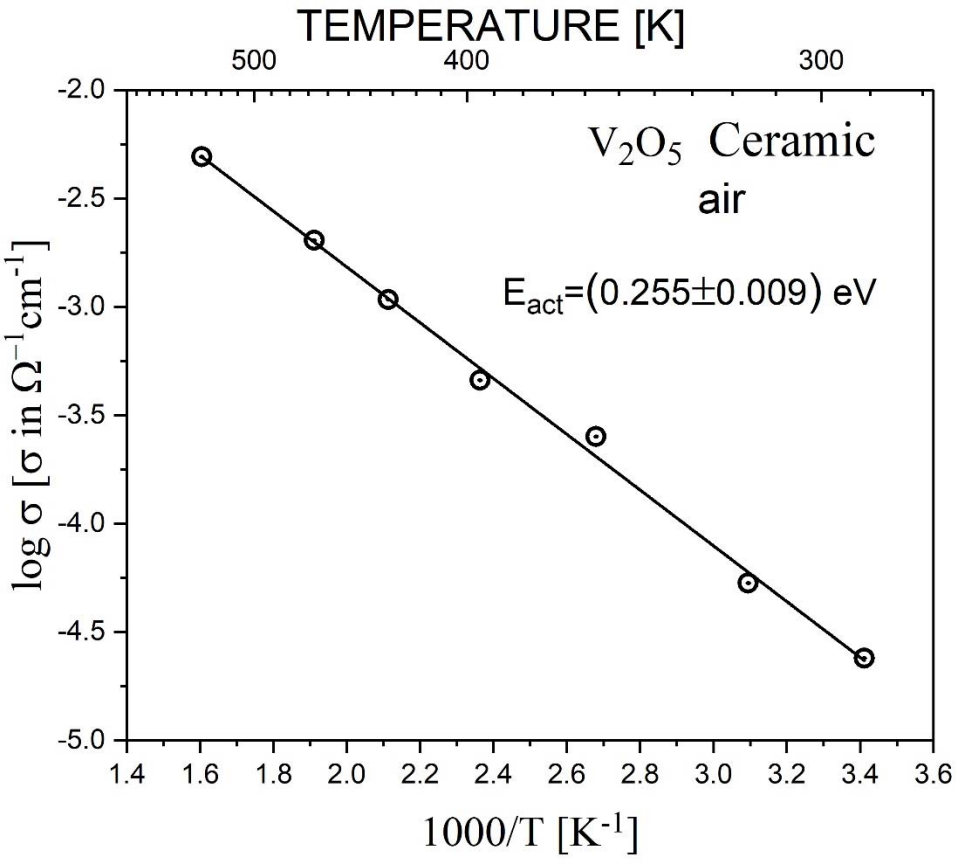

Fig. 4. Temperature dependence of the electrical conductivity (Arrhenius plot) of V_2O_5.

Resistance vs oxygen partial pressure

The results of electrical conductivity as a function of oxygen partial pressure, $p(O_2)$, are presented in Fig. 5.

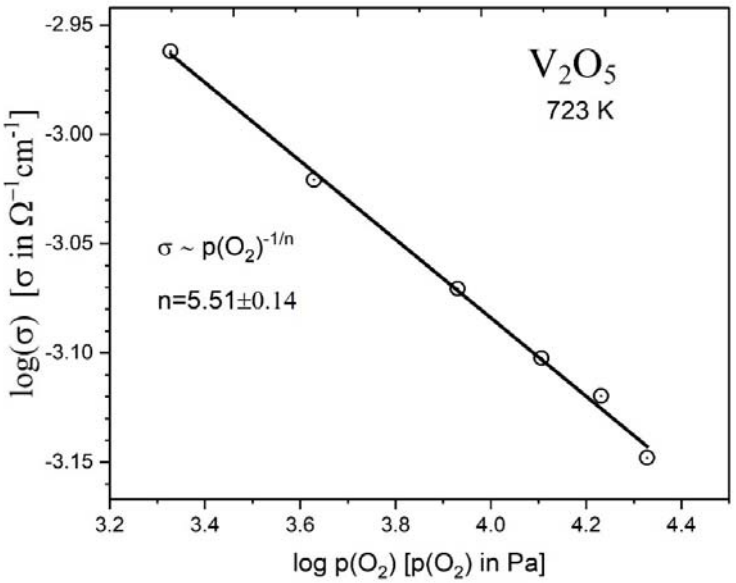

Fig. 5. Electrical conductivity as a function of p(O_2) for V_2O_5 at 723 K.

The decrease of the σ with $p(O_2)$ indicates on n-type extrinsic conductivity of V_2O_5. According to Fig. 4, the dependence of σ as a function of $p(O_2)$ can be approximated by:

$$\sigma = A(T) * p(O_2)^{-1/n} \quad (3)$$

where A is the parameter independent of $p(O_2)$, n is the reciprocal power dependence exponent. The parameter n determined from the slope of the straight-line in Fig. 5. assumes the value of n=5.51±0.14. Similar value of the parameter n= (5.24±0.09) has been reported for V_2O_5 thin film at 623 K [25].

Hence, below we will discuss point defect structure in vanadium pentoxide. Vanadium pentoxide belongs to oxygen-deficit nonstoichiometric compounds [25, 30]. Thedepart from stoichiometry results from the reaction (Kröger-Vink, commonly accepted, the point defect notation is used):

$$O_O \Leftrightarrow V_O^x + \frac{1}{2}O_{2(g)} \quad (4)$$

where V_O^x denotes non-ionized oxygen vacancy, which may undergoes to ionization according to the following reactions:

$$V_O^x \Leftrightarrow V_O^\bullet + e' \quad (5)$$

and:

$$V_O^\bullet \Leftrightarrow V_O^{\bullet\bullet} + e' \quad (6)$$

The mass action law applied to the equilibria (6)-(8) results in the following equation:

$$K_j = [V_O^{j+}][e']^{-j} p(O_2)^{-1/2} \quad (7)$$

where j=0, 1, 2.

Considering the intrinsic equilibria (4)-(6), assuming that only one type defect predominates in the lattice and taking into account electroneutrality condition:

$$[V_O^{\bullet}] + 2[V_O^{\bullet\bullet}] = [e'] \quad (8)$$

the dependence of the electrical conductivity may be expressed as a function of oxygen partial pressure:

$$\sigma = A_0(T)p(O_2)^{-\frac{1}{\infty}} = A_0(T) \text{ if } j = 0 \quad (9)$$

$$\sigma = A_1(T)p(O_2)^{-\frac{1}{4}} \text{ if } j = 1 \quad (10)$$

$$\sigma = A_2(T)p(O_2)^{-\frac{1}{6}} \text{ if } j = 2 \quad (11)$$

where A_o, A_1 and A_2 involvingmobility of electrons and K_o, K_1 and K_2, respectively, and theyare independent of $p(O_2)$. Comparison the experimental value of parameter n (Fig. 5) with theoretical values: n=4 and n=6 done by the Eqs(10) and (11), respectively, revealed that electrical conductivity of the studied material results from the presence of singly ($V_O^{\bullet}$) and doubly ionized oxygen vacancies, ($V_O^{\bullet\bullet}$), with $[V_O^{\bullet\bullet}] > [V_O^{\bullet}]$.

Metal-insulator transition (MIT)

Fig. 6 illustrates dependence of V_2O_5 electrical resistance as a temperature function. Such dependence is typical to semiconductors. No abrupt change of the resistance is observed, in particularly at temperature close to 530K, where the MIT was postulated for the nano-structured V_2O_5materials(such as thin films [26-28] and nanowires [29]).

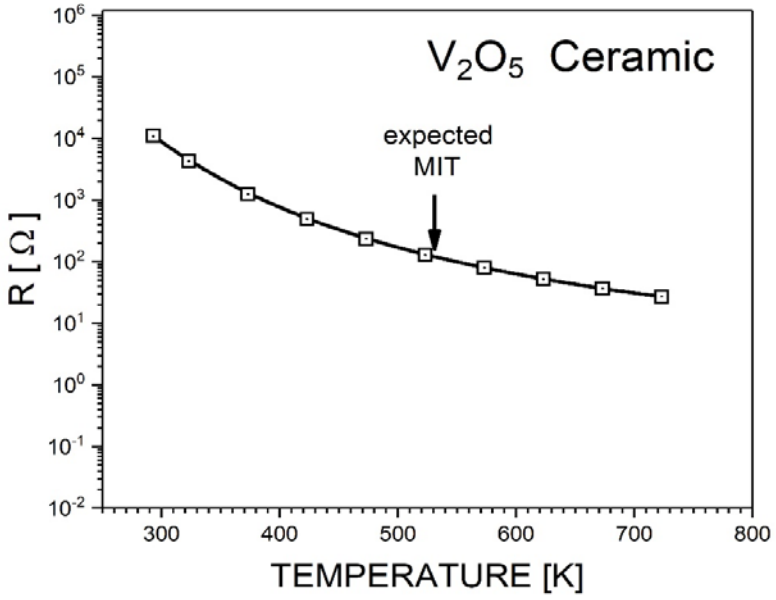

Fig.6. Dependence of electrical resistance on temperature. Arrow show expected (according to literature reports) metal-insulator transition, MIT.

Some interesting result was observed in the experiment presented on Fig.7. Similarly to the results displayed on Fig.6, electrical resistance was measured as a function of temperature at air gas atmosphere. The sample showed semiconductor properties. Then at 723 K the gas atmosphere was changed from air to 10% H_2/Ar. The abrupt change of electrical resistance was observed similar to the MIT phenomenon. Moreover, the sample had metallic properties at 10% H_2/Ar atmosphere with temperature coefficient resistance, TCR=$1.7 \cdot 10^{-4}$ K^{-1}, which is typical to metals. The XRD analysis (Fig. 8.) showed that V_2O_5 sample reduced to V_2O_3metallic phase (forV_2O_3 T_{trans}= 163 K). So, displayed in Fig. 7 plot did not illustrate MIT phenomenon (during typical MIT phenomenon the material doesn't change the chemical composition, but only undergoes the polymorphic phase transition. The observed change of resistance of the studied sample at 723 K resulted from the chemical reaction i.e. reduction of V_2O_5 to V_2O_3 at strongly reduced gas atmosphere.

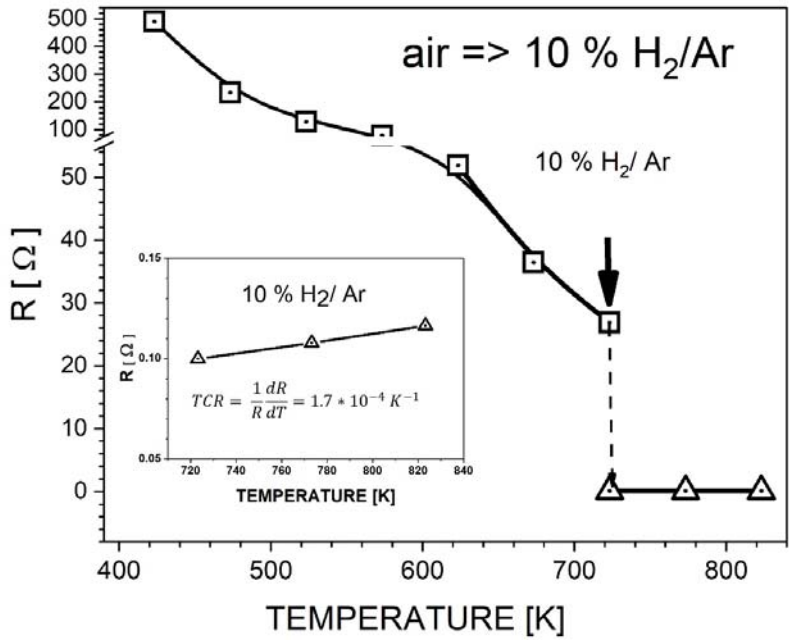

Fig. 7. Temperature dependence of V_2O_3 resistance at air and 10% H_2/Ar gas atmospheres.

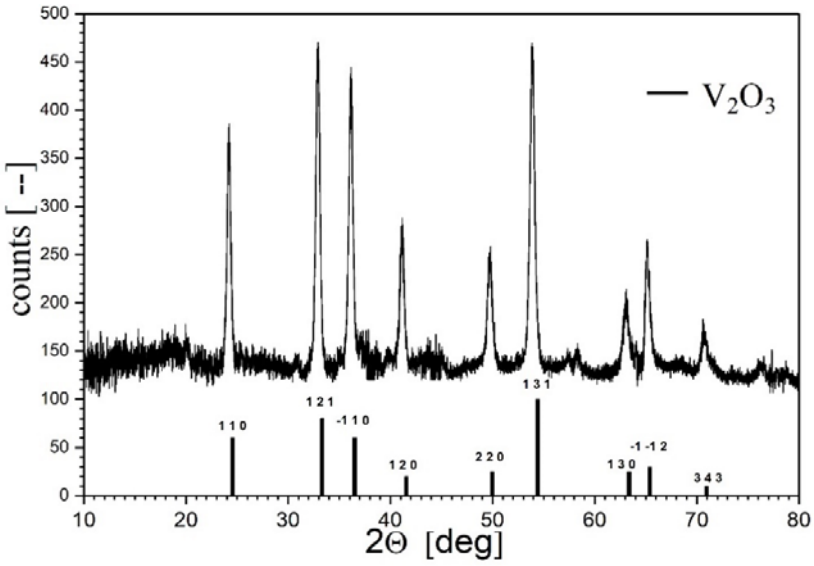

Fig. 8.X-ray diffraction patterns for V_2O_5 sintered in 10 %H_2/Ar.

CONCLUSIONS

In this paper the structural and electrical properties of polycrystalline vanadium pentooxide materials were studied. According to XRD analysis the studied material exhibitorthorhombic structure. Determined crystallite sizes are within 0.42 ÷ 0.49 nm.

The electrical properties of the V_2O_5were investigated with the use ofanalysis of the complex impedance spectra at the frequencies ranging from 0.1 Hz to 1.4 MHz as a function of temperatures within 270 K÷ 723K, and oxygen partial pressure extending from 600 Pa to 21 kPa.It was found that material exhibits n-type extrinsic conductivity. Activation energy of theelectrical conductivity was E_{act}= (0.255 ± 0.009) eV.

The interaction of the solid oxide with oxygen effects on the results of impedance spectra. It is postulated that both singly and doubly ionized oxygen vacancies and electrons are the product of these interactions**.**

No metal-insulator transition (MIT) was observed for V_2O_5 phase. The MIT-like phenomenon can be observed by change of the surrounding gas phase from air to 10%H_2/Ar. However, this process could not be interpreted as MIT, because the chemical reaction (i.e. reduction) takes place. XRD analysis revealed that the product of this reaction was metallic phase of V_2O_3.

The near future research will be concentrated on the use of vanadium pentoxide (both ceramics and thin films) in construction a new generation of resistive gas sensors. According to our experiments [14,37] the highest

sensitivity of V_2O_5 –based sensors in respect to reducible gases (hydrogen, hydrocarbons) is observed at temperatures close to postulated metal-insulator transition (ca. 530 K).

Acknowledgements
This work was supported by the National Science Centre of the Republic of Poland, under Grant No 2016/23/B/ST8/00163**.** The authors would like to thank Dr. Magdalena Ziąbka for her assistance during the microscopy studies.

REFERENCES

[1] Pollini I., Mosser A., Parlebas J.C., Electronic, spectroscopic and elastic properties of early transition metal compound*, Phys. Rep*. 2001, 355, 1-72
[2] Brahlek M., Zhang L., Lapano J., Zhang H-T., Opportunities in vanadium-based strongly correlated electron systems*, MRS Comm*. 2017, 7, 27-52
[3] K. Held, G. Keller, V. Eyert, D. Vollhardt, V.I. Anisimov, Mott-Hubbard metal-insulator transition in paramagnetic V_2O_3: An LDA+DMFT(QMC) study, *Phys.Rev. Lett*. 2001, 86, 5345-5348
[4] Joshi A., Ma M., Zhang F.C., Theory for phase transitions in insulating V_2O_3, *Phys. Rev. Lett*. 2001, 86, 5743-5746
[5] Weckhuysen B.M., Keller D.E., Chemistry, spectroscopy and the role of supported vanadium oxides in heterogeneous catalysis. *Catal.Today*2003, 78, 25-46
[6] Grzybowska-Swierkosz B., Trifiro F., Vedrine J.C., Vanadia Catalysts for Selective Oxidation of Hydrocarbons and Their Derivatives *J. Appl. Catal. A* 1997, 157, 1-45
[7] Andersson G., Studies on vanadium oxides, *Acta Chem. Scand.* 1954, 8, 1599-1606
[8] Wadsley A.D., Nonstoichiometric metal oxides. Order and disorder, *Nonstoichiometric Compounds* 1963, 39/2, 23-36
[9] Yang Z., Ko C., Ramanathan S., Oxide electronics utilizing ultrafast metal-insulator transitions, *Annu. Rev. Mater. Phys.* 2011, 41, 337-367
[10] A.I. Pergament, G.B. Stefanovich, A.A. Vasilenko, Oxide electronics and vanadium dioxide perspective: A.review, *Journal on Selected Topics in Nano Electronics and Computing* 4 (2013) 24-43
[11] Hermann K., Witko M., in: D.P. Woodruff (Ed.), *The Chemical Physics of Solid Surfaces: Oxide Surfaces,* 2001, 9, Elsevier Science 136 (Chapter 4), *and references therein.*

[12] Kumar S., Lenoble D., Maury F. , Synthesis of vanadium oxide films with controlled morphologies: Impact on the metal-insulator transition behavior, *Phys. Stat. Solidi* 2015, 212, 1582-1587.

[13] Jin W. , Yan S., An L, Chenb W., Yang S., Zhao C., Dai Y, Enhancement of ethanol gas sensing response based on ordered V_2O_5 nanowire microyarns, *Sensors and Actuators B* 206, 2015, 284–290

[14] Schneider K., Lubecka M., Czapla A., V_2O_5 thin films for gas sensor applications, *Sensors and Actuators B* 2016, 236, 970-977

[15] Habdank-Wojewódzki, Habdank J., Cwik P., Zimowski S., Characterizations and electrical modeling of sensory samples formed from synthesized vanadium (V) oxide and copper oxide graphene quantum tunnelling composites (GQTC) applied in electrotribology, *MDPI-Sensors* 2016, 16 , 58-69.

[16] Yang Y., Yang D., Ki M., Schmuki P., Vertically aligned mixed V_2O_5–TiO_2 nanotube arrays for supercapacitor applications*,Chem. Commun*. 2011, 47, 27, 7746–7748

[17] Hua L., Ma Z., Shi P., Rui K., Zhou J., Liu X, Zhu J., Sun.G., Ultrathin and large-sized vanadium oxide nanosheets mildly prepared at room temperature for high performance fiber-based supercapacitors *, J. Mater.Chem. A* 2017, 5, 2483-2487

[18] Patil C.E., Electrochromic properties of vanadium oxide thin films prepared by PSPT: Effect of substrate temperature *, AIP Conference Proceedings,* 2013, 1536, 517

[19] Meenakshi M., Sivakumar R., Perumal P., Sanjeeviraja C*.,* .Studies on electrochromic properties of rf sputtered vanadium oxide: Tungsten Oxide *Thin Films, Materials Today Proc., 3, Supplement 1, 2016, Pages S30-S39*

[20] Arico A.S., Bruce P., Scrosati B., Tarascon J.M., van Schalkwij W., Nanostructured materials for advanced energy conversion and storage devices –Review article, *Nature Mater.* 2005, 4, 366-377.

[21] Augustyn V., Simon P., Dunn B., Pseudocapacitive oxide materials for high-rate electrochemical energy storage, *Royal Society of Chemistry,* 2014 , 7, 1597-1614.

[22] Tian X., JIn S., Chua c.K., Tor S.B., Zhou K., Emerging 3D-printed electrochemical energy storage devices: A critical review*, Energy Mater*. 2017, 7, 1700127*,* DOI: 10.1002/aenm.201700127

[23] Yue Y., Liang H., Review: Micro- and nano-structured vanadium pentoxide (V_2O_5) for electrodes of lithium-ion batteries, *Advanced Energy Materials* 2017, 1602545 DOI: 10.1002/aenm.201602545.

[24] Mei J., Liaso T., Sun Z.,Two-dimensional metal oxide nanomaterials for nxt-generation rechargeable batteries, *Adv. Mater.* 2017, 29, 1700176*,* doi: 10.1002/adma.201700176. pub 2017 Apr 10

[25] Yao J., Li Y., Masse R.C. Uchaker E., Cap G.,Revitalized interest in vanadium pentoxide as cathode material for lithium-ion batteries and beyond*, Energy Storage Materials, 2018, 11, 205*

[26] Fleischmann S., Leistenschneider D. , Lemkova V. , Krüner B., Zeiger M., Borchardt L., Presser V., Tailored mesoporous carbon/vanadium pentoxide hybrid electrodes for high power pseudocapacitive lithium and sodium intercalation, *Chemistry of Materials,* 2017, 29, 20, 8653

[27] Cao A.-M., Hu J.-S., Liang H.-P., Wan L.-J., Self-assembled vanadium pentoxide (V_2O_5) hollow microspheres from nanorods and their application in lithium-ion batteries, *Angew. Chem. Int. Ed*. 2005, 44, 28, 4391–4395

[28] Kruse P.W., Uncooled thermal imaging: arrays, systems, and applications, *SPIE Press, Bellingham, Wash*., USA, 2001

[29] Pergament A., Stefanovich G., Kuldin N., Velichko A., On the problem of metal–insulator transitions in vanadium oxides, *ISRN Condensed Matter Physics,* vol. 2013, 2013, 1-6.

[30] Liu W-T., Cao J., Fan W., Hao Z., Martin M.C., Shen Y.R., Wu J. , Wang F., Intrinsic optical properties of vanadium dioxide near the insulator - metal transition, *Nano Letters*, 2011, 11, 466-470

[31] Pergament A., Stefanovich G., Andreev V., Comment on 'Metal-insulator transition without phase transition in V_2O_5 film', *Appl. Phys.Lett*. 2013, 102, 176101

[32] Pergament A.L., Metal-insulator transition temperatures and excitonic phases in vanadium oxides. *ISRN Condensed Matter Physics*, 2011 Article ID 605913

[33] Hanawalt J.D., Rinn H.W., Frevel L.K., Chemical analysis by x-ray diffraction, *Ind. Eng. Chem.Anal*. Ed. 10, 1938, 457–512

[34] Wyckoff R.W.G., Crystal structures, 2nd ed., *Interscience, New York*, 1964 v.2

[35] Enjalbert R., Galy J., An refinement of the structure V_2O_5, *Acta Crystallogr. Sect. C:* R. *Cryst. Struct. Commun*. 1986, 42, 1467-1469

[36] Chakrabarti A., Hermann K., Druzinic R., Witko M., Wagner F., Petersen M., Geometric and electronic structure of vanadium pentoxide: A density functional bulk and surface study, *Phys.Rev. B*, 1999, 59, 10583-10590

[37] Schneider K., Defect structure of V_2O_5 thin film gas sensor, *Proc.of SPIE*, 2016, 10161, 109-1 – 109-9

[38] P. Kang, I. Kim, S. Kim, H.Y. Park, Metal-insulator transition without structural phase transition in V_2O_5 film, Appl.Phys.Lett., 98(2011) 131907-131916

[39] E.E. Chain, Optical properties of vanadium dioxide and vanadium pentoxide thin films, *Appl. Opt*. 30 (1991) 2782-2787

[40] P. Kiri, G. Hyett, R. Binions, Solid state thermochromic materials nanocomposite thin films, *Adv.Mater.Lett*. 1 (2010) 86-105

[41] T.Wu, C.J. Patridge, S. Banerjee, G. Sambandamurthy, Metal-insulator in individual nanowires of doped V_2O_5, American Physical Society, APS Meeting, March 15-19 2010, abstract #V16.007

[42] Kofstad P. in: Nonstoichiometry, diffusion and electrical in binary metal oxides, 1972, Wiley, Intersci., NY, London, Sydney, Tokyo.

Xenon recovery from natural gas by gas hydrate crystallisation: calculation of the distribution coefficient

*Maria Sergeeva, Anton Petukhov, Vladimir Malyshev, Vladimir Vorotyntsev
Nanotechnology and Biotechnology Department, Nizhny Novgorod State Technical University n.a. R.E. Alekseev, Nizhny Novgorod, RUSSIA
e-mail: sergeeva.m.s@rambler.ru

Keywords :*xenon, natural gas, gas hydrate crystallisation, mixed gas hydrates*

ABSTRACT

The distribution coefficients for a four-component natural gas mixture based on methane with impurity components (H_2S=2.5 vol.%, CO_2=2.5 vol.%, *Xe*=0.15 vol.%) are determined. For this mixture the formation of gas hydrates was simulated in the temperature range (268 ÷ 278 K)and for pressures between the dissociation pressure of the gas hydrate mixture and the dissociation pressure of methane gas hydrate. The model of ideal solid clathrate was used for calculating the gas hydrates equilibrium in the four-component gas system. It is shown that the average fraction of *Xe*-filled cavities and the *Xe* distribution coefficient increases with temperature and pressure of the gas mixture. It is shown that the maximum *Xe* distribution coefficient is 5.23 at the natural gas mixture pressure of 4845 kPa and the temperature of 278 K.

INTRODUCTION

Xenon is used in many lines of industry as a fill-gas by manufacturing lamps [1-3], in functional biosensors [4],in the medicine as a general anaesthetic [5].Liquid xenon is used in calorimeters [6]. It is used in instruments for radiation detection, e.g., neutron and X-ray counters and bubble chambers and is a gaseous propellant in the electrostatic ion machines [7].

Xenon occurs in slight traces in the atmosphere of Earth about 0.087 ppm [8]. Itis manufactured on a small scale by the fractional distillation of liquid air [9-13]. Xenon is the heaviest element in the air. The case the xenon extraction from the air, the cost of xenon is overly high due to the necessity to process over 15 million m^3 of air to produce only 1 m^3 of xenon. Therefore the process of extracting xenon from the air is technically complicated and highly energy-consuming. The world extraction of xenon from the air is limited (by about 10 000 m^3 of xenon per annum), and there is no growth tendency due to the fact that the production of xenon is environmentally unfriendly and thus "problematic" [9].

The xenon content in the natural gas equals to 0.15 vol.% (or even more), this is on four orders of magnitude greater of xenon than in the air [9]. Consequently, recovery of xenon from the natural gas is a priority direction. More than ten basic impurities are contained in the natural gas. The highest content of nonhydrocarbon

impurities CO_2 and H_2S. According to [14],their content in the natural gas equals near to 5 vol.%.

For the recovery of xenon from mixtures of the natural gas may also be used the distillation and membrane methods, but they have the same disadvantages as when recovering it from the air.

Recently, the method of gas hydrate crystallisation for the recovery of useful and harmful gases from gas mixtures are used. Gas hydrate crystallisation is used for capturing$CO_2$from the gas stream [15-17], to extractSF_6 [18], to separate noble gases (*Ar*, *Kr*, *Xe*) from the air [19]. Method of recovery the helium from natural gas was patented [20].The mixtures of CH_4+CO_2 [21], CO_2+N_2 [22], CH_4+N_2[23] are separated by the gas hydrate crystallisation.

The method of gas hydrate crystallisation provides efficient separation and recovery of the necessary product from various gas mixtures at a temperature about 273 K, which it is more energy efficient than traditional methods of xenon recovery, and the apparatus is characterized by simpler instrumentation and it may be used either individually or as a the final stage of the technological route in the hybrid processes. Due to the clathrate structure this technology allow concentrating large volumes of gas in a small volume of the gas hydrate, for example, 1 m^3 of xenon gas hydrate at 273 K contains 167 m^3 of xenon gas.

The presented work focus on the calculation the gas hydrate equilibrium in the four-component gas mixture based using the model of ideal solid clathrate. Gas mixture approximating composition of the natural gas (CH_4=94.85 vol.%,H_2S=2.5 vol.%,CO_2=2.5 vol.%,*Xe* = 0.15 vol.%) was chosen for modeling. Modeling of the process of formation of gas hydrates in the temperature range(268 ÷ 278 K)and with an increase the dissociation pressure of the gas hydrate mixture to the dissociation pressure of methane gas hydrate at a given temperatures was carried out. The influence of the temperature and the pressure of the gas mixture on the degree of filling of the small and the large gas hydrate cavities and the *Xe* distribution coefficientare considered.

MATERIALS AND METHODS

Gas hydrates are crystalline molecular complexes formed from mixtures of water and gas molecules. The crystal lattice is made up of water molecules strongly hydrogen bonded [24].

Gas hydrates are nonstoichiometric crystalline solids. Gas hydrates are described by a general formula $M \cdot n\ H_2O$, where M – the gas molecule that forms a gas hydrateat certain of temperature and pressure, n – the number of the water molecules per one gas molecule [25].

The process of formation and growth of gas hydrates on the water surface conditionally divided into two stages. The nucleation is the first stage of the gas

hydrates formation. This stage characterised by the formation of the nucleus of crystallisation from water, supersaturated with gas [26], around which the intensive growth superficial-film hydrate before full overlapping of the free water surface is observed. The second stage is characterised by the volume-diffusive formation of gas hydrate, when the gas diffuses through the formed hydrate to the water surface. After this initial hydrate formation stage, gas continues diffusing into the liquid water from the gas phase supporting further hydrate growth [27].

The formation of the gas hydrate requires the following three conditions:

1) the hydrate-forming agent mustn't chemically interact with water;

2) the diameter of a gas molecule must be less than the free diameter of the cavity of the gas hydrate;

3) the pressure of the gas in the system must be greater than dissociation pressure of the gas hydrate*(P_{dis})*. Dissociation pressure is the minimum pressure at which the hydrate formation process is possible, i.e. pressure, at which the gas hydrate is in a state of thermodynamic stability.

There are three known structures of gas hydrates: the cubic structure-I(*CS-I*), the cubic structure-II(*CS-II*) and the hexagonal structure-III(*HS-III*) [28].The gases CH_4, H_2S, CO_2, *Xe* form of the gas hydrate *CS-I* [29].The structure of the gas hydrates consists of large and small cavities. The cavities of the crystal lattice of the gas hydrate are polyhedron [30].

Multicomponent gas mixture will be formed a mixed the gas hydrate. During the formation of the mixed the gas hydrate distribution of gases in the cavities of the gas hydrate occurs depending on the temperature and pressure.

Because of the regular structure of the gas hydrates their thermodynamic properties may be represented by statistical thermodynamics.The model of ideal solid clathrate, developed by van der Waals, was used for defining the properties of gas hydrates [31,32].

Adsorption of gas molecules by small and large cavities of the hydrate lattice is described the model of Langmuir [31]. The Langmuir constant may be calculated to the spherically smoothed potential function of the *w(r)*at the radial distance *r* from the centre of the cavity to the gas molecule and taking into account the deviation of the molecules from the spherical shape, itis given by the equation:

$$C_{ij} = \left[\frac{4\pi}{kT} \int_0^{R_{qj}} e^{\frac{-w(r)}{kT}} \cdot r^2 dr \right] \cdot \left[\exp\left(- A_j \cdot \left(U_i \cdot \left(\frac{\sigma}{R_{qj} - a} \right) \frac{\varepsilon}{kT} \right)^{l_j} \right) \right], \quad (1)$$

where*i*– the type of a gas molecules; *j*–the type of a gas hydrate cavity; C_{ij}– the Langmuir constant, 1/Pa; *k*– the Boltzmann's constant, J/K; *T*– the temperature of the gas hydrate formation process, K;*q*– the layer number of the water molecules; R_{qj} – the radius of the cavity of the *q*-layer,*Å*; A_j,l_j– the empirical parameters depending on

the cavity type; U_i– the empirical parameter that takes into account the shape of the gas molecules, $U(CH_4)=0, U(Xe)=0, U(H_2S)=0.100, U(CO_2)=0.225$ [33].

The gas molecule is located mainly near the centre of the cavity and is never farther 0.5-1 *Å* from this center [34].TheKihara potentialparametersis usedfordetermining the potential function *w(r)* [35],as this potential maybe applied to nonspherical molecules. The spherically smoothed potential function of the cell may be defined as[24]:

$$w(r) = 2Z\varepsilon\left[\frac{\sigma^{12}}{R_{qj}^{11}\cdot r}(B^{10}+\frac{a}{R_{qj}}\cdot B^{11})-\frac{\sigma^{6}}{R_{qj}^{5}\cdot r}(B^{4}+\frac{a}{R_{qj}}\cdot B^{5})\right], \quad (2)$$

Where Z – the coordination number of the cavity; ε– the depth of the intermolecular potential well, J; σ the distance between molecular coresat with the binary interaction potential becomes zero, *Å*; a–the radius of core of the interaction molecules, *Å*. In the work[36]theKihara potentialparametersfor water molecule as well as the mixing rules are shown.

$$B^n = \frac{1}{n}\left[(1-\frac{r}{R_{qj}}-\frac{a}{R_{qj}})^{-n}-(1+\frac{r}{R_{qj}}-\frac{a}{R_{qj}})^{-n}\right], \quad (3)$$

n takes the 4, 5, 10 and 11.

On the stability of the gas hydrate is influenced by the number of layers of water molecules [37]. Three layers of water molecules are determined the general potential of the cell. For calculations by Eq. (1) the radius of the third layer of water molecules is used, as this radius is as close as possible to the size of the gas hydrate. In work [33] the characteristics of the cells necessary for calculating the Langmuir constant are presented.

The hydrate formation process is possible at a pressure greater than dissociation pressure of the gas hydrate. The vapour pressure of waterover the crystal lattice decreases during hydrate formation. The formation of a solid hydrate phase becomes thermodynamically possible when $P_w^{0(I)} \le P_w^{liq,ice}$ [38], where $P_w^{0(I)}$–the equilibrium vapour pressure of water over the empty hydrate lattice*CS-I*, Pa;$P_w^{liq,ice}$– the equilibrium vapour pressure of water over liquid water or ice, respectively, Pa [39].

The equilibrium vapour pressure of water over the empty hydrate lattice *CS-I*($P_w^{0(I)}$)is determined using the experimentally equationin the temperature range 260 ÷ 290 K [40].

Critical condition for forming the hydrate phase[41]:

$$\ln\left(\frac{P_w^{0(I)}}{P_w^{liq,ice}}\right) = \frac{h}{(1+h)\cdot m}\ln(1+\sum_i C_{1i}\cdot P_i)+\frac{1}{(1+h)\cdot m}\ln(1+\sum_i C_{2i}\cdot P_i), \quad (4)$$

where$h$ – the ratio of numbers of large/small cavities in the unit cell of the gas hydrate (for *CS-Ih*=3 [41]); m– the number of water molecules per one the gas hydrate cavity (for*CS-Im*=5.75 [41]);C_{1i}– the Langmuir constant for small cavities, 1/Pa; C_{2i}– the Langmuir constant for large cavities, 1/Pa;P_i– the partial pressure of the$i$-gas, kPa.

The fraction of gas-filled cavities (Q_{ij})follows the Langmuir's isotherm [31]:

$$Q_{ij} = \frac{C_{ij} \cdot P_i}{1 + \sum C_{ij} \cdot P_i}, \quad (5)$$

The average of the fraction of gas-filled cavities (Q_i) [19]:

$$Q_i = \sum_j N_j Q_{ij}, \quad (6)$$

where N_j–the fraction of cavities of$j$-type in the gas hydrate.

According to the method of Carsonand Katz [42], using the analogy between solid and liquid solutions, the molecules distribution of the main substance and impurities in the cavities of the gas hydrate is described by the distribution coefficient (K_i):

$$K_i = \frac{y_i}{x_i}, \quad (7)$$

where y_i– the mole fraction of the i-gas in the hydrate phase; x_i– the mole fraction of the i-gas in the gas phase.

The gas hydrate distribution coefficient:

$$K_i = \frac{Q_i \cdot \sum P_i}{P_i \cdot \sum Q_i} \quad (8)$$

RESULTSANDDISCUSSION

The Kihara potential parameters must be defined for calculating the fraction of gas-filled cavities (Eq.5) and the distribution coefficient (Eq.8). The Kihara potential parameters used to calculate the dissociation pressure of the mixture were chosen by a numerical method(Tab. 1). Deviation from experimental [33] is 0.4 ÷ 4.5%, which is commensurate with experimental residual standard deviation is 7 ÷ 10% [43-45].

Tab. 1. The Kihara potential parameters

Parameters	CH_4[33]	CH_4*	CO_2[33]	CO_2*	H_2S [33]	H_2S*	Xe [33]	Xe*
ε/k, K	197.4	199.2	506.3	508.3	478.9	493.3	314.5	328.7
σ, $\dot{A}$	3.50	3.47	3.41	3.39	3.48	3.37	3.65	3.48
a, $\dot{A}$	0.26	0.26	0.68	0.68	0.49	0.49	0.25	0.25

* Calculated in our work

The Kihara potential parameters influence the Langmuir constants for small and large cavities. The Langmuir constants were obtained for the gases as a result of the calculation by the Eq. (1).The Langmuir constants decrease with increasing ε and with decreasing σ, consequently, the dissociation pressures calculated according to Eq. (4)are decreased.For example, the calculated the Langmuir constants and the dissociation pressures of individual gases at T=273 K, calculated for the corrected ε and σ, are presented in Tab. 2.

Tab. 2. The Langmuir constants for small (C_1) and large (C_2) of the gas hydrate cavities and the dissociation pressures of individual gases at T=273 K

Absorption molecule	C_1, 1/kPa	C_2, 1/kPa	P_{dis}, kPa	
CH_4	$7.1502 \cdot 10^{-4}$	$1.6332 \cdot 10^{-2}$	2630 [31]	2628*
CO_2	$7.4417 \cdot 10^{-7}$	0.8464	1230 [46]	1232*
Xe	$1.0257 \cdot 10^{-2}$	0.4092	153[46]	151*
H_2S	$3.3006 \cdot 10^{-3}$	3.6371	110 [47]	112*

*Calculated in our work

The deviations the calculated of dissociation pressures from experimental for these individual gases are 0.09 ÷ 1.47%.Therefore, the model of ideal solid clathrate allows calculating the dissociation pressure of the considered gas mixture. The dependence of the average of the fraction of gas-filled cavities (Eq.6) on the temperature and dissociation pressures of the gas hydrates is shown in Tab. 3.

Tab. 3. The dependence of the average of the fraction of gas-filled cavities on the temperature and dissociation pressures of the gas hydrates

T, K	CH_4		CO_2		H_2S		Xe	
	P_{dis}, kPa	Q_i, %	P_{dis}, kPa	Q_i, %	P_{dis}, kPa	Q_i, %	P_{dis}, kPa	Q_i, %
268	2148	17.92	849	12.51	82	54.99	117	0.576
269	2241	18.18	900	12.47	86	54.81	122	0.579
270	2324	18.44	956	12.43	92	54.63	128	0.581
271	2416	18.73	1024	12.38	98	54.45	135	0.585
272	2520	19.04	1136	12.34	104	54.28	144	0.588
273	2628	19.36	1232	12.30	112	54.10	151	0.592
274	2970	20.26	1692	12.27	135	54.03	174	0.608
275	3330	21.07	2317	12.23	164	53.93	198	0.623
276	3776	21.94	3216	12.19	199	53.84	228	0.638
277	4287	22.75	4579	12.15	238	53.73	262	0.652
278	4845	23.61	6401	12.11	284	53.62	301	0.666

The average fraction ofgas-filled cavities depends not only on the temperature and pressure of the gas mixture but also on the solubility of gases in water (Tab. 3).The solubility of CO_2 and H_2S in water is greater by order of magnitude than the solubility of CH_4andXe[48]. Therefore, as the temperature increases the average fraction of

theCO_2, H_2S-filled cavities decreases by 3.22% and 2.48%, respectively, the fraction of theCH_4, *Xe*-filled cavities increases by 31.73% and 15.54%,respectively.The fraction of gas-filled cavitieswith increasing temperature is increased from 86% to 90%.

The dependence of the fraction of the *Xe*-filled cavities from the dissociation pressure of the gas mixture with increasing temperature is shown in Fig. 1.

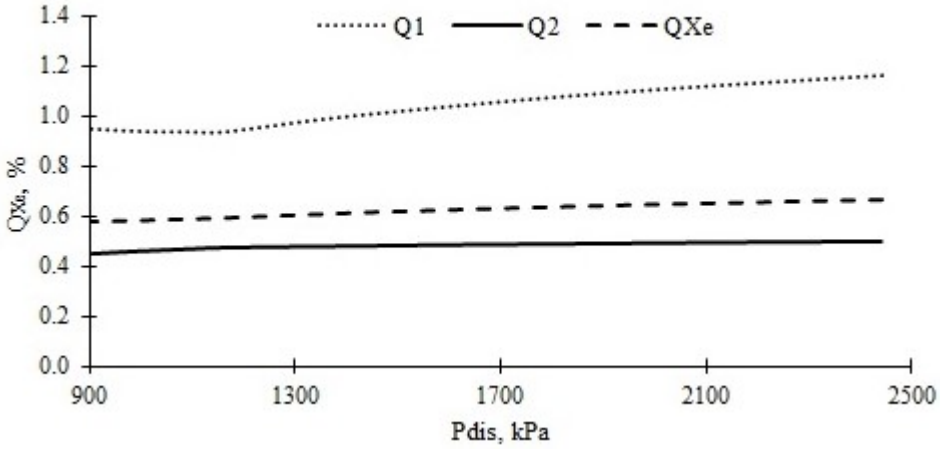

Fig. 1. The dependence of the fraction of the *Xe*-filled small (Q_1), large (Q_2) gas hydrate cavities and the average of the fraction of *Xe*-filled cavities(Q_{Xe}) from the dissociation pressure of the gas mixture$CH_4+H_2S+CO_2+Xe$

Fig. 1shows that with an increase in the dissociation pressure of the gas mixture$CH_4+H_2S+CO_2+Xe$the average of the fraction of *Xe*-filled cavities increases. At a low dissociation pressure of the gas mixture (T<273 K, P_{dis}<1161 kPa) the fraction of small gas hydrate cavities filled by *Xe* and H_2S slightly decreases. Because in these conditions the moleculesCH_4andCO_2 displaces the molecules *Xe* and $H_2S$from small cavities of mixed gas hydrate. The identical behaviour of the moleculesH_2S and *Xe* are related to the close the Langmuir constants for small cavities of the gas hydrate. At T>273 K and P_{dis}>1161 kPa the fraction of gases-filledCH_4, H_2S, CO_2, *Xe* of small cavities increases.

The fraction of large cavities of the gas hydrate, gases-filled$CH_4$and*Xe*,increases.The fraction of large cavities of the gas hydrate, gases-filledH_2SandCO_2,decreases.This is due to that the moleculesof the gas with the highest concentration in this mixture (CH_4) displace the gas molecules, contained in a small amount (H_2S, CO_2),from large cavities of the gas hydrate. The concentration of *Xe* in this mixture is minimal, the Langmuir constants for large cavities of the molecules*Xe*and$CH_4$are close. Therefore the main component (CH_4) will not displace the impurity component (*Xe*) from the large cavities of the mixed gas hydrate.

The *Xe* distribution coefficients in the temperature range 268÷278 K and with an increase in the dissociation pressure of the gas hydrate mixture to the dissociation pressure of methane gas hydrate at a given temperature were determined (Tab. 4 and Fig. 2).

Tab. 4. The *Xe* distribution coefficients from the temperature and gas mixture pressure

T, K	P_{dis}, kPa	K_{Xe}	P_{mix}, kPa	K_{Xe}	P_{mix}, kPa	K_{Xe}	P_{mix}, kPa	K_{Xe}	P_{mix}, kPa	K_{Xe}
268	905	4.47	1216	4.66	1526	4.81	1837	4.91	2148	5.00
269	947	4.49	1271	4.68	1594	4.82	1917	4.92	2241	5.00
270	993	4.50	1325	4.69	1658	4.82	1991	4.93	2324	5.01
271	1043	4.52	1386	4.70	1729	4.83	2073	4.93	2416	5.01
272	110	4.55	1456	4.72	1811	4.85	2166	4.94	2520	5.02
273	1161	4.57	1527	4.73	1894	4.86	2261	4.95	2628	5.03
274	1362	4.65	1764	4.80	2166	4.92	2568	5.00	2970	5.07
275	1566	4.72	2007	4.86	2448	4.97	2889	5.05	3330	5.11
276	1823	4.80	2311	4.93	2799	5.02	3288	5.10	3776	5.15
277	2099	4.87	2646	4.98	3193	5.07	3740	5.14	4287	5.19
278	2441	4.93	3042	5.04	3643	5.12	4244	5.18	4845	5.23

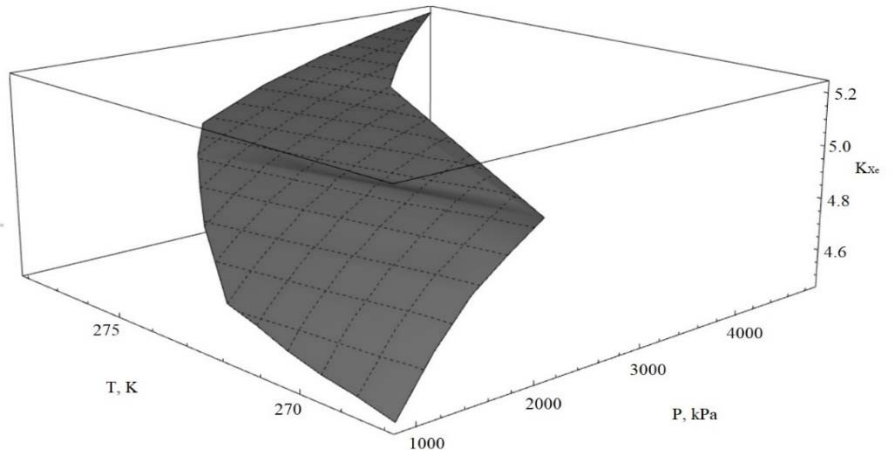

Fig. 2. The dependence of the *Xe* distribution coefficients on the temperature and pressure of the gas mixture$CH_4+H_2S+CO_2+Xe$

Fig. 2 shows thatwhen the temperature and pressure of the mixture$CH_4+H_2S+CO_2+Xe$increasethe*Xe*distribution coefficientincreases. As the temperature and pressure of the gas mixture increase, the average fraction of *Xe*-filled cavities in the gas hydrate increases from 0.576%to 0.666%, hence the *Xe* distribution coefficient increases from 4.47 to 5.23.

CONCLUSIONS

The dependence of the *Xe* distribution coefficient on hydrate formation conditions has been shown. It has been shown that the average fraction of *Xe*-filled

cavities and the *Xe* distribution coefficient increases with temperature and pressure of the gas mixture. It is shown that even using the natural gas mixture with 94.85% methane, the gas hydrate method can be used to recovery xenon. The maximum *Xe* distribution coefficient in the gas mixture under consideration (K_{Xe}) is 5.23 at T=278 K and P=4845 kPa.

ACKNOWLEDGEMENTS

Thisworkwassupported by the Russian Science Foundation (grant no. 17-79-20286).

SYMBOLS

P_{dis} dissociation pressure of gas hydrate, kPa

P_{mix} pressure of mixture, kPa

$P_w^{0(I)}$ equilibrium vapour pressure of water over the empty hydrate lattice *CS-I*, Pa

$P_w^{liq,ice}$ equilibrium vapour pressure of water over ice or over liquid water, respectively, Pa

P_i partial pressure of the*i*-gas, kPa

C_{ij} Langmuir constant, 1/Pa

C_{1i} Langmuir constant for small cavities, 1/Pa

C_{2i} Langmuir constant for large cavities, 1/Pa

r radial distance from centre of the cavity up to the gas molecule, *Å*

$w(r)$ spherically smoothed potential function of the cell attheradialdistance*r*,J

k Boltzmann's constant, J/K

T temperatureofthegashydrateformationprocess, K

R_{qj} radius of the cavity of the q-layer, *Å*

Z coordinationnumberofthecavity

ε depth of the intermolecular potential well, J

σ distance between molecular cores at with the binary interaction potential becomes zero, *Å*

a core radius of interacting molecules, *Å*

A_j empirical parameters, depending on the cavity type

l_j empirical parameters, depending on the cavity type

U_i empirical parameter, that takes into account the shape of the gas molecules

h ratio of numbers of large/small cavities in the unit cell of a gas hydrate

m number of water molecules per one gas hydrate cavity

Q_{ij} fraction of gas-filled cavities, %

Q_i average fraction of gas-filled cavities, %

N_j fraction of cavities of j-type in the gas hydrate
K_i coefficient of gas hydrate distribution
y_i mole fraction of the$i$-gas in the hydrate phase
x_i mole fraction of the$i$-gas in the gas phase

Abbreviations
CS-I cubic structure-I
CS-II cubic structure-II
HS-III hexagonal structure-III

Index
i type of gas molecules
j type of gas hydrate cavity
q layer number of water molecules

REFERENCES

[1] Zundu L. et al., Xenon flash lamp pumped self-frequency doubling NYAB pulsed laser, *Chin. Phys. Lett.*, 1989, 6, 10, 440–443, DOI: 10.1088/0256-307X/6/10/003

[2] Matsuda O., Yaguchi T., 1995. *Filling composition for incandescent lamp, and incandescent lamp containing the same and its use*. Patent USA, No. US5432408A

[3] Neiger M., Hoppstock R., Kleiner B., 1990. *Xenon short arc discharge lamp*.Patent USA, No. US4937496A

[4] Spence M.M. et al., Development of a functionalized xenon biosensor, *J. Am. Chem. Soc.,* 2004, 126, 46, 15287–15294, DOI: 10.1021/ja0483037

[5] Sanders R.D., Ma D., Maze M., Xenon: elemental anaesthesia in clinical practice, *Br. Med. Bull.,* 2005, 71, 1, 115–135, DOI: 10.1093/bmb/ldh034

[6] Gallucci G., The MEG liquid xenon calorimeter, *J. Phys.: Conf. Ser.,* 2009, 160, 1, 74-80, DOI: 10.1088/1742-6596/160/1/012011

[7] Challoner A.D., Poeschel R.L., 1955. *Spacecraft with modulated thrust electrostatic ion thruster and associated method*.Patent USA, No. US4825646A

[8] Godish T., Davis W.T., Fu J.S., Chapter in the book: Atmosphere, *Air quality,CRC Press,* 2014

[9] Smetannikov V.P., Orlov A.N., Malinin N.N., 2010. *Method of xenon concentrate extraction from natural combustible gas, products of its processing, including anthropogenic off gases and the device for its realization (variants)*. Patent RF, No. RU2466086C2

[10] Hahn E., Rohde W., Voit J., 2002. *Method for extracting xenon*. Patent USA, No. US6351970 B1
[11] Wyn R.N., 1955. *Fractional separation of air*. Patent USA, No. US2700282A
[12] Bonnaud H., 1957. *Method for obtaining krypton and xenon*.Patent USA, No. US2793511A
[13] Oleynik A.V., Oleynik V.S., Sedov V.P., 2000. *Method for extracting krypton and xenon from process waste gases*. Patent RF, No. RU2150758C1
[14] Faramawy S., Zaki T., Sakr A..-E., Natural gas origin, composition, and processing: A review, *J. Nat. Gas Sci. Eng.,* 2016, 34, 34–54, DOI: 10.1016/j.jngse.2016.06.030
[15] Duc N.H., Chauvy F., Herri J.M., CO_2 capture by hydrate crystallization – A potential solution for gas emission of steelmaking industry, *Energy Convers. Manage.,* 2007, 48, 4, 1313–1322, DOI: 10.1016/j.enconman.2006.09.024
[16] Surovtseva D., Amin R., Barifcani A., Design and operation of pilot plant for CO_2 capture from IGCC flue gases by combined cryogenic and hydrate method, *Chem. Eng. Res. Des.,* 2011, 89, 1752–1757, DOI:10.1016/j.cherd.2010.08.016
[17] Tajima H., Yamasaki A., Kiyono F., Energy consumption estimation for greenhouse gas separation processes by clathrate hydrate formation, *Energy,* 2004, 29, 11, 1713–1729, DOI: 10.1016/j.energy.2004.03.003
[18] Lee E.K. et al., Pure SF_6 and SF_6−N_2 mixture gas hydrates equilibrium and kinetic characteristics, *Environ. Sci. Technol.,* 2009, 43, 20, 7723–7727, DOI: 10.1021/es901350v
[19] Vorotyntsev V.M., Malyshev V.M., Calculating the separation coefficient in argon, krypton and xenon gas mixture separation by gas hydrate crystallization, *Russ. J. Phys. Chem.*, 2011, 85, 11, 2131–2136, DOI: 10.1134/S0036024411110343
[20] Kinney P.J., Kahre L.C., 1963. *Helium recovery from natural gas*. Patent USA, No. US3097924A
[21] Zhong D.-L. et. al., Evaluation of CO_2 removal from a CO_2 + CH_4 gas mixture using gas hydrate formation in liquid water and THF solutions, *Appl. Energy,* 2015, 158, 133–141, DOI: 10.1016/j.apenergy.2015.08.058
[22] Seo Y.-T. et al., Hydrate phase equilibria for gas mixtures containing carbon dioxide: A proof-of-concept to carbon dioxide recovery from multicomponent gas stream, *Korean J. Chem. Eng.,* 2000, 17, 6, 659–667, DOI: 10.1007/BF02699114
[23] Zhong D.-L., Daraboina N., Englezos P., Recovery of CH_4 from coal mine model gas mixture (CH_4/N_2) by hydrate crystallization in the presence of

cyclopentane, *Fuel,* 2013, 106, 425–430, DOI: 10.1016/J.FUEL.2013.01.029

[24] John V.T., Holder G.D., Choice of cell size in the cell theory of hydrate phase gas-water interactions, *J. Phys. Chem.,* 1981, 85, 13, 1811–1814, DOI: 10.1021/j150613a010

[25] Byk S.S., Fomina V.I., Gas Hydrates, *Russ. Chem. Rev.*, 1968, 37, 6, 469–491, DOI: 10.1070/RC1968v037n06ABEH001654

[26] Yuhara D. et al., Nucleation rate analysis of methane hydrate from molecular dynamics simulations, *Faraday Discuss.,* 2015, 179, 463–474, DOI: 10.1039/C4FD00219A

[27] Jung J.-W., Santamarina J.C., Hydrate formation and growth in pores, *J. Cryst. Growth.,* 2012, 345, 1, 61–68, DOI: 10.1016/j.jcrysgro.2012.01.056

[28] Kirchner M.T. et al., Gas hydrate single-crystal structure analyses, *J. Am. Chem. Soc.,* 2004, 126, 30, 9407-9412, DOI: 10.1021/ja049247c

[29] Byk S.Sh., Makogon Yu. F., Fomina V.I., Chapter in the book: Experimental study of the basic physico-chemical properties of gas hydrates, *Gas hydrates, Khimia,* 1980

[30] McMullan R.K., Jeffrey G.A., Polyhedral clathrate hydrates. IX. Structure of ethylene oxide hydrate, *J. Chem. Phys.*, 1965, 42, 8, 2725–2732, DOI:10.1063/1.1703228

[31] Van der Waals J. H., Platteeuw J.C., Clathrate solutions, *Adv. Chem. Phys.,* 1959, 2, 1–57, DOI: 10.1002/9780470143483.ch1

[32] Vorotyntsev V.M., Malyshev V.M. Gas hydrates, a new class of impurities in high purity gases and gas–vapour mixtures, *Russ. Chem. Rev.,* 1998, 67, 1, 81–92, DOI:10.1070/RC1998v067n01ABEH000318

[33] Holder G D., John V.T., Thermodynamics of multicomponent hydrate forming mixtures, *Fluid Phase Equilib.,* 1983, 14, 353–361, DOI:10.1016/0378-3812(83)80141-1McKoy V., Sinanoğlu O., Theory of dissociation pressures of some gas hydrates, *J. Chem. Phys.,* 1963, 38, 12, 2946–2956, DOI: 10.1063/1.1733625

[34] Kihara T., The second virial coefficient of non-spherical molecules, *J. Phys. Soc. Jpn.,* 1951, 6, 5, 289–296, DOI: 10.1143/JPSJ.6.289

[35] Holder G.D., Hand J.H., Multiple-phase equilibria in hydrates from methane, ethane, propane and water mixtures, *AIChE J.,* 1982, 28, 3, 440–447, DOI:10.1002/aic.690280312

[36] John V.T., Holder G.D., Contribution of second and subsequent water shells to the potential energy of guest-host interactions in clathrate hydrates, *J. Phys. Chem.,* 1982, 86, 4, 455–459, DOI: 10.1021/j100393a008

[37] Byk S.Sh., Makogon Yu. F., Fomina V.I., Chapter in the book: Thermodynamics of hydrate formation, *Gas hydrates, Khimia,* 1980

[38] Nikolsky B.P., Chapter in the book: equilibrium temperatures and pressures (heterogeneous equilibria), *Chemical Handbook, Khimia,* 1966

[39] Byk S.Sh., Fomina V.I., Narozhenko A.F., Natural gas hydrates, *Gazovaya promyshlennost',* 1971, 2, 35–40

[40] Barrer R.M., Stuart W.I., Non-stoicheiometric clathrate compounds of water, *Proc. R. Soc. London,Ser. A,* 1957, 243, 1233, 172–189

[41] Carson D.B., Katz D.L., Natural gas hydrates, *Trans. Am. Inst. Min., Metall. Pet. Eng.*, 1942, 146, 1, 150–158, DOI: 10.2118/942150-G

[42] Malyshev V.V., Description of the potential of Kihara interaction of octahedral molecules. Similarity of molecular systems SF_6, MoF_6, WF_6, UF6, *Teplofizika Vysokikh Temp*., 1974, 12, 5, 1114–1118

[43] Vorotyntsev V.M., Malyshev V.M., Taraburov P.G., Calculation of the coefficient of distribution of admixtures for the process of forming gas hydrates in sulfur hexafluoride, *Russ. J. Phys. Chem. A.,* 2001, 75, 1, 121-125

[44] Vorotyntsev V.M., Malyshev V.M., Gas hydrates: nanosized phases in the separation and purification of substances by crystallization, *Russ. Chem. Rev.,* 2011, 80, 10, 971–991

[45] Istomin V.A., Yakushev V.S., Chapter in the book: Phase equilibria, composition and properties of gas hydrates, *Gas hydrates in natural conditions, Nedra,* 1992

[46] Forcrand R, Villard P., Sur la composition des hydrates d'hydrogene sulfure et du chlorure de methyle, *C. R. Acad. Sci.,* 1888, 106, 849–851

[47] Dean J.A., Chapter in the book: Physical properties, *Lange's handbook of chemistry,McGRAW-HILL,* 1999

Influence of liquid flowrate on size of nanobubbles generated by porous-membrane modules

*Karol Ulatowski, Paweł Sobieszuk
Faculty of Chemical and Process Engineering, Warsaw University of Technology, Warsaw, POLAND
e-mail: Karol.Ulatowski.dokt@pw.edu.pl

***Keywords**: nanobubbles, porous membranes, size distribution*

ABSTRACT

The aim of this work was to investigate the influence of distilled water flowrate in two different porous-membrane modules on size of generated nitrogen nanobubbles. Modules had different diameter and number of membrane tubes inside the module. As bubbles are cut off from the membrane surface by the shear stress induced by the liquid flow, the change in linear velocity of liquid should result in change of generated bubble diameter. For both modules, higher flowrate of liquid induced generation of smaller bubbles, what was consistent with expectations. This effect can help us in generation of bubbles of desired size.

INTRODUCTION

Nanotechnology began to be when scientists found means to measure objects in nanoscale. That's when the extraordinary properties of such objects started to be discovered and described. When we start to decrease the size of object, starting at macroscale, initially most of its physicochemical properties are constant. However, when the size approaches nanoscale, mentioned properties start to change linearly or even nonlinearly [1]. This change is linked to increasing fraction of atoms located on the surface of the object.

For most of the time, nanotechnological studies were focused on investigation of solid nanoparticles. However, this focus starts to shift in favour of nanoobjects which involve liquids (nanodroplets, nanoemulsions) or gas nanobubbles which are described further in this paper. Nanobubbles can be further bisected on bulk nanobubbles (which are not adhered to any solid surface and are homogenously dispersed in liquid) and surface nanobubbles (adhered to the solid surface). In this work, under the term 'nanobubbles', we assume bulk nanobubbles. In case of nanobubbles, the nanoscale starts just under the size of $1\,\mu m$, as this is the approximate boundary of rapid change in physicochemical properties of gas bubbles [2]. Nanobubbles possess extraordinary characteristics which distinguish them from their macroscale counterparts. First of all, nanobubbles have nearly non-existent rising velocity [2, 3] and their paths in liquid can be described by Brownian motion [2, 4]. Such small value of rising velocity is caused by very high density of gas inside of

bubble. High density is caused by significant pressure difference between inside and outside of bubble [2, 3].This difference is caused by surface tension and can be described using Young-Laplace equation even for such small bubbles [5]:

$$\Delta P = \frac{4\sigma}{d} \tag{1}$$

Such high pressure difference, if we apply equations relevant to bubbles in macroscale, should result in almost instantaneous dissolution of bubbles in liquid [6]. Surprisingly, nanobubbles are extremely stable and can last unchanged in liquid for days or even months[4]. Most scientists agree that the main reason of such stability is presence of electrical charge accumulated on the surface of object [7]. In case of nanobubbles, mentioned charge is the result of hydroxyl anions adhesion on bubble surface. They form a firm layer which impedes the mass transfer and coalescence with surrounding bubbles [8, 9]. To overcome this charge external energy must be delivered [8] and amount of said energy can be approximated by zeta potential measurements. The higher the absolute value of zeta potential, the more energy is needed to perform coalescence or mass transfer. The value of absolute zeta potential can be lowered by addition of alcohol or salts [9]. However, there are numerical simulations which show that addition of surfactants, which are known to lover the surface tension between gas and liquid, to liquid phase in contact with surface nanobubbles can destabilize bubbles and result in their dissolution [10]. That means that both the surface tension and high value of zeta potential are needed to ensure the stability of bubbles.

Nanobubbles display unexpected usability in various branches of science in industry. For instance, they are commonly used in wastewater treatment, both in biochemical and in mechanical parts of wastewater treatment plants. As for chemical treatment, oxygen bubbles, starting from microscale, have the ability to mass produce hydroxyl radicals. High oxidation potential of radicals is the reason of destruction of various chemical pollutants [11, 12]. When ozone micro- and nanobubbles are generated, even more hydroxyl radicals are produced [13]. Bubbles of both oxygen and ozone have the ability to reduce COD of wastewater by even 90% [14]. Because of this fact, nanobubbles of this gases were used to reduce the concentration of pesticides in both water and ground originating from heavy polluted fields [15], as well as to decolorize wastewater by decomposing dyes from textile industry [16]. In both cases the efficiency of considered processes have been vastly increased.

In case of mechanical treatment of wastewater, micro- and nanobubbles are used in flotation of solid particles and oils. Because of their extremely low rising velocity, bubbles of this scales are able to disperse in whole volume of the flotation tank and reach zones which cannot be penetrated by bubbles of bigger size [14]. The

usefulness of bubbles in flotation increases with decreasing bubble diameter. Smaller bubbles can adhere to smaller oil droplets or solid particles. Also, in case of larger droplets and particles, the smaller the bubble diameter, the higher the number of bubbles which can adhere to single droplet or particle. It is important, as the combined drag force of numerous bubbles is able to lift the contaminants to the surface with higher rising velocity than with macrobubbles [17]. When we also consider the fact, that freely dispersed nanobubbles have nearly non-existent rising velocity and fill the whole volume of flotation tank, it becomes evident that dispersed bubbles can react immediately on presence of contaminants [17].

Micro- and nanobubbles are also used in disinfection by inactivation of bacteria, viruses or yeast cells [18], even when treatment with atmosphere of the same gas proves to be inefficient [19]. Also, bubbles of this scales can promote growth of plants, fish and animals [20, 21]. In every case, treatment with bubble saturated water resulted in higher food intake and bigger size (higher body mass, longer leaves, etc.) [20, 21].

There are methods which allow generation of bulk micro- and nanobubbles, but they are not studied as thoroughly as their applications. In general, generation methods can be divided into three groups, based on main phenomenon that leads to generation: electrolysis of salts [22], gas-liquid circulation and compression-decompression methods [23]. During electrolysis of salts gas products are released on the electrodes in form of bubbles in solution. This methods leads to producing multimodal distribution of bubble sizes ranging from nanometers to millimeters [22]. Compression-decompression methods are based upon compressing the two-phase system, what leads to increasing the solubility of gas in liquid, and rapid reduction of pressure causing micro- and nanobubble generation [23]. The most common methods are part of gas-liquid circulation group. Using this methods, one pressurizes the gas into pre-generated liquid flow or vortex. The bubbles are formed by cutting them of the surface by shear stress caused by the liquid flow or centrifugal force [23]. One of this methods is generation using porous membrane modules, which will be described further below.

Using porous membranes for nanobubble generation is possible, but requires the knowledge and understanding of phenomena that accompany transfer of gas through pores of micrometric size. Immersing the membrane in liquid and pressurizing gas through pores is not sufficient for generating bubbles in micro- and nanoscale [24]. During the formation of bubbles on the membrane surface, the surface tension and adhesion forces prevent bubbles from breaking off the membrane surface, what leads to them growing in size by filling with more and more gas. If this adhesion is not impeded by any means, the growing will continue until the buoyancy overcomes the forces of adhesion. That leads to generation of bubbles which sizes are even two magnitudes larger than the diameter of membrane pores [24]. Because of this fact, it

is essential to generate the turbulence or shear stress which will help overcoming the adhesion and allow cutting the bubbles off the membrane surface (see Fig. 1.). The easiest way to generate higher shear stress is to increase the flowrate of liquid.

Other fact, which is important when one consider overcoming the adhesion of bubbles, is wettability of surface and in consequence the contact angles of bubble on the surface. Hydrophobic membranes (characterized by low wettability) advantage the adhesion of gas to membrane when used with polar liquids, such as water. It is caused because the adhesion forces between membrane surface and liquid are much lower than cohesion forces of liquid, what allows the bubble to cover large area of membrane and be resistant to shear stress [24]. So it is necessary to use membranes of wettability adequate to polarity of liquid.

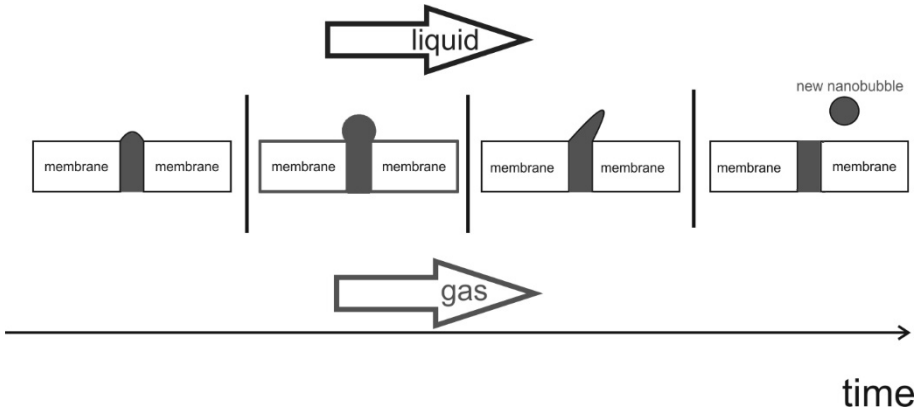

Fig. 1. Scheme of nanobubble generation mechanism by porous membranes

MATERIALS AND METHODS

Porous-membrane modules

During the experiments, two different porous membrane modules were used (denoted Module 1 and Module 2, respectively). Module 1was made from 98% porous silicon carbide with 31 round channels (φ3mm). Module 2 contained single porous-membrane tube (internal/external diameter of 6 mm/16 mm) inside stainless steel external tube. Silicon carbide is characterized by high wettability (contact angles ~45-50º [25]).

Experimental set-up

Fig.2. shows the scheme of experimental setup. Deionized water stored in tank is pumped by centrifugal pump and flows to inner tube/channels of porous-membrane module. Pressurized nitrogenfrom the cylinder flows through pores of the membrane to the liquid flow, which cuts off bubbles that are forming onto the membrane surface. Water containing nanobubbles is returned to storage tank.

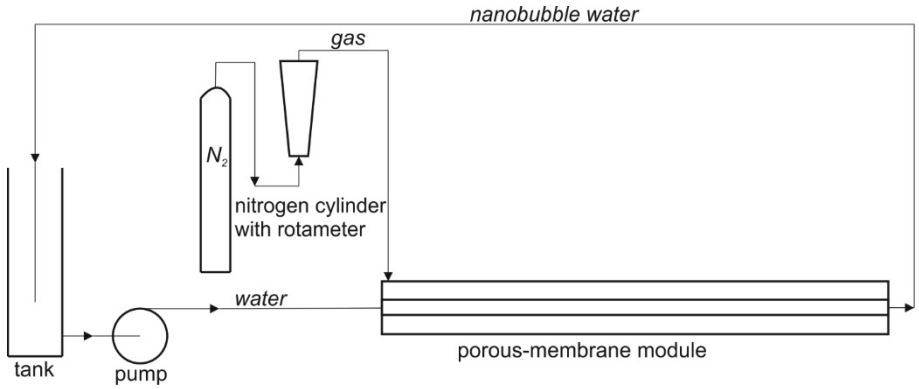

Fig. 2. Scheme of experimental setup

For each module, two distinct liquid flowrates were chosen and each experiment was labeled with consequent numbers, as shown in Table 1. Each generation charge last 2 hours after which two samples were collected. Three charges were performed for each Experiment.

Tab. 1. Flowrates of media for performed experiments

Module	Experiment	Liquid flowrate [dm^3h^{-1}]	Gas flowrate [dm^3h^{-1}]
Module 1	Experiment 1	1900	850
Module 1	Experiment 2	950	850
Module 2	Experiment 3	900	200
Module 2	Experiment 4	600	200

Size distribution measurement

Size distribution of bubbles in samples was measured using Malvern Zetasizer Nano using Dynamic Light Scattering (DLS) technique. This technique is correlating the rate of change of scattered light spectrum with diffusion rate of dispersed objects. Next, to obtain the size of mentioned objects in liquid, the Stokes-Einstein equation is used:

$$D = \frac{k_B \cdot T}{3\pi \cdot \mu \cdot d} \tag{2}$$

For each sample, three measurements were performed. For each measurement Sauter mean diameter (d_{32}) were calculated according to Eq. (3).

$$d_{32} = \frac{\sum n_i d_i^3}{\sum n_i d_i^2} \tag{3}$$

n_i is the number fraction of bubbles of diameter d_i. Three obtained Sauter diameter values were averaged to acquire the value of mean diameter in given sample.

RESULTS AND DISCUSSION

Size distributionsof nanobubbles for each of all four Experiments were obtained and illustrated in Fig. 3-6. As one can see, nanobubbles are polydispersed. For System 1 (Fig. 3 and 4) there is no definite single dominant fraction, the distribution is very wide and has numerous maxima. For System 2 (Fig. 5 and 6.) one can observe dominant fraction of diameter in range 400-600 nm. That may show that higher roughness of the membrane surface favours generation of bubbles of single diameter. It is also important to note, that for Experiment 2 and 4 (Fig. 4 and 6), which were performed using lower water flowrate, we observe bubbles of larger diameter than for Experiments 1 and 3, where water flowrate was higher.

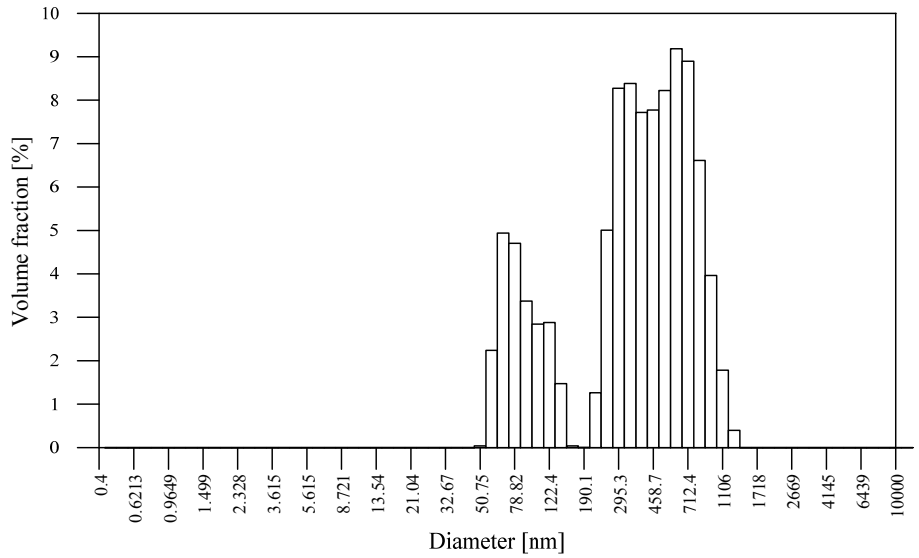

Fig. 3. Size distribution of bubbles obtained in Experiment 1 System 1 (water flowrate 32 L/min).

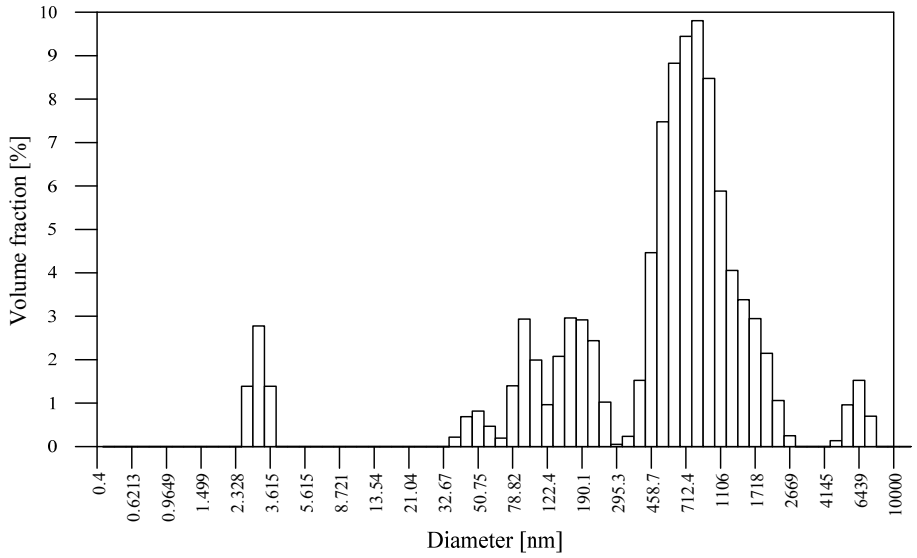

Fig. 4. Size distribution of bubbles obtained in Experiment 2 System 1 (water flowrate 16 L/min).

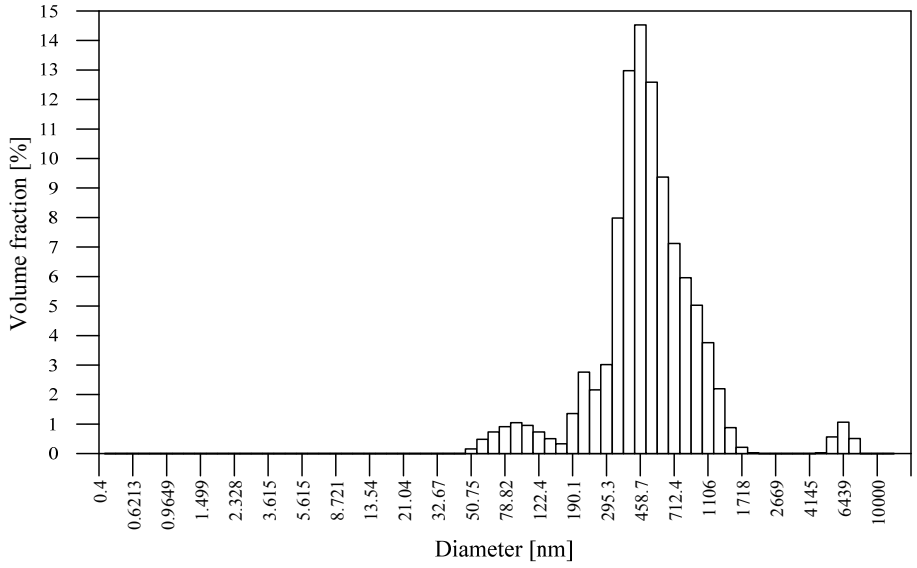

Fig. 5. Size distribution of bubbles obtained in Experiment 3 System 2 (water flowrate 15 L/min).

In Fig. 7-9., the Sauter mean diameter values were presented. Fig. 7. shows results obtained for Experiment 1 (water flow rate of 32 dm^3/min) and Experiment 2 (water flow rate of 16 dm^3/min). In Fig. 8., one can see the results for Experiment 3 (water flow rate of 15 dm^3/min) and Experiment 4 (water flow rate of 10 dm^3/min). Each bar represents results acquired for one generation charge for every experiment. Fig. 9. shows averaged results for each experiment.

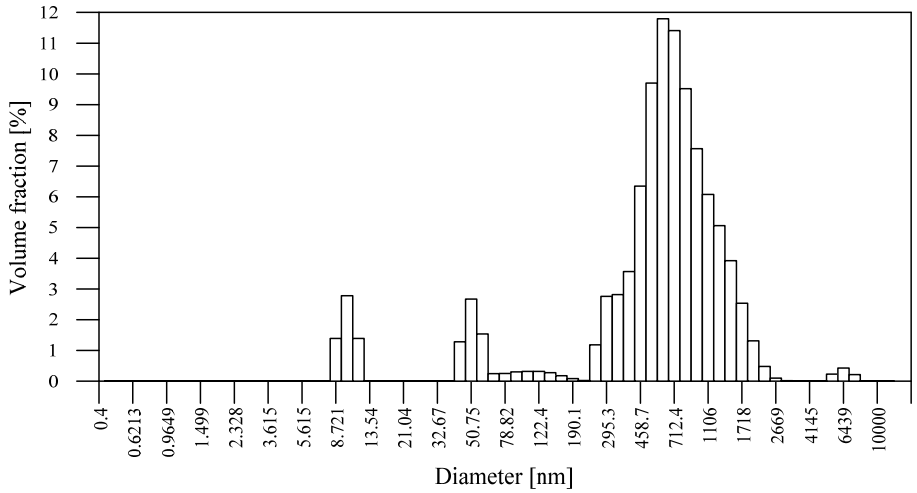

Fig. 6. Size distribution of bubbles obtained in Experiment 4 System 2 (water flowrate 10 L/min).

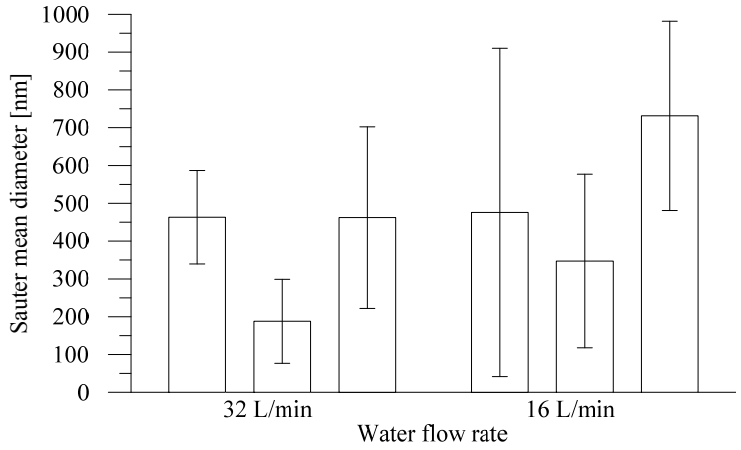

Fig. 7. Sauter mean diameter of bubbles for Experiment 1 (left, 32 L/min) and Experiment 2 (right, 16 L/min). Each bar represents distinct generation charge.

As one can see in both Fig.7. and Fig.8., for higher value of liquid flowrate, the mean diameter of bubbles and the value of standard deviation are lower. That fact is even more visible in Fig. 9. It should be noted, that despite being placed in the same Figure, two leftmost bars represent experiments performed in System 1, and two rightmost ones represent experiments performed in System 2.

We can assume that, as expected, the higher values of liquid flowrate allow generation of smaller bubbles because they generate higher shear stress. For that reason, bubbles can be cut off from the membrane surface earlier, i.e. before they are able to grow. What's interesting, one can see in Fig. 9, that for System 2 (Experiments 3 and 4), despite lower liquid flow rate, bubbles of approximately similar size were obtained. It may be linked to higher roughness of membrane in System 2.

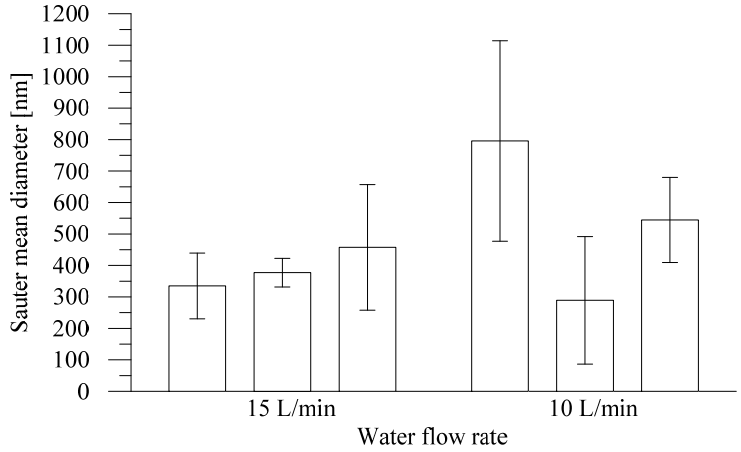

Fig. 8. Sauter mean diameter of bubbles for Experiment 3 (left, 15 L/min) and Experiment 2 (right, 10 L/min). Each bar represents distinct generation charge.

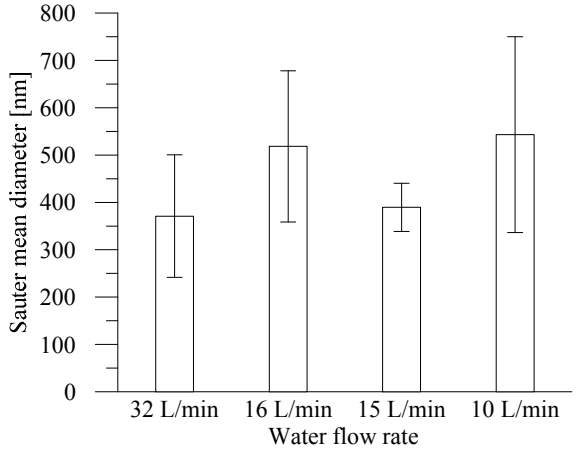

Fig. 9. Averaged results of Sauter mean diameter of bubbles for each experiment. From left to right: Experiment 1, Experiment 2, Experiment 3, Experiment 4.

CONCLUSIONS

Experiments were performed in two porous-membrane systems for different water flow rates to check whether higher liquid flow rates bubbles of smaller diameter would be generated. Size distributions and Sauter mean diameters were obtained. For both experimental systems smaller bubbles were generated for higher value of water flow rate. Additionally we concluded that higher surface roughness favours generation of smaller bubbles even for lower flow rates.

NOTATION

D - diffusion coefficient, m^2s^{-1}

d - bubble diameter, m

d_{32}- Sauter mean diameter, m

d_i - diameter of bubbles in fraction *i*, m

k_B - Boltzmann constant, J K^{-1}

n_i - number of bubbles in fraction *i*, -

T - temperature, K

ΔP - pressure difference, Pa

μ - dynamic viscosity, Pa s

REFERENCES

[1] Cademartiri L., Ozin G.A., Lehn J.-M., *Concepts of Nanochemistry*, *Weinheim: Wiley-VCH,* 2009

[2] Tsuge H., *Micro- and Nanobubbles. Fundamentals and applications, Pan Stanford Publishing,* 2015

[3] Li H., Hu L., Song D., Lin F., Characteristics of Micro-Nano Bubbles and Potential Application in Groundwater Bioremediation, *Water Environmental Research,* 2014, 86, 9, 844-851, DOI: 10.2175/106143014X14062131177953

[4] Takahashi M., Base and technological application of micro-bubble and nanobubble, *Materials Integration*, 2009,22, 2–19

[5] Matsumoto M., Tanaka K., Nano bubble-Size dependence of surface tension and inside pressure, *Fluid Dynamics Research*, 2008, 40, 7–8, 546–553, DOI: 10.1016/j.fluiddyn.2007.12.006

[6] Zhang L. J., Chen H., Li Z. X., Fang H. P., Hu J., Long lifetime of nanobubbles due to high inner density, *Sciencein China Series G-Physics, Mechanics and Astronomy*, 2008, 51, 2, 219–224, DOI: 10.1007/s11433-008-0026-5

[7] Bunkin N. F., Kochergin A. V., Lobeyev A. V.,Ninham B. W., Vinogradova O. I., Existence of charged submicrobubble clusters in polar liquids as revealed by correlation between optical cavitation and electrical conductivity, *Colloids and Surfaces A: Physicochemical and Engineering Aspects*, 1996, 110, 2, 207–212, DOI: 10.1016/0927-7757(95)03422-6

[8] Ghosh P., Coalescence of bubbles in liquid, *Bubble Science, Engineering & Technology*, 2009, 1, 1–2, 75–87.

[9] Srinivas A., Ghosh P., Coalescence of bubbles in aqueous alcohol solutions, *Industrial and Engineering Chemistry Research*, 2012, 51, 2, 795–806, DOI: 10.1021/ie202148e

[10] Xiao Q., Liu Y., Guo Z., Liu Z., Zhang X., How nanobubbles lose stability: Effects of surfactants, *Applied Physics Letters*, 2017, 111,13, 131601, DOI: 10.1063/1.5000831

[11] Sreekanth R., Prasanthkumar K. P., Sunil Paul M. M.,Aravind U. K.,Aravindakumar C. T., Oxidation Reactions of 1- and 2-Naphthols: An Experimental and Theoretical Study, *The Journal of Physical Chemistry A*, 2013, 117, 44, 11261–11270, DOI: 10.1021/jp4081355
[12] Sunil Paul M. M., Aravind U. K., Pramod G., Aravindakumar C. T., Oxidative degradation of fensulfothion by hydroxyl radical in aqueous medium, *Chemosphere*, 2013, 91, 3, 295–301, DOI: 10.1016/j.chemosphere.2012.11.033
[13] Von Gunten U., Ozonation of drinking water: Part I. Oxidation kinetics and product formation, *Water Research*, 2003,37, 7, 1443–1467, DOI: 10.1016/S0043-1354(02)00457-8
[14] Kutty S. R. M., Winarto F. E. W., Gilani S. I. U., Anizam A. A., Karimah W. W. Z., Isa M. H., Chapter in the book: Degradation of organic matter using a submerged microbubble diffuser in a biological wastewater treatment system, *Waste Management and the Environment V, WIT Press*, 2010
[15] Ikeura H., Kobayashi F., Tamaki M., Removal of residual pesticide, fenitrothion, in vegetables by using ozone microbubbles generated by different methods, *Journal of Food Engineering*, 2011, 103, 3, 345–349, DOI: 10.1016/j.jfoodeng.2010.11.002
[16] Chu L. B., Xing X. H., Yu A. F., Zhou Y. N., Sun X. L., Jurcik B., Enhanced ozonation of simulated dyestuff wastewater by microbubbles, *Chemosphere*, 2007, 68, 10, 1854–1860, DOI: 10.1016/j.chemosphere.2007.03.014
[17] Etchepare R., Azevedo A., Calgaroto S., and Rubio J., Removal of ferric hydroxide by flotation with micro and nanobubbles, *Separation and Purification Technology*, 2017, 184, 347–353, DOI: 10.1016/j.seppur.2017.05.014
[18] Khadre M. A., Yousef A. E., Kim J.-G., Microbiological Aspects of Ozone Applications in Food: A Review, *Journal of Food Science*, 2001, 66, 9, 1242–1252. DOI: 10.1111/j.1365-2621.2001.tb15196.x
[19] Kobayashi F., Ikeura H., Ohsato S., Goto T., Tamaki M., Disinfection using ozone microbubbles to inactivate Fusarium oxysporum f. sp. melonis and Pectobacterium carotovorum subsp. carotovorum, *Crop Protection*, 2011, 30,11, 1514–1518, DOI: 10.1016/j.cropro.2011.07.018
[20] Ebina K., Shi. K., Hirao, M., Hashimoto, J. Kawato, Y., Kaneshiro, S., Morimoto, T., Koizumi K., Yoshikawa, H., Oxygen and Air Nanobubble Water Solution Promote the Growth of Plants, Fishes, and Mice, *PLoS One*, 2013, 8, 6, 2–8, DOI: 10.1371/journal.pone.0065339
[21] Park J. S., Kurata K., Application of microbubbles to hydroponics solution promotes lettuce growth, *HortTechnology*, 2009, 19, 1, 212–215
[22] Kikuchi K., Tanaka Y., Saihara Y., Maeda M., Kawamura M., Ogumi Z., Concentration of hydrogen nanobubbles in electrolyzed water, *Journal of Colloid and Interface Science*, 2006, 298, 2, 914–919, DOI: 10.1016/j.jcis.2006.01.010

[23] Terasaka K., Hirabayashi A., Nishino T., Fujioka S., Kobayashi D., Development of microbubble aerator for waste water treatment using aerobic activated sludge, *Chemical Engineering Science*, 2011, 66, 14, 3172–3179, DOI: 10.1016/j.ces.2011.02.043
[24] Zimmerman W. B., Tesa V., Butler S., Bandulasena H. C. H., Microbubble Generation, *Recent Patents on Engineering,* 2008, 2, 1–8, DOI: 10.2174/187221208783478598
[25] Zhong W. W., Huang Y.F., Gan D., Xu, J.Y., Li H., Wang G., Meng S., Chen X. L., Wetting behavior of water on silicon carbide polar surfaces, *Physical Chemistry Chemical Physics*, 2016, 18, 40, 28033–28039, DOI: 10.1039/C6CP04686J

Cultures of non-adherent HL-60 cells in a wave-type agitated single-use bioreactor

*Kamil Wierzchowski[1], Maciej Pilarek[1], Iwona Grabowska[2]
[1] Faculty of Chemical and Process Engineering, Warsaw University of Technology, Warsaw, POLAND
[2] Faculty of Biology, University of Warsaw, Warsaw, POLAND
e-mail: kamil.wierzchowski.dokt@pw.edu.pl

Keywords*: wave-type agitation, single-use bioreactor, non-adherent cell culture, HL-60 human cell line*

ABSTRACT

Wave-type agitated single-use bioreactors are commonly applied for scaling-up of *in vitro* cultures of animal cells. The oscillating movement of the bioreactor's tray induces waves in the two-phase culture system, and thus enhancing the mass transfer between liquid and gas phases inside the disposable culture bag. The *ReadyToProcess* WAVE^{TM}25 bioreactor system equipped with 2 dm^3 polymer-based culture bag, has been applied for studying batch culture of non-adherent HL-60 animal cells. The results of the studies undoubtedly confirmed the applicability of the single-use bioreactor system with wave-induced agitation as the right platform for proceeding the submerged culture of non-adherent animal cells.

INTRODUCTION

Nowadays, the biopharmaceutical industry is searching for the technologies, which could reduce time and costs of bioprocesses performed on large scale. The single-use technology is commonly recognized as the solution which eliminates troublesome and time-consuming steps of bioprocessing, such as cleaning-in-process and cleaning validation as well. Another advantage of the application of disposable culture bag for every new culture charge is elimination of the risk of microbial or cross contamination of culture vessel. Such great merit is really benefitting for modern bioprocess industry, due to possibility of transforming a single-product profile of production into multiproduct facilities. It should also be noted that the single-use technology is reducing a capital cost of the plant constructions in opposite to typical constructions made of glass or stainless steel[1-3]. Currently, single-use culture bags are multilayered films composed of: (i) polyethylene-based outer layer, which determines mechanical properties of whole vessel; (ii) ethylene-vinyl-alcohol-based barrier layer, which prevents permeability of gases and liquids; (iii) ultra-low-density-polyethylene-based biocompatible contact layer, which determines applicability of the bag for bioprocesses[4].

In the wave-agitated bioreactors the oscillating movement of the apparatus's tray induces waves in the two-phase (i.e. gas phase and liquid broth) culture system filling the polymer-based disposable culture bag [5]. During the wave-induced agitation, the interfacial area formed between gas phase and culture medium is continuously renewed, and therefore the bubble-free surface aeration of the culture broth is accomplished (Fig.1)[6]. Simultaneously, such gentle wave-type agitation significantly limits the level of shear forces, as well as inhibit the shear stress effects, which negatively influence the fragile biomass in submerged *in vitro* culture system [7].

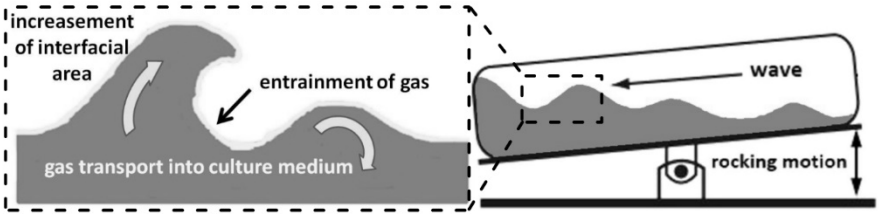

Fig. 1. Scheme of the idea of a wave-type agitation by continuous rocking motion (based on [8]).

Up to date, wave-type agitated single-use bioreactor systems, which utilize effectiveness of waves for continuous aeration and mixing of culture medium, have been readily and successfully applied in the wide range of bioprocesses focused mainly on cultures of isolated animal (A) and insect (I) cells/tissues, or plant (P)cells/organs [9-14], what is briefly shown in Tab. 1:

Tab. 1. Applications of wave-type agitated single-use bioreactor for bioproducts production.

bioreactor	biomass (cell line)	bioproduct	working conditions	reference
WAVE (GE Healthcare; US)	293 EBNA (A)	glycoprotein gp120	α =7 [°] ω =18 [min^{-1}]	[9]
	Drosophila Schenider S2 (I)	monoclonal antibody	α =8 [°] ω=22 [min^{-1}]	[10]
	DHFR- CHO (A)	monoclonal antibody	α=6÷8 [°] ω=20÷27 [min^{-1}]	[11]
Cultibag RM, (Sartorius; DE)	Sf-9(I)	recombined proteins	α=6 [°] ω=18÷32 [min^{-1}]	[12]
Biowave (Sartorius; DE)	HEK-293 EBNA (A)	resistin	α = 6 [°] ω = 30 [min^{-1}]	[13]
AppliFlex (Applikon; US)	*Nicotiana tabacum* BY-2 (P)	M12 antibody	α=8÷10 [°] ω=30÷42 [min^{-1}]	[14]

The aim of the study was to compare the effectiveness of submerged batch culture of suspended non-adherent HL-60 cells performed in the disposable culture bag under defined conditions of wave-type agitation provided by WAVE 25 bioreactor system, with the results of the cells growth noted for static (i.e. non-mixed) culture flask.

MATERIALS AND METHODS

Single-use bioreactor system

Bioreactor *ReadyToProcess* WAVE^{TM}25 (WAVE 25, supplied by GE Healthcare Bio-Sciences AB,US), has been applied to perform *in vitro* culture of non-adherent HL-60 cell line (Fig. 2).

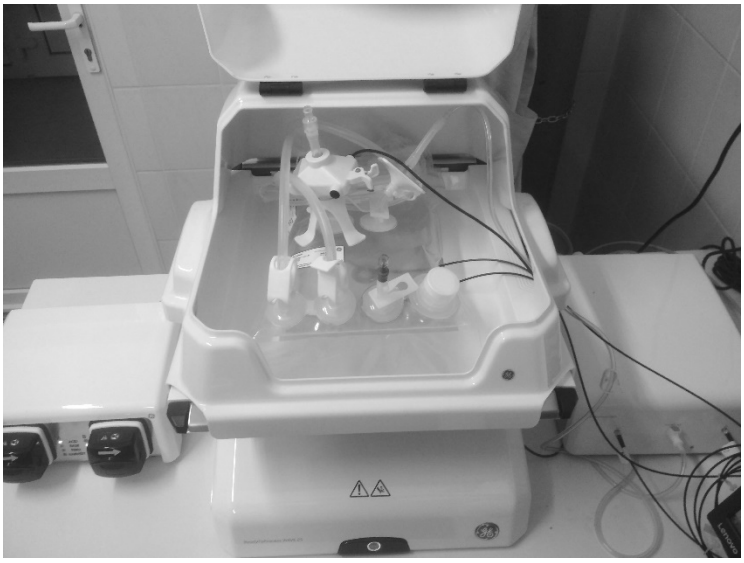

Fig. 2. Bioreactor *ReadyToProcess* WAVE^{TM}25.

The system of WAVE 25contains of:

(i) the rocking tray with parameters of oscillating movement ranged from 2º to 12º in the case of oscillations angle (α) and from 2 min^{-1} to 40 min^{-1} in the case of oscillations frequency (ω), and equipped with built-in thermoelectric heater, as well as weighing scale;

(ii) the 2-litre pre-sterilized polymer-based disposable CELLBAG^{TM} (GE Healthcare, US) as the flexible culture vessel with the working volume ranged from 0.1 dm^3 to 1 dm^3 of culture medium possible to dose inside the culture bag;

(iii) the bioreactor control unit (CBCU),which allows to control parameters of an *in vitro* environment, such as: pH and dissolved oxygen (DO) concentration (*via* miniaturized optical (i.e. spectrophotometric) sensors built-in inside the bottom of culture bag connected with optical fibers), concentration
of oxygen in inlet gas mixture (*via* built-in gas mixer specifically dosing gases
to the culture vessel in following range of concentrations: from 0% to 50%

in the case of O_2, from 0% to 15% in the case of CO_2, as well as from 0.1 $dm^3 \cdot min^{-1}$ to 1.0 $dm^3 \cdot min^{-1}$ in the case of the total gas flow rate);

(iv) the double-set of peristaltic pumps, which allows dosing medium into, or harvesting sample from the culture bag, with the working parameters of every single peristaltic pump ranged from 0.25 $cm^3 \cdot min^{-1}$ to 95.0 $cm^3 \cdot min^{-1}$;

(v) the thermostatic chamber which allows maintaining a steady temperature in culture vessel.

Culture medium

HL-60 cell line was maintained in the culture medium composed of: 89%of Roswell Park Memorial Institute 1640 medium (RPMI)with 2 $g \cdot dm^{-3}$ of glucose, 10% supplementation with Fetal Bovine Serum (FBS) and 1% of antibiotics mixture (PenStrep). All liquid media applied in cell cultures have been supplied by Gibco (US) and they were certified and approved for animal cell cultures.

HL-60 cells

HL-60 is a continuous line of non-adherent human promyelocytic leukemia white blood cells isolated from blood of a 36-year-old woman. HL-60 cells have been supplied by ATCC (US).

Culture of HL-60 cells in WAVE 25

Initially, the culture bag was filled with 0.3 $dm^3$of culture medium. Next the system was stabilized to obtain 37°C, as well as 100% saturation of culture medium with O_2 from sterile dosed CO_2-enriched (5%) atmospheric air (0.5$dm^3 \cdot min^{-1}$). The working parameters of cultures performed in WAVE 25 has been shown in Tab. 2.The initial concentration of HL-60 cells in the culture medium equaled to10^5 $cell \cdot cm^{-3}$. The culture was conducted for6 days, and the samples were harvested daily. In order to compare the results of bioreactor cultures, a typical non-mixed (i.e. static) cultures of HL-60 in 75 cm^2 culture flasks (NEST Biotechnology, US) were performed referentially for 6 days. All samples harvested from both compared culture systems, were subjected to the following tests:

(i) manually counting HL-60 cells pre-stained by 0.4% trypan blue solution in the hemocytometer to determine concentration, as well as viability of the cells in culture medium;

(ii) BioMaxima-LDH test to determine the activity of extracellularly secreted lactate dehydrogenase (LDH),as the quantitative parameter correlated with negative influence of hydrodynamic conditions of the culture process caused on the suspended cells;

(iii) PrestoBlue test determining the metabolic activity of the cells;

(iv) BioMaxima-glucose test to quantitatively determine glucose concentration in sample of culture medium and specific glucose consumption rate.

Tab. 2. Workingparametersof WAVE 25 established for wave-type agitated cultures of HL-60 cells.

parameter	value	unit
angle of oscillations (α)	6	[º]
frequency of oscillations (ω)	20	[min^{-1}]
gas flow rate (Q_G)	0.5	[$dm^3 \cdot min^{-1}$]
volume of culture medium (V_L)	0.3	[dm^3]
concentration of O_2in inlet gas phase (C_{O2})	21	[%]
concentration of CO_2in inlet gas phase (C_{CO2})	5	[%]
temperature (T)	37	[ºC]

Analytical methods

To determine the viability of cells, the sample of suspension of the cells harvested from culture vessel has been equimolarly mixed with 0.4% trypan blue aqueous solution (ThermoFischerScientific, US), incubated at room temperature for 3 minutes to distinguish living cells from dead ones. Then the stained cells were counted with Eclipse TS100 microscope (Nikon, JP).The density (X) and the viability (Z) of HL-60 cells were finally calculated using following equations:

$$X = \frac{x}{k} \cdot d \cdot 5 \cdot 10^5 \quad \left[cell \cdot cm^{-3}\right] \tag{1}$$

$$Z = \frac{z}{x} \cdot 100\% \tag{2}$$

$$x = z + m \tag{3}$$

where x is the total number of cells counted in hemocytometer, k is the number of squares occupied by cells, d is the dilution of the sample, z is the number of alive (unstained) cells and m is the number of dead (stained) cells.

The activity of LDH in the culture medium has been determined according to manufacturer procedure of the BioMaxima-LDH test (BioMaxima, PL). 10 µl of filtered (φ = 0.2 µm) culture medium was added to 1 cm^3 of Biomaxima-LDH reagents, and the absorbency of the reaction mixture were spectrophotometrically (GENESYS 20; ThermoFisherScientific, US) determined and noted in 1-minute intervals. The mixture of1 cm^3 of LDH reagents and 10 µl of double-distilled water has been used as the reference blank sample. The measurements were carried out at analytical wavelength λ=340 nm. The LDH activity (a_{LDH})has been finally calculated using the following equations:

$$a_{LDH} = \frac{V_t \cdot 10^5}{\varepsilon \cdot l \cdot V_s} \cdot \Delta A \quad [U \cdot dm^{-3}] \tag{4}$$

$$a_{LDH} = 2672 \cdot \Delta A \quad [\mu kat \cdot dm^{-3}] \tag{5}$$

where ΔA is the absorbency change per minute, V_t is the total volume of reaction mixture (i.e. 1.01 cm^3), ε is the molar coefficient of NADH absorbency at λ=340 nm (i.e. $6.3 \cdot 10^2$ $m^2 \cdot mol^{-1}$), l is the optical path length (i.e. 1.0 cm^3), V_s is the volume of the sample (i.e. 0.01 cm^3).

To monitor the metabolic activity of the cells suspended in culture medium, the PrestoBlue test (ThermoFischerScientific, USA) has been used. 0.1 cm^3. PrestoBlue reagents were added to 0.9 cm^3 suspension of the cells. Referentially,0.9 cm^3 of culture medium (i.e. without the cells)and 0.1 cm^3PrestoBlue reagents was applied. All samples were incubated at room temperature for 10 minutes. The measurements were carried out at analytical wavelength λ=570 nm (with λ=600 nm as reference). The metabolic activity of the cells (a_M)has been finally calculated using the following equation:

$$a_M = 37.04 \cdot A_W \quad [\mu kat \cdot dm^{-3}] \tag{6}$$

where A_W is the specific absorbency of the sample.

To monitor the daily changes of glucose concentration in the culture medium, the BioMaxima-glucose test (BioMaxima, PL) has been used. 20 µl of the filtered culture medium was mixed with 1 cm^3BioMaxima-glucose reagents. Referentially, 1 cm^3 of BioMaxima-glucose reagents has been mixed with 20 µl of distilled water and then used as the blank sample. All samples were incubated at room temperature for 20 minutes. The measurements on spectrophotometer were carried out at analytical wavelength λ=550 nm. Values of the density of HL-60 cells (X) in culture medium, as well as the daily changes of glucose concentration in the culture medium (ΔC_{glc}) was used to finally calculate the specific glucose consumption rate ($r_{glc/cell}$) using the following equation [15]:

$$r_{glc/cell} = -\frac{\Delta C_{glc}}{\Delta t \cdot X} \quad \left[g \cdot dm^{-3} \cdot h^{-1} \cdot cell^{-1}\right] \tag{7}$$

where Δt is the time interval between two measurements.

RESULTS AND DISCUSSION

The level of DO concentration as a function of time of HL-60 cells culture performed in disposable culture bag fixed to WAVE 25 bioreactor has been presented in Fig. 3A. The level of pH of culture medium noted for subsequent days of culture performed under conditions of wave-induced mixing has been introduced in Fig. 3B. In the case of DO characteristic, it can be clearly seen that only at the 6th day of the culture process the DO concentration noticeably decreased below the almost constant value of DO concentration noted for previous days. However the aerobic conditions

of cell culture have been undeniably provided by WAVE 25 system for whole studied period of the process, i.e. from inoculation of the culture medium up to the 6th day of culture. In the case of the pH level, it decreased monotonically from the 2nd day of the culture, but it was still in the range of optimal values of pH level preferred by HL-60 cells.

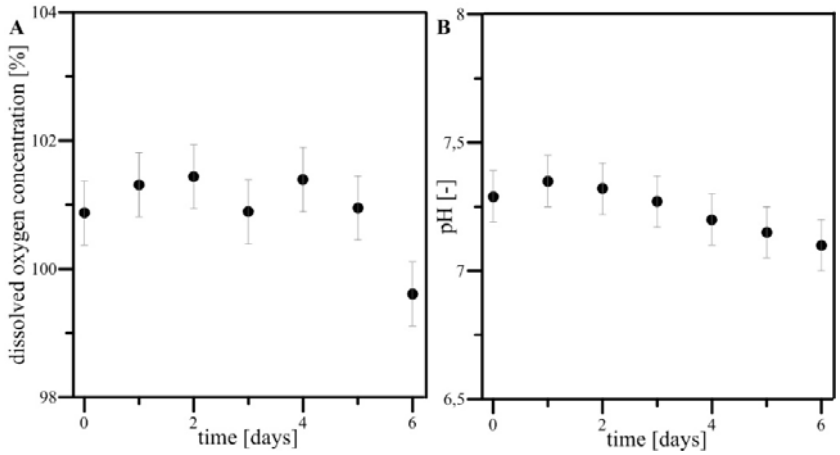

Fig. 3. The time-course of DO (A) and pH levels (B)measured for wave-type agitated culture of HL-60 cells in WAVE 25.

The comparison of HL-60 cells density in the culture medium harvested from the reference (i.e. static) and WAVE 25 systems has been presented in Fig. 4A, and the viability of HL-60 cells in both compared culture systems has been showed in Fig. 4B.It turned out, that from the 3rd day of cultures the density of non-adherent cells was significantly higher for the culture subjected to wave-type agitation, than in the reference static culture. Values of the viability of HL-60 cells determined for the WAVE 25 system were always higher than for the biomass cultured without mixing.

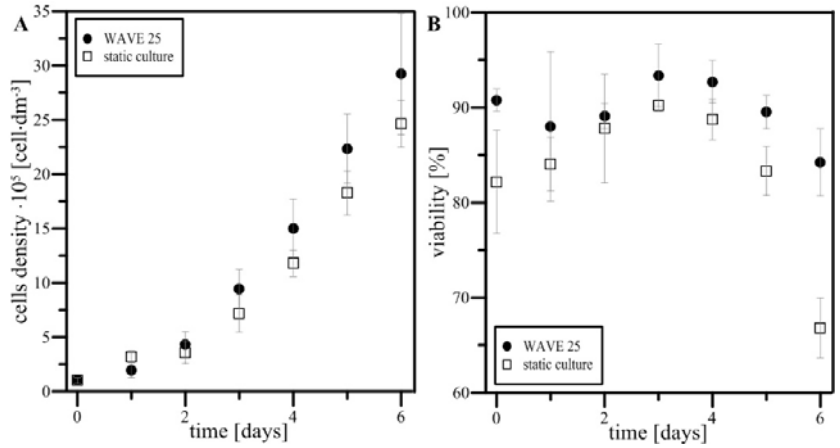

Fig. 4. The comparison of values of the cell density (A) and the viability (B) of HL-60 cells cultured in wave-type agitated WAVE 25 system and in the reference system without mixing.

The values of LDH activity in culture medium and PrestoBlue assay, which both may be interpreted as the quantitative parameters characterizing metabolic condition of HL-60 cells, have been presented in Fig. 5A and Fig 5B, respectively. Much higher values of LDH activity observed in samples of culture medium harvested daily from the static system (Fig. 5A), if compared to rather low values noted for culture performed in WAVE 25, indicated on the negative influence of the static system, what has been proved by leaking of LDH from cytosol through the cell membrane of HL-60 cells into culture medium in such system. This is in line with the results of PrestoBlue assay performed for both compared culture system, because the metabolic activity determined for HL-60 cells cultured in WAVE 25 system was higher than for cells maintained referentially in the static system (see Fig. 5B).

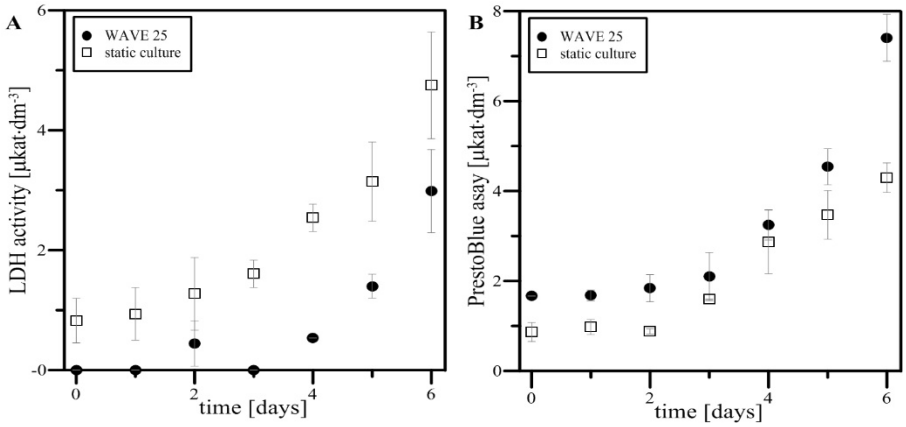

Fig. 5. Comparison of values of LDH activity determined in culture medium (A) and results of PrestoBlue assay (B) noted for the samples harvested from cultures of HL-60 cells performed in WAVE 25, as well as in the reference system.

Values of $r_{glc/cell}$, as the parameter calculated *per* single cell, have been showed in Fig. 6. The higher values of HL-60 cells density, which have been noted in the culture performed in WAVE 25 system, resulted in smaller values of $r_{glc/cell}$ if compared to values of analogue parameter determined in less concentrated cell suspension maintained in the static culture system. The highest values of $r_{glc/cell}$ (i.e. $1.83 \cdot 10^{-8}$g·dm^{-3}·h^{-1}·cell^{-1} for WAVE 25 system and $2.60 \cdot 10^{-8}$ g·dm^{-3}·h^{-1}·cell^{-1} for the reference culture)have been observed at the 2nd day of cultures performed in both compared systems.

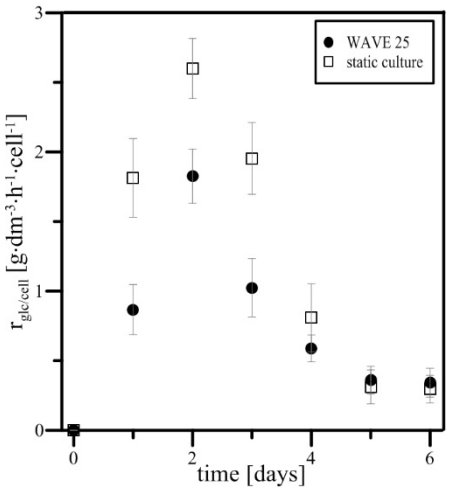

Fig. 6. Values of $r_{glc/cell}$ calculated individually for subsequent days of cultures of HL-60 cells performed in WAVE 25 and the reference system.

CONCLUSION

Based on the results of experiments it can be clearly concluded that the cultures of HL-60 cells performed in WAVE 25 bioreactor system were characterized by higher yields of biomass, in relationship to the results of cell densities noted for typically applied static culture system. Furthermore, the viability of cells maintained in WAVE 25 was significantly higher than in the reference non-agitated cultures. In the case of metabolic activity of HL-60 cells, higher values of Presto-Blue assay, as well as much lower activity of extracellularly secreted LDH, which have been detected in samples of culture medium harvested from culture performed in WAVE 25, in relation to results of the same enzymatic-based tests done for the reference cultures. Summarizing, the advantages of the wave-type agitated culture system have been unequivocally indicated, and WAVE 25 can be recognized as the right platform to performing batch cultures of non-adherent cells.

ACKNOWLEDGEMENTS

This work has been supported by the budget sources for The National Centre for Science, Poland, Grant no. DEC-2015/17/B/ST8/00631.

SYMBOLS

A_W	[-]	specific absorbency of the sample
a_{LDH}	[µkat·dm^{-3}]	activity of lactate dehydrogenase
a_M	[µkat·dm^{-3}]	metabolic activity of the cells
α	[º]	angle of oscillations
C_{CO2}	[%]	CO_2 concentration in the gas phase
C_{O2}	[%]	O_2 concentration in the gas phase

d	[-]	dilution of the sample
ΔA	[-]	absorbency change per minute
ΔC_{glc}	[g·dm^{-3}]	glucose concentration change
Δt	[h]	time interval between two measurements
k	[-]	number of square occupied bycells
l	[cm]	optical path length
m	[cells]	number of dead cells
$r_{glc/cell}$	[g·dm^{-3}·h^{-1}·cell^{-1}]	specific glucose consumption rate
T	[ºC]	temperature
Q_G	[dm^3·min^{-1}]	gas flow rate
V_L	[dm^3]	volume of the culture medium
V_s	[cm^3]	volume of the sample
V_t	[cm^3]	the volume of the reaction mixture
ω	[min^{-1}]	frequency of oscillations
X	[cell·dm^{-3}]	density of HL-60 cells in the culture medium
x	[cells]	number of the cells counted in hemocytometer
Z	[%]	viability of the cells
z	[cells]	number of alive cells
ε	[m^2·mol^{-1}]	molar coefficient of NADH absorbency at λ=340nm
λ	[nm]	wavelength

REFERENCES

[1] Sette A., Barbaroux M., Properties of materials used in single-use flexible containers: requirements and analysis, *BioPharm International*, 2006, 6, 1-8.

[2] Shukla A. A., Gottschalk U., Single-use disposable technologies for biopharmaceutical manufacturing, *Trends in Biotechnology*, 2012, 31, 147-154, DOI:http://dx.doi.org/10.1016/j.tibtech.2012.10.004.

[3] Gottschalk U., Brorson K., Shukla A. A., The need for innovation in biomanufacturing, *Nature Biotechnology*, 2012, 30, 489-492, DOI:10.1038/nbt.2263.

[4] Larroche C., Sanroman M. A., Du G., Pandey A., Current Developments in Biotechnology and Bioengineering: Bioprocess, Bioreactors and Controls, *Elsevier*, 2016.

[5] Eibl R., Löffelholz C., Eibl D., Chapter in the book: Single-use bioreactors – an overview, *Single-use Technology in biopharmaceutical manufacture*, *John Wiley & Sons*, 2011.

[6] Eibl R., Werner S., Eibl D., Disposable bioreactors for plant liquid cultures at litre-scale, *Engineering in Life Sciences*, 2009, 9, 156-164, DOI:10.1002/elsc.200800102.

[7] Nienow A. W., Scott W. H., Hewitt C. J., Thomas C. R., Lewis G., Amanullah A., Kiss R., Meier S. J., Scale-down studies for assessing the impact of different stress parameters on growth and product quality during animal cell culture, *Chemical Engineering Research and Design*, 2013, 91, 2265-2274, DOI:https://doi.org/10.1016/j.cherd.2013.04.002.
[8] Pilarek M., Sobieszuk P., Wierzchowski K., Dąbkowska K., Aplikacyjność bioreaktora single-use z mieszaniem typu wave w bioprocesach prowadzonych w warunkach tlenowych, *Inżynieria i Aparatura Chemiczna*, 2017, 4, 136-137.
[9] Sather D. N., Armann J., Ching L. K., Mavrantoni A., Selhorn G., Caldwell Z., Yu X., Wood B., Self S., Kalams S., Stamatatos L., Factors associated with the development of cross-reactive neutralizing antibodies during Human Immunodeficiency Virus type 1 infection, *Journal of Virology*, 2009, 83, 757-769, DOI:10.1128/JVI.00283-09.
[10] Wang L., Hu H., Yang J., Wang F., Kaisermayer C., Zhou P., High Yield of Human Monoclonal Antibody Produced by Stably Transfected Drosophila Schneider 2 Cells in Perfusion Culture Using Wave Bioreactor, *Molecular Biotechnology*, 2012, 52, 170-179, DOI:10.1007/s12033-011-9484-5.
[11] Clicke M. F., Mölleryd C., Zhang Y., Lindskog E., Walsh K., Chotteau V., Study of a recombinant CHO cell line producing a monoclonal antibody by ATF or TFF external filter perfusion in a WAVE Bioreactor™, *BMC Proceedings*, 2011, 5, P105, DOI:https://doi.org/10.1186/1753-6561-5-S8-P105.
[12] Imseng N., Steiger N., Frasson D., Sievers M., Tappe A., Greller G., Eibl D., Eibl R., Single-use wave-mixed versus stirred bioreactors for insect-cell/BEVS-based protein expression at benchtop scale, *Engineering in Life Sciences*, 2014, 14, 264-271, DOI:10.1002/elsc.201300131.
[13] Marks D. M., Equipment design considerations for large scale cell culture, *Cytotechnology*, 2003, 42, 21-33, DOI:10.1023/A:1026103405618.
[14] Raven N., Schillberg S., Kirchhoff J., Brändli J., Imseng N., Eibl R., Chapter in the book: BY-2 Cell-Based Plantibody Production, *Single-use Technology in biopharmaceutical manufacture*, *John Wiley & Sons*, 2011.
[15] Pilarek M., Grabowska I., Ciemerych M. A., Dąbkowska K., Szewczyk K. W., Morphology and growth of mammalian cells in a liquid/liquid culture system supported with oxygenated perfluorodecalin, *Biotechnology Letters*, 2013, 35, 1387-1394, DOI:10.1007/s10529-013-1218-2.

Adsorption equilibrium of carbon dioxide on zeolite 13X at high pressures

*Kamila Zabielska, Tomasz Aleksandrzak, Elżbieta Gabruś
Faculty of Chemical Technology and Engineering, West Pomeranian University of Technology, Szczecin, POLAND
e-mail: kamila.zabielska@zut.edu.pl

Keywords: *carbon dioxide, zeolite 13X, adsorption equilibrium, adsorption isotherm*

ABSTRACT

Carbon dioxide (CO_2) is a compound responsible for the greenhouse effect. One of the methods of CO_2 capture from the gas stream is adsorption process. In this paper, the adsorption equilibrium isotherms of CO_2 on zeolite 13X were measured at different temperatures (293.15K, 303.15K, 313.15K, 323.15K, 333.15 K, 348.15 K, 373.15 K, 393.15 K) and under pressures up to 2 MPa. These data were obtained using an Intelligent Gravimetric Analyzer (IGA-002, Hiden Isochema, UK). Selected multitemperature adsorption isotherm equations, namely Toth, Langmuir-Freundlich, and Langmuir were correlated with experimental data.

INTRODUCTION

The greenhouse effect is caused by the emission of compounds such as water vapor, carbon dioxide, methane, ozone, and freon into the atmosphere. These gases can be originated in both natural sources and human activity. Carbon dioxide is the main greenhouse gas that contributes to global warming. It is emitted into the atmosphere in the processes of electricity and heat generation based on fuel combustion [1, 2].

According to the Kyoto Protocol from 1997 the greenhouse gas emission was intended to be reduced in 2008-2012 by 5% in relation to the level in 1990. The protocol imposed a requirement to monitor greenhouse gas emission and prepare annual reports. The energy and climate package consists of four legal acts. One of them is a commitment signed by the European Union Member States about 20% reduction of greenhouse gas emissions to the atmosphere by 2020. To achieve this goal the development of clean coal technology should take place simultaneously with the development of CO_2 capture and storage technologies (CCS) [3-6].

There are five main technologies of carbon dioxide capture: pre-combustion capture, post-combustion capture, oxy-fuel combustion, combustion with flue gas recirculation of O_2/CO_2 and chemical looping combustion. In each of the capture methods separation processes such as absorption, adsorption, membrane filtration and cryogenic techniques can be used [6, 7].

The absorption methods allow obtaining a high purity product. The process can be carried out due to chemical or physical absorption. During the chemical absorption the flue gas is passed through the absorption column, where it reacts with a liquid capturing CO_2. This process is used when high degree of component removal is required. Typically amines are used as a solvent such as *monoethanolamine* (MEA), diethanolamine (DEA) as well as aqueous ammonia solution. In the physical absorption process, CO_2 can be absorbed by the solvent according to Henry's law and regenerated by pressure reduction at increased temperature [6-9].

Membrane separation of gases is based on difference in physical or chemical interaction between components present in a gas mixture with the membrane material. Membranes can be used to separate gas mixture or to absorb a gas component when concerning carbon dioxide capture [6, 8, 9].

CO_2 removed by the cryogenic method must be compressed and cooled to the temperature at which it can be separated in a liquid form.

This paper is focused on adsorption process of gas mixture separation. It is commonly used in industry for gas streams purifying and component recovery [6, 9]. Physical adsorption takes place as a result of adhesion of molecules, atoms or ions on the surface or boundary of physical phases, causing local concentration changes on surface of solid adsorbent. Adsorption is more effective at low temperature and high pressure [10-12].

The effective adsorbent should have a high specific surface area and high adsorption capacity of carbon dioxide. The following adsorbents are mainly used: activated carbons, carbon and zeolite molecular sieves and silica gels. The 13X zeolite was selected in this studies because of its unique structure, resistance to high temperatures and its high regeneration degree.

Zeolites are crystalline aluminosilicates of alkali metals and divalent metals.Their structure is composed of elementary tetrahedrons of SiO_4/AlO_4 connected with other oxygen ions. The combined tetrahedrons form polyhedrons. Various molecular sieves can be obtained by different arrangement and connection of polyhedrons. These adsorbents have homogeneous pores and the shape and size of pores determine which molecules are able to enter pore and be adsorbed on its surface. Zeolites can be divided into three types: A, X and Y [10-15].

Mostly, adsorbent is placed in column with the form of a fixed bed, which operates in cycles. The cyclic adsorption process consists of two stages: adsorption and regeneration of an adsorbent. In the adsorption stage a gas stream flows through a column with a packed adsorbent bed. As a result of the adsorption process CO_2 is removed from gas stream by an adsorbent. When the adsorbent is saturated then regeneration stage is occur Various cyclic adsorption processes can be used for separation of carbon dioxide:

- Pressure Swing Adsorption (PSA) which the adsorption step takes place at increased pressure;
- Temperature Swing Adsorption (TSA) in which the adsorbent is regenerated by raising its temperature;
- Electrothermal Swing Adsorption (ETSA) in which the adsorbent is regenerated by passing a low-voltage electric current;
- Vacuum Pressure Swing Adsorption (VSA) in which the adsorbent is regenerated by using vacuum [12, 14].

Most papers concerning adsorption equilibrium isotherms of CO_2 on zeolite 13X determined under pressures below 2 MPa [16-26]. Cavenati et al. [27] measured mentioned above equilibrium using gravimetric method at temperatures 298.15 K, 303.15 K, 323.15 K and under pressures up to 3.4 MPa for about 20 pressure measurement points. Siriwardane et al. [28] used the same method for temperatures 303.15 K and 393.15 K and pressures up to 2.5 MPa for 12 pressure measurement points.

In this paper, the adsorption equilibrium isotherms of CO_2 on zeolite 13X were determined at temperatures 293.15 K, 303.15 K, 313.15 K, 323.15 K, 333.15 K, 348.15 K, 373.15 K, 393.15 K and under pressures up to 2 MPa. The experiments were performed for 33 pressure measurement points allowing to determine the multitemperature adsorption isotherm of the studied system with high accuracy.

MATERIALS AND METHODS

Characteristics of adsorbent and adsorbate

Experimental research concerned adsorption equilibrium of carbon dioxide onto zeolite 13X, which was manufactured by Polskie Odczynniki Chemiczne S.A. (Gliwice, Poland). Basic physical properties of the adsorbent (Figure 1) are presented in Table 1.

Tab. 1. Physical properties of zeolite 13X [12]

Property	Value
BET surface area, m^2/g	726
bulk density, kg/m^3	689
density, kg/m^3	1100
bed porosity	0,374
pellet porosity	0,247
pellet diameter, m	0,0036
pore radius, nm	23

Fig. 1. Molecular sieves 13X

Description of experimental apparatus and measurement methodology

Studies of adsorption equilibrium were performed using Intelligent Gravimetric Analyzer (IGA-002, Hiden Isochema, United Kingdom) (Figure 2). The main element of the IGA system is a precision balance with weighing resolution of 0.1 μg [29].

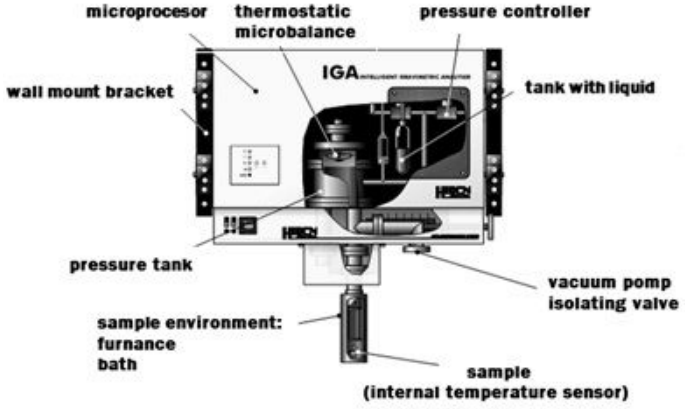

Fig.2. General construction of the IGA-002 system [29]

The sample of adsorbent (about 82 mg) was placed on a stainless steel sieve which was suspended on the balance inside the metal reactor using a gold chain and a tungsten wire. At the condition of ultra-high vacuum the reactor was thermostated using a circulation water bath GR 150 (Grant Instruments, United Kingdom) or heated with electric furnace Cryofurnace (Hiden Isochema, United Kingdom). The sample temperature measured using a Pt 100 sensor was regulated by the PID controller with accuracy of +/-0.05°C for the water bath and +/-0.1°C for the furnace. The reactor pressure was measured using a manometer with the resolution of +/-0.625 Pa. Before each measurement, the sample was degassed "in situ" for 2 hours at the temperature of 200 °C at vacuum of 10^{-6} Pa. Such low pressure was obtained by the system of two vacuum pumps: the MD 1 membrane pump (Vacuumbrand, Germany) and the TMU 071 P turbomolecular pump (Pfiffer Vacuum Technology, Germany) [29].

After degassing the sample, the adsorption equilibrium measurement was made for set values of temperature and pressure. The source of CO_2 was the gas cylinder (purity of CO_2 was 99.995%). IGA controlled pressure inside the chamber, in which a sample was located by adjusting automatically the input and output valves of the reactor. For each measuring point (set pressure and temperature values) real time processor (RTP) was responsible for recording of sample weight changes and predicting an asymptotic value of mass sample. After reaching 99.9% of the predicted weight value, the IGA system continued the measurement in the next isotherm point (next setpoint pressure). When all set point pressures were examined the sample was degassed and the measurement was performed for the next temperature value [29].

Types of adsorption equilibria

As a result of gas phase contact with the solid surface, part of the gas phase molecules are adsorbed on the surface of the solid. The amount of adsorbed substance per unit of adsorbent weight is called adsorption capacity. Adsorption is a surface phenomenon that occurs at any pressure and temperature [10, 14, 15].

Number of molecules adsorbed in equilibrium conditions on the surface of the adsorbent q^* depends on the process temperature T and the partial pressure of the adsorbed substance p:

$$q^* = f(T, p) \tag{1}$$

As there are three parameters in the above equation, the equilibrium may be described in three ways:

- at constant temperature T - adsorption isotherm:

$$q^* = f(p)_T \tag{2}$$

- at a constant vapor pressure p - adsorption isobar:

$$q^* = f(T)_p \tag{3}$$

- at constant concentration of adsorbed component on the solid phase q – adsorption isostere:

$$q^* = f(T)_q \tag{4}$$

The adsorption equilibrium is considered mostly as an adsorption isotherm which can be classified according to the recommendation of the International Union of Pure and Applied Chemistry classification (IUPAC) as one of 6 different types [10, 14, 15].

Adsorption isotherm models

Practical application of measured adsorption isotherms at various temperatures requires presenting them in the form of mathematical equations. To correlate equilibrium models with the experimental data, the multitemperature adsorption isotherm equations of Toth, Langmuir−Freundlich and Langmuir were selected [30].

Langmuir equation

Isotherm model developed by Langmuir in the years 1916-1918 describes the adsorbed component - the adsorbent system in which the surface is coated by the adsorbed component and confined to the monomolecular layer [31]. The equation was formulated on the basis of dynamic equilibrium between the adsorbed phase and the gas (vapour) phase. It was found that the rate at which the gas molecules of the adsorbed component hit the surface of the adsorbent is proportional to the partial pressure p and the size of the adsorbent surface, which has not been covered by the adsorbed substance and is available as adsorption places. Langmuir supposed that the rate of desorption from the adsorbent surface is straight proportional to the surface occupied by the adsorbed substance. The Langmuir isotherm equation can be written as [14, 15, 30, 31]:

$$q = q_m \frac{b(T) \cdot p}{1 + b(T)p} \tag{5}$$

The mathematical form of multitemperature Langmuir adsorption isotherm is:

$$q = q_m \frac{b_1 \exp\left(\frac{c_1}{T}\right) p}{1 + b_1 \exp\left(\frac{c_1}{T}\right) p} \tag{6}$$

where the q_m, b are characteristic coefficients for the adsorbed substance – adsorbent system, p is the partial pressure of the adsorbate, T is the temperature and b_1, and c_1 are the isotherm parameters.

Langmuir made several simplifying assumptions while deriving his equation: heat of adsorption is constant and independent of the degree of adsorbent coverage (as a consequence, there is no interaction between molecules); each adsorbed molecule can occupy only one active centre; adsorption is located (the molecule stays in place until the desorption process occurs) [12, 14, 15, 30, 31].

Langmuir-Freundlich equation

In order to achieve greater flexibility, the equation of the Langmuir and Freundlich isotherms were combine into the form of an empirical relation which can be presented as [12, 15]:

$$q = q_m(T)\frac{b(T)\cdot p^{n(T)}}{1+b(T)\cdot p^{n(T)}} \tag{7}$$

In the equation (7) q_m, b and n are characteristic coefficients for adsorbed component - adsorbent system and depend on the temperature T according to the relations:

$$q_m(T) = a_0 + \frac{a_1}{T} + \frac{a_2}{T^2} \tag{8}$$

$$b(T) = \exp\left(b_0 + \frac{b_1}{T} + \frac{b_2}{T^2}\right) \tag{9}$$

$$n(T) = n_0 + \frac{n_1}{T} \tag{10}$$

After substituting the equations (8) - (10) into equation (7) the mathematical form of multitemperature Langmuir−Freundlich adsorption isotherm is obtained:

$$q = \left(a_0 + \frac{a_1}{T} + \frac{a_2}{T^2}\right)\frac{\left(\exp\left(b_0 + \frac{b_1}{T} + \frac{b_2}{T^2}\right)\right)p^{\left(n_0+\frac{n_1}{T}\right)}}{1+\left(\exp\left(b_0 + \frac{b_1}{T} + \frac{b_2}{T^2}\right)\right)p^{\left(n_0+\frac{n_1}{T}\right)}} \tag{11}$$

where a_0, a_1, a_2, b_0, b_1, b_2, n_0, and n_1 are the isotherm parameters, T is the temperature and p is the partial pressure of the adsorbate [10, 12, 15].

Toth equation

The Toth model is a semi-empirical equation which describes adsorption in monolayer.This equation is related to the heterogeneity of the surface and interactions of the adsorbed molecules. Relation developed by Toth in 2001 [32] has the following form:

$$q = q_m\frac{p}{\left(b(T)+p^n\right)^{1/n}} \tag{12}$$

In the equation (12) the coefficient *b* depends on the temperature according to the formula:

$$b(T) = b_0 \cdot \exp\left(-\frac{n \cdot \Delta H}{R \cdot T}\right) \tag{13}$$

After substituting equation (13) into the equation (12) the mathematical form of multitemperature Toth adsorption isotherm is obtained:

$$q = q_m \frac{p}{\left(b_0\left(-\frac{n \cdot \Delta H}{R \cdot T}\right) + p^n\right)^{1/n}} \tag{14}$$

where ΔH is the heat of adsorption, p is the partial pressure of the adsorbate, R is the universal gas constant, T is the temperature and b, b_0, n, and q_m are the isotherm parameters [12, 15, 32].

Values of model parameters were calculated by nonlinear regression of experimental data using Statistica 13.1 (Statsoft).The average relative error δ, which is the measure of fitting quality was calculated as follows:

$$\delta = \frac{1}{N}\sum_{i=1}^{N}\left|\frac{q_{\exp} - q_{sim}}{q_{\exp}}\right| 100\% \tag{15}$$

where q_{exp} is the experimental adsorption capacity, q_{sim} is the calculated adsorption capacity, and N is the number of experimental points. In addition the coefficients of determination R^2 were calculated for each isotherm model.

RESULTS

As a result of measurements the adsorption isotherms for carbon dioxide – zeolite 13X system were determined at temperatures: 293.15 K, 303.15 K, 313.15 K, 323.15 K, 333.15 K, 348.15 K, 373.15 K, 393.15 K and under pressures up to 2 MPa. All isotherms are type I according to the IUPAC classification [14].

The multitemperature adsorption isotherm models of Toth, Langmuir – Freundlich, and Langmuir were fitted to the experimental data. The obtained values of isotherm parameters are shown in Tables 2 through 4. Average relative errors and coefficients of determination R^2 for all the equilibrium models are presented in Table 5.

Tab. 2. Adsorption isotherm parameters for the Toth model

Parameters	q_m,mol/kg	b_o, Pa^{-n}	n,-	ΔH, J/mol
Value	6.437	576.902	0.464	31864.04

Tab. 3. Adsorption isotherm parameters for Langmuir-Freundlich model

Parameters	a_0, mol/kg	a_1, mol·K/kg	a_2, mol·K^2/kg	b_0, Pa^{-n}	b_1, Pa^{-n}·K	b_2, Pa^{-n}·K	n_0, -	n_1, -
Value	6.159	13.673	0.567	-11.28	2912.8	17.37	1.03	-144.97

Tab. 4. Adsorption isotherm parameters for Langmuir model

Parameters	q_m, mol/kg	a_1, mol/kg·Pa	b_1, Pa^{-1}	c_1, K
Value	1.641	378.063	0.0003	1514.889

Tab. 5. Average relative errors δ and coefficients of determination R^2 for the carbon dioxide-zeolite 13X system for selected of equilibrium models

Equilibirum model	δ, %	R^2, -
Toth	8.57	0.9948
Langmuir-Freundlich	18.79	0.9961
Langmuir	22.89	0.9657

The experimental and isotherms correlated by means of the Toth model for the studied adsorption system at various temperatures and under pressures up to 2 MPa and up to 0.1 MPa are presented in Figure 3 and Figure 4, respectively.

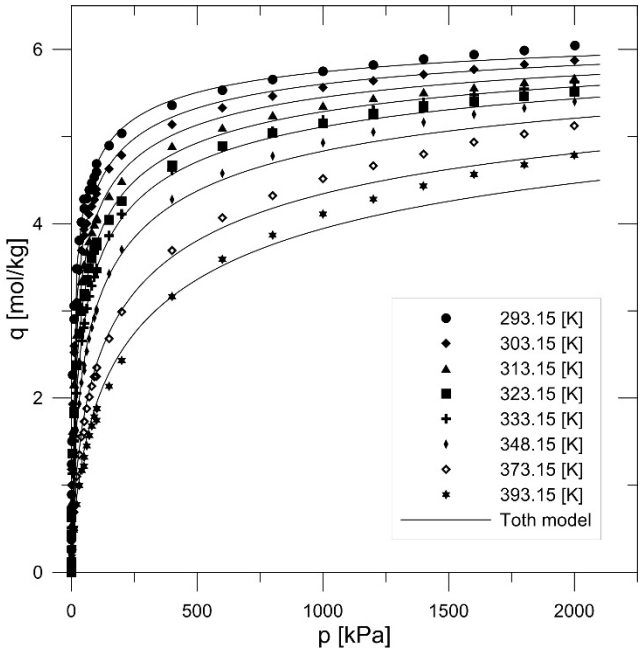

Fig. 3. Experimental and correlated (Toth equation) isotherms for carbon dioxide adsorption onto zeolite 13X at various temperatures.

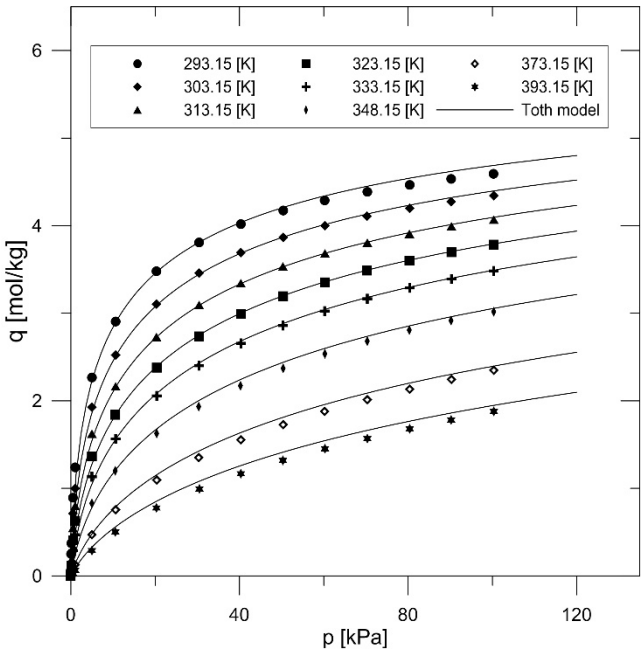

Fig. 4. Experimental and correlated (Toth equation) isotherms for carbon dioxide adsorption onto Zeolite 13X at various temperatures.

The comparison of measured experimental isotherm equilibria for the carbon dioxide - zeolite 13X system at temperatures 293.15 K with results obtained by Lee at al. [17], Costa et al. [18] and Ling et al. [26] is shown in Figures 5 to 6. Another comparison was made for isotherm measured at 323.15 K with the use of results obtained by Wang and LeVan [16], Cavenati et al. [23], Hyun and Danner [19], Maring and Webley [20] and Merel et al. [25] (Figures 7 and 8). The range of pressure values used in our studies presented in Figures 6 and 8 was limited according to the range of data taken from literature sources in order to increase readability of results.

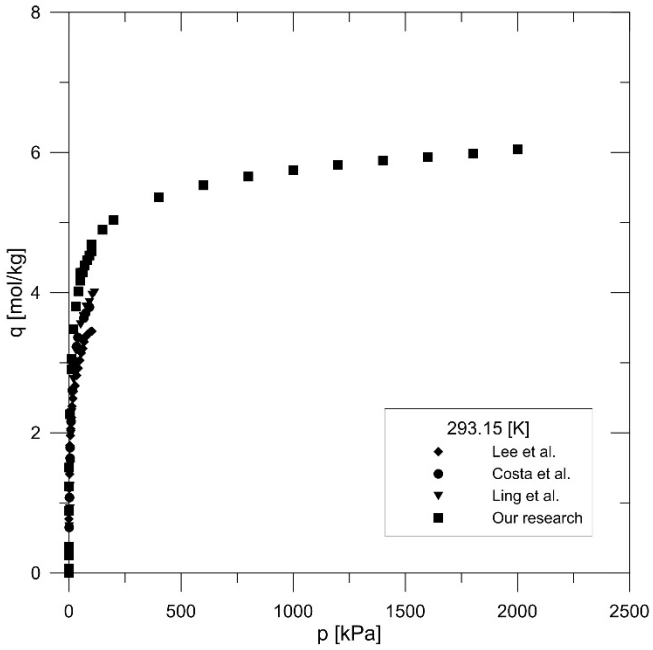

Fig. 5. Comparison of experimental isotherms for carbon dioxide adsorption onto zeolite 13X at 293.15 K in the whole range of pressure measurements.

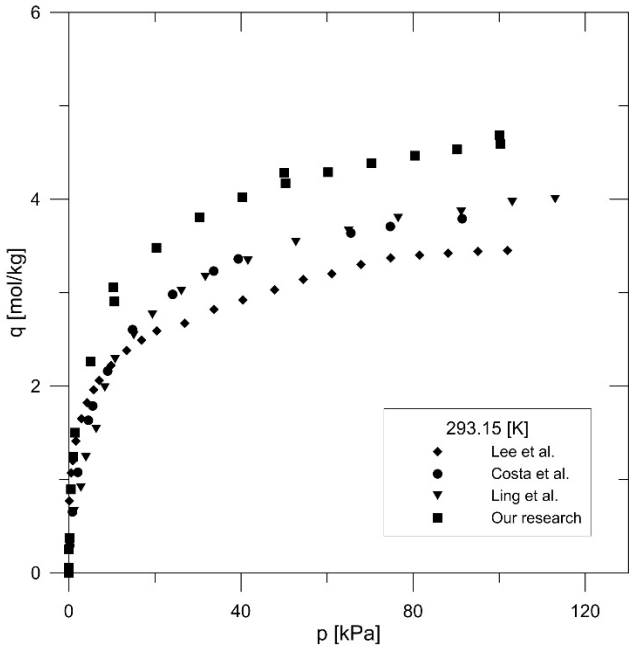

Fig. 6. Comparison of experimental isotherms for carbon dioxide adsorption onto zeolite 13X at 293.15 K.

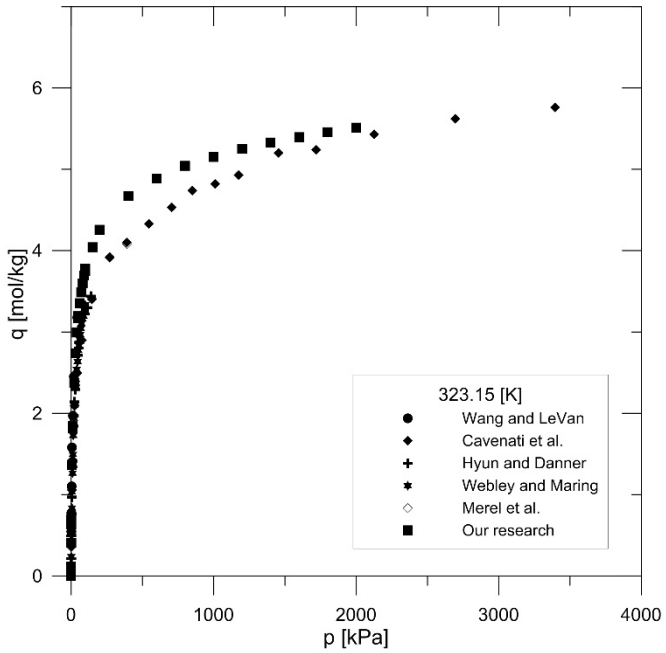

Fig. 7. Comparison of experimental isotherms for carbon dioxide adsorption onto zeolite 13X at 323.15 K in the whole range of pressure measurements.

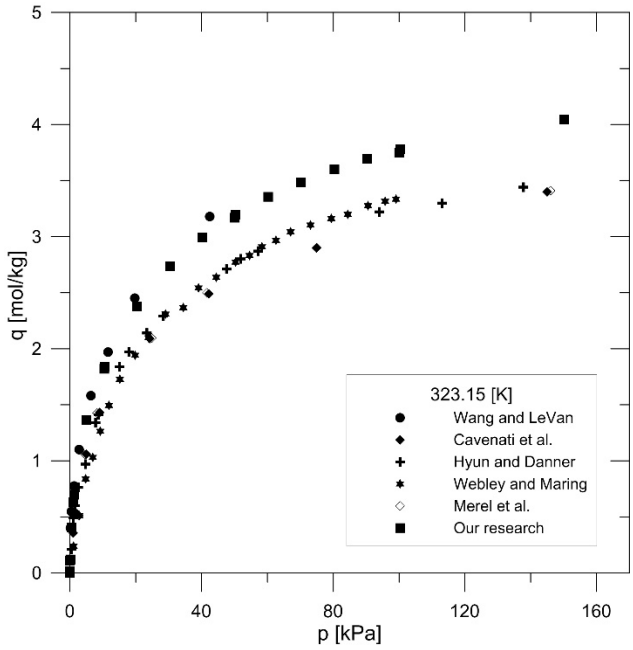

Fig. 8. Comparison of experimental isotherms for carbon dioxide adsorption onto zeolite 13X at 323.15 K.

CONCLUSIONS

The adsorption isotherms of carbon dioxide on zeolite 13X were measured at 293.15, 303.15, 313.15, 323.15 K, 333.15 K, 348.15 K, 373.15 K, 393.15 K and pressures up to 2 MPa. The selected multitemperature equilibrium models of Toth, Langmuir−Freundlich and Freundlich were correlated with the experimental equilibrium data. The analysis of computed average relative errors δ and coefficients of determination R^2 of models fitting to experimental data showed that the best agreement was obtained for the Toth model (8.57% and R^2 =0.9948). The fitting quality was found to be much better for partial pressure range limited to 0.1 MPa (Fig. 4). In the whole studied pressure range the calculated isotherm values were underestimated in comparison with measured values obtained at temperatures 373.15 K and 395.15 K within pressure ranged from 0.5 to 2 MPa (Figure 3).

It was shown that zeolite 13X is characterized by high adsorption capacity and it can be used in the process of carbon dioxide capture. The highest measured adsorption capacity of 6.04 mol/kg was achieved at 293.15 K and 2 MPa.

The results of our research were compared with those obtained by other authors for two temperatures: 293.15 K and 323.15 K at 2 MPa. In most cases the distinct discrepancies between them were observed (Figures 6 and 8) except the isotherm determined experimentally by Wang and LeVan [16] for carbon dioxide adsorption onto zeolite 13X at 323.15 K (Fig. 8). It can be caused by different properties of the used adsorbent or different conditions of adsorbent regeneration.

The experimental and simulation results can be used for modeling of cyclic adsorption processes, for example temperature swing adsorption (TSA) or pressure swing adsorption (PSA). They can also be the basis for modeling multicomponent adsorption equilibrium using interpolative models.

REFERENCES

[1] Kotowicz J., Janusz K., Manners of the reduction of the emission CO_2 from energetic processes, *Rynek Energii*, 2007, 1, 10-18

[2] Lin C.-C., Liu W.-T., Tan C.-S., Removal of Carbon Dioxide by Adsorption in a Rotating Packed Bed, *Industrial and Engineering Chemistry Research*, 2003, 42, 2381-2386, DOI:10.1021/ie020669+

[3] Stewart C., Hessami M. A., A study of methods of carbon dioxide capture and sequestration-the sustainability of a photosynthetic bioreactor approach, *Energy Conversion and Management*, 2005, 46, 403-420, DOI: 10.1016/j.enconman.2004.03.009

[4] Kyoto Protocol to the United Nations Framework Convention on Climate Change, 1998

[5] Miłek M., Problemy z pakietem klimatyczno-energetycznym, *Wydawnictwo PWSZ*, 2009

[6] Nowak W., Majchrzak-Kucęba I., Wawrzyńczak D., Bieniek J., Srokosz K., Błeszyński L., Zajączkowska J., Adsorpcyjne usuwanie CO_2 ze spalin kotłowych, *Energetyka*, 2014, 1, 15-19
[7] Kidnay A.J., Parrish W.R., Fundamentals of Natural Gas Processing, *CRC Press*, 2006
[8] Yang H., Xu Z., Fan M., Gupta R., Slimane R. B., Bland A. E., Wright I., Process in carbon dioxide separation and capture: A review, *Journal of Environmental Sciences*, 2008, 20, 14-27, DOI: 10.1016/S1001-0742(08)60002-9
[9] Creamer A. E., Gao B., Carbon Dioxide Capture: An Effective Way to CombatGlobal Warming, *SpringerBriefs in Green Chemistry for Sustainability*, 2015, DOI 10.1007/978-3-319-17010-7
[10] Paderewski M.L., Procesy adsorpcyjne w inżynierii chemicznej, *WNT*, 1999
[11] Sarbak Z., Adsorpcja i adsorbenty. Teoria i zastosowanie, *Wydawnictwo Naukowe Uniwersytetu im. Adama Mickiewicza*, 2000
[12] Nastaj J., Modelowanie wybranych procesów adsorpcyjnych i biosorpcyjnych w ochronie środowiska, *BEL Studio Sp. z o.o.*, 2013
[13] Małecki Z., Rajewski J., Czas zeolitów, *Świat szkła*, 2008, 116, 55-57
[14] Keller J., Staudt R., Gas Adsorption Equilibria: Experimental Methods and Adsorption Isotherms, *Springer*, 2005
[15] Thomas W. J., Crittenden B., Adsorption Technology and Design, *Butterworth-Heinemann*, 1998
[16] Wang Y., LeVan M. D., Adsorption Equilibirum of Carbon Dioxide and Water Vapor on Zeolites 5A and 13X Silica Gel: Pure Components, *Journal of Chemical and Engineering Data*, 2009, 54, 2839-2844, DOI: 10.1021/je800900a
[17] Lee J.-S., Kim J.-H., Kim J.-T., Suh J.-K., Lee J.-M., Lee C.-H., Adsorption Equilibria of CO_2 on Zeolite 13X and Zeolite X/Activated Carbon Composite, *Journal of Chemical and Engineering Data*, 2002, 47, 1237-1242, DOI: 10.1021/je020050e
[18] Costa E., Calleja G., Jimenez A., Pau J., Adsorption Equilibrium of Ethylene, Propane, Propylene, Carbon Dioxide, and Their Mixtures on 13X Zeolite, *Journal of Chemical and Engineering D*ata, 1991, 36, 218-224, DOI: 10.1021/je00002a020
[19] Hyun S.H., Danner R.P., Equilibrium Adsorption of Ethane, Ethylene, Isobutane, Carbon Dioxide, and Their Binary Mixtures on 13X Molecular Sieves, *Journal of Chemical and Engineering Data*, 1982, 27, 196-200, DOI: 10.1021/je00028a029
[20] Maring B. J., Webley P. A., A new simplified pressure/vacuum swing adsorption model for rapid adsorbent screening for CO_2 capture applications,

International Journal of Greenhouse Gas Control, 2013, 15, 16-31, DOI: 10.1016/j.ijggc.2013.01.009

[21] Delgado J. A., Agueda V. I., Uguina M. A., Sotelo J. L., Brea P., Grande C. A., Adsorption and Diffusion of H_2, CO, CH_4, and CO_2 in BPL Activated Carbon and Zeolite 13X Zeolite: Evaluation of Performance in Pressure Swing Adsorption Hydrogen Purification by Simulation, *Industrial and Engineering Chemistry Research*, 2014, 53, 15414-15426, DOI: 10.1021/ie403744u

[22] Li G., Xiao P., Webley P., Zhang J., Singh R., Marshall M., Capture of CO_2 from high humidity flue gas by vacuum swing adsorption with zeolite 13X, *Adsorption*, 2008, 14, 415-422, DOI:10.1007/s10450-007-9100-y

[23] Cavenati S., Grande C. A., Rodriques A. E., Removal of Carbon Dioxide from Natural Gas by Vacuum Swing Adsorption, *Energy and Fuels*, 2006, 20, 2648-2659, DOI: 10.1021/ef060119e

[24] Hefti M., Marx D., Joss L., Mazzotti M., Adsorption equilibirum of binary mixtures of carbon dioxide and nitrogen on zeolites ZSM and 13X, *Microporous and Mesoporous Materials*, 2015, 215, 215-228, DOI: 10.1016/j.micromeso.2015.05.044

[25] Merel J., Clausse M., Meunier F., Experimental Investigation on CO_2 Post-Combustion Capture Thermal Swing Adsorption Using 13X and 5A Zeolites, *Industrial and Engineering Chemistry Research*, 2008, 47, 209-215, DOI: 10.1021/ie071012x

[26] Ling J., Ntiamoah A., Xiao P., Xu D., Webley P. A., Zhai Y., Overview of CO_2 Capture from Flue Gas Streams by Vacuum Pressure Swing Adsorption Technology, *Austin Chemical Engineering*, 2014, 1(2), 1009

[27] Cavenati S., Grande C.A., Rodrigues A.E., Adsorption Equilibrium of Methane, Carbon Dioxide, and Nitrogen on Zeolite 13X at High Pressures, *Journal of Chemical and Engineering Data*, 2004, 49, 1095-1101, DOI: 10.1021/je0498917

[28] Siriwardane R. V., Shen M.-S., Fisher E., Adsorption of CO_2 on Zeolites at Moderate Temperatures, *Energy and Fuels*, 2005, 19, 1153-1159, DOI: 10.1021/ef040059h

[29] Nastaj J., Aleksandrzak T., Comparison of static and dynamic methods of adsorption isotherms determination, *20th International Congress of Chemical and Process Engineering*, 2013, 25-29

[30] Do D. D., Adsorption Analysis: Equilibria and Kinetics, *Imperial College Press*, 1998

[31] Langmuir K., Adsorption of Gases on Plane Surfaces of Glass, Mica and Platinum, *Journal of the American Chemical Society*, 1918, 40, 1361-1403

[32] Toth J., Adsorption: Theory, Modelling, and Analysis, *Marcel Dekker*, 2001

Articles

Evaluation of the absorbing pervaporation technique for ammonia recovery after the Haber process

*Artem Atlaskin, Anton Petukhov, Nail Yanbikov, Vladimir Vorotyntsev, Ilya Vorotyntsev
Nanotechnology and Biotechnology Department, Nizhny Novgorod State Technical University n.a. R.E. Alekseev, Nizhny Novgorod, RUSSIA
e-mail: atlaskin@gmail.com

Keywords*: gas separation; absorbing pervaporation; ammonia; process intensification; membrane.*

ABSTARCT

The absorbing pervaporation technique is proposed for ammonia recovery. The ammonia-containing gas mixtures separation efficiency evaluation of an absorbing pervaporation technique in a comparison with conventional membrane method was performed experimentally. The process of ammonia recovery from the gas mixture is studied using two gas mixtures containing ammonia as a target component and nitrogen and hydrogen as impurities. The influence of poly-ethylene glycol-400 (PEG-400) content in aqueous solutions (0-20 wt.%) used as a liquid absorbent on a separation efficiency is studied. It was experimentally shown, that absorbing pervaporation technique always outperforms the conventional membrane method by more than an order of magnitude.

INTRODUCTION

One of the fields of chemical technology, where the membrane gas separation [1–7] approach may be successfully applied is the ammonia production, which is the largest in the world. At present, the annual production of ammonia makes more than 150 million tons [8], with most of it being converted into carbamide (urea) and the rest being used in the industry, including the manufacture of nitric acid and ammonium nitrate. The ammonia synthesis technology has not undergone significant change since its invention by Haber and Bosch, and the ammonia recovery stage requires considerable energy supply due to cooling the gas mixture to the ammonia condensation temperature. Thus, the development of advanced physicochemical approaches focused on improving the performance of purification technology is of great importance, especially concerning the enhancement of separation efficiency, maximization of productivity and reduction of energy consumption. Because of that, the membrane-based separation technique may be considered as a perspective approach instead of conventionally applied cryogenic purifiers.

As it is well known, ammonia has a high solubility in water, but because of its physical properties, such as high volatility and low boiling point, it is impossible

to use water as an absorbent for ammonia in modern technological schemes. However, in a number of works it has been shown that its use in combination with organic solvents, for example, poly-ethylene glycol (PEG) aqueous solutions, allows achieving increase in gas solubility rate [9,10]. Poly-ethylene glycol 400 (PEG-400) is an important industrial solvent, which may be used in the cleaning of exhaust air and gas streams from industrial production plants because of its favorable properties, such as low vapor pressure, low toxicity, high chemical stability, and low melting point. On the other hand, PEG presents native hydrogen bonding sites, which are increasing the solubility of aggressive gases like NH_3 and SO_2.

In the current study, the novel hybrid method – absorbing pervaporation [11,12] is proposed for ammonia recovery process intensification. That hybrid separation technique is a combination of gas absorption by liquid absorbent (PEG-400 aqueous solution) displaced on the membrane and further pervaporation (vaporization of gases at the permeate side of the membrane). Additionally, this process can be performed without any phase transition, in a one-volume mass-exchange apparatus and with a liquid absorbent-membrane system, which provides higher selectivity due to high NH_3 solubility. Furthermore, absorbing pervaporation apparatus does not require any heat supply/removal, characterized with scalable design and may be applied individually and as a final stage in technology route or in point-of-use operation. The absorbing pervaporation separation efficiency is studied experimentally during the separation of binary gas mixtures consisting of an ammonia and attendant impurities – nitrogen and hydrogen using the elastomeric poly(dimethylsiloxane)-poly(diphenylsilsesquioxane) LESTOSIL™ membrane-PEG aqueous solution system. During the experimental study, the separation efficiency depending on the rate of ammonia recovery and absorbent composition was investigated. It was clearly demonstrated that the proposed hybrid scheme may offer promising perspectives for ammonia recovery in comparison with other membrane-based techniques, e.g. membrane contactors.

MATERIALS AND METHODS

Test gas mixtures

In order to study and optimize the system it is of interest to perform the experimental study using two binary gas mixtures consisiting of ammonia and attendant impurities – nitrogen and hydrogen. According to that purpose the NH_3/N_2 and NH_3/H_2 gas mixtures were prepeared with NH_3 content of 50vol.% for separation on commercially available elastomeric poly(dimethylsiloxane)-poly(diphenylsilsesquioxane) membrane (LESTOSIL™) covered with uniform layer of PEG-400 aqueous solution. The LESTOSIL™ membrane was purchased from Vladimir PolimerSintez JSC (Vladimir, Russia) and had a composite structure with a thin 5 μm skin layer on porous fluoropolymer support. High purity single gases:

hydrogen (99.9999vol.%), nitrogen (99.9999vol.%) and ammonia (99.9999vol.%) were purchased from Monitoring Ltd. (Moscow, Russia). Pressurized test mixture were prepared in cylinders by a static volumetric method.

The pure component permeances through different membrane-PEG-400 aqueos solution systems were measured according to Dynes-Barrer technique [13,14] in a constant-volume variable-pressure apparatus for gas permeability measurements at the initial transmembrane pressure of 110 kPa and at ambient temperature (25˚C). The experimental procedure is well illustrated in our previous works [4,7].

Experimental setup

The experimental setup designed for separation efficiency evaluation of different membrane-PEG-400 aqueous solution systems is shown schematically in Fig. 1. The test unit is equipped with gas chromatography (GC) system based on Chromos GC-1000 (Chromos Ltd, Russia). Gas chromatograph equipped with a Valco PDHID system (D-2-I model, VICI, USA) for analysis of a retentate flow sample composition.

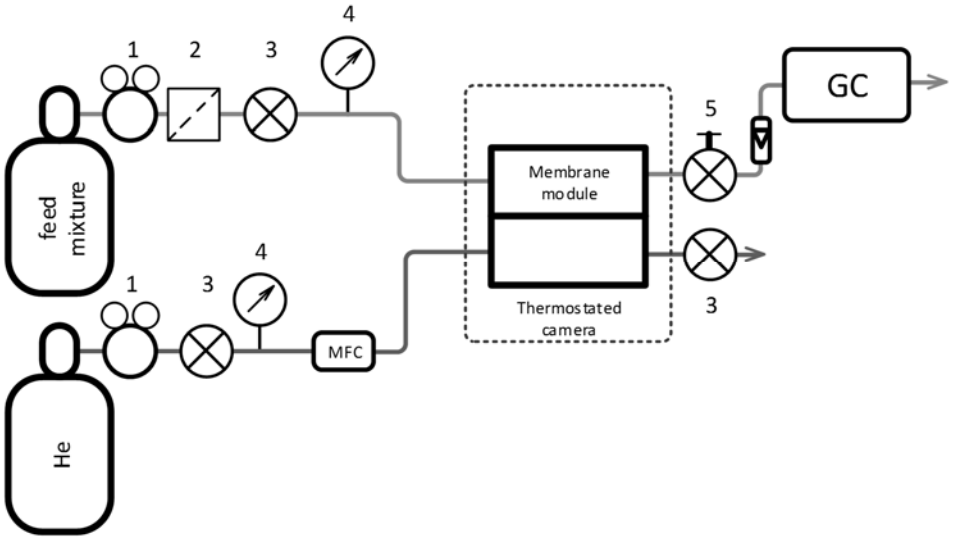

Fig. 1. The principal scheme of the experimental setup. 1 – pressure regulator; 2 – filter; 3 – valve; 4 – pressure gauges; 5 – needle valve.

Gas mixture is continuously supplied from the cylinder to the feed side of the membrane module through a pressure regulator (1) and a filter (2) with a constant pressure maintained at (300±5) kPa. Permeated components removed from the cell by a sweep gas (He), aslo used as a gas carrier in GC system. The pressures of both the feed and permeate sides are monitored by pressure gauges (4) with an accuracy of 0.4% of full scale. The retentate withdrawal flow is regulated by the needle valve (5) and introduced into the flow-through sampling valve of the gas

chromatograph and then neutralized. During the analysis the components of the sample are separated in the chromatographic column under isothermal conditions and detected by the pulsed discharge helium ionization detector. Carrier gas flow controller serves to supply the required flows of the carrier gas (Helium 99.9999+%). The detailed GC-analysis conditions are presented in Tab. 1. GC determination of nitrogen and ammonia using Porapak Q column is also presented in details in [15–17].

Tab. 1. The operating conditions of the GC system.

Component of the GC	Characteristics
Detector	PDHID D-2-I, 100°C
Chromatographic column	Porapak Q, 80/100 mesh, 60°C
	3 m × 2 mm i.d. stainless steel tube
Sample loop	1.6 ml, 70°C
Carrier gas	He 99.9999%, 25 ml/min

The key component of the setup is a radial absorbing pervaporation membrane module made of AISI 316 stainless steel with PTFE sealing. The mathematical model and experimental investigation of gas purification process in membrane module of this type were presented by Vorotyntsev et al. in [18,19]. Fig. 2 shows the schematic design and the principle flow scheme of the membrane module used.

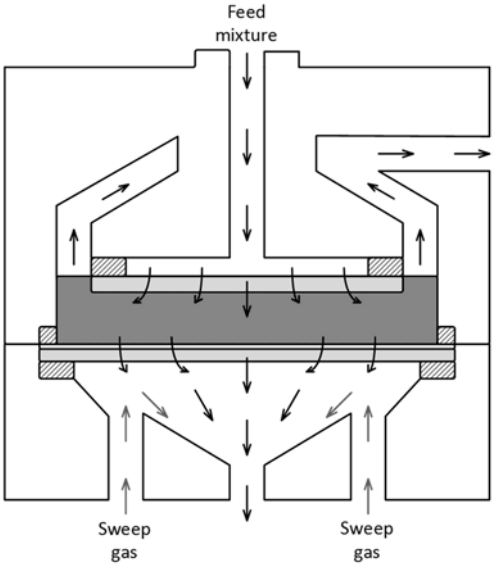

Fig. 2. Principle flow scheme of the radial absorbing pervaporation membrane module.

A flat-sheet membrane covered with a uniform liquid absorbent layer with the same size as the inner diameter of the module is placed on a porous stainless steel support inside the module and dividing the system into upstream and downstream compartments. A PTFE sealing is used to prevent gas leakage at the film edge from

the upstream to the downstream side of the module and to avoid gas exchange between the compartments of the module and the exterior atmosphere.

The feed gas enters the center of the module and flows radially from the center to the periphery of a stainless steel supporting disc and then introduced to the liquid absorbent placed on the high-permeable membrane. Soluted gas is moved through the absorbent to the low-pressure compartment and removed with the sweep-gas flow. This principle eliminates any trapped gas or dead zones in the module. The main separation action takes place in the liquid absorbent, while the membrane serves as a support and provides withholding of a liquid under the pressure gradient between two compartments.

The diameter of the membrane area available for separation is 4.2 cm, corresponding to a membrane area of approximately 13.85 cm^2. The practical active volume of the feed side available for gas separation is situated in a 2 mm gap between the distribution disc and the membrane and equals to approximately 2.8 cm^3.

Stability test of the LESTOSIL™ membrane

The stability of the LESTOSIL™ membranes in the absorbent was first investigated. The film were immersed in PEG-water solution at room temperature for two weeks. After cleaning with ethanol and pure water, the film was then dried in oven for attenuated total reflectance-Fourier transform infrared spectrometry (ATR-FTIR) and contact angle (CA) analysis. ATR-FTIR was used to check the chemical composition, while CA test was used to examine the variation of membrane hydrophobicity.

Moreover, a study of the LESTOSIL™ membrane stability was performed at the room temperature of 25ºC under the pressure of (300±5) kPa during the 90 days to determine the ability of the polymer to maintain mass transfer properties under the influence of ammonia for a long time. As can be seen from Fig. 3, the membrane permeability varies within the instrument error, which indicates the stability of the material.

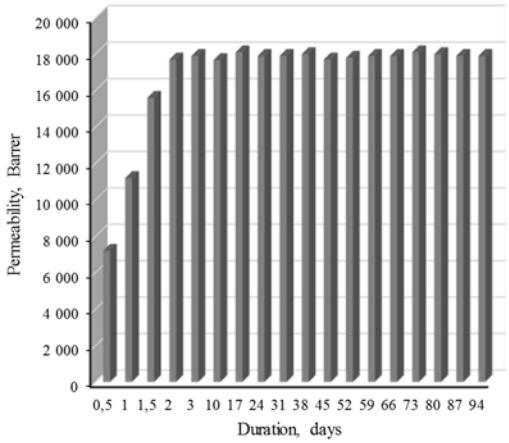

Fig. 3. The LESTOSIL™ Membrane permeability for NH_3.

PEG-water solution preparation

PEG-400, purchased from LLC «Zavod sintanolov» (Dzerzhinsk, Russia) was dehydrated by using molecular sieves before preparing the co-solvent mixtures. All PEG-400 aqueous solutions were prepared by mass, using an Shimadzu AUW220D analytical balance with sensitivity ±0.01 mg, in quantities of 10 g. In order to cover all compositions range, the mass fractions of PEG-400, of the three binary mixtures prepared varied by 0.1 from 0.80 to 1.

RESULTS AND DISCUSSIONS

During the experimental comparison of the two approaches to the ammonia removal from the gas mixtures containing the hydrogen and nitrogen as impurities, the permeability of the single gases were determined through the LESTOSIL™ membrane and combined system of membrane covered with liquid absorbent PEG-400 and its aqueous solutions. An experimental efficiency comparison of the methods described above was performed using the laboratory setup, which is described in the experimental section. Moreover, the membrane material stability was evaluated and the degradation degree under the influence of ammonia as the time function was found. This approach provides a possibility of comprehensive assessment of the proposed technique – absorbing pervaporation for the ammonia recovery from the syngas in the Haber process.

Single gases permeability test

To obtain and compare the values of mass transfer properties the permeability of NH_3, N_2 and H_2 single gases were measured through the LESTOSIL™ membrane and combined system consisting of the membrane and liquid absorbent PEG-400 and its aqueous solutions. The results shown in Tab. 2. The choice of these gases is

justified by the gas mixture composition entering cryogenic purifier in Haber process technological scheme. In that case, ammonia is the target component to be recovered and the nitrogen and hydrogen are attendant impurities to be removed.

Tab. 2. Pure gas permeability coefficients and selectivitys.

Gas	Membrane gas separation, Barrer	Absorbing pervaporation, Barrer PEG 400 content in solution, wt.%.		
		100	90	80
NH_3	17 900	11 950	22 710	25 400
N_2	960	60	150	33
H_2	2210	78	120	63

Measured at 25 °C, 110kPa. 1 Barrer = 3.346 · 10^{-16} mol m s^{-1} m^{-2} Pa^{-1}

Tab. 3. The ideal selectivity for binary gas mixtures.

Gas	Membrane gas separation, Barrer	Absorbing pervaporation, Barrer PEG 400 content in solution, wt.%.		
		100	90	80
NH_3/N_2	18.65	199.0	151.4	769.7
NH_3/H_2	8.00	153.0	189.3	403.2

The measurement of the membrane permeability for the chosen gases was carried out in the steady-state system operational mode. The results of the experiment confirmed the conclusion made in the previous section that the membrane material is able to maintain its mass-transfer properties for a long time. In addition, it was shown that the ammonia permeability exceeds the permeability of hydrogen and nitrogen by more than an order of magnitude. In the case of the membrane-liquid absorbent system, the ammonia permeability increases with the increase of water content of the solution. Wherein the nitrogen and hydrogen permeability decreases, which in turn increases the combined system selectivity (Tab. 3). However, it is important to note that to determine the nature of this dependence, additional experimental studies on a wider range of solutions are required, for example, with a step of 5 wt.% of water in solutions.

Absorbing pervaporation efficiency evaluation

The efficiency of absorbing pervaporation cell was evaluated in a comparison with the conventional single-stage membrane module. The separation efficiency, determined as a natural logarithm of ammonia concentration ratio at the inlet C_{in} (feed) and outlet C_{out} (retentate) of the cell (1) of both methods was evaluated

depending on the process productivity, represented as the target product (ammonia) recovery rate in percent (2)

$$F = \frac{C_{in}}{C_{out}} \tag{1}$$

$$r = \frac{l_{ret}}{l_{feed}}, \tag{2}$$

where l_{ret} and l_{feed} are the flow rates of the feed and retentate flows. Results are shown in Fig. 4. and Fig. 5 for NH_3/N_2 and NH_3/H_2 gas mixtures separation respectively. The graphs clearly demonstrate the dependence of the separation efficiency of the setup on overall productivity. It is experimentally shown that an increase in productivity reduces the product purification degree. Moreover, the gas mixture separation efficiency dependence on the absorbent content was determined and compared with conventional membrane separation technique.

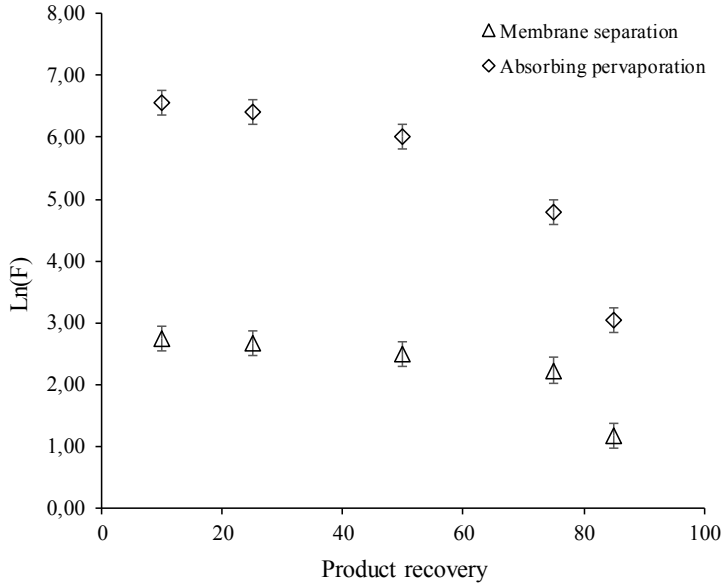

Fig. 4. Evaluation of absorbing pervaporation and membrane separation efficiency during separation of NH_3/N_2 gas mixture.

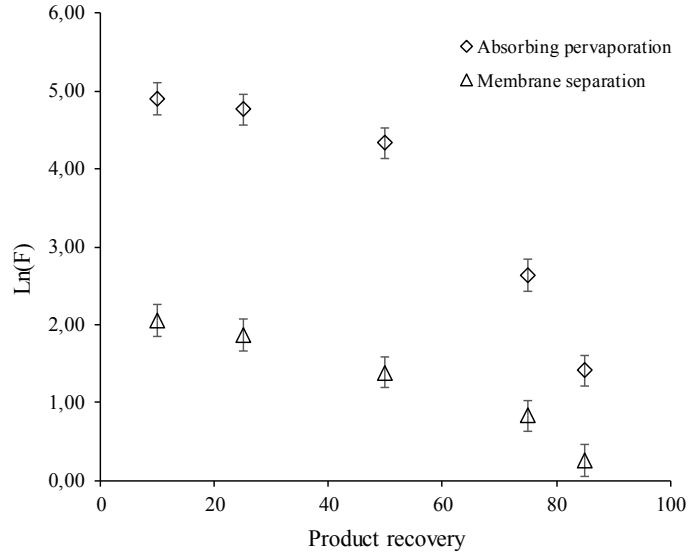

Fig. 5. Evaluation of absorbing pervaporation and membrane separation efficiency during separation of NH_3/H_2 gas mixture.

It is important to note, that trends, illustrated by graphs are similar for all studied systems and increas in productivity decreases the separation efficiency. That system behaviour easily explained by two factors: limitation of absorbent ability to sorb the ammonia and the membrane permeability. As the permeate is continuously refreshed with sweep gas, the concentration gradient through the membrane is maximal and constant. And the membrane-liquid absorbent system provides the maximal permeate flow rate as it is possible for chosen conditions (pressure, temperature, active membrane area etc.). Therefore, to achieve the balance in product purity vs productivity the system optimisation is required.

The gas mixture separation efficiency using PEG-400 aqueous solutions with various compositions in dependence on process productivity was performed. The results shown in Fig. 6 and Fig. 7. As it is seen from grapghs the absorbing pervaporation technique always outperforms traditional membrane gas separation method, and the increase in water content leads to increase in separation efficiency. This is due to the high solubility of the target component compared to the rest of the gases, with the corresponding absorbent, and the realization of the multiplicative separation effect. It is important to note that obtained results well correlate with results achieved in single gases permeability test and forms similar trends.

The selectivity of the absorbing pervaporation process is mainly determined by the absorbent ability to solve one component and not to interact with others, in addition, the selectivity of the membrane also contributes to the separation process. Thus, gases with low solubility in water are well separated from ammonia, which

provides high selectivity of the ammonia/nitrogen and ammonia/hydrogen systems. It should be noted that this process will not demonstrate high separation efficiency for gas pairs with similar solubility in water, since in this case the selectivity of the process will be determined only by the membrane selectivity.

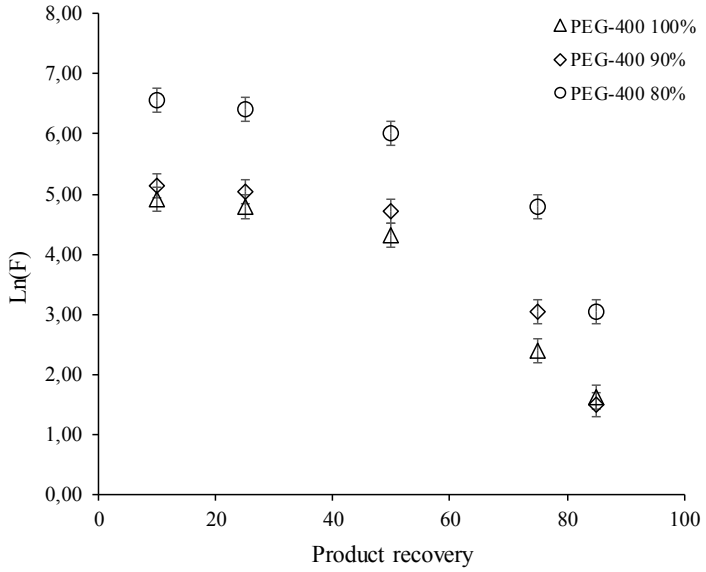

Fig. 6. Evaluation of absorbing pervaporation separation efficiency using PEG-400 aqueous solutions with various compositions during the separation of NH_3/N_2 gas mixture.

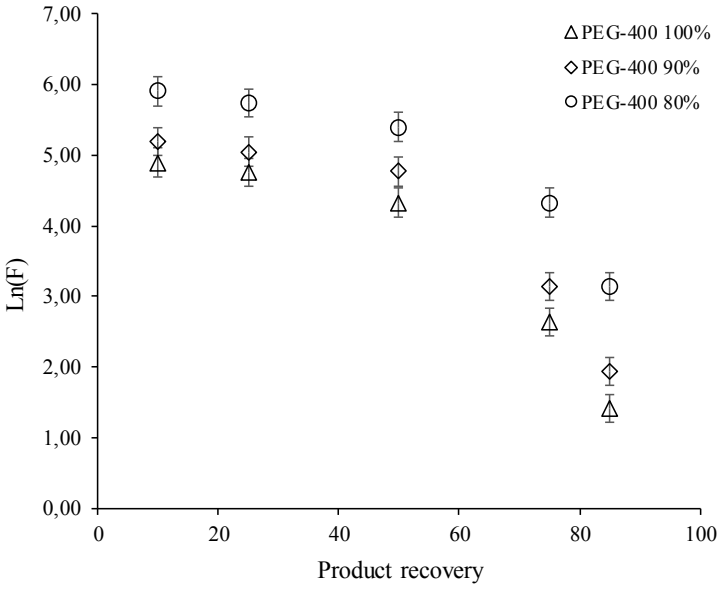

Fig. 7. Evaluation of absorbing pervaporation separation efficiency using PEG-400 aqueous solutions with various compositions during the separation of NH_3/H_2 gas mixture.

CONCLUSIONS

In current work the appliance of the absorbing pervaporation technique in process of ammonia recovery is studied experimentally, taking into account the engineering aspects (separation cell configuration, technological scheme, analytical support etc.).

A detailed experimental evaluation and comparison with conventional membrane gas separation method during the ammonia recovery from binary gas mixtures is performed.

The influence of liquid absorbent composition, that is PEG-400 content in aqueous solutions, on separation efficiency is studied experimentally.

It was clearly demonstrated that the absorbing pervaporation technique may offer a promising perspectives for ammonia recovery process, where an improved separation performance is of great importance. Nevertheless, more rigorous parametric optimization strategy has to be developed for this technique in order to quickly, efficiently identify the best set of operating parameters for a given system, and target performance.

ACKNOWLEDGEMENTS

This work was supported by the Russian Science Foundation (grant no. 17-79-20286).

REFRENCES

[1] Vorotyntsev I. V., Shablykin D.N., Drozdov P.N., Trubyanov M.M., Petukhov A.N., Battalov S. V., Separation of ammonia-containing gas mixtures in a one-compressor multistage membrane apparatus, *Pet. Chem.* 2017, 57, 172–181, DOI:10.1134/S0965544116110153

[2] Vorotyntsev V.M., Drozdov P.N., Vorotyntsev I. V., Manokhina S.N., Knysh S.S., Fine purification of silane for removal of chlorosilanes by membrane gas separation, *Pet. Chem.* 2013, 53, 627–631, DOI:10.1134/S0965544113080161

[3] Vorotyntsev V.M., Drozdov P.N., Vorotyntsev I. V., Pimenov O.A., Separation and concentration of a low-penetrating impurity by membrane gas separation, *Pet. Chem.* 2012, 52, 631–635, DOI:10.1134/S0965544112080129

[4] Trubyanov M.M., Drozdov P.N., Atlaskin A.A., Battalov S.V., Puzanov E.S., Vorotyntsev A.V., Petukhov A.N., Vorotyntsev V.M., Vorotyntsev I.V., Unsteady-state membrane gas separation by novel pulsed retentate mode for improved membrane module performance: Modelling and experimental verification, *J. Memb. Sci.* 2017, 530, 53-64, DOI:10.1016/j.memsci.2017.01.064

[5] Akhmetshina A.A., Davletbaeva I.M., Grebenschikova E.S., Sazanova T.S.,

Petukhov A.N., Atlaskin A.A., Razov E.N., Zaripov I.I., Martins C.F., Neves L.A., Vorotyntsev I. V., The Effect of Microporous Polymeric Support Modification on Surface and Gas Transport Properties of Supported Ionic Liquid Membranes., *Membranes*, 2015, 6, DOI:10.3390/membranes6010004

[6] Akhmetshina A.I., Gumerova O.R., Atlaskin A.A., Petukhov A.N., Sazanova T.S., Yanbikov N.R., Nyuchev A.V., Razov E.N., Vorotyntsev I.V., Permeability and selectivity of acid gases in supported conventional and novel imidazolium-based ionic liquid membranes, *Sep. Purif. Technol*., 2017, 176, DOI:10.1016/j.seppur.2016.11.074

[7] Davletbaeva I.M., Nurgaliyeva G.R., Akhmetshina A.I., Davletbaev R.S., Atlaskin A.A., Sazanova T.S., Efimov S.V., Klochkov V.V., Vorotyntsev I.V., Porous polyurethanes based on hyperbranched amino ethers of boric acid, *RSC Adv.*, 2016, 6, DOI:10.1039/C6RA21638B

[8] Marcu A., Stoefs W., Tuokko K., Egenhofer C., Renda A., Simonelli F., Genoese F., Storti E., Drabik E., Hähl T., Overgaag M., Grave K., Koper M., Luchetta G., Freudenthaler M., Bolognini A., *Composition and drivers of energy prices and costs: case studies in selected energy-intensive industries FINAL REPORT*, 2016

[9] Zhang J., Liu L., Huo T., Liu Z., Zhang T., Wei X., Absorption of dilute sulfur dioxide in aqueous poly-ethylene glycol 400 solutions at T = 308.15 K and p = 122.60 kPa, *J. Chem. Thermodyn.*, 2011, 43, 1463–1467, DOI:10.1016/J.JCT.2011.04.016

[10] Zhang N., Zhang J., Zhang Y., Bai J., Wei X., Solubility and Henry's law constant of sulfur dioxide in aqueous polyethylene glycol 300 solution at different temperatures and pressures, *Fluid Phase Equilib.,* 2013, 348, 9–16, DOI:10.1016/J.FLUID.2013.03.006

[11] Vorotyntsev I.V., Atlaskin A.A., Trubyanov M.M., Petukhov A.N., Gumerova O.R., Akhmetshina A.I., Vorotyntsev V.M., Towards the potential of absorbing pervaporation based on ionic liquids for gas mixture separation, *Desalin. Water Treat.*, 2017, 75, DOI:10.5004/dwt.2017.20400

[12] Vorotyntsev I. V., Drozdov P.N., Shablikin D.N., Gamajunova T. V., Ammonia separation and purification by absorbing pervaporation, *Desalination*, 2006, 200, 379–380, DOI:10.1016/j.desal.2006.03.382

[13] Barrer R.M., Rideal E.K., Permeation, diffusion and solution of gases in organic polymers, *Trans. Faraday Soc.*, 1939, 35, 628, DOI:10.1039/tf9393500628

[14] Daynes H.A., The Process of Diffusion through a Rubber Membrane, *Proc. R. Soc. A Math. Phys. Eng. Sci.*, 1920, 97, 286–307, DOI:10.1098/rspa.1920.0034

[15] Trubyanov M.M., Mochalov G.M., Vorotyntsev I. V., Vorotyntsev A. V.,

Suvorov S.S., Smirnov K.Y., Vorotyntsev V.M., An improved back-flush-to-vent gas chromatographic method for determination of trace permanent gases and carbon dioxide in ultra-high purity ammonia, *J. Chromatogr. A.*, 2016, 1447, 129–134, DOI:10.1016/j.chroma.2016.04.020

[16] Vorotyntsev V.M., Mochalov G.M., Matveev A.K., Malyshev A. V., Vorotyntsev I. V., Determination of Trace Impurities of H2, O2, Ar, N2, CO, CO2, and Hydrocarbons in High-Purity Monosilane by Gas Chromatography, *J. Anal. Chem.*, 2003, 58, 156–159, DOI:10.1023/A:1022310222267

[17] Vorotyntsev V.M., Mochalov G.M., Suvorov S.S., Shishkin A.O., Gas-chromatographic determination of the impurity composition of permanent gases, methane, carbon monooxide, and carbon dioxide in high-purity monogermane, *J. Anal. Chem.,* 2010*,* 65, 634–639, DOI:10.1134/S1061934810060146

[18] Vorotyntsev V.M., Drozdov P.N., Vorotyntsev I. V., Mathematical modeling of the fine purification of gas mixtures by absorption pervaporation, *Theor. Found. Chem. Eng.* 2011, 45, 180–184, DOI:10.1134/s0040579511020163

[19] Vorotyntsev V.M., Drozdov P.N., Kolotilov E.Y., Gas mixtures separation by an absorbing pervaporation method, *Desalination,* 2002, 149, 23–27, DOI:10.1016/S0011-9164(02)00686-0.

Membrane gas separation module with pulsed retentate for low-permeable component recovery

*Stanislav Battalov, Maxim Trubyanov, Egor Puzanov, Tatyana Sazanova, Pavel Drozdov, Ilya Vorotyntsev
Laboratory of Membrane and Catalytic Processes, Nanotechnology and Biotechnology Department, Nizhny Novgorod State Technical University n.a. R.E. Alekseev, Nizhny Novgorod, RUSSIA
e-mail: sv.battalov@gmail.com

Keywords*: membrane gas separation; unsteady-state operation; process intensification; separation efficiency; membrane module*

ABSTRACT

The paper presents the experimental study of a novel unsteady-state membrane gas separation approach for recovery of a slow-permeant component in the membrane module with periodical retentate withdrawals. The case study consisted in the separation of binary test mixtures based on the fast-permeant main component (N_2O, C_2H_2) and the slow-permeant impurity (1%vol. of N_2) using a radial counter-current membrane module. It has been shown that the novel semi-batch withdrawal technique allows to intensify the separation process and provides up to 40% increase in separation efficiency compared to a steady-state operation of the same productivity.

INTRODUCTION

A specific part of modern engineering approaches to membrane gas separation is focused on the development and optimization of unsteady-state operating conditions for the enhancement of the separation performance [1–5]. It is known that transient regimes could give a considerable increase in separation efficiency compared to a steady-state operation, however, at the expense of a loss in productivity [1]. Recently it has been shown that novel pulsed retentate separation approach holds great promise for the improvement of a single membrane module separation ability without productivity loss [3]. The enhancement of the separation efficiency up to 80% (depending on the membrane selectivity) was demonstrated on the example of a fast-permeant impurity removal during pulsed retentate operation in comparison with a steady-state process. Current research aims at exploring the capabilities of the novel process intensification logic for slow-permeant component recovery. The principal objective is to achieve higher separation performance of a single module by the periodical product withdrawals keeping the desired level of productivity. Such a technique constitutes the essential novelty as compared to the intensification methods considered in the literature so far [1].

In this study, the separation of two binary mixtures under unsteady-state operational conditions has been studied against the conventional steady-state separation in order to identify the influence of the operating parameters and compare the behavior of the novel separation technique both for fast-permeant impurity removal and for slow-permeant component recovery.

MATERIAL AND METHODS

The two-step semi-batch separation process with pulsed retentate was realized for the high-efficient countercurrent radial membrane module [6] through the cyclic alternation of a so-called "closed mode" operation (no product flow) [7] and a short-time product withdrawal according to the description given elsewhere [3]. The experimental setup designed for testing the performance of a steady-state and a pulsed retentate operation is shown schematically in Fig. 1.

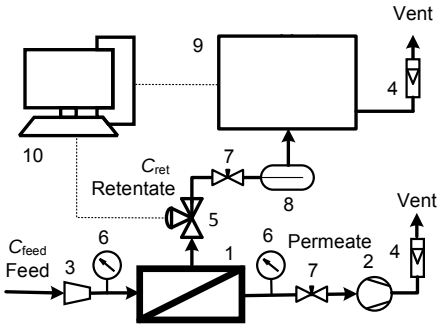

Fig. 1. Principal scheme of the experimental setup for testing the performance of a pulsed retentate operation: 1 – radial counter-current membrane module; 2 – vacuum pump; 3 – feed pressure regulator; 4 – flow meters; 5 – automated pneumatic valve; 6 – high precision pressure gauges; 7 – needle valves; 8 – mixing chamber; 9 – GC/TCD system; 10 – workstation.

The crucial component of the setup is a radial countercurrent membrane module made of AISI 316 stainless steel with PTFE sealing. Fig. 2 shows the schematic design and the principal flow scheme of the membrane module used. An automated pneumatic valve was mounted on the retentate line to carry out periodical withdrawals of impurity concentrate. The high-performance elastomeric poly(-arylate-siloxane) SILAR™ membrane with 5 μm selective layer was chosen for the case study of separation of binary test mixtures based on a fast-permeant basic component (nitrous oxide, acetylene) and a slow-permeant impurity (1 vol. % of nitrogen). Gas mixture was supplied from the cylinder to the feed side of the membrane module through a pressure regulator with a constant pressure maintained at 120 ± 5 kPa. Permeate was evacuated by a vacuum pump with a constant flow of 100 cm^3/min controlled by a flowmeter. In a steady-state operational mode the retentate flow was regulated by a needle valve in the range of 4–100 cm^3/min. The

impurity concentration variation during the separation process was monitored by the gas chromatography with thermal conductivity detector system (GC/TCD) CvetAnalitik (Dzerzhinsk, Russia). Controlled operating parameters included time of a "closed mode" operation (enrichment time), time of retentate withdrawal, flow and amount of retentate sample withdrawal, transmembrane pressure, feed and permeate flows. The system automatically executed 50 cycles of retentate withdrawals at a given set of operating parameters (opening and closing times, transmembrane pressure, feed and permeate flow rates, and retentate sample amount), and then the average composition of the retentate sample is determined by starting the GC/TCD analysis. The experimental procedure was analogous to that described in detail elsewhere [3].

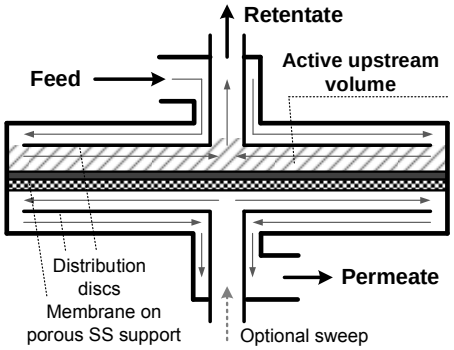

Fig. 2. Principal flow scheme of the radial countercurrent membrane module [6].

RESULTS AND DISCUSSION

According to the research aim, the behavior of the pulsed retentate mode under different operating parameters (enrichment time, time of retentate withdrawal, flow and amount of retentate sample withdrawal) was experimentally studied for slow-permeant component recovery, and its performance was compared with the conventional steady-state process.

At the first step of the cyclic process, the membrane module operates in a so-called "closed mode" implying continuous supply of the feed mixture under constant pressure, continuous evacuation of the permeate, and zero retentate flow (pneumatic valve is closed for the given period of time referred to as τ_{close}). During this step, some near-stationary state is gradually achieved in the upstream side of the membrane module, and the concentration profile is established in the active upstream volume (Fig. 2) from the feed inlet towards the retentate outlet along the membrane.

During the first set of experiments, the "closed mode" operation of the membrane module was studied in order to determine the time needed to reach the near-stationary state of the closed operation. The retentate valve closing duration was varied stepwise from 3 to 60 s at other operating parameters set as described in the experimental section. The valve opening duration for a retentate sample withdrawals

was 0.5 s. The experimental results are presented in Fig. 3 showing the value of the separation degree $F = C_{ret}/C_{feed}$ determined as the ratio of the retentate/feed slow-permeant component concentration depending on the closing time τ_{close} (enrichment time) for 9 different τ_{close}. Six to eight parallel measurements were carried out for each experimental point giving an error less that 7%. It was calculated as the uncorrected sample standard deviation according to the method described in [8].

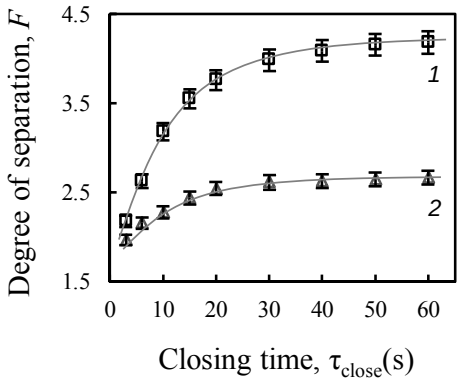

Fig. 3. Approaching a near-stationary state during the "closed mode" operation: 1 – N_2O/N_2 system; 2 – C_2H_2/N_2 system.

As it can be seen from the graph the concentration ratio in the upstream side of the membrane module gradually increases with time and approaches a stable value similarly to the total reflux operation of a batch distillation column. During the "closed mode" operation, the maximum separation degree can be achieved inside the membrane module, and the maximum slow-permeant component concentration is realized in the active upstream volume near the retentate outlet.

The small portion of this slow-permeant-enriched mixture is to be withdrawn as a retentate sample at the second step of the cyclic process when the retentate line is opened for the given period of time referred to as τ_{open} (withdrawal time). The practical active volume of the feed side available for gas separation is situated in the 1 mm gap between the distribution disc and the membrane (shaded area in Fig. 2) and equals to approximately 50 cm^3 (V_0). Fig. 4 reflects the variation of the slow-permeant component concentration depending on the retentate sample volume (V_s) withdrawn after the "closed mode" operation for 8 different V_s. The volume of the retentate sample was varied stepwise from 1.2 cm^3 to about 40 cm^3 by changing the opening duration of the retentate withdrawal valve and the withdrawal flow. The closing time period was set corresponding to the time required to reach the near-stationary state. Such experimental technique allows to estimate the concentration profile being established in the active upstream volume during the "closed mode" operation from the center ($V_s/V_0 \rightarrow 0$) to the periphery ($V_s/V_0 \rightarrow 1$). The graph shows that the

concentration of the slow-permeant component in the withdrawn sample is the highest if the (Vs/V_0) value is close to zero which means that the smallest possible retentate sample is withdrawn from the center part of the active upstream volume. Then the concentration in withdrawn samples decreases exponentially with the increase of the retentate sample amount.

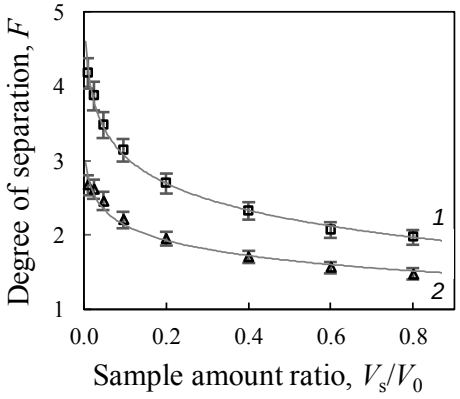

Fig. 4. The concentration of the slow-permeant component depending on the retentate sample amount: 1 – N_2O/N_2 system; 2 – C_2H_2/N_2 system.

Similar trends were obtained earlier for the case of the fast-permeant impurity removal by the same periodical retentate withdrawal technique [3]. It should be noted that the current dependencies correlate very well with the previously obtained results, but slightly less pronounced due to the fact that the membrane module used for the experiments generally exhibits lower separation efficiency for the case of concentrating the slow-permeant component in comparison with the removal of the fast-permeant impurity [6]. Nevertheless, it is of immediate interest to compare the novel semi-batch pulsed separation approach with the conventional steady-state process concerning the performance of the slow-permeant component recovery.

Since in our case the retentate flow is the target product flow enriched with the slow-permeant component, the ratio between the retentate flow (L_{ret}) and the feed flow (L_{feed}) directly reflects the process productivity. During the steady-state separation tests the retentate flow constantly goes through the sampling valve of the gas chromatograph for on-line determination of the impurity content. Therefore, it is possible to estimate the variation of the separation degree ($F = C_{ret}/C_{feed}$) against the process productivity. The obtained experimental data for the various pulsed retentate conditions were summarized in terms of separation efficiency – productivity tradeoff. Fig. 5 shows the performance of the two modes for the selected gas mixtures depending on the productivity. For the pulsed retentate operation, the time-averaged retentate flow which depends both on the opening and closing times was calculated from the experimental data on the volume of withdrawn retentate samples.

As it can be seen from the graphs, the unsteady-state operation provides enhanced separation performances observed under the decrease of L_{ret}/L_{feed} ratio, which means that just the use of a pulsed product withdrawal technique allows to improve the separation ability of the membrane module while keeping the productivity level same as for the steady-state withdrawal. The same behavior was demonstrated for the case of the fast-permeant impurity removal [3], thus the conclusion that can be drawn from the obtained results is that the novel process intensification logic is based on some universal principle of dynamic driving force increase in the module. The periodical disturbances of the near-stationary state established in the module under the "closed mode" conditions promote a higher average driving force for more intense mass transfer process. During the pulsed retentate withdrawals the concentration gradient cyclically established in the active upstream volume of the membrane module may become higher than that of a steady-state operation depending on the opening and closing time periods, sample volume, and the total cycle time. Besides that, it is possible to optimize the total cycle time for a given productivity, selecting a longer cycle time, which is desired from an operating standpoint as less frequent valve switching will be favorable for process control and operation.

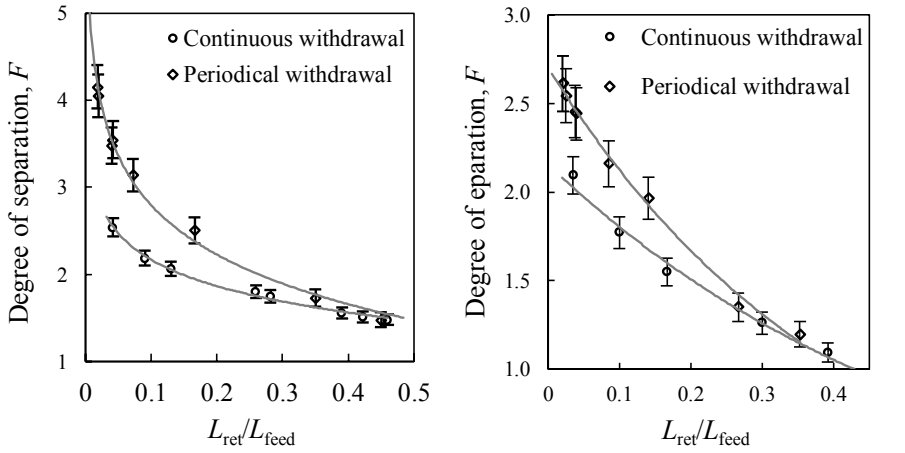

Fig. 5. Comparison of a continuous withdrawal mode and a periodical withdrawal mode in terms of productivity and efficiency during low-permeable component recovery: (left) N_2O/N_2 system; (right) C_2H_2/N_2 system.

CONCLUSIONS

The experimental study of the unsteady-state membrane gas separation process with pulsed retentate withdrawals has been done for the case of a slow-permeant component recovery showing the possibility of increasing the separation performance of the membrane module as compared to the conventional steady-state operation. The kinetics of the "closed mode" operation has been studied

experimentally as well as the dependence of the separation efficiency on the retentate withdrawals for different test systems has been obtained. The improvement of the membrane module separation ability in the pulsed retentate operation is associated with the higher driving force of unsteady-state cyclic process in which the module periodically works at a distance from the stationary-state "closed mode" condition attempting to achieve it. The enhancement of the separation efficiency obtained for the slow-permeant impurity recovery under the unsteady-state operation was up to 40% depending on the selectivity of the membrane as compared to the conventional steady-state process of the same productivity. The experimental evidence clearly shows that the periodical withdrawal technique is efficient both for the slow-permeant component recovery as well as for the fast-permeant impurity removal (according to [3]) thus providing a universal and simple way to intensify the separation process keeping the desired productivity. Much longer cycle time can be used compared to the transient permeation processes [1], which is favorable from the operational point of view. The transmembrane pressure difference is not affected in this process, consequently, there is no additional costs to increase the pressure difference.

The novel semi-batch membrane separation technique can be particularly beneficial and useful in analytical applications (impurity pre-concentration) and also may offer a series of promising perspectives for use in continuous membrane column apparatuses, comprising of both the stripping and enrichment sections to which the periodical withdrawals technique can be applied. A semi-empirical optimization model needs to be developed for evaluation of the each operating parameter contribution and identifying the best set of operating conditions for a given system and target performance.

ACKNOWLEDGEMENTS

This work was supported by the Russian Science Foundation, Project № 17-79-10464.

REFERENCES

[1] L. Wang, J.-P. Corriou, C. Castel, E. Favre, A critical review of cyclic transient membrane gas separation processes: State of the art, opportunities and limitations, J. Memb. Sci. 383 (2011) 170–188. doi:10.1016/j.memsci.2011.08.052.

[2] I.N. Beckman, A.B. Shelekhin, V.V. Teplyakov, Separation of gas mixtures in unsteady-state conditions, J. Memb. Sci. 55 (1991) 283–297. doi:10.1016/S0376-7388(00)80583-9.

[3] M.M. Trubyanov, P.N. Drozdov, A.A. Atlaskin, S. V. Battalov, E.S. Puzanov, A. V. Vorotyntsev, A.N. Petukhov, V.M. Vorotyntsev, I. V. Vorotyntsev, Unsteady-state membrane gas separation by novel pulsed retentate mode for

improved membrane module performance: Modelling and experimental verification, J. Memb. Sci. 530 (2017) 53–64. doi:10.1016/j.memsci.2017.01.064.
[4] J.-P. Corriou, C. Fonteix, E. Favre, Optimization of a pulsed operation of gas separation by membrane, AIChE J. 54 (2008) 1224–1234. doi:10.1002/aic.11443.
[5] Y. Chen, D. Lawless, X. Feng, Pressure-vacuum swing permeation: A novel process mode for membrane separation of gases, Sep. Purif. Technol. 125 (2014) 301–310. doi:10.1016/j.seppur.2014.01.053.
[6] P.N. Drozdov, Y.P. Kirillov, E.Y. Kolotilov, I. V. Vorotyntsev, High purification of gas in radial membrane element, Desalination. 146 (2002) 249–254. doi:10.1016/S0011-9164(02)00482-4.
[7] P.N. Drozdov, I. V. Vorotyntsev, Closed mode of gas-separation membrane modules, Theor. Found. Chem. Eng. 37 (2003) 491–495. doi:10.1023/A:1026046810040.
[8] G. Upton, I. Cook, A Dictionary of Statistics, Oxford University Press, 2014. doi:10.1093/acref/9780199679188.001.0001.

Influence of molecular structure on helical twist sense for liquid crystalline compounds and their mixtures

*Anna Drzewicz, Marzena Tykarska
Institute of Chemistry, Military University of Technology, Warsaw, POLAND
e-mail: anna.drzewicz@wat.edu.pl

***Keywords**: liquid crystals, SmC_A^* phase, helicoidal structure, helical twist sense*

ABSTRACT

The Gray and McDonnel theory does not work for compounds with chiral smectic liquid crystalline phase. Within one homologue series compounds with chiral center at the same type of absolute configuration and located at the same distance from the rigid core exhibit differential dependence parameters of helicoidal structure on temperature within one liquid crystalline phase. The effect of helical twist sense inversion phenomenon may be explained by the presence of different conformers promoting opposite handedness, which concentration may change with temperature. In this work types of compounds with various helicodal structure and also their mixtures have been presented.

INTRODUCTION

The helicoidal structure in the liquid crystalline molecule has been formulated, when the chiral center (for instance asymmetric carbon atom) has been presented in the structure. Such helix is characterized by two parameters. Firstly, the helical pitch, which inform about the distance at which director rotates by 360° around the normal to smectic layers. Secondly, the helical twist sense, which is defined as (+) for a right-handed twist or (-) for a left-handed twist.

The helical pitch strongly depends on temperature. For smectic chiral liquid crystalline phase with antiferroelectric properties (SmC_A^*) the value of this parameter may increase upon heating or cooling or increase for lower temperatures and decrease for higher temperatures [1-3]. On the other hand the helical pitch independs of temperature for smectic chiral liquid crystalline phase with ferroelectric properties (SmC^*) [4,5].

According to the Gray and McDonnel theory [6] the type of helical handedness depends on the chiral center (especially on the type of absolute configuration of the chiral carbon atom and its position related to the rigid core). Right-handed helix is formulated, when the carbon atom of **R** (**S**)-type of absolute configuration is in the **o**dd (**e**ven) position from the rigid core of molecule – **Rod** (**Sed**). In contrast the left-handed helix has been obtained for **R** (**S**)-type of absolute configuration of chiral carbon atom in the **e**ven (**o**dd) position – **Rel** (**Sol**). This theory was upgraded by Goodby and Chin who examined influence of the spontaneous

polarization on the helical twist sense [7]. The helical handedness may change during the transition from one phase to another for the same substance [8,9] or within one phase [10-12]. The effect of helical twist sense inversion phenomenon may be explained by the presence of different conformers promoting opposite handedness, which concentration may change with temperature [13-15].

In this paper the influence of the length of non-chiral alkyl chain on type of helicoidal structure for chosen compounds and also the behavior of helix in the mixtures have been examined.

MATERIALS AND METHODS

Liquid crystalline compounds with general acronym **3FmHF** (where **3F** means C_3F_7 group, **m** is the number of methylene groups in the non-chiral terminal chain, **H** and **F** are hydrogen and fluorine atoms in the benzene ring), with S-type of absolute configuration and formed SmC_A^* and/or SmC^* phases, have been examined. The structure of them is presented in Fig. 1.

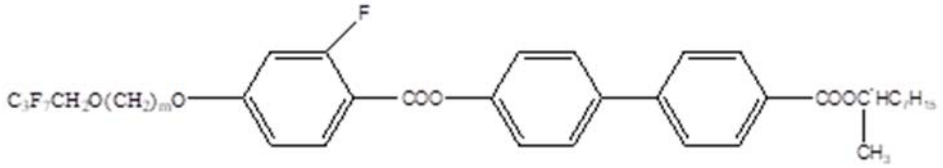

Fig. 1. The general structure of examined compounds, where m = 3,5,7.

The Olympus BX51 polarizing microscope in conjunction with Linkam THMS-600 heating stage and Linkam CI94 temperature controller to record phase transition temperatures has been used. The measurements in both cooling and heating cycles with a temperature rate 1°C/min have been realized. The values of phase transition temperatures have been also determined using DSC Setaram 141 microcalorimeter in both cooling and heating cycles with scan rate 2°C/min.

The method based on the selective light reflection phenomenon to determine the helical pitch using the Shimadzu UV-Vis-NIR spectrometer with AMLWU7 temperature controller and Peltier element for changing temperature has been used [16-18]. The measurements in the range of wavelength: 360-3000 nm and in the range of temperature: 2-110°C have been realized. The value of wavelength for the minimum of transmission must be divided by average refractive index (which is equal to 1.5 [19]) to obtain the value of helical pitch.

The polarimetry method using OptaTech MPM-349 polarizing microscope in conjunction with Linkam THMSE-600-2 heating stage and Linkam T95-STD temperature controller to determine the helical twist sense has been used. The measurements were carried out at different temperatures for SmC^* and SmC_A^* phases.

There are two methods to determine the temperature of helical twist sense inversion. The direct method involves the comparison of transmittance at different

temperatures. At inversion temperature, when the helix is completely unwinded, the line in the spectrum has the lowest transmission. A more precise indirect method uses the results of the measurement of the helical pitch [3]. At the inversion temperature, the helical pitch goes to infinity, so the inverse of the helix (1/p) goes to zero. Therefore, the inversion temperature of the helix determines the zero point of the line describing the temperature dependence on the inverse of helical pitch led through the measurement points, where values for the right-handed structures are marked with the sign "+", and for the left-handed structures with the sign "-". This method of determining the inversion temperature is illustrated on Fig. 2

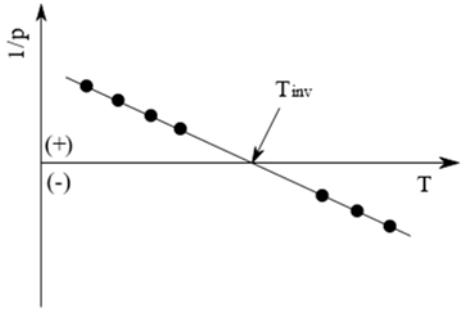

Fig. 2. The scheme of indirect method of inversion temperature determination.

RESULTS

The results of measurements of phase transition temperatures and the parameters of helicoidal structure for compounds series 3FmHF and their mixtures have been presented.

Phase transition temperatures

All of examined compounds have SmC_A^* phase in the broad range of temperatures. The compounds with longer alkyl chain (m = 5 or 7) have also SmC^* phase. The values of phase transition temperatures obtained during microscopic and DSC measurements in Tab. 1 have been showed.

Tab.1. The phase transition temperatures for examined compounds.

3FmHF	Cr	T_{mic} [°C] T_{DSC} [°C]	SmC_A^*	T_{mic} [°C] T_{DSC} [°C]	SmC^*	T_{mic} [°C] T_{DSC} [°C]	SmA	T_{mic} [°C] T_{DSC} [°C]	Iso
3F3HF	*	45.4	*	84.7	-	-	-	-	*
		43.4		82.5		-		-	
3F5HF	*	35.0	*	90.3	*	96.0	-	-	*
		34.1		86.2		91.2		-	
3F7HF	*	34.0	*	85.8	*	95.8	*	97.7	*
		32.8		82.2		92.4		93.7	

T_{mic} [°C] is the temperature obtained from microscopic measurements in the cooling cycle; T_{DSC} [°C] is the temperature from DSC method

Helicoidal structure of compounds

On Fig. 3 the helical pitch dependences upon temperature for examined compounds have been presented. For compound with three methylene groups in the alkyl chain (m=3) the values of helical pitch in the SmC_A^* phase increase upon heating and the right-handed helix has been observed (Fig. 3a). On the other hand for compound 3F7HF in the SmC_A^* phase the helical pitch increase upon cooling with left-handed helix and in the SmC^* phase this parameter does not change with temperature (Fig. 3c). Moreover for compound 3F5HF the helical twist sense inversion phenomenon has been registered with the inversion temperature (obtained for the spectrum line with the minimum of transmission) equal to 65°C (Fig. 3b). The same temperature has been obtained as the zero point for the indirect method (Fig. 3d).

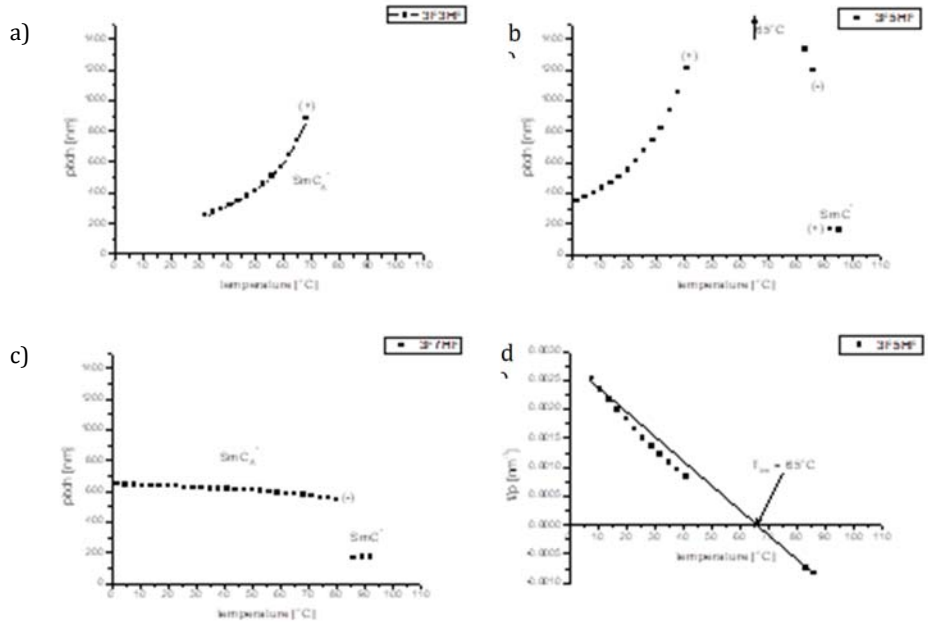

Fig. 3. The helical pitch dependence on temperature for: a) 3F3HF; b) 3F5HF; c) 3F7HF compounds and d) the inverse of helical pitch dependence on temperature for 3F5HF compound.

Phase transition temperatures and helicoidal structure of mixtures

The mixtures from examined compounds have been prepared. These compounds are mixed in the SmC_A^* phase without restrictions. The eutectic point occurs in 0.5 mole fraction for 3F7HF+3F3HF mixture.

For the mixture of compounds with different helical handedness (3F7HF+3F3HF) the left-handed helix is unwinded with the addition of 3F3HF compound (Fig. 4). The inversion of helical twist sense for the 0.6 and 0.8 mole fraction has been observed.

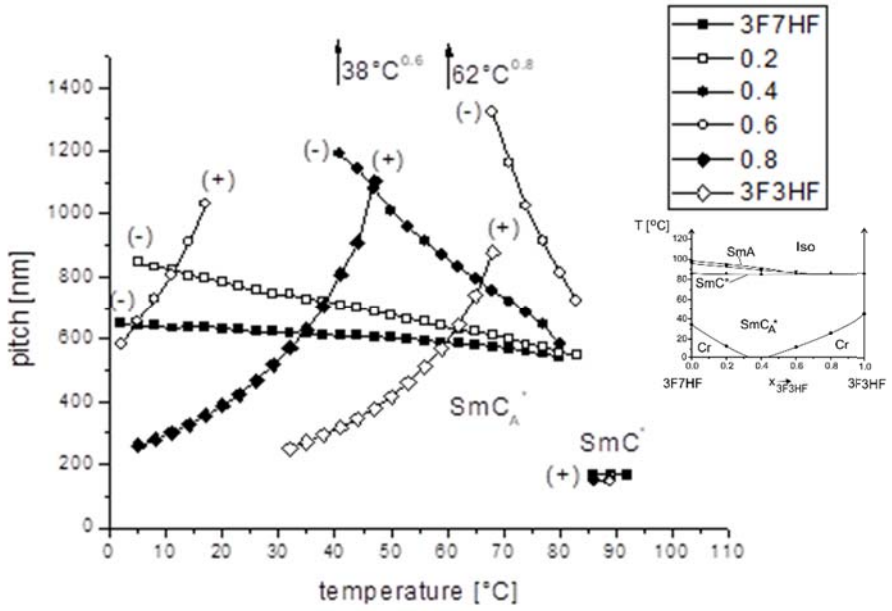

Fig. 4. The helical pitch dependence on temperature and the phase transition diagram for mixture 3F7HF+3F3HF.

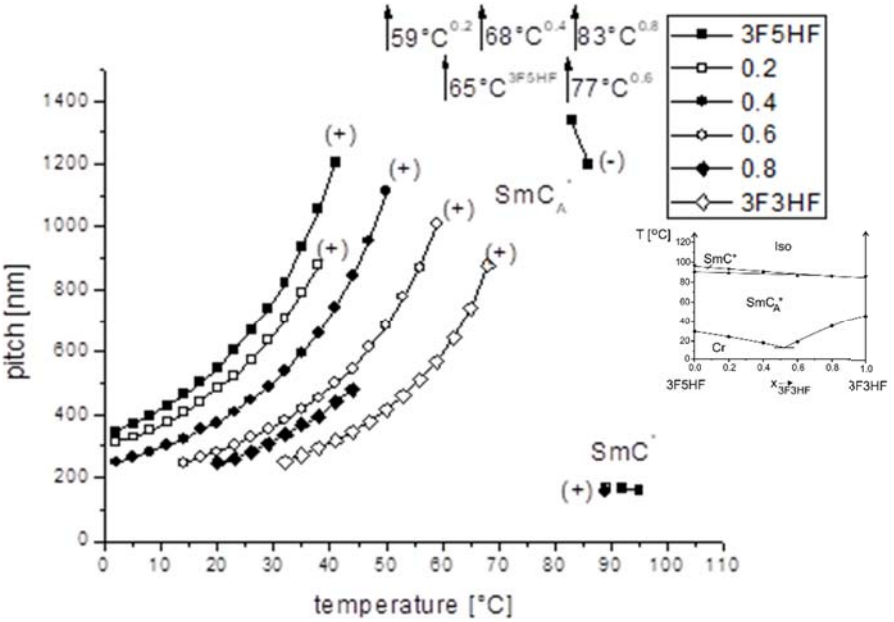

Fig. 5. The helical pitch dependence on temperature and the phase transition diagram for mixture 3F5HF+3F3HF.

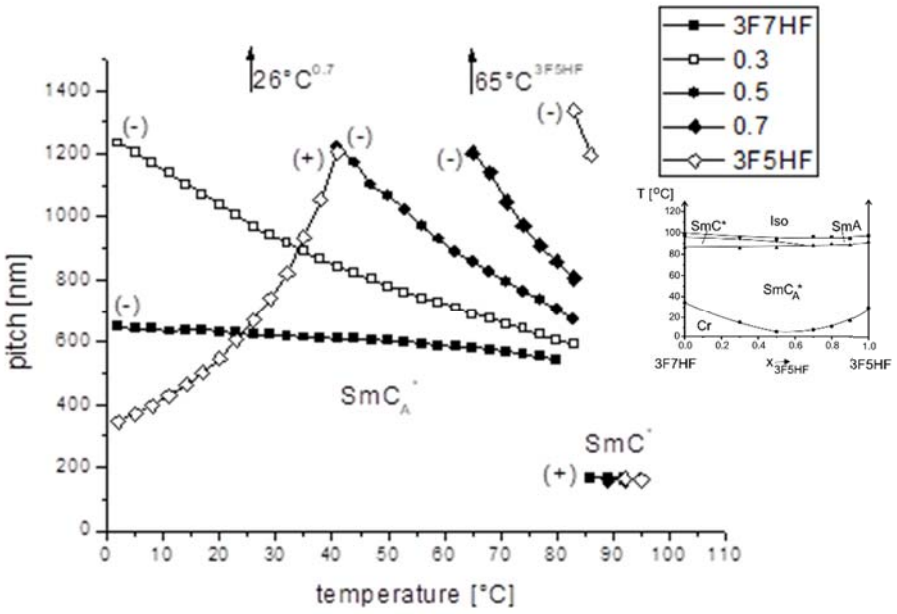

Fig. 6. The helical pitch dependence on temperature and the phase transition diagram for mixture 3F7HF+3F5HF.

For the mixture of compounds when one of them has the inversion of helical handedness and one of them has right-handed helix (3F5HF+3F3HF) this helix winded with the addition of 3F3HF compound (Fig. 5). The inversion of helical twist sense for all mole fractions has been observed.

For the mixture of compounds when one of them has the inversion of helical handedness and one of them has left-handed helix (3F7HF+3F5HF) this helix unwinded with the addition of 3F5HF compound (Fig. 6). The inversion of helical twist sense for 0.7 mole fraction has been observed.

CONCLUSIONS

The compounds and their mixtures of 3FmHF (m=3,5,7) series have been examined. For the compound with the shortest non-chiral alkyl chain (m=3, right-handed helix) the different helical pitch dependence on temperature in SmC_A^* phase have been registered than for compound with the longest non-chiral alkyl chain (m=7, left-handed helix). Therefore, for compound with five methylene groups two types of helical handedness in SmC_A^* phase have been observed. In the SmC^* phase for all compounds the helical pitch independents of temperature.

In the mixtures of compounds with different type of helical twist handedness the helix may be winded or unwinded with the addition of one compound to another.

Moreover in this case for mixtures the helical twist sense inversion phenomenon has been observed.

ACKNOWLEDGEMENTS
This work was supported by RMN 08/687.

REFERENCES

[1] Li J., Takezoe H., Fukuda A., Novel Temperature Dependences of Helical Pitch in Ferroelectric and Antiferroelectric Chiral Smectic Liquid Crystals, *Jpn. J. Appl. Phys.*, 1991, 30, 3, 532-536, DOI: 10.1143/JJAP.30.532

[2] Tykarska M., Czerwiński M., Miszkurka J., Influence of temperature and terminal chain length on helical pitch in homologue series nH6Bi, *Liq. Cryst.*, 2010, 37, 4, 487-495, DOI: 10.1080/02678291003686880

[3] Tykarska M., Czerwiński M., The inversion phenomenon of the helical twist sense in antiferroelectric liquid crystal phase from electronic and vibrational circular dichroism, *Liq. Cryst.*, 2016, 43, 4, 462-472, DOI: 10.1080/02678292.2015.1118769

[4] Glogarova M., Novotná V., Kašpar M., Hamplová V., Unusual behaviour of binary mixtures of ferroelectric and antiferroelectric liquid crystal with three chiral centers, *Opto-Electron. Rev.*, 2002, 10, 47-52, DOI: 10.1117/12.472131

[5] Panov V.P., Seomun S.S., Shytkov N.M., Vij J.K., Nguyen H.T., The Biaxiality of the Chiral Smectic Subphases in Very Thin Freestanding Films, *Ferroelectrics*, 2002, 278, 47-55, DOI: 10.1080/00150190214473

[6] Gray G.W., McDonnell D.G., The Relationship Between Helical Twist Sense, Absolute Configuration and Molecular Structure for Non-Sterol Cholesteric Liquid Crystals, *Mol. Cryst. Liq. Cryst.*, 1976, 34, 9, 211-217, DOI: 10.1080/15421407708083708

[7] Goodby J.W., Chin E., Helical Twist and Spontaneous Polarization Direction in Ferroelectric Smectic Liquid Crystals, *J. Am. Chem. Soc.*, 1986, 108, 4736-4742, DOI: 10.1021/ja00276a009

[8] Chandani A., Górecka E., Ouchi Y., Takezoe H., Fukuda A., Antiferroelectric Chiral Smectic Phases Responsible for the Tristable Switching in MHPOBC, *Jpn. J. Appl. Phys.*, 1989, 28, 7, 1265-1268, DOI: 10.1143/JJAP.28.L1265

[9] Seomun S., Gouda T., Takanishi Y., Ishikawa K., Takezoe H., Bulk optical properties in binary mixtures of antiferroelectric liquid crystal compounds showing V-shaped switching, *Liq. Cryst.*, 1999, 26, 2, 151-161, DOI: 10.1080/026782999205281

[10] Tykarska M., Czerwiński M., Żurowska M., The temperature and concentration dependence of helical pitch in the mixtures of antiferroelectric compounds with

the opposite helical twist sense, *Liq. Cryst.*, 2011, 38, 5, 561-566, DOI: 10.1080/02678292.2011.558217

[11] Takezoe H., Lee J., Ouchi Y., A. Fukuda, Ferrielectric Chiral Smectic Liquid Crystalline Phase, *Mol. Cryst. Liq. Cryst.*, 1991, 202, 85-90, DOI: 10.1080/00268949108035660

[12] Kašpar M., Górecka E., Sverenyák H., Hamplová V., Glogarová M., Pakhomov S.A., Helix twist inversion in ferroelectric liquid crystals with one chiral center, *Liq. Cryst.*, 1995, 19, 5, 589-594, DOI: 10.1080.02678299508031072

[13] Slaney A., Nishiyama I., Styring P., Goodby J.W., Twist Inversion in a Cholesteric Material containing a Single Chiral Center, *J. Mater. Chem.*, 1992, 2, 8, 805-810, DOI: 10.1039/jm9920200805

[14] Cieplak B., Kocot A., Merkel K., Wrzalik R., Praniuk R., Dielectric and Optical Studies of FLC Sample with Helix Inversion, *Ferroelectrics*, 2004, 311, 83-95, DOI: 10.1080/00150190490511275

[15] Watson M.J., Horsburgh M.K., Goodby J.W., Takatoh K., Slaney A.J., Patel J.S., Styring P., A phenomenological approach to the inversion of the helical twist sense in the chiral nematic phase, *J. Mater. Chem.*, 1998, 8, 9, 1963-1969, DOI: 10.1039/a804413i

[16] Kurp K., Tykarska M., Drzewicz A., Lapanik V., Sasnouski G., Effect of ferroelectric liquid crystalline quaterphenyl structure and handedness on helical pitch length in bicomponent mixtures, Liquid Crystals, 2016, DOI: 10.1080/02678292.2016.1226975

[17] Drzewicz A., Tykarska M., Szala M., Żurowska M., Wpływ struktury molekularnej na strukturę helikoidalną i na charakter widm NMR chiralnych estrów ciekłokrystalicznych, Biuletyn WAT, 2017, LXVI, 2, 25-35, DOI: 10.5604/01.3001.0010.1887

[18] Drzewicz A., Tykarska M., Żurowska M., Wpływ długości łącznika alkilowego oraz podstawienia atomami fluoru na charakter widm w podczerwieni chiralnych estrów ciekłokrystalicznych, Biuletyn WAT, 2017, LXVI, 3, 63-74, DOI: 10.5604/01.3001.0010.5391

[19] Raszewski Z., Kędzierski J., Perkowski P., Piecek W., Rutkowska J., Kłosowicz S., Zieliński J., Refractive Indices of the MHPB(H)PBC and MHPB(F)PBC Antiferroelectric Liquid Crystals, *Ferroelectrics*, 2002, 276, 289-300, DOI: 10.1080/00150190214411

DSC and helix parameters measurements for chiral smectic liquid crystalline mixtures

*Anna Drzewicz, Marzena Tykarska
Institute of Chemistry, Military University of Technology, Warsaw, POLAND
e-mail: anna.drzewicz@wat.edu.pl

***Keywords**: liquid crystals, SmC_A^* phase, SmC^* phase, helicoidal structure, differential scanning calorimetry*

ABSTRACT

The chiral esters with three ring rigid core and terminal chains: one 1-methylheptyloxycarbonyl group and another one 1-(1,1,1-trifluoromethyl)-heptyloxycarbonyl group were studied. These compounds are liquid crystals having chiral smectic phases with ferroelectric (SmC^*) and antiferroelectric (SmC_A^*) properties. The phase transition temperatures and enthalpies received by polarized optical microscopy and differential scanning calorimetry, respectively, are given. The measurements of helical pitch were based on a selective light reflection phenomenon.

In this work the influence of molecular structure of chiral smectic liquid crystals and their mixtures on the helicoidal structure and DSC spectra have been presented.

INTRODUCTION

Helix is one of the most representative examples of chiral forms occurred in nature. It is characterized by two basic parameters: the helical pitch and the helical twist sense. The helical pitch is the distance at which director rotates 360° around the normal to layers. The helical twist sense is defined as positive for a right-handed helix and negative for a left-handed helix.

According to Gray and McDonnel theory [1] compounds with S-type of absolute configuration of chiral center and even position from the rigid core (Se) as well as R-type of absolute configuration and odd position (Ro) have right-handed helical twist sense. While left-handed helix is obtained by compounds with Re and So combination.

We have recently reported [2] that in the SmC_A^* phase for compounds characterizing by the same type of chiral center (the same type of absolute configuration and the same position related to the rigid core), the helical pitch increase with temperature and the helix is right-handed (for compound with short alkyl chain, m=3) or the helical pitch increase upon cooling and the helix is left-handed (for compound with long alkyl chain, m=7). Nonetheless for compound with five methylene groups in the alkyl chain the inversion of helical twist sense phenomenon has been observed.

Moreover for the same compounds the temperature dependence of helical pitch is different in various smectic phases. For example Panov et al. [3] have presented that the value of helical pitch of the SmC_A^* phase is constant and independent of temperature changes. On the other hand results of Li et al. [4] measurements show strongly dependence helical pitch upon temperature. In comparison, in the SmC^* phase the helical pitch usually does not change with temperature [5]. Lagerwall et al. [6] have given the theoretical explanation why the helical structure of SmC_A^* and SmC^* phases have opposite handedness in the same compound.

The aim of this work is to present results of DSC measurements of systems with helical twist sense inversion phenomenon. The changes of helical pitch value and helix handedness in the SmC_A^* phase upon temperature are reported.

MATERIALS AND METHODS

Chiral smectic liquid crystalline esters (Fig. 1) with general acronym **3FmXY** (where **3F** means C_3F_7 fragment, **m** is the number of methylene groups in the non-chiral alkyl chain, **X** and **Y** are hydrogen or fluorine atoms in the benzene ring) have been examined.

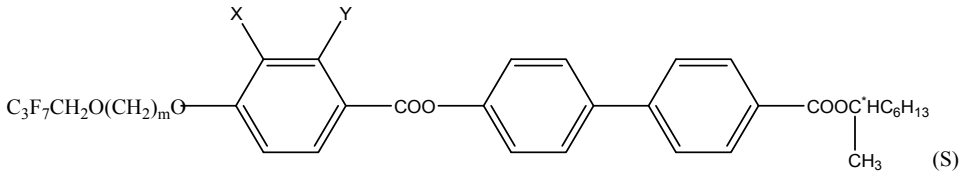

Fig. 1. The general structure of examined compounds, where m = 4,5,7; X or Y = H or F.

The measurements of phase transitions temperatures by the polarizing optical microscope Olympus BX51 with the heating stage Linkam THMS-600 and the temperature controller Linkam CI94 have been made.

The differential scanning microcalorimeter DSC 141 SETARAM to perform the calorimetric measurements has been used. The measurements were carried out in a heating and cooling process. Both scan rates of heating and cooling were constant and equal to 2°C/min. For measuring temperatures and enthalpies of phase transitions the same weighed amounts for all samples were used with a mass of about 10 mg each, while for measuring the specific heat capacities the weighed amounts with a mass of about 40 mg each were used. The specific heat capacity was determined by the continuous method with a standard sample (aluminium oxide, α-Al_2O_3). The excess specific heat capacity was calculated as the difference between the value of specific heat capacity for SmC_A^* to SmC^* transition from DSC measurement and the value of specific heat capacity for this transition from theoretically calculations. The

specific heat capacity for pure compounds is zero. The calculations of value of excess enthalpy are analogous as the calculations of excess specific heat capacity.

The helical pitch measurements are based on the selective light reflection phenomenon [7]. The spectrophotometer Shimadzu UV-Vis-NIR in the range of 360-3000 nm was used to measure the light transmission and to determine the value of helical pitch. The tested compounds were placed on a glass plate with an oriented N-cethyl-N,N,N-trimethylammonium bromide (CTAB) layer to ensure the homeotropic alignment. The temperature range of measurement was 2-110°C and for changing the temperature the temperature controller MLW U7 with Peltier element was used. The results were obtained only during cooling process. The result of the measurement is the wavelength of selectively reflected light λ_s as a function of temperature. According to the Bragg's law the values of λ_s should be divided by double refractive index for SmC^* phase or by refractive index for SmC_A^* phase (the value of average refractive index for this class of materials is about 1.5 [8]) to obtaining the values of helical pitch.

The helical twist sense of chiral phases was based on a polarimetry technique for chiral compounds. The aligned sample was placed between crossed polarizers and the top polarizer was rotated relative to the bottom one. According to Shtykov and Vij [9] a clockwise rotation of analyzer indicates a dextro or left-handed helix and anticlockwise rotation indicates a laevo or right-handed helix when λ_s is bigger than used light.

RESULTS

The phase transitions temperatures, the parameters of helicoidal structure and DSC results of measurements for compounds series 3FmXY and their mixtures have been presented.

Phase transition temperatures

Each of examined compounds have SmC_A^* and SmC^* phases. Compounds with four methylene group in the alkyl chain and with two hydrogen or two fluorine atoms as X or Y symbols (3F4HH and 3F4FF) do not have SmA phase. The values of phase transition temperatures obtained from polarizing microscope and DSC measurements as well as the values of enthalpies for tested compounds in Tab. 1 have been presented.

Tab.1. The phase transition temperatures and enthalpies for examined compounds [10].

3Fm XPhY	Cr	T_{mic} [°C] T_{DSC} [°C] *ΔH [kJ/mol]*	SmC_A^*	T_{mic} [°C] T_{DSC} [°C] *ΔH [kJ/mol]*	SmC^*	T_{mic} [°C] T_{DSC} [°C] *ΔH [kJ/mol]*	SmA	T_{mic} [°C] T_{DSC} [°C] *ΔH [kJ/mol]*	Iso
3F4H PhH	*	62.7 60.3 29.1	*	108.4 109.5 0.06	*	130.5 130.0 6.9	-		*
3F7H PhH	*	60.0 57.8 32.0	*	117.8 116.3 0.058	*	122.1 120.4 1.03	*	124.5 123.0 3.84	*
3F5H PhF	*	- 28.1 34.9	*	99.0 97.0 0.1	*	100.2 - -	*	101.0 99.0 5.4	*
3F7H PhF	*	- 25.1 13.1	*	96.3 94.7 0.072	*	100.9 99.2 0.78	*	102.7 100.9 3.7	*
3F4F PhH	*	75.1 73.1 28.0	*	96.9 95.5 0.044	*	114.6 113.4 1.46	*	115.6 114.5 4.1	*
3F7F PhH	*	- 37.4 25.6	*	103.7 103.1 0.065	*	106.0 104.3 0.77	*	110.7 109.1 3.8	*
3F4F PhF	*	79.4 81.45 27.3	*	87.6 - -	*	104.0 101.9 5.4	-		*
3F7F PhF	*	- 50.2 22.0	*	106.3 104.6 0.044	*	107.6 105.9 0.68	*	110.8 109.1 3.8	*

T_{mic} [°C] is the temperature obtained from microscope measurements in the cooling cycle; T_{DSC} [°C] is the temperature from DSC method; ΔH [kJ/mol] is the enthalpy.

Helix parameters of compounds and their mixtures

The plot of the helical pitch as a function of temperature for HH mixture is presented on Fig. 2a. The right-handed helix is unwinded with the addition of compound 3F7HH with longer alkyl chain (m=7). Moreover the addition of this compound causes the inversion of helicoidal structure in the mixtures. The signals from left-handed helix for mixtures and for SmC^* phase could be out of the temperature range of measurement.

The similar situation for SmC_A^* phase is observed for the FH mixture, which plot is presented on Fig. 2c. In the SmC^* phase the helical pitch does not depend on the temperature and it is created the right-handed helix.

On Fig. 2b is presented the plot of HF mixture. The inversion of helical pitch is causes by compound with shorter alkyl chain (m=5). In the SmC_A^* the left-handed helix is unwinded with increasing the content of compound 3F7HF. The characteristic of right-handed helix in the SmC^* phase is independent of temperature.

For the FF mixture, which plot is presented on Fig. 2d, we observe the same situation as earlier. The signals from mixtures in the SmC_A^* phase are not visible, because of the appearance of them out of the range of spectrometer.

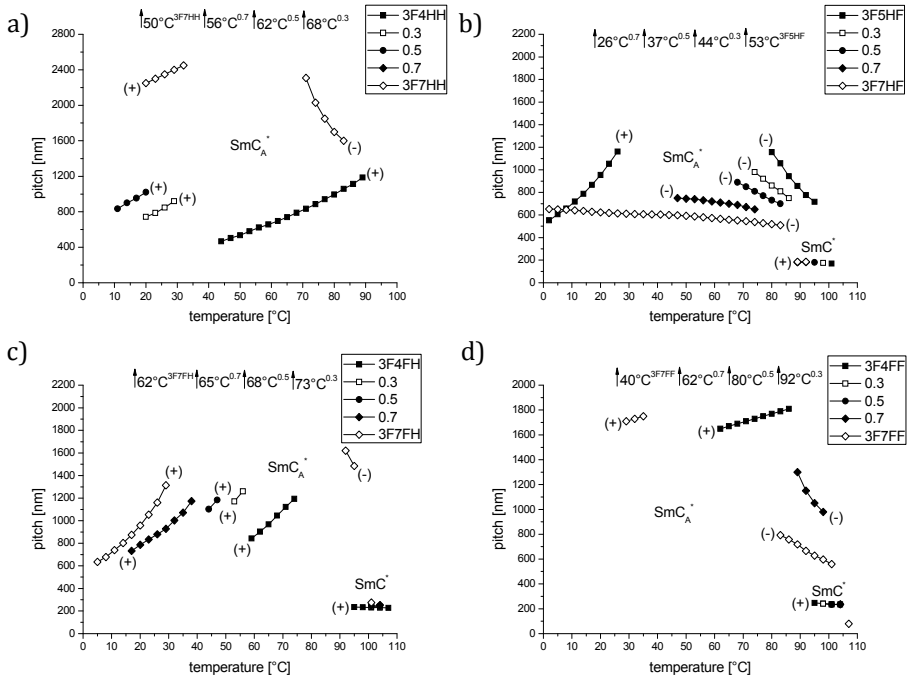

Fig. 2. The helical pitch dependence upon temperature for: a) 3F4HH+3F7HH; b) 3F5HF+3F7HF; c) 3F4FH+3F7FH; d) 3F4FF+3F7FF mixture.

DSC results

The plot of excess specific heat capacity versus content of tested mixtures in SmC^* and SmC_A^* is presented in Fig. 3. Despite the full miscibility of SmC_A^* phase of pure compounds of bicomponent mixtures, the excess specific heat capacity is additive for compounds without fluorine atom in the rigid core and negative for systems with fluorine atom. For SmC^* phase the values of excess specific heat capacity are lower than for SmC_A^* phase in the same mixture. The curves for mixtures with fluorine atoms have the similar shapes, moreover the excess specific heat capacity has higher for HF system.

The plot of excess enthalpy as a function of concentration of mixtures for transition from SmC_A^* to SmC^* is presented in Fig. 4. The excess enthalpy of phase transition SmC_A^* - SmC^* is more symmetrical according equimolar concentration for the FH and FF mixtures than for HH and HF mixtures. The convex shape of the excess enthalpy curves suggests that mixing compounds is connected with absorption of heat, so interactions between molecules in the mixtures are stronger than in the pure compounds.

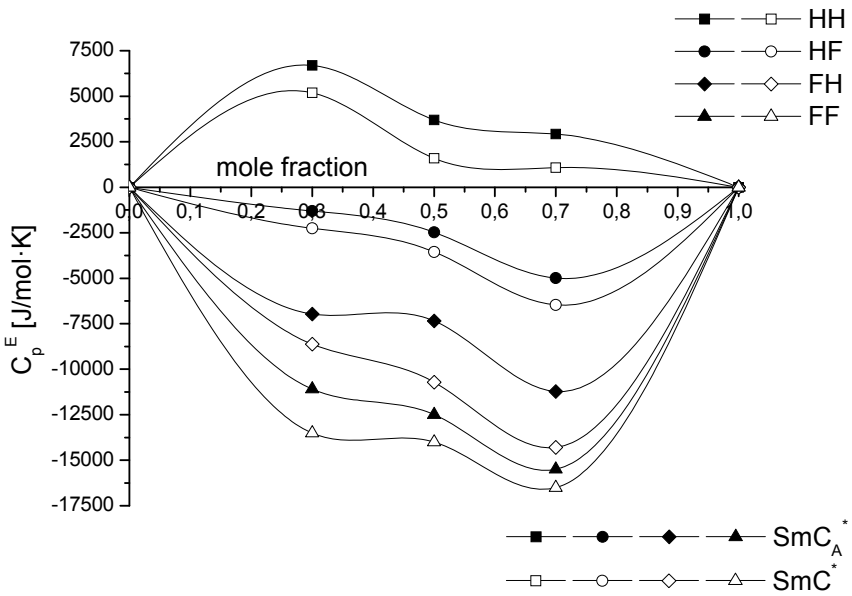

Fig. 3. The excess specific heat capacity dependence on mole fraction of examined mixtures in SmC* and SmC$_A$* phases.

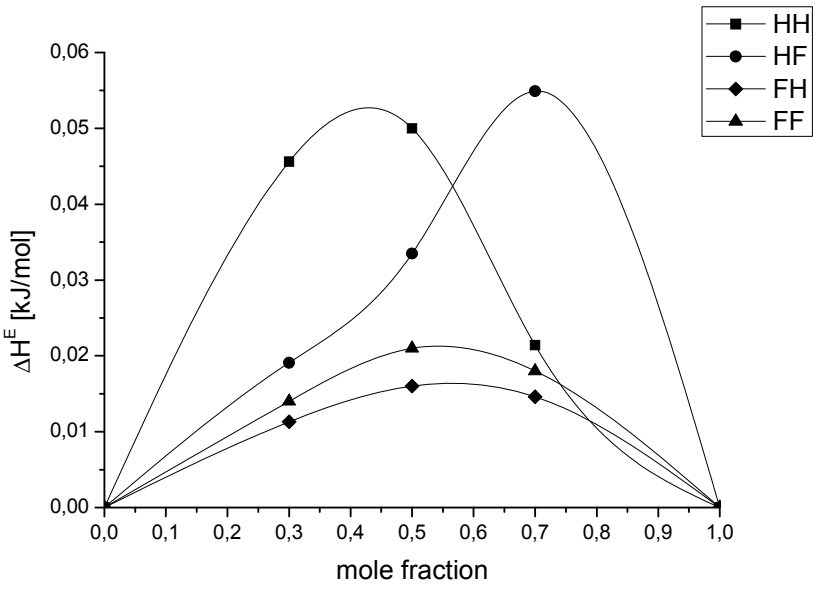

Fig. 4. The excess enthalpy dependence on mole fraction of examined mixtures during the transition from SmC$_A$* phase to SmC* phase.

CONCLUSIONS

The compounds and their mixtures of 3FmXY (m=4,5,7; X,Y=H,F) series have been examined. The influence of molecular structure on the helicoidal structure has been observed. Compounds with longer alkyl chain (m=7) and with two hydrogen atoms in the benzene ring (HH), two fluorine atoms (FF) or with fluorine atom in 2 position (FH) have the phenomenon of the helical twist sense inversion, as well as compound 3F5HF. In the mixtures of compounds with different alkyl chain length and the type of helical handedness, but with the same type of substitution of the benzene ring, the helix may be unwinded with the addition of one compound to another.

On DSC spectra the value of excess specific heat capacity is positive for compounds with unsubstituted benzene ring, however is negative for compounds with one or two fluorine atoms in the rigid core. Moreover this parameter is higher in the SmC_A^* phase than in the SmC^* phase for all compounds and their mixtures. The convex shape of the excess enthalpy curves suggests that mixing compounds is connected with absorption of heat, so interactions between molecules in the mixtures are stronger than in the pure compounds.

ACKNOWLEDGEMENTS

This work was supported by RMN 08/687.

REFERENCES

[1] Gray G.W., McDonnell D.G., The Relationship Between Helical Twist Sense, Absolute Configuration and Molecular Structure for Non-Sterol Cholesteric Liquid Crystals, *Mol. Cryst. Liq. Cryst.*, 1976, 34, 9, 211-217, DOI: 10.1080/15421407708083708

[2] Tykarska M., Czerwiński M., Żurowska M., The temperature and concentration dependence of helical pitch in the mixtures of antiferroelectric compounds with the opposite helical twist sense, *Liq. Cryst.*, 2011, 38, 5, 561-566, DOI: 10.1080/02678292.2011.558217

[3] Panov V.P., Seomun S.S., Shytkov N.M., Vij J.K., Nguyen H.T., The Biaxiality of the Chiral Smectic Subphases in Very Thin Freestanding Films, *Ferroelectrics*, 2002, 278, 47-55, DOI: 10.1080/00150190214473

[4] Li J., Takezoe H., Fukuda A., Novel Temperature Dependences of Helical Pitch in Ferroelectric and Antiferroelectric Chiral Smectic Liquid Crystals, *Jpn. J. Appl. Phys.*, 1991, 30, 3, 532-536, DOI: 10.1143/JJAP.30.532

[5] Glogarova M., Novotná V., Kašpar M., Hamplová V., Unusual behaviour of binary mixtures of ferroelectric and antiferroelectric liquid crystal with three chiral centers, *Opto-Electron. Rev.*, 2002, 10, 47-52, DOI:10.1117/12.472131

[6] Lagerwall J.P.F., Giesselmann F., Osipov M., On the change in helix handedness at transitions between the SmC^* and phases in chiral smectic liquid crystals, *Liq. Cryst.*, 2006, 33, 6, 635-633, DOI:10.1080/02678290500371392

[7] Kurp K., Tykarska M., Drzewicz A., Lapanik V., Sasnouski G., Effect of ferroelectric liquid crystalline quaterphenyl structure and handedness on helical pitch length in bicomponent mixtures, Liquid Crystals, 2016, DOI: 10.1080/02678292.2016.1226975

[8] Raszewski Z., Kędzierski J., Perkowski P., Piecek W., Rutkowska J., Kłosowicz S., Zieliński J., Refractive Indices of the MHPB(H)PBC and MHPB(F)PBC Antiferroelectric Liquid Crystals, *Ferroelectrics*, 2002, 276, 289-300, DOI: 10.1080/00150190214411

[9] Shytkov N.M., Vij J.K., Dielectric and optical rotatory power investigations of an antiferroelectric liquid crystal 12OF1M7 in a homeotropic cell: implications for models of the structure of ferrielectric phases, *Liq. Cryst.*, 2001, 28, 11, 1699-1704, DOI: 10.1080/02678290110068974

[10] Żurowska M., Dąbrowski R., Dziaduszek J., Czupryński K., Skrzypek K., Filipowicz M., Synthesis and Mesomorphic Properties of Chiral Esters Comprising Partially Fluorinated Alkoxyalkoxy Terminal Chains and a 1-methylheptyl Chiral Moiety, *Mol. Cryst. Liq. Cryst.*, 2009, 495, 145/[497]-157/[509], DOI: 10.1080/15421400802432428

The investigation and improvement of hydrothermal gasification parameters on microalgal biomass

*Daniel Fozer[1], Cintia Farkas[1], Bernadett Kiss[2], Laszlo Lorincz[1], Andras Jozsef Toth[1], Anita André[1], Tibor Nagy[1], Ariella Janka Tarjani[1], Eniko Haaz[1], Nora Valentinyi[1], Aron Nemeth[2], Edit Szekely[1], Peter Mizsey[1,3]

[1]Department of Chemical and Environmental Process Engineering, Budapest University of Technology and Economics, Budapest, HUNGARY

[2]Department of Applied Biotechnology and Food Science, Budapest University of Technology and Economics, Budapest, HUNGARY

[3]Department of Fine Chemicals and Environmental Technology, University of Miskolc, Miskolc, HUNGARY

e-mail: fozer.daniel@mail.bme.hu

Keywords*: Hydrothermal Gasification, Microalgae Biomass, Chlorella vulgaris, Biogas production*

The investigation of hydrothermal gasification (HTG) of microalgae biomass is carried out in order to produce biogas and upgrade its composition. Microalgae are suitable microbes which able to mitigate the negative environmental and social impacts of climate change, as well as capture and transform carbon dioxide into valuable compounds, such as biofuels.

In our work we investigated the role of temperature (525-575°C), pressure (250-280 bar), catalyst loading (5-15 w/w%) and ratio of homogenous catalysts (K_2CO_3/KOH) on biogas composition, gasification efficiency and total gas yield. *Chlorella vulgaris* is selected to cultivate and test as feedstock for HTG process. The biogas composition (H_2, CH_4, CO_2, CO) and the biological composition (CNHO, ash, volatile matter, fixed carbon) of the biomass arealso determined.

It is found that the application of homogenous catalyst mixture increasing significantly the biogas and hydrogen yields at elevated temperature level. The highest total gas yield is found to be 38.69 mmol g^{-1} while the H_2 yield is 24.69 mmol g^{-1} dry microalgae.

Through our work we attained high carbon gasification efficiency (>20%) and hydrogen yield in several cases. The experimental results are statistically evaluated and the main effects of influencing factors are determined.

INTRODUCTION

The application of fossil fuels affects unfavourably the environment due to the related emission of greenhouse gases such as CO_2 which contribute significantly to global climate change[1]. Moreover, the worldwide growing energy demand makes necessary the investigation of environmentally friendly, clean and sustainable

processing pathways and energy sources[2]. Biomass (e.g., microalgae) is considered as a suitable substitute that provide abundant renewable energy.

Microalgae are cultivated in diluted suspension which brings difficulties at downstream processing because the evaporation of excess water requires immense energy which makes challenging economic operation[3]–[5]. Hydrothermal treatment of biomass received great attention recently because eliminates biomass drying-step and therefore contribute to more ecological processing of wet biomass[6].

Hydrothermal gasification (HTG) is a thermochemical process that produces biogas, containing mainly H_2, CH_4, CO_2 and CO where the constituent ratio can be controlled by reaction conditions. The process performed atelevated temperatures (up to 600°C)[7] and therefore the reduction of operation temperature is desirable to achieve energy efficient operation. One way to do so is applying catalysts. Homogenous catalysts such as alkali metals (K_2CO_3, KOH, Na_2CO_3, NaOH) already reported in literature in case of model compounds such as humic acids, cellulose, mannose, horse manure[8]–[13]. Catalysts can also be used for upgrading biogas improving their quality [14]. In this study we investigated the role of temperature, pressure, catalyst loading and the ratio of homogenous catalyst mixtures on biogas composition, carbon gasification efficiency and biogas yield.

MATERIALS AND METHODS

Microalgae cultivation

Chlorella vulgaris was purchased from the Mosonmagyaróvár Algal Culture Collection (Széchényi István University). BG11 medium was used for the fermentations with the following composition (in g L^{-1}): $NaNO_3$, 1.500; K_2HPO_4, 0.040; $MgSO_4 \cdot 7H_2O$, 0.075; $CaCl_2 \cdot 2H_2O$, 0.036; Citric acid, 0.006; $FeNH_4SO_4$, 0.006; $EDTANa_2$, 0.001; Na_2CO_3, 0.020 and 1 ml of trace metals solution[15].

The microalgae were cultivated in 4.25 L stirred tank reactors. Artificial irradiation was provided by an RGB-LED lighting platform (UTEX Culture Collection of Algae) where the illumination duration was set to 16:8 hours light and dark photoperiod. The light intensity was measured by a lux meter (IEC 6 LF 22, CosiluxTungram) and it was kept constant at 352 μmolphoton m^{-2} s^{-1}. The aeration was set to 1.00 vvm, where the air was filtered with a sterile filter (0.2 μm, PTFE, Sartorius Midisart 2000). An autoclave (3870ELV, Tauttnauer) was used for the sterilization of fermenter and media at 121°C for 20 minutes.

The fermentations were monitored by measuring optical density (OD) at 560 nm (Pharmacia LKB·Ultraspec Plus Spectrophotometer). Gravimetric method was applied to determine the dry weight of microalgae. 10 ml suspension was filtered through a nitrocellulose membrane (0.22 μm, MILLIPORE), and dried at 105°C for 2 hours. The dry weight was determined by Eq. 1:

$$DW = \frac{(A - B) \cdot 100}{SV} \quad (1)$$

where DW is the dry weight (g L^{-1}), A is the weight of the microalgae and the filter (g), B is the weight of filter (g), SV is the volume of algae suspension (ml).

The biomass concentration was determined with calibration based on the following equation:

$$DW = 0.3903 \cdot OD_{560} - 0.1560, R^2 = 0.9753. \quad (2)$$

The elemental composition of microalgae biomass was determined by Liebig- and Dumas-methods with LECO FP-528 analyzer. Proximate analysis was carried out based on ASTM D3172 (DENKAL 1.4/1000).

Hydrothermal gasification

The overall flowsheet of microalgae cultivation and hydrothermal gasification process performed in the experiments is shown in Figure 1. A 2 m length tubular reactor was placed in an oven where the pressure was generated and maintained with HPLC pumps (Jasco PU-980, Gilson Model 303). Throughout hydrothermal gasification the residence time and biomass concentration held constant at 120 sec and 2.6wt.%, respectively.

The composition of the produced biogas was determined by gas chromatography (HP5890A/TCD/FID, stainless steel column packed with Porapak Q 80/100 mesh, 1/8 inch OD, 1.9 m).

The carbon gasification efficiency (GE_C) was calculated by dividing the carbon content of the gas product and carbon content of the biomass (Eq. 3.).

$$GE_C(\%) = \frac{m_{C,gas}}{m_{C,feed} - m_{C,residue}}, \quad (3)$$

where $m_{C,gas}$ is the carbon contentof biogas (g min^{-1}), $m_{C,feed}$ is the carbon content of biomass, $m_{C,residu}$ is the carbon content of residue. The total carbon content of the residue was determined by Shimadzu TOC/VCSH.

The gasification yield was determined using the following equiation (Eq. 4.):

$$Y_{biogas} = \frac{n_{biogas}}{m_{biomass}}, \quad (4)$$

where Y_{biogas} is the total yield of biogas (mmol g^{-1}), n_{biogas} is the mole number of gas product (mmol), m_{biomas} is the mass of dried biomass (g).

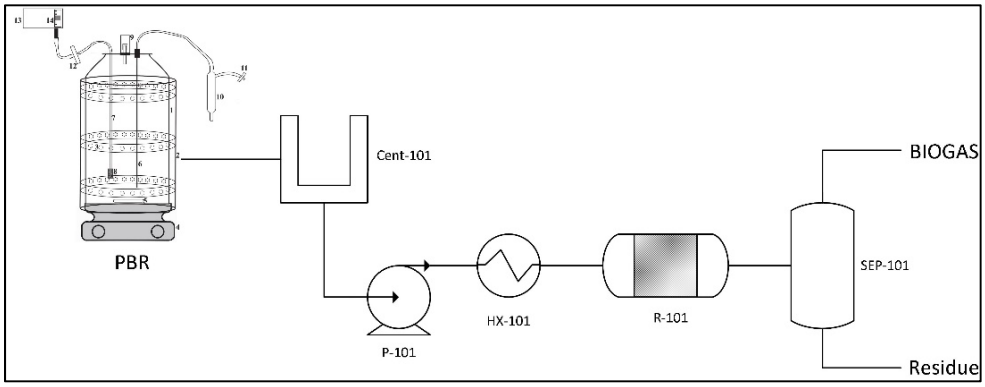

Fig. 1. Flowsheet of microalgae cultivation and hydrothermal gasification of *C. vulgaris* biomass.

Experimental design

Design of Experiments software Statistica 13.1 was used for planning the experiments andstatistical evaluation of the experimental results. $2^{(4-1)}$ fractional factorial design was applied for the investigation of factors such as temperature (525-575°C), pressure (250-280 bar), catalyst loading (5-15 wt.%) and catalysts (K_2CO_3 and KOH) ratio (2:1-1:2) on biogas composition, carbon gasification efficiency and biogas yield.

RESULTS

The proximate and ultimate analyses are presented in Table 1, the results of HTG experiments are listed in Table 2. Experiments were conducted under different temperature, pressure, catalyst loading and catalyst ratios. Non catalytic hydrothermal gasification of microalgae is also investigated for comparison purposes with catalytic HTG. It is found that applying homogenous catalyst increases hydrogen yield, while decreases CO and CO_2content of biogas which is in agreement with the findings of previous studies [9][13][16]. However, it turned out thatapplication of catalyst mixtures increase further the hydrogen yield compared to unmixedcatalysts.Applying elevated temperature and mixed homogenous catalystsraised hydrogen yield from 4.83 mmol g^{-1} to 24.69 mmol g^{-1}. The highest H_2 yield was achieved at 575°C, 280 bar, 15 wt.% catalyst loading, 2:1 catalyst ratio and it was found to be 24.69 mmol g^{-1} dry microalgae which is twice as high as reported with model compounds such as mannose [11], horse manure [10] or different heterogeneous catalysts [9].

In our findings the highest hydrogen yield paired with the highest total gas yield (38.69 mmol g^{-1}). The highest hydrogen mol fraction was 66.83 mol% at 525 °C, 250 bar, 15 wt.% catalyst loading and 2:1 catalyst ratio, though the total biogas yield was one of the lowest, only 12.55 mmol/g.

Tab.1. Proximate and elemental analysis of microalgae biomass.

Biomass	Proximate analysis (wt.%)			Ultimate analysis (wt.%)			
	Volatile matter	Fixed carbon	Ash	C	N	H	O
Chlorella vulgaris	74.20	19.43	6.37	57.65	9.73	5.30	27.32

Tab.2. $2^{(4-1)}$ fractional factorial design and the results of hydrothermal gasification.

Run	Temperature (°C)	Pressure (bar)	Cat. loading (wt.%)	K_2CO_3/ KOH ratio	H_2 (mol %)	CH_4 (mol %)	CO_2 (mol %)	CO (mol %)	GE_C (%)	Y_{biogas} (mmol/g)
0	550	250	-	-	17.83	4.11	7.54	70.52	30.49	27.14
1	525	250	5	1:2	49.73	3.31	7.42	33.59	17.23	19.58
2	575	250	5	2:1	64.39	9.24	8.68	17.54	25.95	35.78
3	525	280	5	2:1	53.58	3.48	6.87	26.26	9.60	11.47
4	575	280	5	1:2	54.13	5.51	8.66	31.35	26.35	28.12
5	525	250	15	2:1	66.83	5.06	5.92	21.53	8.54	12.55
6	575	250	15	1:2	65.68	6.45	8.56	19.31	23.43	32.44
7	525	280	15	1:2	50.03	3.17	6.36	35.31	15.85	16.03
8	575	280	15	2:1	63.81	8.12	6.44	21.33	29.07	38.69

The methane yield of biomass was increased from 1.12 mmol g^{-1} to 3.31 mmol g^{-1} algae which is almost a triple growth, while the total biogas yield was increased by 42.56% applying homogenous catalyst mixtures.

Comparing the results to the non-catalytic hydrothermal gasification, augmented hydrogen yields result in a decreasing carbon gasification efficiency. The main reason for this phenomena can be explained bythat homogenous catalysts diminish the CO content of biogas which ultimately decrease the carbon gasification efficiency.

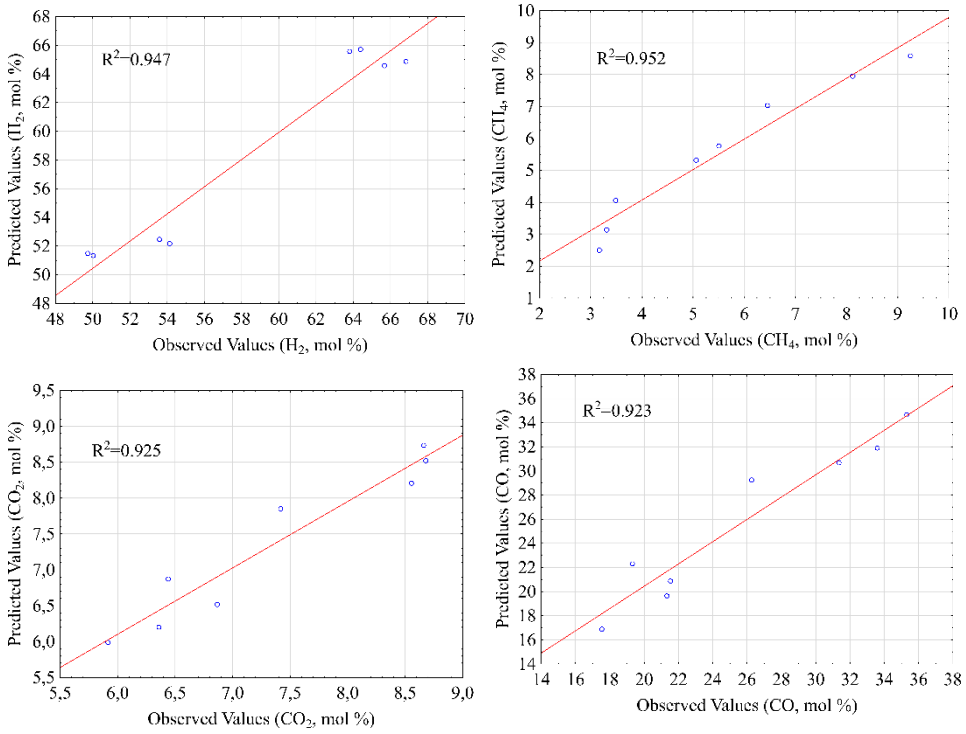

Fig. 2. Predicted and observed values from statistical model.

The statistical analysis of experimental data shows that temperature has significant effect on all independent variable (H_2, CH_4, CO_2, CO fraction, GE_C and Y_{biogas}). All dependent variables have significant effect on H_2 production (R^2=0.947). It is also turned out that both temperature and catalyst ratio are significant factors in case of CO content. The predicted and the observed values are adequate, as showed in Figure 2, and thus the experimental data fits well the applied statistical models (R^2>0.9 in all cases).

CONCLUSIONS

This study aims to explore hydrothermal gasification of microalgae biomass under different reaction parameters. *C. vulgaris* was cultured and converted into biogas, and the impact of temperature (525-575°C), pressure (250-280 bar), catalyst loading (5-15 wt.%) and catalyst ratio (K_2CO_3:KOH = 2:1;1:2)on the yield of the process was investigated based on $2^{(4-1)}$ fractional factorial experimental design.

The investigated statistical models are satisfactory and fits well experimental results.

The highest total biogas and hydrogen yield arefound to be 38.69 and 24.69mmol g^{-1}, respectively. It is demonstratedthat higher H_2 and biogas yield can be achieved by catalyst mixtures compared to single homogenous or heterogeneous

catalysts. The experimental data shows thatusing different reaction conditions, in situ upgrading of biogas becomespossible due to the augmented concentration and yield of H_2 and CH_4.

ACKNOWLEDGEMENT

This work was supported by the ÚNKP-17-3-I New National Excellence Program of The Ministry of Human Capacities. The authors are grateful for the financial support from the János Bolyai Research Scholarship of the Hungarian Academy of Sciences and the Hungarian National Research Foundations (OTKA) project: Capture of CO_2 from biogases and industrial flue gases, project nr.: 112699. This research was supported by the European Union and the Hungarian State, co-financed by the European Regional Fund in the framework of the GINOP-2.3.4-15-2016-00004 project, aimed to promote the cooperation between the higher education and industry.

REFERENCES

[1] Korre A., Nie Z., Durucan S., Life cycle modelling of fossil fuel power generation with post combustion CO2 capture, *Energy Procedia*, 2009, 1, 1, 3771–3778, DOI: 10.1016/j.ijggc.2009.08.005

[2] Kumar G., Shobana S., Chen W.H., Bach Q.V., Kim S.H., Atabani A.E. Chang J.S., A review of thermochemical conversion of microalgal biomass for biofuels: chemistry and processes,*Green Chem.*, 2017, 19, 1, 44–67, DOI:10.1039/C6GC01937D

[3] Fozer D., Valentinyi N., Racz L., Mizsey P., Evaluation of microalgae-based biorefinery alternatives, *Clean Technol. Environ. Policy*, 2017, 19, 2, 501–515, DOI: 10.1007/s10098-016-1242-8

[4] Karimi I.A., Kawi S., Technoeconomic perspectives on sustainable CO2 capture and utilization,*Environ. Sci. Pollut. Res.*, 2016, 23, 22, 22223–22225, DOI:10.1007/s11356-016-7838-z

[5] Laurens L.M.L., Markham J., Templeton D.W., Christensen E.D., Wychen S., Vadelius E.W., Chen-Glasser M., Dong T., Davis R., Pienkos P.T., Development of Algae Biorefinery Concepts for Biofuels and Bioproducts; a Perspective on Process-compatible Products and Their Impact on Cost-Reduction, *Energy Environ. Sci.*, 2017, 10, 1716-1738, DOI: 10.1039/C7EE01306J

[6] Patel B., Guo M., Izadpanah A., Shah N., Hellgardt K., A review on hydrothermal pre-treatment technologies and environmental profiles of algal biomass processing, *Bioresour. Technol.*, 2016, 199, 288–299, DOI: 10.1016/j.biortech.2015.09.064

[7] Kumar M., Oyedun A.O., Kumar A., A review on the current status of various hydrothermal technologies on biomass feedstock,*Renew. Sustain. Energy*

Rev., 2018, 81, 1742–1770, DOI: 10.1016/j.rser.2017.05.270

[8] Madenoğlu T.G., Sağlam M., Yüksel M., Ballice L., Hydrothermal gasification of biomass model compounds (cellulose and lignin alkali) and model mixtures,*J. Supercrit. Fluids*, 2016 115, 79–85, DOI: 10.1016/j.supflu.2016.04.017

[9] Chakinala A.G., Brilman D.W.F., Van SwaaijW.P.M., Kersten S.R.A., Catalytic and Non-catalytic Supercritical Water Gasification of Microalgae and Glycerol,*Ind. Eng. Chem. Res.*, 2010, 49, 3, 1113–1122, DOI: 10.1021/ie9008293

[10] Nanda S., Dalai A.K., Gökalp I., Kozinski J.A., Valorization of horse manure through catalytic supercritical water gasification, *Waste Manag.*, 2016, 52, 147–158, DOI: 10.1016/j.wasman.2016.03.049

[11] Madenoğlu T.G, Cengiz N.Ü., Sağlam M., Yüksel M., Ballice L., Catalytic gasification of mannose for hydrogen production in near- and super-critical water,*J. Supercrit. Fluids*, 2016, 107, 153–162, DOI: 10.1016/j.supflu.2015.09.003

[12] Gong M., Nanda S., Romero M.J., Zhu W., KozinskiJ. A., Subcritical and supercritical water gasification of humic acid as a model compound of humic substances in sewage sludge,*J. Supercrit. Fluids*, 2017, 119, 130–138, DOI: 10.1016/j.supflu.2016.08.018

[13] Onwudili J.A., Lea-Langton A.R., RossA. B., WilliamsP. T., Catalytic hydrothermal gasification of algae for hydrogen production: Composition of reaction products and potential for nutrient recycling,*Bioresour. Technol.*, 2013, 127, 72–80, DOI: 10.1016/j.biortech.2012.10.020

[14] Khan I.U., Othman M.H.D., Hashim H., Matsuura T., Ismail A.F., Rezaie-DashtArzhandi M., Azelee I.W., Biogas as a renewable energy fuel – A review of biogas upgrading, utilisation and storage,*Energy Convers. Manag.*, 2017, 150, 277–294, DOI: 10.1016/j.enconman.2017.08.035

[15] CCAP, BG11 media, 2017, https://www.ccap.ac.uk/media/documents/BG11.pdf (Accessed 22.01.2018)

[16] Peng G., Vogel F., Refardt D., Ludwig C., Catalytic Supercritical Water Gasification: Continuous Methanization of Chlorella vulgaris,*Ind. Eng. Chem. Res.*, 2017, 56, 21, 6256–6265, DOI: 10.1021/acs.iecr.7b00042

Diagnosis of lung cancer using Matlab

*Magdalena Fryc[1]
[1]Institute of Material Science, University of Silesia, Katowice, POLAND
e-mail: magdalena_fryc@o2.pl

***Keywords**: Matlab, lung cancer, MRI*

ABSTRACT

The aim of the paper was the subject of the BA thesis realized in the Institute of Computer Science at the Department of Informatics and Material Science of Silesian Institute.The purpose of this work is to create an author's program in Matlab to facilitate the diagnosis and analysis of lung cancer based on a series of MRI images. The program was created to facilitate the oncologist's work. It is possible to indicate the part of the lung where the tumor change is located, in order to automatically calculate the area of the lung and the tumor change and to select the appropriate treatment for the patient. Thanks to the program it ispossible to analyze lung tumor changes and rapid diagnosis, leading to the choice of further treatment of the patient.

INTRODUCTION

Novelty in the presented paperis a program for the diagnosis and analysis of neoplastic changes. So far no work related to the use of generally available programs as a method for analyzing cancerous changes has been published. Available programs analyzing neoplastic changes currently used in hospitals are not available to third parties. Only doctors and hospital staff have access to them. Therefore, the aim of this work was to create a program analyzing cancerous changes from magnetic resonance images, using the Matlab environment, so that the program can be available to the public.

Lung cancer is one of the most developing diseases in Poland and in the world, especially in developing countries. This disease affects more and more people, both men and women, the majority of whom are habitual smokers and people exposed to harmful chemicals such as nickel, asbestos or radon. Lung cancer is one of the few, virtually incurable diseases. A small percentage of patients with lung cancer are healed, however, thanks to the progress of medicine and such sciences as medical physics or biomedical engineering, it is possible to significantly extend the lives of people affected by this disease. There are many options for treating lung cancer depending on its type, i.e. the histopathological division of lung cancer. From chemotherapy through bronchoscopy, or radiotherapy, to surgical treatment, which in rare cases allows complete removal of the tumor. The main tools for detecting lung cancer are x-ray (X-ray), computed tomography (CT), positron emission tomography

combined with computed tomography (PET CT), but also in special cases magnetic resonance imaging (MRI)

The purpose of the following publication is to propose a method of computer image processing and analysis, which is to help diagnose lung cancer changes by oncologists in the field of adjusting the appropriate treatment for individual patients.

The images subjected to processing and analysis are image sequences for various lung planes obtained from magnetic resonance.

In particular, the following issues were considered:

1. objective assessment of the possibility of using computer analysis of magnetic resonance images for lung cancer changes,
2. segmentation of the lung cancer lesion, using its own proposals for the extraction of changes through image binarization and the isolation of interesting fragments,
3. calculation of the distance between the two most distant cancer lesion points,
4. calculation of the surface area of the isolated lung cancer lesions and the volume of the final lung cancer change for each of the loaded series of images,
5. depicting graphs of designated lengths of neoplastic changes at the widest point,
6. displaying graphs of changes in the surface area of neoplastic lesions on subsequent images of a series of downloaded images,
7. automatic saving of results to a spreadsheet with images of isolated neoplastic lesions,
8. making a preliminary diagnosis and matching the appropriate treatment for an exemplary patient.

MATERIALS AND METHODS

Matlab package

The Matlab program (MATrix and LABoratory) is a package with a universal environment that allows for complex scientific and technical calculations, through access to various and effective computational algorithms. It allows you to visualize the obtained results in the form of various graphs and three-dimensional graphics. Matlab allows the analysis of images not only obtained from cameras, but also from magnetic resonance and other medical devices, such as CT, X-ray or ultrasound. Therefore, the aim of the work, which was to present the analysis of neoplastic changes in relation to the volume of the lungs, was possible thanks to the functionality of the Matlab package.

TNM CLASSIFICATION OF NON-SMALL CELL LUNG CANCER

The severity of non-small cell lung cancer is determined by the international classification of TNM, in which three features are considered:

• T-characteristic of the primary tumor in the lung

• N-character evaluating the presence of metastases in the lymph nodes
• M-feature evaluating the presence of distant metastases.

The next step to assess the clinical stage of non-small cell lung cancer is the analysis of the dependence of individual TNM traits, which is important in the choice of the treatment method, especially for the patient's qualification for surgery [3].

The choice of treatment for non-small cell lung cancer depends on the severity of the TNM-mediated classification as demonstrated (Tab. 1.)

Tab.1. Methods of treatment of non-small cell lung cancer depending on its severity [3].

The severity of cancer stage	Treatment method
I II	Surgical treatment and chemotherapy after surgery
IIIA	Operative treatment and possibly chemotherapy and / or radiotherapy before surgery
IIIB	Radiotherapy possibly combined with chemotherapy
IV	Palliative chemotherapy or symptomatic treatment of organ system efficiency and the general condition of the patient

RESULTS

As part of the presented work with the Matlab package, a program was created to diagnose and analyze lung cancer changes. A program was created using the procedure shown in Fig. 1.

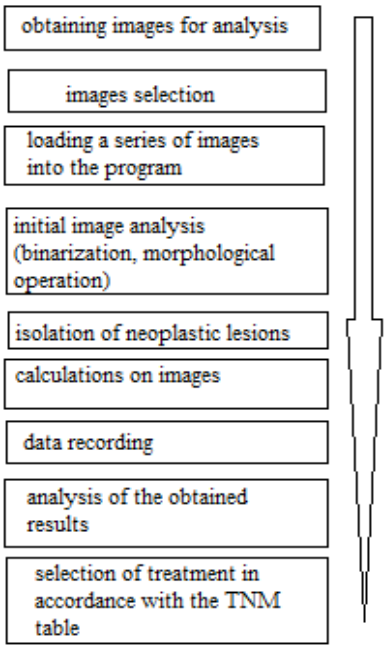

Fig. 1. The process of proceeding during the analysis and diagnosis of lung cancer changes in the Matlab environment.

Selection of images for analysis

In each series of images received for analysis, a selection was carried out, in which images were rejected where the neoplastic changes were not visible and on which, despite properly performed binarization and morphological operations, the neoplastic change was impossible to isolate. As a result, a much larger fragment was extracted (Fig. 2). change in the binarization threshold caused that the surface area decreased, or the neoplastic change disappeared, which caused an erroneous diagnosis, which is why it was decided to reject several images during the analysis.

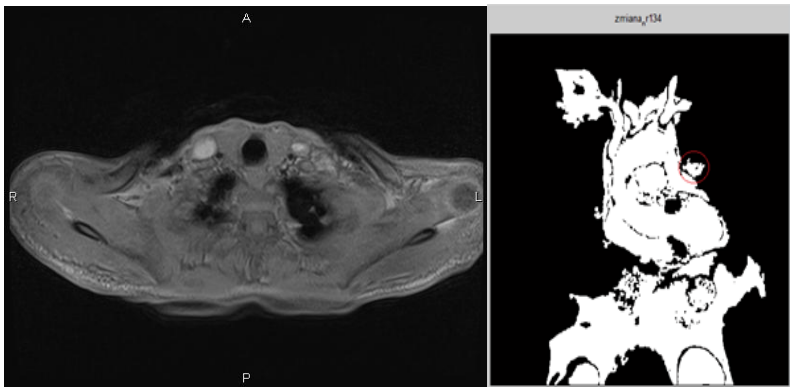

Fig. 2. Examples of rejected images without visible cancerous changes.

Loading a series of images, binarization and morphological operations on binary images

At the beginning of the analysis, a series of MRI images is loaded in a loop and displayed in the following graphic windows (Fig. 3). Each image loaded from the series has been properly described and numbered automatically by calling the 'i' variable defined at the beginning of the loop.

```
pam=[];
for i = 1:1:7
   L=imread(['C:\acces\dcm\',mat2str(i),'.jpg']);
          figure;
          imshow(L);
title(['obraz nr',num2str(l)]);
```

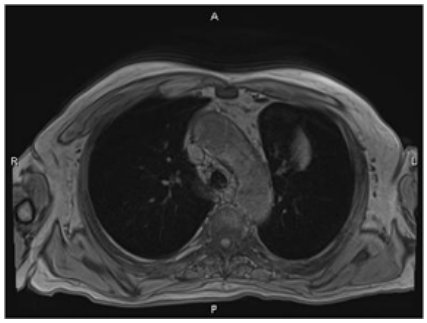

Fig. 3. Loaded image with lung cancer change transverse plane view.

Then, a histogram is displayed for each image to match the neutral binarization threshold. After the obtained histograms, one binarization threshold was chosen that was appropriate for all loaded images of a given series. For example, for the first loaded series of images, the binarization threshold is 50 [X] in the gray scale, after switching to double 0.25 [X]. To ensure that the binarization was carried out correctly, a histogram was displayed (Fig. 4). All the above operations are presented in the following code:

```
L=double(L)/255;
figure; imhist(L);
grid;
        set(gcf,'Color',([1 1 1]));
        ylabel(pixel's number,'FontSize',15,'FontName','Arial CE');
L1=L>0.25;
figure; imshow(L1);
figure; imhist(L1);
```

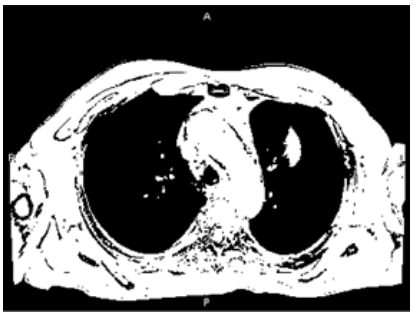

Fig. 4. Image with tumor change after binarization.

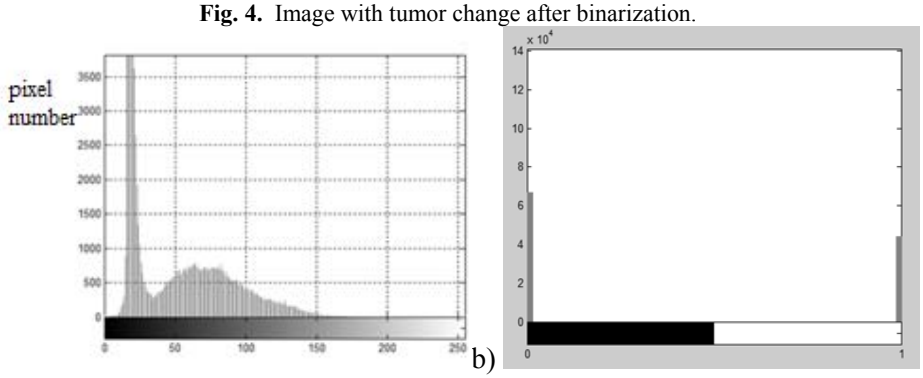

a) b)

Fig.5. Histograms for thumor image showen on fig. 4 a) before and b) after binarization.

After the binarization of images, subsequent morphological operations were carried out (Fig.6), shown in the following code:

```
BW2 = bwmorph(L1,'erode');
        figure ;imshow(BW2) ;
BW3 = bwmorph(BW2,'dilate');
        figure ;imshow(BW3) ;
bw=bwmorph(BW1,'open');
        figure ;imshow(bw) ;
end
```

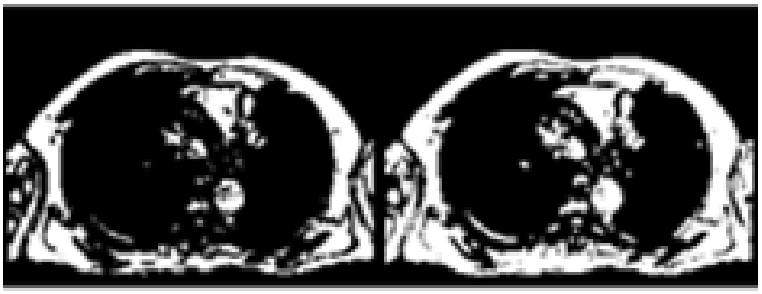

Fig.6. Morphological operations: erosion and dilatation.

Extraction of the lung cancer changes

Isolation of lung cancer changes was performed in the loop. The applied 'ginput' function allows to manually select a cancerous lesion on a binary image and in addition to each of the images it can be used repeatedly if the analyzed changes in the lungs are disseminated, as in the case of small-cell lung cancer, or if there are metastases to other organs or nodes lymph. This function, despite the fact that it is time-consuming for the user, avoids a computer error that could bypass any of the changes or mark a different structure that is not considered to be cancerous. The following code is responsible for extracting neoplastic lesions and displaying the selected change in a new graphics window (Fig. 7).

```
L5=bwlabel(BW3);
        figure; imshow(L5);
[x,y,k]=ginput(1);
nr=L5(round(y),round(x));
L6=L5==nr;
        figure; imshow(L6);
title(['zmiana nr',num2str(i)]);
```

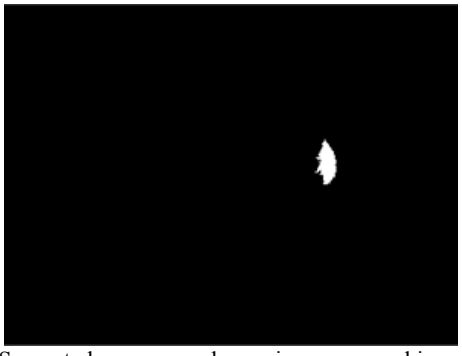

Fig. 7. Separated cancerous change in a new graphics window.

In order to illustrate individual stages of image processing, we display them in the proper order in a new graphics window (Fig. 8), which allows additional step-by-step analysis of the image to ensure that every operation performed on the image has been carried out correctly and whether it requires additional amendments. The

following code shows how to correctly display all images in a single graphics window with the description and numbering of subsequent series of images.

```
figure; imshow([L,L1,BW2,BW3,L6]);
```

Fig. 8. Graphic window with individual stages of image processing.

Calculations on images

In order to analyze and make any initial diagnosis it is important to make some calculations on the analyzed images. Due to the TNM division of tumors, the first parameter to be calculated is the length of the neoplastic lesion at its widest point. Next, the surface area of each previously separated neoplastic lung lesion will be calculated. The final step will be to calculate the total volume of neoplastic lung cancer.

Calculating the length of neoplastic lesion at the widest point

Due to the irregular shape of neoplastic lesions, the length of each shift is calculated at its widest point, in other words between the two most distant points. In order to calculate this parameter, additional memory was created, which stores the data concerning the length of the change and the loop in which the new variable 'm' was introduced, causing the angle of rotation for each previously separated neoplastic lesion. In addition, the entire result must be multiplied to obtain the appropriate units. In our case, the expected result should be given in millimeters [mm], therefore, the unit through which our images are represented, i.e. pixels [X] must be converted to millimeters by multiplying the given sum by a unit corresponding to 1 X mm. The series of images used in the presented work was made by magnetic resonance, in which 1x1x1 [X] corresponds to 1 voxel represented by 3x3x3 [mm]. The correct calculation of the length of neoplastic change is presented in the following code:

```
pam1=[]
for m= 0:180
   L10=imrotate(L6,m);
pam1=[pam1;[m sum(sum(L10,1)>1)]*3];
end
pam1=sortrows(pam1,-2);
pam1(1,2)
```

Area and volume of neoplastic lesion

The surface area is a simple parameter to be determined, which can be determined with high accuracy. In order to determine the area, we need to count the

points of the image fragment whose field interests us. Then, after determining the actual distance which corresponds to the designated points of the fragment we are interested in, we obtain the result of measurement in the appropriate units for our measurement. In order to obtain the surface area in the appropriate units [mm^2], it is necessary to multiply the value obtained twice by 3. All calculated data are saved to the common memory created at the beginning of the program. These operations show the following fragment of the program:

```
bwarea(L6)
pam=[pam;[i,sum(sum(L6))*3*3,pam1(1,2)]];
```

In order to obtain the final result, i.e. the volume of the isolated tumor change for a given series of images, it is necessary to multiply the appropriate value by 3 again, in this way we obtain the result in [mm^3]. The following code fragment shows the correct calculation of the volume of neoplastic lung cancer:

```
sum(pam(:,2)*3)
```

CREATING CHARTS

Plots of surface area and length of tumor changes for particular images of the loaded series.

After calculating the surface area and the length of individual lung cancer lesions, charts were generated showing the change of surface area for subsequent images of the loaded series as well as the length of tumor change between the two most distant points in order to compare the results and carry out further analysis of the images. A linear chart was selected, obtained by calling the 'plot' function (Fig. 9). The obtained graph can be modified automatically by calling appropriate commands corresponding to min. for choosing the line style, color, size, adding markers and appropriate description of the X and Y axes, giving the title and legend, the font selected and defined in the code:

```
Figure;
plot(pam(:,1),pam(:,2));
line (pam(:,1),pam(:,2),'linestyle','-','marker','*')
xlabel (’image number','FontSize',15,'FontName','Arial CE')
ylabel (’area’,'FontSize',15,'FontName','Arial CE')
title(’area of simple image, 'FontSize', 15, 'FontName','Arial CE')
grid on ;legend (’area of image’)
```

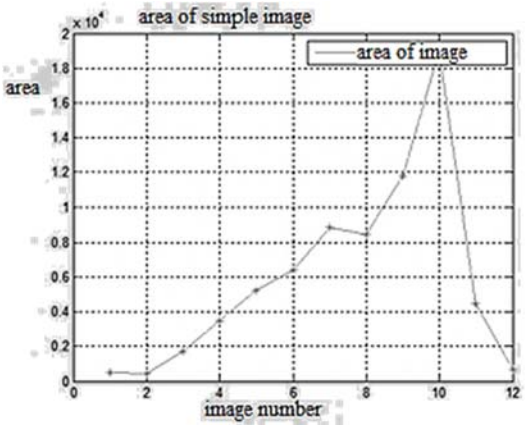

Fig. 9. Surface area plot for a sample series of images.

Recording the image sequence of the extracted cancerous lesion into a folder together with a spreadsheet containing calculation data

The recording of the sequence of images of isolated lung cancer changes into a new folder allows for a subsequent detailed analysis of the cancerous changes that are interesting, without the need to re-isolate them from the original images. This is a great help for technicians and doctors because they are analyzing a suitably isolated change without the need to reprocess the images. In addition, importing data on cancer length and its area to a spreadsheet is another convenience that allows you to analyze data and create any charts in your worksheet and carry out your own analyzes.

```
imwrite(L6,['C:\Users\Ola\Desktop\dane\change1',mat2str(i), '.jpg'])
xlswrite('C:\Users\Ola\Desktop\dane\area1',pam);
```

RESULTS ANALYSIS

After the obtained results for neoplastic lesions for one patient from three series of magnetic resonance images for different body sections, the analysis of the area results of the separated lesions was performed for selected images, where the tumor lesion was visible and for which it was possible to isolate it in a new graphics window. After comparing the results, it can be concluded that the number of analyzed images is different for each patient. The results of the length between the two most distant points, the surface area and the final volume of the neoplastic change differ significantly between the analyzed series of images of three sample patients, with the largest number of images, i.e. 39, for the last series of images taken in the cross section of the frontal plane while the first series of images counted in the cross-section in the transversal plane of 8 neoplastic lesions and the second series also in cross-section in the transverse plane 12.

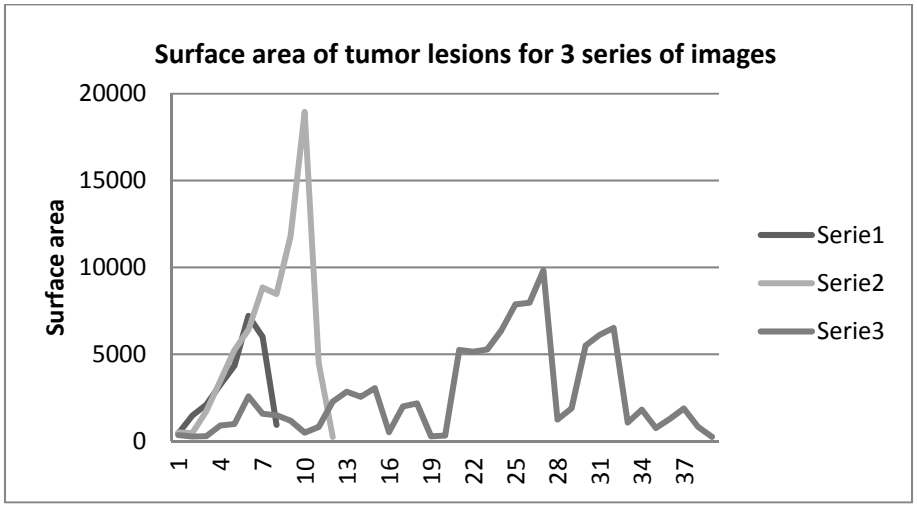

Fig. 10. Comparative graph of changes in surface area for particular series of images.

Although the largest area of neoplastic lesion recorded was in the second loaded series of images, the largest final volume occurred in the third loaded series of images, where the images analyzed were the most numerous. The final volume of each series of images is shown (Fig. 10).

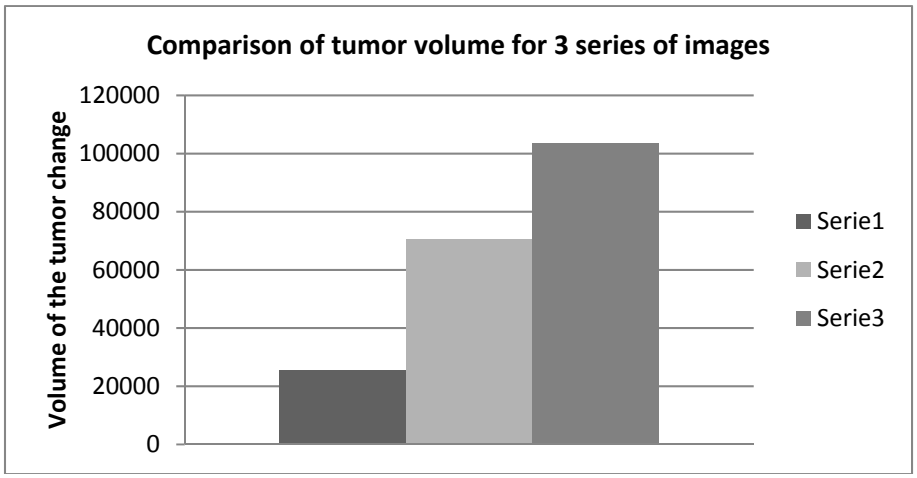

Fig. 11. The comparison of the volume of tumor change for individual series of images.

In order to issue a preliminary diagnosis it is necessary to enter the T parameter from the TNM classification, which is responsible for min. for the diameter of the neoplastic lesion, i.e. the distance between the two outermost points of the analyzed neoplastic lesion. To give an initial diagnosis, a comparative chart of the length of the analyzed neoplastic lesions is presented for three loaded series of images (Fig. 11).

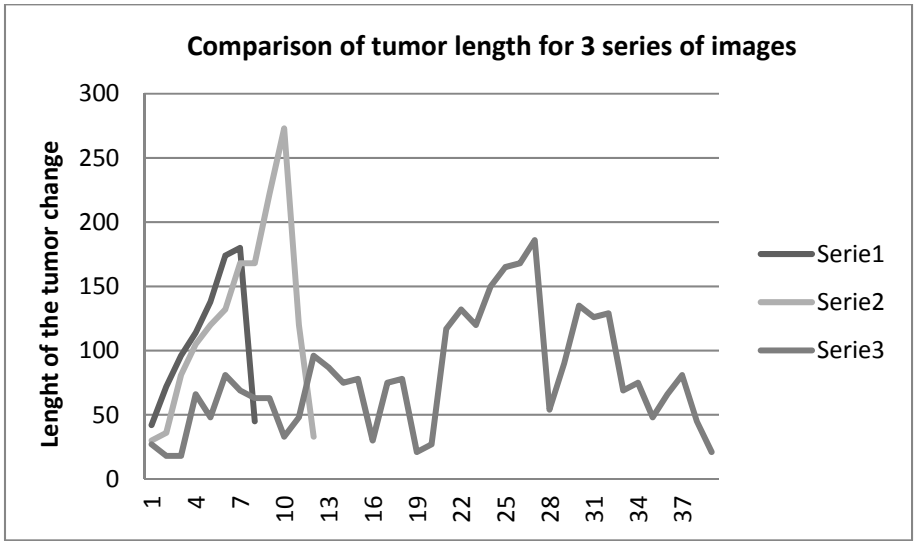

Fig. 12. The comparison of the length of tumor change for individual series of images.

After analyzing the individual graphs, it can be concluded that in the second series where the neoplastic change has reached the largest surface area and length. After analyzing the data on the area of the final volume and the length of the tumor changes, it can be noticed that there is a significant relationship between the field, the surface and the length of neoplastic changes, while the volume resulting from the area of all neoplastic lesions of a given series does not affect the diagnosis.

The maximum length of neoplastic lesions from each series of images can be the basis for making a preliminary diagnosis based on the T parameter from the TNM classification.

After the results obtained and their comparison with the TNM values - T is T4, because the tumor length is greater than 3 cm and the tumor infiltrates structures such as mediastinum, heart, large vessels. The occurrence of infiltrates on other structures was found due to the inability to separate tumor changes from such organs as the heart during the binarization process. However, the features N and M receive X values, i.e. that the assessment of regional lymph nodes as well as the assessment of metastases distant to other organs are impossible. Both features: N and M are impossible to assess due to the analysis of images of only the area of the chest limited to the structure of the lungs.

After the obtained results T4, Nx and Mx, the next step to issue a preliminary diagnosis is to determine the stage of cancer. After comparing the results with the table values, we can qualify the analyzed cancer lesion as the stage IIIB of cancer advancement.

The final step is to choose the patient's treatment (Table 1). According to the stage of cancer of IIIB, the appropriate treatment for the patient according to Table 3 is radiotherapy optionally combined with chemotherapy.

CONCLUSIONS

The performed binarization on images has a huge impact on the result of the surface area. An incorrectly chosen binarization threshold can drastically change the area of cancerous lesions. What is associated with falsification of results and consequently leading to an incorrect diagnosis.

The final volume of neoplastic change is influenced by the number of images analyzed, even when the field of individual neoplastic changes in a given series is not too large. However, this is not enough to give an initial diagnosis.

The maximum length of a neoplastic lesion can be the basis for making a preliminary diagnosis based on the T parameter from the TNM classification.

The created program for the analysis and preliminary diagnosis of tumors may be a facilitation for physicians analyzing photos from magnetic resonance in order to select the appropriate treatment for patients suffering on cancer.

Thanks to the data archiving function of the program, you can quickly return to the patient's results without having to re-analyze the images of neoplastic changes. This feature is additionally useful when comparing new test results after appropriate treatment with pre-treatment results to verify whether the patient's treatment has the expected results.

The program itself is only a facilitation for doctors and technicians working in hospitals, but without the proper knowledge of physicians, the program is not able to decide on the patient's future, which is why the human factor is an indispensable element in the diagnosis and the treatment of patients.

REFERENCES

[1] Pratap R., *Matlab 7 dla naukowców i inżynierów*, Warszawa: Wydawnictwo Naukowe PWN SA, 2013, str. 280

[2] Wróbel Z., Koprowski R., *Praktyka przetwarzania obrazów z zadaniami w programie Matlab,* Warszawa: Akademicka Oficyna Wydawnicza EXIT, 2012, str. 278

[3] Rzyman W., *Rak płuca*, Gdańsk: Katedra i Klinika chirurgii klatki Piersiowej Akademii Medycznej, T. 2, 6/2008, 407–419

Effect of tantalum addition on the structure of ferromagnetic shape memory alloy Ni-Co-Mn-In

*Magdalena Fryc[1], Krystian Prusik[1], Maciej Zubko[1]
[1]Institute of Materials Science, University of Silesia, POLAND
e-mail: magdalena_fryc@o2.pl

***Keywords**: Ferromagnetic shape memory alloys (FSMA), SEM, TEM, X-ray.*

ABSTRACT

In the present work the effect of tantalum addition on the structure of the Ni-Co-Mn-In FSMA were investigated. During the structural studies the chemical composition of the studied samples was determined by SEM. The phase analysis was performed using XRD and TEM. Tantalum-containing alloys have a lot of precipitates of the high content of Ta, Mn and Ni, but were poor in Co and In. The matrix of the studied alloys consisted mainly of Ni, Mn, Co. X-ray and TEM phase analysis confirmed the presence of a high-order $L2_1$ austenite and a seven-layer modulated 14M martensite structures.

INTRODUCTION

A new class of intelligent materials was recently appeared, are called Ferromagnetic Shape Memory Alloys (FSMA). In FSMA, the change of shape is caused by applying an external magnetic field and takes place through two mechanisms i.e. reverse martensitic transformation or reorientation of martensite tiles caused by the movement of twin boundaries. The disadvantages of existing FSMA such as high brittleness, difficulties in their production and high production costs significantly limit their practical applications in certain areas of life. Therefore, numerous studies are underway to find suitable materials that will find wider practical applications.

So far, it has been confirmed that several alloys exhibit the characteristics of FSMA, including: Ni-Mn-Ga [1], Ni-Mn-Sn [2], Co-Ni-Ga [3], Co-Ni-Al [4], Ni-Fe-Ga [5], Ni-Mn-Al [6]. Among which the most popular representative is the monocrystalline Ni-Mn-Ga alloy [7]. However, due to the high price of pure gallium and the difficulties associated with the growth of monocrystals, alternative alloys are being sought for Ni-Mn-Ga, whose production costs will be lower, while maintaining or improving their properties.

In recent years, interest in polycrystalline alloys based on Heusler's phase, i.e. Ni-Mn-In and Ni-Co-Mn-In [8] has increased, which exhibit many important physical properties, such as the magneto-caloric effect or the magnetic shape memory effect. However, despite many advantages, they also have disadvantages that limit their practical application in industry, technology or medicine. Ni-Mn-X alloys (X=In,

Co+In) are very fragile. Therefore, studies are underway to improve the plasticity of these alloys (e.g. by doping them). Despite its high fragility of the Ni-Mn-X (where X=In, Co+In) alloys, they can be a viable alternative to the Ni-Mn-Ga alloy [9]. Therefore, it seems important to conduct further research aimed at analyzing the influence of other elements on the structure and mechanical properties of FSMA Ni-Mn-X (where X=In, Co+In).

Due to the lack of previous studies on the effect of tantalum addition on the structure and properties of FSMA were tested. The aim of the work was to examine the effect of tantalum addition on the structure, chemical and phase composition of FSMA Ni-Co-Mn-In. Due to the physical and chemical properties of tantalum, the expected effect is to improve the mechanical properties of the Ni-Co-Mn-In alloy, mainly his plasticity and strength, while maintaining his structure (austenite and martensitic phases).

MATERIALS AND METHODS

The chemical composition of alloys and the technology of their production were chosen so that the martensitic transformation occurred near room temperature. Based on the literature review [8, 9], it was found that the above conditions meet the alloy with the chemical composition **$Ni_{45,5-x}Co_{4,5}Mn_{36,6}In_{13,4}Ta_x$ (where, x=0, 1, 3, 5)** (Tab. 1).

Tab.1. Chemical composition of alloys.

	Chemical composition %.at				
Determination of alloys	Ni	Mn	Co	In	**Ta**
Ta0	45.5	36.6	4.5	13.4	**0**
Ta1	44.5	36.6	4.5	13.4	**1**
Ta3	42.5	36.6	4.5	13.4	**3**
Ta5	40.5	36.6	4.5	13.4	**5**

Material of research

The 15 g buttons of $Ni_{45.5-x}Co_{4.5}Mn_{36.6}In_{13.4}Ta_x$ (x = 0, 1, 3, 5) chemical composition were produced by arc melting technique at the Institute of Materials Science in Chorzow, in a protective atmosphere of argon and at a temperature up to 3000^{o}C at a current up to 140 A, generated with the TIG VIPER 325-DC inverter. The alloys have been obtained from high purity metals: Ni-99.95%, Co-99.95%, Mn-99.9%, In-99.99999% and Ta-99.99%.

Test methods

To determine the chemical composition of Ni-Co-Mn-In-Ta alloys and surface morphology, scanning electron microscopy was used, using a JEOL type JSM 6480 microscope equipped with an EDS detector. Observations of surface morphology were carried out using a secondary electron detector (SED) and backscatter electron detector (BSE) using an acceleration voltage up to 20 keV. In order to analyze the chemical composition of the matrix and precipitates occurring in the alloys, the energy dispersion method (EDS), the detector of the IXRF company and the EDS 2006 software integrated with the microscope were used.

The X-ray phase analysis was carried out using a PANalitical model Empyrian diffractometer. A copper anode lamp (CuKα = 1.54178 Å) was used with a nickel filter, supplied with a current -30 mA and 40 kV. The data was recorded using the "step-scanning" method with 0.0132° step and the counting time of 900 seconds per measuring step in the range from 20° to 140° 2θ.

Thin films for TEM analysis, after previous mechanical processing, were made using ion polishing. The research was carried out using a high-resolution electron microscope JEOL type JEM 3010. During measurements, the transmission electron microscope worked at an accelerating voltage up to 300 kV. All images received were recorded using a Gatan digital CCD camera.

RESULTS

During the analysis of the recorded images, numerous secretions on the surface of the samples were observed. The Ta0 sample has a homogeneous structure without precipitates. Metal inclusions created during the technological process were observed on the surface of the Ta0 sample. Ta1-Ta5 samples are characterized by a multiphase structure, in which the matrix and surface separations can be distinguished. Studies on the chemical composition of alloys showed that the current releases (Fig. 1) are rich in Ta and for samples Ta3 and Ta5 also in Ni and Mn. For all studied alloys containing tantalum, the secretions are very poor in In and Co (Tab. 2).

Tab. 2. The average chemical composition of the matrix and the precipitated samples.

Sample	Matrix [% at.]±0,5%					Precipitates [% at.] ±0.5%				
	Ni	Co	Mn	In	Ta	Ni	Co	Mn	In	Ta
Ta0	45.5	4.5	36.6	13.4	0	-	-	-	-	-
Ta1	40.0	4.1	43.2	11.6	1.1	4.7	0.9	5.8	1.3	87.3
Ta3	38.5	3.4	45.7	12.4	1.2	22.0	14.0	16.0	0.7	47.5
Ta5	38.3	3.1	46.3	12.3	1.5	36.0	18.4	26.3	1.7	17.7

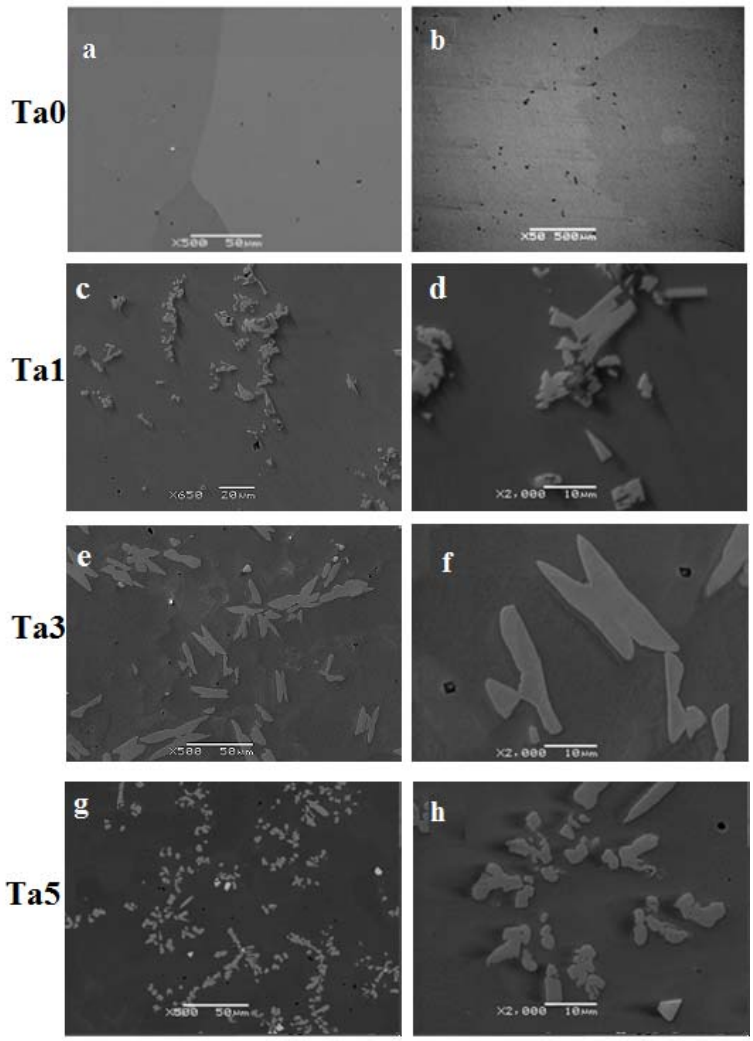

Fig. 1. SEM images of the Ta0-Ta5 sample microstructure of backscattered electrons (a, g) and secondary electrons (b, c, d, e, f, h).

The X-ray phase analysis carried out showed that in all the tested samples there is an austenite phase with an ordered structure L21 (Fig. 2). The occurrence of a martensitic phase in all tested alloys was also recorded. The existing martensitic phase is a modulated seven-layer martensite, which is designated as 14M (space group P2/m). Additionally, in the Ta1 alloy, the presence of a very rich Ta solid solution was confirmed by the results of the chemical composition carried out by the EDS method (Ta contents of 87.3% at. In the Ta1 samples). In comparison with the Ta0 sample, the diffractograms of tantalum-containing alloys occur a lot more reflections from the austenite phase. In order to provide exact parameters of elementary cells (a, b, c, a, β, ɤ) of the identified phases,

Rietveld analysis was carried out using the PANalytical X'Pert HighScore Plus computer program. The obtained parameters are summarized in Tab. 3.

Tab.3. Parameters of unit cells of phases occurring in the tested alloys.

Alloy	**Phase**	**Spatial group**	**Lattice parameter a [Å], b [Å], c [Å]**	**Angle β [°]**
Ta0	$L2_1$	Fm-3m	5,99	90
Ta1	$L2_1$	Fm-3m	5.99	90
	14M	P2/m	a=4.40 b=5.55 c=12.95	86
	Ta	Fm-3m	4.22	90
	Co-Ta(1)	Pm-3m	3.07	90
	Mn-Ni	Pm-3m	2.89	90
Ta3	$L2_1$	Fm-3m	5.99	90
	14M	P2/m	a=4.40 b=5.55 c=12.95	86
	$Ta(CoNi_2)$	P63/mmc	a=5.17 b=5.17 c=4.19	90 ɤ=120
	Co-Ta(2)	Fd-3m	6.79	90
	$Mn_{0.85}Co_{0.15}$	Pm-3m	3.07	90
	Ta	P4132	6.32	90
Ta5	$L2_1$	Fm-3m	5.99	90
	14M	P2/m	a=4.40 b=5.55 c=12.95	86
	$Ta_{0,8}Co_{2,2}$	Fd-3m	6.79	90
	Mn-Ni	Pm-3m	2.89	90

The resulting diffractograms are shown in Fig. 2. The observed phases are marked on the diffraction patterns corresponding to the test samples, respectively. The highest intensities correspond to the austenite phase with structure $L2_1$. Numerous peaks with lower intensity correspond to the martensitic phase 14M and come from the other identified phases (Co-Ta(1,2), Mn-Ni, $Ta(CoNi_2)$, $Mn_{0,85}Co_{0,15,}$ $Ta_{0,8}Co_{2,2}$).

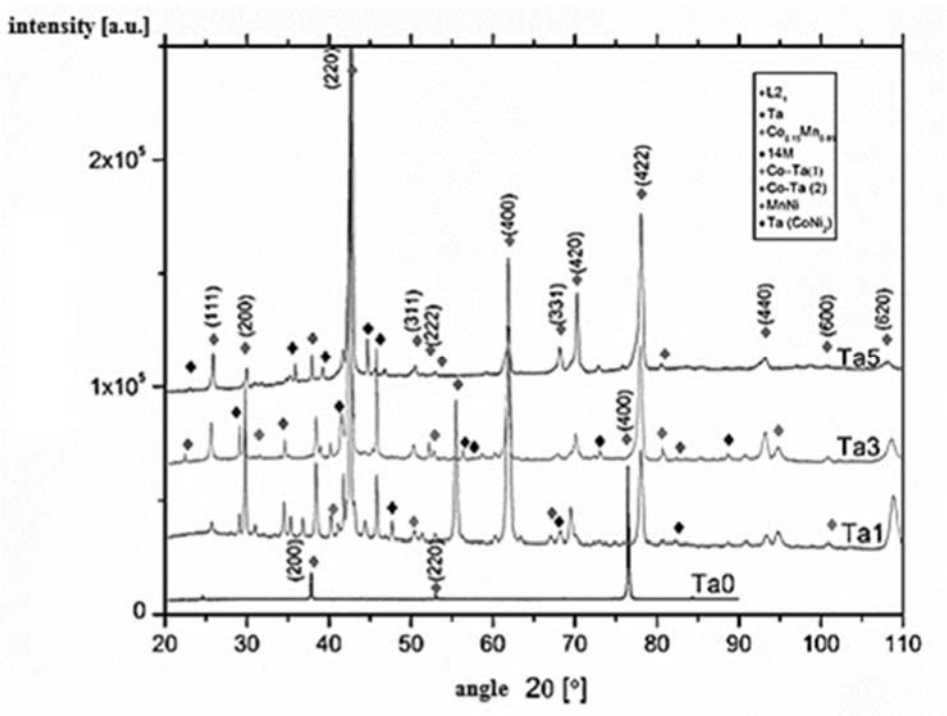

Fig.2. X-ray diffraction pattern of tested alloys.

During the X-ray phase analysis, the presence of numerous phases containing Ta was observed. The identified phases were characterized by the presence of Ta, Ni, Co and Mn, while none of the registered phases contained In.

Based on the analysis of the obtained electronograms (Figure 3), the parent phase was identified as an ordered structure of $L2_1$.

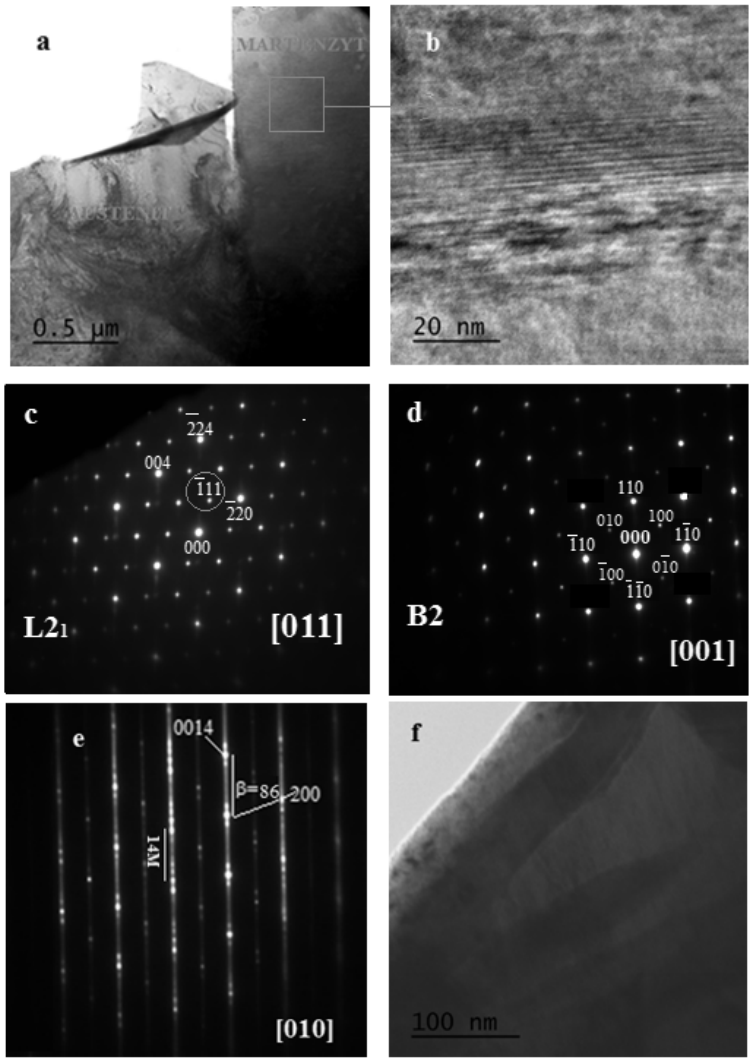

Fig. 3. a) A bright field image of parent and martensitic phase microstructures; b) a high resolution image of the enlarged area of the martensite phase; c-e) electronograms a, b-mother phase (α-L21 superstructure, b-B2 structure), e-martensite14M (7M); f) an image in a bright field of the martensite structure.

The {111} reflections that are typical of the L21 superstructure are observed on the parent phase electronograms in the orientation [011]. The electronograms in the orientation [001] also show reflections of type {001} showing the ordering of phase B2 (Figure 43d). The structure of the martensitic phase based on the obtained electronograms and visible satellite reflections was clearly identified as a seven-layer martenite modulated by 14M (Fig. 43e). The identified phases: parental and martensitic, are consistent with the results obtained during X-ray phase analysis.

During mechanical tests it was proved that the addition of tantalum has a positive effect on the mechanical properties of the alloys tested.

With the increase of Ta content, the following occurs:

- decrease of microhardness of precipitates by approx. 57% (from 1134 $\mu HV_{0.05}$ -Ta1 to 502 $\mu HV_{0.05}$-Ta3), while the increase of microhardness of the matrix by approx. 50% (from 313 $\mu HV_{0.05}$ -Ta0 to 458 $\mu HV_{0.05}$ - TA3),
- increasing the compressive strength by over 300% (from 313 MPa -Ta0 to 1006 MPa -Ta1),
- increase in the maximum compression strain by approx. 57% for a sample with an addition to 1% at. This in comparison with the sample without tantalum Ta0, and its decrease by approx. 57% for the sample containing 5% at. tantalum.

CONCLUSIONS

Tantalum-containing alloys have a lot of precipitates of the high content of Ta, Mn and Ni, but were poor in Co and In. The matrix of the studied alloys consisted mainly of Ni, Mn, Co. The addition of tantalum does not affect the structure of the austenite phase. X-ray and transmission electron microscopy phase analysis confirmed the presence of a high-order L21 austenite and a seven-layer modulated 14M martensite strutures.

After the structural studies carried out using scanning electron microscope, analysis of chemical composition by EDS energy dispersion method and after phase analysis carried out with X-ray diffraction and transmission electron microscopy, the following conclusions were made:

1. Addition of tantalum was strongly affected on the structure of Ni-Co-Mn-In alloys causing numerous precipitates in the alloy matrix;
2. The precipitates of the high content of Ta can affect the mechanical properties of the Ni-Co-Mn-In ferromagnetic alloys, improving their plastic properties;
3. In this work, structural tests of samples in the initial state were carried out. In the further course of work, analogous structural studies of alloys with Ta addition after heat treatment should be performed;
4. Addition of tantalum to 5% at. does not change the structure of the austenite (high-order L21 phase), which is present in all tested alloys;
5. Addition of tantalum to 5% at. does not cause the disappearance of the martensitic phase, which occurs in the form of seven-layer modulated 14M martensite, thanks to which martensitic transformation in these alloys is possible.
6. Addition to 1% at. tantalum increases compressive strength by more than 300% and increase in maximum compression strain by approx. 57%.

REFERENCES

[1] A. Sozinov et al., Giant Magnetic-Field-Induced Strain in NiMnGa Seven Layered Martensitic Phase, *Applied Physics Letters,* 2002*, 80, 10,* 1746-1748.

[2] A. Auge, et al., The magnetic shape memory alloy Ni-Mn-Sn in thin films, Bielefeld: Department of Physics University of Bielefeld, 2012.

[3] M. Wuttig, et al., A new ferromagnetic shape memory alloy system," *Scripta Materialia,* 2001, *44, 10,* 2393-2397.

[4] K. Oikawa, et al., Promising ferromagnetic Ni-Co-Al shape memory alloy system, *Applied Physics Letters, 2001, 79, 20,* 3290-3292.

[5] K. Oikawa, et al., Magnetic and martensitic phase transitions in ferromagnetic Ni–Ga–Fe shape memory alloys, *Applied Physics Letters, 2002, 81,* 5201-5203.

[6] A. Fujita, et al., Magnetic properties and large magnetic-field-induced strains in off-stoichiometric Ni-Mn-Al Heusler alloys, *Applied Physics Letters,* 2000, 77, 19, 3054-3056.

[7] Ullakko K. et al., Large magnetic-field-induced strains in Ni2MnGa single crystals, *Applied Physics Letters, 1996, 69, 13,* 1966-1968.

[8] K. Prusik,TEM study o f Ni-Mn-Co-In ferromagnetic shape memory alloys, *Solid State Phenomena, 2012, 186,* 271-274.

[9] S.Yang et al., Microstructure, martensitic transformation, mechanical and shape memory properties of Ni–Co–Mn–In high-temperature shape memory alloys under different heat treatments, *Department of Material Science and Engineering Xiamen University* 2002.

The electrochemical properties of La doped $BiFeO_3$ ceramics

*Małgorzata Dziubaniuk[1], Jan Wyrwa[1], Mieczysław Rękas[1], Kamila Kluczewska[2]
[1]Faculty of Materials Science and Ceramics, AGH University of Science and Technology, Cracow, Poland
[2]Institute of Technology, Pedagogical University, Cracow, Poland
*e-mail: dziubaniuk@o2.pl

Keywords: *bismuth ferrite, solid state synthesis, solid state ionics, electrochemical impedance spectroscopy*

ABSTRACT

The aim of presented study was the determination of impact of gaseous atmosphere composition on undoped and La-doped BFO electrical properties. The first step consisted of materials synthesis by solid state route using analytically pure oxides. The materials nominal compositions were $BiFeO_3$, $0.05La_2O_3$-$0.9BiFeO_3$, and $0.1La_2O_3$-$0.8BiFeO_3$. The microstructure of sintered bodies was revealed by SEM technique and phase compositions were verified by XRD method. The electrical properties of sintered pellets supported by silver electrodes were determined by Electrochemical Impedance Spectroscopy.

INTRODUCTION

Multiferroics is a group of materials in which at least two of three possible orders, i.e. ferromagnetic (ferromagnetic, antiferromagnetic or ferrotoroidal) ferroelectric or ferroelastic occur. Even though the mentioned phenomena were discovered as far back as in 60', its practical application becomes possible in late 90'. Among the prototypical appliances based on multiferroics materials presented up to now, it is worth to list magnetic field sensors, gas sensors as well as devices for energy storage and conversion [1].

One of these multiferroic materials, which is especially interesting on account of fundamental properties as well as possible usage, is the bismuth ferrite $BiFeO_3$ (BFO). At room temperature, in the BFO phase the ferroelectric and antiferromagnetic orders coexist (Neel antiferromagnetic temperature is 643 K and ferroelectric Curie temperature is 1100 K). BFO exhibits rhombohedrally distorted perovskite (ABO_3) crystal structure with R3c space group. In this case the polarization is mostly caused by the lone pair (s^2 orbital) of Bi^{3+}, so that the polarization comes from the A site while the magnetization comes from the B site (Fe^{3+}). The local spin ordering of Fe^{3+} forms a cycloidal spin structure.

The synthesis of single-phase BFO is still challenging due to the narrow temperature range of ABO_3 perovskite phase stabilization. The difficulty in obtainment pure phase material breed the opinion that BFO is in fact metastable in

air [2]. First of all, the $BiFeO_3$ compound is prone to decompose into Fe_2O_3 and Bi_2O_3. Secondly, according to the Bi_2O_3/Fe_2O_3 phase diagram, beside the desired $BiFO_3$, the parasitic $Bi_{25}FeO_{39}$ and $Bi_2Fe_4O_9$ phases can appear as products of reaction between the oxides, which indeed occur mainly at grain boundaries and impurities. The presence of the secondary phases in BFO leads to large leakage current and restricts its application.

In order to improve the purity of the material, different methods have been explored including wet chemical and mechanical methods, such as sol gel [3], conventional solid-state reaction route [4], co-precipitation [5], rapid liquid sintering [6], and mechanical activation [7]. BFO properties modification is possible by doping with controlled amounts of metal ions. Several research group have reported that the aliovalent substitution with Ba^{2+}, Pb^{2+}, Sr^{2+} and Ca^{2+} at bismuth site results in stabilization of low symmetric crystal structure which can enhance the magnetoelectric and optical properties of the doped BFO [8-9]. Moreover, it is observed that the BFO electrical properties can be improved by doping with trivalent rare earth ions, i.e. La^{3+}, Sm^{3+}. Y^{3+}, Pr^{3+}. This modification was demonstrated to effectively reduce the concentration of charge defects and dielectric losses [10-13].

Hence, properties emerging by rare-earth doping at B-site are worth of comparison with undoped BFO.

The largest part of studies about BFO regard new synthesis methods, structural properties by the use of SEM, phase analysis by XRD and FT-IR, dielectric properties basing on dielectric constant and tangent losses measurements in function of temperature, ferroelectric, magnetic and optical properties [14]. About material characterization, there are no reports dealing with the influence of gas atmosphere composition on electrical properties of BFO material. On top of that, there are no data about the effect on rare-earth dopant on BFO electrical conductivity. Hence, the work presented here aimed to add information about the BFO physicochemical properties, in relation to possible applications in gas sensing or hydrogen generating processes.

MATERIALS AND METHODS

A series of $Bi_{1-x}La_xFeO_3$ (x=0, 0,1 and 0,2) was synthesized by conventional solid state reaction method using powders of Bi_2O_3 (99,9%), La_2O_3 (99.99%) and Fe_2O_3 (99,8%) in their stoichiometric ratio. After mixing with isopropanol and ball milling for 24h with 350 rpm, the mixtures were dried in 373 K for 24h. The obtained powder was pressed into pellets and calcinated in 923 K for 1h. The products were crushed, grinded in agate mortal into powder and pellets of 10mm and 0.5g weight were formed. The materials were sintered in air at 1073K for 1 h.

Sintered pellets were examined by X-ray diffraction (XRD) method. The measurements were done in air at room temperature using CuK_α radiation (Philips X'Pert) within the 2Θ range 10-90° with the scan ratio 0.008°/s.

The surface morphology of sintered materials was observed using ultrahigh-resolution scanning electron microscope with field emission (FEG-Schottky emitter; Nova Nano-SEM 200, FEI Europe BV) cooperating with EDAX EDS analyzer.

The pellets were prepared for EIS measurements by covering on both sides with Ag paste provided by Pelco and fireing at 1073 K for 5 minutes.

The EIS measurements were performed in controlled atmospheres using a frequency analyzer (Solartron model FRA 1260) coupled with Dielectric Interface (model 1296) in the temperature range 473 - 773K. The frequency range was 0.1 Hz - 32MHz, the amplitude of sinusoidal voltage signal was 20 mV. The measurements were performed in the following atmospheres: synthetic air (series no 1, 3 and 5), 3000 ppm NH_3 in argon (series no 2), 10% H_2 in argon (series no 4). The series no 3 and 5 in synthetic air were conducted in order to determine the reversibility of the material impedance response in H_2 and NH_3 rich atmospheres. The values of the resistances were derived using Zview software (version 2.2, Scribner Associates, Inc.).

RESULTS AND DISCUSSION

Spectra from XRD are presented in Fig. 1.

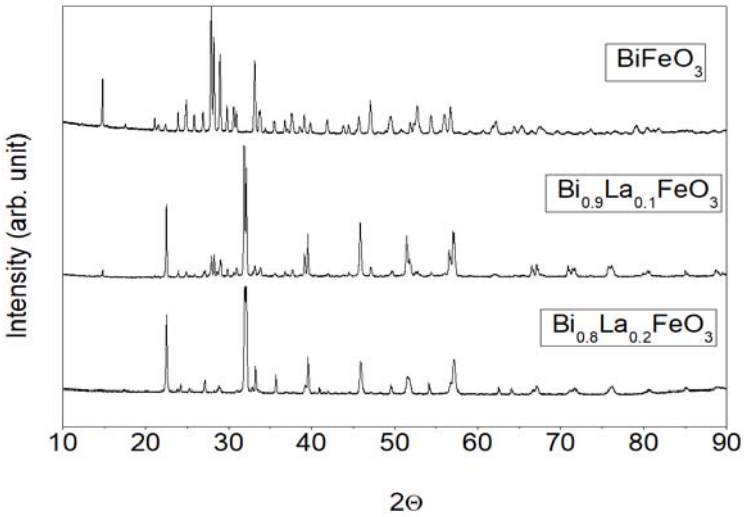

Fig. 1. XRD patterns for sintered bodies.

Undoped material exhibited some extra peaks coming from $Bi_2Fe_4O_9$ and $Bi_{36}Fe_2O_{57}$ secondary phases. The spectra were obtained for 10at.% and 20%at. La doped exhibits mainly peaks characteristic for $BiFeO_3$ crystallizing in distorted perovskite structure with rhombohedral lattice type and R3C space group. This means that doping with La hinders the formation of undesirable phases.

SEM images are presented in Fig. 2-4. The investigated ceramic materials are comprised of well developed grains with clearly separated boundaries. Undoped BFO contains the biggest grains and some empty spaces. In case of 10at.% La doped material the analysis of grain size was performed. The diameter of grains is about 250 nm. $Bi_{0.9}La_{0.1}FeO_3$ is characterized by higher homogeneity than pure BFO. The neighboring grains closely adhere to each other and there are no empty spaces visible. Material with the highest content of La is composed of the smallest grains. The results indicate that the addition of La ions improve the sinterability of the materials.

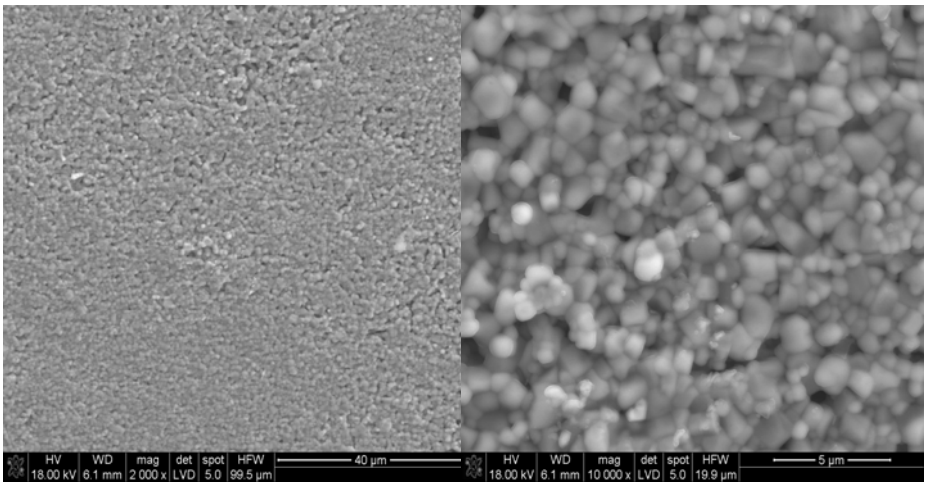

Fig. 2. SEM images for $BiFeO_3$ sintered body.

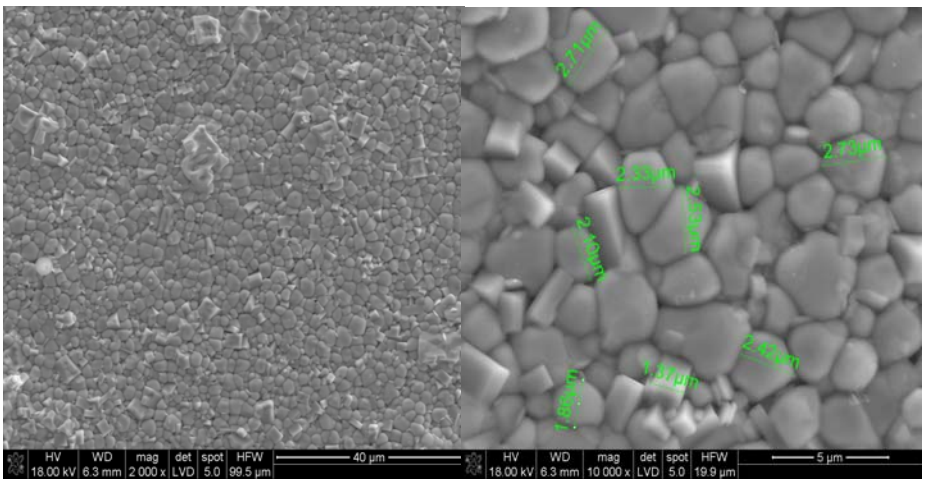

Fig. 3. SEM images for $Bi_{0.9}La_{0.1}FeO_3$ sintered body.

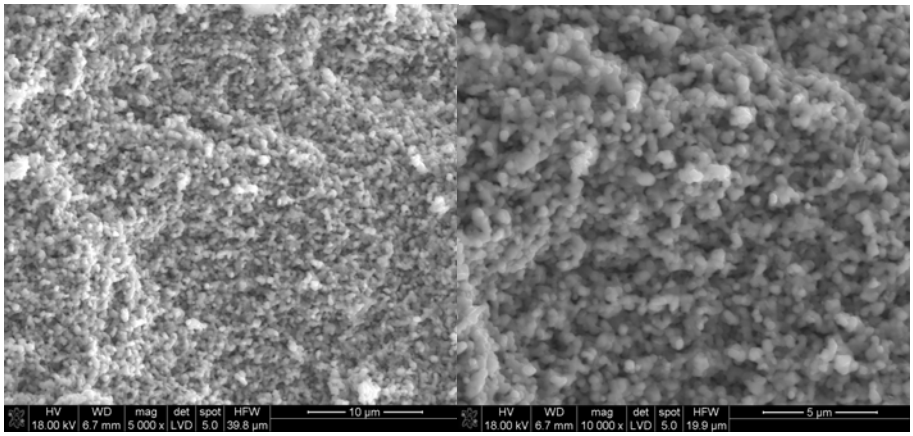

Fig. 4. SEM images for $Bi_{0.8}La_{0.2}FeO_3$ sintered body.

The electrochemical properties were investigated by EIS spectra analysis realized by dedicated software. The specific conductivities were calculated using values of specimens resistance obtained by analysis of the spectra taking account of the pellets geometry. The results of these conductivities are presented in form of Arrhenius plots in Fig. 5-7. For the undoped and 10% at. La doped BFO the conductivity increases with temperature according to Arrhenius law in every atmosphere. In these cases the linear regression analysis was performed and the values of activation energy were determined. The values about 1 eV are close to the half of reported theoretical optical band-gap at room temperature ranging from 2.3-2.8 eV, which reveals intrinsic conduction phenomena occurring in the specimen [14]. Intrinsic mechanism of electrical conductivity results from the equilibrium:

$$\text{nill} = e' + h^{\bullet}. \tag{1}$$

In contrast, the energy of activation value from series no 5 for undoped material is about twice lower. It shows, in this case, that the extrinsic conduction mainly affects the observed electrical properties. In turn, basing on available data, for undoped BFO it is difficult to explain the highest value of E_a about 2 eV from H_2 rich atmosphere. It may be caused by the Fe^{3+}/Fe^{2+} reduction and the creation of some unexpected phases. However, this hypothesis needs further verification.

The processes occurring in 20at.%. La doped specimen are more complicated than what the theory assumes. It may depend on several simultaneous reactions with opposing effects. 10 and 20%at. La doped materials show much higher electrical conductivity in comparison to undoped material. It should be noted that in H_2 reach atmosphere at temperatures of 400 and 500°C for all samples the conductivities are visibly higher than in the air, which can be explained by the proton conduction realized by the dissociation and adsorption of hydrogen at high temperatures. The

$Bi_{0,8}La_{0,2}FeO_3$ specimen shows much higher resistance in ammonia rich atmosphere than in air. However, further investigation is necessary to explain these phenomena.

In order to investigate the reversibility of the reaction between materials supported with silver electrodes and reductive atmospheres, after the measurements in H_2 and NH_3 containing atmospheres, the following measurements in air were performed. In general, the spectra did not achieve their initial state, which indicate that used reductive gases introduced permanent modifications in specimens.

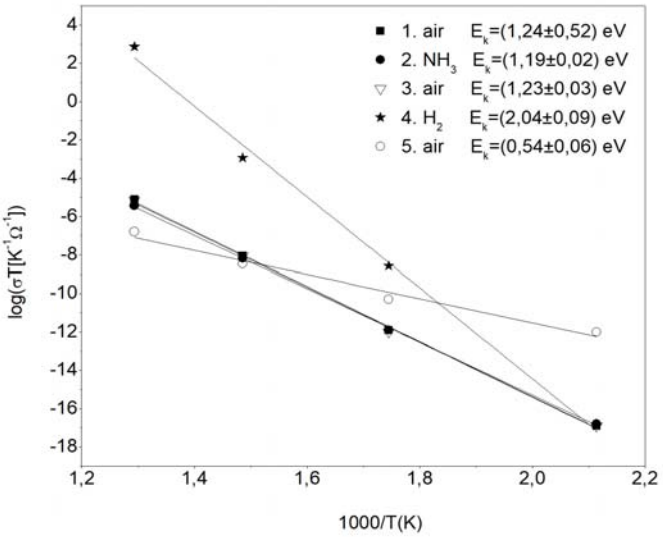

Fig. 5. Arrhenius plots for $BiFeO_3$.

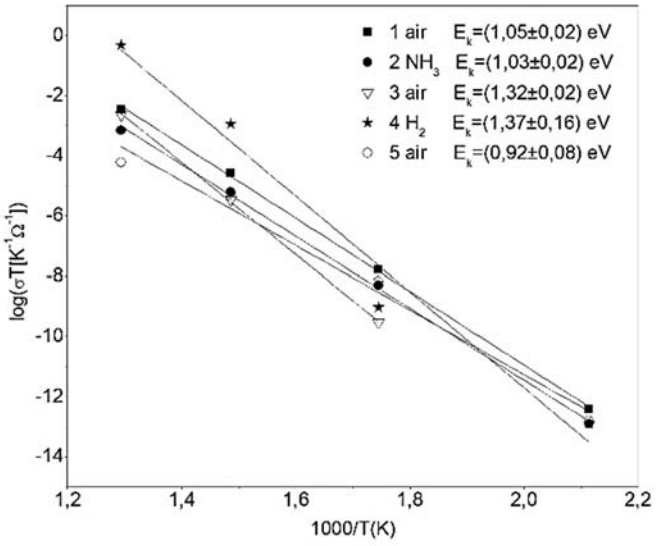

Fig. 6. Arrhenius plots for $Bi_{0.9}La_{0.1}FeO_3$.

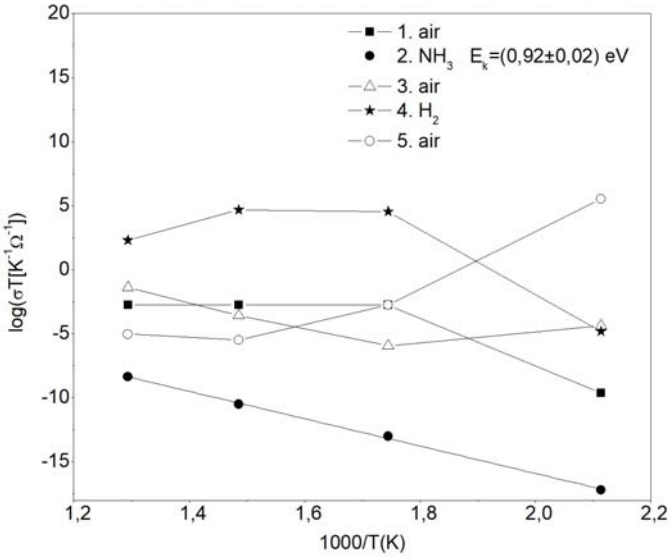

Fig. 7. Arrhenius plots for $Bi_{0.8}La_{0.2}FeO_3$.

CONCLUSIONS

Mechanically stable sintered bodies featured by the nominal compositions $Bi_{1-x}La_xFeO_3$ (x=0, 0.1 and 0.2) were prepared by the mechanosynthesis route. The presence of La^{3+} ions stabilized the desired rhombohedral crystallographic structure and improved the sinterability of the selected ceramic powders. The investigated materials supported with silver electrodes reacted with gaseous hydrogen in irreversible way, which was demonstrated by the modification of permanent electrical properties. Material containing the highest content of La reacts with ammonia, leading to decrease of its electrical conductivity. The mechanisms of observed reactions seems a complex topic, needing more detailed o explain the nature of investigated phenomena in materials based on BFO.

ACKNOWLEDGMENTS

This work was supported by the National Science Centre of the Republic of Poland, under Grant No 2016/23/B/ST8/00163.

REFERENCES

[1] Spaldin N.A., Fiebig M., The reneissance of magnetoelectricmultiferroics, *Science* 2005, 309, 391-392, DOI: DOI: 10.1126/science.1113357

[2] Palai R, Katiyar R.S., Schmid H., Tissot P., Clark S.J, Robertson J., Redfern S.A.T., Catalan G., Scott J.F., β phase and γ−β metal-insulator transition in multiferroic $BiFeO_3$, *Physical Review B*, 2008, 77, 014110 DOI: https://doi.org/10.1103/PhysRevB.77.014110

[3] Xu J-H, Ke H., Jia D-C, Wang W., Zhou Y., Low-temperature synthesis of $BiFeO_3$nanopowders via a sol–gel method, *Journal of alloys and Compounds*, 2009, 472/1-2, 473, DOI: http://www.sciencedirect.com/science/article/pii/S0925838808007366

[4] Bhole C. P., Patil S. L. and Rewatkara K. G., Synthesis and Characterizations of $BiFeO_3$, Ceramics by Solid State Method, International Conference on Benchmarks in Engineering Science and Technology ICBEST 2012, DOI: research.ijcaonline.org/icbest/number3/icbest1031.pdf

[5] Shetty S., Palkar V. R., Pinto R., Size effect study in magnetoelectric $BiFeO_3$ system, *Pramana – Journal of Physics* 58, 2002, 5-6, 1027-1030 DOI: http://www.ias.ac.in/article/fulltext/pram/058/05-06/1027-1030

[6] Y. P. Wang, L. Zhou, M. F. Zhang, X. Y. Chen, J.-M. Liu, Z. G. Liu, Room-Temperature Situated Ferroelectric Polarization in BiFeO3 Ceramics Synthesized by Rapid Liquid Phase Sintering, *Applied Physics Letters* 2004, 84, 10, 1731-1733 DOI: 10.1063/1.1667612

[7] Maurya D., Thota H., Singh K., Nalwa, Garg A., $BiFeO_3$ ceramics synthesized by mechanical activation assisted versus conventional solid-state-reaction process: A comparative study, Journal of Alloys and Compounds 2009, 477, 780–784 DOI: https://doi.org/10.1016/j.jallcom.2008.10.155

[8] Khomchenko V.A.,.Kiselev D.A, Vieira J.M. ,Jian L. , Kholkin A.L. , Lopes A.M.L., Pogorelov Y.G., Araujo J.P., MaglioneM.,Effect of diamagnetic Ca, Sr, Pb, and Ba substitution on the crystal structure and multiferroic properties of the $BiFeO_3$perovskite, *Journal of Applied . Physics*, 2008, 103, 024105, DOI: http://aip.scitation.org/doi/abs/10.1063/1.2836802

[9] Jaiparkash, Kumar J., Chauhan R.S., Kumar R., Study of dielectric properties of single phase $Bi_{1-x}Ca_xFeO_3$ (x = 0.1, 0.3, 0.5), Solid State Sciences 2011, 13, 1869-1873, DOI:https://doi.org/10.1016/j.solidstatesciences.2011.07.021

[10] Cheng Z. X., Li1 A. H., Wang X. L.,Dou S. X.,Ozawa K, Kimura H. ,Zhang S. J., Shrout T. R., Structure, ferroelectric properties, and magnetic properties of the La-doped bismuth ferrite, *Journal of Applied Physics* 2008, 103, 07E507; DOI: https://doi.org/10.1063/1.2839325

[11] Verma V., Beniwal A., Ohlan A., Tripathi R., Structural, magnetic and ferroelectricproperties of Pr dopedmulti-ferroicsbismuthferrites, *Journal of Magnetism and Magnetic Materials*, 2015, 394, 385-390, DOI: https://doi.org/10.1016/j.jmmm.2015.06.067

[12] Cheng Z. X., Li A. H., Wang X. L., Dou S. X., Ozawa K., Kimura H., Zhang S. J, Shrout T. R., Structure, ferroelectricproperties, and magneticproperties of the La-dopedbismuthferrite, *Journal of Applied Physics*2008, 103, 07E507, DOI:https://doi.org/10.1063/1.2839325

[13] Rao T. D., Karthik T., Asthana S., Investigation of Structural, magnetic and opticalproperties of rareearthsubstitutedBismuthFerrite, Journal of RareEarths 2013, 31, 370-375 DOI: http://dx.doi.org/10.1016/S1002-0721(12)60288-9
[14] Catalan G., Scott J.F., Physics and Applications of BismuthFerrite, Advanced Materials 2009, 21, 2463–2485, DOI: 10.1002/adma.200802849

Analysis of *wake* structures in bubbly flows using *Particle Image Velocimetry* (PIV)

*Björn Lewandowski[1,2], Micha Fertig[2], Georg Krekel[2], Mathias Ulbricht[1]
[1] Chair of Technical Chemistry II, University of Duisburg-Essen, Essen, DE
[2] Faculty of Chemistry, Niederrhein University of Applied Sciences, Krefeld, DE
e-mail: Bjoern.Lewandowski@hs-niederrhein.de

***Keywords**: Bubbly flow, Particle Image Velocimetry, wake analysis, flow characteristics, high-speed imaging*

ABSTRACT

The flow structure around rising single air bubbles in water and their characteristics, such as equivalent diameter, rising velocity and shape, was investigated using Particle Image Velocimetry (PIV) and Shadowgraphy in a transparent apparatus with a volume of 120 ml. The effect of different volumetric gas flow rates, ranging from 4 µl/min to 2 ml/min on the liquid velocity was studied. Ellipsoidal bubbles were observed with a rising velocity of 0.25 – 0.29 m/s. It was found that a Kármán vortex street existed behind the rising bubbles. Furthermore, the wake region expanded with increasing volumetric gas flow rate as well as the number and size of the vortices.

INTRODUCTION

Multiphase gaseous-liquid flows play an important role in the chemical industry, e. g. in bubble column reactors [1]. A detailed insight into flow patterns and rising velocities is possible with optical methods, like PIV [2]. Application to multiphase flows is, however, challenging due to the presence of different phases and the complex flow structures. In particular, unwanted reflections of irradiated light at the phase boundaries complicate the analysis. Furthermore, shadow regions appear due to light refraction and reflection, so that some information is lost. Additionally, illuminated particles behind the rising bubbles are captured due to the transparency of the gaseous phase (see Fig. 1.). Such particles will also be considered in the analysis, if the images are used untreated, and thus lead to wrong vectors.

Many researchers have already investigated the flow field around and the wake structures of single bubbles as well as bubble swarms [3]-[8]. Still, some controversial reports about the wake structure of bubbles are present in literature [9]. Reasons for this may be the different purities of the water used, which has a significant influence on the bubble boundary and thus on the bubble movement itself [10]-[12]. Furthermore, two bubbles rising within a very short time interval tend to interact with each other, which has also a great impact on the bubble characteristics and therefore on the wake structure [9]. *Sam et al.* proposed for this reason a bubble

frequency of less than 80 bubbles per minute to reduce the interaction of two consecutive bubbles [11], [13].

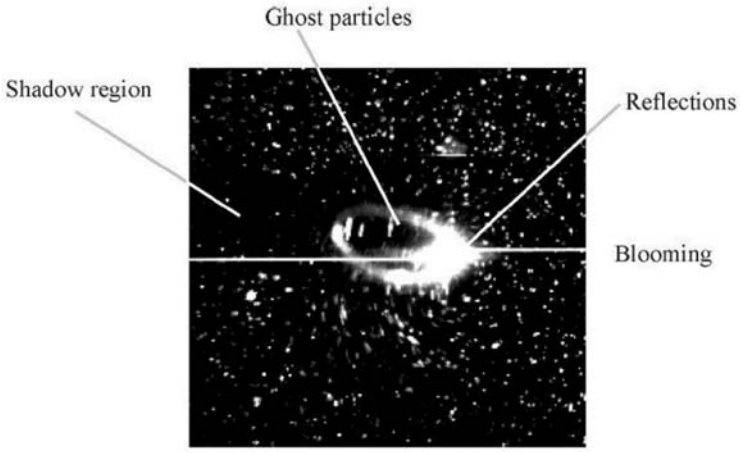

Fig. 1. Problems of multiphase PIV [5].

MATERIALS AND METHODS

Air bubbles were filmed rising in a water filled transparent apparatus made of three millimetre thick poly(methyl methacrylate) (PMMA) plates. A schematic drawing of the experimental set-up is given in Fig. 2. A continuous wave (c. w.) Nd:YAG laser with a wave length of 532 nm and a maximum power output of 5 W (supplier: Dantec Dynamics) was used to illuminate the flow. A high-speed CMOS camera (type: Olympus iSpeed TR) with a 12x zoom lens) with F-Mount (supplier: Navitar) in combination with a 0.5x lens attachment (supplier: Navitar) was used as optical system. High-speed monochrome 8 bit grayscale image sequences were captured at a frame rate of 300 fps. Thus, approx. 36 images were obtained for each bubble. The image resolution was 1280 x 1040 px. In addition to the c. w. laser, a LED backlight illumination (supplier: Dantec Dynamics) with 55,000 lux at continuous illumination mode was used to obtain Shadowgraphy images for the determination of bubble characteristics, such as equivalent diameter d_B, rising velocity w_B and elongation f_e as morphological parameter.

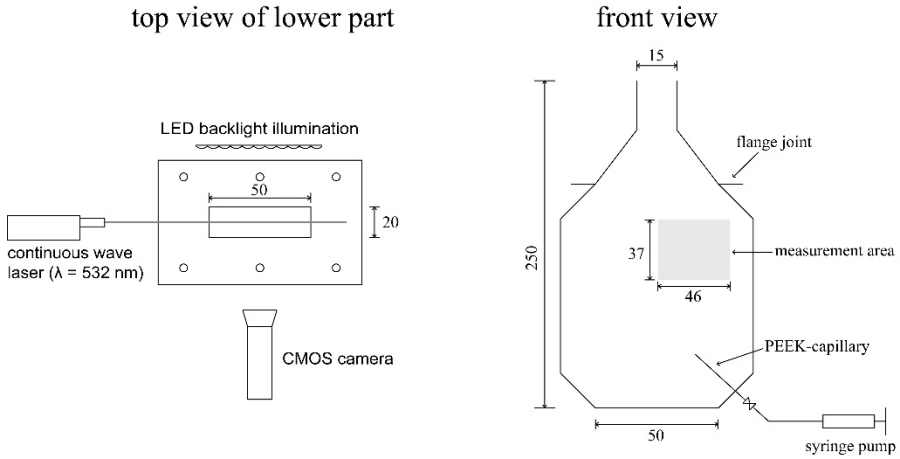

Fig. 2. Experimental set-up for PIV experiments (all dimensions in mm).

The equivalent bubble diameter was calculated under the assumption of rotational symmetry using the maximum and minimum axes of a fitted ellipse [14]:

$$d_B=\left(d_{max}^2 \cdot d_{min}\right)^{1/3} \tag{2}$$

The elongation is calculated using equation (3). Its domain ranges from 0 for a perfect circle to 1 for an infinite line (= infinitely stretched bubble):

$$f_e=1-\frac{d_{min}}{d_{max}} \tag{3}$$

The conditions for the conducted experiments are given in Tab. 6. A poly(ether ether ketone) (PEEK) capillary with an internal diameter of 250 µm (supplier: Techlab) was introduced into the apparatus at the bottom at an angle of 45°. The capillary was connected to a 5 ml gastight syringe (supplier: Hamilton) filled with ambient air in a syringe pump (type: KDS 200, supplier: Cole-Parmer). Distilled water was used as liquid. The water was first degassed at 50 mbar for approx. 15 minutes before filling the apparatus. This procedure reduced the amount of unwanted gas bubbles attached to the PMMA surface in the measurement area. Polyamide seeding particles with a mean diameter of 20 µm (supplier: LaVision) were added to the water, so that at least 10 particles were present per interrogation area.

Tab. 6. Experimental conditions.

Test conditions:	
Internal capillary diameter d_i in µm	250
Volumetric gas flow rates $\dot{V}_g$ in ml/min	0.004, 0.050, 2.000
Position of measurement area above capillary in mm	60
Environmental temperature in °C	22
Gas properties [10]:	**Air**
Dynamic viscosity η_g in mPa s	0.0183
Density ϱ_g in kg/m^3	1.18
Liquid properties [10]:	**Water**
Dynamic viscosity η_l in mPa s	0.957
Density ϱ_l in kg/m^3	997.75
Surface tension γ_{lg} in N/m	0.072

The image sequences were analysed using the adaptive correlation in Dynamic Studio v4.00 (supplier: Dantec Dynamics). The size of the interrogation area was set to 16 x 16 pixel, which corresponds to 0.6 x 0.6 mm, with an overlap of 25 %. A peak validation with a factor of 0.5, a neighbourhood size of 5 x 5 pixel and an acceptance factor of 0.20 were applied for the vector validation. The liquid velocity w is calculated using the scalar map function, with V as velocity in x and U as velocity in y direction:

$$w=\sqrt{V^2 \cdot U^2} \tag{4}$$

The vorticity is analysed as a measure of the vortex strength. Since only planar PIV images are present in this work, only the rotation around the z axis ω_z is determined. The local velocities ∂V and ∂U are differentiated with respect to the location ∂x and ∂y, respectively:

$$\omega_z=\frac{\partial V}{\partial x}-\frac{\partial U}{\partial y} \tag{5}$$

RESULTS AND DISCUSSION

For the characterisation of the rising bubbles, a set of dimensionless numbers is used [16], [17]. These are the bubble Reynolds number Re:

$$Re=\frac{w_B \cdot d_B \cdot \varrho_l}{\eta_l} \tag{6}$$

The Eötvös number Eo:

$$Eo=\frac{g \cdot (\varrho_l-\varrho_g) \cdot d_B^2}{\gamma_{lg}} \tag{7}$$

And the Morton number M as description for the physical properties of the fluid:

$$M=\frac{g\cdot(\varrho_l-\varrho_g)\cdot\eta_l^4}{\varrho_l^2\cdot\gamma_{lg}^3} \tag{8}$$

The results for the bubble characteristics are given in Tab. . The standard deviations are with less than 3 % negligible and therefore not listed in the table. From Tab. it can be concluded that with an increase of $\dot{V}_g$ the bubble diameter increases from 2.53 to 2.70 mm. The same applies to the rising velocity, which increases from 0.25 to 0.29 m/s, and the elongation, which increases from 0.26 to 0.36. The measured rising velocity is in accordance with literature data from *Clift et al.* for a pure water system [16]. The bubble Reynolds number varied in a range of 659 to 809, the Eötvös number varied from 0.86 to 0.98 and the Morton number was constant at $2.14 \cdot 10^{-11}$. According to bubble shape maps found in literature, the observed bubbles are in the ellipsoidal regime [16], [17]. This is in consensus with the visual impression gained from the image sequences as well as the determined elongation (compare Tab. 2).

Tab. 2. Bubble characteristics.

$\dot{V}_g$ in ml/min	d_B in mm	w_B in m/s	f_e	Re	Eo	M
0.004	2.53	0.25	0.26	659	0.86	$2.14\ 10^{-11}$
0.050	2.55	0.29	0.34	762	0.87	$2.14\ 10^{-11}$
2.000	2.70	0.29	0.36	809	0.98	$2.14\ 10^{-11}$

A typical resulting vector plot for the data analysis is given in Fig. 3. The wake structure behind the bubbles can clearly be identified. Alternating clockwise and anti-clockwise vortices can be seen, representing a typical Kármán vortex street. Additionally, the typical flow structure around the bubble is presented according to other observations in literature [16]. The flow in front of the bubble is directed in the same direction as the bubble trajectory, while a circulating flow is present at the sides. Behind the bubble, the flow is again directed in direction of the bubble trajectory.

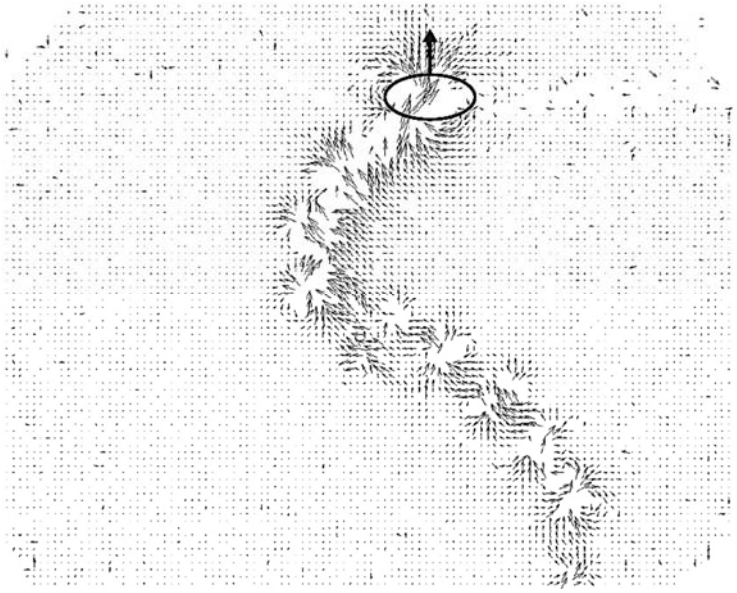

Fig. 3. Resulting vector plot for a rising bubble 117 ms after entering the measurement area (bubble position and direction of movement marked at the top of the image).

The resulting velocities and vorticities for the different volumetric gas flow rates are presented in Fig. 4. At a low volumetric gas flow rate $\dot{V}_g$ of 4 µl/min, most parts of the measurement area are calmed. In the wake region far behind the rising bubble, velocities of about 0.015 m/s can be observed. Directly behind the bubble, higher velocities of approx. 0.035 m/s were measured. The vorticity plot shows alternating clockwise (blue) and anti-clockwise (yellow) vortices according to a Kármán vortex street. The vortices are not located in the region directly behind the bubble, but at a certain distance. The amount and size of clockwise vortices is dominant.

An increase of $\dot{V}_g$ to 0.05 ml/min leads to an expanding wake structure behind the rising bubble (see Fig. 4., centre). Furthermore, the region of higher velocities directly behind the bubble increases. The mean velocity in this area is approx. 0.045 m/s. The vorticity plot shows again a typical Kármán vortex street. The size and number of the vortices is higher than at a $\dot{V}_g$ of 4 µl/min.

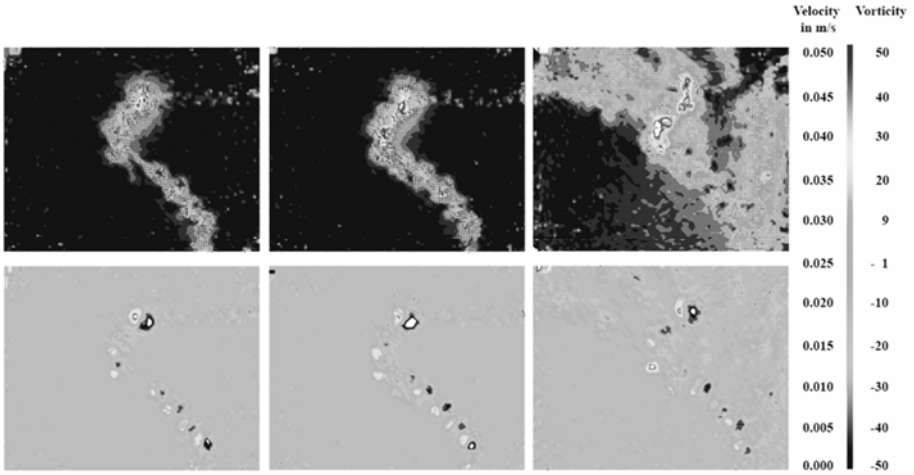

Fig. 4. Liquid velocity (top) and vorticity (bottom) for volumetric gas flow rates $\dot{V}_g$ of 0.004 ml/min (left), 0.05 ml/min (centre) and 2.0 ml/min (right) for rising air bubbles in distilled water 100 ms after the bubble entered the measurement area.

Additionally, vortices can be seen in the immediate region behind the bubble. The wake structure seems more closed which is also reflected in the closed region of the wake in the velocity plot.

At $\dot{V}_g$ of 2.0 ml/min nearly 50 % of the measurement area show velocities greater than zero. However, the main bubble trajectory according to the two lower volumetric gas flow rates may still be recognized in the velocity plot. A mean velocities of 0.050 m/s is present in the vicinity of the rising bubble. Furthermore, the flow seems to expand to the right-hand side and to the top left corner of the measurement area. At the right-hand side an overall downwards movement is present with some recirculating areas. These recirculation areas may be caused due to the small distance to the apparatus wall (compare to Fig.). The flow in the top left corner is mainly directed upwards due to the induced turbulence of the rising bubble. In the vorticity plot more regions of turbulence are present than before. The amount of clockwise rotating vortices is dominant and only some anti-clockwise vortices can be identified. Compared to the vorticity plots of the other two volumetric gas flow rates, the intensity of the vorticity increases, which is indicated by darker shades of blue and yellow/red for clockwise and anti-clockwise rotation, respectively.

CONCLUSIONS

An investigation of the bubble characteristics and wake structure of rising air bubbles in water in dependency of the volumetric gas flow rate was carried out using optical methods like Shadowgraphy and Particle Image Velocimetry (PIV). The bubble Reynolds number was in a range of 659 to 809 and the Eötvös number was in a range of 0.86 to 0.98 with a constant Morton number of $2.14 \cdot 10^{-11}$.

It was found that with increasing volumetric gas flow rate the bubbles became larger and their rising velocity increased. Furthermore, the bubbles became more ellipsoidal. Using PIV for the investigation of the flow structure it was found that the wake structure behind the rising bubbles expanded with increasing volumetric gas flow rate. Additionally, higher liquid velocities were observed in the region directly behind the bubbles. At a flow rate of 2 ml/min the turbulent flow structure included nearly the complete measurement area. Using the vorticity as representation for the turbulence a Kármán vortex street with alternating clockwise and anti-clockwise rotating vortices was observed. An increase of the volumetric flow rate produced more and larger vortices. The clockwise vortices were always dominant. Additionally, recirculation areas were found at higher volumetric gas flow rates at the right-hand side of the measurement area, which may be caused by the short distance to the apparatus wall.

NOMENCLATURE

CMOS	Complementary metal-oxide-semiconductor	$\dot{V}_g$	Volumetric gas flow rate
c. w.	Continuous wave	w	Liquid velocity
d_B	Equivalent bubble diameter	w_B	Rising velocity of bubbles
d_i	Capillary internal diameter	Eo	Eötvös number
f_e	Elongation	Re	Bubble Reynolds number
g	Acceleration due to gravity	M	Morton number
LED	Light-emitting diode	γ_{lg}	Surface tension between liquid and gaseous phase
PIV	Particle Image Velocimetry	η_l/η_g	Dynamic viscosity of liquid/gas
U	Velocity in y direction	ϱ_l/ϱ_g	density of liquid/gas
V	Velocity in x direction	ω_z	Vorticity as rotation around z axis

REFERENCES

[1] Kraume, M., *Transportvorgänge in der Verfahrenstechnik*, *Springer*, 2012

[2] Raffel, M. et al., *Particle Image Velocimetry: A practical guide*, *Springer*, 2007

[3] Bröder, D., *Anwendung optischer Messtechniken zur Untersuchung disperser Gas-Flüssigkeits-Strömungen, Ph. D. Thesis*, Martin-Luther Universität Halle-Wittenberg, 2003

[4] Sommerfeld, M., *Bubbly flows*, *Springer*, 2004

[5] Brücker, C., *PIV in two-phase flow* in *Particle Image Velocimetry and associated techniques*, *Lecture series*, Rhode-St-Genèse, 2000-2001

[6] Liu, Z., Zheng, Y., *PIV study of bubble rising behavior*, *Powder technology*, 2006, 168, 10-20, DOI: 10.1016/j.powtec.2006.05.020

[7] Liu, Z., Zheng, Y., Jia, L., Zhang, Q., *Study of bubble induced flow structure using PIV*, *Chemical Engineering Science*, 2005, 60, 3537-3552, DOI: 10.1016/j.ces.2004.03.049

[8] Kim, S., Yi, S., Kim, H., Kim, J., Kim, K., *Dynamic analysis of bubble-driven liquid flows using time-resolved particle image velocimetry and proper orthogonal decomposition techniques*, *Journal of Visualization*, 2010, 13, 213-220, DOI: 10.1007/s12650-010-0029-y

[9] Brücker, C., *Structure and dynamics of the wake of bubbles and its relevance for bubble interaction*, *Physics of Fluids*, 1999, 11, 1781-1796, DOI: 10.1063/1.870043

[10] Li, Y., Zhu, T., Liu, Y., Tian, Y. Wang, H., *Effects of surfactant on bubble hydrodynamic behavior under flotation-related conditions in wastewater*, *Water Science & Technology*, 2012, 65, 1060-1066, DOI: 10.2166/wst.2012.933

[11] Saito, T., Sakakibara, K., Miyamoto,Y., Yamada, M., *A study of surfactant effects on the liquid-phase motion around a zigzagging-ascent bubble using a recursive cross-correlation PIV*, *Chemical Engineering Journal*, 2010, 158, 39-50, DOI: 10.1016/j.cej.2008.07.021

[12] Sam, A., Gomez, C., Finch, J., *Axial velocity profiles of single bubbles*, *International Journal of Mineral Processing*, 1996, 47, 177-196, DOI: 10.1016/0301-7516(95)00088-7

[13] Rafiei, A., Robbertze, M., Finch, J., *Gas holdup and single bubble velocity profile*, *International Journal of Mineral Processing*, 2011, 98, 89-93, DOI: 10.1016/j.minpro.2010.10.011

[14] Grau, R., *An investigation of the effect of physical and chemical variables on bubble generation and coalescence in laboratory scale flotation cells*, *Ph. D. Thesis*, Helsinki University of Technology, 2005

[15] VDI Gesellschaft, *VDI heat atlas*, *Spinger*, 2010

[16] Clift, R. et al., *Bubbles, Drops, and Particles*, *Academic Press*, 1978

[17] Fan, L., Tsuchiya, K., *Bubble wake dynamics in liquids and liquid-solid suspensions*, *Butterworth-Heinemann*, 1990

The study of ruthenium-based catalysts used in homogeneous transfer hydrogenation of acetophenone

Filip Mikołajczyk, Kamil Kamiński
Faculty of Process and Environmental Engineering, Lodz University of Technology, Łódź, POLAND
e-mail: mikolajczyk.filip.pl@gmail.com

Keywords: *ruthenium-based catalysts, transfer hydrogenation, ketones, catalysis,* $RuCl_2(PPh_3)_3$

ABSTRACT

A detailed comparison of catalytic properties of two different ruthenium-based catalysts in the reaction of homogeneous hydrogenation of acetophenone was performed. Additionally, methods of synthesis of both catalysts were tested and optimized in order to achieve the best possible quality and purity of the final catalysts.

NMR analysis was used to analyze and identify the composition of ruthenium compounds and gas chromatography was used to analyze the conversion rate of hydrogenation reactions.

It was determined that $RuCl_2(PPh_3)_3$ obtained with a modified method described by Shaw's group [1] had the best catalytic properties in the reaction performed under conditions described in Liang Wang's publication [2]. It was also determined that for concentration ratio of substrate to $RuCl_2(PPh_3)_3$ amounting to 250:1 the conversion rate was much higher than for the reaction performed with a double dose of the catalyst. Results of experiments also show that samples of the post-reaction solution should be analyzed right after the reaction, because even if they are stored in low temperature the amount of product can change up to 3-5% compared to the base sample and this change is not predictable.

These findings have significant implications for further research of the reaction of homogeneous transfer hydrogenation of ketones. With the right catalysts and methods of their synthesis other parameters of this reaction can be optimized. The most important one is a change of solvent from isopropyl alcohol to a less toxic substance like water. This may result in increasing the value of this reaction in green chemistry and chemical industry.

INTRODUCTION

The reaction of hydrogenation of multiple bonds withgaseous hydrogen in presence of homogeneous metallic catalysts has beenknown in organic chemistry since 1938, when it was observed for the first time by Otto Roelen. Since then it was determined that performing this type of reaction has some significant advantages over these, where heterogeneous catalysts have been used. Homogeneous catalysts are very

effective and selective even when the reaction is performed under mild conditions. It also allows scientists to study the mechanism and kinetics of the reaction. Its usage is also beneficial for the industry – it does not require a high hydrogen pressure and hazardous reducing reagents. Thanks to these features, the interest of this reaction type is steadily growing, what has resulted in a great number of decisive publications, like invention of optically active homogeneous catalysts in 1968 by William Knowles and Leopold Horner. Simultaneously to the studies of the reaction based on using gaseous hydrogen a new approach was taken. In 1952 it was suggested that it might be possible to perform a reaction of catalytic hydrogen transfer from an organic molecule to various organic acceptors under mild conditions. It could be realized in photochemical or biological processes, heterogeneous, homogeneous and also photochemical catalysis.

The reaction of hydrogenationwas one of several possible hydrogen transfer processes, which were classified by Braude and Linstead as follows [3]:

- hydrogen migrations, which take place within one molecule,
- hydrogen disproportionation, that takes place between two identical molecules, where one accepts the role of a donor and the other one acts like an acceptor,
- reaction of transfer hydrogenation-dehydrogenation, which occurs between two different molecules that act like a pair of donor and acceptor.

A lot of different hydrogen donors are used, but primary and secondary alcohols are usually a preferred choice. During the hydrogenationthey are oxidized to the corresponding ketone or aldehyde but depending on the choice of the catalyst and the conditions of the reactions formation of various amounts of unconventional products can be observed.

Choice of the right catalyst is also very important. In industrial heterogeneous reaction of hydrogenation usually compounds of metals like iron, nickel and chromium are used due to their low cost and decent catalytic properties. They are also often used in their metallic form [5]. In homogeneous reaction organic transition metal complexes are usually used as catalysts. In these compounds not only the type of the central atom is important, but also the type of ligands is extremely significant. Usually derivatives of aliphatic compounds are used, because derivatives of aromatic compounds may lead to too aggressive oxidation and removing an oxygen molecule from the oxidized compound. They also may lead to unwanted side reactions of saturationof the aromatic ring or a reaction of hydrogenolysis. The type of ligand also determines thesolubility of the catalyst in the reaction environment. Groups like CO, CN and PPh_3 are very effective in an organic environment, while ligands like amino sulfonamides are soluble in inorganic solvents. Some groups, like TPPTS (3,3′,3″-phosphanetriyltris(benzenesulfonic acid) trisodium salt) are soluble in both types of solvents. In order to maximize the effectiveness of the reaction transition metals like

ruthenium [4], nickel [6] and platinum [4] are often used as a central atom due to their good catalytic properties. Sometimes other metals are also used because they have some special properties even though they are worse catalysts in general. For example, osmium minimizes the probability of side reactions occurring and iridium, which is a mediocre catalyst in this type of reactions is extremely efficient in the reaction of hydrogenation of hexane-2,5-dioneto 2,5-dimethyltetrahydrofuran [4].

The reaction of hydrogenation is a reaction between molecular hydrogen and another compound or element. The general mechanism of this reaction can be summarized with a simplified equation (A is substrate, B is a product of the reaction):

$$A + H_2 \rightarrow B \qquad (1)$$

The exact mechanism of the reaction highly depends on the type of the catalyst and type of the substrate. Due to the large amount of energy needed for breaking a chemical bond in particles of the substrate usually a catalyst is used during reaction. The reaction can be carried out without it, but then it requires very high temperature and pressure [7]. Generally, when heterogeneous catalysts are used the mechanism of the reaction can be summarized in a few steps:

- Adsorption of reagents on surface of the catalyst,
- Dissociation of the particle of gaseousH_2,
- Creation of a bond between one of the carbon atoms of ketone and dissociated hydrogen atom,
- Creation of a bond between the second carbon atom of ketone and dissociated hydrogen atom,
- Product of the reaction leaves surface of the catalyst.

In the case of homogenous catalysts, the reaction mechanisms are different for different types of transition metals complex compounds. All of these mechanisms assume that reaction starts with adirect interaction between the complex compound and molecules of hydrogen. This triggers a cycle of reactions that leads to the transformation of complex compound and reagents. The reaction ends when the reaction product is created and the catalyst particles are regenerated.

The mechanism of the reaction is also dependent on the type of hydrogen donor. If the source of hydrogen molecules is different than gaseous hydrogen the reaction is called transfer hydrogenation. In the case of homogeneous hydrogenation of acetophenone studied in this research isopropyl alcohol is used as a donor of hydrogen. This reaction can be summarized by an equation:

$$C_6H_5COCH_3 + (CH_3)_2CHOH \rightarrow CH_3CH(C_6H_5)OH + CH_3OCH_3 \qquad (2)$$

As stated before this type of reaction requires large amounts of energy, what means that an optimization of the reaction conditions is crucial for profitability. It is also worth mentioning that if homogeneous catalysts are used, the temperature of the

reaction should not exceed the decomposition temperature of the catalyst. In this case catalysts have to be activated with potassium hydroxide and temperature.

Majority of current research is based on optimal parameters stated in other publications. Therefore, the aim of this research was to find the effect of change of crucial reaction parameters on the amount of the product. Two different catalysts were compared, and also additional parameters of the reaction were studied.

METHODS

Firstly, both catalysts were synthesized in the laboratory. For $RuCl_2(PPh_3)_3$ instructions from Michigan University [8] were used. It is a multistep reaction summarized by an equation:

$$2RuCl_3 \cdot 3H_2O + 7PPh_3 \rightarrow 2RuCl_2\left(PPh_3\right)_3 + 2HCl + 5H_2O + OPPh_3 \quad (3)$$

For this reaction 300 mg $RuCl_3 \cdot H_2O$, 1800 mg PPh_3 and 50 ml of pure, degassed and anhydrous methanol were used. They were mixed in a distillation flask and set to boil under argon atmosphere. After an hour the reaction mixture was filtered. The collected precipitate was washed three times with 10 ml of unstabilized diethyl ether. Then it was dried with a rotary evaporator and a vacuum pump and analyzed with NMR.

Second sample was synthesized with instructions from the other publication [1]. It was very similar to the first method, the only differences between them were the amount of methanol (65 ml instead of 50 ml) and duration of the reaction (2,5 hours instead of 1 hour). All other steps were identical to those from the first method.

Reaction was performed in the atmosphere of inert gas, what reduced the probability of a reaction between ruthenium compounds and oxygen occurrence [9]. ^{31}P spectrain D_2O inNMR of catalysts produced in both reactions were obtained.

$RuCl_2(PPh_3)_3$obtainedduring synthesis with the first methodwas contaminated with unreacted substrates. The yield of produced catalyst was not very high, what is shown in Fig. 1. (first peak from the left). Results for the catalyst obtained during the second reaction were significantly better, as shown in Fig. 2. Due to this reason the first sample was not used during the reaction of hydrogenation, instead the reaction was carried out with the second sample. Reaction was also carried out without the synthesized catalyst – instead $RuCl_3 \cdot 3H_2O$ and PPh_3 were added to check if synthesizing the catalyst before the reaction of hydrogenation would improve the rate of the reaction.

The second catalyst, the $RuCl_2(TPPTS)_2 \cdot 6H_2O$, was synthesized with the procedure shown by Herrmann. It assumed that the molar ratio of reagents was as follows: $RuCl_3 \cdot 3H_2O$:TPPTS=1:5 [10]. Firstly, 0,355 g TPPTS was dissolved in 15 ml of water. Then 0,0325 g of $RuCl_3 \cdot 3H_2O$ was added. They were mixed and heated up to 50°C. After 24 hours the mixture was dried with a rotary evaporator and a vacuum drier. Then solid product of the reaction was collected and closed in a

container filled up with argon. Second sample was prepared the same way, but proportion of TPPTS and $RuCl_3 \cdot 3H_2O$ was reduced to $RuCl_3 \cdot 3H_2O$:TPPTS=1:2,5. This time 206 mg TPPTS and 38 mg of $RuCl_3 \cdot 3H_2O$ were used, the amount of other reagents stayed the same. Both samples were analyzed with NMR and their ^{31}P spectra in D_2O were obtained.

Tab. 1. Mass of catalysts used in the reaction of hydrogenation.

Catalyst	Comments	Mass of substances [g]
$RuCl_2(PPh_3)_3$	Reaction performed without the synthesized catalyst	$RuCl_3 \cdot 3H_2O$: 0,0261 PPh_3: 0,1567
$RuCl_2(PPh_3)_3$	Synthesized in an argon atmosphere	0,1739
$RuCl_2(TPPTS)_2 \cdot 6H_2O$	First sample	0,1699
$RuCl_2(TPPTS)_2 \cdot 6H_2O$	Second sample	0,3118

The reaction of hydrogenation was performed in the same way for every catalyst. Firstly, 3g of acetophenone, 30cm^3 isopropyl alcoholand 0,0784g KOH were mixed in a distillation flask. Then the amount of chosen catalyst shown in Table 1 was added to the flask. The mixture was mixed and heated up to 60°C in an atmosphere of argon. After 6 hours the reaction was stopped. The reaction mixture was poured into smaller containers and left for 5 minutes in order to let the precipitate fall to the bottom of a container. Then the sample was analyzed with gas chromatography in order to determine the composition of a post-reaction mixture [2]. The amount of used catalysts was calculated in a way that ensured that the same amount of ruthenium is present in every sample. Results of these calculations are shown in Table 1.

RESULTS

For $RuCl_2(TPPTS)_2 \cdot 6H_2O$ the amount of the obtained catalyst for both samples was similar, but the first sample (synthesized with higherexcess of reagents) was more contaminated.

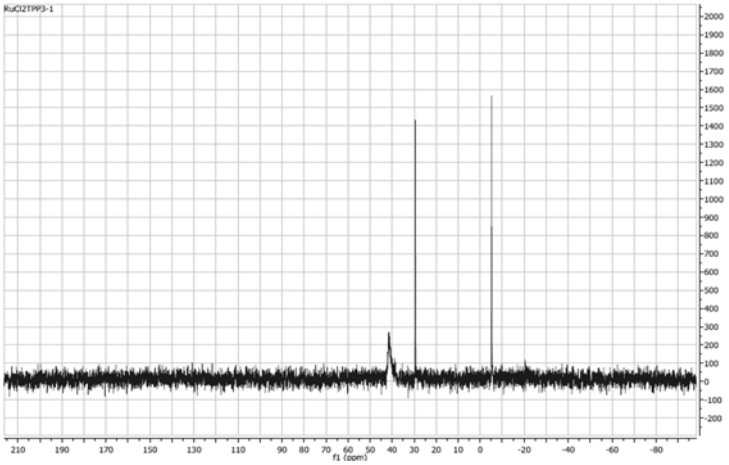

Fig.1. ^{31}P spectrumof $RuCl_2(PPh_3)_3$sampleproduced in the first reaction.

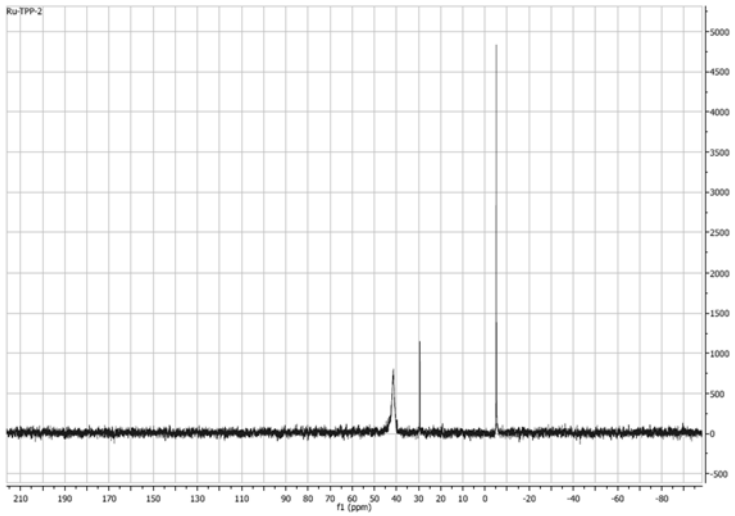

Fig. 2. ^{31}P spectrum of $RuCl_2(PPh_3)_3$sampleproduced in the second reaction.

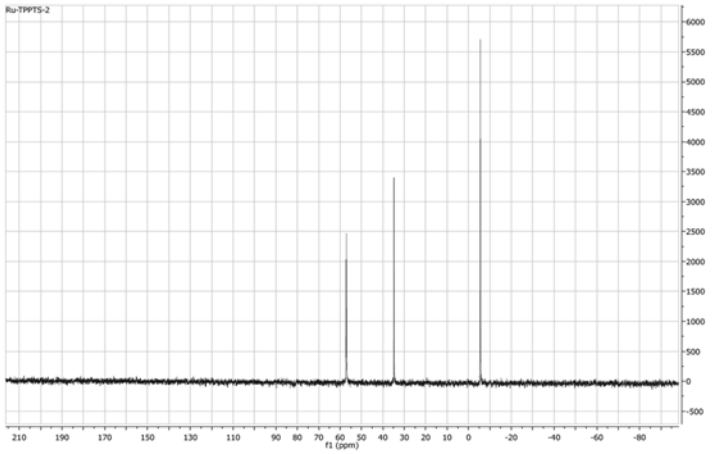

Fig.3. ^{31}P spectrum of $RuCl_2(TPPTS)_2$sampleproduced in the first reaction.

As shown on Fig. 3. the post-reaction reaction mixture contains not only $RuCl_2(TPPTS)_2$ (57 ppm), but also TPPTS that have not reacted (-4,8 ppm) and some contaminations (34,2 ppm). According to literature [11] it is probably OTTPTS.

The reaction of hydrogenation was carried out with catalysts listed in Table 1. twice for each catalyst. The results of the reaction are listed in Table 2. Additional reactions were carried out in order to examine the impact of other reaction parameters on the amount of produced 1-phenylethanol. For $RuCl_2(PPh_3)_3$ two reactions were carried out with the double amount of catalyst and for the other two duration of the reaction was increased from six to ten hours. Results of these reactions are presented in Table 3.

Tab. 2. Amounts of reagents in post reaction mixture for standard parameters of the reaction.

Catalyst	Comments	$m_{acetophenone}$ [g]	$m_{1\text{-}phenylethanol}$ [g]	$n_{acetophenone}$ [mol]	$n_{1\text{-}phenylethanol}$ [mol]
$RuCl_2(PPh_3)_3$	Reaction performed without the synthesis of the catalyst	2,944	0,056	$2,450*10^{-2}$	$4,590*10^{-4}$
$RuCl_2(PPh_3)_3$	Reaction performed without the synthesis of the catalyst	2,946	0,054	$2,452*10^{-2}$	$4,399*10^{-4}$
$RuCl_2(PPh_3)_3$	Second sample	2,422	0,578	$2,016*10^{-2}$	$4,727*10^{-3}$
$RuCl_2(PPh_3)_3$	Second sample	2,427	0,573	$2,020*10^{-2}$	$4,687*10^{-3}$
$RuCl_2(TPPTS)_2$	First sample	2,905	0,095	$2,417*10^{-2}$	$7,808*10^{-4}$
$RuCl_2(TPPTS)_2$	First sample	2,904	0,096	$2,417*10^{-2}$	$7,865*10^{-4}$
$RuCl_2(TPPTS)_2$	Second sample	2,899	0,101	$2,413*10^{-2}$	$8,231*10^{-4}$
$RuCl_2(TPPTS)_2$	Second sample	2,899	0,101	$2,413*10^{-2}$	$8,249*10^{-4}$

Tab. 3. Amounts of reagents in post reaction mixture for modified parameters of the reaction.

Catalyst	Comments	$m_{acetophenone}$ [g]	$m_{1\text{-}phenylethanol}$ [g]	$n_{acetophenone}$ [mol]	$n_{1\text{-}phenylethanol}$ [mol]
$RuCl_2(PPh_3)_3$	Increased amount of the catalyst	2,570	0,430	$2,139*10^{-2}$	$3,524*10^{-3}$
$RuCl_2(PPh_3)_3$	Increased amount of the catalyst	2,570	0,430	$2,139*10^{-2}$	$3,524*10^{-3}$
$RuCl_2(PPh_3)_3$	Extended reaction time	2,133	0,867	$1,775*10^{-2}$	$7,095*10^{-3}$
$RuCl_2(PPh_3)_3$	Extended reaction time	2,139	0,861	$1,780*10^{-2}$	$7,045*10^{-3}$

The conversion rate of acetophenone for each reaction was calculated based on the obtained data. Results are shown in Table 4.

Tab. 4. Conversion rate of acetophenone.

Catalyst	Comments	Reaction parameters	Conversion rate of acetophenone[%]
$RuCl_2(PPh_3)_3$	Reaction performed without the synthesis of the catalyst	6 hours	1,869
$RuCl_2(PPh_3)_3$	Reaction performed without the synthesis of the catalyst	6 hours	1,791
$RuCl_2(PPh_3)_3$	Second sample	6 hours	19,251
$RuCl_2(PPh_3)_3$	Second sample	6 hours	19,085
$RuCl_2(TPPTS)_2$	First sample	6 hours	3,179
$RuCl_2(TPPTS)_2$	First sample	6 hours	3,203
$RuCl_2(TPPTS)_2$	Second sample	6 hours	3,352
$RuCl_2(TPPTS)_2$	Second sample	6 hours	3,357
$RuCl_2(PPh_3)_3$	Synthesized in an argon atmosphere	6 hours, increased amount of catalyst	14,348
$RuCl_2(PPh_3)_3$	Synthesized in an argon atmosphere	6 hours, increased amount of catalyst	14,344
$RuCl_2(PPh_3)_3$	Synthesized in an argon atmosphere	10 hours	28,893
$RuCl_2(PPh_3)_3$	Synthesized in an argon atmosphere	10 hours	28,689

In order to examine the impact of storing conditions of the samples of post reaction mixture on the quality of the measurements it was decided that an additional experiment should be performed.Four samples (without the precipitate) were collected from post reaction mixture obtained in the reaction catalyzed by $RuCl_2(TPPTS)_2$ (second sample, with smaller amounts of reagents).Two of them were stored in a freezer in constant temperature of -15°C for 19 hours, the others were stored in 20°C for the same time. Results are shown in Table 5.

Tab. 5. Conversion rate of acetophenone after 19 hours.

Catalyst	Storage conditions	Conversion rate of acetophenone[%]	Change in relation to base sample [%]
$RuCl_2(TPPTS)_2$	20°C	3,656	+ 9,062
$RuCl_2(TPPTS)_2$	20°C	3,596	+ 7,130
$RuCl_2(TPPTS)_2$	-15°C	3,478	+ 3,766
$RuCl_2(TPPTS)_2$	-15°C	3,535	+ 5,307

DISCUSSION

Carrying out the reaction of hydrogenation with $RuCl_2(PPh_3)_3$ without prior synthesis of the catalyst is highly ineffective and leads to minimal production of 1-phenylethanol. Time saved by skipping the reaction of synthesis does not compensate the negligible conversion rate of acetophenone. It may be an effect of low concentration of the catalyst in the solution and possible side reactions of ruthenium compounds. Due to the low conversion rates further research of this type of reaction was suspended.

The results obtained during the reaction with $RuCl_2(TPPTS)_2$ were disappointing. Obtained conversion rates were significantly lower than those obtained in other publications [2]. It may be a result of high contamination of this catalyst what is shown on Fig 3. The amount of unwanted substances was noticeable, but their identification was not possible with available methods of analysis. It is also worth noting that $RuCl_2(TPPTS)_2$ is usually recommended for two-phase systems [2]. In order to increase the rate of reaction in future research addition of water to reaction environment is planned. It is also worth adding that decreasing the amount of TPPTS during catalyst synthesis has positive effect on the catalytic properties of the final product, but the conversion rate increase is negligible. It is still a desirable effect, because using smaller increase of TPPTS results in much smaller cost of the final catalyst. It was also determined that TPPTS is not an inhibitor of the reaction of hydrogenation of ketones.

$RuCl_2(PPh_3)_3$occurred to be a very good catalyst for this type of reaction. Obtained conversion rates were high, but during the synthesis of the catalyst a large amount of side products (as it is shown on Fig. 1. and Fig. 2.), like e.g. oxidized compounds of ruthenium were observed. It is planned to develop new methods of purification of $RuCl_2(PPh_3)_3$and optimizing the parameters of the reaction before

starting new research [12]. It is also worth noting that increasing the amount of the catalyst in this reaction resulted in lower conversion rates. Usually, this should increase the rate of the reaction due to more possibilities of collision between the molecule of the substrate and the catalyst. When the concentration of the catalyst is already high enough, the reaction rate should stay more or less the same. In the case of $RuCl_2(PPh_3)_3$ this is a bit different due to the presence of particles of PPh_3. They inhibit the reaction of formation of coordinatively unsaturated molecules and they also react with the free coordination place in the central atom of the complex. This prevents the coordination of ketone and the whole reaction of hydrogenation [13]. This could also cause changing a reaction route. Increasing the time of reaction from 6 to 10 hours resulted in almost 50% increase of the conversion rate.

Results from table 5. show that the analysis of the post-reaction mixture should be made as fast as possible, because the reaction does not stop even in low temperature. To add more, the increase of the product was noticeably different even in the case of samples stored under the same conditions.

The results of this research are very promising. The research can be further developed by changing the donor of hydrogen to a more environmentally friendly substance like ethanol to check if this reaction can be used in green chemistry. Due to the homogeneous nature of the reaction, methods of recovering the catalyst have to be invented. To add more, other parameters of the reaction also have to be optimized in order to increase the possibility of practical application of this process in industry.

CONCLUSIONS

In the homogeneous reaction of hydrogenation of acetophenone in organic environment$RuCl_2(PPh_3)_3$ is much more effective as a catalyst than $RuCl_2(TPPTS)_2$. The reaction of hydrogenation and synthesis of both catalysts should be carried out in the atmosphere of an inert gas in order to minimize the amount of unwanted side products. Increasing the amount of TPPTS during synthesis of $RuCl_2(TPPTS)_2$ above a certain value is not recommended as it results in only a slight increase of the amount of the produced catalyst. An increase of the time of reaction results in a rise of conversion rate of reagents. An increase of $RuCl_2(PPh_3)_3$ amount above some value can result in a decrease of the conversion rate of acetophenone. Samples of the reaction product should be analyzed immediately after experiments in order to obtain reliable results.

REFERENCES

[1] Shaw A. P., Ryland B. L., Norton J. R., Buccella D., Moscatelli A., *Electron Exchange Involving a Sulfur-Stabilized Ruthenium Radical Cation*; Inorganic Chemistry 2007, 46, p. 5805-5812

[2] Wang L., Ma H., Song L., Li L., Wang Y., Wang H., *Transfer hydrogenation of acetophenone in an organic aqueous biphasic system containing double long-chain surfactants*; RSC Advances 2013, 4., p. 1567-1569
[3] Brieger G., Nestrick T. J.,*Catalytic transfer hydrogenation*; Chem. Rev 1974, 74(5), p. 567-580
[4] Ryandler P. N., *Catalytic Hydrogenation in Organic Syntheses*; Academic Press. Inc., San Diego 1979, p. 82-88
[5] Grzywa E., Molenda J., *Technologia podstawowych syntez organicznych. Tom 2*; WydawnictwaNaukowo-Techniczne, Warszawa 2000, p. 11-121
[6] Hurd C. D., Perletz P*., Aryloxyacetones*; *J. Am. Chem. Soc.*, 1946, 68 (1), pp 38–40
[7] http://www2.chemistry.msu.edu/courses/cem415/CEM415,%202013/Experiment%203.pdf
[8] Gatsis J. G., *American patent,* US 3635838 A, January 18, 1972
[9] Ugo R., *Aspects of homogeneous catalysis. Volume 1*; Carlo Manfredi, Milano 1970, p. 46-48
[10] Herrmann W. A., Brauer G., *Synthetic Methods of Organometallic and Inorganic Chemistry. Volume 9: Transition Metals, Part 3;* Thieme Medical Publishers, Stuttgart 2000
[11] Bhanage B. M., Divekar S. S. Deshpande R. M., Chaudhari R. V., *Selectivity in Sulfonation of Triphenyl Phosphine*; Organic Process Research & Development 2000, 4, p. 342-345
[12] Cho C. S., Kim B. T., Kim T., Shim S. C., *An Unusual Type of Ruthenium-Catalyzed Transfer Hydrogenation of Ketones with Alcohols Accompanied by C-C Coupling*; J.Org. Chem. 2001, 66, p. 9020-9022
[13] Houghton R. P., *Kompleksy metali w chemii organicznej;* Warszawa 1985, Państwowe Wydawnictwo Naukowe, p. 248-257

Influence of metal layers on a spectral characteristics in a tapered optical fiber

*Joanna Moś[1], Leszek R. Jaroszewicz[1]
[1]Faculty of New Technology and Chemistry, Military University of Technology, Warsaw, POLAND
e-mail: joanna.musial@wat.edu.pl

***Keywords**: surface plasmon resonance, tapered optical fiber, metal layers, optical sensor, tapered technology.*

ABSTRACT

Theoretical part describes propagation of light in optical fiber tapers, as well as applications of different metal layers. Technological part describes the FOTET arrangement used for manufacturing fiber-optic tapers, as well as parameters' characteristics of the produced elements. Technology of a deposition of metal layers on the taper and evaluation of surface morphology of the manufactured elements were also presented. The research part describes transmission measurements for selected elements depending on the used material (gold, silver), layer's thickness (25 nm, 50 nm, 100 nm) and length of the tapered optical fiber (about 15 mm and about 30 mm).

INTRODUCTION

One of the technics used in fiber-optic technology is the tapered optical fiber [1]. There are used to make couplers [2], supercontinuum generation [3], optical sensors [4]. Tapered optical fibers have unique physical and optical properties, which we cannot find in standard optical fibers. As a result of the technological process the fiber diameter is decreasing. The light propagating in the core begins to leak into the cladding like evanescent field. As a result, we have a possibility of interacting the light beam with the surroundings Fig.1.

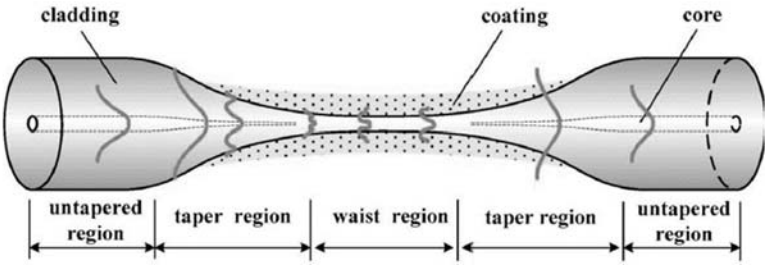

Fig. 1. Scheme of a tapered optical fiber [7].

Directly with this change, there are observed changes of the boundary conditions due to the large difference in refractive indices between the cladding and the surrounding starting to enclose a taper waist. In opposite to the standard optical fiber where difference between core and cladding reflective index is of about 1% Fig.2 [1].

This effect is widely used in optical sensors. The surrounding of a tapered optical fiber is changed by application of an extra material. Changes of optical properties (reflective index) of the extra material are caused by a change transmission in the optical fiber.

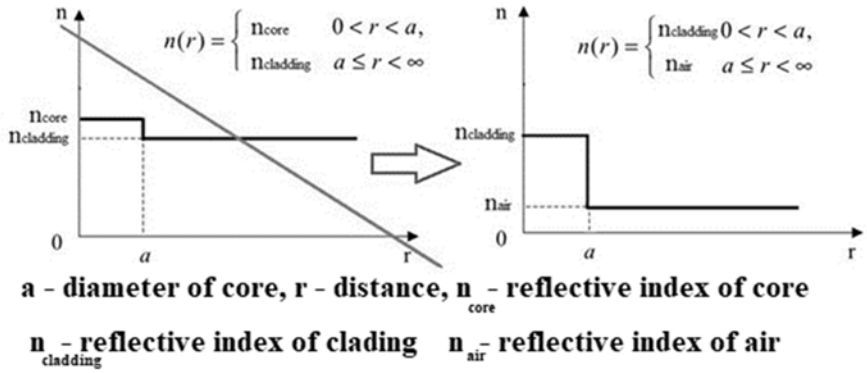

Fig. 2. Change of boundary conditions (difference in reflective index) from the standard optical fiber to the tapered optical fiber.

In order to improve sensitivity, additional materials are used to measure specific physical, chemical or biological properties. The tapered optical fibers are surrounded by liquid crystals [8], alkanes [9], thermosetting layers [7], materials used in our life like gelatin [10] and metals [11]. Sputtered metal layers on the tapered optical fiber induce surface plasmon resonance (SPR) at the boundary of metal-dielectric media [12, 13]. Sensors based on this phenomenon are highly sensitive to changes in refractive index and allow for a direct monitoring of chemical and biological reactions. Main applications include environmental monitoring, food quality assurance, or use of such sensors in medical diagnostics [14]. SPR detection structures offer many interesting features, also small in size and robustness. Most commonly used in biological sensors are gold and silver [15]. Other metals such as aluminum (Al) copper (Cu), palladium (Pd), titanium (Ti) were also used for SPR sensors [11, 16, 17]. At present, combinations of these elements are used to increase sensors' sensitivity [15, 17]. The miniaturization of SPR-based sensors is of great interest. Different approaches to reducing the size and complexity of the sensor can be observed. Particular attention is attracted by sensors based on optical fibers. Not only standard single-mode fibers, but also photonic optical fibers are used [18-20]. In

addition to performing tapered optical fiber, technique of polishing the cladding [18, 21] or bending the optical fiber [22] are used. The most novel direct research which is connect with this effect is localized SPR. This kind of SPR- sensors use nanoparticles of metals [23].

The main purpose of the research is to optimize the parameters of the structure consisting of tapered optical fiber and the metal layer for future applications.

MATERIALS AND METHODS

Single Mode Fiber (SMF) with a core diameter of 8.2 μm, a cladding diameter of 125 ± 0.7 μm and a loss of 0.18 dB/km for 1550 nm was used for the research. The set-up FOTET (Fiber Optic Taper Element Technology) has been used to prepare tapered optical fibers with different diameters and optimize tapered optical fiber parameters. This process consisted of heating the fiber section to a softening temperature of glass and, then its elongation to the appropriate length with stepper motors. The system was controlled by a computer. During testing, the tapered optical fibers were characterized by the parameters shown in Tab. 1.

Tab. 1. Parameters of used tapered optical fibers.

Tapered optical fiber symbol	Loss [db]	Move of torch [mm]	Lenght of elongation [mm]	Diameter of tapered optical fiber [μm]
5x30	0.22 ± 0.12	5	30.27 ± 0.22	5.90 ± 0.25
5x15	0.22 ± 0.14	5	15.28 ± 0.27	18.56 ± 0.46

The structure was secured by aluminum which allowed the metal to be sputtered on the tapered optical fiber. In this study the sputtered layers were of gold and silver with a thickness of about 25nm, 50nm, 100nm. These metals were chosen because they are the most popular coating materials which are used in measurement and control technology. Sputter EM SCD 005 Leica Miscrosystems to added metal layers was used. The gold target was characterized by purity of the material equal to 99.9 % and density of 19.3 g/cm^3 and for silver target purity of the material was 99.99 % and density of 10.5 g/cm^3. The thickness of the metal layer was determined by the thickness gauges EM. Parameters used during sputtering process and thickness of layers are shown in Tab. 2.

Tab. 2. Parameters used for coating metallic layers.

Current [mA]	Target	Sputtering time [s]	Thickness of layer [nm]
22	Gold	180	25.12 ± 0.70
		360	52.42 ± 1.08
		645	99.98 ± 0.67
30	Silver	90	24.06 ± 0.65
		160	46.75 ± 0.74
		310	93.26 ± 1.08

It is worth to underline that the sputtering process is a very important element. There may be problems during sputtering like parallelism of the tapered optical fiber to the ground. In order to make the layer sprayed uniformly, the tapered optical fiber should be perfectly parallel. If this is not possible, there may be the shadow effect which causes uneven overlap. In addition, the problem may be the samples' rotation itself. Devices allowing the metal layer to be sprayed do not have a rotary table. The sample is sprayed on one side and then rotated and sprayed on the other. Hence, a non-uniform metal layer can be formed on the cylindrical tapered optical fiber. In order to check the quality of the sputtered layers PHENOM electron microscope was used. The images show that the entire tapered optical fiber was covered evenly with the metal layer Fig. 3.

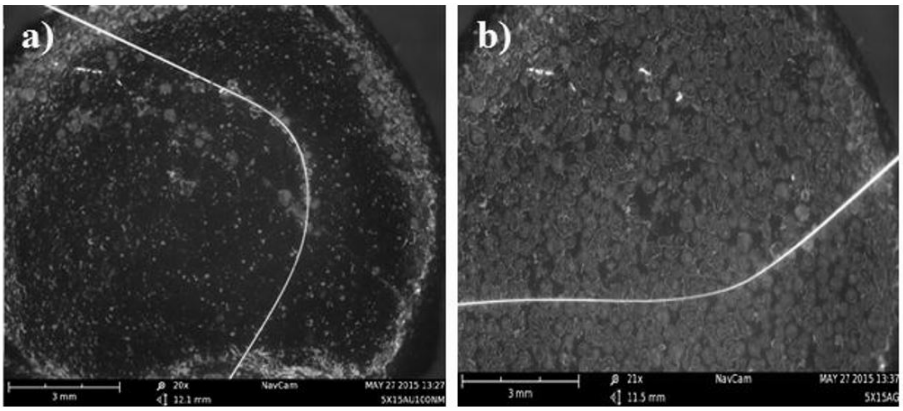

Fig. 3. Tapered optical fiber with metal layer a) gold b) silver.

RESULTS

The built measurement system consisted of a source of light type supercontinuum SC450-4-AOTF Fianium, which has an almost flat spectrum in range of 420-2000 nm, as well as of an optical spectrum analyzer AQ6319 Yokogawa, which makes possible the measurement of the spectral characteristics in the range of 600 nm - 1700 nm (Fig. 4).

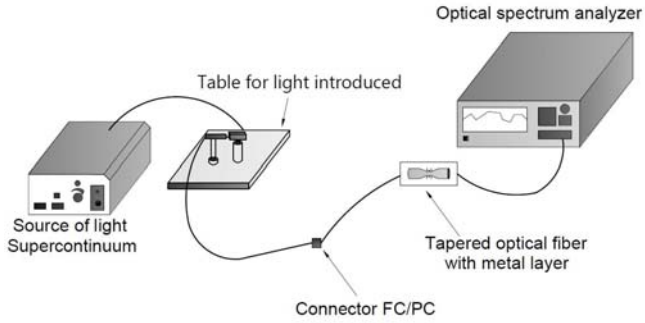

Fig. 4. Scheme of the arrangement for measurements of the spectral characteristics.

The research for series of samples of 5x15 and 5x30 with different thickness of metals was obtained. It turned out that the effect does not occur for 5x30 tapered optical fibers. The metal layer introduces very high losses which results in lack of transmission for all thickness of metals (gold, silver). In Fig. 5 the light emission is presented. As can be seen from the picture below, the power loss is located on the side of the light source in the transition area of the tapered optical fibers.

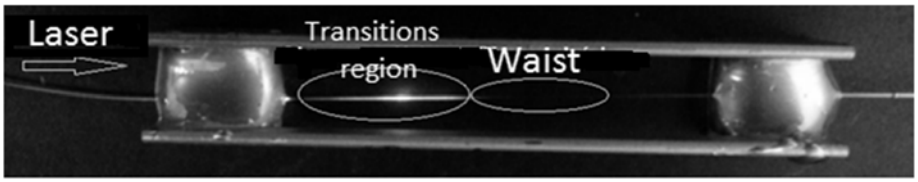

Fig. 5. Tapered optical fiber 5x15 with a metal layer. The light is held within transitions region.

Spectral characteristics in the range of 600-1700 nm for 5x15 were obtained. Both for the gold and silver layers, as the metal thickness increases, the loss of power by tapered optical fiber increases too (Fig. 6, 7a). This is due to the interaction of the field with the surrounding metal that grows with increasing wavelengths, which results in greater power being driven out of the fiber structure and greater interaction of the metal with the guided light.

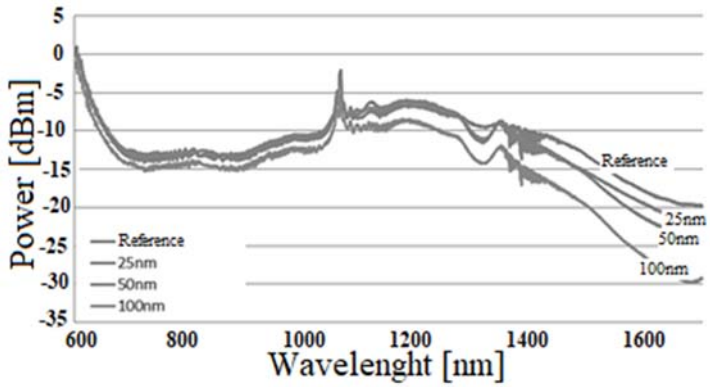

Fig. 6. Spectral characteristics in the range of 600-1700 nm for the tapered optical fiber with gold layer.

In Fig. 7b the interference of cladding modes with basic mode is very well shown. This characteristics can be derived directly from the real and imaginary dielectric constant of silver.

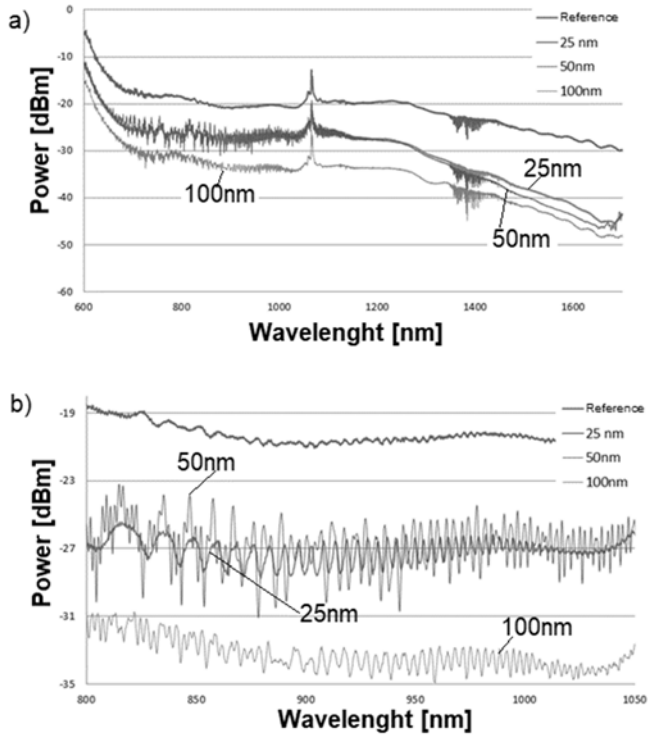

Fig. 7. Spectral characteristics for the tapered optical fiber with silver layer a) in the range of 600-1700 nm, and b) in the range of 800-1050 nm.

CONCLUSIONS

From transmission measurements it was noted that the 5x30 structures are too small and cannot record transmission because the power radiates out of the fiber structure. This is due to the fact that high power is propagated outside the fiber structure as the evanescent field and strongly interacts with the sprayed metal layer, resulting in are very high losses. After the research was done, it turned out that the transmission is possible for a 5x15 structure. The influence of metal layers on the propagation of the light beam in the tapered optical fiber has been demonstrated, depending on the layer's thickness. For structure consisted on tapered optical fibers and gold or silver layer there is observed the following dependency, increase of the layer thickness causes the increase of power loss. The optimum solution is a 25-50 nm layer of metal, and further research will be done in this direction.

REFERENCES

[1] G. Brambilla, Optical fibre nanowires and mikrowires: review, *Journal of Optics*, 2010, 12, 1-19 DOI: 10.1088/2040-8978/12/4/043001

[2] R. G. Lamont, D. C. Johnson, K. O. Hill, Power transfer in fused bioconical taper single-mode fiber couplers: dependance on external reflactive index *Applied Optics*, 1985, 24, 3, 327-332 DOI: 10.1364/AO.24.000327

[3] S. Leon-Sava, T.A.Briks, W. Wadsworth, P. S. J. Russell, Supercontinuum generation in submikron fibre waveguides, *Optics Express*, 2004, 12, 13, 2864-2869 DOI: 10.1364/OPEX.12.002864

[4] L. Zhang, J. Lou, L. Tong, Micro/Nanofiber Optical Sensors, Photonic *Sensors*, 2011, 1, 1, 31-42 DOI: 10.1007/s13320-010-0022-z

[5] Y. Tian, W. Wang, N. Wu, X. Zou, W. X, Tapered Optical Fiber Sensor for Label-Free Detection of Biomolecules, *Sensors*, 2011, 11, 4, 3780-3790 DOI: 10.3390/s110403780

[6] L.Tong, J.Lou, E.Mazur, Single mode guiding properties of subwavelenght diameter silica and silicon wire waveguides, *Optics Express*, 2004, 12, 6, 1025-1035 DOI: 10.1364/OPEX.12.001025

[7] S. Zhu, F. Pang, T.Wang, Single-mode tapered optical fiber for temperature sensor based on multimode interference, *Optical Sensors and Biophotonics*, 1-6, 2011 DOI: 10.1117/12.904444

[8] J.E. Moś, M. Florek, R. Wonko, K. A. Stasiewicz, Leszek R. Jaroszewicz, Influence temperature and electric field on propagation properties of a nematic liquid crystals optical fiber device, *Optical Fibers and Their Applications 2017*, *SPIE*, 10325, 2017 DOI: 10.1117/12.2271042

[9] K.A. Stasiewicz, J. Musial, Threshold temperature optical fibre sensors, *Optical Fiber Technology*, 2016, 32, 111-118, DOI: 10.1016/j.yofte.2016.10.009

[10] L. Zhang, F. Gu, J. Lou, X. Yin, L. Tong, Fast detection of humidity with a subwavelength-diameter fiber taper coated with gelatin film, *Optics Express*, 2008, 16, 17, 13349-13353 DOI: 10.1364/OE.16.013349

[11] D. Monzón-Hernández, J. Villatoro, Fast detection of hydrogen with nano fiber tapers coated with ultra-thin palladium layers, *Optics Express*, 2005,13, 13, 5087-5092 DOI: 10.1364/OE.16.013349

[12] R. Slavík J. Homola, J. Čtyroký, Single-mode optical fiber surface plasmon resonance sensor, *Sensors and Actuators B*, 1999 54, 1-2, 74-79 DOI: 10.1109/19.728812

[13] Maier S.A., Chapter in the book: Plasmonics: Fundamentals and Applications, *Springer*, 2007

[14] J. Homola, Surface Plasmon Resonance Sensors for Detection of Chemical and Biological species, *Chemical Reviews*, 2008, 108, 2, 462-493 DOI: 10.1021/cr068107d

[15] H. Moyyed I.T. Leite, L. Coelho, J.L. Santos, D. Viegas, Analysis of Phase Interrogated SPR Fiber Optic Sensors with Biometallic Layers, *Sensors* Journal, IEEE. 2014, 14, 10, 3662 – 3668 DOI: 10.1109/JSEN.2014.2329918

[16] C. Perrotton Javahiraly M. Slaman B. Dam,P. Meyrueis, Fiber optic Surface Plasmon Resonance sensor based on wavelength modulation for hydrogen sensing, *Optics Express*, 2011, 19, S6, 1175-1183 DOI: 10.1364/OE.19.0A1175

[17] S. Ju S. Jeong , Y. Kim , P. Jeon, Min-Su Park , H. Jeong, Experimental demonstration of surface plasmon resonance enhancement of the tapered optical fiber coated with Au/Ti thin film, *Journal of Non-Crystalline Solids*, 2013, 383, 146- 152 DOI: 10.1109/JSEN.2014.2356251

[18] H. Esmaeilzadeh, M. Rivard, E. Arzi, F. Légaré, A.Hassani, Smart textile plasmonic fiber dew sensors, OPTICS EXPRESS, 2015, 23, 8576-8582, DOI:10.1364/OE.23.014981

[19] N. Luan, R. Wang, W. Lv, and J. Yao, Surface plasmon resonance sensor based on D-shaped microstructured optical fiber with hollow core, *OPTICS EXPRESS,* 2015, 23, DOI: 10.1364/OE.23.008576

[20] A. A. Rifat, G. A. Mahdiraji, D. M. Chow, Y. G. Shee, R. Ahmed, F.R. M. Adikan, Photonic Crystal Fiber-Based Surface Plasmon Resonance Sensor with Selective Analyte Channels and Graphene-Silver Deposited Core, *Sensors*, 2015, 15(, 11499-11510; DOI:10.3390/s150511499

[21] Z. Liu, Y. Wei, Y. Zhang, C. Liu, Y. Zhang, E. Zhao, J. Yang, L.Yuan, Compact distributed fiber SPR sensor based on TDM and WDM technology, *OPTICS EXPRESS*, 2015,23, DOI:10.1364/OE.23.024004

[22] A. K. Sharma R. Jha, B.D. Gupta, Fiber- Optic Sensor Based on Surface Plasmon Resonance: A Comprehensive Review, IEEE SENSORS JOURNAL, 2007, 7, 1118-1128, DOI: 10.1109/JSEN.2007.897946
[23] K.M. Mayer, J. H. Hafner, Localized Surface Plasmon Resonance Sensors, *Chem. Rev*., 2011, 111, 3828–3857, DOI: 10.1021/cr100313v

Preparation and Characterization of Chitosan Obtained from Honey Bee

*Paulina Pędziwiatr
Faculty of Process and Environmental Engineering, Lodz University of Technology, Lodz, POLAND
e-mail: paulina.pedziwiatr@o2.pl

***Keywords**: chitin, chitosan, honey bee corpses, deacetylation*

ABSTRACT

Chitosan is non-toxic polysaccharide, characterized by a biocompatibility and biodegradability. The concept of the chitosan production from an alternative source such as naturally died honeybees is described in this paper. Chitin was extracted from the honey bees' corpses. The procedure of chitin isolation consists of removal from the bees' bodies substances such as waxes, minerals, proteins and natural pigments - melanin. Process of deacetylation (hydrolysis of N-acetylglucosamine groups) was conducted by chemical method. Obtained bee chitosans were characterized using the Fourier transform infrared (FT-IR) spectroscopy.

INTRODUCTION

Chitosan is a copolymer composed of β-(1→4)-linked N-acetyl-D-glucosamine (GlcNAc) and β-(1 →4)-linked D-glucosamine (GlcN). Monomers, as in the case of chitin, are connected by a glycosidic bond. During the chemical or enzymatic deacetylation of chitin, some or all the acetyl groups are removed from the N-acetylglucosamine monomers [1].

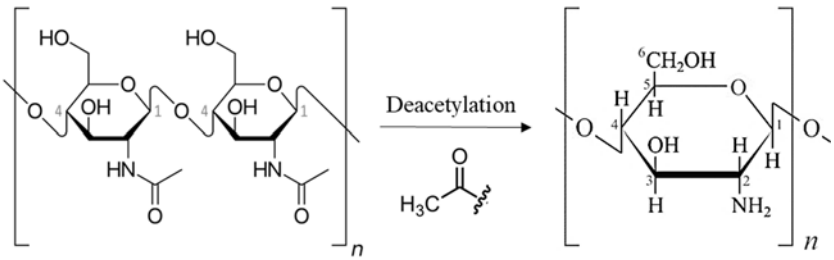

Fig. 1. Chemical structure of chitin and deacetylated chitin (chitosan).

The interesting properties of chitosan such as biocompatibility, low allergenicity, biodegradability and cationic character make this polysaccharide a relevant candidate in the field of industrial and biomedical applications [2]. Nowadays, because of unique chemical and biological properties, chitosan is one of the most well-studied biomaterials [3]. It is a suitable as a component of drug delivery

systems, flocculants for protein recovery, flocculants to clarify water and for the development of biodegradable films, encapsulating nanoparticles and scaffolds for tissue engineering [4,5].

The main source of chitin used for the chitosan production, until recently, were two crustaceans - shrimps and crabs. Due to ecological reasons, their catches have been significantly reduced and alternative sources of chitin have been developed. The corpses of honey bees consist of dead, dried bees' bodies, collected during the spring cleaning work in the apiary. The bodies of honey bees consist of chitin (23 to 32%), proteins (35-45%), mineral salts (2-3%), and pigment - melanin (30-40%). In spring, a bee family is renewed by 60–80%. Due to winter losses of the worker bees, the annual global volume of bee corpses reaches 210 000 tones, as it is shown in Table 1. [6,7]

Tab. 1. Annual production of bee chitin.

	Number of bee colonies	**The weight of bee corpses [t]**	**The weight of chitin [t]**
Poland	1 504 623	3 950	1 106
European Union	15 800 000	41 475	11 613
World	80 000 000	210 000	58 800

Large-scale beekeeping waste (honey bee corpses) is a valuable but undeveloped source of chitin [8]. Moreover, the production of chitosan from proposed source is independent of the limited supply of chitin from marine processing, which with the growing demand for chitosan creates the possibility of industry interest on presented method. In this study, the author introduces the methodology of chitosan production from bees' corpses in two different methods.

EXPERIMENTAL

Materials

Chitin source - corpses of European honey bee (*Apis mellifera*) were collected from apiary located in central Poland in April 2016, as part of cleaning works. The material also contains the body of the external parasitic mite *(Varroa destructor)*. Varrora mite is an arthropod with chitin-melanin exoskeleton.

Fig. 2. Source of chitin - a) honey bees' corpses, b) components of source: honey bees and varrora's bodies and fragments.

Chemicals

Analytical Grade Reagents: Ethyl alcohol Absolut 99,8% (POCH), hydrochloric acid 35-38% (CHEMPUR), sodium hydroxide (CHEMPUR), hydrogen peroxide 30% (CHEMPUR). Deionized water (from laboratory Water Purification System Direct-Q 3 UV). Medical chitosan, DD 82,6-87,5% (HEPPE Medical chitosan GmbH) for comparative purposes.

METHODS

Before the chemical treatment bees had been dried at 50°C in the laboratory dryer for 24h. Then the corpses were minced and dried for 24 h once again. Bee powder was suspended in water to remove water-soluble substances. The procedure of chitin isolation consists of removal from the bees' bodies substances such as waxes, minerals, proteins and natural pigments – melanin. To obtain chitosan, isolated chitin was deacetylated.

1. **Removing of waxes** - waxes from the bodies of naturally died bees were removed by extraction in the Soxhlet apparatus with ethyl alcohol as a solvent. The process was completed after five cycles. The obtained fractions were dried at 50°C for 24h.
2. **Demineralization -** to remove mineral substances (mainly $CaCO_3$) material was treated with the solution of 1M HCl with constant stirring. After a treatment with acid the solid material was separated on MPW-56 centrifuge (2000 rpm, 4 min) and washed with deionized water to obtain pH=7.
3. **Deproteinization** - to remove proteins obtained material was treated with 3% sodium hydroxide. The reaction was conducted at 80°C for 180 min with constant stirring. The solid material was separated and washed with deionized water.

4. **Depigmentation** – substance responsible for the colour of insects, including honeybees, is natural pigment – melanin. Discoloration of the chitin–melanin complex was conducted at 85°C for 2,5h with 18% hydrogen peroxide as an oxidizing agent. Blenched solid material was separated and washed with deionized water.
5. **Deacetylation** - comprises hydrolysis of N-acetylglucosamine groups was conducted by chemical method. Two different NaOH solution were prepared (1M and 25M). Bee chitin was resuspended in NaOH and deacetylated by heating at 100°C for 40 h with stirring. Then two obtained chitosans were washed several times with deionized water to pH 7.0 and dried at 50°C.

The molecular structure of chitosan isolated from the honey bee was characterized using the Fourier transform infrared spectroscopy by the Thermo Scientific Nicolet iS50 FT-IR spectrometer. The samples of chitosan from different concertation of NaOH in deacetylation process, were compared to the IR spectrum of commercial chitosan.

RESULTS AND DISCUSSION

The results obtained for chitosan samples prepared in synthesis I and II are shown in Fig. 2. To compare the result the sample of commercial chitosan was also analysed.

Depending on the literature source, the characteristic IR absorption frequencies of chitosan functional groups indicates different wave length. The most common and averaged were collected in Tab.2 [1, 11].

Tab. 2. Characteristic IR Absorption Frequencies of Chitosan Functional Groups [1].

Wave length, cm^{-1}	Functional group
3450	OH
3360	NH, stretching
2920, 2880, 1430, 1320	CH_2, stretching
1730	-C=O, stretching
1655	-C=O, stretching
1560	-NH, bending
1590	$-NH_2$, cutting
1380	$-CH_3$
1150-1040	C-O-C

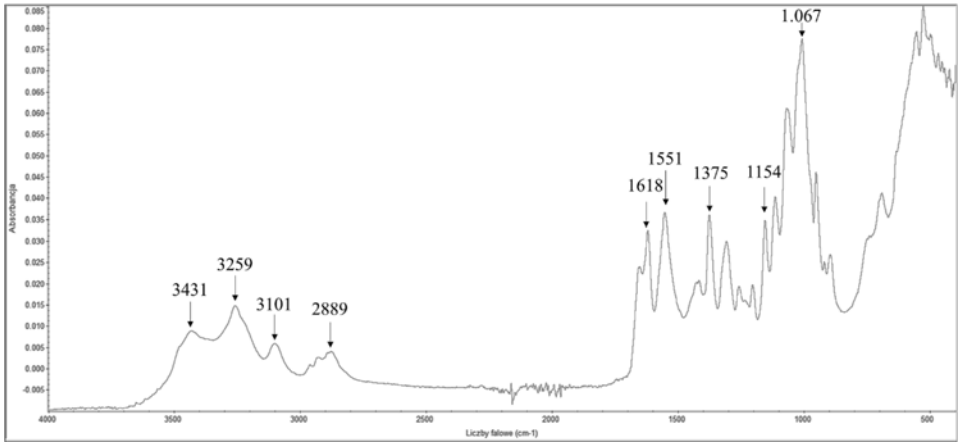

Fig. 3. Infrared spectra as a wave length function displayed for chitosan I.

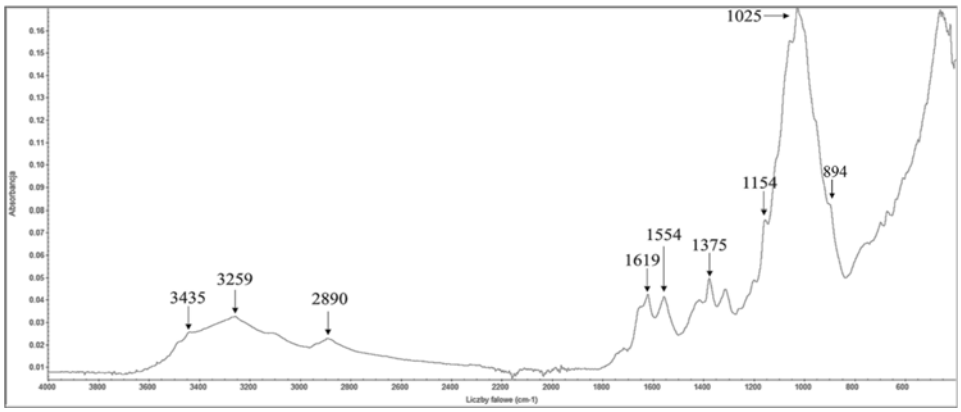

Fig. 4. Infrared spectra as a wave length function displayed for chitosan II.

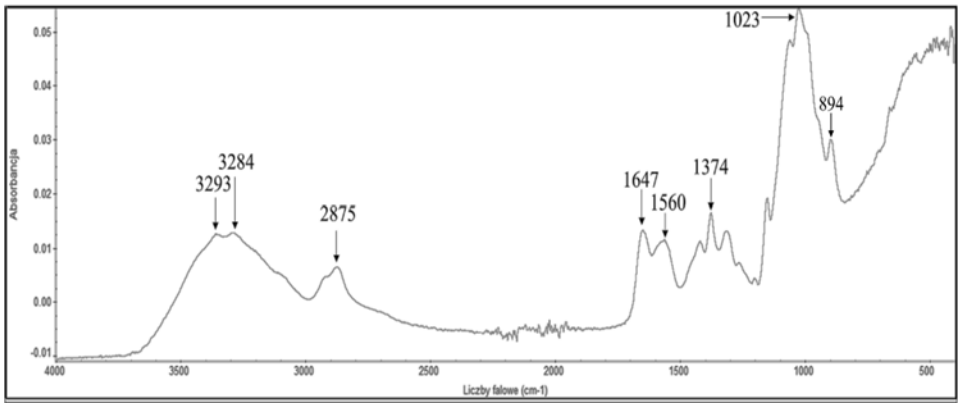

Fig. 5. Infrared spectra as a wave length function displayed for commercial chitosan.

Characteristic of the three chitosans was shown by a broad absorption band in the range 3000 to 3500 cm^{-1} which is attributed to O-H stretching vibrations. The

strongest peak in the 3259 cm^{-1} (vibration of NH) was observed for chitosan I. The stretching vibrations of methylene C-H at 2880 cm^{-1} was displayed for all three chitosans. Absorption peak at 1590 cm^{-1} correspond to the NH_2. The amide II band is used as the characteristic band of N-acetylation [10]. The spectra of chitosans showed the different vibration that occurs after deacetylation process in different conditions. Weaker vibration C = O at 1627 cm^{-1} region for chitosan II. and commercial chitosan, indicates that the vibration of C = O has been reduced (because of removing acetyl groups from chitin). Sharp peak at 1618 cm^{-1} for chitosan I. indicate low degree of deacetylation. Chitosan I. was deacetylated in 1M NaOH what demonstrate insufficient concertation of alkali solution to hydrolysis majority of N-acetylglucosamine groups. A number of sharp peak at range 1000-1500 cm^{-1} shows other functional groups and probably pollutants. According to the molecular structure chitosan II. is physiochemically similar to commercial chitosan.

CONCLUSIONS

To sum up, honey bees' corpses could be successfully used as an alternative source of chitin for chitosan production. The procedure of chitin isolation require removal from the bees' bodies substances such as waxes, minerals, proteins and natural pigments - melanin. Process of effective deacetylation depends on concertation of sodium hydroxide solution. Reaction with 25M NaOH provide higher degree of deacetylation. Temperature, reaction time and concentration of reagents in every process (demineralization, deproteinization, depigmentation and deacetylation) effect on final chitosan physicochemical properties. The IR spectrum of commercial chitosan allow to compare obtained chitosanas and confirm that chitosan II has similar molecular structure to commercial chitosan.

The main aim of this paper was to explore the opportunity of obtaining chitosan from honey bees' corpses. Moreover, global demand for chitosan is growing year-by-year, consequently unconventional methods of the chitosan production should be developed. The production of bee chitosan could be used to dispose of dead honeybees, which bodies contain parasites. Extreme conditions for purification and deacetylation processes guarantee the purity of the obtained product. Removal of waxes and protein substances allows to use chitosan in the biomedicine and pharmaceutics by persons, who are allergic to bee products.

REFERENCES

[1] Mucha, M. (2010). Chapter in the book: Parametry charakterystyczne chitozanu, *Chitozan: wszechstronny polimer ze źródeł odnawialnych. Wydawnictwa Naukowo-Techniczne*.

[2] Mucha, M., Balcerzak, J., Michalak, I., & Tylman, M. (2011). Biopolymeric matrices based on chitosan for medical applications. *e-Polymers,* 11(1), 21-28, DOI: 10.1515/epoly.2011.11.1.21

[3] Elieh-Ali-Komi, D., & Hamblin, M. R. (2016). Chitin and chitosan: production and application of versatile biomedical nanomaterials. *International journal of advanced research*, 4(3), 411.

[4] Rinaudo, M. (2006). Chitin and chitosan: properties and applications. *Progress in polymer science*, 31(7), 603-632, DOI: 10.1016/j.progpolymsci.2006.06.001

[5] Tylman, M., & Mucha, M. (2014). Chitosan scaffolds with nanosilver layer for bone implantation obtained by electrolytic method. *Materials Science and Technology*, 30(5), 582-586, DOI: 10.1179/1743284713Y.0000000497

[6] P. Semkiw, Sektor pszczelarski w Polsce w 2016 roku, Instytut Ogrodnictwa Zakład Pszczelnictwa w Puławach, Puławy, 2016.

[7] Report Bee Health in Europe - Facts&Figures, OPERA Research Centre, 2013.

[8] Nemtsev, S. V., Zueva, O. Y., Khismatullin, M. R., Albulov, A. I., & Varlamov, V. P. (2004). Isolation of chitin and chitosan from honeybees. *Applied Biochemistry and Microbiology*, 40(1), 39-43, DOI: 10.1023/B:ABIM.0000010349.62620.49

[9] Marei, N. H., El-Samie, E. A., Salah, T., Saad, G. R., & Elwahy, A. H. (2016). Isolation and characterization of chitosan from different local insects in Egypt. *International journal of biological macromolecules*, 82, 871-877, DOI: 10.1016/j.ijbiomac.2015.10.024

[10] Islam, M. M., Masum, S. M., Rahman, M. M., Molla, M. A. I., Shaikh, A. A., & Roy, S. K. (2011). Preparation of chitosan from shrimp shell and investigation of its properties. *International Journal of Basic & Applied Sciences*, 11(1), 116-130.

[11] Rumengan, I., Suryanto, E., Modaso, R., Wullur, S., Tallei, T., & Limbong, D. (2014). Structural Characteristics of Chitin y Chitosan Isolated from the Biomass of Cultivated Rotifer, *Brachionus rotundiformis*. Int. J. Fish. Aquat. Sci, 3, 12-18.

Investigation of the chitosan solutions flow behavior using rotational and oscillatory measurements

*Anna Rył, Piotr Owczarz
Lodz University of Technology, Faculty of Process and Environmental Engineering, Department of Chemical Engineering, Lodz, POLAND
e-mail: anna.ryl@dokt.p.lodz.pl

***Keywords**: sol-gel phase transition, chitosan hydrogels, rheometry measurements, oscillatory shear, rotational shear*

ABSTRACT

This paper will discuss the influence of the deformation type on the flow behaviour and the ability to gelation thermosensitive chitosan hydrogels. Application of the shear rate determined based on the conducted oscillatory measurements leads to other shapes of the experimental curves of dynamic viscosity. Simultaneously, higher viscosity values in rotational measurements may indicate a stronger crosslinking of the polymer structure. Furthermore, the results of isothermal measurements indicate a faster formation of a gel structure with a unidirectional shear.

INTRODUCTION

In recent years, thermosensitive chitosan hydrogels are the object of interest of many researchers. The colloidal chitosan solution has a natural ability to undergo a sol-gel phase transition [1, 2]. This leads to the possibility of preparing injection scaffolds for applications in tissue engineering [3] formed in vivo. This is due to the application of minimally invasive, low viscosity sol phase [4,5]. In order to precisely determine the gelation conditions and the mechanical properties of the obtained hydrogels, oscillatory rheometry measurements are commonly carried out [6–9].It results from an easy interpretation of the experienced data obtained and their unambiguous. Furthermore, these measurements are characterized by low invasiveness - they almost do not damage the internal structure of the tested medium. Nevertheless, the use of this type of deformation leads to oscillatory shear bidirectional. The high unidirectional shear strengths generated in the syringe during injection can affect the sol-gel phase transition conditions. It seems reasonable to determine the effect of these unidirectional stress on the ability to gelation of the colloidal chitosan solutions. In the literature, no studies have been found to determine the effect of unidirectional shear on phase transition conditions of chitosan hydrogels. However, there are studies indicating a change in the spatial configuration of chitosan chains in solutions with disodium β-glycerophosphate under unidirectional shear [1]. Thus, it seems reasonable to determine the effect of unidirectional shear as the only type of applied deformation on the kinetics and

conditions of the sol-gel phase transition of chitosan solutions.

The purpose of this article is to investigate the influence of rotational deformations on the sol-gel phase transition condition of low-concentration chitosan solutions.The obtained results were compared with data obtained during classical oscillatory tests carried out under conditions of comparable shear.

MATERIALS AND METHODS

Materials

Colloidal solutions of chitosan (Sigma Aldrich) were prepared by dissolving 0.4 g of biopolymer (DD = 81.8%, Mw = 680 kDa) in 16 ml of 0.1 M hydrochloric acid (Fluca). A suspension of sodium β-glycerophosphate (Sigma Aldrich) - obtained by dissolving 2.0g of salt into 2.0ml of distilled water - was added to the prepared chitosan solutions.During the preparation of the research material, the procedures described in the literature were followed [7, 8, 10].

Methods

Rheometric measurements were carried out in a cone-plate measurement system (50 mm diameter, 1° slope angle, 48 μm truncation) of Anton PaarPhysica MCR 301 rotational rheometer.In order to determine the influence of the direction of the applied mechanical deformation, oscillatory and rotational measurements were carried out with constant deformation under isothermal and non-isothermal conditions.

The shear rate ($\dot{\gamma}$=0.03s^{-1}) in rotational measurements has been determined from the calculation of the deformation in the oscillatory measurements (strain amplitude γ=1%, angular frequencyω=5 s^{-1}) the known geometry (diameter and slope angle) of the measurement system.

RESULTS AND DISCUSSION

The results of the measurements carried out under non-isothermal conditions are shown in Fig. 1.The unidirectional shear leads to a different shape of the dynamic viscosity curve η compared to the experimental curve obtained in the oscillatory measurements – the real part of the complex viscosity η'.In the initial stage of the measurement up to 10 °C, an increase in the dynamic viscosity η was noted by almost a decade.This phenomenon was not observed in the case of oscillatory measurements.In this case, the real part of the complex viscosity decreases -the viscosity of the medium decreases due to the increase in temperature.The polymerization of chitosan chains may be hindered by the action of oscillatory movements.

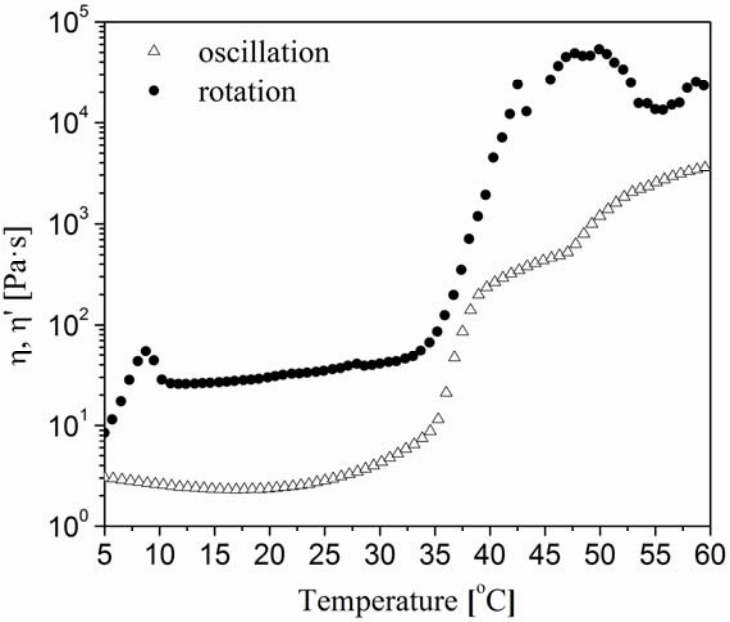

Fig. 1. The experimental curves of dynamic viscosity η and the real part of the complex viscosity η' obtained in non-isothermal measurements.

Further heating of the experimental medium leads to a continuous slow increase in the dynamic viscosity and the real part of the complex viscosity. Slow polymerization occurs, limited by the diffusion of polymer molecules. At 35 °C, regardless of the type of deformation applied, a rapid increase in the value of both quantities, which is associated with the fastest changes occurring in the sample, is observed.The increase in temperature, and thus the decrease in the viscosity of the medium, causes an increase in the diffusion rate of the polysaccharide molecules.Above 43 °C, the dynamic viscosity curve η reaches the second plateau. In the case of oscillatory measurements, this area is identified with a range of slow gelation, in which the existing polymer structure is being expanded[6].Above 52 °C, partial destruction of the structure is observed - the values of dynamic viscosity η are falling. Such a result is not obtained during oscillatory measurements. In the tests carried out, the real part of the complex viscosity η' increases. This means that oscillatory measurements as less invasive do not damage the internal structure.Simultaneously, the analysis of the conducted oscillatory measurements indicates that occurrence of the second plateau was not observed. This indicates that the final, highly cross-linked polymer structure was not formed during the measurement. It was also found that in the whole range of temperatures, the values of dynamic viscosity were higher compared to value of the real part of the complex viscosity. It should be noted that the experimental values obtained at

the beginning of the measurements reached nearly the same values regardless of the applied deformation.

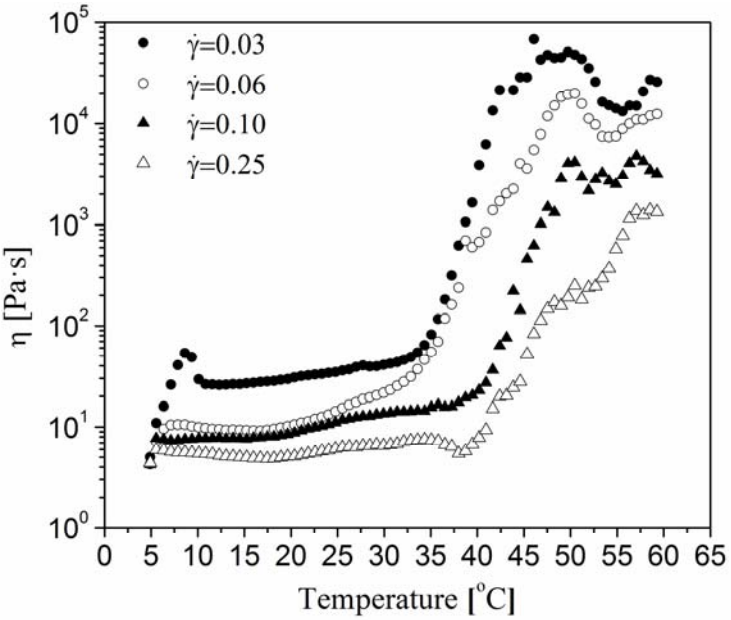

Fig. 2. Influence of shear rate on the change of the dynamic viscosity value η in non-isothermal measurements.

Fig. 2 shows changes in dynamic viscosity values in non-isothermal rotational measurements depending on the deformation used. The analysis of the obtained experimental data shows that the value of shear rate significantly influences the shape of the experimental curves. In the initial heating stage (up to approximately 10 °C), an increase in the shear rate causes a decrease in the dynamic viscosity value. The shapes of the experimental curves almost do not change to a temperature of approximately 30°C - viscosity values independent of the temperature change. In this range only the curve determined for the shear rate of 0.06 s^{-1} differs slightly from the others. It was also found that as the shear rate increased, the rapid change in the shape of the experimental curve and the increase in dynamic viscosity shifted towards higher temperatures. Above 55 °C, the occurrence of the second plateau is observed for all of the shear rates tested. However, with the increase of the deformation used, lower values of dynamic viscosity were obtained.This may indicate a lower degree of cross-linking of the polymer structure.

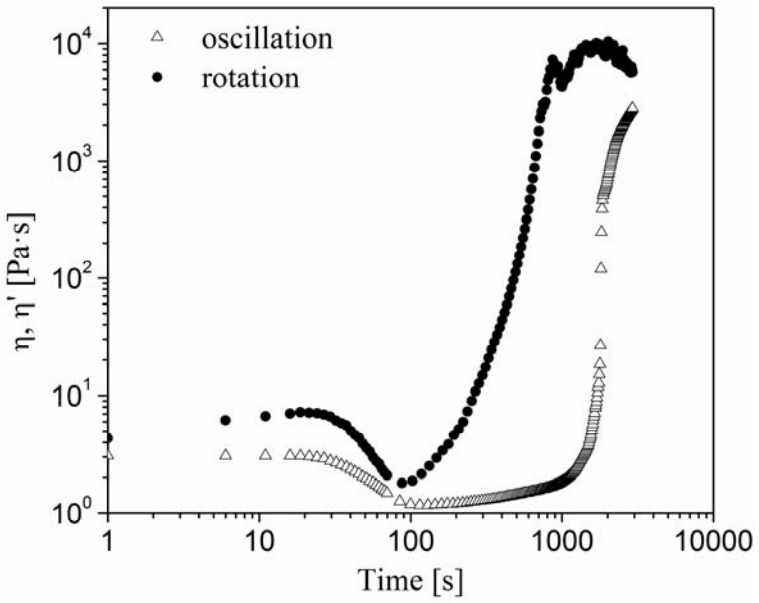

Fig. 3. The phase-change sol-gel kinetics in rotational and oscillatory measurements.

The results of isothermal measurements (at 37°C) at constant deformation are shown in Fig. 3. Analyzing the obtained results, the impact of the applied deformation on the sol-gel phase transition kinetics is even greater. The experimental curve of dynamic viscosity is consistent with the experimental curve of the real part of complex viscosity obtained in oscillatory measurements. The initial decrease in the viscosity value is related to the rapid heating of the test medium to the set storage temperature. After reaching the minimum value, a rapid increase in the dynamic viscosity is observed by almost 4 decades.The second plateau is reached after approximately 940 seconds. It is seen that more than three times longer storage at 37°C under oscillating shear does not lead to the occurrence of the second plateau region. This means that this time was not enough to form an infinite three-dimensional polymer structure. The biggest differences between oscillatory and rotational measurements are in the range of times from 100s to 1000s.In this range, in the oscillatory measurements, small changes in value of real part of the complex viscosity are observed. Simultaneously in this range, the most rapid changes in the value of dynamic viscosity was observed.

It was also found that at each stage of forming the structure, the values of dynamic viscosity are expressly higher than the values of the real part of complex viscosity.

CONCLUSIONS

The obtained results indicate a significant influence of the type of applied deformations on changes in rheological properties of colloidal,

low-concentration chitosan solutions. The experimental curves of rotational measurements are consistent with the characteristic regions of experimental curves obtained in oscillatory measurements for thermosensitive chitosan hydrogels. Application of very low values of shear rate, during unidirectional shear, can increase the mobility of molecules and leads to changing their spatial configuration (disentangling of entangled polymer chains) - thus accelerating the gelation process. The acceleration of sol-gel phase transition during unidirectional shear can also result from the ordering of the entangled long polymer chains along the shear field. The investigations carried out are consistent with the literature[1] determining the effect of unidirectional shear on gelation of colloidal chitosan solutions. Simultaneously it was found that shear of the formed, unlimited polymeric structure causes its destruction. This phenomenon is not observed during oscillatory measurements. Further development of the problem undertaken in the article seems justified due to the potential application of colloidal solutions of chitosan as injectable scaffolds in tissue engineering and high shear forces occurring in the syringe during their application.

REFERENCES

[1] Owczarz P., Ziółkowski P., Modrzejewska Z., Kuberski S., Dziubiński M., Rheo-Kinetic Study of Sol-Gel Phase Transition of Chitosan Colloidal Systems, *Polymers*, 2018, 10, 47, DOI:10.3390/polym10010047

[2] Rwei S.P., Chen T.Y., Cheng Y.Y., Sol/gel transition of chitosan solutions, *J. Biomater. Sci. Polym. Ed.,* 2005, 16, 1433–1445, DOI: 10.1163/156856205774472290

[3] Chenite A., Chaput C., Wang D., Combes C., Buschmann M.D., Hoemann C.D., *et al.*, Novel injectable neutral solutions of chitosan form biodegradable gels in situ, *Biomaterials,*2000, 21, 2155–2161, DOI: 10.1016/S0142-9612(00)00116-2

[4] Liu M., Zeng X., Ma C., Yi H., Ali Z., Mou X., *et al.*, Injectable hydrogels for cartilage and bone tissue engineering, *Bone Res.*, 2017, 5, 17014, DOI: 10.1038/boneres.2017.14

[5] Solouk A., Mirzadeh H., Amanpour S., Injectable scaffold as minimally invasive technique for cartilage tissue engineering: in vitro and in vivo preliminary study, *Prog. Biomater.*, 2014, 3, 143–151, DOI: 10.1007/s40204-014-0031-x

[6] Cho J., Heuzey M.-C., Bégin A., Carreau P.J., Chitosan and glycerophosphate concentration dependence of solution behaviour and gel point using small amplitude oscillatory rheometry, *Food Hydrocoll.,*2006, 20, 936–945, DOI: 10.1016/j.foodhyd.2005.10.015

[7] Chenite A., Buschmann M., Wang D., Chaput C., Kandani N., Rheological characterisation of thermogelling chitosan/glycerol-phosphate solutions, *Carbohydr. Polym.*, 2001, 46, 39–47, DOI: 10.1016/S0144-8617(00)00281-2
[8] Owczarz P., Rył A., Modrzejewska Z., Dziubiński M., The influence of the addition of collagen on the rheological properties of chitosan chloride solutions, *Prog. Chem. Appl. Chitin Its Deriv,.* 2017, 22, 176–189, DOI: 10.15259/PCACD.22.18
[9] Jiang Y., Meng X., Wu Z., Qi X., Modified chitosan thermosensitive hydrogel enables sustained and efficient anti-tumor therapy via intratumoral injection, *Carbohydr. Polym.,*2016, 144, 245–253, DOI: 10.1016/j.carbpol.2016.02.059
[10] Kamińska M., Kuberski S., Maniukiewicz W., Owczarz P., Komorowski P., Modrzejewska Z.,Thermosensitive chitosan gels containing calcium glycerophosphate for bone cell culture, *J. Bioact. Compat. Polym.,*2017, 32, 209–222, DOI: 10.1177/0883911516671150

Application of porogenes in the process of production of porous polymers by supercritical foaming

*Katarzyna Sawicka, Katarzyna Kosowska, Marek Henczka
Faculty of Chemical and Process Engineering, Warsaw University of Technology, Warsaw, Poland
e-mail: saw.kasia@gmail.com

***Keywords**: tissue engineering, supercritical fluids, foaming, poly(ε-caprolactone), porogenes*

ABSTRACT

Biocomposite foam scaffolds of poly(ε-caprolactone) with different porogenes were produced with batch foaming technique using supercritical carbon dioxide ($scCO_2$) as a blowing agent. In performed experiments composites were prepared from graphene-oxide (nGO), nano-hydroxyapatite (nHA) and nano-cellulose (nC), with various concentrations. The objective of the study was to explore the effect of porogen concentration and foaming process parameters on morphology and mechanical properties of the three-dimensional porous structures that can be used as temporary scaffolds in tissue engineering. The structures were manufactured with $scCO_2$, at two various foaming pressures (9 MPa and 18 MPa), at three different temperatures (323 K, 343 K and 373 K) for different saturation times (0,5 h, 1 h and 4 h). In order to examine the utility of the porogenes, a number of tests, such as static compression tests, thermal analysis and scanning electron microscopy, were performed. By analyzing the results of carried out research, considered materials have demonstrated high mechanical strength and wide range of pores sizes. Results suggest that obtained PCL composites could be promising materials as biodegradable and biocompatible scaffolds for tissue engineering.

INTRODUCTION

The development of chemical engineering is directly related to tissue engineering, an emerging interdisciplinary field aiming to produce biodegradable scaffolds that restore, maintain and improve damaged organs or tissues. A tissue scaffold is a three-dimensional structure that plays a crucial role as a temporary support for cell adhesion and it is used to facilitate the transport of metabolites and nutrients [1]. Over the last years, a variety of tissue scaffolds fabrication techniques have been developed, including solvent-casting, particulate-leaching and freeze drying. However, these conventional methods suffer various limitation. The main disadvantages are the use of large amounts of organic, not environment friendly solvents or high temperature required [2]. For this reason, novel methods are of interest and the foaming process with the use of supercritical fluids, has the potential

to overcome these drawbacks. The most commonly used supercritical fluid is carbon dioxide, due to its desirable attributes as readily available and inexpensive, nontoxic, nonflammable, low critical parameters (T_c=304,1 K and P_c=73,8 bar) [3]. The properties and characteristics of porous structures are dependent not only on the fabrication technique but also on the type of the materials. Synthetic polymers are promising scaffolding materials. Poly(ε-caprolactone) (PCL) is a semi-crystalline polymer of low melting temperature of approximately 59-64ºC. It has always been a popular biomaterial due to its biocompatibility and slow degradation rate (up to 2 years) [2]. One of fundamental properties of scaffold in tissue engineering is its sufficient mechanical strength, that should closely match the mechanical strength of the neotissue. However, no single component polymer materials can perform all functional requirements. Therefore, fabrication of composite materials seems to be an attractive strategy to develop multifunctional tissue scaffolds. In an attempt to improve mechanical properties and porosity of solid foams, bioactive calcium particle as hydroxyapatite has attracted lot of attention because of its similarity to the natural bone [4]. Nanocellulose, a natural polymer material extracted from native cellulose, possesses diverse characteristic different from tradional materials, including high Young's modulus (up to 167 GPa), high-surface area, possibility for chemical modifications and hydrophilicity. Materials based on this constituent are reported to be promising biomedical materials because of their excellent physical and biological properties, in particular their low cytotoxicity, biocompatibility and biodegradability [5]. Also graphene-based materials have undergone rapid development in recent years due to their unique structure and excellent mechanical, optical and electrical properties. Graphene oxide (GO) is highly oxidized form of graphene that structure consists of functional groups such as hydroxyls, carbonyls, carboxyls, and epoxides. It is reported that the addition of GO to the polymer matrix enhances the mechanical and thermal properties of commonly used biomaterials in tissue engineering [6].

MATERIALS AND METHODS

In performed experiments the PCL pellets (D~3mm) with number-average molecular weight Mn= 80,000 were obtained by Sigma Aldrich (Italy) and were used as a model polymeric material. Carbon dioxide (CO_2) with purity grade of 4,5, which was used as a blowing agent in foaming experiments, was purchased from Linde Gaz (Poland). Nano-hydroxyapatite powder and nano-cellulose powder were manufactured by Sigma Aldrich (Italy). Graphene oxide suspension in ethanol was supplied by Nanomaterials (Poland). Polymer-based nanocomposites were obtained by blending of the biodegradable polymer- PCL and the reinforcement materials-porogenes. Composites with 0-12wt% of nHA, 0-12wt% of nC and 0-1,5wt% of nGO were prepared.

In the first part of experimental investigation, poly(ε-caprolactone) scaffolds incorporating hydroxyapatite, cellulose and graphene oxide nanoparticles were fabricated by supercritical gas foaming technique by using high-pressure experimental system shown in Fig.1.

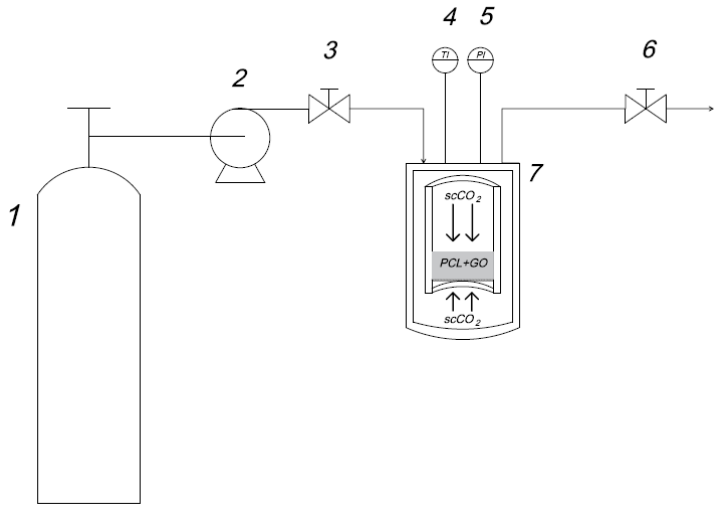

Fig.1. Schematic diagram of the experimental system: (1) Carbon dioxide tank, (2) $scCO_2$ pump, (3) valve, (4) temperature indicator, (5) pressure indicator, (6) back pressure regulator, (7) high pressure vessel.

The composites foaming experiments were conducted in a three-step batch process. First, the stainless steel high pressure vessel was filled with 3 grams of composite material, that was melted and saturated with a carbon dioxide under certain conditions. The structures were treated with $scCO_2$, at two various foaming pressures: 9 MPa and 18 MPa, at three different temperatures 323 K, 343 K and 373 K. Gas absorption led to formation of a homogeneous carbon dioxide-polymer mixture. This stage lasted 30 minutes, 1 hour or 4 hours. Thereafter, the mixture was cooled to 25ºC and kept for 30 minutes under the constant pressure in order to enable nucleation of cells in the polymer matrix. The final stage of foaming process, was a rapid decompression to atmospheric pressure, that led to the growth of foam bubbles. Finally, the composite porous structure was taken out from the stainless steel vessel and the residues of CO_2 were removed by evaporation.

In the second part of performed experiments the mechanical properties and morphology of solid foams were analysed using specialized analytical methods.

Scanning Electron Microscopy

The morphology of cross-section fracture and side section of the porous structures was analyzed by using Phenom scanning electron microscope (SEM). Sectioned foams were attached on SEM stubs using double-sided tape. Thereafter they

were coated with gold for 2 min under an argon atmosphere with a K550x sputter coater. SEM microphotographs were taken at two different magnifications (600x, 2000x). Image software analysis (Axiovison, Carl Zeiss) was used to identify the average pore sizes of scaffolds materials, by applying the following equation

$$D = \frac{\sum_{i=1}^{n} \sqrt{\frac{4 \cdot P_i}{\pi}}}{n} \quad (1)$$

where D is an average pore size, n is a number of pores identified in an analyzed sample and P_i is each pore area in an analyzed sample.

Differential Scanning Calorimetry (DSC)

The thermal analysis was performed using a Mettler Toledo scanning calorimeter. Sample of about 8 mg was placed in a platinum crucible. Measurements were performed at temperature range of 30-120ºC with temperature increasing rate of 10°C/min under an argon flow rate 30mL/min. The degree of crystallinity of polymer X_c was calculated based on the melting enthalpy value (ΔH) obtained from DSC thermogram with respect to melting enthalpy for 100% crystalline PCL (ΔH^0_{PCL}=142 J/g) [6], by using equation

$$X_c = \frac{\Delta H}{x \cdot \Delta H^0_{PCL}} \quad (2)$$

where x is the weight fraction of PCL in the sample.

Static Compression Test

Static compression tests were used to investigate the mechanical properties of obtained scaffolds. Three cuboids samples (5mm x 5mm x 8mm) were tested for each solid foam. Measurements were carried out by the universal testing machine Instron. Scaffolds were compressed to a total strain of 70% using a compression speed of 0,4 mm/min. The Young's modulus of solid foams was determined as the slope of the initial linear portion of stress-strain profile. Also the compression strength was identified on the basis of that curve.

RESULTS AND DISCUSSION

A balance between porous architecture sufficient to allow cells to adhere, proliferate, differentiate and mechanical properties of scaffolds used for tissue engineering is of critical importance [8]. Solid foams based on poly(ε-caprolactone) supplemented with 5% nHA, 5 % nC, 0,2% nGO have demonstrated these requirements for tissue regeneration.

The morphology and mechanical properties of porous materials prepared via the scCO2 foaming process are strongly dependent on the operating conditions such as pressure, saturation time and temperature.

SEM analysis allowed to identify the microstructure of polymer-based composite materials obtained under various foaming process conditions. The effect of pressure on the scaffolds' morphology was studied at a constant saturation temperature of 343 K and saturation time of 1 h. SEM microscope images of the cross-sections of the investigated composite porous structures evidencing the effect of the process pressure on the morphology of the samples are shown in Fig.2.

	Porogene's concentration		
Pressure [MPa]	5 % nHA	5 % nC	0,2 %nGO
9	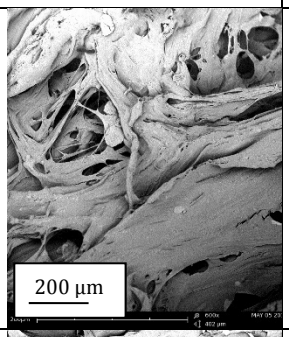	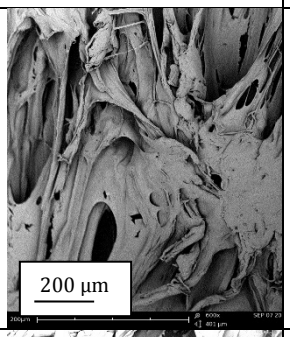	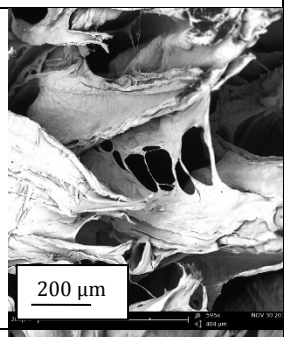
18	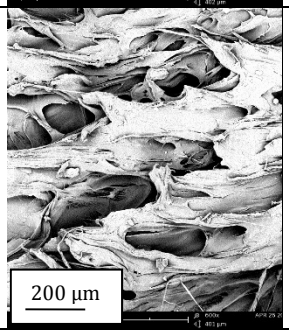	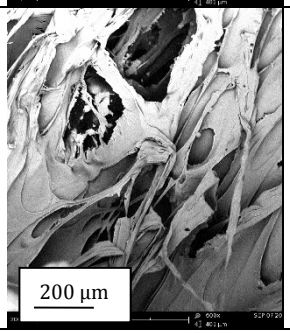	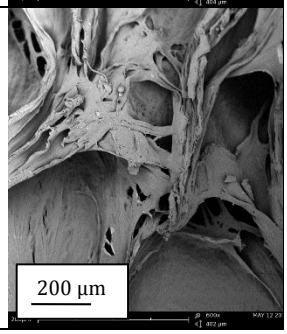

Fig. 2. Effect of a process pressure on morphology of porous structures obtained at constant saturation temperature (343 K) and saturation time (1 h).

As presented in SEM microphotographs (Fig. 1), the pore sizes decreased with increase of pressure of polymer saturating. At constant temperature, when the pressure increases more fluid is dissolved into the polymer matrix. This enhances the nucleation process and growth of pores. Moreover, a larger number of nuclei, which act as the centre of cells growth, are created. In general, much more pores with smaller size are formed at higher process pressure. The structures of all analyzed porous composite foams are non- uniform, also different pore shapes are noticed. In principle, such scaffold's microstructure is the most desirable for biomedical application.

The optimal pore size for porous structure is strictly dependent on the type of regenerated tissue. The values of an average pores of composite structures obtained under constant pressure (18 MPa) and different saturation time, temperature are summarized in Table 1.

Overall, application of supercritical carbon dioxide in the foaming process allowed to obtain composite porous structures with wide range of average pore sizes. The effect of temperature on the average pore size of a final porous structure was identified. As presented in Tab. 1 the average pore size increased with increase of foaming temperature from 323 to 343 K. At higher temperature the CO_2 solubility in the composite matrix decreases what causes that there is less dissolved fluid into this structure which is essential for the nucleation and growth of pores. Performing saturation of composite material at 343 K led to fabrication of scaffolds with the largest average pore size.

Tab. 1. Effect of foaming conditions on average pore size.

Average pore size [μm]				
Pressure [MPa]		18		
Porogene's concentration		5 % nHA	5 % nC	0,2 %nGO
T_{sat} [K]	323	11,17 (±0,84)	5,21 (±0,46)	23,19 (±2,54)
	343	22,43 (±1,61)	17,72 (±1,79)	23,97 (±2,96)
	373	15,27 (±1,86)	7,80 (±1,12)	15,54 (±1,76)
t_{sat} [h]	0,5	14,56 (±1,51)	16,06 (±1,48)	16,02 (±1,56)
	1	22,43 (±1,61)	17,72 (±1,79)	23,97 (±2,96)
	4	11,01 (±1,28)	15,67 (±2,53)	31,85 (±2,70)

It was observed that an increase in saturation time leads to creation of larger pores. The longer saturation time more fluid could dissolve into polymer matrix. It enables pore sizes to develop to a greater extent than in the case of relatively short saturation times.

DSC assays were conducted to investigate the effects of nanoparticles on the crystallization behavior of the PCL matrix. As presented in Fig. 3, the melting temperature was determined as the peak temperature of heating curve. Applying $scCO_2$ to polymer foaming process led to a decrease in the melting point of analyzed materials. The melting temperature of obtained composite porous structures was lower than the melting point of 100% crystalline PCL. On the basis of DSC thermographs foams degrees of crystallinity were defined. The largest value of this parameter was observed for 5 wt% of nHA (Tab. 2).

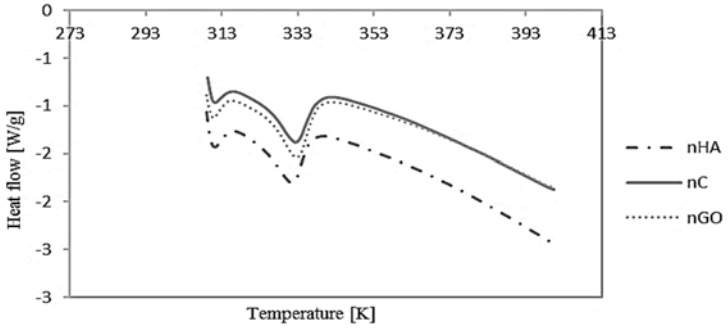

Fig. 3. DSC thermogram of the investigated composite porous structures obtained under the foaming conditions P_{sat}=18 MPa, T_{sat}=343 K, t_{sat}=1 h.

Static compression test was done to determine the mechanical properties of porous scaffolds that are strictly dependent on their porosity and density [9]. The results of carried out experiments are summarized in Tab. 2. It was observed that for a relatively short saturation time of 0,5 h, the highest values of Young's modulus and compressive strength of composite scaffolds were achieved. The Young's modulus values increased with increase of pressure, whereas for a compressive strength values the opposite effect was observed. The increase of the saturation temperature led to increase of mechanical properties of solid foams.

Tab. 2. Compression Test and Differential Scanning Calorimetry results of composite foams.

Porogene's concentration	Foaming process parameter		Static compression test		DSC	
			Young's modulus [MPa]	Compression strength [MPa]	Degree of crystallinity [%]	Melting temperature [ºC]
Foaming process conditions: T_{sat}=343 K, t_{sat}=1 h						
5 % nHA	Pressure [MPa]	9	1,446 (±0,21)	0,462 (±0,04)	22,10 (±2,19)	54,83 (±0,41)
		18	1,193 (±0,09)	0,507 (±0,05)	23,50 (±2,19)	53,83 (±0,41)
5 % nC		9	1,303 (±0,20)	1,595 (±0,16)	18,55 (±1,85)	55,17 (±0,32)
		18	1,575 (±0,17)	1,331 (±0,47)	16,53 (±1,85)	55,17 (±0,32)
0,2 % nGO		9	1,470 (±0,26)	14,872 (±4,81)	18,33 (±0,62)	54,50 (±0,22)
		18	1,698 (±0,09)	1,091 (±0,38)	17,38 (±0,62)	55,83 (±0,22)
Foaming process conditions: P_{sat}=18 MPa, t_{sat}=1 h						
5 % nHA	Temperature [K]	323	1,702 (±0,19)	0,784 (±0,20)	23,16 (±2,19)	53,83 (±0,41)
		343	1,193 (±0,09)	0,507 (±0,05)	23,50 (±2,19)	53,83 (±0,41)
		373	1,098 (±0,23)	0,617 (±0,16)	23,56 (±2,19)	54,50 (±0,41)
5 % nC		323	0,600 (±0,01)	0,676 (±0,05)	22,45 (±1,85)	54,50 (±0,32)
		343	1,575 (±0,17)	1,331 (±0,47)	16,53 (±1,85)	55,17 (±0,32)
		373	2,235(±0,12)	2,382 (±0,21)	19,70 (±1,85)	55,83 (±0,32)
0,2 % nGO		323	1,478 (±0,05)	1,036 (±0,03)	19,33 (±0,62)	55,83 (±0,32)
		343	1,698 (±0,09)	1,091 (±0,38)	17,38 (±0,62)	55,83 (±0,22)
		373	1,893 (±0,14)	5,189 (±4,23)	19,21 (±0,62)	55,83 (±0,22)
Foaming process conditions: P_{sat}=18 MPa, T_{sat}=343 K						
5 % nHA	Saturation time [h]	0,5	0,422 (±0,14)	0,816 (±0,26)	10,20 (±2,19)	56,50 (±0,41)
		1	1,193 (±0,09)	0,507 (±0,05)	23,50 (±2,19)	53,83 (±0,41)
		4	1,136 (±0,11)	0,448 (±0,12)	23,86 (±2,19)	55,17 (±0,41)
5 % nC		0,5	1,459 (±0,08)	4,127 (±2,17)	9,40 (±1,85)	55,83 (±0,32)
		1	1,575 (±0,17)	1,331 (±0,47)	16,53 (±1,85)	55,17 (±0,32)
		4	0,998 (±0,26)	0,736 (±0,35)	19,84 (±1,85)	53,83 (±0,32)
0,2 % nGO		0,5	3,281 (±0,40)	9,767 (±4,91)	21,80 (±0,62)	55,83 (±0,22)
		1	1,698 (±0,09)	1,091 (±0,38)	17,38 (±0,62)	55,83 (±0,22)
		4	0,633 (±0,10)	1,058 (±0,20)	19,99 (±0,62)	55,83 (±0,22)

CONCLUSIONS

The performed experimental investigations demonstrated that porogen concentration and foaming process parameters have significant impact on mechanical properties and morphology of the obtained three-dimensional porous structures. The most appropriate foam for biomedical application was supplemented with graphene-oxide (0,2 wt%) and obtained at temperature 343 K, under the pressure 18 MPa for

the period of saturation time 0,5h. This structure was characterized by large average pore size and high mechanical and thermal properties. No negative changes in foams structure and properties, that would limit the usability of the porogenes in polymer foaming process, were observed. Results ensured that all obtained foams are suitable for potential application in tissue engineering.

REFERENCES

[1] Chen, C. X., Liu, Q. Q., Xin, X., Guan, Y. X., Yao, S. J., Pore formation of poly(ε-caprolactone) scaffolds with melting point reduction in supercritical CO2 foaming. Journal of Supercritical Fluids, 2016, 117, 279–288, DOI: 10.1016/j.supflu.2016.07.006

[2] Kramschuster, A.,Turng, L.-S., Fabrication of Tissue Engineering Scaffolds. Handbook of Biopolymers and Biodegradable Plastics. Elsevier, 2013, 17, 427-446, DOI: 10.1016/B978-1-4557-2834-3.00017-3

[3] White, L. J., Hutter, V., Tai, H., Howdle, S. M.,Shakesheff, K. M., The effect of processing variables on morphological and mechanical properties of supercritical CO2 foamed scaffolds for tissue engineering. Acta Biomaterialia, 2012, 8(1), 61–71, DOI: 10.1016/j.actbio.2011.07.032

[4] Velasco, M. A., Narváez-Tovar, C. A., Garzón-Alvarado, D. A., Design, materials, and mechanobiology of biodegradable scaffolds for bone tissue engineering. BioMed Research International, 2015, DOI: 10.1155/2015/729076

[5] Dumrah Dumanli, A., Nanocellulose and its Composites for Biomedical Applications. Current Medicinal Chemistry, 2017, 24(5), 512–528. DOI: 10.2174/0929867323666161014124008

[6] Ahadian, S., Ramalingam, M., Khademhosseini, A., The Emerging Applications of Graphene Oxide and Graphene in. Biomimetics, 2013, 279–300.

[7] Diaz-Gomez, L., Concheiro, A., Alvarez-Lorenzo, C., García-González, C. A., Growth factors delivery from hybrid PCL-starch scaffolds processed using supercritical fluid technology. Carbohydrate Polymers,2016, 142, 282–292, DOI: 10.1016/j.carbpol.2016.01.051

[8] Loh, Q. L., Choong, C., Three-Dimensional Scaffolds for Tissue Engineering Applications: Role of Porosity and Pore Size. Tissue Engineering Part B: Reviews, 2013, 19(6), 485–502, DOI: 10.1089/ten.teb.2012.0437

[9] Fröhlich, M., Grayson, W. L., Wan, L. Q., Marolt, D., Drobnic, M., Vunjak-Novakovic, G., Tissue engineered bone grafts: biological requirements, tissue culture and clinical relevance. Current Stem Cell Research & Therapy, 2008, 3(4), 254–64. DOI: 10.2174/157488808786733962

Staining techniques as a tool for assessing surface hydrophobicity of the contact lenses

*Sylwia Stiler[1], Sylwia Golba[1]
[1]Faculty of Materials Science, University of Silesia in Katowice, POLAND
e-mail: stiler.sylwia@wp.pl

***Keywords**: contact lenses, staining techniques, Sudan IV*

ABSTRACT

Almost half of people using contact lenses experience dryness and discomfort of the eyeball. These sensations are caused by changes in the surface of lens during their use as a result of surface deposition of proteins and lipids.

Protein adsorption proceeds predominantly on hydrophobic surfaces. The surface of contact lens is hydrophilic. However, the hydrophobic domains can locally occur in them. Studies on the adsorption of various contaminants are important in the design of biocompatible surfaces, where reduction or elimination of protein deposition improves their functionality.

The presence of proteins on biomaterial surfaces can be detected by selective staining using appropriate probes. Dyeing is a technique that enables detecting of interesting sites without isolating them.

The studies included the identification of hydrophobic domains in hydrogel lenses. Lipophilic dye, Sudan IV, was used. The analysis of the results allowed to determine the percentage of hydrophobic domains on the surface of the lens material.

INTRODUCTION

Among those who use contact lenses, almost half of these population experience discomfort related to dryness in the eyeball. This effect has mostly been recorded a few hours after using contact lenses due to changes in the surface of the hydrogel or silicone hydrogel material (depending on the lens used) caused by the deposition of proteins and lipids on their surface [1].

Contact lenses are most effective when they are well suited to individual patients. Their influence on the eye organ is undeniable, although proper adjustment of their shape and properties to the anatomy of the patient's eyeball allows them to be more tolerant.

Knowledge about the basic structures occurring in the eyeball is necessary, as it helps to prevent the negative effects of the use of contact lenses, and also allows the development of contactology.

The human eye is approximately a sphere with a diameter of 25 millimeters. The eyeball is surrounded by a membrane, which can be divided into three layers. The outer layer is formed by the fibrous membrane of the eyeball, which is transparent in

the front part and is called the cornea, while the remaining part, which is opaque, is called the sclera. The middle layer is called the choroid, which in the front part forms the ciliary body and the iris. The inner membrane, for the most part, is made of retina.

The individual elements play following roles:

• sclera - a protective layer of the eyeball. Eye muscles are attached to it, which are responsible for moving the eyeball.

• cornea - the main part of the optic system of the eye. Her main tasks are: refraction of light rays and protection of the eye (thanks to strong irradiation, it reacts to foreign bodies)

• choroid - thanks to strong vascularization nourishes the layers of the eye, which are located deeper. It becomes swollen to the front, grows into the eye (forming a ciliary body), participates in the accommodation process.

• iris - part of the vascular membrane that surrounds the hole called the pupil. Iris muscles give the possibility of increasing or decreasing the inflow of light by adjusting the size of the pupil [2].

The cornea fulfills the functions of the protective film and places through which the light rays have the ability to reach the retina. It is transparent, due to its homogeneous structure, lack of vessels and edema. The hydration status of the cornea and the lack of edema can be maintained thanks to the active carbonate pump that is formed by the endothelium and the epithelium and endothelium that perform the function of a barrier. Endothelium is more important in the mechanism of hydration than the epithelium, so its damage make a serious health issue. The destruction of endothelial cells causes corneal edema and the loss of its transparency, which may persist due to limited regenerative possibilities.

Evaporation of water from the front of the tear film causes its increased tension. This process, as well as direct evaporation, are water-distracting agents from the surface of the cornea to maintain a proper hydration.

The penetration of drugs through the intact cornea is two-phase. Fat soluble compounds can penetrate through the intact epithelium, whereas water soluble compounds can penetrate intact epithelium. Therefore, in order for the drugs to penetrate the cornea, they should be dissolved in both fats and water [3].

Since the introduction of contact lenses on the market, it has been obvious that tear film components are deposited on their surface [4]. In particular, the proteins contained in the tear film lead to feelings of discomfort, worsening vision and the occurrence of inflammation. In human tear film, almost 500 different proteins are distinguished, however, only four of them are present in high concentration – these are: lipocaine, lysozyme, lactoferrin and secretory immunoglobulin A (sigA) [5]. All of these proteins are produced by the lacrimal gland: the three mentioned first are secreted in the staphylococcal cell clusters, while sigA is secreted by interstitial plasmocytes [6].

The most important proteins found in the tear film help to prevent eye infections and are responsible for the health of the eye organs. Mainly lysozyme, which is a strong antibacterial enzyme, allows the hydrolysis of chemical bonds in the outer cell walls of bacteria [7].

The most important bacteria that occur in the tear film and are controlled by lysozyme are streptococcal and staphylococcal bacteria that can cause conjunctivitis.

The proteins present in the tear film quickly settle on the surface of the lens material - even within a few hours. Protein deposition is closely related to the type of material. From a clinical point of view, protein deposition on the surface of contact lenses is considered an undesirable effect [8].

Adsorption of proteins takes place on hydrophobic surfaces, which is very important from the point of view of contact lenses suitability. By implication, the surface of the hydrogel lenses is hydrophilic, whereas silicone hydrogels can have silicone hydrophobic domains.

Polymeric materials have a wide range of biomedical applications. Depending on the type of application, protein adsorption is a desired phenomenon (mainly in the case of biosensors) or undesirable (in the case of contact lenses). Most proteins tend to physically adsorb to polymers, which reduces their functionality. Research on their adsorption is extremely important for the design of biocompatible surfaces, where the reduction or elimination of protein deposition improves their functionality.

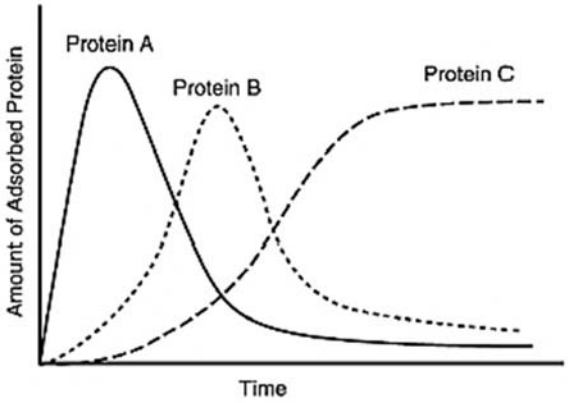

Fig. 1. Scheme of changes caused by adsorption and desorption of proteins on the surface of the biomaterial depending on time leading to the determination of the dynamic balance (Vroman effect) [10].

Adsorption of proteins on the surface is a result of three steps: transport, adsorption and repulsive forces. It shows that the diffusion of small molecules (Protein A) is faster than large proteins (Protein C) (Figure 1), therefore they adsorb small proteins first. Due to the larger contact area, large proteins bind more strongly to the

surface, which may force the desorption of smaller proteins during diffusion on the surface. The result is a local maximum that can be observed on the temporal dependence of protein adsorption.

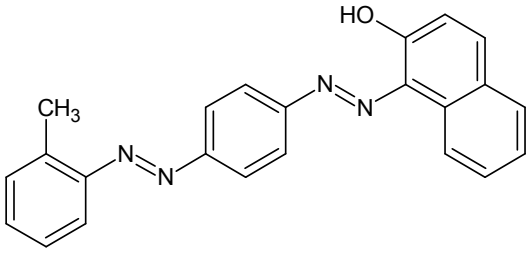

Fig. 2. Structural formula of Sudan IV dye.

The presence of proteins on biomaterial surfaces can be detected by selective staining using appropriate probes. Dyeing is an important biochemical technique that allows to visually detect interesting places on the material without isolating them. Sudan IV (Figure 2) is a fat-soluble pigment. It is used to stain lipids, triglycerides and lipoproteins. It has the form of red-brown crystals whose melting point is 199 ° C, and the maximum absorbance occurs at 520 nm. Its presence is an unambiguous marker of the hydrophobic nature of the surface [9].

MATERIALS AND METHODS

In this work the hydrogel "one-day" lenses available commercially were studied. Before testing they have been conditioned in four selected environments: artificial tears, liquids for their storage, saline solution and distilled water. Before immersing the material in the solutions, each lens was rinsed with distilled water for 40 minutes, in order to remove from their surface ingredients coming from the liquid in which they are stored in the package.

The lenses have been subjected to surface hydrophilicity tests. To this end, a solution of an indicator showing affinity for hydrophobic areas (Sudan IV) in silicone oil was prepared in accordance with the procedure proposed in the literature [9]. For this purpose, 0.1 g of Sudan IV was added to 4.9 g of silicone oil. The solution was then stirred for 30 minutes using a magnetic stirrer. After this time, the saturated solution was poured into vials and centrifuged for 5 minutes. The supernatant was then pipetted as a clear solution, 7.5 g of silicone oil was added thereto and again mixed with a magnetic stirrer resulting in an intense red clear solution.

Two lens storage times were used in Sudan IV solution: 30 minutes (experiment 1) and 24 hours (experiment 2). This allowed to obtain a color on their surface, in places where there is a hydrophobic character of the surface. Due to its chemical structure, this dye is capable of selective adsorption on surfaces of a hydrophobic nature, becoming a specific marker. After removing from Sudan IV, the

lens was rinsed in distilled water for 30 minutes to get rid of impurities from their surface. Next, the lenses were analyzed in the ImageJ program (producer: National Institutes of Health., Available free of charge, 2017), in order to calculate the% share of the color on their surface.

RESULTS

After studied the pictures were read into the program, processed into an 8-bit image, binarized and analyzed to calculate the percentage of color on the surface of the lens. According to the description presented in the theoretical part of the work, places that have been stained are places of potential deposition on the lens surface of proteins and impurities, which has a significant impact on the comfort of their use.

Table 1 shows the conditions for conducting the conditioning process prior to the staining of the lenses, together with the results of the share of the surface capable of selective adsorption of the dye.

Tab. 1. Conditions for conditioning before dyeing together with the percentage of stained surface.

CL storage environment			NaCl	PDPS	SzŁ	WD
color factor	polymer matrix	time				
Sudan IV	Hy (1D)	30 min	11%	10%	18%	11%
	Hy (1D)	24 h	19%	12%	24%	16%

The lenses under study were conditioned in four environments. Places stained with Sudan IV are places of potential deposition on the surface of lipids and other impurities of organic origin, which is disadvantageous to the user of the lenses.

Figure 3 and Figure 4 show photos of hydrogel lenses (1 day) after storing in four environments: PDPS (commercial liquid for lens storage), NaCl (saline solution 0,9%), SZŁ (artificial tears) and WD (distilled water), as well as images processed in the ImageJ program, thanks to which the degree of surface coloring was determined.

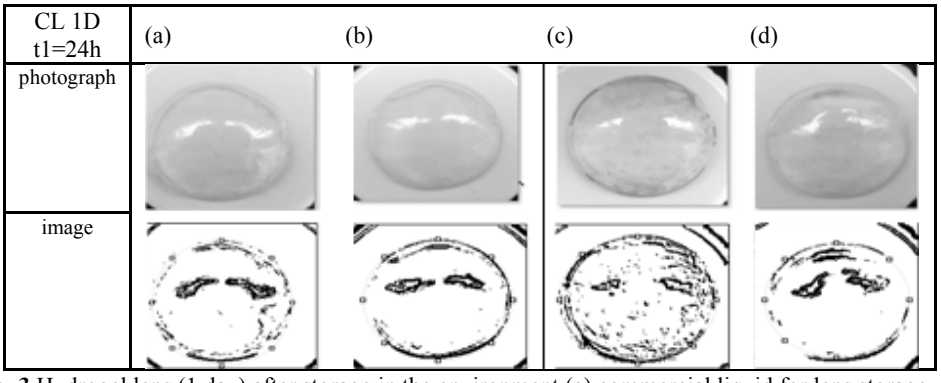

Fig. 3 Hydrogel lens (1 day) after storage in the environment (a) commercial liquid for lens storage, (b) saline solution (0.9% NaCl), (c) artificial tears, (d) distilled water, t1 = 24 h.

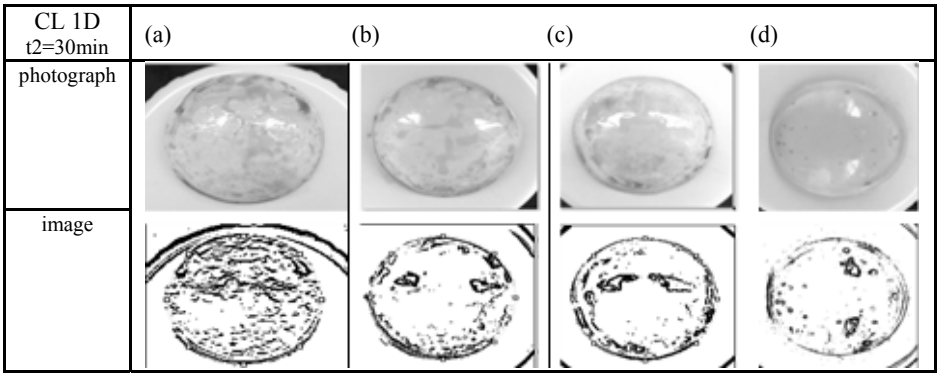

Fig. 4 Hydrogel lens (1 day) after storage in the environment (a) commercial liquid for lens storage, (b) saline solution (0.9% NaCl), (c) artificial tears, (d) distilled water, t2 = 30 min.

As can be seen in figures 3 and 4, the tested lenses, despite not being worn by patients, have stained sites (hydrophobic domains).

The environment that had the greatest impact on the formation of hydrophobic spots on the surface of the lenses are artificial tears. The smallest number of these places was recorded in distilled water.

CONCLUSIONS

The conducted research allowed to determine changes in the hydrophilicity degree of hydrogel materials.

It has been observed that hydrogel contact lenses have hydrophobic regions on their surface. Both the basic structure of the matrix and the environment in which the lenses are stored have an impact on the area covered by the hydrophobic compound.

The highest amount of dye was adsorbed on the surface of the lens stored in artificial tears, which indicates the most hydrophobic character of the surface. Attempts should be made to reduce the occurrence of these areas, due to the susceptibility of these areas to the adhesive attachment of protein structures.

Determination of the content of the hydrophobic surface indicates the susceptibility of these areas to the adsorption of protein-derived sediments constituting the first stage in the process of creating a bacterial biofilm. It has been shown that the presence of hydrophobic surfaces in hydrogel materials is already affected by their storage in conditioning solutions. In the next step, tests of lens used by patients should be carried out, so that the results can be applied to clinical applications.

REFERENCES

[1] T. Edwards K. Kura, D. Nissanke, H. Ketelson, J.T. Jacob. Hydrophobic Domains in Silicone Hydrogels Contact Lenses. *Investigative Ophthalmology & Visual Science*, 2012.

[2] K. Pecold M. Krawczyński. Oczodół, powieki i układ łzowy. Wrocław: Wydawnictwo medyczne Elsevier&Partner, 2003.

[3] P. Riodan-Eva P.J. Whitcher. *Okulistyka Vaughana i Asbury'ego. Wydawnictwo Czelej*, 2011.

[4] S. Eriksen, Cleaning hydrophilic contact lenses: an overview. *Annals of Ophthalmology* 1975; 7: 1223-6, 1229-32.

[5] L. Jones, V. Franklin, K. Evans, R. Sariri, B. Tighe, Spoilation and clinical performance of monthly vs. three monthly Group II disposable contact lenses. *Optometry and Vision Science* 1996; 73: 16-21.

[6] K.W. Gellatly, N.A. Brennan, N. Efron, Visual decrement with deposit accumulation of HEMA contact lenses. *American Journal of Optometry and Physiological Optics* 1988; 65: 937-941.

[7] C. Skotnitsky, P.R. Sankaridurg, D.F. Sweeney, B.A. Holden, General and local contact lens induced papillary conjunctivitis (CLPC). *Clinical and Experimental Optometry* 2002; 85: 3 193-197.

[8] J. Tiffany, The normal tear film. *Developments in Ophthalmology* 2008; 41: 1-20

[9] A. Guzman-Aranguez, B. Colligris, J. Pintor, Contact Lenses: Promising Devices for Ocular Drug Delivery. *Journal of Ocular Pharmacology and Therapeutics*, 2013. 189-199.

[10] W. Mathers, Evaporation from the ocular surface. *Exp Eye Res.*, 2004. 389-394.

Contact lenses as controlled release drug systems on the example of timolol

*Sylwia Stiler[1], Sylwia Golba[1]
[1]Faculty of Materials Science, University of Silesia in Katowice, POLAND
e-mail: stiler.sylwia@wp.pl

***Keywords**: contact lenses, controlled release drug systems, timolol*

ABSTRACT

The first attempts to use contact lenses as drug release dies took place as early as in the 1960s. Initially, the main method of applying the drug in a hydrogel lens was dipping it in the drug solution, and then immediately applying it to the patient.

The aim of the research was to study the sorption and desorption of timolol in polymer matrices. The newly opened lens was thoroughly rinsed with distilled water and its absorption spectrum was recorded. The material was then placed in a vessel filled with a solution of timolol and held for a given time (1 day, 3 days or 7 days) to allow diffusion of the substance molecules in the polymer matrix.

The drug substance used for the study gives promising results in terms of its use in contact materials as controlled drug release systems, because during the use of the drug directly into the eyeball it remains in it only a few minutes, while from the lens is released for several dozen minutes.

INTRODUCTION

Hydrogels appeared in 1960, when Wichterle and Lim for the first time proposed the use of hydrophilic networks made of poly (2-hydroxyethyl methacrylate) (PHEMA). Since then, there has been increased interest in hydrogels and their use in biomedical and pharmaceutical applications. [1]

Compared to other synthetic biomaterials, hydrogels possess physical properties similar to living tissue due to high water content, plasticity and elasticity. In addition, due to the low interfacial tension they have a minimal tendency to adsorb proteins from body fluids. In the literature, when referring to these polymers, the terms gel and hydrogel are used interchangeably, without taking into account the differences that occur in their physical properties, only their chemical similarities are taken into account. [2-3]

Hydrogels, using the prefix "hydro" are identified with water gels, but this term should be defined as a swellable in water or biological fluids synthetic material that is spatially crosslinked, and also composed of hydrophilic natural polymers, capable of absorbing large amounts of water at preserving its three-dimensional structure. In the hydrogel, water is a transport medium for the diffusion of substances,

while the degree of matrix cross-linking affects the possibility of their transport through the material. [4-5]

The first attempts to use contact lenses as drug release matrices took place as early as in the 1960s. Initially, the main method of applying the drug in a hydrogel lens was dipping it in the drug solution, and then immediately applying it to the patient. This method was more effective than eye drops, but it lengthened the possibility of drug application by several hours compared to the original method.

After the development of silicone hydrogel lenses, tests were carried out in which the lenses were immersed in the antihistaminic drug solution. The obtained results were quite promising, after soaking the lens for 3 days in the drug solution its release from the matrix took over 24 hours. The application of such a lens made it possible to obtain results similar to the four-fold application of drops to the conjunctival sac. Also, a more stable concentration of the formulation in the tear film allows for greater effectiveness of the drug and minimizes possible side effects of treatment.

The results obtained by scientists have already allowed the initial use of silicone hydrogel lenses as drug carriers. Due to the enormous potential of contact materials, several methods have been developed that allow to increase the saturation of the material with the drug, as well as extend its release to several or even several dozen days. [6-8]

MATERIALS AND METHODS

One-day lenses that were used for testing are soft hydrogel lenses, while two-week and monthly lenses are silicone hydrogel lenses. According to the manufacturer's data, they contain a minimum of 46% water and a suitable polymeric material.

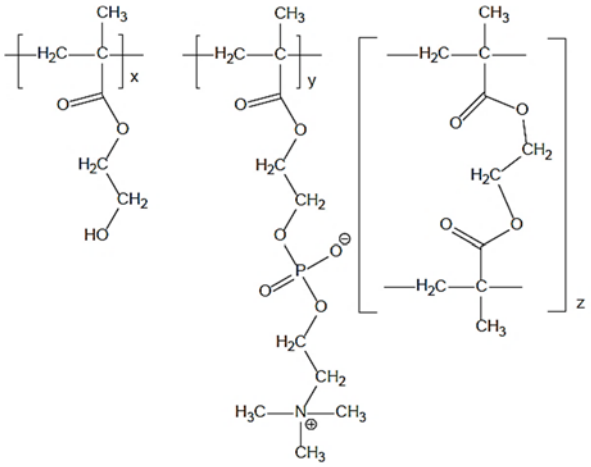

Fig. 1. Structural formulas of polymers forming the Omafilcon B lens network [9].

One-day lenses contain Omafilcon hydrogel material (Figure 1) and are made in PC technology. This means that they are made with phosphorylcholine molecules (Figure 2) that are biocompatible with the human body and have hydrophilic properties. The Omafilcon A material is built from poly (2-hydroxyethyl methacrylate), which is doped with ethylene glycol diacrylate. The PC coating is colored with the addition of reactive blue.

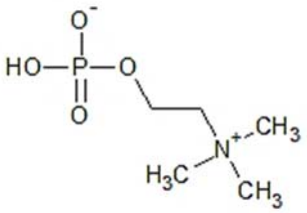

Fig. 2. Structural formula of phosphorylcholine.

The composition of the solution of the drug used:

• timolol (Tim): active substance timolol, 2.5 mg (CAS: 26921-17-5, M = 432.49 g), auxiliary substances: benzalkonium chloride 0, 05 mg, sodium bisphosphate x 2 H_2O 8.00 mg, sodium hydrogen phosphate x 12 H_2O 32.00 mg, water for injections up to 1.00 ml.

A 3 ml solution was prepared at a standard therapeutic concentration: Tim - 0.2% (consulted with ophthalmic units).

The newly opened lens was thoroughly rinsed with distilled water and its absorption spectrum was recorded. The material was then placed in a drug-filled vessel and held for a given time (1 day, 2 days or 7 days) to allow diffusion of the substance molecules in the polymer matrix. The lenses were then removed, rinsed to clean the surface adsorbed molecules and placed in a measuring cuvette in order to register the spectrum.

Absorptive spectra for solutions and for lenses after their retention in solutions have been recorded. Next, curves for the release of drug substance from polymer matrices were registered. The desolation study of timolol was carried out using a UV VIS spectrophotometer. The lens was placed on the bottom of a quartz cuvette and flooded with 2 ml of distilled water, then the spectra were recorded at 30 second intervals until the obtaining of the identical solution spectrum was stabilized for 5 consecutive measurements.

RESULTS

The tested drug was timolol (Tim), which is used as a treatment for glaucoma, because it reduces intraocular pressure. The initial concentration of active ingredient was 0.2%. Three samples were tested, differing in the time they were kept in the drug

solution (1, 3 and 7 days). After this time, their absorption spectra were taken out and recorded to determine if the drug was absorbed.

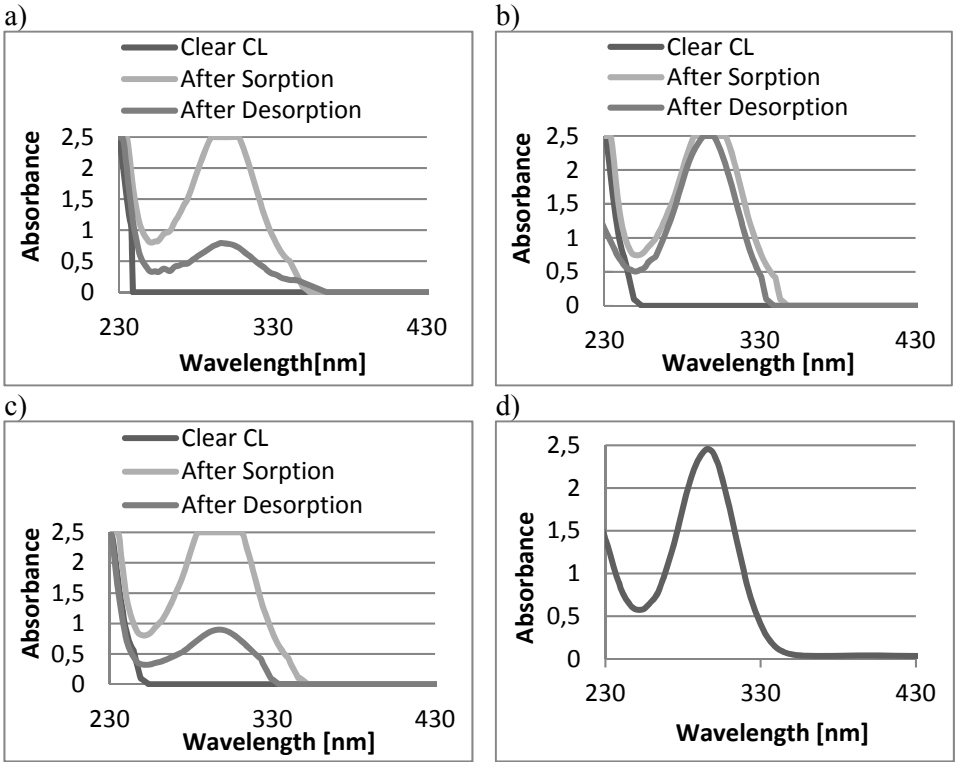

Fig. 3. Absorption spectra recorded for lenses sorptioned in aqueous Tim and desorption in water for a) 1 day, b) 3 days, c) 7 days, d) spectrum for Tim (dilution in a ratio of 1: 1).

The Figure 3 show the spectra for pure lens material, for the lens after sorption and after desorption. On the curve it is possible to observe the characteristic band for Tim in all three samples (Figure 3), which did not appear for the pure lens material. After desorption of the drug, the absorbance in this range decreased, which indicates its release from the polymer matrix. The spectrum for the pure drug is shown after its dilution in a 1: 1 ratio, because the primary spectrum exceeded the measuring range of the apparatus. As a result, it was possible to determine the wavelength at which there is a characteristic absorption band for this substance. Based on the recorded spectrum, 296 nm was assumed as the analytical wavelength.

On the basis of the curves obtained, it was possible to calculate what amount timolol has been absorbed into the lens. To this end, Lambert Beer's law was applied and dependence:

$$c_{witE} = \frac{A_{ps}}{\varepsilon * l}$$

where:

c_{witE} - amount of absorbed vitamin, [%]
A_{ps} - absorbance value for sorption material (λ = 296 nm), [au]
ε - an analog of the molar absorption coefficient determined from the experimentally obtained calibration curve, [$\%^{-1} \cdot cm^{-1}$]
l - thickness of the absorbing layer, [cm].

On the basis of the obtained results, the relationship between the storage time of the lens in the drug and the concentration of the drug that was absorbed into its interior was drawn (Figure 4).

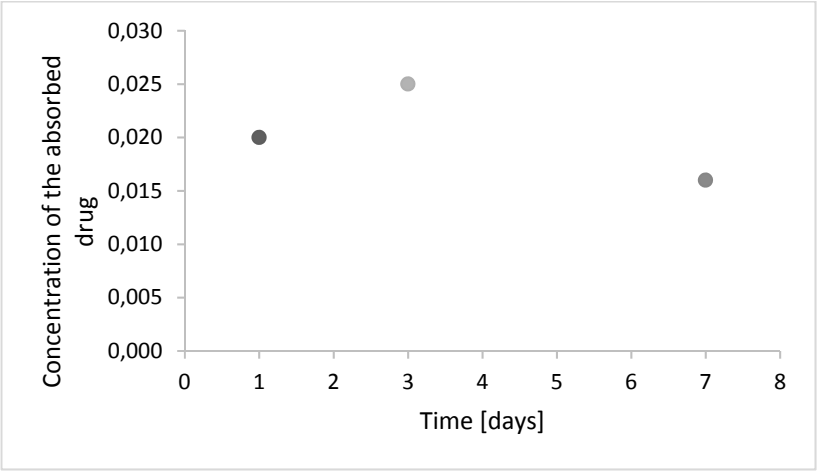

Fig. 4. The relationship between the concentration of the absorbed drug and the time the lens was stored in Tim solution.

It has been observed that the most effective sorption for Tim can be obtained after storing the lens in the drug solution for a period of 3 days.

After removing the lens from the solution after one day and recording its absorption spectrum, analysis of drug release from the lens was started. For this purpose, it was placed in a quartz cuvette. Then 2 ml of distilled water were added and the absorption spectra were recorded, in the initial period of drug release, when it was more rapid the spectra were recorded every 30 seconds, then at 1 minute intervals. The measurement was carried out until the maximum value of the absorbance registered by the apparatus was exceeded, which lasted 57 minutes for the first sample (1 day in solution), 74 minutes for the second sample (3 days in solution) and 3 minutes for the third sample (7 days in solution). This may indicate that the period of 7 days is too long to store the lens in this drug because it has become less elastic, softer and the release of the drug is too rapid.

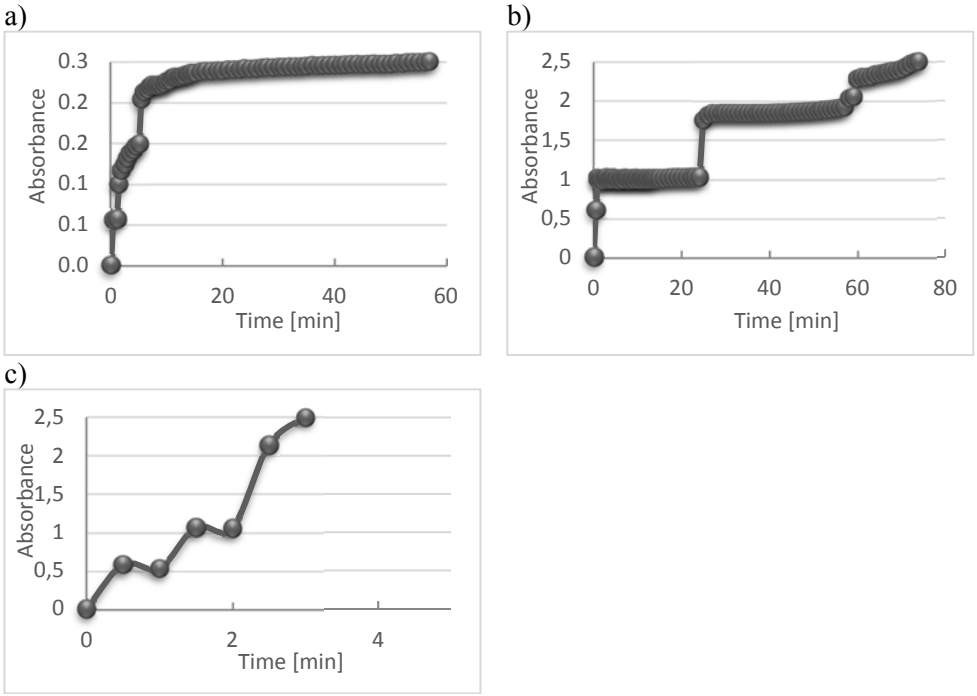

Fig. 5. Tim desorption curve in aqueous solution - a) CL1 - 1 day, b) CL2 - 3 days, c) CL3 -7 days.

The obtained results were analyzed in order to plot the timolol desorption graph depending on the time for the lenses. For each of the storage times of the lens in the drug (Figure 5), very rapid diffusion of drug molecules from the hydrogel matrix can be observed in the first phase of the experiment. This may indicate that the tested system was not in a state of equilibrium, which results in drug-matrix interactions that are subject to abrupt tearing and cause a large portion of the drug to be ejected into the measuring cuvette space.

CONCLUSIONS

The drug substance used for the study gives promising results in terms of its use in contact materials as controlled drug release systems, because during the use of the drug directly into the eyeball it remains in it only a few minutes, while the lens is released for several dozen minutes.

It has been shown that hydrogel matrices have the potential to be used as carriers of ophthalmic drugs. The next research series should be carried out taking into account the influence of parameters such as the concentration of the active substance and the type of hydrogel matrix. They will allow for detailed

determination of the usefulness of polymer matrices as materials for the controlled release of drugs.

REFERENCES

[1] P.Gupta K.Vermani, S.Garg. *Hydrogels from controlled release to pH-responsive drug delivery.* DDT, 2002. 10 : 569-578.

[2] N.A. Peppas E.W.Merrill. *Hydrogels for controlled drug delivery.* Biomaterials, 1984. 5 : 27-36.

[3] N.A.Peppas. *Hydrogels and drug delivery.* Current Opinion in Colloid and Interface Science,1997. 2: 531-537.

[4] B.D.Ratner A.S.Hoffman. *Synthetic hydrogels for biomedical applications.* Hydrogels for Medical and Chemical Society, 1976. : 1-36.

[5] C.L.Bell N.A.Peppas. *Biomedical membranes from hydrogels and interpolymer complexes.* Advanced Polymer Science, 1995. 122 : 125-175.

[6] H.P.Filipe J.Henriques, P.Reis et.al. *Contact lenses as drug controlled release systems : narrative review.* Revista Brasiliera de Oftamologia, 2016. 75 : 241-247.

[7] X. Hu L. Hao, H.Wang, et. al. *Hydrogel Contact Lens for Extended Delivery of Opthalmic Drugs.* International Journal of Polymer Science, 2011.

[8] L.U.Changhai B.Roshan, M.Kociolek, et. al. *Hydrogel Containing Silica Shell Cross-Linked Micelles for Ocular Drug Delivery.* Journal of Pharmaceutical Science, 2013. : 627-637.

[9] French K. *Contact lens material properties. Part I - Wettabiity.* Optician, 2005. 230 : 20-28. (6022).

Thermogravimetric studies of hydrogel contact lenses

*Sylwia Stiler[1], Sylwia Golba[1]
[1]Faculty of Materials Science, University of Silesia in Katowice, POLAND
e-mail: stiler.sylwia@wp.pl

***Keywords**: contact lenses, thermogravimetric studies, hydrogel*

ABSTRACT

An important parameter characterizing these systems is the equilibrium water content (EWC). It is extremely important from a clinical point of view, because it directly affects many usable parameters of the lens.

Before the test, the samples were placed in individual solutions for a period of 24 hours.

After desorption, the lenses were re-sorbed in analogous solutions to determine if the lens returned to its original mass (before desorption).

Thermogravimetric analysis showed great variation in the course of the dynamics of the drainage process, indicating the interaction of the polymer matrix with each of the environments in a specific way.

INTRODUCTION

Contact lenses are most effective when they are well suited to individual patients. Their influence on the eye organ is undeniable, although at the time of proper adjustment of their shape and properties to the anatomy of the patient's eyeball, it allows them to be more tolerant.

Knowledge about the basic structures occurring in the eyeball is necessary, as it helps to prevent the negative effects of the use of contact lenses, and also allows the development of contactology.

Contact lenses are a safe, accurate and comfortable method of correction of vision defects. They make it possible to correct the majority of sight defects, while at the same time giving the patients comfort.

The use of contact lenses can unfortunately give some complications. They can be kept to a minimum, if the patient follows the basic rules of hygiene and care of the lenses, as well as observes the time and the mode of wearing them. The most common causes of symptoms in the eye are corneal hypoxia, allergies, infectious agents as well as toxic effects of fluid components for care.

Oxygen is essential for the cornea to function properly. It is taken up by epithelial cells by diffusion from atmospheric air. The most common pathophysiological symptom observed in patients who use contact lenses is corneal hypoxia. This is due to the limitation of oxygen access to epithelial cells, which are covered with a contact lens. Most often, in the abnormally oxygenated cornea,

swelling of its epithelium, swelling of its specific substance, as well as microcyst and vacuoles are observed.

Infections and inflammations are rare in patients. Exposure to infections results in two basic factors: corneal epithelial injury, and the presence of microbes. Factors that cause infection there are inadequate hand hygiene, uncommon replacement of the fluid and container for lens care, as well as failure to observe the time of wearing them (causes the deposition of protein deposits on the lenses, which constitute a nutrient for the bacteria).

Thanks to better parameters, silicone hydrogel lenses disrupt the corneal physiology to a lower extent, which is very beneficial from the point of view of the user. They are characterized by better oxygen permeability, which allows avoiding complications and the possibility of a longer uninterrupted time of wearing them. The permeability of the material of which the lens is made is different to the permeability of the finished product.

In the case of the final lens, its thickness and shape should also be taken into account. Oxygen permeability can be characterized by two parameters: permeability (Dk), and permeability (Dk/t), where t is the thickness of the lens. The permeability parameter is determined on the basis of flow resistance measurements, it describes the permeability of the lens material without considering its thickness. It allows you to estimate the availability of oxygen for lenses of different power, thickness and geometry. The permeability parameter is measured for the lens which is placed between the chamber devoid of air and the chamber containing oxygen. This parameter is the result of measuring the maximum lens's ability to deliver oxygen to the eye through the given area. During the measurement, only the front surface of the material is in contact with the air [1-2].

An important parameter characterizing these systems is the equilibrium water content (EWC). It determines the degree of material hydration, it is related to the material's ability to bind water under given environmental conditions. It is extremely important from a clinical point of view, because it directly affects many usable parameters of the lens.

The degree of hydration of the material is defined by the following relationship:

$$EWC = \left(\frac{m_o - m_k}{m_o}\right) \cdot 100\% \qquad (1)$$

where:
EWC - equilibrium water content,
m_o - initial mass of the sample (mass of hydrated polymer) [g],
m_k - final mass of the sample (mass of dry polymer) [g] [3].

Hydrogel and silicone hydrogel lenses are very different. In hydrogel lenses, the oxygen contained in the material corresponds to the water contained in the material, while in silicone hydrogels, silicone fragments transport oxygen.

Water is an integral part of these materials in the hydrated state that water molecules interact with the polymer chains. The effect of these interactions is the change of water properties, among others, it does not crystallize at 0°C.

Taking into account thermodynamic properties, water in hydrogels can be divided into two main groups: bound water (division into strongly bound and loosely bound water) and unbound water.

Strongly bound water forms direct hydrogen bonds with polar groups or strongly interacts with ionic residues, it is so strongly bound to the polymer that it does not boil at 100°C. The loosely bound water forms loose hydrogen bonds with the polymer, which causes it to freeze at temperatures below 0°C. Free water does not react with the polymer matrix and therefore retains the properties of pure water.

Water in the lenses is very important, and parameters such as: water content, free to bound water ratio and the degree of dehydration, are the main features that affect the comfort of wearing, as well as oxygen permeability [4].

Dehydration is dehydration of hydrogels, a process in which due to changes in the environment in which the material is placed, the water's equilibrium content is reduced. Dehydration of contact lenses occurs at the moment when the lens is placed on the eye and lasts until it reaches the balance with the surroundings [5].

The evaporation from the front surface of the lens primarily leads to loss of water. Probably a small amount of water is drained from the material along with tears, nasolabial tubules and conjunctival capillaries [6].

Dehydration also leads to changes on the surface of the material. The parameter whose change in particular works to the disadvantage is the wettability of the surface. In the case of hydrogels, adequate wettability is ensured only in conditions of full hydration, however in the case of contact with the environment, along with the loss of water, the surface tension is reduced, so that the wettability of the material is reduced [7].

Factors that affect the acceleration of dehydration can be divided into three groups: related to the material, related to the environment, as well as related individuals with the patient [8].

MATERIALS AND METHODS

The aim of the research was to determine the curves of dehydration of hydrogel lenses. The tests were carried out using a laboratory scale and a laboratory dryer (at 37°C, which allowed for the simulation of lenses' use conditions). The debrocation curves, dehydration and rehydration coefficients obtained during the measurements of the lens masses before dehydration, during and

after the dehydration of the lenses were determined and the equilibrium water content (EWC) in the tested material determined.

In the case of dehydration studies, the solutions in which the lenses were stored were: artificial tears, lens storage liquid and physiological saline. The compositions of the solutions are as follows:

• artificial tears: sodium hyaluronate 0.2%, auxiliary agents: disodium phosphate, sodium dihydrogenorthophosphate, sodium chloride, sodium edetate, benzalkonium chloride, water for injections, preservative: benzalkonium chloride

• lens storage fluid: hyaluronan, sulfobetaine, poloxamine, boric acid, sodium borate, disodium ethylenediaminetetraacetic acid, sodium chloride, 0.00013% polyaminopropyl biguanide solution and 0.0001% polymeric quaternary ammonium salt

• physiological saline: 0.9% sodium chloride solution, purified water

• distilled water: it contains dissolved gases, e.g. nitrogen, oxygen, carbon dioxide and impurities with volatile organic substances.

First, desorption tests were carried out (distilled water, artificial tears, lens storage liquid and saline solution), which consisted in measuring changes in the mass of the tested material during desorption after storage in a given environment. The tests were carried out at 37°C to simulate the conditions in the body.

Fig.1. Laboratory dryer Memmert UNE 500.

Before the test, the samples were placed in individual solutions for a period of 24 hours. Then they were put into a laboratory dryer (Figure 1) and the mass was determined by analytical balance at intervals of 5 minutes until it stabilized, which meant the end of desorption. Two samples were tested for each of the solutions.

From the data obtained in the measurements, the desorption curves of solutions from contact lenses and the desorption coefficient were determined.

After desorption, the lenses were re-sorbed in analogous solutions to determine if the lens returned to its original mass (before desorption). The resorption was carried out analogously at 37°C.

From the obtained data, the resorption curves of the solutions were determined, as well as the resorption coefficient for each of the lenses.

RESULTS

The lenses have been placed in four environments: in distilled water, saline solution, liquid for lens storage and artificial tears. Individual environments were used to modify the lens material.

When placed in distilled water, the lenses are placed in a container, and then placed in a laboratory dryer at 37°C. Every 5 minutes their mass was read until they stabilized in three subsequent measurements, which meant the end of the dehydration process. Next, the dehydration and rehydration curve was made. A comparison of the lens masses before dehydration was made and after it, as well as the loss of mass, the dehydration and rehydration coefficients were calculated (Table 1).

The dehydration factor is a parameter that determines the rate of the dewatering process. It is calculated according to the following formula:

$$DR = \left(\frac{m_t - m_{t-1}}{m_t}\right) \cdot 100\% \quad (2)$$

where:
m_t - mass of the lens at time t [g],
m_{t-1} - mass of the lens at time t-1 [g].

The coefficient of rehydration, which was determined based on the following formula, was calculated in an analogous manner:

$$WR = \left(\frac{m_k}{m_p}\right) \cdot 100\% \quad (3)$$

where:
m_k - mass of the lens after rehydration [g],
m_p - mass of the lens before dehydration [g].

Tab.1. List of the mass of lenses stored in selected environments.

Solution	Contact lens	Mass before [g]	Mass after [g]	Loss of weight [g]	Dehydration factor [%]		Rehydration factor [%]	
					DR	$\overline{DR}$	WR	$\overline{WR}$
NaCl	CL1	0.0443	0.0139	0.0422	77	76.5	126	116
	CL2	0.0554	0.0139	0.0453	76		106	
SzŁ	CL1	0.0409	0.0137	0.0272	69	72	98	95
	CL2	0.0433	0.0140	0.0293	75		92	
PDPS	CL1	0.0446	0.0139	0.0307	69	67	89	94
	CL2	0.0397	0.0142	0.0255	65		99	
WD	CL1	0.0571	0.0137	0.0427	67	67.5	75	84
	CL2	0.0559	0.0136	0.0571	68		93	

The aim of the thermogravimetric analysis was to determine the dynamics of the dewatering process of the tested samples, in which the dehydration factor (DR) is helpful. The calculated DR values are presented as a function of time on the graphs. For each chart, the same scale was used, which allows to better assess the differences between individual materials.

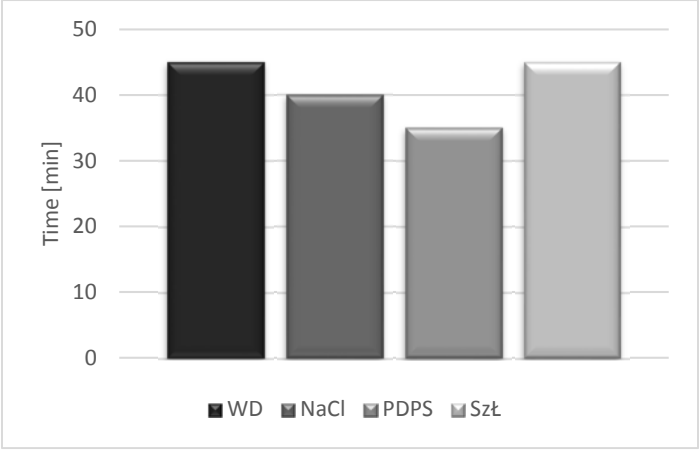

Fig. 2. Time necessary to achieve a balance with the surroundings for individual lenses.

The graph (Figure 2) presents the time necessary to achieve a balance with the surroundings in the samples tested. The results indicate that this time differed depending on the environment used - the longest was recorded for distilled water, the shortest for NaCl and the lens storage fluid. This indicates the contribution of the components of individual fluids in the dehydration process that affect with water molecules contained in the structure of the polymer matrix.

The average degree of reversibility of the dehydration process for individual environments was as follows: NaCl solution - 106%; SzŁ - 97.5%; PDPS - 97.5%; WD - 86.5%. From the parameters obtained during dehydration and rehydration of contact lenses stored in four environments, it was possible to determine their EWC parameter, i.e. the equilibrium water content. From the obtained results it was observed that the dehydration process for the investigated lenses was reversible and their hydration level returned to its original value. The degree of reversibility increases in order: NaCl, SzŁ, PDPS, WD. The biggest change was recorded for pure distilled water, which can be explained by rinsing the absorbed ingredients from the liquid out of the package during the experiment.

CONCLUSIONS

The dehydration factor determined on the basis of gravimetric measurements indicates that the dewatering rate is the highest for the material retained in the NaCl

environment (DR = 76.5%), then for artificial tears (DR = 72.0%), and comparable for a fluid for lens storage (DR = 67.0%) and distilled water (DR = 67.5%).

Subsequent resorption process showed at the same time that the changes are the most dynamic in the environment of NaCl (WR = 116.0%), artificial tears (WR = 95.0%) and fluid for lens storage (WR = 94.0%), a minimum for distilled water (WR = 84.0%) indicating the penetration of fluid components into the material during the storage of the lenses.

Thermogravimetric analysis showed great variation in the course of the dynamics of the drainage process, indicating the interaction of the polymer matrix with each of the environments in a specific way. For individual samples, changes in the DR coefficient indicate at least two dehydration areas for each of the environments, with the indication that the individual steps are differently distributed over time.

It influenced the time necessary to achieve the balance with the environment in the tested samples, which was the shortest in the most strongly interacting environment (NaCl), similar to the fluid for lens storage, and the shortest for distilled water. This indicates the contribution of components of particular fluids in the dehydration process, which interact with water molecules contained in the structure of the polymer matrix.

REFERENCES

[1] B.Holden S.Stretton, P.L.de la Jara, K.Ehrmann, D.LaHood. Przyszłość soczewek kontaktowych: Dk rzeczywiście jest istotne. *Kontaktologia*, 2006.

[2] N.A.Brennan M.L.Chantal Coles, T.L.Comstock, B.Levy. A 1-year prospective CLinical trial of Balafilcon A (PureVision) silicone-hydrogel contact lenses used on a 30-day continuous wear schedule. *Opthalmol*, 2002. : 1172-1177.

[3] K.Krysztofiak. Badanie procesu dehydratacji w hydrożelowych i silikonowo-hydrożelowych soczewkach kontaktowych, *Uniwersytet im. Adama Mickiewicza w Poznaniu*, 2015.

[4] M.Covey D.F.Sweeney, P.R.Sankaridurg, B.A.Holden. Hypoxic effect on the anterior eye of high Dk soft lens wearers are negligible. *Optometry&Vision Science*, 2001. : 95-99.

[5] I.Tranoudis N.Efron. Parameter stability of soft contact lenses made from different materials. *Cont Lens Anterior Eye*, 2004. 27 : 115-131.

[6] W.Mathers. Evaporation from the ocular surface. *Exp Eye Res.*, 2004. 78 : 389-394.

[7] 37. French K. Contact lens material properties. Part I - Wettabiity. *Optician*, 2005. 230 : 20-28.

[8] 38. P. Ramamoorthy LT. Sinnott, JJ. Nichols. Contact lens material characteristics associated with hydrogel lens dehydration. *Opthalmic Physiol Opt. [I]*, 2010. 30 : 160-166.

The influence of the physical parameters on the transmission spectra of the long period grating

*Renata Zawisza, Leszek R. Jaroszewicz
Institute of Applied Physic, Military University of Technology, Warsaw, POLAND
e-mail: renata.wonko@wat.edu.pl

***Keywords**: long period grating, optical sensor, optical fiber, optical measurement*

ABSTRACT

In the last decade long period grating-based sensors have achieved relevant interest by the researcher due to the low cost, insensitivity to the electro- magnetic field and the most important their ability to assess good quality and safety. Taking into account the industry requirements of the precise detection of the biological and chemical factors, the long period grating working close to the turning point is desired. The ultra-high sensitivity of such periodic structure for ambient physical parameters changes allows to detect the refractive index, temperature, strain perturbation or even gas flow changes with resolution of 10^{-6}. It means that a detection system with a spectral resolution of 1 pm, is capable of measuring changes as small as 10^{-6} per refractive index unit. In terms of exceeding the resolution of such sensors, the long period grating can be combined with another physical structure like thin layer or evanescent field. In this paper we present the literature review of the long period grating-based sensors with a single and dual resonance for the physical parameters detection. The characteristic of the long period grating transmission spectra in terms of refractive index and temperature fluctuations are carried out by authors of this papers.

INTRODUCTION

The optical fibers with micro- periodic structure provide new possibility for the light guiding and control that have not been obtainable with the conventional optical fibers [1]. In general, the photosensitivity of the optical fibers refers to possibility of a permanent change in the fiber core's refractive index (RI) when is exposed to UV- light radiation [2]. Of course, there are another methods of LPG fabrications [3-5], however the UV radiation-based method allows to obtain relatively small periods with good geometry accuracy. In this case, the long period gratings should be written in photosensitive fiber. Photosensitization techniques, including hydrogen loading, flame brushing and co-doping (e. g. boron, europium, cerium, erbium, phosphorous, antimony and tin) in fiber core are able to increase the photoinduced index modulations in the fiber core up to the order of 10^{-3} - 10^{-2}. The most common classification of this kind of fiber devices comprises fiber Bragg grating (FBG) [6] and long period grating (LPG) [7]. The fabrication method of both structure

is very similar, whereas the difference lies in the period of structure, i.e. the FBG has sub-micron structure and the LPG's period is in the range of 0,1 – 1 mm [8]. This distinction leads to two different physical phenomena occurring in the optical structure during light guiding. The LPG promotes coupling between the propagating core mode and co-propagating cladding modes resulting in several attenuation bands on the transmission spectrum at discrete wavelength (Fig. 1) [9].

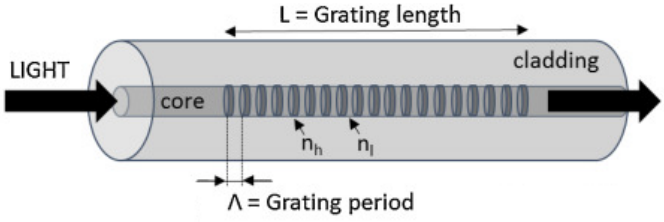

Fig. 1. Mode coupling in long period grating [10].

The position of the wavelength resonances λ_{res} is determined by the propagation constants of the core and cladding modes, which, in their turn, depend on the average constraints of the fiber grating structure such as: the refractive index (RI) profile, the cladding radius (Eq. 1), and the RI of the surrounding medium [7].

$$\lambda_{res} = (n_{eff}^{co} - n_{cleff}^{cl}) \cdot \Lambda \tag{1}$$

where, $n_{eff}^{co}\ and\ n_{cleff}^{cl}$ are effective refractive index of optical fiber core and cladding, respectively. Λ is the period of refractive index modulation.

On the other hand, the FBG couples light from the forward-propagating core mode of the optical fiber to a backward, counter-propagating mode [6]. In general, LPGs are more sensitive to environmental perturbations than FBGs, which could be unprofitable for the LPG-based telecommunications devices. However, this feature of LPGs can be well exploit when they are intended to be used as a sensor platform.

As long as the boundary conditions of LPG do not change, the transmission spectrum is stable. In the case of any perturbation will effect on the LPG surface, the transmission spectrum will be varied. Such phenomenon leads to exploit the LPG as a platform for physical [11], chemical [12], and biological [13] sensors. Most of them require special LPG's surface modification which make them selective and more sensitive. The purpose of this work is to present the fundament of the LPG-based sensor and experiment results of the selected physical parameters detection.

OPERATION PRINCIPLE OF LPG-BASED SENSOR

As it was mentioned above, the cladding modes are weakly guided and suffer from high attenuation, and thus, the transmission spectrum of the typical LPG consists

of a series of attenuation bands at discrete wavelengths (Fig. 2). This mode coupling can be analyzed by the most often used coupled-mode theory (CMT) [14].

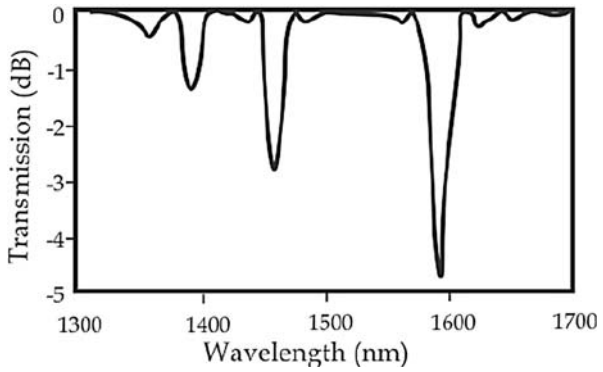

Fig. 2. Example of transmission spectrum of a long-period grating [15].

The resonance wavelength of LPG is a strong function of external perturbations like surrounding RI, temperature and strain. Appearance of these ambient perturbations affects the coupling strength between the core and cladding modes, which could lead to both wavelength and amplitude shift of the attenuation peaks on the LPG transmission spectrum. The shift of the resonance peaks can be determined using an optical spectrum analyzer (OSA). A complete analysis of the LPGs sensitivity to the external changes is necessary prior to practical device design. The investigation of the shift in the center of the resonance wavelength of the LPG $\Delta\lambda_m$ in terms of temperatureΔT, strain $\Delta\varepsilon$ and surrounding RI Δn_{surr} perturbation can be expressed as [16]:

$$\Delta\lambda_m = \left(\frac{d\lambda_m}{dT}\right)\Delta T + \left(\frac{d\lambda_m}{d\varepsilon}\right)\Delta\varepsilon + \left(\frac{d\lambda_m}{dn_{surr}}\right)\Delta n_{surr} \qquad (2)$$

where, $\frac{d\lambda_m}{dT}$, $\frac{d\lambda_m}{d\varepsilon}$ and $\frac{d\lambda_m}{dn_{surr}}$ are temperature, strain and RI sensitivity, respectively.

When it comes to the chemical and biological sensors, the principle of operation is very similar. Major of the chemical or biological samples can be detected due to the difference in RI of the samples or ability to adhere the particles to the surface of the LPG. In this case, the change of boundary condition is determined by the thickness of the surrounding medium. Such approach can be justified only when the LPG's surface is functionalized [17].

RESULTS AND DISCUSSION

LPG's sensitivity to the external RI perturbation

The LPG-based sensors have become very attractive regarding to another proposed RI sensors based on optical fiber, i.e. surface plasmon resonance-based sensors, which special technology results in questionable repeatability and relatively low mechanical strength. The external RI perturbations change the effective index of the cladding mode and will lead to both amplitude and wavelength shift of the resonance dips in the LPG transmission spectrum. The higher order cladding mode coupled with the $LP_{0,1}$ mode, the greater sensitivity to changes in external RI is achieved. This is due to the fact, that these modes extend further out into the area exterior to the fiber [18]. When the external RI is lower than RI of cladding material, the total internal reflection analysis can be adopted. In this case, the resonance peak blue-shifts. Once the external RI is closer to the RI of the cladding material, the sensitivity is higher and leads to larger wavelength shift. In case of matching the external RI with that of the cladding, rejection bands disappear, and the transmission spectrum gets flattened. Finally, when the external RI is higher than cladding RI, the cladding modes no longer experience total internal reflection and Fresnel reflection can be used to explain the mode structure [19]. Hence, the resonance peaks reappear at slightly longer wavelengths (red shift).

In general, the RI sensor based on standard LPG is well known and many of reports was published [20-22]. For this reason the new field of research was started. Hence, the dispersive nature of LPG leads to appearance so-called dual resonance long period grating (DR-LPG) [23]. However, to achieved such phenomena, the cladding diameter of LPG needs to be reduced by for instance etching in hydrochloric acid. For this reason, phase matching conditions are changed and the fundamental mode couples with very higher cladding mode. Here, the DR-LPG sensitivity for external RI perturbation is one order of magnitude higher comparing with standard LPG [24]. The transmission spectra for different RI solution made from appropriate amount of water with glycerin was obtained and present on the Fig. 3. The long period grating was fabricated by exposing a part of hydrogenated standard germanium-doped Corning SMF-28 fiber to the UV radiation using chromium mask technique. Then, in order to release the thermal stresses the LPG was annealed at a temperature of 150°C for 90 minutes.

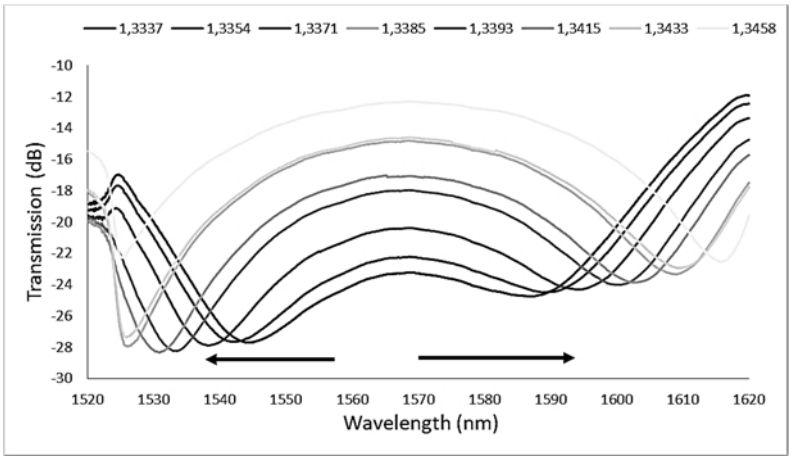

Fig. 3. RI sensitivity response of dual resonance long period grating with Λ=217 nm and etched cladding up to 90 μm.

Both notches of DR-LPG shift in the opposite direction under external RI changes. For this reason, it is possible to employ some mathematical tools to obtain ultra-high RI sensitivity. It is also worth to mentioned, that the decreasement of the amplitude of both resonance peaks is disproportionate. This phenomena provides replacement of an expensive optical spectrum analyzer by the optical power meter.

LPG's sensitivity to the external temperature perturbation

The temperature sensitivity of the LPGs arises from two major contributions: changes in the differential refractive index of the core and the cladding due to the thermo-optic and thermo-expansion effects, as well as changes in the LPG's period caused by the temperature. This first contribution is strongly dependent of different fiber types, which have different thermo-optic coefficients. Hence, the concentration of the dopants in silica (e. g. SiO_2, GeO_2, B_2O_3) determines the sensitivity of the temperature sensor. The appearance of the GeO_2 dopants causes a larger thermo-optic coefficient comparing with SiO_2 dopants, whereas B_2O_3 characterized in a positive thermo-optic coefficient. In the case of standard fiber, the core contains SiO_2 and GeO_2 and the cladding contains only SiO_2. Thus, the thermo-optic coefficient of the core will be higher than that of the cladding. As a result when the temperature increases, the LPG made on these fibers will show a peak shift toward longer wavelengths [25]. On the other hand, the boron co-doped fibers provide a wavelength shift toward shorter wavelengths due to the negative thermo-optic coefficient. When it comes to avoid cross-sensitivity of LPG-based sensor, the possibility to choose the sensor response direction is a great opportunity.

As in the case of RI measurement, the DR-LPG has a higher sensitivity than standard one in terms of the temperature detection. Fig. 4. shows the influence of external temperature perturbation on the transmission spectra of the DR-LPG. The

measurement was carried out on the same LPG as in RI measurement. The LPG was immersed in water and heated up to 50°C. The higher temperature resulted evaporation of water from vessel.

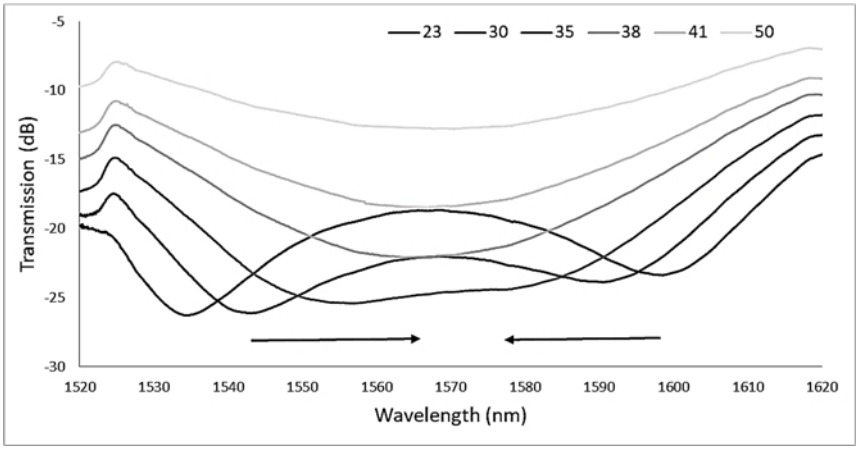

Fig. 4. Temperature sensitivity response of dual resonance long period grating with Λ=217 nm and etched cladding up to 90 μm.

As one can see, the DR-LPG notches move in the opposite direction. However, comparing with external RI sensor response, the peaks converge into one another. After 38°C, peaks unite into one and the amplitude increases. Here, it is important to mention that such peak's connection is caused by the occurrence of the dispertion turning point [26], where dispersion changing from positive to negative. Such region is very sensitive to any perturbation.

CONCLUSIONS

In conclusion, in this paper we have presented a principle of LPG sensitivity to various physical parameters. Moreover, we presented the influence of the external RI and temperature perturbation on the transmission spectra of the DR-LPG. As it can be seen from measurements, LPGs are sensitive to almost every physical perturbation, and are used currently in sensor applications, as well as filters in the telecommunication. The LPG-based sensors have main advantage with respect to fiber Bragg grating-based systems is the lower fabrication cost, since they can be inscribed in almost any type of fiber using a wide range of techniques. In terms of the constant pursuit of improvement, the influence of external perturbation on the transmission spectrum characteristic of the LPG with dual resonance was presented. One of the main drawback of the DR-LPG-based sensors is the very low extinction ratio, which may cause ambiguous determination of the wavelength of the resonance peak. However, this can be alleviated by using interferometric structure, for instant fiber

loop mirror or Mach-Zender interferometer. In this case, the interference pattern could have sharpen the DR-LPG peaks by superposition.

REFERENCES

[1] Pilla P., Trono C., Baldini F., Chiavaioli F., Giordano M., Cusano A., Giant sensitivity of long period gratings in transition mode near the dispersion turning point: an integrated design approach, *Optics Letters*, 2012, 37, 19, 4152–4154, DOI: 10.1364/OL.37.004152

[2] Kowal D., Statkiewicz-Barabach G., Mergo P., Urbanczyk W., Inscription of long period gratings using an ultraviolet laser beam in the diffusion-doped microstructured polymer optical fiber, *Apply Optics*, 2015, 54, 20, 6327-6333. DOI: 10.1364/AO.54.006327

[3] Yonemura M., Hasegawa K., Fabrication of long-period fiber gratings using end-coupled ultrafast laser pulses, *Optics Express*, 2017, 25, 10, 11340-11346, DOI: 10.1364/OE.25.011340

[4] Ivanov O. V., Fabrication of long-period fiber gratings by twisting a standard single-mode fiber, *Optics Letters*, 2005, 30, 24, 3290-3292, DOI: 10.1364/OL.30.003290

[5] Martínez-Gaytán A., Soto-Olmos J., Oropeza-Ramos L., Hernandez-Cordero J., Fabrication of Low-Cost Long-Period Fiber Gratings Using Tapered Optical Fibers Embedded in Polymer, *Latin America Optics and Photonics Conference*, 2012, LS2C.3

[6] Hill K.O., Meltz G., Fiber Bragg grating technology fundamentals and overview, *Journal of Lightwave Technology*, 1997, 15, 8, 1263 – 1276, DOI: 10.1109/50.618320

[7] Libish, T. M., Chapter in the book: Design and Development of Fiber Grating Based Chemical and Bio Sensors, *Fiber Gratings: Basic Theory and Sensing Principle, Shodhganga,* 2016

[8] Erdogan T., Cladding-mode resonances in short- and long-period fiber grating filters: Errata, *Journal of Optical Society of America A*, 2000, 17, 11, 2113, DOI: 10.1364/JOSAA.17.002113

[9] Bhatia V., Applications of long-period gratings to single and multi-parameter sensing, *Optics Express*, 1999, 4, 11, 457-466, DOI: 10.1364/OE.4.000457

[10] Urrutia A., Goicoechea J., Ricchiuti A. L., Barrera D., Sales S., Arregui F. J., Simultaneous measurement of humidity and temperature based on a partially coated optical fiber long period grating, *Sensors and Actuators B: Chemical*, 2016, 227, 135-141, DOI: 10.1016/j.snb.2015.12.031

[11] Singha A., Ranaa Sh. B., Singhb M., Sharma A., Study and investigation of long period grating as refractive index sensor, *Oplik*, 2014, 125, 7, 1860-1863, DOI: 10.1016/j.ijleo.2013.10.002

[12] Tang J., Chiang T., Chang H., Wang J., Long-period grating-based sensor for chemical sensing applications, *2005 Pacific Rim Conference on Lasers & Electro-Optics*, 2005, 975-976

[13] Pissadakis S., Anglos D., Klini A., Konstantaki M., Long period optical fiber grating outcladding overlaid sensors: a versatile photonic platform for health and bio applications, *2011 International Workshop on Biophotonics*, 2011, 978-980

[14] Erdogan T., Cladding-mode resonances in short- and long-period fiber grating filters: Errata, *Journal of Optical Society of America A*., 2000, 17, 11, 2113, DOI: 10.1364/JOSAA.14.001760

[15] Estudillo-Ayala J. M., Mata-Chávez R. I., Hernández-García J. C., Rojas-Laguna R., Chapter in book: Fiber Optic Sensors, *Long Period Fiber Grating Produced by Arc Discharges, INTECH,* 2015

[16] Shu X., Zhang L., Bennion I., Sensitivity characteristics of long-period fiber gratings, *Journal of Lightwave Technology*, 2002, 20, 2, 255-266, DOI: 10.1109/50.983240

[17] Koba M., Śmietana M., Brzozowska E., Górska S., Mikulica P., Cusanoe A., Bock W. J., Detection specificity studies of bacteriophage adhesin-coated long-period grating-based biosensor, *24th International Conference on Optical Fibre Sensors*, 2015, 9634

[18] Patrick H. J., Kersey A. D., Bucholtz F., Analaysis of the long period fiber gratings to external index of refraction, *Journal of Lightwave Technology*, 1998, 16, 9, 1606-1642, DOI: 10.1109/50.712243

[19] Hiroshi T., Urabe K., Characterization of Long-period Grating Refractive Index Sensors and Their Applications, *Sensors*, 2009, 9, 6, 4559-4571, DOI: 10.3390/s90604559

[20] James S. W., Korposh S., Lee S., Tatam R. P., A long period grating-based chemical sensor insensitive to the influence of interfering parameters, *Optics Express*, 2014, 22, 7, 8012-8023, DOI: 10.1364/OE.22.008012

[21] Li Q., Zhang X., Shi J., Xiang D., Zheng L., Yang Y., Yang J., Feng D., Dong W., An Ultrasensitive Long-Period Fiber Grating-Based Refractive Index Sensor with Long Wavelengths, *Sensors*, 2016, 16, 12, 2205, DOI: 10.3390/s16122205

[22] Dissanayake K. P. W., Wu W., Nguyen H., Sun T., Grattan K. T. V., Graphene oxide-coated Long Period Grating-based fibre optic sensor for relative humidity and external refractive index, *Journal of Lightwave Technology*, 2017, PP, 99, DOI: 10.1109/JLT.2017.2756097

[23] Liu Q., Chiang K. S., Lor K.P., Dual resonance in a long-period waveguide grating, *Applied Physics B*, 2007, 86, 1, 147–150, DOI: 10.1007/s00340-006-2433-5

[24] Yan Z., Sun Q., Wang C., Sun Z., Mou C., Zhou K., Liu D., Zhang L., Refractive index and temperature sensitivity characterization of excessively tilted fiber grating, *Optics Express*, 2017, 25, 4, 3336-3346, DOI: 10.1364/OE.25.003336

[25] Mizunami T., Fukuda T., Hayash A., Fabrication and characterization of long-period-grating temperature sensors using Ge–B-co-doped photosensitive fiber and single-mode fiber, *Measurement Science and Technology,* 2004, 15, 8, 1467–1473, DOI: 10.1088/0957-0233/15/8/006

[26] Shu X., Zhang L., Bennion I., Sensitivity characteristics near the dispersion turning points of long-period fiber gratings in BGe codoped fiber, *Optics Letters*, 2001, 26, 22, 1755-1757, DOI: 10.1364/OL.26.001755

Abstracts

Continuous membrane column configurations for gases high purification: comprehensive experimental study and efficiency evaluation

*Artem Atlaskin, Maxim Trubyanov, Nail Yanbikov, Pavel Drozdov, Vladimir Vorotyntsev, Ilya Vorotyntsev

Nanotechnology and Biotechnology Department, Nizhny Novgorod State Technical University n.a. R.E. Alekseev, Nizhny Novgorod, RUSSIA

e-mail: atlaskin@gmail.com

Keywords*: gas separation; membrane column; ultra-purification; process intensification; radial membrane module.*

Constantly growing requirements for the characteristics of substances: purity, quality, environmental friendliness directly form a trend in the design and development of energy-efficient methods and technologies of purification. In the field of ultra-purification applications, the membrane-based separation technique may be considered as an attractive alternative to conventional, energy-intensive processes such as those based on sorption, crystllization, cryofiltration, etc. Moreover, the membrane-based process provides separation without any phase transition, at ambient temperature, does not require heat supply or removal, and apparatuses are characterized by hardware design simplicity and may be applied individually and as a final stage in technology route or in point-of-use operation.

In the present work, the gas ultra-purification efficiency of a novel membrane column configuration comprising of three high-performance counter-current radial membrane modules has been evaluated experimentally in two regimes and compared with the original membrane column. The process of high-permeable impurity removal from low-permeable target component is studied using three model gas mixtures of high (94.3), medium (15.7) and low (2.5) selectivities for a commercially available silicone membrane.

Total reflux operation has been considered and the influence of the enrichment section on the performance of the stripping section has been evaluated. Achieved target component purity reaches 99.999995% for nitrogen with 2% acetylene impurity at 50% product recovery rate.

It was clearly demonstrated that the novel membrane column configuration offers promising perspectives for gases high-purification applications, where high separation performance and simplicity of the hardware design are more important than ensuring large capacity of the production process.

Acknowledgements

This work was supported by RFBR, according to the research project No. 16-38-60174 mol_a_dk.

Evaluation of the absorbing pervaporation technique for ammonia recovery after the Haber process

*Artem Atlaskin, Anton Petukhov, Nail Yanbikov, Vladimir Vorotyntsev, Ilya Vorotyntsev
Nanotechnology and Biotechnology Department, Nizhny Novgorod State Technical University n.a. R.E. Alekseev, Nizhny Novgorod, RUSSIA
e-mail: atlaskin@gmail.com

Keywords*: gas separation; absorbing pervaporation; ammonia; process intensification; membrane.*

The ammonia synthesis technology since its invention by Haber and Bosch has not undergone significant change, and the ammonia recovery stage requires considerable energy supply due to cooling the gas mixture to the ammonia condensation temperature. The membrane-based separation technique may be considered as a perspective approach instead of conventionally applied cryogenic purifiers.

In the current study, the novel hybrid method – absorbing pervaporation is proposed for ammonia recovery process intensification. This hybrid separation technique is a combination of gas absorption by liquid absorbent (PEG) displaced on the membrane and further pervaporation (vaporization of gases at the permeate side of the membrane). Additionally, this process can be performed without any phase transition, in a one-volume mass-exchange apparatus and with a liquid absorbent-membrane system, which provides higher selectivity due to high NH_3 solubility. Furthermore, absorbing pervaporation apparatus does not require any heat supply/removal, has a scalable design and may be applied individually and as a final stage in technology route or in point-of-use operation.

The absorbing pervaporation separation efficiency is studied experimentally during the separation of binary and ternary gas mixtures consisting of an ammonia and attendant impurities – nitrogen and hydrogen using the PTFE membrane-PEG system. During the experimental study, the separation efficiency depending on the rate of ammonia recovery and absorbent composition (PEG+H_2O) was investigated. It was clearly demonstrated that the proposed hybrid scheme may offer promising perspectives for ammonia recovery in comparison with other membrane-based techniques, e.g. membrane contactors.

Acknowledgements
This work was supported by the Russian Science Foundation (grant no. 17-79-20286).

Membrane gas separation module with pulsed retentate for low-permeable component recovery

*Stanislav Battalov, Maxim Trubyanov, Egor Puzanov, Pavel Drozdov, Ilya Vorotyntsev
Nanotechnology and Biotechnology Department, Nizhny Novgorod State Technical University n.a. R.E. Alekseev, Nizhny Novgorod, RUSSIA
e-mail: sv.battalov@gmail.com

Keywords*: membrane gas separation; unsteady-state operation; membrane modules and cascades; optimization; separation efficiency.*

Improvement of product specification level and the need to reduce production costs encourages chemical engineers to intensify the implementation of energy-efficient separation methods and search for novel ways of optimizing the existing technological solutions. The purpose of the present work is consideration of unsteady-state operational conditions of a single gas separation membrane module for increasing its separation ability.

Principally new approach is realized by two steps:1. a membrane module operates in a "closed" mode (without retentate flow, analogous to total reflux operation in distillation) 2. a small amount of a gas mixture is withdrawn. A variety of cases including removal of a fast-permeant impurity of 1 vol.% (N_2O, CO_2, CH_4) from a slow-permeant target component (N_2) and also enrichment of a slow-permeant impurity of 1 vol.% (N_2) during removal from fast-permeant target component (N_2O) have been considered. The experimental verification of the presented calculation was made with the radial membrane module. The concentrations during separation were measured by gas chromatography analysis.

The separation efficiency of a pulsed retentate operation has been compared to that of a steady-state operation depending on the productivity of the process both through the simulation study and the experiments. A unique model for optimizing the pulsed retentate mode is developed taking into account all operational parametrs (flow rates, valve closing times, valve opening times, retentate sample size, and membrane selectivity) that affect the separation effect of the membrane apparatus, furthermore the estimated data conforms with experimental results. For the first time it has been experimentally and theoretically shown that novel pulsed retentate approach during membrane gas separation provides higher separation efficiency as compared to conventional steady-state operation at the same productivity. The dependence of the separation ability on the operating conditions was determined.

Acknowledgements
This work was supported by the Russian Science Foundation, Project № 17-79-10464.

Modelling of radial membrane gas separation module for integration in Aspen Plus

*Stanislav Battalov, Egor Puzanov, Maxim Trubyanov, Alina Kozlova, Pavel Drozdov, Ilya Vorotyntsev
Nanotechnology and Biotechnology Department, Nizhny Novgorod State Technical University n.a. R.E. Alekseev, Nizhny Novgorod, RUSSIA
e-mail: sv.battalov@gmail.com

Keywords*: membrane gas separation, radial membrane module, simulation, Aspen Plus, user model*

Reducing the material and energy costs of production is the basis for increasing the competitiveness of chemical enterprises. To compare the efficiency of various technological schemes and to choose the optimal values of the operating parameters, process simulation tools are widely used. There are limited studies on the design of membrane systems using commercial process simulator due to the lack of built-in membrane separation models.

In this work, for the first time, the rigorous model of a counter-current radial membrane gas separation module has been incorporated in the environment of Aspen Plus process simulation tool as a user defined unit operation. The regimes of ideal displacement (plug flow), perfect mixing, and ideal displacement with longitudinal dispersion were implemented into the Aspen Plus user model using the Fortran subroutine. The main benefit of the developed model is that it can be easily incorporated into a commercial simulator and used as a unit operation model in complex technological schemes.

The obtained simulation results for the case of a steady-state gas purification process with removal of fast-permeant impurity correlate well with the experimental results. The developed Aspen Plus user model of a radial membrane module makes it possible to conduct rigorous simulation and techno-economic evaluation of membrane apparatuses with recycling, membrane cascades, continuous membrane columns, and hybrid processes combining membrane gas separation with other purification methods in the Aspen Plus process simulation environment.

Acknowledgements
This work was supported by RFBR (research projects No. 16-38-60174 mol_a_dk and 17-38-50100 mol_nr) (program development), and by the Russian Science Foundation (grant № 17-79-10464) (theoretical modelling).

Silicon Oxycarbide glasses as protective coatings on TiAl based alloys

*Maciej Bik, Maciej Sitarz
AGH University of Science and Technology, Faculty of Materials Science and Ceramics, Cracow, POLAND,
e-mail: mbik@agh.edu.pl

***Keywords**: Silicon oxycarbide, TiAl alloys, sol-gel, dip-coating*

The hot-temperature corrosion is one of the most difficult challenge for many branches of industry such as power engineering or automotive. Materials for such applications should provide with prominent mechanical properties combined with low density and high corrosion resistance. The group of materials which drew an attention in last 30 years, are TiAl based alloys. Due to their high content of aluminum, when exposed to harsh gaseous environment, heat-resistant Al_2O_3 scale is created. However, similar thermodynamic potential of Al_2O_3 and TiO_2 creation during oxidation in the form of mixed non-protective scale, still generates a need to look for new solutions such as protective coatings, in order to improve the corrosion behavior over 700°C.

The material proposed in the form of anti-corrosive coatings are so-called black glasses. These ceramic materials are of amorphous silica network, in which defined number of oxygen ions are replaced by carbon anions. Such an replacement provides with an improvement in mechanical and thermal properties and chemical stability, as a result of a local increase in the bond density.

The main objective of this study was to characterize structure and microstructure of black glasses coatings on TiAl based alloys.

Coating material was obtained by the means of sol-gel method, where obtained sol was deposited on samples by the dip-coating technique. After drying, layers were pyrolyzed in 800°C in an argon atmosphere in order to obtain black glasses coatings. Their appropriate structure was confirmed by a series of structural studies (MIR, XRD, EDS). In the next part, microstructural studies (Confocal, SEM) revealed an acceptable degree of coatings' homogeneity and tightness. In the end, there were performed thermogravimetric analyses (TGA) of selected samples in 800°C in a laboratory air atmosphere for 100 h, which showed a slight mass gain decrease of samples during oxidation.

Acknowledgements
This research was financed by Polish Ministry of Science and Higher Education from the budget for science in the years 2017-2020, as a research project under the program "Diamond Grant" (grant no. DI2016 004046). Also, Maciej Bik has been partly supported by the EU Project POWR.03.02.00-00-I004/16.

Studies on corrosion inhibition of black glasses coatings/TiAl based alloys system

*Maciej Bik, Maciej Sitarz
AGH University of Science and Technology, Faculty of Materials Science and Ceramics, Cracow, POLAND,
e-mail: mbik@agh.edu.pl

Keywords: *black glasses, corrosion, intermetallic phases, microstructure*

Materials based on intermetallic phases, have been investigated during last 30 years for applications, where high corrosion resistance together with low density play major roles. One of these group of alloys, based on TiAl, have found many applications as lightweight materials with good mechanical properties in a broad range of temperature. However, for temperatures higher than 700°C, there occurs a problem with selective oxidation of aluminum, which leads to thermodynamically favored creation of TiO_2 and pitting corrosion. The most promising solutions include use of the III generation alloys with additions of i.e. Nb or surface modifications, such as protective coatings. Hence, there has been proposed a brand new coating material based on "black glasses".

These are ceramic materials of v-SiO_2 structure, where controlled replacement of oxygen ions with carbon ones, generates local increase in density of bonds in glass network. As a result, highly beneficial mechanical and thermal properties are obtained together with a satisfactory corrosion resistance.

The main aim of this work was to investigate anti-corrosive properties of the black glasses coatings/TiAl based alloys system.

Coatings were obtained by using the sol-gel method in which as precursors there were used ladder-like polysilsesquioxanes. The dip-coating technique allowed to deposit homogenous layers on different TiAl alloys substrate, which were dried and then heat treated in 800°C.

Corrosive studies were conducted in 800°C and 1000°C in laboratory air atmosphere for 100 h. After oxidation, structure (XRD, Raman, EDS) and microstructure (SEM, Confocal) of surface and cross sections of samples, were examined. Initial studies revealed that in 800°C, coatings improved the corrosion inhibition, however in 1000°C the whole system underwent serious degradation.

Acknowledgements
This research was financed by Polish Ministry of Science and Higher Education from the budget for science in the years 2017-2020, as a research project under the program "Diamond Grant" (grant no. DI2016 004046). Also, Maciej Bik has been partly supported by the EU Project POWR.03.02.00-00-I004/16.

Investigations of ceramic membrane fouling in ultrafiltration process of protein aqueous solution

*Martyna Borysiak, Elżbieta Garbuś
Faculty of Chemical Technology and Engineering, West Pomeranian University of Technology, Szczecin, POLAND
e-mail: borysiak.martyna@zut.edu.pl

***Keywords**: ultrafiltration, ceramic membrane, chicken egg white*

Macromolecular solutions can be separated by low pressure membrane filtration, such as microfiltration (MF) or ultrafiltration (UF). The driving force of the processes is transmembrane pressure, and the separation is based on particles size – diameter (in MF) or molecular weight (in UF). This kind of separation mechanism is based on a sieve effect and is realized through fine pores of the membrane. Operating parameters, such as transmembrane pressure, cross-flow velocity and temperature, have crucial influence on separation efficiency. In case of ultrafiltration, additional parameters are often taken into account, i.e. pH value of solution. Ultrafiltration is used widely for separation and concentration of proteins, polysaccharides, etc., mainly in food processing industry.

This paper presents a study on ceramic membrane ultrafiltration of chicken egg white aqueous solution. Experiments were conducted with 3-channel ceramic TiO_2/Al_2O_3 ultrafiltration membrane (cut-off 150 kDa, separation area 0.009375 m^2, length 0.25 m, outer diameter 10 mm) obtained from TAMI Industries, placed in a stainless steel tubular module. Separation process was performed at constant temperature (293 K) and different operating parameters: transmembrane pressure (105-310 kPa), cross-flow velocity (2.73-4.55 m/s). As pH adjustment factors, 0.1M HCl and 0.1M NaOH were used to achieve pH 5. Feed stream chicken egg white protein concentration was 0.2 g/L.

The obtained results have been presented as permeation curves with fitted pore blocking models, as well as tables of operating parameters, initial and steady-state permeate flux for each of the test runs. The highest value of permeate flux (8.91E-05 m^3/m^2s) was achieved at transmembrane pressure 310 kPa and cross-flow velocity 4.55 m/s. Mass transport resistances have been calculated using resistance-in-series model. Applying pore blocking models to the experimental data allowed to determine the dominant fouling mechanism for chicken egg white ultrafiltration.

Manufacture of the anodic aluminium oxide on the surface of Fe-Al.alloy

*Paulina Chilimoniuk, Tomasz Czujko, Wojciech J. Stępniowski
Department of Advanced Materials and Technologies, Faculty of Advanced Technology and Chemistry, Military University of Technology, Warszawa, POLAND
e-mail: paulina.chilimoniuk@wat.edu.pl

Keyword: *anodization, pores, intermetallics, oxides*

Electrochemical surface oxidation is a method commonly used in the industry to create protective coatings and for decorative purposes. Moreover, using this method, a highly ordered, hexagonal morphology of anode oxide aluminum oxide (AAO) nanopores can be obtained. Oxides obtained as a result of the anodization process attract the attention of researchers from around the world due to the unlimited potential in many disciplines, including: nanofabrication, construction of sensors, materials with a high angle of wetting, photonic crystal production, ecological production of photovoltaic cells and biomaterials. The process of anodization can be carried out both on pure metals and their alloys. An example here can be alloys based on aluminum and alloys based on intermetallic phases with the participation of aluminum, an example here is the Ni_3Al phase or also phases from the Ti-Al. Between the parameters of the anodization process and the obtained porous morphology geometry created in this process occurs very special relationship. Manipulating process parameters directly interferes with the final appearance and properties of the oxide nanostructure, which in turn influences the application possibilities of the obtained layer.

On the basis of studies the parameters for the conduct of process of anodize were established. The potential of anodization was taken as a varying parameter. The voltage ranging from 5 to 20 V with a step of 2.5 V. The time (60s) as well as the temperature (0^oC) of anodization were constant parameters of the process.

Based on the obtained study of the conducted process it was found that it is possible by appropriate selection of the anodization process parameters to obtain a nanoporous oxide structure on the alloy surface on the FeAl intermetallic phase matrix. It was also found that the anodization process on the FeAl substrate was significantly shortened compared to the formation of anodic oxide coatings produced on high purity aluminum.

Co/Pd based mixed oxide catalysts for methane combustion: structure and activity studies

*Damian K. Chlebda[1], Magdalena A. Chrzan[1], Przemysław J. Jodłowski[2], Roman J. Jędrzejczyk[3], Joanna Łojewska[1]

[1]Faculty of Chemistry, Jagiellonian University, Kraków, POLAND

[2]Faculty of Chemical Engineering and Technology, Cracow University of Technology, Kraków, POLAND

[3]Malopolska Centre of Biotechnology, Jagiellonian University, Kraków, POLAND

e-mail: damian.chlebda@uj.edu.pl

***Keywords**: methane combustion, catalysts, palladium oxide, cobalt oxide, Raman spectroscopy*

The activation of methane molecule has been studied many years, and various catalysts has been tested and proposed. However, the problem of the rational development of catalysts demands usage of spectroscopic methods that give information about the active sites and their role in general process. The activation of methane molecule is still unsolved with a lot of controversies.

In this study, we investigated spectroscopic properties and the application in methane combustion of different cobalt–palladium and mixed oxide-based catalysts supported on Al_2O_3. The catalysts engaged in this study were prepared by means of incipient wetness impregnation and by the sonication method to obtain the reduction of particle size of oxides. Additional to compare the spectral characteristic of catalysts the reference material in a form oxides palladium and cobalt oxide were prepared by simple calcination of precursors.

Spectroscopic properties of the surface of those materials has been studied by *in situ* micro-Raman method. The structures of the adsorbed metal oxides particles were characterized in details. The Raman spectra disclosed that the active cobalt form of the catalysts in catalytic combustion is Co_3O_4 spinel structure, and for the palladium-based catalysts, the PdO oxide is dominant phase. For the sonicated cobalt catalyst, the cobalt–alumina spinel structure was observed as an additional shoulder on the bands around 500–510 cm^{-1}. The band positions for different series of catalysts and for the prepared reference materials were not stable. The activity test for methane abatement under oxidative conditions proved the higher activity of catalyst prepared by application of ultrasound.

Acknowledgements

This study was supported by National Science Centre, Poland research grant No. 2015/19/N/ST8/00181.

Post processing and biological evaluation of the titanium implants fabricated by Selective Laser Melting

Agnieszka Chmielewska[1,2], Bartłomiej Wysocki[1,2,], Karol Szlązak[1,2], Joanna Idaszek[2], Wojciech Święszkowski[2]
[1]Materialscare LLC, Bialystok, POLAND
[2]Faculty of Materials Science and Engineering, Warsaw University of Technology, Warsaw, POLAND
email: bartlomiej.wysocki@materialscare.eu

Keywords: *Titanium implants, Veterinary implants, Selective Laser Melting, Computer Aided Design*

Titanium and its alloys are widely used in the medical applications due to the biocompatibility and non-toxicity in the human body environment. Titanium and its alloys have a lowest elastic modulus from popular biocompatible alloys which can be further adjusted to match an elastic modulus of the human bone. The elastic modulus can be easily decreased by introducing open porosity to the implant. Implants which have elastic modulus similar to this of humane bone minimalize stress shielding effect and prevent natural bone from demineralization in the implant surrounding. Due to the complex shape of natural bones and the possibility to produce implants with controlled porosity the most attractive method of fabrication bone replacement implants are Additive Manufacturing (AM) techniques such as Selective Laser Melting (SLM). In the SLM method implants can be produced directly from the CAD model by using a high-energy laser beam.

In this work, patient-specific veterinary implants were fabricated by SLM technique from raw titanium powder. After fabrication sintered to the surface powder particles were removed by chemical polishing with different mixtures of hydrofluoric and nitric acids. Influence of chemical polishing on the cell proliferation and differentiation in different polishing baths was studied using human mesenchymal stem cells.

Chemical polishing not only improved implant surface but also restored CAD model dimensions what was confirmed by Scanning Electron Microscopy observations and microtomography reconstruction.

Acknowledgments
The authors would like to thank the NCBiR (National Center for Research and Development) for providing financial support to project iTE - Method of treatment of large bone defects in oncological patients using in vivo tissue engineering approach (Grant No. STRATEGMED3/306888/NCBR/2017).

Modeling and fabrication of custom designed veterinary implants

*Agnieszka Chmielewska[1,2], Bartłomiej Wysocki[1,2], Karol Szlązak[1,2], Jerzy Gawor[3], Wojciech Święszkowski[2]
[1]Materialscare LLC, Bialystok, POLAND
[2]Faculty of Materials Science and Engineering, Warsaw University of Technology, Warsaw, POLAND
[3]ArkaVeterinary Clinic
email: agnieszka.chmielewska@materialscare.eu

Keywords: *titanium implants, veterinary implants, Selective Laser Melting, Computer Aided Design*

Personalized veterinary implants are more increasingly used for a treatment of defects caused by injury or cancellous bone resection. Due to the fact, that dog patients depending on the race have a different anatomical structure it is a very difficult to design implants in size series that will match all cases. The complex shape of the natural bone causing difficulties with using conventional manufacturing methods favors an increasing need for custom implants for the veterinary market. Individual modeling ensures creating an implant that is perfectly adapted to the anatomical bone shape of the particular patient. The most attractive method of fabrication complex-shaped individual bone-replacement implants are Additive Manufacturing (AM) techniques like Fused Deposition Modeling (FDM) and Selective Laser Melting (SLM). Depending on the intended use, both polymeric and metallic implants can be manufactured.

In this work, personalized veterinary bone replacement implants were designed based on the computed tomography data provided by veterinary doctors. Firstly, the defected bone area was virtually removed and the visualization of the implant was created. The implant with fixing plates was modeled to closely match resected or missing bone fragment. Designed structures were manufactured from pure titanium powder with Selective Laser Melting (SLM) technique. To improve surface properties and cell adhesion post-processing chemical polishing was performed in a mixture of hydrofluoric and nitric acids.

Acknowledgments
The authors would like to thank the NCBiR (National Center for Research and Development) for providing financial support to project iTE - Method of treatment of large bone defects in oncological patients using in vivo tissue engineering approach (Grant No. STRATEGMED3/306888/NCBR/2017).

Modeling of the patient-specific cutting guides and surgical instruments

*Agnieszka Chmielewska[1,2], Bartłomiej Wysocki[1,2], Karol Szlązak[1,2], Maciej Rysz[3], Wojciech Święszkowski[2]
[1]Materialscare LLC, Bialystok, POLAND
[2]Faculty of Materials Science and Engineering, Warsaw University of Technology, Warsaw, POLAND
[3]The Maria Skłodowska-Curie Institute of Oncology in Warsaw, Warsaw, POLAND
email: agnieszka.chmielewska@materialscare.eu

Keywords: *surgical cutting guides, surgical instruments, Selective Laser Melting, Computer Aided Design*

Personalized cutting guides and surgical instruments are increasingly used during maxillofacial operations to help surgeons in the cancellous bone resection and reconstruction using fibula. Pre-operative cutting guides and surgical instruments are constructed by engineers based on the computed tomography data provided by doctors and adapted to the anatomical dimensions of the patient. Bone resection surgeries performed without using personalized pre-operative tools were not only more complicated but also in some cases impossible to perform. Now, 3D printing techniques are used to produce patient-specific guides and surgical instruments which match complicated anatomical bone structure. Personalized cutting guides reduce the risk of making a mistake and allow surgeons to perform maxillofacial surgeons faster. Shortening of the operation time brings many benefits such as shortening the ischemic time of fibular graft which leads to lower overall health lose and faster patient recovery.

In this work patient-specific cutting guides and surgical instruments have been designed and fabricated for different oncological patients. The diseased part of the bone was virtually removed and replaced by fibula. Based on the virtual reconstruction custom designed cutting guides were modeled and 3D printed using biocompatible polycaprolactone (PCL) in Fused Deposition Modelling (FDM) technology.

Acknowledgments
The authors would like to thank the NCBiR (National Center for Research and Development) for providing financial support to project iTE - Method of treatment of large bone defects in oncological patients using in vivo tissue engineering approach (Grant No. STRATEGMED3/306888/NCBR/2017).

Hydrothermal microwave synthesis and characterization of hydroxyapatite nanoparticles

*Agnieszka Chodara[1,2], Sylwia Kuśnieruk[1], Tadeusz Chudoba[1], Jacek Wojnarowicz[1], Witold Łojkowski[1]

[1]Laboratory of Nanostructures, Institute of High Pressure Physics, Polish Academy of Sciences, Warsaw, POLAND

[2]Faculty of Materials Engineering, Warsaw University of Technology, Warsaw, POLAND

e-mail: a.chodara@labnano.pl

***Keywords**: hydroxyapatite, nanopowder, hydrothermal, microwaves, biocompatybility*

Hydroxyapatite (HA, $Ca_{10}(PO_4)_6(OH)_2$) is an inorganic component of hard tissues such as bones and teeth. Hydroxyapatite possesses exceptional biocompatibility and bioactivity properties with respect to bone cells and tissues, probably due to its similarity with the hard tissues of the body. It has been used extensively for biomedical applications.HAp is commonly the material of choice for various biomedical applications, e.g. bone implants, scaffold layers, drug delivery agent, dental materials.Various processes for the preparation of HApowders have been developed in the past.

Hydroxyapatite nanopowder were synthesized by hydrothermal synthesis using microwave reactor MSS2 (Microwave Solvothermal Synthesis). The starting materials include pharmaceutical grade substrates: calcium hydroxide $Ca(OH)_2$ and orthophosphoric acid H_3PO_4 as substrates to obtain ceramic nanoparticles.

Obtained nanoparticles have average grain size in range of 8 - 45 nm. Thanks to a wide variety of grain size crystallinity it can be used in different application depending on desired resorption time of hydroxyapatite. The water is the single by-product. Nanopowder has been characterized by several methods: X-ray diffraction(phase purity), SEM(morfolofy), BET (Specific Surface Area) and helium pycnometry(skeleton density).

To sum up, microwave synthesis allows easily and precisely control the grain size of nanoparticles.The grain size average was controlled by synthesis conditions, such as time, pressure and temperature. Obtained hydroxyapatite is similar to the bioapatite.

Water wettability of activated composite surfaces

*Michał Chodkowski[1], Konrad Terpiłowski[2]
[1]Department for the Modelling of Physico-Chemical Processes, Faculty of Chemistry, Maria Curie-Skłodowska University, Lublin, POLAND
[2]Department of Physical Chemistry-Interfacial Phenomena, Faculty of Chemistry, Maria Curie-Skłodowska University, Lublin, POLAND
e-mail: michal@chodkowski.eu

Keywords: *wettability, water, contact angle, plasma, composite materials*

A composite material is made by combining two or more materials – often of different properties. The two materials work together to give the composite unique properties. Most composites are made of just two materials. The greatest advantage of modern composite materials is that they are both light and strong.

Surface properties of composite materials can be modified for special applications. Nowadays a very popular method of surface modification is the plasma technique. One of the results of this type of modification is wettability change. It is alternative to traditional methods of surface modification (e.g. by chemical methods).

The aim of the experiment was determination of surface properties of paper composite materials after plasma treatment. Contact angle measurements by the sessile droplet method were made in order to examine wettability changes. To get information about the surface structure, optical profilometry was also performed.

It was found that after plasma modification wettability and topology of each surface were changed. The surfaces obtain more hydrophilic properties and changes in surface roughness were observed.

Determination of phase transition temperature of silicon by water contact angle measurements

*Michał Chodkowski[1], Paweł Bryk[1]
[1]Department for the Modelling of Physico-Chemical Processes, Faculty of Chemistry, Maria Curie-Skłodowska University, Lublin, POLAND
e-mail: michal@chodkowski.eu

***Keywords**: wettability, silicon, wetting, phase transition, contact angle*

When the solid surface is exposed to the environment of the coexisting liquid and vapor, two different events can happen. If the molecules of the liquid interact strongly with the surface, the liquid will spread across the surface in a thick film and the surface is said to be wet. However, if the surface is weakly binding, so that the interactions between the liquid molecules are stronger than those with the surface, the liquid will clump around itself and will not wet the surface. If a surface is non-wet at a given temperature, it will usually become wet at a higher temperature. The temperature at which the surface becomes completely wet is the wetting temperature (T_w). The transition from the non-wet surface to the wet surface due to the temperature rise is called the wetting transition.

Advancing and receding water contact angles on the silicon surface were measured in order to determine temperature of wetting phase transition. Measurements were made using the sessile drop technique as follows: a 6 µl droplet was settled on the examined surface and the advancing contact angle was measured, then 2 µl of water was sucked from the droplet into the syringe and the receding contact angle was measured in the temperature range from 5°C to 50°C with 5°C steps. Then at each temperature the equilibrium contact angle was calculated using the Tadmor's approach and the phase transition temperature was determined.

It was found that the temperature of the wetting phase transition is equal to 76.95°C. Moreover, the wetting transition is first-order phase transition.

Surface properties of 3-bromopyruvic acid deposited on plasma-activated substrates

*Michał Chodkowski[1], Konrad Terpiłowski[2]
[1]Department for the Modelling of Physico-Chemical Processes, Faculty of Chemistry, Maria Curie-Skłodowska University, Lublin, POLAND
[2]Department of Physical Chemistry-Interfacial Phenomena, Faculty of Chemistry, Maria Curie-Skłodowska University, Lublin, POLAND
e-mail: michal@chodkowski.eu

Keywords*: plasma, surface properties, 3-bromopyruvate, contact angle*

3-bromopyruvic acid ($C_3H_3BrO_3$, 3BrPA, 3-bromopyruvate) is the brominated derivative of pyruvic acid. There have been several reports of the use 3-bromopyruvate in the anticancer therapy. In the literature there is a number of papers about its effects in cells and organisms. The acid appears to disrupt glycolysis and is thus suspected to have a Warburg effect against the tumor cell metabolism.

Surface properties of various materials can be modified using the plasma technique which nowadays is one of the most popular techniques. One of the consequences of this type of modification is wettability change.

The aim of the study was determination of surface properties of 3-bromopyruvic acid deposited on various substrates such as: stainless steel, glass, Teflon (PTFE) and polyether ether ketone (PEEK). The substrates were activated by air, nitrogen and argon plasma during 60 s before deposition of 3BrPA. Contact angle measurements by the sessile droplet method were made in order to examine wettability of obtained surfaces. Optical microscope images were also obtained to get more information about structure of surfaces.

It was found that surface properties of substrates depend on type of plasma. Wettability of surfaces was changed after plasma modifications. Moreover, crystalline structures were observed on the obtained surfaces.

Metal oxide catalysts for methane combustion: in situ FTIR study of active centres

*Magdalena A. Chrzan[1], Damian K. Chlebda[1], Ewelina Salamon[1], Przemysław J. Jodłowski[2], Joanna Łojewska[1]
[1]Faculty of Chemistry, Jagiellonian University, Krakow, POLAND
[2]Faculty of Chemical Engineering and Technology, Cracow University of Technology, Krakow, POLAND
e-mail: magdalena.chrzan@uj.edu.pl

Keywords*: active centres, methane combustion, probe molecules, oxide catalysts, infrared spectroscopy*

Methane unquestionably seems to be the most abundant of the fossil fuels, but its combustion appears as an important problem for many practical reasons connected with energy and environmental issues. From a scientific point of view, the mechanism of methane oxidation is still unresolved and is continual interesting issue. One of the difficulty is huge energetic barrier of the C-H bond breakage which follows in compliance with the radical mechanism. In spite of the *in situ* FTIR attempts of several groups [Demoulin, 2005; Sehmal, 2006; Zhang, 2016] to assign the stable surface intermediate products of methane oxidation on Pd-based catalysts, the band assignment is still unclear and questionable. Thus it hinders determination parallel-consecutive oxidation pathways for methane surface evolution. It is contentious issue whether the methane oxidation proceeds via adsorption step by forming methoxy groups or without adsorption.

In this study, metal oxide catalysts (Fe, Co, Pd) on different metal oxide supports (CeO_2, ZrO_2, TiO_2, SiO_2, Al_2O_3) were selected based on their activity in the methane combustion reaction. The evaluation of active centres was done by in situ FTIR method coupled with application of various probe molecules e.g. carbon monoxide, methanol, methane. The obtained IR vibrations of the surface intermediates have been assigned to different products: formates, carbonates on different active centres.

The assignment of the IR intermediates bands allowed to distinguish of active centres on the catalysts' surface and classificate to acidic, basic and redox. Moreover the presence of methoxy groups on the surface of the working catalyst during the experiments performed in situ with FTIR detection proved the Langmuir-Hinschelwood mechanism for methane catalytic oxidation.

Acknowledgements
This work was supported by the National Science Center Poland based on the decision No. 2017/25/N/ST8/01029.

Formation non-equilibrium high-aluminum phases in the eutectic area by powder metallurgy

*Sylwia Ciołek, Stanisław Jóźwiak
Department of Advanced Materials and Technologies, Military University of Technology, Warsaw, POLAND
e-mail: sylwia.ciolek@wat.edu.pl

***Keywords**: powder metallurgy, FeAl, diffusion, high – aluminum phases, eutectic*

In the Fe-Al equilibrium system, at ambient temperature, there are three high-aluminum phases ζ-$FeAl_2$, η-Fe_2Al_5 and θ-Fe_4Al_{13} (FeA_{l3}), which due to low symmetry and large volume of crystalline cells are characterized by high hardness, which predisposes them to use as reinforcing phases. According to the equilibrium system, the eutectic point is located at the content of about 2% wt iron. At other contents of this element, as a final result, an eutectic mixture of aluminum or $FeAl_3$ is obtained. It is also possible to distinguish the occurrence of less-studied high-aluminum phases in the eutectic region. A careful analysis of the Al-Fe equilibrium system in the eutectic area shows that depending on the technological parameters such as temperature, the cooling rate, in addition to the stable $FeAl_3$ phase, can also occur during the crystallization of the alloy of approximately eutectic composition, metastable structures such as $FeAl_6$, $FeAl_m$ or $FeAl_x$, Fe_2Al_9 and $FeAl_p$. In the connection with the above, tests were carried out to check which of the above phases is the easiest to form by diffusion.

The paper presents an analysis of the impact of production parameters such as temperature and annealing time on the shape and size of precipitations of high-aluminum phases formed in a powder mixture with a content of 95.5% by weight Al and 4.5% by weight Fe. Samples were produced by powder metallurgy, recording during the simulation of the sintering process (DTA) changes in the heat flux to determine the temperature of the changes taking place. In order to pre-verify the obtained structures, microscopic observations (SEM) and analyzing its chemical composition were carried out. The share and shape of the precipitated high-aluminum phases were determined. Also, using microhardness tests using Mayer's law and Kick's similarity law, analysis of the effect of high-aluminum phases on the strengthening of the material produced was made.

Based on the data analysis the following conclusions were made, that under the applied process conditions, the resulting secretions were identified as a metastable, rarely described in the literature phase Fe_2Al_9.

The first synthesis of enantiopure cinchona-binaphthalene derivatives and their application as organocatalysts in asymmetric *Michael* addition

Gyula Dargó[1], Sándor Nagy[1], Péter Kisszékelyi[1], Péter Huszthy[1], *József Kupai[1]
[1]Faculty of Chemical Technology and Biotechnology, Budapest University of Technology and Economics, Budapest, HUNGARY
e-mail: jkupai@mail.bme.hu

Keywords*: organic solvent nanofiltration, organocatalysis, cinchona alkaloids, Michael reaction, catalyst recovery*

The use enantiopure 2,2'-disubstituted 1,1'-binaphthalene as a chiral scaffold is well established in asymmetric catalysis. The bifunctional binaphthalene-based organocatalysts containing hydrogen bond donor moieties have been found useful in asymmetric *Michael* addition, in *Morita–Baylis–Hillman* reaction and in *Henry* reaction.

Multistereogenic binaphthyl-cinchona derivatives (for example see **4** on Figure) were successfully applied in *Michael* addition between β-nitrostyrene and 1,3-dioxo compounds. High enantiomeric excesses were achieved (up to 97%) in different solvents. The applied hydrogen-bond organocatalysts were synthesized using commercially available, and relatively cheap starting materials such as (*R*)-binaphthol (**1**), quinine (**3**) and dimethyl squarate (**2**) that gave the squaramide unit which is frequently used as building blocks of H-bond organocatalysts.

The feasibility of the application of these catalysts can be potentially expanded by using OSN (Organic Solvent Nanofiltration) technique. This method is widely used for separation of molecules based on the differences between those molecule's sizes. With the help of the OSN technique, the applied organocatalysts can be recyclable, due to its high molecular weight.

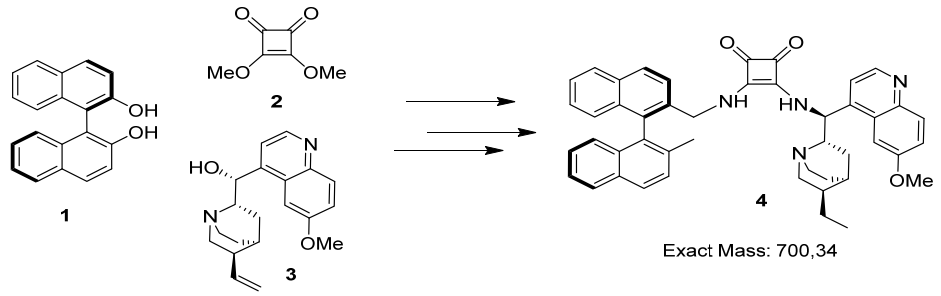

Synthesis of new organocatalyst with central and axial chirality

Acknowledgements
Financial support: Servier Beregi Scholarship, Hungarian Scientific Research Fund (OTKA K112289)

The new generation of microwave reactors for hydro- and solvothermal nanopowder synthesis

*Sylwia Dąbrowska[1,2], Jacek Wojnarowicz[1], Tadeusz Chudoba[1], Agnieszka Chodara[1,2], Andrzej Majcher[3], Witold Łojkowski[1]

[1]Institute of High Pressure Physics, Warsaw, Poland

[2]Warsaw University of Technology, Faculty of Materials Science and Engineering, Warsaw, Poland

[3]Institute for Sustainable Technologies NRI, Radom, Poland

e-mail: s.dabrowska@labnano.pl

Keywords: *microwave, reactor, zinc oxide, hydroxyapatite, nanopowder*

Nowadays more and more bioactive materials are used in medical applications, which can support osseointegration. Bioactive hydroxyapatite (HAP) is one of the inorganic component of hard tissues, which is manufactured in The Institute of High Pressure Physics (IHPP PAS) and it is called GoHAP^{TM}.

Microwave solvothermal synthesis (MSS) is an example of microwave assisted wet chemical synthesis process and nowadays it is counted as one of the most popular chemical methods of obtaining nanomaterials, like HAP, ZnO, ZrO_2 and other. The morphology, grain size and specific surface area of the nanopowder can be controlled thanks to the microwave reactor and the high pressure consolidation technology for ceramic materials. Microwave heating enables a better control of the reaction time, fast heating and reducing the thermal gradients. This results in a better crystallinity of the nanoparticles comparing to the precipitation process. An additional advantage is a reduced synthesis temperature, so no powder calcination is needed.

At our laboratory, we have been developing new type microwave reactors for nanomaterials synthesis for more than 10 years. The use of the microwave radiation and the unique design of the reactor permit precise pressure control and system which allows for an automatic operation in the stop flow or use batch (closed vessel) mode.

MSS2 reactor with Labview software

Acknowledgements

The MSS2 reactor was constructed as a part of the CePT project, reference: POIG.02.02.00-14-024/08, financed by the European Regional Development Fund.

Effect of the properties of selected nebulized inhalation drugs on aerosol characteristics

*Katarzyna Dobrowolska, Tomasz R. Sosnowski
Faculty of Chemical and Process Engineering, Warsaw University of Technology, Warsaw, POLAND
e-mail: katarzyna.dobrowolska.dokt@pw.edu.pl

***Keywords**: inhalation drugs, nebulizers, lung deposition, budesonide*

Nebulized drug therapy uses a direct delivery of medicines via airways to target final destination, for instance in treating illnesses with bronchial contractions (asthma, chronic obstructive pulmonary disease - COPD). A great example of a inhalation drug is budesonide, a synthetic corticosteroid with strong local anti-allergic and anti-inflammatory action.

Inhalers, which disperse liquid medicines to fine droplets, are known as nebulizers. Inhaled aerosol emitted by a nebulizer is partly deposited in the upper respiratory tract, whereas, so called, 'fine particles' (i.e. particles < 5 μm) can penetrate deeper and deposit in the lower respiratory tract. The undoubted advantage of aerosol therapy, in addition to high local concentration of the active substance contained in drug and faster absorption, is the lack of side-effects due to reduction of the total dose obtained by other organs. The effectiveness of aerosol therapy is influenced by many factors, among others: the physicochemical properties of the drug, the properties of inhaled aerosol, individual respiratory parameters and geometry of the respiratory system of a given patient.

This work presents a research on the effects of the properties of inhalation drugs atomized in a jet nebulizer and a vibrating mesh nebulizer on the characteristics of emitted aerosol. The research includes the measurements of selected physicochemical properties (e.g. colloidal stability and the surface tension) of several inhalation drugs based on budesonide, and the determination of their aerosol properties (e.g. mass output rate, droplet size distribution). The results show that some drugs form less stable suspensions due to relatively fast sedimentation of budesonide microparticles. Independently of budesonide concentration, all drugs have a similar surface tension, which can be explained by a comparable content of surface-active drug stabilizers in all tested drugs. The mass output and droplet size distribution depend on the nebulizer type but not on the type of drug. These parameters may have an impact on lung deposition of inhaled aerosols and the efficiency of drug delivery using tested nebulizers.

Synthesis of monomers containing asymmetric diimides for photovoltaic applications

*Anna Drewniak[1], Przemysław Ledwoń[2], Krzysztof Walczak[1]
[1]Department of Organic Chemistry, Bioorganic Chemistry and Biotechnology, Silesian University of Technology, Gliwice, POLAND
[2]Department of Physical Chemistry and Technology of Polymers, Silesian University of Technology, Gliwice, POLAND
email: anna.drewniak@polsl.pl

***Keywords**: diimide, naphthalene, perylene*

Perylenedianhydride (PDA) and naphthalenedianhydrides (NDA) are commonly used as a precursors of perylene diimides (PDIs) and naphthalenediimides (NDIs). PDIs has been used as industrial pigments for many years. PDIs and NDIs derivatives used in this study have shown excellent light harvesting capability and high electron mobility, which makes them a promising material for photovoltaic applications.

However, the current applications of PDIs in the field of organic electronics and photovoltaics generally require PDIs with reasonable solubility in common organic solvents. In this regard, we prepare simple modification of basic dyes by condensation with bulky primary amines in order to achieve good solubility. These bulky *N*-imidosubstituents are forced out of the plane of the PDI chromophore, thereby reducing the π−π stacking of the PDIs and enhance its solubility.

PDIs were synthesized as a result of a single step reaction, while NDIs were obtained in two steps. Generally, PDI monomers were synthesized at higher yields than NDI. The synthesis of PDI monomers was possible in one step while maintaining satisfactory performance, whereas NDI required two steps, the efficiency of which was significantly lower. Polymerization reaction of these monomers was conducted by Suzuki coupling and Stille coupling.

The structures of final monomers and intermediates were confirmed by ^{1}H and ^{13}C NMR spectroscopy.

Acknowledgements
This work was supported by National Science Centre, Poland, under grant no 2015/17/DST5/01343.

Inversion of helical twist sense phenomenon

*Anna Drzewicz, Marzena Tykarska
Institute of Chemistry, Military University of Technology, Warsaw, POLAND
e-mail: anna.drzewicz@wat.edu.pl

***Keywords**: liquid crystals, SmC_A^* phase, helicoidal structure, helical twist sense*

The chirality center in the molecule causes formulation of helicoidal structure, which is characterized by two parameters: the helical pitch and the helical twist sense. The value of first parameter changes with temperature, whereas the second parameter depends on the molecular structure, especially on the type of absolute configuration of chiral carbon atom and its position related to the rigid core (Gray and McDonnel's theory).

This theory does not work for compounds with chiral smectic liquid crystalline phase. Within one homologue series compounds with chiral center at the same type of absolute configuration and located in the same distance from the rigid core exhibit differential dependence parameters of helicoidal structure on temperature within one liquid crystalline phase. The effect of helical twist sense inversion phenomenon may be explained by the presence of different conformers promoting opposite handedness, which concentration may change with temperature.

In this work types of compounds with differential helicodal structure have been presented. The helical pitch was determined by selective light reflection phenomenon, while the helical handedness was evaluated using polarimetry method. The Figure presents one of examined compound with the inversion of helical twist sense.

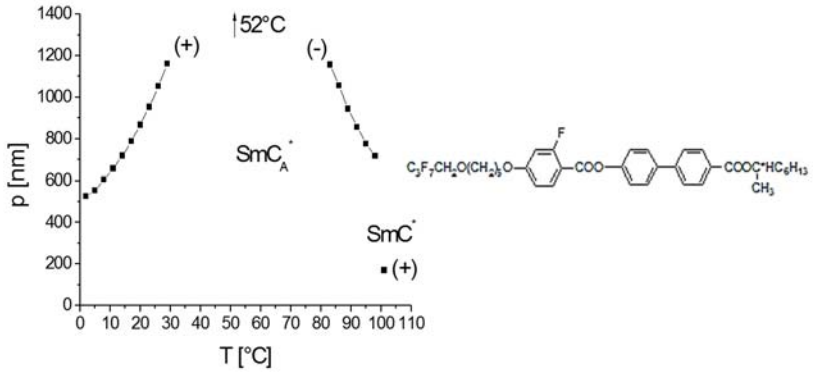

The helical pitch and the helical twist sense dependence on temperature for one of examined compound.

Acknowledgements
This work was supported by RMN 08/687.

Systems with inversion of helical twist sense phenomenon tested by differential scanning calorimetry

*Anna Drzewicz, Marzena Tykarska
Institute of Chemistry, Military University of Technology, Warsaw, POLAND
e-mail: anna.drzewicz@wat.edu.pl

***Keywords**: liquid crystals, SmC_A^* phase, SmC^* phase, helical handedness, differential scanning calorimetry*

It is very important to investigate, why liquid crystalline compounds and their mixtures have different type of helical twist sense during changes of temperature in chiral smectic phase with antiferroelectric (SmC_A^*) properties. In the literature a lot of theories may be found, for example that this effect is causes by the presence of conformers (one of them has the right-handed helix and another has the left-handed helix), which amount may change with heating.

The chiral esters with three ring rigid core and terminal chains: one 1-methylheptyloxycarbonyl group and another one 1-(1,1,1-trifluoromethyl)-heptyloxycarbonyl group were studied. The structure of them is presented on Figure.

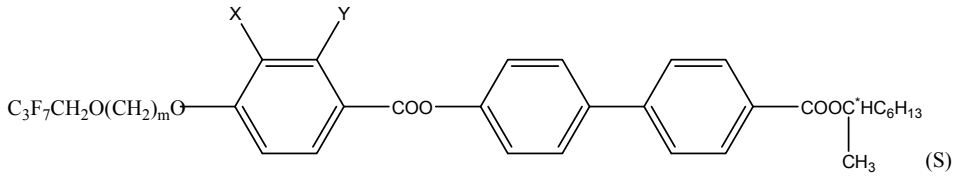

The structure of examined compounds, where m=4,5,7; X,Y=H,F.

In this work the influence of molecular and helicoidal structure of chiral smectic liquid crystalline esters on the differential scanning calorimetry spectra has been presented. The different shapes of these spectra for compounds with various type of benzene ring substitution by hydrogen or fluorine atoms have been observed.

Acknowledgements
This work was supported by RMN 08/687.

Real-time monitoring of the enzymatic production of fructo-oligosaccharides using UV spectroscopy

*Balázs Erdős[1], Maarten Grachten[2], Peter Czermak[3-4-5], Zoltán Kovács[1]
[1]Department of Food Engineering, Szent István University, Budapest, HUNGARY
[2]Department of Computational Perception, Johannes Kepler University, Linz, AUSTRIA
[3]Institute of Bioprocess Engineering and Pharmaceutical Technology, University of Applied Sciences Mittelhessen, Giessen, GERMANY
[4]Department of Chemical Engineering, Kansas State University, Manhattan, USA
[5]Fraunhofer Institute IME-Bioresources, Giessen, GERMANY
e-mail: b.erdos6@gmail.com

***Keywords**: fructo-oligosaccharides, UV spectroscopy, artificial neural networks*

The demand for commercially available fructo-oligosaccharides (FOS) is growing in the food industry. FOS are produced via biocatalysis in a biotechnological route. To ensure an efficient process, strict supervision is needed. Monitoring and quality assurance of the FOS production is carried out by measuring the saccharides composition using conventional chromatographic chemical analysis methods, such as HPLC. Although, being accurate and reproducible, these techniques work with considerably long delay from sampling to obtaining the result. There is a need for a rapid, possibly on-line method to allow tracing the course of the bioconversion.

We propose an alternative method to measure saccharides composition via UV spectroscopy coupled with artificial neural networks (ANN). For the evaluation of the technique, a large number of experimental samples were prepared through operating an enzyme membrane reactor. Subsequently, the saccharides composition and UV spectrum of the samples were recorded in order to be used for teaching an ANN model. The trained model was validated using new observations that were not involved in the training process.

The results suggest, that the proposed method has a great potential to be applied on-line during FOS manufacturing.

Acknowledgements
The preparation of this work was supported by the Marie Skłodowska-Curie grant of the EU FP7 Framework Programme (PCIG11-GA-2012-322219) and the Bolyai Scholarship Programme of the Hungarian Academy of Sciences.

The photocatalytic removal of cytostatic drugs in presence of $Bi_4O_5Cl_{1,3}Br_{0,7}$ - influence of the matrix solution

*Agnieszka Fiszka Borzyszkowska[1], Andrea Conde[2], Patrycja Wilczewska[1], Aleksandra Bielicka–Giełdoń[1], Ewa Maria Siedlecka[1]

[1]Department of Environmental Technology, University of Gdańsk, Gdańsk, POLAND

[2]Escuela Politécnica Nacional, Quito, ECUADOR

e-mail: agnieszka.fiszka@phdstud.ug.edu.pl

***Keywords**: photocatalysis, $Bi_4O_5Cl_xBr_{2-x}$, cytostatic drugs, visible light*

Cytostatic drugs are of particular concern due to the fact that they are potentially mutagenic, carcinogenic and genotoxic even at low concentrations. Most of cytostatic drugs are resistant to biotic and abiotic degradation processes in conventional wastewater treatment. They are also resistant to photolysis. Therefore the photocatalysis would be the main method appropriate for the removal of these compounds. In this work hierarchical bismuth-rich $Bi_4O_5Cl_{1,3}Br_{0,7}$ photocatalyst with optimal ratio between Cl to Br selected from preliminary studies, was applied to removal cytostatic drugs 5-Fluorouracil (5-FU) and Imatinib (IMA).

Hierarchical $Bi_4O_5Cl_{1,3}Br_{0,7}$ microspheres were prepared by a solvothermal method using glycerol as the solvent. The photocatalyst was characterized by UV-Vis spectroscopy, photoluminescence (PL) spectroscopy, X-ray diffraction (XRD) and scanning electron microscopy (SEM). Photocatalytic activity test of $Bi_4O_5Cl_{1,3}Br_{0,7}$ was performed under simulated sunlight and visible light (λ>420 nm) on the photocatalytic degradation of 5-FU and IMA. Additionally the effect of inorganic ions such as Cl^-, SO_4^{2-}, NO_3^- and CO_3^{2-}/HCO_3^- on the decomposition behavior of 5-FU was also investigated. The 5-FU and IMA concentration was analyzed by HPLC-UV method.

The impact of anions on the photocatalytic degradation of drugs by $Bi_4O_5Cl_{1,3}Br_{0,7}$ was investigated using sodium salts which can avoid the potential simultaneous effects of cations. Cl^-, SO_4^{2-}, NO_3^- inhibited the photocatalytic degradation of 5-FU. In contrast, the CO_3^{2-}/HCO_3^- accelerated the degradation rates of 5-FU. During photocatalytic degradation of IMA all examined ions improved the process.

The obtained results also showed that the mechanism of the photocatalytic oxidation of IMA and 5FU drugs are different. The presence of ions in the matrix solution has a significant impact on the photocatalytic removal of studied drugs.

Acknowledgements

This work was supported by BMN 538-8626-B369-17, DEC-2017/01/X/ST5/01136 and DS530-8626-D596-17.

New type of CNW/BiOClBr photocatalysts with high cytostatic drugs removal efficiency

*Agnieszka Fiszka Borzyszkowska, Patrycja Wilczewska, Aleksandra Bielicka–Giełdoń, Ewa Maria Siedlecka
Department of Environmental Technology, University of Gdańsk, Gdańsk, POLAND
e-mail: agnieszka.fiszka@phdstud.ug.edu.pl

***Keywords**: carbon nanowalls, BiOClBr, photocatalysis, cytostatic drugs*

Carbon nanomaterials offer opportunities in enhancement of photocatalytic activity *via* surface modification of semiconductors. Bismuth oxyhalides (BiOX, X = Cl and Br) have been studied recently due to their superior photocatalytic activity for decomposition of micropollutants under simulated solar light irradiation. The advantages advantageous of its application are connected with hierarchical structures (high surface area) and chemical stability. In order to enhance the photocatalytic activity of BiOClBr semiconductor, the modification with B-doped Carbon Nanowalls (CNWs) was applied. CNWs are nanostructures consisting of vertically aligned graphene nanosheets with excellent electrical conductivity, high specific surface area and chemical strength.

Hierarchical BiOClBr microspheres modified by CNWs were prepared by a solvothermal method. The dispersion of CNWs before solvothermal treatment was carried out by sonication. The effect of CNWs amount in the range 0-5 wt% on the photocatalytic degradation efficiency was investigated. CNW/BiOClBr photocatalysts were characterized by photoluminescence (PL) spectroscopy, UV-Vis spectroscopy, scanning electron microscopy (SEM) and X-ray diffraction (XRD). Photocatalytic activities of the prepared composites were evaluated by the degradation of cytostatic drugs: 5-fluorouracil (5-FU) and Imatinib (IMA) under the Xenon lamp irradiation. The 5-FU concentration was monitored by means of HPLC-UV analysis.

The investigation of photocatalytic ability showed that the CNWs/BiOClBr had a higher photocatalytic activity than BiOClBr independently of the used drug. The amount of the CNWs had a significant influence on the photoactivity of CNWs/BiOClBr and the optimal CNWs content was determined to be 1 wt%. In summary, novel CNWs/BiOClBr composite photocatalysts were successfully prepared and are efficient with regard to the degradation of both analyzed drugs.

Acknowledgements
This work was supported by BMN 538-8626-B369-17, DEC-2017/01/X/ST5/01136 and DS530-8626-D596-17.

Life cycle and PESTLE analysis of CCS alternatives

*Daniel Fozer[1], Flora Zita Sziraky[1], Laszlo Racz[1], Tibor Nagy[1], Ariella Janka Tarjani[1], Andras Jozsef Toth[1], Eniko Haaz[1], Tamas Benko[1], Peter Mizsey[1]
[1]Department of Chemical and Environmental Process Engineering, Budapest University of Technology and Economics, Budapest, HUNGARY
e-mail: fozer.daniel@mail.bme.hu

***Keywords**: Life Cycle Assessment, CCS, Environmental impact evaluation, PESTLE, Multi-Criteria Decision Analysis*

The greenhouse gas (GHG) such as CO_2 emission to Earth atmosphere leads to irreversible changes in the nature, thus the investigation of the Carbon Capture and Storage (CCS) process is highly required. Within our research group PESTLE (Political, Economic, Social, Technological, Legal and Environmental) analysis of CCS alternatives (Fossil based, Improved Fossil and Renewable based) is investigated in detail and compared to the direct CO_2 release using Life Cycle Assessment (LCA) methods. Multi-Criteria Decision Analysis (MCDA) is also applied with Multi Attribute Value Theory method (MAVT).

Our results show that applying process improvement (*e.g.*, heat integration) and renewable energy sources (*e.g.,*biogas) for absorbent regeneration result in a CCS technology of much smaller environmental and social impacts, and therefore the CCS technology becomes more favorable than the uncontrolled release. Based on the Ecoinvent database, the environmental impacts of CCS utilizing the frequently used absorbent monoethanolamine gives the result that CCS seems to be more beneficial from the viewpoint of carbon footprint. The PESTLE risk analysis shows that beyond the environmental criteria, economic, social and technological factors also influence the CCS process chain. The results highlight that the highest unfavorable environmental impacts of CCS technology is associated with the absorbent regeneration and compression of the captured CO_2.

Acknowledgements
This work was supported by the ÚNKP-17-3-I New National Excellence Program of the Ministry of Human Capacities.

The investigation and improvement of hydrothermal gasification parameters on microalgal biomass

*Daniel Fozer[1], Cintia Farkas[1], Bernadett Kiss[2], Laszlo Lorincz[1], Andras Jozsef Toth[1], Anita André[1], Tibor Nagy[1], Ariella Janka Tarjani[1], Eniko Haaz[1], Nora Valentinyi[1], Aron Nemeth[2], Edit Szekely[1], Peter Mizsey[1,3]

[1]Department of Chemical and Environmental Process Engineering, Budapest University of Technology and Economics, Budapest, HUNGARY

[2]Department of Applied Biotechnology and Food Science, Budapest University of Technology and Economics, Budapest, HUNGARY

[3]Department of Fine Chemicals and Environmental Technology, University of Miskolc, Miskolc, HUNGARY

e-mail: fozer.daniel@mail.bme.hu

Keywords*: Hydrothermal Gasification, Microalgae Biomass, Optimization, Biogas composition*

The investigation of hydrothermal gasification (HTG) of microalgae biomass is carried out in order to produce biogas and upgrade its composition. Microalgae are a suitable microbe which able to mitigate the negative environmental and social impacts of climate change and capture and transform carbon dioxide into valuable compounds such as biofuels.

In our work we investigate the role of temperature (525-575°C), pressure (250-280 bar), catalyst loading (5-15 w/w%) and ratio of homogenous catalysts (K_2CO_3/KOH) on biogas composition, carbon gasification efficiency and total gas yield. *Chlorella vulgaris* is selected to cultivate and test as feedstock for HTG process. The biogas composition (H_2, CH_4, CO_2, CO) and the biological composition (CNHO, ash, volatile matter, fixed carbon) of the biomass are also determined.

It is found that the application of homogenous catalyst mixture increasing significantly the biogas and hydrogen yields at elevated temperature level. The highest total gas yield is found to be 38.69 mmol g^{-1} while the H_2 yield is 24.69 mmol g^{-1} dry microalgae.

Through our work we attained high carbon gasification efficiency (>20%) and hydrogen yield in several cases. The experimental results are statistically evaluated and the main effects of influencing factors are determined.

Acknowledgements

This work was supported by the ÚNKP-17-3-I New National Excellence Program of the Ministry of Human Capacities.

Diagnosis of lung cancer using Matlab

*Magdalena Fryc[1]
[1]Wydział Informatyki i Nauki o Materiałach, University of Silesia, Katowice, POLAND
e-mail: magdalena_fryc@o2.pl

***Keywords**: Matlab, lung cancer, magnetic resonance imaging.*

The purpose of this work is to create a program in Matlab to facilitate the diagnosis and analysis of lung cancer. We want to present the author's idea of a program designed to analyze lung cancer based on a series of images obtained from magnetic resonance imaging. The program is created to facilitate the oncologist's work, and with the help of the program, a doctor can indicate the part of the lung where the tumor change is located, in order to automatically calculate the area of the lung and the tumor change and to select the appropriate treatment for the patient. Cancer, especially lung cancer, is one of the most developing diseases in the world, in addition to these virtually incurable diseases, but with the advancement of medicine and biomedical engineering it is possible to extend the lives of the sick. The main tools for detecting lung cancer are RTG, PET CT, and in special cases MRI, and because of its virtually complete non-invasive nature, MRI deserves special attention.

The program was created in Matlab environment because it is a package with an universal environment for performing complex scientific and technical calculations by accessing a variety of efficient computational algorithms. It allows visualization of results obtained in various graphs and three-dimensional graphics. Matlab is an interactive environment offering you a range of built-in technical computing, graphics and animations. The program allows you to expand the scope of applications by creating your own scripts and programs in the selected high level programming language. The user has access to reliable mathematical algorithms for use and to numerous expansion modules. The versatility of the program allows for a wide range of applications that can be found in medicine, power engineering, photography and other fields, resulting from its many advantages and functions, and in particular it enables quick results of complex calculations and visualization of results. Matlab allows you to analyze images of different formats.

Final results were obtained using the algorithm a series of MRI image transition procedure, we obtain the final result in the form of a further patient treatment proposal in accordance with the TNM table. Therefore, the aim of this work, which was to present the analysis of tumor changes in relation to lung volume, was made possible by the functionality of the Matlab package. Thanks to the program, it is possible to analyze lung tumor changes and rapid diagnosis, leading to the choice of further treatment of the patient.

Effect of tantalum addition on the structure of ferromagnetic shape memory alloy Ni-Co-Mn-In

*Magdalena Fryc[1], Krystian Prusik[1]
[1]Wydział Informatyki i Nauki o Materiałach, University of Silesia, Katowice, POLAND
e-mail: magdalena_fryc@o2.pl

***Keywords**: Ferromagnetic shape memory alloys (FSMA), SEM, TEM, X-ray.*

Smart materials change their properties under the influence of external conditions. Among them Shape Memory Alloys (SMA) is one of the most interesting group of alloys. In "classic" shape memory alloys (e.g. NiTi), the effect of shape change can be driven by the temperature field.

A special group of SMA are Magnetic Shape Memory (MSM) alloys in which the shape changes under the external magnetic field. In the present work the effect of tantalum addition on the structure of the Ni-Co-Mn-In metamagnetic shape memory alloy system were investigated.

The 15g buttons of Ni45.5-xCo4.5Mn36.6In13.4Tax (x = 0, 1, 3, 5) chemical composition were produced by arc melting technique. During the structural studies, modern electron microscopy (scanning electron microscopy) was used and the EDS energy dispersion method was used to determine the chemical composition of the studied samples. The phase analysis were performed using XRD X-ray diffraction and transmission electron microscopy

Tantalum-containing alloys have a lot of precipitates of the high content of Ta, Mn and Ni, but were poor in Co and In. The matrix of the studied alloys consisted mainly of Ni, Mn, Co. The addition of tantalum does not affect the structure of the austenite phase. X-ray and transmission electron microscopy phase analysis confirmed the presence of a high-order $L2_1$ austenite and a seven-layer modulated 14M martensite structures.

From the obtained results, it was found that the addition of tantalum was influenced on the structure of the ferromagnetic Ni-Co-Mn-In shape memory alloys. Addition of tantalum to 5% at. it does not change the structure of the parental phase L21. In all alloys with the addition of tantalum, the structure of the seven-layer M14 modulated martensite was observed. Addition of tantalum to 5% at. has a favorably affects on the structure of Ni-Co-Mn-In alloys, which may cause their practical application in the future.

Structural studies of glass-carbomer cements

*Magdalena Fryc[1], Małgorzata Karolus[1], Tomasz Kupka[2]
[1]Institute of Materials Science, University of Silesia, Chorzów, POLAND
[2]Medical University of Silesia, Bytom, POLAND
e-mail: magdalena_fryc@o2.pl

***Keywords**: glass-carbomer cements, glass-ionomer cements, dental materials, X-ray.*

Glass-carbomer cement is a new carbomised nano particles containing glass ionomer restorative cement with specially designed filler and fluorapatite/hydroxyapatite particles for reduced solubility, superior compressive and flexural strength and high wear resistance. This material is 100% biocompatible and safe for the dentist, the patient and the environment, during its entire operating cycle of production, processing and loss of products during the wear process.

In glass–carbomer cement, the remineralisation process is improved by applying nanotechnology fluorapatite particles. This material does not contain any resin, solvents and metals and is as such monomer free. The obtained materials were characterized by X-ray diffraction (XRD). Mentioned method was used for structure determination of glass-carbomer cement which is designed for the traditional indications as a replacement for glass ionomer cements and composites in restorative stomatology. Phase analysis of glass-carbomer cement was performed and the crystallites size of nanoparticles and lattice strain were determined. Thanks of scanning electron microscopy the microstructure of tested materials was analyzed.

The measurements for the determination of residual stresses were performed using the Empyrean diffractometer with 5-axes holder at four φ angle directions, 0° (parallel), 45°, 90° (perpendicular to the X-ray beam) and 135° for the diffraction line ($2\theta = 89.89°$) of the main phase identified in studied material. The $\sin^2\psi$ method was used in order to determine the residual stresses.

The residual stresses obtained in all direction have compressive character. Parallel to the X-ray direction, the stress values are about 1.7 GPa. The results obtained for 45°, 90° and 135° direction have similar values and they are in a range of 11 – 14 GPa.

Precursors of chlorates and chlorites in swimming pool water

*Dominika Gajewska[1]
[1]Faculty of Mining Surveying and Environmental Engineering, AGH University of Science and Technology, Cracow, POLAND
e-mail: gajewska@agh.edu.pl

***Keywords**: swimming pools, chlorination, chlorine dioxide, chlorate, chlorite*

Literature reports confirming defects in chlorination have become an incentive to search for and implement new, alternative methods of pool water disinfection. One of the technologies that constitutes a better alternative to the most popular disinfection method is the use of chlorine dioxide. The application of ClO_2 does not cause dangerous chloroorganic compounds. The only danger associated with its use is the formation of inorganic disinfection by-products: chlorate (ClO_3^-) and chlorite (ClO_2^-) ions. Oxidative stress causing changes in red blood cells is the main and consistent finding arising from exposure to chlorite and chlorate. The main objective of research was to understand the impact of ClO_2 application on the reactivity of potential precursors of chlorate and chlorite, so body fluid analogues, solid contaminants introduced with the users of the pool and the inorganic compounds present in the swimming pool water.

In the control laboratory conditions in the test of disinfection by-products formation potential, the reactivity of the inorganic and the organic precursors to the formation of chlorate and chlorite in the swimming pool water and fractions of dissolved and undissolved substances fractionated from swimming pool water, was checked. Samples for laboratory experiments (with the appropriate amount of body fluid analogues) were tested for the test of the potential of chlorate and chlorite formation by applying to the samples fixed doses of ClO_2, followed by incubation at 25^oC for 24 hours, and then by analysis of by-products. Chlorite and chlorate were determined by iodometric titration.

Of the organic compounds, creatinine is the highest reactivity to the formation of chlorate and chlorite, while out of inorganic compounds nitrite is the highest reactivity. Experiments on organic matter fractions have demonstrated that the greatest potential for the formation of chlorate and chlorite is the fraction of pollutants of dissolved organic matter.

In the swimming pool water there is urea in the highest concentrations. This compound is introduced into the water with sweat and bathing urine. Therefore, it is most likely that this precursor in the most real way affects the levels of analyzed by-products. The obtained results of research on inorganic precursors show high reactivity of ClO_2 to inorganic matter, what can find the confirmation in the available literature.

Assessment of water quality in the swimming pool foot bath

*Dominika Gajewska[1]
[1]Faculty of Mining Surveying and Environmental Engineering, AGH University of Science and Technology, Cracow, POLAND
e-mail: gajewska@agh.edu.pl

***Keywords**: swimming pool foot bath, water quality, microbiological contamination*

The cleanliness and sanitation of the swimming pool environment is determined not only by the water quality in the basin, but also by adjacent surfaces and problematic swimming pool foot baths. The passage through this element of the pool hall equipment should ensure the maintenance of better quality of the pool water and the surrounding area. However, the author's observations, research and the lack of clearly defined guidelines concerns the way of their exploitation show, that the water quality in these facilities does not always fulfill the role assigned to them, which is protection against pollution. In connection with this problematic issue, the main objective of the research was to assess the quality of water in this element of the swimming pools, both in terms of microbiological and physicochemical contamination.

The study submitted the water from the swimming pool foot bath for one of the swimming pools in Cracow. On the spot, using a portable photometer, the total and free chlorine concentrations were measured at ten-minutes intervals. The total number of mesophilic and psychrophilic bacteria, pH, conductivity, nitrates, nitrites, ammonium nitrogen, total nitrogen, total organic carbon and ChZT were determined in the samples taken to the laboratory.

The research presented a very high degree of microbiological water pollution. Already after 20 minutes from the total water exchange in the swimming pool foot bath, the total number of microorganisms significantly exceeded the permissible value of 100 [CFU]. Measurements of the free chlorine parameter showed that after 2 hours from the moment of water exchange, its concentration dropped to the value below the range of determination (<0.05 mg/dm^3). The required concentration value of this parameter should be in the range of 1.0 to 2.0 mg/dm^3.

Studies have shown that the quality of the water in the swimming pool foot bath after 2 hours of water exchange is alarming. So that the swimming pool foot bath fulfill their function of preventing the introduction of additional pollution into the swimming pool water by swimmers, the water should be replaced there every 30 minutes. Water quality should be improved after introducing e.g. a separate water treatment system.

The study of ferroelectric liquid crystal mixtures with very shortpitch

*Katarzyna Gaładyk[1], Katarzyna Kurp[2], Jakub Herman[2], Wiktor Piecek[1]
[1]Institute of Applies Physics, Faculty of Advanced Technologies and Chemistry,Military University of Technology (MUT), Warsaw, POLAND
[2]Institute of Chemistry, Faculty of Advanced Technologies and Chemistry, Military University of Technology (MUT), Warsaw, POLAND
e-mail: katarzyna.galadyk@wat.edu.pl

Keywords:*ferroelectric liquid crystal, short pitchp, spontaneous polarization P_s, tilt angle θ*

The ferroelectric liquid crystal mixtures (FLC)with a very short helical pitch (p~150-350 nm at the room temperature), denoted here as SPFLC, are presented. This type of materials with short helical pitch p (p<1 μm) can be utilized to make transducers providing of microsecond switching time. Usually so called Deformed Helix Ferroelectric electrooptical effect (DHF) is induced.This threshold-free effectis observed where a cell gap d is larger than helical pitch$d>>p$as to preserve a helical smectic structure inside.

In this work the selected physical and chemical properties of an example of SPFLC synthesized at MUT are presented. The temperature characteristic of spontaneous polarization $P_s(T)$, tilt angle$\theta(T)$ and helical pitch $p(T)$ are shown. The electrooptical performance of the surface stabilized structures (SSFLC) of SPFLC are presented and discussed.

The studied SPFLCs exhibit high spontaneous polarization P_s up to 250 nC/cm^2 and tilt angle θ~30° at the room temperature, which promise fast highcontrast electrooptical switching.

Acknowledgements
This work was supported by RMN grant 08-691 and PBS 27-652 at MUT.

Magneto-responsive composite ultrafiltration membranes with reversible molecular sieving effects

*Sanae Gassa, Mathias Ulbricht
Lehrstuhl für Technische Chemie II, Universität Duisburg-Essen, Essen, GERMANY
e-mail: sanae.gassa@uni-due.de

***Keywords**: magnetic nanoparticles, thermo-responsive nanogels, core-shell particles, magneto-responsive composite membrane, molecular sieving*

Over the last few decades, stimuli-responsive membranes have attracted attention as they can self-regulate their permeability and selectivity properties in response to a specific stimulus. This project focuses on the advanced design of magneto-responsive ultrafiltration (UF) membranes featuring temporal and remote controlled molecular sieving by an alternating magnetic field (AMF).

For that, magneto-responsive core-shell particles consisting of magnetic iron oxide nanoparticles (IONPs) as local heaters and poly-(*N*-isopropyl acrylamide) (PNIPAM) as thermo-responsive actuator are integrated in the polyether-sulfone (PES) membrane. First, IONPs are synthesized by solvothermal synthesis and then covered with PNIPAM by precipitation polymerization. The core-shell particles are characterized regarding morphology, structure, swelling properties as well as magnetic and heating properties. In the second step, the particles are blended into an anisotropic PES membrane by non-solvent induced phase separation (NIPS). To achieve homogeneous mixed matrix membranes, the composition of the dope solution as well as the preparation conditions are studied by rheology measurements. Lastly, the separation performance of the composite membranes is determined by dextran UF at different conditions (without and with AMF, external heating) to compare its efficiency to traditional heating.

First results have shown that monodispersed amine-functionalized IONPs with an average size of 40 nm were successfully synthesized. In the next step, the particles were treated with potassium hydroxide at high temperature to gain hydroxyl groups which subsequently were partly converted into alkenes by dehydration. FT-IR results revealed the absence of primary amino groups after the treatment and the presence of ether and alkene groups. These groups improve the integration of the particles into PNIPAM by firstly enhancing the hydrophobicity of the IONPs and secondly the alkenes form chemical bonds with NIPAM monomers *via* radical polymerization. In conclusion, the IONPs were successfully synthesized and post-modified and should enable the PNIPAM shell formation.

Bioactivity of layers based on black glasses - preparation and examination

*Magdalena Gawęda[1], Elżbieta Długoń[1], Wojciech Simka[2], Maciej Sitarz[1]
[1]Faculty of Materials Science and Ceramics, AGH University of Science and Technology, Krakow, Poland
[2]Faculty of Chemistry, Silesian University of Technology, Gliwice, Poland
e-mail: mgaweda@agh.edu.pl

***Keywords**: biomaterial, bioactivity, silicon oxycarbide, sol-gel, spectroscopy*

Amorphous materials based on silicon oxycarbide, commonly named black glasses, contain carbon ions bond into the silica network and so-called free carbon. These materials might be obtained as bulk, powder and fibres, as well as fabricated directly on the various substrates in the form of thin layers. Most effective path of preparation of black glasses with the use of appropriate organosilicon precursors containing in their structure the Si-C bond. Examples of such precursors are ladder-like oligo- and polysilsesquioxanes. These compounds possess good adhesion during deposition on the metallic surfaces via e.g. the dip-coating method. To obtain final ceramic material, polymeric precursors need to undergo high-temperature treatment. Such obtained layers might be characterized by high durability, corrosion resistance, chemical and thermal stability, good mechanical properties. Recently, it was also proven they are bioactive and biocompatible. Due to the use of self-synthetized precursors, it is possible to modify properties of black glasses in the wide range. It is possible to control the amount of introduced carbon ions, to enhance already good stability and mechanical features with the use of aluminium, nitrogen, cerium, boron zirconium ions. It is also possible to add to the existing material new properties, such as catalytic or magnetic.

This work focuses on the preparation and modification of black glasses to obtain material most convenient material for biomedical applications. The aim was to fabricate bioactive, biocompatible and osteoconductive layers on titanium substrates. Structural examination of silicon oxycarbide-based materials was done with the use middle infrared spectroscopy (MIR) and X-ray diffraction (XRD). Microstructure and surface properties were analysed with the use of scanning electron microscopy (SEM), laser confocal microscope (LCM) and goniometer. In terms of further applications, crucial corrosion resistance was examined. As the final stage, bioactivity of black glasses was tested.

Acknowledgements:
This work was supported by National Science Centre Poland - No. 2014/15/B/ST8/02827

Structural studies on phosphorus-modified silicon oxycarbide

*Magdalena Gawęda, Elżbieta Długoń, Piotr Jeleń, Maciej Sitarz
Faculty of Materials Science and Ceramics, AGH University of Science and Technology, Krakow, Poland
e-mail: mgaweda@agh.edu.pl

***Keywords**: MIR, XRD, polysesquioxanes, silicon oxycarbide, sol-gel,*

The sol-gel method is one of the *soft chemistry* methods. The process is based on two fundamental processes: hydrolysis and polycondensation, It depends on plenty factors, such as the activity of substrates, temperature, humidity, type of used catalyst. However, it is indispensable if the desired homogeneity and purity of the final material is on the molecular level. One of such material is the black glass, which is based on silicon oxycarbide. Due to the presence of silicon-carbon bond in the amorphous silica matrix, it is impossible to prepare this material with the use of classical melt-quenching method. During the sol-gel synthesis, compounds already containing the crucial Si-C bond are used and this bond is preserved after ceramization of the material. Black glasses might be characterized by high durability, good mechanical properties, corrosion resistance and stability in a hostile environment. It is possible to tailor characteristics of the material by the control of the amount if introduced carbon ions and modification by doping with various ions. For instance, modifications with aluminium or nitrogen ions cause improvement of mechanical properties, the addition of boron ions prevents the tendency to crystallization. The new idea is to dope black glasses with phosphorus ions - the natural compound of the human bones. It might elevate bioactivity, biocompatibility and osteoconductivity of the material.

This work is focused on the formation of phosphorus-doped black glasses based on previously synthesized via the sol-gel method oligo- polysilsesquioxanes. The aim was to discover the path of the substitution process of phosphorus ions in the polymeric precursors as well as ceramized black glass. The proposed sources of phosphorus ions were triethyl phosphate and triethyl phosphite. Samples with various content of modifier were prepared and analysed before and after pyrolysis with the use of middle infrared spectroscopy (MIR), energy dispersive spectroscopy (EDS) and X-ray diffraction (XRD). Results of the analyses enable the description of the structure and composition of both polymeric precursors and phosphorus-doped black glasses.

Acknowledgements:
This work was supported by National Science Centre Poland - No. 2014/15/B/ST8/02827

Controlled synthesis of anodic tin oxide layers with complex internal morphology and their photoelectrochemical properties

*Karolina Gawlak[1], Magdalena Gurgul[1], Leszek Zaraska[1], Grzegorz D. Sulka[1]
[1]Department of Physical Chemistry and Electrochemistry, Faculty of Chemistry, Jagiellonian University, Krakow, POLAND
e-mail: gawlak@chemia.uj.edu.pl

***Keywords**: anodic oxidation, tin oxides, porous layers, photoelectrochemical properties*

Tin oxide is very important wide band gap semiconductor which is extensively investigated due to many potential applications. Anodic oxidation of metallic Sn seems to be an extremely promising strategy for the fabrication of nanoporous SnO_x layers, as it can lead to the formation of the material with precisely designed morphology. Very recently we proposed a new approach to obtain crack-free porous tin oxide layers based on anodic oxidation of Sn in alkaline electrolyte at low applied voltages and the developed method allowed to obtain for the first time nanoporous structures with various pore diameters. One of the most significant advantages of this conclusion is possibility of getting anodic tin oxides layers with complex internal morphologies.

In this study, we present some recent results on the optimization of the procedure for the fabrication of anodic tin oxide layers with complex internal morphologies. The morphology and composition of as synthesized nanostructured electrodes were investigated by various techniques (e.g. SEM, XRD, XPS) and correlated with the conditions applied during fabrication process. Finally, optical band gap energies were determined and photoelectrochemical characterization of samples was carried out using a photoelectric spectrometer.

It was found that tin oxide with ultra-small nanopores (<15 nm in diameter) is formed at the potential of 2 V, while anodizing at 4 V leads to the formation of anodic films with much larger (~50 nm) channels. Applying periodically changed potential resulted in the formation of nanoporous SnO_x layers with the complex internal structure consisted of segments with different nanochannel diameters. Finally, it was confirmed that the internal morphology of oxide layers, i.e. thicknesses of oxide segments can be designed by adjusting of time of anodization carried out at a given anodizing potential.

Acknowledgements
This work was supported by National Science Centre, Poland (Project no. 2016/23/N/ST5/01579).

Novel photoanodes based on anodic tin oxide layers for photoelectrochemical water splitting

*Karolina Gawlak[1], Magdalena Gurgul[1], Leszek Zaraska[1], Grzegorz D. Sulka[1]
[1]Department of Physical Chemistry and Electrochemistry, Faculty of Chemistry, Jagiellonian University, Krakow, POLAND
e-mail: gawlak@chemia.uj.edu.pl

***Keywords**: anodic tin oxide, photoelectrochemical water splitting, band gap engineering*

Photoelectrochemical (PEC) water splitting has recently received much scientific attention as an effective strategy for production of hydrogen from water on a large scale. However, effectively operating photoanode should meet some important requirements. It is necessary for the material to be stable in aqueous environment, resistant to corrosion and photocorrosion as well as nontoxic and environmentally friendly. In case of commonly used semiconductors like SnO_2, which fulfill the aforementioned criteria, the main problem is a relatively high band gap (> 3 eV) allowing the absorption of the visible light only. Therefore, the main challenge in improving energy conversion efficiency of photoanode is to reduce band gap of semiconductor. A very promising way to enhance the performance of photoanode is to form heterojunction by simple coupling of two different semiconductors with different band gaps and band edges positions.

Therefore, here we propose preliminary results of a novel host-guest systems composted of nanoporous anodic tin oxide layers with precisely designed morphology sensitized by α-Fe_2O_3 or CdS nanoparticles. The morphology and composition of as synthesized nanostructured photoanodes were investigated by various techniques (e.g. SEM, XRD, XPS) and correlated with the conditions applied during the fabrication process. Finally, the photoelectrochemical properties of all obtained photoanodes were extensively investigated to find the optimal procedure allowing for the synthesis of the most effective system for PEC water splitting.

It was confirmed that α-Fe_2O_3 or CdS nanoparticles were successfully deposited on the surface of porous anodic SnO_x by simple electrochemical deposition and SILAR method, respectively. Such kind of host-guest systems exhibited strongly enhanced photoelectrochemical activity under visible light when compared to as-received anodic films.

Acknowledgements
This work was supported by National Science Centre, Poland (Project no. 2016/23/N/ST5/01579).

Synthesis of p-conjugated graft copolymers and their electrochemical characteristic

Karolina Gebka[1], Kinga Kepska[1], Agnieszka Stolarczyk[1], Tomasz Jarosz[1,2], Mieczyslaw Lapkowski[1]

[1]Department of Physical Chemistry and Technology of Polymers, Silesian University of Technology, Gliwice, POLAND

[2]Department of Inorganic Chemistry, Analytical Chemistry and Electrochemistry, Silesian University of Technology, Gliwice, POLAND

e-mail: Karolina.Gebka@polsl.pl

Keywords**:** *conjugated polymers, synthesis, poly(3-hexylthiophene), polysiloxane*

Poly(3-hexylthiophene) (P3HT) belongs to the group of organic semiconductor. They find application in many devices such as: organic light emitting diodes, photovoltaic cells, electrochromic windows etc. In presented study graft copolymers based on polysiloxane and regioregular poly(3-hexylthiophene) are synthesized.

Regioregular P3HT vinyl functionality was introduced allowing to attach it using hydrosilylation method to the polymethylsiloxane. As a result new, not described in scientific literature polymethylsiloxane-graft-poly-3-(hexylthiophene)–graft-polyether material was obtained, wherein the P3HT units are dispersed on the molecular level in the polymer siloxane matrix. The developed method of their synthesis makes possible the further modification of the macromolecule properties through the different molecular mass of the polymethylsiloxane matrix, P3HT pendant grafting density and chain length, and the presence and nature of co-grafted polyehter.

The modification of the contents of the two components was carried out by varying the quantity of vinyl group terminated rrP3HT and then saturation of the remaining hydrogen atoms with Poly(ethylene glycol) methyl ether methacrylate. It is worth emphasizing that the entire copolymerization reaction is carried out as eco-friendly one-pot synthesis.

Received compounds were characterized and confirmed by ^{1}H NMR, ^{13}C NMR, IR, GPC. They basic electrochemical properties was investigated by cyclic voltammetry.

The results shows that synthesized copolymers have conducting properties. Moreover we observed interesting features of received copolymers such as major conformational changes in comparison to poly(3-hexylthiophene).

Acknowledgements

This work was financing by NSN in Poland in the framework of project: “Siloxane graft conjugated polymers architectures–novel tailored multifunctional materials for organic optoelectronics” (2016/23/B/ST5/03103).

Corrosion tests of InSb thin films synthesized via pulse electrodeposition

*Dominika Gilek[1], Katarzyna E. Hnida[2], Agnieszka Brzózka[1], Grzegorz D. Sulka[1]
[1]Department of Chemical Chemistry and Electrochemistry, Jagiellonian University, Cracow, Poland
[2]Academic Centre of Materials and Nanotechnology AGH, Cracow, Poland.
e-mail: gilek@chemia.uj.edu.pl

Keywords*: pulse electrodeposition, corrosion, indium antimonide, thin films*

Indium antimonide is a semiconducting material, widely used in many devices, such as sensors, IR detectors and many others. Simultaneously, InSb has one of the more reactive surface among III-V materials. Oxidation features are evident during the wet etching processes. Therefore, it is essential to know, how a surface of this compound behaves in various conditions. It create an opportunity to determine under which conditions the material is more stable.

In this work, the material in the form of thin films was studied. The electrodeposition of indium antimonide was performed using a graphite foil. The electrochemical synthesis was carried out in a citrate bath (0.2 M citric acid, 0.17 M sodium citrate) containing 0.06 M In^{3+} and 0.045 M Sb^{3+}. The pulse electrodepositions took place in a conventional three-electrode cell. The obtained InSb films were tested in alkaline and acidic solutions using electrochemical technics.

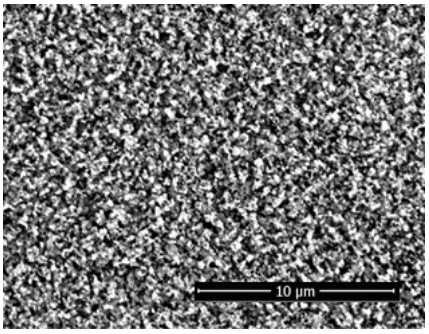

SEM microphotograph of the InSb thin layer obtained by pulse electrodeposition (V_{on} = -2.3V vs. SCE, t_{on} = 1 ms, V_{off} = -0.5 V vs. SCE, t_{off} = 5 ms).

The obtained results indicate that the material behavior significantly depends on pH of the electrolyte what has been confirmed by composition analysis and SEM microphotographs.

Acknowledgements
This work was supported the National Science Centre, Poland (grant no. 2015/17/D/ST5/021332).

Dispersability of silicon carbide powders in aqueous media with TMAH

*Joanna Gnyla, Agnieszka Gubernat, Łukasz Zych, Kamil Kornaus, Zuzanna Góral
Faculty of Materials Science and Ceramics, AGH University of Science and Technology, Kraków, POLAND
e-mail: jgnyla@agh.edu.pl

***Keywords**: silicon carbide, rheology, TMAH, stabilization*

Wide high-temperature application of covalent ceramics like silicon carbide (SiC) products and their typical application as wear-resistant elements requires manufacturing of products with complex shapes. They can be fabricated using the slip casting method. It is important to remove at an early stage of production all microstructural defects which affect properties of sintered, polycrystalline material. Elimination of all problems is difficult, but ceramic slips can be effectively stabilized before the slip casting process which in turn improve properties of the final products.

The dispersion behavior of 40 vol.% water suspensions of commercial SiC powders (UF 10, UF 15, UF 25; HC Starck) was studied. The SiC powders differed both in a specific surface area and the particle size distribution. Tetramethylammonium hydroxide (TMAH) was used as a dispersing agent. The suspensions were stabilized with various amounts of TMAH i.e.; 0.5, 1.0 and 1.5 wt.%. Mixture of sintering activators (10% of Al_2O_3 and Y_2O_3 powders; 3:2 mass ratio) was added to the slips. Mass of the activators was calculated in relation to the SiC powder. Complex viscosity and G' and G'' vs. angular frequency of the SiC slips were measured using a plate-plate system (d=25 mm).

Knowledge of an ability of particles to form stable suspensions is essential when products are formed by casting techniques. The optimum amount of TMAH was determined which was necessary to stabilize suspensions made from the various SiC powders. It was noted, that the optimal amount of TMAH was larger when the SiC powder was finer. In such a case suspensions had the smallest apparent viscosity. All suspensions were stable when pH was higher than 10, as determined by zeta potential measurements. It was found that the rheological properties of the SiC suspensions depended on many factors such as; solid phase volume fraction; particle size distribution and particle shape. The sintering activators caused a slight increase in viscosity of the suspensions. From the point of view of slip casting method, the best SiC powder was UF 10.

Acknowledgements
The work was supported by statutory research realized on Faculty of Materials Science and Ceramics, AGH-UST, No. 11.11.160.617.

Molecular dynamics simulations of iron phosphate glasses

*Paweł Goj, Paweł Stoch
Faculty of Material Science and Ceramics, AGH - University of Science and Technology, Cracow, POLAND
e-mail: pgoj@agh.edu.pl

***Keywords**: molecular dynamics, computer simulations, iron phosphate glasses, Structure, waste vitrification*

Phosphate glasses are characterized by a low chemical durability because of easily hydrated P-O-P bonds. The addition of iron to glass increase its chemical durability due to formation of more hydration resistant Fe-O-P bonds. Iron phosphate glasses, due to their favourable properties such as excellent chemical durability, low melting temperature as well as ability to accommodate large amounts of sulphur compounds and metal oxides can be used in immobilization of hazardous waste. Iron in these glasses can exist in +2 and +3 oxidation states. The $Fe^{2+}/(Fe^{2+}+Fe^{3+})$ molar ratio depends on melting atmosphere, temperature and time. Glass of composition 40Fe2O3–60P2O5 [% mol] has highest chemical durability among others.

In this work molecular dynamics MD modeling was applied to determine influence of gradual substitution of Fe^{3+} by Fe^{2+} on structure 40Fe2O3–60P2O5 [% mol] glass. The molecular dynamics is computer simulation technique consist of the numerical solution of the classical equations of motions when particles interacting through a given force field. This technique is used for example to study glass structure, diffusion or radiation tolerance of materials.

According to the conducted simulation bound lengths of P–O, Fe2+–O, Fe3+–O and O–O are independent of content Fe^{2+} in glass structure their values are 1,49, 1,90, 2,10 and 2,44 Å respectively. Iron in modeled glasses has coordination numbers from 4 to 6. Fe^{2+} prefers higher coordination numbers then Fe^{3+}. Mean coordination numbers of Fe^{2+} and Fe^{3+} to oxygen increase with increasing substitution of Fe^{3+} by Fe^{2+}.

Adhesives based on the polyvinyl acetate dispersion with improved thermal and fireproof properties

*Zuzanna Góral[1], Piotr Izak[1], Joanna Mastalska-Popławska[1], Łukasz Wójcik[1], Marcin Gajek[1]

[1]Faculty of Materials Science and Ceramics, AGH University of Science and Technology, Krakow, POLAND

e-mail: zgoral@agh.edu.pl

Keywords*: wood, adhesives, thermal analysis, fireproof properties*

Wood is the natural material which is commonly used in the furniture or construction industry, although it is a flammable material. Due to this, it is very important to improve wood fireproof properties and fireproof adhesive can be one of the method to achieve this.

The results of the research related to the development of an adhesive formula with reduced flammability for bonding wood and wood-based elements were presented. Influence of the expanded graphite and ammonium polyphosphate on properties of the polyvinyl acetate adhesive dispersion was investigated. To obtain the enhanced fireproof properties, ceramic fire retardants and fillers such as silica, aluminum oxide or talc were also added. In addition, glycerin and distilled water were employed to improve the rheological properties. Prepared mixtures were characterized by measurements of viscosity, thermal properties (DSC-TG), pH, strength and flammability.

The results of thermal analysis have shown lower weight loss of such adhesives (from over 99 wt.% to under 75 wt.%) with increase of graphite and ammonium polyphosphate content in comparison to polyvinyl acetate dispersion without any additives. Viscosity of the tested adhesives mixtures was in the range between 5000 and 8200 mPa·s. Moreover, the flammability tests indicated significant delay in ignition of samples and higher total burning time of them.

The studies revealed improvement of the polyvinyl acetate adhesive properties by using such additives compositions, including positive impact of graphite and ammonium polyphosphate.

Acknowledgements

This work was supported by financial resources under the project “Creating a formulation and technology for the production of glue for wooden and wood-based elements allowing to produce fireproof partitions, together with technology of its application” under the Operational Program Intelligent Development, years 2014-2020, Measure 1.1 "B+R projects of enterprises" (contract No. 5.5.160.998).

Impact of melamine and its derivatives on the polyvinyl acetate wood adhesive properties

*Zuzanna Góral[1], Piotr Izak[1], Joanna Mastalska-Popławska[1], Łukasz Wójcik[1], Marcin Gajek[1]
[1]Faculty of Materials Science and Ceramics, AGH University of Science and Technology, Krakow, POLAND
e-mail: zgoral@agh.edu.pl

Keywords*: wood adhesives, melamine derivatives, fire retardants*

To ensure safety of human life in the case of fire, the suitable fire protection is necessary. It could be implemented by different ways and many stages. For instance, the materials used in building construction need to be fireproofed. On the other hand, it is not always possible to find the right materials on the market. The one example of this could be adhesives. There are several products such as fireproof adhesives, but not all of them are good enough for wood. Too high value of adhesive pH or environmentally harmful composition, e.g. by formaldehyde emission may be the reason.

The studies on formulation of the fireproof adhesive for bonding wood and wood-based elements were shown. The melamine's compounds were added to the polyvinyl acetate dispersion as the fire retardants. The impact of a melamine, melamine phosphate and melamine polyphosphate were compared. To achieve better properties of adhesives, other compounds (fillers) such as glass fiber, aluminum oxide and kaolin were also employed. Thermal analysis (DSC-TG), strength tests, rheology, pH and flammability measurements were made.

The results indicate a better effect of melamine phosphate and melamine polyphosphate on the thermal properties of the adhesive than pure melamine. Thanks to the used additives, an improvement in the strength and fireproof properties of some adhesive mixtures was obtained (compared to the pure polyvinyl acetate dispersion).

The research has shown that some of prepared adhesives could have potential application as fireproof adhesive in the future.

Acknowledgements
This work was supported by financial resources under the project “Creating a formulation and technology for the production of glue for wooden and wood-based elements allowing to produce fireproof partitions, together with technology of its application” under the Operational Program Intelligent Development, years 2014-2020, Measure 1.1 "B+R projects of enterprises" (contract No. 5.5.160.998).

Flow rate influence on foam formation in high speed bottles filling process

*Piotr Grochowiecki, Paweł Kiszelewski, Łukasz Makowski
Faculty of Chemical and Process Engineering, Warsaw University of Technology, Warsaw, POLAND
e-mail: piotrgrochowiecki@gmail.com

***Keywords**: filling, foam, CFD, FMCG*

In fast-moving consumer goods industry (FMCG), a liquid product filling process is a last stage in a production chain. For many reasons, this process is a challenge for engineers. One of questions that rises during development phase is how fast single bottle can be filled to avoid foam formation and achieve maximum capacity of the production line. There is a number of liquid properties to consider but the most important are density, viscosity, surface tension and gas solubility in a case of fizzy drinks. Parameters that can be changed are flow rate and diving nozzle speed.

If above mentioned parameters are choose incorrectly, it is likely for foam to form. This is highly undesired because time required for foam degradation would extend whole filling process multiply, it would prevent filling the bottle to the desired height and eventually to pour liquid over bottle could stain it. Phenomenon that favors foam formation is complex movement (e.g. splash) when gas is entrapped within liquid.

Computational fluid dynamics study of different cases was made using Ansys Fluent software. Volume of Fluid model was chose to predict an gas-liquid interface. The paper considers the influence of the volumetric flow rate, bottle geometry and the depth of immersion of the dosing pipe on the amount of foaming foam. The simulations revealed that the best results are obtained when flow rate is constant or increases gradually and diving nozzle is immersed just below the liquid surface. In addition, a new shape of the dosing tube is presented, the use of which significantly reduces the formation of foam.

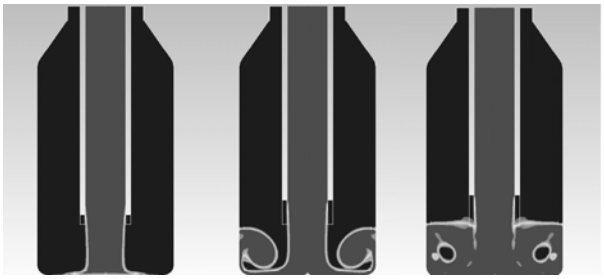

Air (darker) entrapped within water (brighter) during high speed bottle filling, CFD simulation

Complex characterization of novel bacterial electrodes for bioelectrochemical systems' applications

*Joanna Grudzień, Kamil Kamiński, Magdalena Jarosz, Maria Nowakowska, Grzegorz D. Sulka
Department of Physical Chemistry and Electrochemistry, Jagiellonian University, Krakow, POLAND
e-mail: grudzien@chemia.uj.edu.pl

***Keywords**: bioelectrochemical systems, bioelectrodes, lactic acid bacteria*

Bioelectrochemical systems (BESs) are a specific type of electrochemical setups in which microorganisms like bacteria, yeast or algae species are utilized. Those microbes can colonize electrodes or occur as planktonic forms in electrolyte and have ability to convert chemical energy from organic matter, for example pure glucose or mixture of organic compounds from wastewater, to electric energy. However, current efficiency of BESs depends on many biological, thermodynamical and technical factors. Selection of electrode material and type of bacteria species should be mentioned as ones that have the most crucial impact on the power output.

In this research, novel bioelectrodes consisting of copper foil covered by a thin gold film, cationic derivatives of natural polymers and a biofilm from *Lactobacillus rhamnosus* were presented. The morphology of samples was determined by using scanning electron microscopy (SEM), infrared spectroscopy (IR) and atomic force microscopy (AFM). In order to study electrochemical activity of setups, electrochemical measurements, like voltammetry or chronoamperometry, were performed.

Preliminary studies revealed that bacteria formed a well-developed, three-dimensional lace-like network on the investigated substrates. What is more, cyclic voltammetry (CV) studies confirmed that bioelectrodes exhibited electrochemical activity.

Antimony modified germanate oxide glass doped with rare earth ions - structural and optical properties

*Renata Jadach[1], Marcin Kochanowicz[2], Jacek Zmojda[2], Piotr Miluski2, Wojciech Pisarski[3], Joanna Pisarska[3], Maciej Sitarz[1], Dominik Dorosz[1]
[1]Faculty of Materials Science and Ceramics, AGH University of Science and Technology in Krakow, POLAND
[2]Faculty of Electrical Engineering, Bialystok University of Technology, POLAND
[3]Institute of Chemistry, University of Silesia, POLAND
e-mail: rjadach@agh.edu.pl

Keywords: *germanate glasses, gallate glasses, luminescence, structure.*

In recent decade glass have gained wide interest as host material for rare earths (active) dopants in optoelectronics. However, host glass need to possess suitable optical and thermal properties, relatively low phonon energy, good solubility of RE ions and proper mechanical properties. Among glasses which are perspective silicates, phosphates, chalcogenides, fluorides, and germanates ought to be mentioned. In particular gallo-germanate glass are under interest as they have high solubility of RE ions, good thermal stability and relatively low phonon energy.

This research is focused on investigation of glass modifiers influence on luminescent and structural properties of barium-gallo-germanate glasses. Studied glasses were modified with antimony ions on the way of barium ions replacement. Er^{3+} and Dy^{3+} ions were used as dopants to probe the local structure of surrounding environment.

The investigated glass system composition were as follow: GeO_2-Ga_2O_3-(25-x)BaO-xSb_2O_3, where x=0, 5, 10, 15, 20, 25. Structural properties were studied with use of X-ray Diffraction measurements (Panalytical Empyrean powder diffractometer using Cu Kα (λKα = 1.54186 Å)), Scaning Electron Microscope (SEM-FEI Nova 200 NanoSEM) and FTIR spectra (Bruker Company Vertex 70v spectrometer and Horriba Yvon Jobin LabRAM HR micro-Raman spectrometer). Optical properties were analyse on the basis of luminescence spectra (Acton Spectra Pro 2300i monochromator and laser diode).

Acknowledgements
The research activity was granted by the National Science Centre, Poland No. 2016/23/B/ST8/00706.

The effect of modifier additive on Barium-Gallo-Germanate glass structure and optical properties

*Renata Jadach[1], Marcin Kochanowicz[2], Jacek Zmojda[2], Piotr Miluski2, Wojciech Pisarski[3], Joanna Pisarska[3], Maciej Sitarz[1], Dominik Dorosz[1]
[1]Faculty of Materials Science and Ceramics, AGH University of Science and Technology in Krakow, POLAND
[2]Faculty of Electrical Engineering, Bialystok University of Technology, POLAND
[3]Institute of Chemistry, University of Silesia, POLAND
e-mail: rjadach@agh.edu.pl

Keywords: *gallo-germanate glasses, luminescence, spectroscopy, structure.*

Glass materials have been recently widely studied as new materials in optoelectronic. Host glass need to possess suitable thermal and optical properties, good solubility of RE ion, proper mechanical properties and relatively low phonon energy. Gallo-germanate glasses meet most of the mentioned requirements like good solubility of RE ions, low phonon energy and stable thermal properties.

In this paper research on the influence of type and amount of modifier on luminescence efficiency of gallo-germanate glasses were executed. It was also toward to define the correlation between structure and luminescence properties of obtained glasses. The investigated glassy system GeO_2-Ga_2O_3-BaO-xM, where M-modifier (x=5, 10, 15, 20 and 25 mol%) was doped with trivalent lanthanide ions which were used as probe to investigate the local structure of surrounding environment.

Following study of prepared glasses were executed: X-ray Diffraction measurements (Panalytical Empyrean powder diffractometer using Cu Kα (λKα = 1.54186 Å)), SEM/EDS (SEM-FEI Nova 200 NanoSEM), FTIR spectra (Bruker Company Vertex 70v spectrometer and Horriba Yvon Jobin LabRAM HR micro-Raman spectrometer), luminescence spectra (Acton Spectra Pro 2300i monochromator and laser diode).

Acknowledgements:
The research activity was granted by the National Science Centre, Poland No. 2016/23/B/ST8/00706.

Quaternary ammonium salts as stored product insect antifeedants

*Damian Krystian Kaczmarek[1], Michał Niemczak[1], Tomasz Rzemieniecki[1], Daria Czuryszkiewicz[1], Kamil Czerniak[1], Agnieszka Biedziak[1], Anna Turguła[1], Tomasz Klejdysz[2]

[1]Department Chemical Technology, Poznan University of Technology, Poznan, POLAND

[2]Institute of Plant Protection - National Research Institute, Poznan, POLAND

e-mail: damian.rom.kaczmarek@doctorate.put.poznan.pl

Keywords*: quaternary ammonium salts, food deterents, new compounds, synthesis, biological activity*

Antifeedants are chemical substances that prevent feeding insects. These compounds affect thetaste receptors of insects, which results in inhibiting their feed consumption. In effect, insects do not perceive potential food as feed and they move to another place or die of starvation.The most of the available antifeedants are characterized by medium activity or high costs of their synthesis. Therefore, many scientific groups conduct an intensive research on synthesis of novel, eco-friendly and cost-effective antifeedants. One of these possibilities is the use of quaternary salts. These chemicals possess high thermal stability and low volatility, which is often a great advantage in terms of environmental protection.

An efficient method of new bis-ammonium quaternary salts with saccharinate, glycolate and lactate anions was developed as a result of laboratory work. The selected alkyl-1,X-bis(decyldimethylammonium) dibromide and the potassium salts of the above-mentioned anions were used for the synthesis of these compounds. As a result, 15 novel bis-ammonium quaternary salts were obtained with high efficiency by the ion exchange reaction. To confirm their structures proton and carbon nuclear magnetic resonance technique have been utilized. According to Vogel's methodology, the solubility of obtained compounds was tested in 10 representative solvents such as distilled water, methanol, acetone, DMSO, acetonitrile, isopropanol, ethyl acetate, chloroform, hexane and toluene. The final element of the work was to determine the potential of application of synthesized salts. The methodology for testing antifeedant activity described in the literature was used for this purpose.

In the framework of our recent research new quaternary ammonium salts with the bis-ammonium cation and saccharinate, glycolate and lactate anions have been obtained with high yields.The synthesized products proved to possess high deterrent activity and may be described as new antifeedants.

Dicationic triazolium ionic liquids - synthesis and application

Damian Kaczmarek[1], *Kamil Czerniak[1], Tomasz Rzemieniecki[1], Anna Turguła[1], Daria Czuryszkiewicz[1], Agnieszka Biedziak[1]

[1]Faculty of Chemical Technology, Poznan University of Technology, Poznan, POLAND

e-mail: kamil.z.czerniak@doctorate.put.poznan.pl

Keywords*: dicationic ionic liquids, herbicide, fungicide*

Dicationic Ionic Liquids (DILs) comprised of two identical or different monocations linked together by a rigid or flexible organic spacer and paired with two singly charged anions. Recently, DILs comprising imidazolium, ammonium, pyridinium and phosphonium cations or their combinations to make asymmetric salts have be developed and extensively studied. Important advantages of DILs in comparison to monocationic ILs is high thermal and chemical stability, larger liquid ranges, higher solubility of compounds, surface properties and lower volatility.

A series of 20 dicationic ionic liquids were synthesized from commercial triazole fungicide (tebuconazole). Dicationic triazolium compounds, containing different linkers, were prepared *via* acid-base reaction between the corresponding dicationic hydroxides and herbicides in the form of free acids. NMR spectra (^{1}H and ^{13}C) were prepared in deuterated dimethylsulfoxide containing TMS as the internal standard. The herbicidal efficacy was tested in greenhouse experiments, where in the test plants were lambsquarters (*Chenopodium album* L.). Fungicidal activity was measured using agar disk-diffusion method. Six species of fungi obtained from the Institute of Plant Protection-NRI collection were used: *Sclerotinia sclerotiorum*, *Botrytis cinerea*, *Fusarium culmorum*, *Fusarium oxysporum*, *Colletotrichum* and *Monographella nivalis*.

Dicationic triazolium salts show a various activities against fungi. Their efficacy depends mainly on the concentration, the type of anion and the length of the linker. In the case of application of the active substance at concentrations of 100 and 1000 ppm, most of the compounds showed activity similar to the reference substance (tebuconazole). On the basis of the obtained results can be concluded that DILs with the longer linker exhibited the highest activity against the plant pathogen fungi. In addition, performed tests showed, that higher herbicidal activity of compounds is associated with plant growth regulating properties of triazole fungicides.

Surface properties of herbicidal ionic liquids

Damian Kaczmarek[1], Kamil Czerniak[1], Tomasz Rzemieniecki[1], Anna Turguła[1], Daria Czuryszkiewicz[1], *Agnieszka Biedziak[1]

[1]Faculty of Chemical Technology, Poznan University of Technology, Poznań, POLAND

e-mail:agnieszka.l.biedziak@doctorate.put.poznan.pl

Keywords*: ionic liquids, herbicidal ionic liquids, surface activity*

The insertion of the herbicidal anion into the structure of ionic liquids led to the development of a novel group of compounds defined as herbicidal ionic liquids (HILs). Long alkyl chains in the cation provide high surface activity and increase the wettability of the weed leaves which result in enhancement of contact between the solution of the new herbicide and the control plant.

The studied compounds were herbicidal ionic liquids with (alkyl)trimethylammonium cations containing 16, 18 and 22 carbon atoms in the alkyl chain. The source of anion were popular phenoxyacids such as 2.4-dichlorophenoxyacetic acid (2.4-D), 4-chloro-2-methylphenoxyacetic acid (MCPA) and 4-chloro-2-methylphenoxypropionic acid (MCPP-P). The surface tension was determined using the pendant drop method and the basis for the determination of the contact angle is the image of the drop on the examined surface (paraffin).

The surface active parameters were calculated for the obtained salts and the corresponding chlorides. The measured CMC values for $[C_{16}TMA][Cl]$ and $[C_{18}TMA][Cl]$ were 1.41 and 0.34 $mmol \cdot dm^{-3}$, respectively. Increase of the alkyl chain length resulted in the decrease of the measured CMC value from 0.46$mmol \cdot dm^{-3}$ for $[C_{16}TMA][MCPA]$ to 0.043 $mmol \cdot dm^{-3}$ for $[C_{22}TMA][MCPA]$.

As the derivatives of cationic surfactants, all of the obtained salts were characterized by good surface-active and wetting properties. A decrease of the CMC value was observed with the increase of the alkyl chain length in cations of analysed HILs.

Experimental results and calibration of dynamic phase shift measurement system for liquid crystals application

*Aleksandra Kalbarczyk, Leszek R. Jaroszewicz
Faculty of Advanced Technologies and Chemistry, Military University of Technology, Warsaw, POLAND
e-mail: aleksandra.kalbarczyk@wat.edu.pl

***Keywords**: Young interferometer, phase modulation, nematic liquid crystal*

Liquid crystal (LC) devices present strong potential application in dynamic modulation of optical signal. Depth of dynamic phase modulation of light propagating in LC depends on driving signal and mesomorphic properties of LC.

Interferometric setup based on Young experience for direct measurements and analysis of dynamic phase modulation in devices based on LC mixtures is presented in this work. LC cell was inserted in one arm of the interferometer. A dynamic shift of the interference pattern relates to the phase modulation controlled by LC placed in the reference path of the beam of the interferometer. For purpose of this work, the setup was calibrated by varying the distance between reference beam and probe beam. Experimental results for 5μm-thick nematic liquid crystal mixture (6CHBT) with a homogenous orientation are shown. Dynamic phase response of nematic LC is presented for three different waveforms applied to LC cell.

The work proposed Young's interferometer with possibility to control the distance between two point sources for dynamic phase change. The calibration process have been performed to optimize the interferometer. This method allows the examination of LC relaxation phenomena and provides information about the response time of molecular switching in LC.

The proposed device is low cost, has a simple control and high tunability. Used measurement method does not require complex mathematical algorithm to compute the phase shift. Interferometer calibration results show that a small distance between two beams is required. Fringe patterns show very high contrast.

Investigation of liquid crystals with frequency controlled birefringence

*Aleksandra Kalbarczyk, Noureddine Bennis, Przemysław Kula, Leszek R. Jaroszewicz
Faculty of Advanced Technologies and Chemistry, Military University of technology, Warsaw, POLAND
e-mail: aleksandra.kalbarczyk@wat.edu.pl

***Keywords**: liquid crystal, dielectric relaxation, dielectric anisotropy, dynamic phase demodulation*

Liquid crystals (LC) exhibit optical and dielectric anisotropy as crystals. LC director is easily reoriented while supplying a low voltage signal. Due to the optical quality and high birefringence they are extensively used in electro-optical applications. To improve the switching time dual frequency liquid crystals (DFLC) were proposed. A DFLC consists of two types of compounds. One of them is positive and its dielectric anisotropy is positive at low frequencies of the applied electric field, but it decreases with higher frequencies to negative value. The second is negative and its dielectric anisotropy is negative and almost constant in a whole range of frequencies. For this reason, the LC director can be reoriented by varying the frequency of the applied electric field, instead of the amplitude.

In present work, the optical and phase behavior of a novel nematic liquid crystal (NLC) with frequency controlled birefringence and dual frequency liquid crystal (DFLC) have been investigated. A novel nematic mixture with frequency controlled birefringence is a composition of three different dielectrically positive families of rod-like molecules. The frequency dependence of parallel component of electric permittivity is different for each family. Instead of bistable DFLC, this mixture is dielectrically positive in the whole range of frequencies. In this work two setups for measuring the optical and phase behavior of LC were proposed. The transmittance measurements provides a voltage-dependent transmission and phase retardation results. Young's interferometer provides a dynamic phase measurements for LC cell.

In this work, the relationship of frequency modulation and amplitude modulation to the relaxation dynamics of LC was examined. Frequency modulation for this mixture is not affected by the thickness of the cell. This material allows to create a multiple gray levels with a stabilized phase in frequency modulation. Frequency modulation makes this material of a special interest for optical and photonic applications.

Analysis of fatty acids composition in *Tricholoma equestre* fruiting bodies

*Katarzyna Kała[1], Agata Krakowska[2], Jelena Radović[3], Tatjana Kundaković[3], Bożena Muszyńska[1]

[1]Department of Pharmaceutical Botany, Faculty of Pharmacy, Jagiellonian University Medical College, Kraków, POLAND

[2]Department of Inorganic and Analytical Chemistry, Faculty of Pharmacy, Jagiellonian University Medical College, Kraków, POLAND

[3]Department of Pharmacognosy, University of Belgrade, Faculty of Pharmacy, Belgrade, SERBIA

e-mail: kat3kala@gmail.com

***Keywords**: Tricholoma equestre, edible mushroom, fatty acids, analysis, GC-MS*

Tricholoma equestre (L.) P. Kumm. (Man on horseback) is a popular species of edible mushroom. This species was selected for the experiment because it is a commonly consumed mushroom that is allowed to be sold on bazaar in many countries include Poland. It was proven that this species is a good source of zinc and other biologically active substances. Based on scientific data is good known that biologically active constituents of *Tricholoma equestre* − fatty acids, exhibit role in prophylaxis of hypertension and coronary heart disease.

Thereby, the aim of the research was to study content of fatty acids and their profile in lyophilized fruiting bodies of *Tricholoma equestre*. In order to study the chemical composition of fatty acids, their cyclohexane extract was studied using GC-MS. Fatty acids were esterified using 98% H_2SO_4/MeOH anh. to obtain FAMEs (fatty acid methyl esters).

Eleven fatty acids were detected and quantified: myristic acid, pentadecanoic acid, palmitic acid, heptadecanoic acid, stearic acid, oleic acid, vaccenic acid, linoleic acid, arachidonic acid, behenic acid, and lignoceric acid. Palmitic, oleic and linoleic acids were determined in highest amounts (respectively 28.84%, 28.59%, and 28.29% of total content). The analyzed total fatty acids profile contain saturated fatty acids (40.25%), monounsaturated fatty acids (31.12%) and polyunsaturated fatty acids (28.63%).

To ensure the proper functioning of the human body, it is necessary to have a balance between the saturated and unsaturated fatty acids in daily diet. Based on obtained results *Tricholoma equestre* species is a good natural source of unsaturated fatty acids and can be a valuable component of everyday diet.

Study on the release of organic compounds from commercial preparations containing *Bacopa monnieri* to artificial digestive juices

Agata Krakowska[1], *Katarzyna Kała[2], Jan Lazur[2], Agnieszka Szewczyk[2], Bożena Muszyńska[2]

[1]Department of Inorganic and Analytical Chemistry, Faculty of Pharmacy, Jagiellonian University Medical College, Kraków, POLAND

[2]Department of Pharmaceutical Botany, Faculty of Pharmacy, Jagiellonian University Medical College, Kraków, POLAND

e-mail: kat3kala@gmail.com

Keywords*: Bacopa monnieri, phenolic compounds, digestive juices, RP-HPLC analysis*

Bacopa monnieri (L.) Pennell is one of the plants belonging to the Hindu traditional medicine system called Ajurveda. Raw material obtained from this plant was used before the world for the treatment of various ailments and conditions. Clinical studies have confirmed the beneficial effects of *Bacopa monnieri* on the psychological condition of children who are struggling with ADHD.

The aim of the present work was to determine the degree of release of the analyzed organic compounds (protoactechuic acid, *p*-hydroxybenzoic acid, neochlorogenic acid, chlorogenic acid, isochlorogenic acid, coffeic acid, ferulic acid, isoferulic acid, luteoline) from commercial preparations containing *Bacopa monnieri* and biomass obtained from *in vitro* cultures into artificial digestive juices. The test material was incubated in artificial gastric juice at two times: 30 and 60 minutes respectively, while in artificial intestinal juice for 150 minutes. The concentration of the tested compounds in the obtained extracts was determined using the RP-HPLC method.

Based on the analyzes, it was found that prolongation of incubation time in gastric juice had a small effect on the increase of the amount of substances released to the stomach. In addition, organic compounds are released in higher amount into the gastric juice than to intestinal juice (e.g. for isochlorogenic acid – 45.10 mg/L and 0.13 mg/L, respectively). What is more, neochlorogenic acid, chlorogenic acid, isochlorogenic acid, coffeic acid, ferulic acid, isoferulic acid, luteoline were released only from *Bacopa monnieri* biomass from *in vitro* cultures.

In conclusion, there are significant differences between the biological material (*in vitro* cultures of *Bacopa monnieri*) and commercial preparations.

Analysis of selected organic compounds in preparations containing *Bacopa monnieri*

Bożena Muszyńska[1], Agata Krakowska[2], *Katarzyna Kała[1], Jan Lazur[1], Agnieszka Szewczyk[1], Maciej Łojewski[1]

[1]Department of Pharmaceutical Botany, Faculty of Pharmacy, Jagiellonian University Medical College, Kraków, POLAND

[2]Department of Inorganic and Analytical Chemistry, Faculty of Pharmacy, Jagiellonian University Medical College, Kraków, POLAND

e-mail: kat3kala@gmail.com

Keywords*: Bacopa monnieri, dietary supplements, phenolic compounds, RP-HPLC analysis*

Bacopa monnieri (L.) Pennell is a popular medicinal plant used for thousands years in traditional Hindu medicine. Due to its numerous physiologically active compounds (e.g. flavonoids, alkaloids, and triterpene saponins) it is increasingly used in anti-inflammatory, antidepressant and anticancer prevention.

Bacopa monnieri preparations and lyophilized biomass derived from *in vitro* cultures of this species were analyzed in the following research, including phenolic compounds such as: protocatechuic acid, *p*-hydroxybenzoic acid, neochlorogenic acid, chlorogenic acid, isochlorogenic acid, coffeic acid, ferulic acid, isoferulic acid, luteoline. Analysis of these compounds in prepared methanol extracts was performed by RP-HPLC.

The content of the protocatechuic acid (ranged from 0.40 to 3.00 mg/L) and *p*-hydroxybenzoic acid (0.14 – 4.05 mg/L) were only in commercial formulas in amount which was possible to measure. However, the remaining compounds: neochlorogenic acid (6.94 – 7.42 mg/L), chlorogenic acid (15.04 – 73.31 mg/L), isochlorogenic acid (181.16 – 864.79 mg/L) were determined only in *Bacopa monnieri* biomass obtained from *in vitro* cultures.

Based on the conducted studies, it was found that the content of the tested organic compounds was significantly different and depending on the form and origin of the supplement. Hence, these preparations can only be useful to supplement the deficiencies of some organic compounds in the human body.

Sorption properties of MTMS-based aerogel and filters modified with its share

*Mateusz Kamiński[1], Bartosz Nowak[1], Marta Bojarska[1,2]
[1]Faculty of Chemical and Process Engineering, Warsaw University of Technology, Warsaw, POLAND
[2]GVS Filter Technology, Zola Predosa (Bologna), ITALY
e-mail: mateusz.kaminski.dokt@pw.edu.pl

Keywords*: silica aerogel, methyltrimethoxysilane (MTMS), sorption properties, fibrous filters*

The research is focused on sorption properties of aerogel synthesized with methyltrimethoxysilane (MTMS) used as a precursor. The aim of this study was to determine the best MTMS:solvent ratio, and further use it to modify fibrous filters. MTMS-based aerogel have high porosity, hydrophobic and oleophilic properties, thus can be used to enhance oil-sorptive propertiesof filters used to remove oil mist.

The aerogel used in this study was produced in a two-stage, acid-base sol-gel process. The drying of aerogel was carried out at atmospheric pressure. Samples were tested for wettability, their morphology was examined using SEM. The porosity, bulk density and volume shrinkage of aerogel were also determined. The sorption properties of obtained aerogels were tested for three oils (di-ethyl-hexyl-sebacat, diesel, vegetable oil), three alcohols (methyl, ethyl, isopropyl alcohol) and one ketone (propanone).

Research has shown that the MTMS:solvent volume ratio affects the structure and morphology of the synthesized aerogels. Performed studies confirmed hydrophobic and oleophilic properties of tested aerogels. The obtained results indicate that aerogels synthesized at volume ratio 1:10 and 1:8 (MTMS:MeOH) have the best sorption properties for all of the above listed compounds. The results of the study allowed to connect the sorption capacity of the examined aerogels with their morphology and porosity.

Tests conducted for filters showed that oil sorption capacity of filters modified with aerogel increased in comparison to unmodified filters. It was observed that aerogel (for ratios 1:8-1:13) tends to accumulate on the fibers located in the top layer of filter.

Acknowledgements
This work was supported by The National Centre for Research and Development – project "Oil removal from gas and liquid streams thanks to filter media modified by aerogel" LIDER/011/L-6/14/NCBR/2015

3D printing of stainless and acid resistant steel

*Magdalena Karpowicz[1], Marek Polański[1],
[1]Department of Advanced Materials and Technologies, Military University of Technology, Warsaw, POLAND
e-mail: magdalena.karpowicz@wat.edu.pl

***Keywords**: 3D Printing, additive manufacturing, laser engineered net shaping (LENS), stainless steel, austenitic steel*

Therefore that surrounding us environment is becoming increasingly polluted by numerous industrial wastes or chemical reagents and trash this work focuses on the use of stainless steel. The commercial methods of manufacturing stainless steels are of course very well known, but in this work we wanted to show alternative manufacturing technology – 3D Printing with laser as light source and powder melting medium – Laser Engineered Net Shaping (LENS) technology. This technique was selected because from several years this kind of additive technologies are rapidly developing. This techniques have a lot of application in constantly improving areas of technology and industry. During 3D Printing process it is used all commercially available materials, from polymers to pure metals, ceramics or composites and steels.

First part of this work describes the properties of selected stainless steel - which are responsible for its use in many industrial fields such as medicine, automotive, construction, aerospace or military. Austenitic stainless steels have good mechanical properties, very high corrosion resistance and competitive price.

In this part also included a description of the technology used to manufacture test samples – LENS technology. In experimental part of work it was shown the process of selecting production parameters and manufacturing process of steel samples. Thanks to LENS process manufactured consistent and unbroken samples. After LENS process, the samples were examined on an optical and scanning microscope to reveal the microstructure.

After a comprehensive analysis of the research found that microstructure of austenitic stainless steel is substantially different from the microstructure of this kind of steel manufactured by conventional techniques. The resulting microstructure has the appearance of a so-called fish scale or snake skin. The effect of this is on the nature of the process, because LENS process causes columnar crystallization of the powder material which is delivered to the focus of the laser beam.

Alkylbenezenesulfonic acid-doped poly(3-hexylthiophene) as membrane material for gas separation

*Kinga Kepska[1], Agnieszka Stolarczyk[1], Mieczyslaw Lapkowski[1,2]
[1] Department of Physical Chemistry and Technology of Polymers, Silesian University of Technology, Gliwice, POLAND
[2] Centre of Polymer and Carbon Materials, Polish Academy of Sciences, Zabrze, POLAND
e-mail: kinga.kepska@polsl.pl

***Keywords**: conjugated polymers, poly(3-hexylthiophene), chemical doping, membrane gas separation, tailor-made materials*

Membrane gas separation is a promising separation technique, mainly due to energy efficiency compared to other methods. Separation of air components is a challenge due to the small difference in kinetic diameters of the molecules (oxygen: 3.46 Å, nitrogen: 3.64 Å). As a result, differences in the diffusion rates in polymeric membranes are very low if there are no specific interactions with one of the gases. That is why air separation requires tailor-made membrane materials. Doping of conjugated polymers generate charge carriers, like polarons, which may interact with O_2 diradicals facilitating the oxygen transport through the membrane.

Nonregular poly(3-hexylthiophene) (NR PHT) synthesized by means of chemical oxidation with $FeCl_3$ has suitable film-forming properties and mechanical strength for use as membrane material, but does not show selectivity in O_2/N_2 separation. This communication presents the results considering the influence of NR PHT doping with 4-ethylbenzenesulphonic acid (EBSA) on membrane separation parameters such as: permeability coefficients, selectivity and separation coefficients and activation energies of gas transport.

Doping NR PHT with the 0.5 and 1% of EBSA caused decrease of the nitrogen permeability coefficient (from 3.48 to 1.16-1.42 barrer), while the oxygen permeability coefficient was maintained (about 4.5 barrer). That resulted in significant rise in the selectivity coefficient (from 1.29 to 3.75-3.38) and separation coefficient (from 1.06 to 1.99-1.79) of the investigated membranes.

In conclusion, doping PHT membranes with alkylbenzenesulfonic acid, namely EBSA, resulted in an improvement of selectivity and allowed oxygen enrichment of air up to 32.8%.

Acknowledgements
This work was supported by National Science Centre, Poland (PRELUDE 11: 2016/21/N/ST8/01871 grant).

Synthesis and application of oligosaccharide-based cinchona organocatalysts

Péter Kisszékelyi, Bálint Zeller, Sándor Nagy, Petra Kozma, Péter Huszthy, *József Kupai
Faculty of Chemical Technology and Biotechnology, Budapest University of Technology and Economics, Budapest, HUNGARY
e-mail: jkupai@mail.bme.hu

Keywords*: organic solvent nanofiltration, organocatalysis, cinchona alkaloids, cyclodextrin, catalyst recovery*

Organocatalysis has emerged as an efficient solution for the rapid and stereoselective synthesis of enantiomerically enriched molecules. Cinchona alkaloids and their derivatives have proven to be powerful organocatalysts owing to their reactivities, leading to high enantioselectivities.

Organic solvent nanofiltration (OSN) is an emerging technology that allows separation of solutes via pressure gradient in organic media. Attaching cinchona moieties to β-cyclodextrins seems to be an effective way to reach convenient organocatalysts with high molecular weight, leading to easy separation of the catalyst from the reaction mixture.

New β-cyclodextrin-cinchona thiourea and squaramide organocatalysts were prepared starting from commercially available β-cyclodextrin and hydroquinine. These bifunctional organocatalysts were applied successfully (up to 95% yield and 99% e.e.) in asymmetric *Michael* additions between 1,3-dioxo compounds and β-nitrostyrene. After the enantioselective reactions, separation of the products and the cyclodextrin-based catalysts were carried out applying the OSN method with high efficiency, resulting in a green and sustainable organocatalytic method.

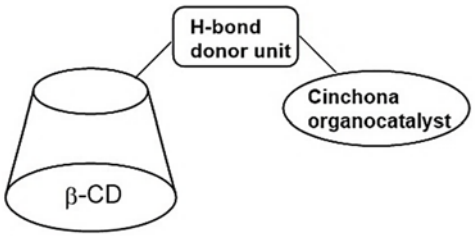

General structure of the new cyclodextrin-cinchona organocatalyst family.

Acknowledgements
Financial support: Richter Gedeon Talentum Fund, Hungarian Scientific Research Fund [OTKA 112289, PD108462], ÚNKP-17-1-I Fund.

The preparation condition influence on $K_{0,5}Bi_{0,5}TiO_3$ electrochemical properties

*Małgorzata Dziubaniuk[1], Jan Wyrwa[1], Mieczysław Rękas[1], Kamila Kluczewska[2], Piotr Czaja[2], Jan Suchanicz[2]

[1]Faculty of Materials Science and Ceramics, AGH University of Science and Technology, Cracow, POLAND

[2]Institute of Technology, Pedagogical University, Cracow, POLAND

e-mail: dziubaniuk@o2.pl

***Keywords**: ferroelectrics, potassium bismuth titanate, solid state synthesis, solid state ionics, electrochemical impedance spectroscopy*

$K_{0,5}Bi_{0,5}TiO_3$ (KBT) and $Na_{0,5}Bi_{0,5}TiO_3$ (NBT) are $A_{0,5}^{+}Bi_{0,5}^{3+}B^{4+}O_3$ type perovskites capable of working in elevated temperatures. The ferroelectric and piezoelectric properties of the materials, exhibited in wide range of temperatures, as well as high environmental and chemical stability make them interesting candidates for applications in devices range from multilayer actuators to buzzers, diesel engine fuel injectors, sonar, ultrasound appliances and nanopositioners in scanning microscopes.

NBT materials have been extensively studied, while research on KBT has rarely been reported due to difficulty to fabricate high density KBT ceramic. Up to now few research reports are available concerning mainly dielectric and pyroelectric measurements, C-V characteristics and DC conductivity.

The main aim of presented studies was determination of impact of applied synthesis conditions on KBT electrical properties in different gas atmospheres of precisely controlled compositions. The first step consisted of materials synthesis by solid state route, using analytically pure bismuth and titanium oxides and potassium carbonate. Samples properties were studied by XRD and SEM. The electrical properties of sintered pellets supported by silver electrodes were determined by electrochemical impedance spectroscopy in three different atmospheres i.e. in synthetic air, 10% H_2 in argon and 3000 ppm NH_3 in argon and in temperature range 200-500°C.

Based on obtained spectra in frequency range 10^{-1}-10^{7} Hz, the mechanism of reaction on three-phase boundaries (ceramic-metal-gas) was proposed as well as the conduction type in samples in different temperatures was determined. The electrochemical properties of KBT samples prepared in varied conditions were compared.

Acknowledgements

This work was supported by the National Science Centre of the Republic of Poland, under Grant No 2016/23/B/ST8/00163.

The electrochemical properties of La doped $BiFeO_3$ ceramics

*Małgorzata Dziubaniuk[1], Jan Wyrwa[1], Mieczysław Rękas[1], Kamila Kluczewska[2]
[1]Faculty of Materials Science and Ceramics, AGH University of Science and Technology, Cracow, POLAND
[2]Institute of Technology, Pedagogical University, Cracow, POLAND
e-mail: dziubaniuk@o2.pl

***Keywords**: bismuth ferrite, solid state synthesis, solid state ionics, electrochemical impedance spectroscopy*

Multiferroics is a group of materials in which at least two of three possible orders i.e. ferromagnetic (ferromagnetic, antiferromagnetic or ferrotoroidal) ferroelectric or ferroelastic occur. Even though the mentioned phenomena were discovered as far back as in 60', its practical application become possible in late 90'. Among the prototypical appliances based on multiferroics materials presented up to now, it is worth to list magnetic field sensors, gas sensors as well as devices for energy storage and conversion.

One of the multiferroic material, which is especially interesting on account of fundamental properties as well as possible usage is bismuth ferrite $BiFeO_3$ (BFO). At room temperature in BFO phase ferroelectric and antiferroelectric order coexist (Neel antiferromagnetic temperature is 643 K and ferroelectric Curie temperature is 1100 K). Modification of physicochemical properties of the material is possible by metal oxide doping.

The main aim of presented studies was determination of impact of gaseous atmosphere composition on undoped and La-doped BFO electrical properties. The first step consisted of materials synthesis by solid state route using analytically pure oxides. The materials nominal composition were $BiFeO_3$, $0.1La_2O_3$-$0.9BiFeO_3$, and $0.2La_2O_3$-$0.8BiFeO_3$. The microstructure of sintered bodies was revealed by SEM technique and phase compositions were verified by XRD method. The electrical properties of sintered pellets supported by silver electrodes were determined by electrochemical impedance spectroscopy in three different atmospheres i.e in synthetic air, 10% H_2 in argon and 3000 ppm NH_3 in argon and in temperature range 200-500°C. Based on obtained spectra in frequency range 10^{-1}-10^7 Hz the mechanism of reaction on three-phase boundaries (ceramic-metal-gas) was proposed as well as the conduction type in samples in different temperatures was determined.

Acknowledgements
This work was supported by the National Science Centre of the Republic of Poland, under Grant No 2016/23/B/ST8/00163.

Impedance spectroscopy of vanadium pentoxide

Kamila Kluczewska[1], Krystyna Schneider[2], *Małgorzata Dziubaniuk[3], Jan Wyrwa[3]
[1]Institute of Technology, Pedagogical University, Cracow, POLAND
[2]Faculty of Computer Science, Electronics and Telecommunications, AGH University of Science and Technology, Cracow, POLAND
[3]Faculty of Materials Science and Ceramics, AGH University of Science and Technology, Cracow, POLAND
e-mail: dziubaniuk@o2.pl

***Keywords**: vanadium pentoxide, impedance spectroscopy, electrical conductivity, defect structure*

Vanadium oxides are used in many technological applications, such as in oxide electronics as electrical and optical switching devices, light detectors. Moreover, they are used as chemical sensors materials and heterogeneous catalysts. Among from ten to twenty known titanium oxides vanadium pentoxide, V_2O_5 is the most popular. Vanadium ions in V_2O_5 have the highest oxidation state; therefore it is the most stable one in the vanadium-oxygen system.

Vanadium pentoxide (V_2O_5) was the subject of studies. X-Ray diffraction (XRD) and scanning electron microscopy (SEM) were used to structural and phase characterization. Electrical properties were determined by means of impedance spectroscopy at the frequencies ranging from 0.1 Hz to 1.4 MHz as a function of oxygen partial pressure from 200 Pa to 210 kPa, at temperatures from room temperature to 620 K.

The distinct effect of the temperature was observed. It was found, that the impedance spectra can be characterized by an equivalent circuit composed from ohmic resistor and non- Debye constant phase element (CPE) connected in parallel. Vanadium pentoxide shows n-type semiconducting properties. Basing on electrical conductivity vs. oxygen partial pressure dependence the defect model has been proposed. The interaction of the solid oxide with oxygen effects on the impedance spectra. It is postulated that both singly and doubly ionized oxygen vacancies and electrons are the product of these interactions.

Acknowledgements
This work was supported by the National Science Centre of the Republic of Poland, under Grant No 2016/23/B/ST8/00163.

Functionalization of ultrafiltration membranes for integration of adsorber properties

Dereck Koch, Mathias Ulbricht
Faculty of Chemistry, University of Duisburg-Essen, Essen, GERMANY
e-mail: dereck.koch@uni-due.de

Keywords: *Polymer enhanced ultrafiltration, ATRP, wastewater treatment, membranes, "click" chemistry*

Water contaminations with heavy metals are a dominant environmental problem. Generated through a rising number of industry processes many waters are loaded with high contents of harmful species. There are several processes to free water of pollutants like chemical precipitation or electrochemical treatment. However most of these processes are only suitable for high amounts of pollutants or lead to secondary treatment of byproducts. Membrane processes have aroused a high interest in the last years for wastewater treatment since they include low operative costs and simple processes. The process of ultrafiltration (UF) could be enhanced by complexing ions with a polymer soluble in water to allow filtration; this procedure is called polymer enhanced ultrafiltration (PEUF).

The aim of this project is to merge the two steps of PEUF into one membrane. For this purpose membrane materials (polysulfone or polyethersulfone) are functionalized to allow a "click" reaction with functional polymers. These polymers have on the one hand groups suitable for "click" chemistry to immobilize them on the surface and on the other hand work as binding agents for metal ions. A good approach is to functionalize commercially available polymers like polyethyleneimine (PEI).

Polysulfone has been successfully chloromethylated to different degrees and azidated afterwards, while PEI with different molar masses has been modified to contain alkyne groups with differing degrees of substitution. Membranes were cast from these polymers and characterized in terms of pore structure and filtration performances. A heterogeneous, catalyzed "click" reaction with modified PEI was performed via infiltration of an aqueous solution and absorption studies were performed.

The obtained results show promising first tendencies for a successful process, while for achieving optimal conditions in terms of membrane performance, parameters have to be further adjusted.

Acknowledgements
This work is part of the project POLINOM (grant number 03XP0106C), supported by the German Ministry of Education and Research (BMBF) as part of the 'Materialien für eine nachhaltige Wasserwirtschaft–MachWAS' initiative.

Determination of oil sorption properties of fibrous media coated with aerogel particles

Juliusz Kondracki[1], *Patrycja Wierzba[1], Bartosz Nowak[1], Andrzej Krasiński[1], Marta Bojarska[1,2]
[1]Faculty of Chemical and Process Engineering, Warsaw University of Technology, Warsaw, POLAND
[2]GVS Filter Technology, Zola Predosa (Bologna), ITALY
e-mail: patrycja.wierzba.dokt@pw.edu.pl

Keywords*: polypropylene fibrous media, hydrophobic organosilica aerogels, wettability, capillary rise test, emulsion separation*

Methyltrimetoxysilane (MTMS)-based aerogels are porous and lightweight materials characterized by high oil sorption capacity and water/oil separation selectivity. Due to the large specific area and strongly hydrophobic properties, they are promising material for removal of oily contaminants from the oil-in-water emulsions.

The aim of this work was determination of oil sorption properties of fibrous polypropylene materials coated with aerogel by capillary rise method. The wettability kinetic of tested porous structures for pure oils and oil-in-water emulsions were measured. The sorption properties were determined in experiments with pure oils: di-ethyl-hexyl-sebacat (DEHS) test oil, diesel fuel and vegetable oil, and with their 10%vol water emulsions. The emulsions were created by vigorous agitation and stabilized by addition of surfactants (Tween® 20 and Span® 80). The fibrous materials used in research were made of polypropylene using melt-blown technique. The aerogels were synthesized via two-step acid-base sol-gel method using different ratios of methyltrimethoxysilane precursor to solvent (methanol) equal to 1:20, 1:15 and 1:10. Depending on the MTMS to methanol ratio different amount of aerogel and its distribution in the filter volume was obtained.

The conducted research showed that aerogel deposition increase the wettability thus improve the wetting kinetic. This also leads to a higher sorption capacity of polypropylene material for pure oils. The experimental data concerning the oil-in-water dispersions show the relatively slow wettability kinetics. Obtained results can be explained by slower migration of the oil droplets into material pores due to emulsion stabilization by surfactant additive.

Acknowledgements
This work was supported by NCBiR project "Oil removal from gas and liquid streams thanks to filter media modified by aerogel" LIDER/011/L-6/14/NCBR/2015

Synthesis methods of magnesium titanate solid solutions by solid state reaction

*Kamil Kornaus, Radosław Lach, Magdalena Szumera, Agnieszka Gubernat
Department of Ceramics and Refractories, AGH University of Science and Technology, Cracow, POLAND
e-mail: kornaus@agh.edu.pl

***Keywords**: Tialite, solid state synthesis, thermal expansion coefficient, stabilization, heterogenic nucleation*

Tialite is synthetic refractory material with Al_2TiO_5 structural formula. The biggest limitation in the potential use of tialite as a refractory material is its thermal instability within the range of 750-1280°C. It was found that the magnesium oxide and silicon oxide introduced into the system in the small amounts effectively limit the decomposition of tialite in this temperature range. $MgTi_2O_5$ is one of the possible, isostructural with tialite, transitions phase occurring during the synthesis. Therefore it is possible to synthesize tialite by introducing into the reaction mixture seeds of $MgTi_2O_5$. Forming of tialite solid solutions with general formula $Mg_xAl_{2(1-x)}Ti_{1+x}O_5$ should result in lowered the temperature of the synthesis, and an increased thermal stability.

The presented results compare three methods of tialite synthesis such as: classical synthesis in solid phase, reaction synthesis using magnesium titanate in-situ synthesis and heterogeneous nucleation with the use of isostructural phases in the form of magnesium titanate. The synthesis was carried out on samples varying in particle size of the starting powders, quantity and type of used additives. Different reaction powders mixtures was formed into cylindrical shaped samples. Influence of simultaneously synthesis and sintering temperature (1250-1550°C) on conversion and density was investigated. Reference samples was made by equimolar mixtures of titanium and alumina oxides. Yield of synthesis reaction was specified by XRD method. In both cases, the synthesis focused on solid solution formation (using magnesium titanate) has managed to achieve fully reacted systems. The highest efficiency of classical synthesis was 93%. An additional advantage of using heterogeneous nucleation was a significant reduction in the temperature of synthesis. In addition, both methods using transition phases showed higher thermal resistance of the obtained materials.

Acknowledgements
This work was performed within statutory research realized on Faculty of Materials Science and Ceramics AGH University of Science and Technology, No. 11.11.160.617.

Investigation of the integrated reactive adsorption process

*Tomasz Kotkowski, Michał Lewak, Eugeniusz Molga
Faculty of Chemical and Process Engineering, Warsaw University of Technology, Warsaw, POLAND
e-mail: Tomasz.Kotkowski.dokt@pw.edu.pl

Keywords: *process integration, reactive adsorption, esterification*

Nowadays the role of sustainable technology increases. Among others an integration of processes is one of the way for practical implementation of this idea.

Reactive adsorption is among others an example of process integration. In this approach the chemical reaction is carried out with simultaneous adsorption of one of the reaction product. This kind of integration is particularly effective for reversible reactions, as it helps to remove one product from the reaction zone, so to shift the reaction equilibrium towards the total conversion of reactants. Additionally, there is no need to separate the products after reaction completion and the non-adsorbed product is relatively pure.

In presented investigations the reactive adsorption process was carried out in the batch reactor. Two series of experiments were carried out: first series was the reaction without the adsorbent, then at the presence of the sorbent. The experiments were executed with use of the testing reversible reaction - esterification of acetic acid with n-butanol. Amberlyst-15 was employed as a catalyst. The molecular sieves 3A were used as a sorbent of the water produced during the reaction progress. Due to removal of water from the reaction zone, the chemical equilibrium of the reaction was shifted towards the ester production, so even a complete conversion of alcohol and acid was possible. The reaction progress was determined with a gas chromatography.

An influence of the temperature, the reactant concentrations, a presence of the catalyst as well as a presence of the sorbent on the reaction progress were investigated.

The mathematical model of the process was formulated, which includes the reaction kinetics and thermodynamics as well as the sorption of the product. Predictions obtained with the elaborated model were compared to the experimental results.

The obtained results indicate that an addition of sorbet into the reaction mixture helps to increase productivity of the reaction.

Physical activation of end-of-life tyre pyrolytic char

Tomasz Kotkowski, *Robert Cherbański, Eugeniusz Molga
Faculty of Chemical and Process Engineering, Warsaw University of Technology, Warsaw, POLAND
e-mail: robert.cherbanski@pw.edu.pl

***Keywords**: physical activation, char, end-of-life tyres, pyrolysis*

About 3.19 million tonnes of end-of-life tyres (ELTs) were managed in Europe in 2015 (ETRMA, 2015). The direct disposal of ELTs in landfills is banned in Europe. Therefore, the management of ELTs is organized in Europe in the form of material recovery and energy recovery. Tyre pyrolysis is an attractive form of material recovery in which char, oil, gas and metal are produced. Estimated yields of the end-products are: 33% char, 35% oil, 20% gas and 12% metal. The gas and oil can be directly used to heat the pyrolysis reactor. The oil can also be distilled to recover certain chemical compounds such as: benzene, toluene, xylenes, limonene. On the other hand, the char need to be activated to obtain the secondary product of relatively high market value.

This work presents experimental results on physical activation of the pyrolysis char. The tyre pyrolysis with subsequent char activation were carried out in a thermobalance TG 209 F1 Libra (Netzsch, Germany) equipped with a micro furnace and a precise ultra-microbalance. The char was analysed in the 3Flex Surface Characterization Analyzer (Micromeritics, USA) showing an influence of the activation temperature and its duration on the total and micropore surface area of the activated char. Figures below present typical results obtained for non-activated pyrolytic char produced at 500°C. The char can be characterized with BET surface area of about 63 m^2/g and t-plot micropore area of about 16 m^2/g.

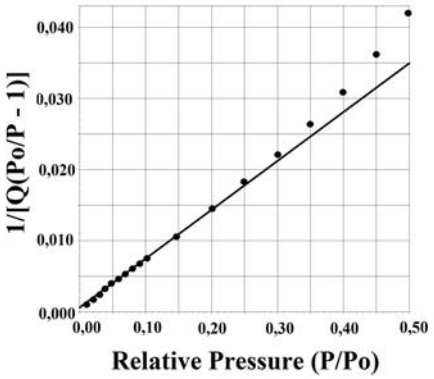

BET Surface Area Plot for the end-of-life pyrolytic char produced at 500°C

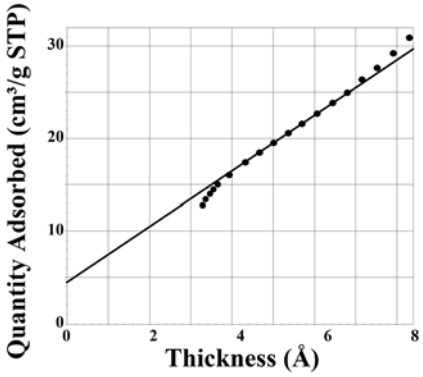

t-Plot for the end-of-life pyrolytic char produced at 500°C

Heat Transfer in Helical Coil Heat Exchanger: Parametric Study

*Krzysztof Kowalski, Dorota Downarowicz
Faculty of Chemical Technology and Engineering, West Pomeranian University of Technology, Szczecin, POLAND
e-mail: krzysztof.kowalski@zut.edu.pl

***Keywords**: helical coil, heat exchanger, condensation, Wilson method, laminar flow, pressure drop*

Helical coil heat exchangers have simple and compact structures and large heat transfer areas. They are widely used in a variety of industry applications such as refrigeration systems, power generation, process plants, heat recovery and air conditioning systems. The exchangers are usually applied as coolers, heaters, condensers or evaporators. A performance evaluation of such devices is necessary for the proper heat transfer process optimization.

The experimental set-up consisted of a heat exchanger with a cooper helical coiled tube (1.7 m length, 4 mm ID × 6 mm OD and curvature ratio of 0.054), a refrigerated circulator (FP ME50, Julabo) and an air–isopropanol (IPA) vapour mixture generation system. The gas mixture and the cooling medium (methylsilicone oil) were passed through the coil and the shell, respectively. The pure or IPA-laden air streams with specified concentrations ranging from 4 to 10.5 g/m^3 were used to the study. The experiments were performed in the following invariability range of operating parameters: air velocity 6-27 m^3/s and the coolant temperature 243 - 273K. The tests were conducted until steady-state was reached, indicated by a stable temperature of gas stream at coil outlet.

The effect of Reynolds number and the operating temperature on the heat transfer performance and the pressure drop in the helical coil for laminar flow conditions was investigated. The heat transfer coefficients and frication factors were determined using the modified Wilson plot method and Ito and White empirical correlations, respectively.

The data analysis was performed for the steady-state conditions. It showed that the overall heat transfer coefficient and the pressure drop are increased with the increase of the gas flow rate. Secondary flow in a coil tube is the potential reason observed dependencies. The pressure drop through the helical coil was even 4-times higher than through a straight tube with the same dimensions. The values of the overall heat transfer coefficient increased with the increase in the IPA vapour concentration and the decrease in the coolant temperature. It is effect a higher heat capacity of the gas mixture then pure air in the same operation condition.

Synthesis of B_4C using monosaccharides and polysaccharides

*Dawid Kozień, Paweł Rutkowski, Mirosław M. Bućko
Department of Materials Science and Ceramics, AGH University of Science and Technology, Cracow, POLAND
e-mail: kozien@agh.edu.pl

***Keywords**: B_4C, monosaccharides, polysaccharides, boron carbide*

The production of powders of covalent materials (carbides, nitrides, borides) of grain size at the nanometer level has long been a technological challenge. The goal of this paper is to investigate the possibilities of the synthesis of boron carbide (B_4C) nanopowders using monosaccharides: glucose from the aldohexose group and fructose which is a simple ketonic monosaccharide and polysaccharides: dextrin and hydroxyethyl starch (HES). Boron carbide due to high density, good wear resistance and high neutron absorption cross-section and so forth is currently used as shielding material in nuclear industry, ball mils.

These substances were prepared at a concentration of about 10% per weight. Boric acid was dissolved in these solutions in such a quantity that the molar ratio of boron to carbon was 1:10. In the first process, the solutions were lyophilized into powders and dried. In the other one the solutions were evaporated and the solids were dried at 90 ° C to constant weight. All powders were placed in graphite crucibles and then heat-treated at a temperature from 1200 to 1700°C for 1h under argon flow. All obtained powders were characterized by the X-ray diffraction (XRD). We conducted a morphological examination of powders by scanning electron microscopy (SEM) with X-ray energy dispersive spectroscopy (EDS).

Results indicated that the morphology of the B_4C depends on the temparature of the synthesis and strongly depends on the carbon source. These findings suggest that lyophilization influences on the shape and size of B_4C. This study is the first step in studying the effects of ketonic monosaccharide and aldohexose monosaccharide on B_4C synthesis.

Synthesis of B_4C using different carbon precursor

*Dawid Kozień, Paweł Rutkowski, Mirosław M. Bućko
Department of Materials Science and Ceramics, AGH University of Science and Technology, Cracow, POLAND
e-mail: kozien@agh.edu.pl

***Keywords**: graphene, soot, boron carbide, active carbon, carbon precursor*

The goal of this paper is to investigate the possibilities of the synthesis of boron carbide (B_4C) nanopowders using active carbon, graphene and soot. Active carbon is a substance consisting mainly of elemental carbon in amorphous form, partly in the form of fine crystalline, soot is a product created during incomplete combustion of fuels and other materials containing significant amounts of carbon in its chemical composition. The main, though not the only, component of carbon black is the amorphous form of carbon graphite, whereas graphene is an allotrope (form) of carbon consisting of a single layer of carbon atoms arranged in an hexagonal lattice.

Nanopowders of boron carbide (B_4C) were produced using ammonium borate prepared by dissolving of boric acid in ammonia solution at 50°C was used as a precursor. A source of carbon were suspensions of graphene, soot and active carbon powders in isopropyl alcohol. Both solution were mixed together and then liquid was evaporated in a drier. All powders were placed in graphite crucibles and then heat-treated at a temperature from 1200 to 1700°C for 1h under argon flow. sults depends on the temparature of the synthesis and strongly depends on the carbon source. All obtained powders were characterized by the X-ray diffraction (XRD). We conducted a morphological examination of powders by scanning electron microscopy (SEM) with X-ray energy dispersive spectroscopy (EDS).

Results indicated that the morphology of the B_4C depends on the temparature of the synthesis and strongly depends on the carbon source. However, with the increase in the order of the carbon precursor structure, the morphology shape and size of the boron carbide (B_4C).

Application of cinchona-squaramide organocatalyst immobilized on polybenzimidazole membrane and its recovery by nanofiltration

Petra Kozma[1],Péter Kisszékelyi[1], Sándor Nagy[1], Péter Huszthy[1],*József Kupai[1]
[1]Faculty of Chemical Technology and Biotechnology, Budapest University of Technology and Economics, Budapest, HUNGARY
e-mail: jkupai@mail.bme.hu

Keywords*: organic solvent nanofiltration, immobilization, membrane cascade reactor, asymmetric synthesis, organocatalyst*

Due to the numerous advantages over conventional transition metal catalysis, organocatalytic methodologies have become an attractive synthetic tool in asymmetric catalysis. However, the cumbersome product purification by column chromatography, and the need for catalyst recovery and reuse call for the design of more flexible and sustainable organocatalytic strategies. Immobilization of organocatalysts on polymer supports was proposed to overcome the separation bottleneck; however, binding a homogeneous catalyst to solid surfaces often led to a deteriorationin catalytic activity and enantioselectivity. Consequently, the scientific and technological challenges of realising highly efficient asymmetricr eactions and simultaneously developing practical separationstrategies are yet to be solved.

Given the achieved yield and enantiomeric excess, we demonstrate an efficient andeminently suitable membrane based strategy for asymmetric organocatalysis. A cinchona squaramide and a polybenzimidazole membrane were successfully modified with azide and propargyl functionalities, respectively. Finally, the catalyst was clicked onto the nanofiltration membrane.

The asymmetric organocatalysis with integrated separation was successfully demonstrated in a two stage membrane cascade reactor. The separation allowed >98% product recovery and 99% unreacted substrate recovery. The *in situ* solvent recovery mitigated the need for solvent addition for purification purposes. The concept of catalyst grafted membrane cascade reactor presented herein enables new possibilities for fine chemical manufacturing, and further boosts growth in the exciting new era of organocatalysis.

Acknowledgements
Financial support of the Hungarian Scientific Research Fund / National Research, Development and Innovation Office (OTKA / NKFIH No. K112289), ÚNKP are gratefully acknowledged.

New method for formaldehyde determination in the air using polyurethane foam passive samplers

*Kucharczyk Aleksandra, Grochowalski Adam
Faculty of Chemical Engineering and Technology, Cracow Univesity of Technology, Cracow, POLAND
e-mail: akucharczyk@chemia.pk.edu.pl

***Keywords**: formaldehyde, air, passive sampling, PUF*

The purpose of the research was development of the method for determination of formaldehyde using passive air sampling with polyurethane foam (PUF) sorbent and derivatizing reagent 2,4-dichlorophenylhydrazine (2,4-DCPH), and determination of this compound in the environment. Formaldehyde, due to various sources of emission often occurs in both the indoor and outdoor air. To enable quantitative determination of formaldehyde in the air calibration of the passive samplers was necessary.

Calibration was based on defining the relationship between the concentration of the compound in the air and the mass of formaldehyde absorbed in a passive sampler. Passive samplers consisted of: a metal casing, a metal rod, which is the support for the PUF discs (1 cm thick, 5.5 cm diameter), and a plastic cover to protect against water getting into the sampler. Apparatus for calibration consisted of: the air pump, two scrubbers (first with deionized water, second - formaldehyde solution), flowmeter, exposure chamber with passive samplers, and temperature and humidity recorder. Steps of analytical procedure: exposure of PUF passive samplers (7 days), elution of formaldehyde from PUF sorbent using deionized water (3×15 ml), derivatization reaction with 2,4-DCPH, enrichment of derivative using SPE technique (Phenomenex, StrataX), and final determination of formaldehyde derivative with RP-HPLC-PDA system with analytical wavelength 276 nm.

Number of analysis of environmental air samples were performed. 11 indoor air samples (furniture shop) and 32 outdoor air samples (3 measurement points in Cracow) were prepared. For indoor air results were obtained in the range of 49 to 886 $\mu g \cdot m^{-3}$, and for outdoor air from value below the LOD (limit of detection) to 325 $\mu g \cdot m^{-3}$.

Developed method can be successfully used for measurements in environmental conditions. Application of reusable, cheap, available PUF sorbent significantly decreases cost of single analysis. This may contribute to the popularization of formaldehyde monitoring in the air. We want to pay attention to the problem of formaldehyde presence in concentrations dangerous to human health.

Synthesis and application of a cinchona-squaramide organocatalyst and its recovery by immobilization on poly(glycidyl methacrylate)

Sándor Nagy[1], Levente Kárpáti[1], Béla Mátravölgyi[1], Péter Kisszékelyi[1], Béla Pukánszky[1], Péter Huszthy[1], *József Kupai[1]

[1]Faculty of Chemical Technology and Biotechnology, Budapest University of Technology and Economics, Budapest, HUNGARY

e-mail: jkupai@mail.bme.hu

Keywords*: polymerization, organocatalysis, cinchona alkaloids, Michael addition, catalyst recovery*

Catalytic transformations play an increasingly important role in organic chemistry today, both in academic laboratories and on an industrial scale. Enzymes, organo- and homogeneous catalysts are expensive, and therefore sensible strategies have to be investigated to obtain maximum catalyst performance, e.g. in terms of selectivity and high turnover numbers. Immobilization on polymer support is one of the most promising methods to achieve these goals.

Cinchona-squaramides were found to be an excellent catalyst for asymmetric *Michael* additions. Therefore, our aim was to immobilize organocatalyst **1** on a chemically stable solid support. For this purpose, poly(glycidyl methacrylate) [poly(GMA)] microspheres of narrow size distribution were prepared in a simple one-step procedure by dispersion radical polymerization. Cinchona-squaramide containing phenolic hydroxylic group **1** was synthesized from commercially available quinine. Finally, **1** was deprotonated in aq. NaOH solution and anchored to poly(GMA) (see scheme below). The obtained heterogeneous organocatalyst **2** was applied successfully in asymmetric *Michael* additions of 1,3-dioxo compounds to β-nitrostyrene.

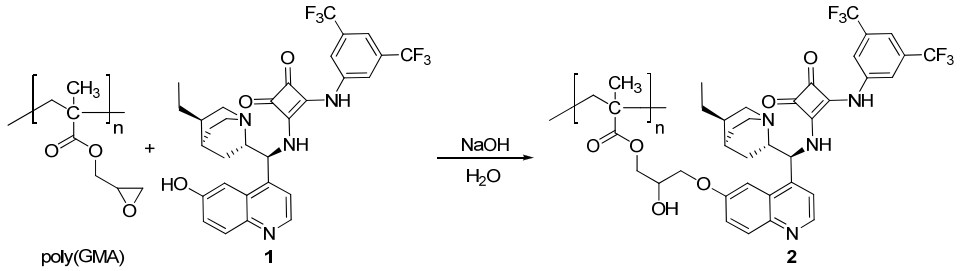

Covalent grafting of cinchona squaramide organocatalyst to poly(glycidyl)methacrylate support.

Acknowledgements:

Servier Beregi Scholarship, Hungarian Scientific Research Fund (OTKA K112289)

Registration of phenomena associated with Rotational Seismology

*Anna Kurzych[1], Leszek R. Jaroszewicz[1], Zbigniew Krajewski[1], Jerzy K. Kowalski[2]
[1]Institute of Technical Physics, Military University of Technology, Warsaw, POLAND
[2]m-Soft Ltd., Warsaw, POLAND
e-mail: anna.kurzych@wat.edu.pl

***Keywords**: interferometer, rotation, seismology, detection*

An earthquake is a release of a stored elastic energy due to a sudden fracture and movement of rocks inside the Earth. The released energy propagates by two types of seismic waves: body and surface waves which arrive at seismic recording stations one after another and travel outward in all directions from the point of an initial rupture. A classical approach in the seismological monographs distinguishes only these linear seismic waves which can vary in such properties like polarization, velocity or direction of the oscillation.

Nevertheless, it does not explain observations of atypical, rotational deformations of architecture structures, for instance tombstones or monuments which appear after earthquakes. A scientific community has revealed several theoretical investigations of the seismic rotational waves but yet there are limited instances of their experimental confirmation. It is caused by the lack of appropriate sensors to detect these movements which are characterized by extremely low signal amplitude even of the order of 10^{-9} rad/s and frequency range from 0.01 Hz to 0.1 Hz.

In this paper we present two sensors basing on the Sagnac effect which give opportunity to record rotational seismic phenomena and their first data recorded in seismological observatory located in Książ, Poland. The obtained signals by both systems are characterized by a high correlation coefficient of the order of 0.97.

Acknowledgements
This work was supported by National Science Centre, Poland under project 2016/23/N/ST10/02508

From low-molecular weight analogues to carbon nanotubes – chemistry of azides toward functionalization of sp^2-nanocarbons

*Anna Kuziel, Anna Kolanowska, Sławomir Boncel
Department of Organic Chemistry, Bioorganic Chemistry and Biotechnology, Silesian University of Technology, Gliwice, POLAND
e-mail: anna.w.kuziel@gmail.com

***Keywords**: carbon nanotubes, azides, surface modification*

Functionalization of carbon nanotubes (CNTs) is of the fundamental importance since it enables their use – due to individualization and/or in-bulk homogenization – in various fields from materials engineering to electronics to medicine. Inter alia, organic azides are useful substrates for numerous organic reactions including azide-alkyne Huisgen cycloaddition, nucleophilic substitution or addition to α,β-unsaturated carbonyl compounds. Nevertheless, so far, the azide-modified CNTs have neither been obtained nor have served as substrates in one-step approaches in the above reactions.

Because of the fact that CNTs may be considered as *quasi*-aromatic structures, the first step of the herein proposed studies was to conduct the initial experiments using low-molecular weight molecules (L-MWMs) (figure below). These compounds (naphthalene, azulene and anthracene) were selected as simplified models potentially mimicking reactivity of the real-morphology nanotubes containing polyaromatic moieties and CNT-wall defects (e.g. Stone-Wales). As the final synthetic target, apart from the comprehensively analyzed L-MWM derivatives (NMR, ESI-MS, FT-IR), azido-multi-wall CNTs shall unveil: (a) full complexity of the sp^2-carbon representatives and (b) possible extension to graphene and its chemical analogues.

Based on a literature survey and the preliminary results, we have indeed selected the most applicable routes of synthesis of azides and their macromolecular counterparts considering high yield, short reaction time and convenient workup.

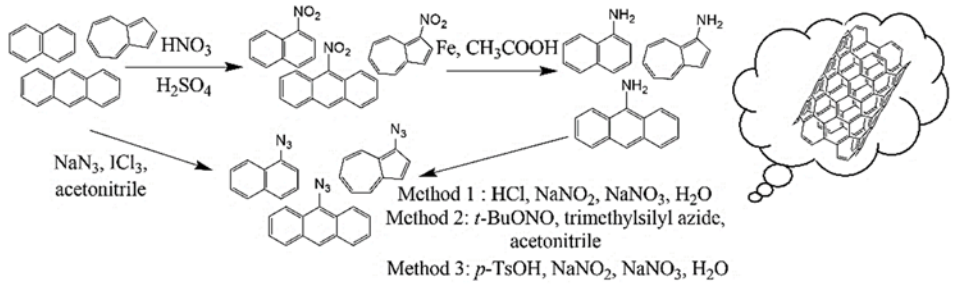

Azide-based modification of L-MWMs as models potentially translatable to CNTs

Acknowledgements
This work was generously supported by The National Centre for Research and Development (Tango, TANGO1/266702/NCBR/2015).

Electrical control depolarization in nematic liquid crystals cells

*Marlena Kwiatkowska, Paweł Marć and Leszek R. Jaroszewicz
Military University of Technology, Warsaw, POLAND
e-mail: marlena.kwiatkowska@wat.edu.pl

***Keywords**: liquid crystal, depolarization, depolarizer, vertically aligned*

Electrically controlled degree of depolarization using liquid crystal has been reported in the literature [Honma and Nose, 2004]. Liquid crystal depolarizer has advantages: can be used for wide wavelength ranges, has a small size. When totally polarized light impinges on liquid crystal, partially un-polarized light may be obtained with negligible scattering and absorption effect. This depolarization found its origin in disordered birefringent medium which cause non-uniform polarization distribution over cross-section of transmitted light [Vena et al. 2014].

A liquid crystal alignment layer could play an important role in depolarizer design and performance. Vertically aligned Nematic (VAN) liquid crystal with zero pretilts in the off state is isotropic for light impinging at normal incidence. Specially prepared measuring system allowed to measure the state and degree of polarization (SOP and DOP). Optical system consisted of crossed polarizer, quarter-wave plate, generator and detector.

Built measuring system allowed to show that the light passing through VAN liquid crystal is depolarized. The degree of polarization depends on the voltage applied to the cell. Minimum degree is about 2%. Obtained results for VAN liquid crystal compared with the result for commercially available polarizer. Result for VAN liquid crystal are better about 40%.

Development and evaluation of an antifouling coating for reverse osmosis membranes which can be applied in modules

*Soraya Laghmari, Mathias Ulbricht
Faculty of Technical Chemistry II, University Duisburg-Essen, 45141 Essen, GERMANY
e-mail: soraya.laghmari@uni-due.de

Keywords: *Reverse osmosis, fouling, desalination, cooling water, steel industry*

The steel industry has a water requirement of 2.3 billion m^3/a for cooling circuits. Due to recirculation as well as evaporation, salts in the cooling water are concentrated during the process and the water is additionally contaminated by particles and oil. In order to maintain the tolerable concentration of salts, a fraction of the circulating water stream has to be removed and replaced by fresh water which seems to be inefficient and not resource-saving. Reverse osmosis (RO) provides a limited alternative for processing water from cooling circuits due to its susceptibility to all types of fouling. Thus, the required performance cannot be achieved without pre-treatment and/or the membranes should be made more resistant to fouling.

In this project, desalination processes based on RO are developed by critically evaluating separation performance of established membranes, by modifying the surface of promising membranes with a suitable antifouling coating and by implementing such membranes in a cooling water circuit for the steel industry. As a first step, the effects of the composition of water from real cooling circuits onto RO performance are examined. Interactions between commercially proven membranes and critical components of the cooling water are investigated in dead-end batch cells with focus on membrane fouling. The membrane performance is then evaluated in a small pilot cross-flow system. Analysis of fouling is complemented by surface characterizations. This provides the basis for the design of antifouling coatings, with amphiphilic properties featuring fouling resistant and fouling release domains. Methods for membrane coating are based on combinations of macro-initiator mediated- and concentration polarization-enhanced grafting and cross-linking reactions, and layer-by-layer assembly of oppositely charged polyelectrolyte building blocks including polyzwitterions. In the last step, the most versatile antifouling coating is transferred to a spiral wound RO membrane module which will be used in pilot scale tests.

Acknowledgements
This work is part of the cooperative project “WEISS” which is funded by the Bundesministerium für Bildung und Forschung (BMBF) within the funding initiative “WavE”.

Synthesis of hydroxyapatite nanoparticles in continuous reactor: preliminary experimental results

*Joanna Latocha, Michał Wojasiński, Paweł Sobieszuk, Tomasz Ciach
Faculty of Chemical and Process Engineering, Warsaw University of Technology, Warsaw, POLAND
e-mail: joanna.latocha.dokt@pw.edu.pl

***Keywords**: hydroxyapatite, nanoparticles,synthesis in continuous reactor*

Among all the methods for producing hydroxyapatite (HAp), synthesis in batch reactor is the most common because of its simplicity. Synthesis in continuous reactor seems to be promising way to obtain a better control over the reaction conditions. Production of hydroxyapatite nanoparticles using ultrasonic tubular microreactor, meso-oscillatory flow reactor, tube-in-tube microchannel reactor, among the others, has been reported in literature. Conducting wet chemical precipitation in continuous reactor is a simple way to produce hydroxyapatite nanoparticles with controlled properties. We present preliminary results of HAp nanoparticles synthesis using a two Y-type microreactors with 1 mm in inner diameter both and 10 mm or 150 mm in length.

We synthesized hydroxyapatite in presence of lecithin (3g/l) by chemical precipitation method using solution of $Ca(NO_3)_2 \cdot 4H_2O$ and solution of $(NH_4)_2HPO_4$ in ultra-pure water as starting media. Ca:P molar ratio was maintained at 1.67 as in a stoichiometric HAp. Synthesis was conducted in continuous reactors under atmospheric pressure and room temperature with each starting media flow rate of 500 ml/h and aged in room temperature. Resulting powders were characterized by Fourier transformed infrared spectroscopy (FTIR), scanning electron microscopy (SEM), nanoparticle tracking analysis (NTA), dynamic light scattering (DLS) and zeta potential measurement.

FTIR spectra shows signals from phosphate PO_4^{3-} and hydroxyl OH^- functional groups characteristic of a typical hydroxyapatite. Analysis of SEM images display structure consisting of spherical particles with size 15±3 nm and 11±2 nm, for short and long microchannel respectively. Both NTA and DLS methods demonstrate broad particle size distribution indicating particles aggregation. Potential zeta around –20 mV confirms their tendency to aggregate.

In conclusion, this preliminary results present a simple and low cost method to produce modified hydroxyapatite in continuous reactor with controlled morphology and particle size dependent on length of microchannel.

Acknowledgements

Funding: “Innovative polymer composites for filling bone defects.” POIR.04.01.04-00-0133/15 Project was financed by European, European Regional Development Fund in frame of Smart Growth Operational Program for 2014-2020, operation 4.1. “Research and development”.

The effect of substituents on direct polycondensation and properties of aliphatic polyester-amides

*Levente Karpati[1], Gergely Hamar[1], Ádám Ganyecz[1], Viktória Vargha[1]
[1]Department of Physical Chemistry and Materials Science, Budapest University of Technology and Economics, Budapest, HUNGARY
e-mail: karpati.levente@mail.bme.hu

***Keywords**: polyester-amides, direct polycondesnsation, substituents, thermal properties*

Polyester amides (PEA) derived from their special structure are promising materials. Their properties can be tuned according to molecular structure and the distribution of ester and amide groups along the polymer backbone. These polymers are biodegradable and biocompatible. In this study amino alcohols have been reacted with adipic acid. We examined the effect of substituents of amino alcohols on the polycondensation reaction and product properties. The studied amino alcohols were 1-amino-ethanol, 2-amino-1-propanol, 2-amino-1-butanol and 2-amino-2-methyl-1-propanol. A two-step direct polycondensation method was used. The reaction products were examined with functional group analysis, gel permeation chromatography (GPC), FTIR and NMR spectroscopy, differential scanning calorimetry (DSC), thermogravimetric analysis (TGA), wide angle X-ray scattering (WAXS) and oscillation rheometry. Pressed plates were made to the practical biodegradability in compost.

Based on the results of functional group analysis and GPC we assume that the substituent had a negative effect on the reactivity of the functional groups resulting in a significant decrease in molecular weight. The FTIR spectra proved the ester-amid structure of the polymers, NMR spectroscopy confirmed the assumed fine structure of the reaction products. According to the DSC data PEA are elastomers with glass transition temperature below room temperature. The DSC and WAXS measurements showed that the crystalic PEA has two different crystal phases. Interestingly we have observed higher complex viscosity with 2-amino-1-butanole, than 1-amino-ethanol which had higher molecular weight. After 25 days in compost the pressed plates completely disappeared.

The results of this study indicate that small substituents like methyl, and ethyl groups can have significant effect on the end-products of direct polycondensation.

Acknowledgements
One of the authors (KL) kindly thanks for the support of the ÚNKP 17-3 Hungarian New National Excellency Program.

Analysis of *wake* structures in bubbly flows using *Particle Image Velocimetry* (PIV)

*Björn Lewandowski[1,2], Micha Fertig[2], Georg Krekel[2], Mathias Ulbricht[1]
[1] Chair of Technical Chemistry II, University of Duisburg-Essen, Essen, GERMANY
[2] Faculty of Chemistry, University of Applied Sciences Niederrhein, Krefeld, GERMANY
e-mail: Bjoern.Lewandowski@hs-niederrhein.de

***Keywords**: Bubbly flow, Particle Image Velocimetry, wake analysis, flow characteristics, high-speed imaging*

Multiphase gaseous-liquid flows play an important role in the chemical industry, e. g. in bubble column reactors. A detailed insight into flow patterns and velocities is possible with optical methods, like *Particle Image Velocimetry* (PIV). Application to multiphase flows is, however, challenging due to the presence of different phases and the complex flow structures. In particular, unwanted reflections of irradiated light at the phase boundaries complicate the analysis.

A detailed study of the flow structure of rising single bubbles of air in water was conducted in a modular apparatus made of poly(methyl methacrylate) using a high-speed camera and a continuous wave laser. The focus of this study was the investigation of the flow structure behind the bubble in the so-called *wake*. Additionally, the liquid flow around the bubble was analysed. The bubble diameter and the bubble creation frequency were manipulated using different volumetric gas flow rates. Furthermore, the bubble surface tension was selectively modified using added surface active reagents.

It could be shown that a vortex street was induced in the *wake* of the bubbles, which influenced the rising path of following bubbles significantly. The vortex street was observed at bubble Reynolds numbers of 500-1000, where a zigzagging rising path was present. At every deflection point of the rising bubble, vortex structures with a diameter of several millimetres were observed. The circumferential speed of these vortices was in a similar scale as that of the rising bubbles. Furthermore, the region with turbulent flow structures was observed to expand in the process volume with rising volumetric gas flow rate. Using surface active reagents, spherical bubbles could be formed. Their flow structure was alike that of rigid spheres.

Investigation of formation and characteristics of heterocoagulates in flotation processes with *Shadowgraphy*

*Björn Lewandowski[1,2], Christina Nielsen[2], Georg Krekel[2], Mathias Ulbricht[1]
[1] Chair of Technical Chemistry II, University of Duisburg-Essen, Essen, GERMANY
[2] Faculty of Chemistry, University of Applied Sciences Niederrhein, Krefeld, GERMANY
e-mail: Bjoern.Lewandowski@hs-niederrhein.de

***Keywords**: Flotation, surface chemistry, high-speed imaging, Shadowgraphy, heterocoagulates*

The flotation process is, with approx. two billion metric tonnes floated crude ore per year, one of the most important processes for the enrichment of valuable minerals. Many works on the investigation of flotation processes are available in literature. However, most of these deal with empirical optimisation of the process parameters. The main goal is often to maximize the separation efficiency. Nevertheless, the process has not yet been fully understood, since modelling of mechanical processes is mainly based on empirical correlations. Optical methods, such as *Shadowgraphy* and *Particle Image Velocimetry* (PIV) could help to improve the understanding of the basic principles of flotation.

In the present work the flotation process was investigated experimentally in a transparent flotation cell made of poly(methyl methacrylate) using glass particles as model system. A design of experiments (DoE) was performed to find optimal process parameters for particle recovery regarding the volumetric gas flow rate, the concentration of collector (hexadecylamine) and the concentration of frother (4-methyl-2-pentanol). Additionally, the surface of the glass particles was selectively modified using different silane reagents, e. g. ethyltriethoxysilane and 1H,1H,2H,2H-perfluorooctyltriethoxysilane. These modified particles were floated without using a collector. Thus, the influence of wetting on particle recovery by flotation could be investigated. Furthermore, image sequences of rising heterocoagulates could be filmed with help of a Shadowgraphy system, consisting of a high-speed camera and a LED backlight illumination.

It was found that the concentration of the collector had the greatest influence on recovery, followed by the concentration of frother. The volumetric gas flow rate had no significant influence in the observed regime. Furthermore, the wetting of particles had a great influence on flotation recovery. Hydrophobic particles were better floated than hydrophilic ones. Different types of formed heterocoagulates were filmed. In most of the cases, bubble clusters with multiple bubbles and multiple particles were observed.

The influence of addition of bismuth oxide on the properties of low-melting glazes

*Ewa Litwinek[1], Piotr Izak[1], Łukasz Wójcik[1], Marcin Gajek[1]
[1]Faculty of Materials Science and Ceramics, AGH University of Science and Technology, Cracow, POLAND
e-mail: ewa.litwinek@gmail.com

***Keywords**: frit, glazes, bismuth oxide, roof tiles*

The market of roof tiles is evolving, looking for more and more solutions. Most ceramic roof tiles are covered with engobes, which improve the properties of tiles and have a decorative function. The demand of espiecially Polish market brings that glossy, dark-coloured, low-melting glazes are used in production of roof tiles. In the final step of production the roof tiles are covered with a thin layer of glaze and then fired at around 1050°C. As a result of these processes, the final product is covered with a homogeneous glossy glaze, which gives a smooth surface. The surface reduces the adhesion of contamination and inhibits to cover the surface of roofing with moss.

The purpose of this study was to investigate the influence of bismuth oxide on the properties of low-melting glazes used as a coating for ceramic roof tiles. The composition of low-melting frits were created and then they were modified by the addition of bismuth oxide. Compositions of glazes were fritted in temperature 1300°C, and on their basis were prepared red wine color glazes. Thermal properties including coefficient of linear thermal expansion was detemined by dilatometry and softening points were determined by heating microscopy. The colour of fired samples was measured by spectrophotometry.

These studies showed that the addition of bismuth oxide affects the properties of the low-melting frits and depends on their composition. Modified frits give rise to a low-melting glazes of red wine color. It is necessary to continue research in order to optimize the composition of the glazes.

Caffeine detection on glassy carbon electrode modified by composed nanoparticles of titanium dioxide – conductive polymer

*Łukasz Magda[1], Katarzyna Wilkosz[1], Władysław W. Kubiak[1]

[1] Department of Analytical Chemistry, Faculty of Materials Science and Ceramics, AGH UST University of Science and Technology, Kraków, POLAND
e-mail: lukasmag@agh.edu.pl

***Keywords**: nanomaterials, nanoparticles, titanium dioxide, electrode modification*

The purpose of this work is to shows the possibility of modifying the voltammetric electrode using ceramic nanopowders such as titanium dioxide (TiO_2). Electrochemical sensors using conductive polymers such as Poli(3,4-etyleno-1,4-dioksytiofen) or other conductive polymers as modifiers are increasingly applied. The advantages of the conductive layers membranes are good durability, high density and time of preparation.

The determined substance is caffeine. This is an organic chemical compound, purine alkaloid found in coffee beans and many other plant raw materials. It can also be obtained synthetically. It was discovered by the German chemist Friedrich Ferdinand Runge in 1819. Depending on the source, it is also called tein (when the source is tea), guaranine (when it comes from guarana) and matein (when it comes from yerba mate). Caffeine is a psychoactive drug from the group of stimulants. It is used as an additive to certain products, including energy drinks, as well as other beverages, mainly carbonated drinks (for example colas). After a longer period of regular caffeine intake, the phenomenon of tachyphylaxis (tolerance) occurs, ie a gradual weakening of the biological response of the body.

Voltammetric methods, due to its numerous advantages are a tool often used by the modern scientists. They are characterized by high sensitivity, selectivity for molecules electroactive, a wide range of linearity, portable, inexpensive apparatus and a large variety used electrodes. The great advetage is possibility to determine very low concentrations of substances in very small samples. The research technique used is cyclic voltammetry. This technique is most popular in experiments of quality and diagnostic

Acknowledgements
This study was carried out within the AGH – University of Science and Technology (Kraków), Grant Number. 15.11.160.017.

The influence of nanopowder on the analytical signal from caffeine

*Łukasz Magda[1], Katarzyna Wilkosz[1], Władysław W. Kubiak[1]
[1] Department of Analytical Chemistry, Faculty of Materials Science and Ceramics, AGH UST University of Science and Technology, Kraków, POLAND
e-mail: lukasmag@agh.edu.pl

***Keywords**: caffeine, nanopowders, analytical signal, voltametry, conductive polymers*

Titanium oxide is characterized by very good photocatalytic properties thanks to its application in many branches of technology. This work shows the use of titanium oxide (TiO_2) nanoparticles of varying degree of fineness for the modification of glassy carbon electrodes used in voltammetry. This experiment shows the possibility to use nanoparticles as a possibility of further modification of the measurement electrodes in order to improve their operational parameters.

Voltammetry is an analytical technique, which is based on the measurement depending on the current - electric potential in a working electrode and a reference immersed in a solution containing the test determined the substance and electrolyte primary. Voltammetric methods, due to its numerous advantages are a tool which is often used by the modern scientists. They are characterized by high sensitivity, selectivity for molecules electroactivity, a wide range of linearity, portable inexpensive apparatus and a large variety used electrodes. The great advantage is possibility to determine extremly low concentrations of substances in very small samples. The research technique that is used it is a cyclic voltammetry. This technique is the most popular in experiments of quality and diagnostic. Measuring system consists of three electrodes such as working electrode, reference electrode and auxiliary electrode. These electrodes are immersed in the solution containing the analyte analyzed.

The conductive layer was prepared using electropolymerization of the nanopowder suspension in conductive polymers. The glassy carbon electrode was polished on the polishing cloth with nanopowders Al_2O_3 and washed with deionized water . The solution before electropolymerization had been mixed using a magnetic stirrer.

For received layers there were taken pictures of Scanning Electron Microscope(SEM) and energy dispersive spectroscopy (EDS), then analysed in order to illustrate their structure.

Acknowledgements
This study was carried out within the AGH – University of Science and Technology (Kraków), Grant Number. 15.11.160.017.

The development of an innovative method of bioreceptor layer deposition in biosensor construction

*Szymon Malinowski[1], Justyna Jaroszyńska-Wolińska[1], Cecylia Wardak[2]
[1]Faculty of Civil Engineering and Architecture, Lublin University of Technology, Lublin, POLAND
[2]Maria Curie-Skłodowska University, Faculty of Chemistry, Lublin, POLAND
e-mail: s.malinowski@pollub.pl

Keywords: *laccase, biosensor, soft plasma polymerization method, laccase bio-reception layer*

Biosensors are devices widely used in many areas of industry and science in chemical compounds quantitative determination. They are composed of two key parts: (I) biologically active reception layer (bio-reception layer) and (II) transducer. Bio-reception layer is created by immobilization biologically active species i.e. enzymes, antibodies, nucleic acids and is responsible for creation of signal which is subsequently transformed into useful analytical signal by transducer. Most of biosensors are devices with enzymes i.e. acetylocholinesterase, acid phosphatase, alkaline phosphatase, glucose oxidase, lipase or especially laccase. Laccase enzymes are popular in biotechnology for biosensor construction because of their redox properties. Currently laccase biosensors are constructed on the way "wet" methods of bio-reception layer deposition, which are complex and time consuming. In many cases these procedures need overnight storing of electrode in enzyme solution in order to immobilization and receiving of bio-reception layer.

The main aim of this work was elaboration of new, faster, one-step method of bio-receptor layer deposition by soft plasma polymerization method. The basis of this method is deposition of biological precursor introduced into corona discharge plasma reaction zone in He carrier gas stream. Application of this method allow to biosensor construction without conditioning of electrode in enzyme solution.

The development of a new, faster and greener way to obtain bioreceptor layer is extremely important due to their increasing demand in the production of biosensors, especially in the era of the growing importance of environmental protection.

Acknowledgements
We acknowledge support from Polish Ministry of Science and Higher Education within the statutory research number S-12/II/B/2017.

Influence of carrageenan and cationic surfactants on the stability of the alumina suspension

*Jakub Matusiak, Elżbieta Grządka
Department of Radiochemistry and Colloid Chemistry, Maria Curie-Skłodowska University, Lublin, POLAND
e-mail: jakub.matusiak@umcs.pl

***Keywords**: stability, colloids, polysaccharide, carrageenan, adsorption*

Colloidal systems are unstable in time. There are different factors that influence stability of such systems, e.g. temperature, addition of surfactants or macromolecules, pH etc. The addition of polymer to the system can change its properties. Regarding to the situation whether the polymer adsorbs on the surface of the colloidal particles or not, different mechanisms of stability can be distinguished. The most common one is the steric stabilization, which occurs in the situation when the polymer is adsorbed on the solid surface. The consequence of that is the higher repulsion between the colloidal particles. The electrosteric mechanism is similar to the steric stabilization, but the difference is the ionic character of the adsorbed polymer. In the situation when the polymer does not adsorb on the surface of colloidal particles, the depletion stabilization can occur. Free non-adsorbed polymer chains situated in the bulk of the solution reduce the interactions between the colloidal particles. The addition of macromolecules might cause the destabilization of the system as well. Two different types of destabilization such as bridging and depletion flocculation can be mentioned. Both mechanisms result in the destabilization of the system which is the consequence of the aggregation or sedimentation of the colloidal particles.

As it was mentioned above, the addition of surfactants can influence the stability of the studied systems as well. Because of the interactions between polymers and surfactants, different structures can (or not) be formed. As a result of that, properties of the studied systems can change drastically.

The main goal of this research was to investigate the influence of the addition of carrageenan, its concentration and the addition of surfactants (MTAB, S-106-a, Silquat J2) on the stability of the colloidal suspensions of alumina. For the full examination of such system, the adsorption measurements have to be conducted.

The obtained results indicate, that the stability of alumina suspension increases with the concentration of carrageenan as well as after the addition of surfactants. Based on the conducted measurements, it can be stated that stability mechanism in this system is the electrosteric stabilization.

Tensiometric and conductometric studies of the cationic starch/anionic surfactants complexes

*Jakub Matusiak, Elżbieta Grządka
Department of Radiochemistry and Colloid Chemistry, Maria Curie-Skłodowska University, Lublin, POLAND
e-mail: jakub.matusiak@umcs.pl

***Keywords**: starch, polymers, surfactants, complexes, surface tension*

Surface active agents (surfactants) are the compounds that possess the ability to lower the surface tension. There are different types of such molecules, for example conventional hydrocarbon surfactants, fluorinated surfactants and silicon ones. What makes them so special is their structure. Surfactants are composed of the hydrophilic head and hydrophobic tail. Because of the electrical charge of the head, they can be divided into cationic, anionic, zwitterionic and non-ionic. When placed in a liquid solution, at certain concentration surfactants start to aggregate to form micelles. This concentration is called critical micelle concentration (CMC).

Addition of different macromolecular compounds, such as polymers, can change the properties of the surfactant solution. Due to the interactions between surfactants and polymers, different structures can be formed. In this case, the critical aggregation concentration has to be described. It is the concentration, in which the polymer starts to interact with the surfactant. Polymer/surfactant complexes are very important problem in many branches of science and industry. The addition of polymers to the surfactant solutions can help to achieve better properties, for example to overcome the negative influence of the surfactants on the human organism. It is especially important in the cosmetic and pharmaceutical formulations. There are different methods that can be used to study the interactions between polymer and surfactants, such as tensiometry, conductometry, microcalorimetry, voltammetry and NMR spectroscopy.

Main goal of this research was to investigate the influence of cationic starch on the surface tension of three different anionic surfactants: fluorinated Capstone FS-91, conventional SDS and silicon Silphos A-100. The obtained results show, that cationic starch can form complexes with some of the mentioned surfactants, resulting in lower surface tension values for the polymer/surfactant solutions than for pure surfactant solutions.

Adsorption and electrokinetic properties of the cationic starch/silica system

*Jakub Matusiak, Elżbieta Grządka
Department of Radiochemistry and Colloid Chemistry, Maria Curie-Skłodowska University, Lublin, POLAND
e-mail: jakub.matusiak@umcs.pl

***Keywords**: starch, polymers, surfactants, complexes, surface tension*

The adsorption of organic compounds plays an important role in many branches of industry as well as in the academic research. The process of the polymer adsorption is complicated and the final outcome depends on many factors e.g. the type of polymer and its molecular weight, the type of used adsorbent and other environmental factors such as temperature. The addition of macromolecules is used in many industrial formulations in order to gain stable products under different conditions. Depending on the fact, whether the polymer adsorbs on the surface of the colloidal particles or not, different mechanisms of the stabilization can be observed. This is the reason why the measurements of the adsorption of such molecules are very important. For the full description of the colloidal systems the electrokinetic properties such as zeta potential and surface charge density can be used.

The polymer used in the studies was cationic starch (CS), which is a cationic polyelectrolyte produced by chemical reaction of starch with various reagents possessing positively charged groups (amino, ammonium, imino, sulphonium, phosphonium). Introducing a positively charged group to starch provides good mineral binding properties. Many commercial products widely used in different fields contain cationic starch. Among them, the most important are papermaking chemicals, drug delivery systems, daily chemicals and petroleum.

The aim of this study was to investigate the adsorption of cationic starch on the surface of silicon dioxide as well as the electrokinetic properties of the SiO_2/CS/NaCl system. To determine cationic starch adsorption, Dubois colorimetric method was used. The influence of both factors: the concentration as well as pH on the zeta potential was investigated. In order to determine the changes in the zeta potential of the silicon dioxide suspensions before and after the addition of cationic starch, the dynamic light scattering method was used. Obtained values of the electrophoretic mobility were calculated into the zeta potential using the Smoluchowski equation. Potentiometric titration was used to determine the surface charge density of the studied systems.

Electrochemical synthesis of nanostructured ZnO in sodium hydroxide electrolyte

*Krystyna Mika[1], Leszek Zaraska[1], Grzegorz D. Sulka[1]
[1]Department of Physical Chemistry and Electrochemistry, Faculty of Chemistry, Jagiellonian University, Kraków, POLAND
e-mail: mika@chemia.uj.edu.pl

***Keywords**: zinc oxide, anodization, sodium hydroxide*

Nanostructured semiconducting materials are excellent candidates for both: photoelectrochemical water splitting and photocatalysis. These two applications are especially important due to the gradual depletion of fossil fuels as well as increasing environment pollution, respectively. Zinc oxide (ZnO) due to its properties, which can be further improved by using nanostructured architecture, is very promising material for these applications.

Anodic oxidation (anodization) seems to be simple and inexpensive method for the synthesis of various ZnO nanostructures. Appropriate optimization of anodization conditions, e.g. the value of applied potential, electrolyte composition, duration and temperature of the process allows to obtain certain ZnO nanostructures. A big advantage of anodization is also possibility to prepare semiconducting nanostructures directly on the metallic surface. It provides a direct electric contact between semiconductor and conductor (that is especially beneficial in photoelectrochemical applications) and significantly improves mechanical stability of the photoelectrode.

Here we present some recent studies on electrochemical fabrication of nanostructured zinc oxide layers. ZnO nanostructures were obtained by anodic oxidation of metallic zinc in sodium hydroxide with different concentrations. Anodization was performed at various anodizing potentials at room temperature. Various sets of parameters including applied potential, electrolyte concentration and time of the process were examined to check morphology changes of the anode surface and to establish the mechanism of nanostructures growth. The morphology of the obtained ZnO layers was analysed by using a Field Emission Scanning Electron Microscope. The crystallinity and phase composition of the obtained ZnO nanostructures were examined by XRD measurements.

Acknowledgements
This work was partially supported by National Science Centre, Poland (Project no. 2014/13/D/ST5/02750).

The study of ruthenium-based catalysts used in homogeneous transfer hydrogenation of ketones

Filip Mikołajczyk, Kamil Kamiński
Faculty of Process and Environmental Engineering, Lodz University of Technology, POLAND
e-mail: mikolajczyk.filip.pl@gmail.com

Keywords: *ruthenium-based catalysts, transfer hydrogenation, ketones, catalysis,* $RuCl_2(PPh_3)_3$

A detailed comparison of catalytic properties of two different ruthenium-based catalysts in reaction of homogeneous hydrogenation of acetophenone was performed. Additionally, methods of synthesis of both catalysts were tested and optimized in order to achieve the best possible quality and purity.

NMR analysis was used to analyze and identify composition of ruthenium compounds and gas chromatography was used to analyze conversion rate of reactions of hydrogenation.

It was determined that $RuCl_2(PPh_3)_3$ obtained with modified method described by Shaw's group had the best catalytic properties in reaction performed under conditions described in Liang Wang's publication. It was also determined that for concentration ratio of substrate to $RuCl_2(PPh_3)_3$ amounting to 250:1 conversion rate was much higher than for reaction performed with double dose of catalyst. Results of experiments also shows that samples of post-reaction solution should be analyzed right after reaction, because even if they are stored in low temperature amount of product can change up to 3-5% compared to base sample and this change is not predictable.

These findings have significant implications for further research of reaction of homogeneous transfer hydrogenation of ketones. With right catalysts and methods of their synthesis other parameters of this reaction can be changed and optimized. The most important one is a change of solvent from isopropyl alcohol to less toxic substance. This may result in increasing value of its reaction in green chemistry and chemical industry.

Acknowledgements
This research was supported by Department of Process Thermodynamics and Department of Numerical Modeling located at Faculty of Process and Environmental Engineeringat Lodz University of Technology. In performing this work, we also had help and guidance of Mr. Jerzy Petera and Mr. Radosław Bonikowski from Lodz University of Technology.

The effect of connecting a tapered optical fiber with a liquid crystal mixture

*Joanna Moś, Karol Stasiewicz, Leszek R. Jaroszewicz
Institute of Technical Physics, Military University of Technology, Warsaw, POLAND
e-mail: joanna.musial@wat.edu.pl

***Keywords**: tapered optical fiber, liquid crystal mixture, optical sensors*

This paper presents an analysis of a theoretical and experimental properties of a light beam propagation in an optical taper fiber with a liquid crystal clad. Heating and stretching in a high temperature a small optical fiber segment causes decreasing of the fiber's dimension simultaneously providing a leakage of a light beam which propagates in that fiber taper. Discussed phenomenon is accompanied by the possibility of changing the propagation parameters of the beam by applying an additional material which forms the clad of a "new fiber". In presented research it is an anisotropic material – a liquid crystal mixture.

Tapered optical fibers are manufactured using the Fiber Optic Taper Element Technology (FOTET) Device. Fibers are characterized by the following parameters: loss lower than 0.5 dB for a broad range, diameters of a taper waist equal to 15.5 ± 0.5 μm. In the next part of research, parameters of the built liquid crystal cell – with an indium tin oxide (ITO) layer (which gives a possibility to change orientation of a liquid crystal molecules by an applied electric field) and alignment layers (which give the initial orientation of molecules) are described. The cell is filled with a liquid crystal mixture of 1550 characterized by the parameters of the extraordinary reflective index n_e=1.5276 and the ordinary reflective index n_o= 1.4618 measured for wave length 532 nm.

The results show changes of a spectral characteristics depended on temperature in a range of 20-50^{o}C and applied electric field in the range of 0-180 V with and without modulation of the electric signal with a frequency of 1-10 Hz.

As the voltage and temperature increase, the power of the propagating light beam in an optical fiber increases. The liquid crystal cell with a tapered optical fiber transfers the modulation of the electrical signal to spectral characteristics. The results may be the basis for the construction of optical devices such as sensors and filters.

Optimization and homogeneous catalysis of aza-*Markovnikov* reaction using cinchona organocatalysts and their recycling by organic solvent nanofiltration

Sándor Nagy, Zsuzsanna Fehér, Péter Kisszékelyi, Péter Huszthy, *József Kupai
Faculty of Chemical Technology and Biotechnology, Budapest University of Technology and Economics, Budapest, HUNGARY
e-mail: jkupai@mail.bme.hu

Keywords*: organic solvent nanofiltration, organocatalysis, cinchona alkaloids, aza-Markovnikov, catalyst recovery*

Aza-*Markovnikov* addition is a type of useful nitrogen-carbon bond-forming reaction. It is especially important to synthesize bioactive *N*-heterocycle derivatives with a nitrogen-carbon linkage which could be achieved by an addition reaction. 1-[*N*-(*N*-Heterocycle)] alkyl esters possess valuable biological activities and can act as, amongst others, acaricides, antitumor drugs, and (H^+–K^+)-ATPase inhibitors.

Three cinchona catalysts were tested in aza-*Markovnikov* additions of different *N*-heterocycles to different esters. Quinine is a commercially available versatile organocatalyst, which was used as starting material for preparing three organocatalysts, its amino and squaramide derivatives.

The feasibility of the application of these catalysts was expanded by using OSN (Organic Solvent Nanofiltration) technique. The chemically stable polybenzimidazole membrane was used for separation of molecules. The pore size of membranes was adjusted by their preparation. With the help of OSN technique the applied organocatalysts became recyclable, furthermore the products of reactions are separable from the reaction mixture. The feasibility of membrane-based separation for catalyst recovery was demonstrated with a potential to keep the catalyst loss below 1% using a two stage cascade configuration (see figure below).

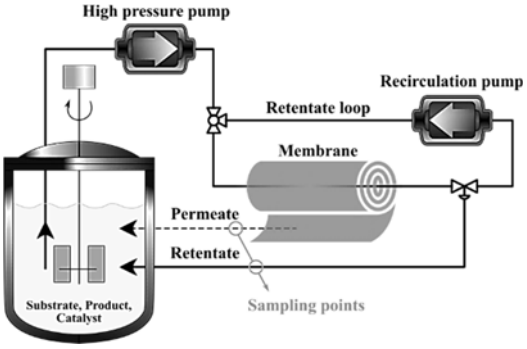

Process scheme of the experimental set-up for cross-flow membrane filtration.

Acknowledgements
Financial support: Servier Beregi Scholarship, Hungarian Scientific Research Fund (OTKA K112289)

Formation and examination of well-attached layer to the amorphous metal surface

*Jolanta Nieorda[1,2], Andrzej Rybak[2], Maciej Sitarz[1]
[1]Faculty of Materials Science and Ceramics, AGH University of Science and Technology, Krakow, POLAND
[2]ABB Corporate Research Center, Krakow, POLAND
e-mail: jolanta.nieroda@agh.edu.pl

***Keywords**: metallic glass, adhesive layer, tetraethoxysilane, 1,2-Bis(triethoxysilyl)ethane,*

Metallic glass foil is one of the newest material used in transformers manufacturing. As it is characterized with low magnetic losses and high electrical resistivity it has been used for laminated core production. Transformers equipped with this kind of magnetic core exhibit up to 70% lower core losses in relation to standard devices (Ramanan, 2012). Despite such a good achievement, researches related to this material are still continued. In order to obtain well-attached layer to metal surface, used compound should contain hydroxide groups. Well-known materials with reactive hydroxide groups are silanes in hydrolysed forms. As they can form metal-oxane bonding (M-O-Si), they are a perfect candidates to be applied on metal surface.

Presented work contains results of covering Metglas 2605 foil with layers based on different silane precursors. Two types of silanes were used: tetraethoxysilane (TEOS) and dipodal 1,2-Bis(triethoxysilyl)ethane (BTSE). Both of them were prepared with acidic hydrolysis, while TEOS was additionally processed with base catalyzed hydrolysis. Samples of Metglas 2605 foil was covered with one or two layers of obtained solutions and were characterized with scanning electron microscopy, confocal microscopy and Raman spectroscopy.

The selected analytical methods were used to compare the received layers in order to select the best surface modification characterized by smooth coating without cracks on amorphous metal foil. Moreover, chemistry of obtained layers was studied and differences were indicated.

Applied methodology allow to choose an appropriate silane layer and manufacturing parameters in order to obtain well-attached and uniform layer on Metglas 2605foil.

Influence of plasma treatment factors on final properties of metallic glass surface

*Jolanta Nieroda[1,2], Andrzej Rybak[2], Maciej Sitarz[1]
[1]Faculty of Materials Science and Ceramics, AGH University of Science and Technology, Krakow, POLAND
[2]ABB Corporate Research Center, Krakow, POLAND
e-mail: jolanta.nieroda@agh.edu.pl

***Keywords**: metallic glass, plasma, design of experiments*

Plasma treatment is a well-known method for surface energy activation. It combines both cleaning and oxidizing pretreatment if adequate working gases are used. During plasma treatment, the applied energy causes gas activation and as a consequence an ionized gas called plasma is obtained. In contact with surface, plasma removes some atoms from surface and/or apply other compounds from used gas. Final effect of plasma treatment is dependent on the four parameters, namely: power, time, pressure, and gas composition. Appropriate matching of these factors allows to obtain a highly reactive surface.

In the presented work, influence of plasma parameters on surface free energy and wetting properties of metallic glass foil Metglas 2605 by polar solvent was studied. Design of experiments method (DOE) was used and four factors were variable: 10-80% of plasma power, 1-5 minutes of treatment time, 0.1-0.4 mbar of gas pressure and different gas composition: 90% of argon + 10% of oxygen or 10% of argon + 90% of oxygen. Surface free energy and wetting properties of treated samples were measured by means of contact angle measurements with sessile drop method.

Used parameters led up to 117% of relative increase of surface free energy of tested amorphous steel. Moreover, impact of plasma treatment parameters on wetting properties with polar solvent for each single factor as well as for their combinations was calculated.

The very high improvement of material properties was achieved, what confirms appropriateness of plasma treatment application in order to modify Metglas 2605 foil. Moreover, obtained results allow to select the most appropriate values of plasma treatment in order to obtain the best surface properties as possible.

Numerical simulation of LVAD inflow cannula effect on stagnation and recirculation zones in left ventricular

*Mikhail Nosov[1], Vladimir Malgichev[2]
[1]Department of Biological and Medical Physics, Moscow Institute of Physics and Technology, Moscow, RUSSIAN FEDERATION
[2]Dona-M Ltd, Moscow, RUSSIAN FEDERATION
e-mail: mikhail.nosov@phystech.edu

Keywords*: left ventricular assist device (LVAD), inflow cannula, thrombosis, OpenFOAM, heart*

Cardiovascular diseases are globally the most common cause of death today. Each year it causes over 4.3 million deaths in Europe, 48% of all deaths. In the USA statistics show that for the 50,000 patients awaiting heart transplant only 2,500 donor hearts become available each year.

Left Ventricular Assist Device (LVAD) is a mechanical circulatory device used to support failed heart by pumping blood from left ventricle to the aorta. The inflow cannula is the connection between the apex of left ventricle and the pump of LVAD. Due to deficit of donor hearts, for many patients this is the only chance to survive.

Pump thrombosis is one of the main causes for device malfunction, and patients are exposes to the risk of sudden death. Thrombus formation arises from the combined effect of elevated shear stress levels and recirculating flow patterns in specific regions within a device.

To investigate the correlation between LVAD cannula tip design and potential for stagnations and recirculation zones formation in left ventricular, analysis of the intraventricular flow field was numerically computed by computation fluid dynamics (OpenFoam-extend_3.2). Seven different cannula tips were simulated, blunt (5 mm, 15 mm), trumpet, beveled, caged, crown (Incor), blunt 25 mm (AVK-N).

The results showed that the cannula tip design affected the stagnation and recirculation zones size. Among these seven cannulas, caged, crown and trumpet cannulas owned the minimal zones thrombosis formations size. The study indicated that the caged tip is the most suitable for LVAD.

The influence of addition of the zirconium oxide on some technological parameters of the raw porcelain glaze

*Katarzyna Pasiut[1], Janusz Partyka[1]
[1]Faculty of Materials Science and Ceramics, AGH University of Science and Technology, Kraków, POLAND
e-mail: kpasiut@agh.edu.pl

***Keywords**: glazes, zirconium oxide, viscosity, HSM*

The research focused on the influence of addition of zirconium oxide on some technological parameters of porcelain ceramic glazes, which were created to fire at temperature 1230°C. The examined glazes had a constant molar ratio of SiO_2/Al_2O_3 = 4, CaO/MgO = 1 and Na_2O/K_2O = 1. To these glazes, the zirconium oxide was added in five different amounts (1.5; 3; 6; 12; 24 wt%). Glazes were ground in a planetary mill for 30 minutes and dried. Raw glazes were used to designate the characteristic temperature at High Stage Microscopy (HSM). Fired glazes were used to dilatometric measurements.

As the result of examination some parameters were obtained such as: characteristic temperatures obtained by HSM and dilatometric measurements by mechanical dilatometer, coefficient of thermal expansion by dilatometric method and the viscosity of glaze as a function of temperature, using *Vogel* – Fulcher –*Tammann models.*

The obtained results indicate on a lot of important dependencies between the content of zirconium oxide in glaze and examined properties such as decreasing characteristic temperatures and viscosity and increasing of the coefficient of thermal expansion of analysed glazes.

Acknowledgements
This research work has been carried out thanks to financing in the framework of NCBiR (Polish National Research and Development Committee) program PBS1/B5/17/2012

The influence of addition of the zirconium oxide on some surface parameters of the raw porcelain glaze

*Katarzyna Pasiut[1], Janusz Partyka[1]
[1]Faculty of Ceramic and Refractory Materials, AGH University of Science and Technology, Kraków, POLAND
e-mail: kpasiut@agh.edu.pl

Keywords: *glaze, porcelain, zirconium oxide, whiteness, gloss, roughness*

The appearance of a surface of glazed products gives information about a quality of products. Whereas it is important to take into account not only parameters describing the appearance of the surface and also parameters describing the properties related to the use of a product, eg. chemical durability or stain resistance. These researches were carried on the influence of adding the zirconium oxides on the surface parameters, for firing temperature 1230°C. The examined glazes had a constant of molar ratio of $SiO_2/Al_2O_3 = 4$ and $Na_2O/K_2O = 1$ and variable of a molar ratio of CaO/MgO and amount of added of zirconium oxide (1.5; 3; 6; 12 and 24 wt%).

During this research, some parameters such as: whiteness in CIE L*a*b* in system, gloss by glossmeter and roughness of the surface by the confocal microscope, were measured. In addition, studies of chemical durability were made.

The obtained results show that the addition of zirconium oxide and variable of molar ratio of the alkaline earth oxides in an interesting way affects on the appearance and parameters of the surface of glaze. Addition of zirconium oxide improve some analysed parameters but this changes strongly depends on the system to which this oxide was added.

Acknowledgements
This research work has been carried out thanks to financing in the framework of NCBiR (Polish National Research and Development Committee) program PBS1/B5/17/2012

Impact of different functionalization of anodic TiO_2 layers on the cells response and drug delivery process

*Anna Pawlik[1], Grzegorz D. Sulka[1]
[1]Department of Physical Chemistry and Electrochemistry, Faculty of Chemistry, Jagiellonian University, Cracow, POLAND
e-mail: pawlika@chemia.uj.edu.pl

***Keywords**: titanium dioxide, surface modification, cell response, drug delivery,*

Recently, nanoporous anodic titanium oxide (TiO_2) (ATO) layers are thoroughly investigated as drug delivery systems and scaffolds for cell culture. It is noted that the surface chemistry and topography play a crucial role. Therefore, the modification of ATO surface can improve the cells behavior.

Nanoporous TiO_2 layers were fabricated via a three-step anodization process. ATO layers were modified with 0.5 M sodium hydroxide (NaOH) for 15 min. In order to obtain anatase phase, TiO_2 samples were annealed in air for 2 h at 400 °C. The samples non-annealed and annealed NaOH-modified samples were immersed in 1% ethanolic solution of different silane derivatives ((3-aminopropyl)triethoxysilane (APTES), (3-glycidyloxypropyl)trimethoxysilane (GPTMS) and (3-mercaptopropyl)-trimethoxysilane (MPTMS)) for 2 hours. Ibuprofen, a nonsteroidal anti-inflammatory drug, was loaded inside nanopores and, then, released in a 0.01 M phosphate buffer solution (PBS, pH = 7.4) at 37 °C. A desorption-desorption-diffusion (DDD) model was fitted to the obtained drug release profiles. In biological studies, the osteoblast-like cells line MG-63 were seeded on TiO_2 layers and incubated for 2, 24 or 72 h. MTS assay was carried out to examine cell viability and proliferation on different samples. The morphology of adhered osteoblast-like cells was investigated using a fluorescent microscope and scanning electron microscope.

The data showed that the modification of nanoporous TiO_2 layers with small chemicals such as silane derivatives enhanced metabolic activity of adhered cells. In addition, the cells were well dispersed. It was demonstrated that modified with silane derivatives nanoporous TiO_2 layers could be successfully applied as drug delivery systems. In conclusion, both amorphous nanoporous TiO_2 anatase layers can be successfully modified with NaOH and silane derivatives (APTES, GPTMS, MPTMS) and the modified samples can be used as drug delivery systems and scaffolds for osteoblasts-like cells culturing.

Acknowledgements
This work was supported by the National Science Centre, Poland (Grant number 2016/21/N/ST5/00872).

Chitosan-coated anodic TiO_2 layers as a potential drug delivery system

*Anna Pawlik[1], Grzegorz D. Sulka[1]
[1]Department of Physical Chemistry and Electrochemistry, Faculty of Chemistry, Jagiellonian University, Cracow, POLAND
e-mail: pawlika@chemia.uj.edu.pl

***Keywords**: anodic titanium dioxide layers, chitosan, drug delivery, apatite*

Recently, anodic titanium dioxide (TiO_2) (ATO) layers are widely investigated as an implant material. In addition, nanoporous TiO_2 layers can be coated with biocompatible polymers, such as chitosan. Chitosan has antibacterial and osseointegration properties. The polymeric coating reduces the burst release of drugs and extends overall release.

Nanoporous TiO_2 layers were synthesized via a three-step anodization process. The samples were annealed in air at 400 and 600 ºC in order to obtain anatase or mixture of anatase and rutile phases, respectively. The samples were coated with chitosan applying the dip-coating process. The modified TiO_2 layers were studied as potential drug delivery systems. Ibuprofen, a nonsteroidal anti-inflammatory drug, was used in drug release studies. The release studies were carried out in a 0.01 M phosphate buffer solution (PBS, pH = 7.4) at 37 °C. The drug concentration was determined using UV-Vis spectrophotometry. A desorption-desorption-diffusion model of the drug release was fitted to the resulting profiles. The apatite-forming ability of chitosan-coated nanoporous ATO layers was examined in simulated body fluid (SBF). In order to form calcium phosphate crystals on ATO surfaces, the samples were soaked in SBF for 1, 3, 5, 7, 14 and 21 days and, then, were characterized by scanning electron microscopy (SEM) and energy-dispersive X-ray spectroscopy (EDS).

Based on the results, it was demonstrated that coating of nanoporous TiO_2 samples with chitosan inhibited the process and reduced the fraction of the drug released in the first stage ("burst" effect). The desorption from the surface and nanopores was slower, however the diffusion process is faster, for polymer-coated samples than non-coated. It was noted that chitosan coated anatase and mixed anatase/rutile samples exhibited apatite forming ability. In conclusion, the nanoporous TiO_2 layers could be successfully coated with chitosan and the coated samples are a promising implant material.

Acknowledgements
This work was supported by the National Science Centre, Poland (Grant number 2016/21/N/ST5/00872).

Apatite-forming ability of anodic titanium dioxide layers synthesized at different anodization potential

*Anna Pawlik[1], Grzegorz D. Sulka[1]
[1]Department of Physical Chemistry and Electrochemistry, Faculty of Chemistry, Jagiellonian University, Cracow, POLAND
e-mail: pawlika@chemia.uj.edu.pl

***Keywords**: anodization, anodic titanium dioxide layers, calcium phosphate, simulated body fluid*

Due to their good mechanical properties and great biocompatibility, titanium and its alloys are commonly used as bone implantable materials. However, Ti-based implants exhibit poor osseointegration and bioactivity. The process of chemical bonding between the biomaterial and surrounding bones is long-lasting because it occurs via an oxide layer formed on the material surface. In order to tackle this problem anodic titanium oxide (ATO) layers can be formed before implantation via anodization process. The length and diameter of nanopores/nanotubes can be easily controlled by anodizing voltage. In addition, it was reported that formation of hydroxyapatite on anodic TiO_2 layers is accelerated by the presence of anatase or rutile phases. Typically, the samples are soaked in simulated body fluid (SBF).

Nanoporous TiO_2 layers were synthesized via a three-step anodization process in an ethylene glycol electrolyte under a constant voltage ranging from 30 to 70 V. The duration of the first and second anodizing step was 3 h, while the third step lasted 10 min. The anatase and a mixture of anatase and rutile phases were obtained by annealing the as-prepared amorphous TiO_2 layers in the air for 2 h at 400 and 600 °C, respectively. The samples were soaked in a simulated body fluid for 1, 3, 5, 7, 14 and 21 days. Then, they were washed gently with distilled water. ATO layers were characterized by scanning electron microscopy (SEM) and energy-dispersive X-ray spectroscopy (EDS).

Based on the results, it was demonstrated that annealed samples exhibited better apatite-forming abilities than amorphous ATO layers. Moreover, anodizing voltage had an impact on the formation of calcium phosphate crystals on ATO samples. Samples anodized at 60 and 70 V exhibited the best apatite-forming abilities. In coclusion, the anodization potential and crystalline structure have an influence of apatite-forming ability of anodic titanium dioxide layers.

Acknowledgements
This work was supported by the National Science Centre, Poland (Grant number 2016/21/N/ST5/00872).

Exploring the potential of lactic acid bacteria for the production of high-purity galacto-oligosaccharides

*Melinda Pázmándi[1-2], Anna Maráz[1], Zoltán Kovács[2]
[1]Department of Microbiology and Biotechnology, Szent István University, Budapest, HUNGARY
[2]Department of Food Engineering, Szent István University, Budapest, HUNGARY
e-mail: pazmandi.melinda@hallgato.uni-szie.hu

***Keywords**: galacto-oligosaccharides, lactic acid bacteria, selective fermentation*

Galacto-oligosaccharides (GOS) are prebiotic substances that can promote human health by selectively stimulating the growth of prebiotic bacteria in the large intestine. GOS is produced via enzymatic conversion from lactose. The reaction results in a mixture composed of mono- (MS), di- (DS), and oligosaccharide (OS) fractions. In industrial practice, the purification of OS from the less valuable MS and DS is achieved via liquid chromatography. The high cost of the chromatographic separation directs attention at alternative methods, such as selective fermentation.

This study focuses on the possibility of using lactic acid bacteria (LAB) for the selective fermentation of MS and DS from OS fractions. Various *Lactobacillus* and *Lactococcus* strains have been investigated in regards to their nutrient needs and fermentation characteristics.

Experimental results indicate that due to the high nutrient needs of the LAB strains, the GOS mixture requires organic nitrogen source supplementation. Obtained results show that some LAB strains (*Lactobacillus rhamnosus* PB9, *Lactobacillus plantarum* 2018 and *Lactobacillus acidophilus* N2) are able to selectively ferment mono- and disaccharides to a high degree in the presence of GOS molecules.

The application of LAB strains for the fermentation of GOS-containing saccharides mixtures may result in development of products with pleasant organoleptic quality with a potential to be marketed as prebiotic drinks.

Acknowledgements
The preparation of this work was supported by the Marie Skłodowska-Curie grant of the EU FP7 Framework Programme (PCIG11-GA-2012-322219) and the Bolyai Scholarship Programme of the Hungarian Academy of Sciences.

Preparation and Characterization of Chitosan Obtained from Honey Bee

Paulina Pędziwiatr
Faculty of Process and Environmental Engineering, Lodz University of Technology, Lodz, POLAND
e-mail: paulina.pedziwiatr@o2.pl

***Keywords**: chitin, chitosan, honey bee corpses, deacetylation*

Chitosan is non-toxic polysaccharide consisting of two kinds of polymers; i.e. glucosamine and N-acetylglucosamine, characterized by a biocompatibility and biodegradability. The concept of the chitosan production from an alternative source such as naturally died honeybees is described in this paper.

Chitin was extracted from the corpses of the European honey bee (*Apis mellifera*) collected in spring 2017, in author's bee yard located in Central Poland. Two different methods were tested to obtain bee chitosan. The procedure of chitin isolation consists on removal from the bees' bodies substances such as waxes (by extraction in Soxhlet apparatus), minerals, proteins and natural pigments - melanin. Process of deacetylation comprises hydrolysis of N-acetylglucosamine groups was conducted by chemical method with two different concentration of NaOH solution (1M and 25M) in 100°C. Obtained chitosans were characterized using the Fourier transform infrared (FT-IR) spectroscopy.

The FTIR spectra of chitosan I and II, exhibited a characteristic band at 3448 cm^{-1} (-NH and -OH groups), band at 2885 cm^{-1} (aliphatic C-H), the characteristic carbonyl C = O stretching at 1627 cm^{-1} (amide I band) and 1558 cm^{-1} (N-H deformation of amide II). Chitosan from method I (1M NaOH) contain additional sharp bands from 1550 cm^{-1} to 1100 cm^{-1}.

The selecting of conditions for each of stages has a significant impact on the quantity and physicochemical properties of the resulting product. Bee chitosan obtained by chemical deacetylation in 25M NaOH result in better quality (less amount of pollution) than deacetylation in 1M NaOH. Honey bee could be use as an alternative source of chitin for chitosan production. Obtained chitosan (from II method) is physiochemically similar to commercial chitosan.

Acknowledgements:
This work was supported by PhD Michał Tylman and Department of Process Thermodynamics.

Use of a mixture of technically pure iron and aluminum powders to shaping the surface of Fe-Al sinter using 3D printing technology

*Magda Pęska[1], Krzysztof Karczewski[1]
[1]Department of Advanced Materials and Technologies, Military University of Technology, Warsaw, POLAND
e-mail: magda.peska@wat.edu.pl

***Keywords**: intermetallic, laser engineered net shaping, iron aluminides, additive manufacturing*

In industries such as petrochemical, energy or aviation, materials suitable for use in high temperatures and resistant to aggressive action of chemical environments are used. Therefore, new materials with unique qualities that meet increasing requirements are being sought, such materials like iron- aluminum alloys based on intermetallic phases can be included to this group. Prospective use involves two phases occurring in this system: Fe-Al and Fe3Al. Unfortunately, Fe-Al phase-based materials received by conventional methods as powder metallurgy is characterized by low plasticity and brittleness, so new technologies are being sought for their manufacture.

3D printing belongs to such modern technologies, it is an additive technique where the material is being built gradually, layer by layer. It allows to obtain elements of a very complex shape adapted to a specific application, and by controlling the appropriate parameters you can receive materials of a certain structural and phase structure. Additionally it gives the possibility of producing details of complicated shapes, including spatial thin-walled structures which are impossible to implement with traditional methods. One of the techniques of 3D printing is Laser Engineered Net Shaping (LENS).

The main aim of this work is to evaluate the possibility of shaping the surface layer of Fe-Al sinter using LENS technology. Using powder metallurgy, the substrates with differed atomic composition of Fe and Al were received. The next step was to prepare mixtures of different atomic compositions (so that the formed elements have different phase structure). Then, using the LENS technique, elements from the prepared mixtures were deposited on the previously obtained substrates. The experimental part also included studies on chemical composition, phase analysis of built elements.

Based on the data analysis the following conclusions were made: LENS technique have been found to be an alternative to conventional methods of obtaining the Fe-Al intermetallic alloys. Using a mixture of pure technical powders it is possible to receive a product with a preset chemical composition and appropriate phase structure.

The effect of the solvent type on the structure of chitosan hydrogels formed at the physiological body temperature

*Katarzyna Pieklarz[1], Zofia Modrzejewska[1], Michał Tylman[2]
[1]Department of Environmental Engineering, Faculty of Process and Environmental Engineering, Lodz University of Technology, Lodz, POLAND
[2]Department of Process Thermodynamics, Faculty of Process and Environmental Engineering, Lodz University of Technology, Lodz, POLAND
e-mail: katarzyna.pieklarz@dokt.p.lodz.pl

***Keywords**: chitosan, natural polymer, thermosensitive hydrogels, structural properties*

Over the past few years has been a noticeable increase interest of hydrogels made of synthetic and natural polymers. The main reason for this trend is the enormous potential for their use in biomedical engineering, which is an interdisciplinary field of knowledge covering process and material engineering. Hydrogels can be used for the controlled release of bioactive molecules and as scaffolds in tissue engineering.

The aim of the research is to analyze the effect of the solvent type on the structure of chitosan hydrogels formed at physiological body temperature. Chitosan from crab shells with low viscosity of a degree of deacetylation SD ~ 79.5% and molecular weight of 86 kDa and lactic, hydrochloric and acetic acid at a concentration of 0.1 M were used for preparation of hydrogels. Sodium β-glycerophosphate was used as a neutralizing and buffering agent. The structure of gels was investigated by FTIR spectroscopy. The crystallinity of gel structure was determined by X-ray diffraction analysis (XRD).

Based on the FTIR analysis it could be observed changes in the wide band of 3000-3500 cm-1, amine band, 1100-700 cm-1 band corresponding to the saccharide structure and the bands associated with the presence of phosphate ions. The obtained diffraction patterns show that the chitosan chloride gels contain crystalline phases due to presence of sodium β-glycerophosphate and precipitation of NaCl during drying, while the lactate gels are practically amorphous.

Studies have shown the significant effect of chitosan salt on the structure of the obtained gels. Thermosensitive gels prepared with the use of chitosan salts can be an interesting material both as a drug carrier and as a material for scaffolds in tissue engineering.

Chitosan hydrogels formed at the physiological body temperature containing nano-ingredients

*Katarzyna Pieklarz[1], Zofia Modrzejewska[1], Michał Tylman[2]
[1]Department of Environmental Engineering, Faculty of Process and Environmental Engineering, Lodz University of Technology, Lodz, POLAND
[2]Department of Process Thermodynamics, Faculty of Process and Environmental Engineering, Lodz University of Technology, Lodz, POLAND
e-mail: katarzyna.pieklarz@dokt.p.lodz.pl

***Keywords**: chitosan, hydrogels, nano-ingredients, graphene oxide (GO)*

In recent years, the development of nanotechnology sciences has been observed, focusing mainly on the study of carbon nanostructures. Nanoparticles are more and more often used in many fields of science, including medicine or biomedical engineering as systems transporting various active substances to well-defined tissues of the human body. The use of graphene, a two-dimensional form of carbon, discovered in 2004 by A. Geim and K. Novosolov, seems to be particularly promising.

The aim of the research is creation of a new generation of thermosensitive chitosan gels containing graphene oxide and silica nanoparticles for biomedical applications. Chitosan from crab shells, lactic, hydrochloric or acetic acid at a concentration of 0.1 M, graphene oxide (GO) with an atomic ratio of C/O = 2.2 and silica were used for preparation of gels. Sodium β-glycerophosphate was used as a neutralizing and buffering agent. The structural characteristics of hydrogels were based on the analysis of XRD and FTIR spectra.

Based on the FTIR analysis, after introducing GO into the structure of chitosan lactate gels, were observed changes in the wide asymmetric band range for the 3300 cm-1 wave number and bands for the 1080 and 980 cm^{-1} wave numbers with a small arm for 970 cm^{-1}. Whereas in the case of chitosan chloride gels, the intensity of bands corresponding to O-H vibrations decreases with increasing GO concentration. The diffraction patterns show that the chloride gels crystalline structure after the addition of GO does not change.

Thermosensitive chitosan gels formed at physiological body temperature can contain nano-ingredients in their structure (for example: graphene oxide or silica). The chosen direction of research is innovative and extremely promising, and is the basis for further experiments using other carbon nanostructures.

Warm isostatic pressing technology for polymer- hydroxyapatite composites

*Elżbieta Pietrzykowska[1,2], Agnieszka Chodara[1,2], Barbara Romelczyk[2], Witold Łojkowski[1]

[1]Institute of High Pressure Physics, Polish Academy of Sciences, Warsaw, POLAND
[2]Faculty of Materials Science and Engineering, Warsaw University of Technology, Warsaw, POLAND
e-mail: e.pietrzykowska@labnano.pl

Keywords: *warm isostatic pressing, hydroxyapatite, composites*

Orthopaedics employs implants made of materials that are characterised by high strength and are not resorbable in the organism, such as metal alloys, ceramic materials. Their application involves negative effects such as bone weakening, allergies, complications, another operation of implant removal. The currently applied bioresorbable implants include polymer materials, but their application is limited by poor mechanical properties. Numerous bioresorbable material solutions are known and employed but there is no solution of a bioresorbable implant that would be overgrown by bone tissue. The aim of the presented research is to produce an osteoinductive composite of nano-hydroxyapatite and biodegradable polymer. This material is similar to natural bone as regards chemical, physical and mechanical properties.

Used warm isostatic pressing technology permits to obtain dense ceramic with mechanical properties close to the natural bone. The work shows mechanical properties of consolidated HAP-polymer composite. The consolidation process was carried out in extreme pressure up to 1GPa and temperature under 200°C.

The mechanical properties of this nanoceramic were investigated and the compressive strength reach assign value above 130 MPa (natural bone is in range from 100 to 200 MPa). The produced nano-hydroxyapatite / polymer composite is a promising biomaterial for application in orthopaedics in bioresorbable arthroscopic screws and wedges. The applied cryogenic milling method enabled obtaining a material containing 50% of PLA and 50% of nHAP.

Acknowledgements

This work was supported by the STRATEGMED III iTEProject and it is founded by The National Centre for Research and Development. The Project entitled: Tissue engineering method of bone loss treatment for oncological patients. Grant STRATEGMED3/306888/3/NCBR/2016.

Influence of Au NPs on electrooptical properties of liquid crystals

*Natalia Przybysz[1], Paweł Marć[1], Emilia Tomaszewska[2], Jarosław Grobelny[2], Leszek R. Jaroszewicz[1]

[1]Advanced Technologies and Chemistry Faculty, Military University of Technology, Warsaw, POLAND

[2]Department of Materials Technology and Chemistry, Faculty of Chemistry, University of Lodz, Lodz, POLAND

*e-mail: natalia.przybysz@wat.edu.pl

Keywords: *nematic liquid crystals, gold nanoparticles, mixtures of AuNPs and LC*

Doping a nematic liquid crystals mixtures (LC) with gold nanoparticles (Au NPs) have drown our attention because of possibilities to influence on the electrooptical properties of these material and to measure localized plasmon resonance of the mixture within the range of 200 to 1100 nm.

Due to physicochemical properties of LC mixtures, gold nanoparticles were synthesized in dedicated process to obtain molecules with specific sizes. Prepared Au NPs were transferred from water to an organic medium to provide dispersion of nanoparticles in nematic liquid crystal mixtures – the process was optimized by using particular molecules' surface modifier.

Stable mixtures of Au NPs and LC were prepared for two different sizes of nanoparticles and various concentrations. The liquid crystal cells (LCC) (thickness 5 μm) were filled up with these mixtures and thane their thermo-optical properties were investigated. Using cross polarizers technique we have measured light transmission of the LCC with changes of the temperature in range of 30 to 50^{o}C. With increasing temperature changes of refractive indices and optical birefringencewere observed.

As the next step of measurement the Mueller matrix, UV-Vis spectrometry and surface plasmon resonance will be carry out for tested samples.

Photonic Crystal Fiber Transducers for an Optical Fiber Multilevel Temperature Threshold Sensor

*Natalia Przybysz[1], Paweł Marć[1], Leszek R. Jaroszewicz[1]
[1]Advanced Technologies and Chemistry Faculty, Military University of Technology, Warsaw, POLAND
*e-mail: natalia.przybysz@wat.edu.pl

Keywords: *photonic crystal fiber, temperature threshold sensor, PCF, alkanes*

We have presented three pairs of PCF transducers filled with pure and Au NPs doped selected n-alkanes. The transducer was fabricated as a patch cord with one piece of a PCF partially filled with a prepared mixture and spliced in between two pieces of standard single mode telecommunication fibers.

In a single temperature test we have used a pair of transducers with the same n-alkanes. In the experiment we have used n-nonadecane, n-heneicosane and n-octacosane. For each of them there were prepared 1:1 mixtures with organic colloid of Au NPs. The intention to use the NPs was reducing hysteresis between On and Off states which appears because of melting points and crystallization temperature differences of the used n-alkanes. The concentration of NPs used in tested transducers allows only to slightly reduce their hystereses, but the slopes of On or Off states are sharper and characteristics of on state are more smoother and stable. In the next step of the research we will test higher concentration of NPs.

Experimental study of influence of process parameters and reactor geometry on process of molybdenum disulphide nanoparticles formation in impinging jet reactors

*Przybysław Przybyt, Ewelina Bielecka, Michał Wojtalik, Łukasz Makowski
Faculty of Chemical and Process Engineering, Warsaw University of Technology, Warsaw, POLAND
e-mail: przybyslaw.przybyt@gmail.com

***Keywords**: molybdenum disulphide, nanoparticles, impinging jet reactors*

The subject of this study was to determine an influence of process parameters and reactor geometry on the process of molybdenum disulphide nanoparticles formation in impinging jet reactors. MoS_2 has numerous applications such as a lubricant or a catalyst in petrochemistry and electromagnetic material. Therefore obtaining nanoparticles in a cheap way may be crucial to improving many industries.

In order to synthesize MoS_2 reaction of ammonium heptamolybdate with ammonium sulphide in presence of citric acid was performed. Experiments were carried out in two jet reactors of coaxial and tangential type. These micro-mixers were investigated because of their ability to achieve the high mixing efficiencies. Measurements of products characteristics were performed with DLS (Dynamic Light Scattering) and laser diffraction techniques using particle size distribution analyzers Beckman&Coulter and Malvern ZetaSizer. Process parameters such as feeding reactant concentrations and feeding volumetric flow have significant influence on MoS_2 nanoparticles size distribution. Study shows that with higher feeding volumetric flow the lower nanoparticles average diameter. Lower nanoparticles average diameter was also obtained with lower feeding reactant concentrations. The tendency to form nanoparticles which have lower average diameter has been noticed in coaxial reactor type rather than in tangential. All measurements characterize with narrow particle distribution.

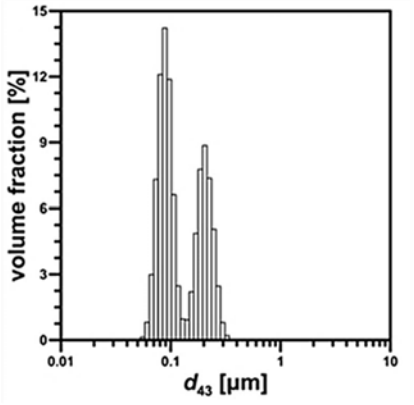

MoS_2 PSD histograms, jet-mixer, u_{jet} = 0.2 m s^{-1}, 2:1 CA:Mo molar ratio, c_{Mo}= 0.1 mol dm^{-3}

Qualitative and quantitative characterization of microstructural constituents in Ni-based superalloy

*Łukasz Rakoczy[1], Małgorzata Grudzień[2], Anna Zielińska-Lipiec[1]
[1]Department of Physical and Powder Metallurgy, AGH University of Science and Technology, Cracow, POLAND
[2]Foundry Research Institute, Cracow. POLAND
e-mail: lrakoczy@agh.edu.pl

***Keywords**: superalloy, gamma prime, stereology, carbides, volume fraction*

Ni-based superalloys are the materials used for turbine blades of aerospace jet engines and stationary gas turbines, due to their superior strength, and resistance to oxidation and hot corrosion. The high performance of superalloys during operating at elevated temperature depends largely on their microstructural stability.

This research examined the stereological parameters and chemical composition of microstructural constituents in commercially used Ni-Cr-Co-W superalloy. For accurate analysis, the microstructure was observed in both unetched and chemically etched condition in order to clearly reveal phase contrast and morphology. The observation was carried out with the use of light and scanning electron microscopy equipped with an energy dispersive x-ray (EDS) detector.

The results clearly show that analyzed material is characterized by the substantially large volume fraction of γ' phase. In dendrite core γ' precipitates dominates in nearly cubic shape, whereas in interdendritic spaces as eutectic islands. Moreover, complex shape carbides were observed mainly in the close neighborhood of eutectic island. Chemical analysis reveals that independently of the morphology, blocky and Chinese script carbides were enriched with refractory elements like Ta, while along grain boundaries Cr-rich carbides occurred.

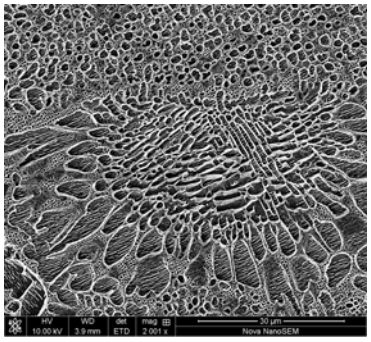

Eutectic γ/γ' in rosette morphology

Acknowledgements
This work was supported by the National Science Centre under grant 2017/25/N/ST8/02368.

Influence of shell mould composition on microstructure of cast nickel alloy

*Łukasz Rakoczy[1], Małgorzata Grudzień[2], Rafał Cygan[3], Anna Zielińska-Lipiec[1]
[1]Department of Physical and Powder Metallurgy, AGH University of Science and Technology, Cracow, POLAND
[2]Foundry Research Institute, Cracow. POLAND
[3]CPP Consolidated Precision Products, Rzeszow, POLAND
e-mail: lrakoczy@agh.edu.pl

***Keywords**: shell mould, investment casting, lost wax-casting, equiaxed*

The earliest application of lost-wax casting was primarily in the production of airfoil shapes like blades and vanes used in the jet engine. This has become a specialized area of investment casting technology requiring various processing techniques to insure the suitable metallurgical purity.

Equiaxed Ni-based superalloy was used as a base metal for the experiment. The molten metal was poured into ceramic shell moulds produced through "dip and stucco" technique. Microstructure characterization and analyses were carried out by using the following techniques: light microscopy, scanning electron microscopy, x-ray spectroscopy and Vickers hardness. Images captured during observation were subjected to image analysis. The mean size, area, perimeter and number of grains per mm^2 were calculated with the use of ImageJ software. Microstructural observation reveals dendritic structure of casting with high chemical inhomogeneities, which originated from decreasing of solubility of elements in the γ-matrix during the solidification process. The high volume fraction of intermetallic γ' phase indicates on high mechanical properties which were confirmed by Vickers hardness.

The intensive analysis shows the influence of investment casting process parameters on macro- and microstructure of Ni-based superalloy. Casting moulds differed in the type of metal powders that were added to strengthen the ceramic mould. This proved to be effective, besides, by changing the powder, the size of the grain can be controlled. From the selected elements, Al allowed obtaining the largest average grain diameter desired from the point of view of service at high homologous temperature.

Acknowledgements
This research work was supported by the Polish Ministry of Science and Higher Education, Grant No. 11.11.110.299. The investigated alloys were made as a part of the project LIDER/227/L6/14/NCBR/2015.

Nanotechnological approach to bacterial cellulose/nanohydroxyapatite biocomposites fabrication for bone regeneration

*Julia Rogowska-Tylman[1,2], Nabanita Saha[3], Agnieszka Chodara[1,2], Oyunchimeg Zandraa[3] , Witold Łojkowski[1], Petr Sáha[3]

[1]Laboratory of Nanostructures, Institute of High Pressure Physics, Polish Academy of Sciences, Warsaw, POLAND

[2]Faculty of Materials Science and Engineering, Warsaw University of Technology, Warsaw, POLAND

[3]Centre of Polymeric Systems, University Institute, Tomas Bata University in Zlin, CZECH REPUBLIC

e-mail: juliaRT@labnano.pl

Keywords*: bacterial cellulose, nanohydroxyapatite, biosynthesis, nanocomposites, bone regeneration*

Bacterial cellulose (BC) is a promising biomaterial for the development of new composites for biomedical applications especially for bone regeneration. Due to its good mechanical properties, water sorption capacity, porosity, stability and conformability, BC has been successfully used in tissue engineering of cartilage, blood vessels and in the wound healing. Authors proposed new route of BC-based nanocomposites fabrication by direct introduction of synthetic nanohydroxyapatite (nHA) particles in the cellulose biosynthesis. nHA itself, exhibit high affinity to natural human bone mineral phase. Thus, fabrication of composites based on BC and nHA can serve as a new material for bone regeneration.

The modification of the existing cellulose biosynthesis method in HS (Hestrin-Schramm) medium enabled to obtain uniform BC fibers net with entangled nHA agglomerates. Various initial nHA concentrations in BC matrix were prepared (0.1%, 0.5%, 1% nHA) which was also associated with changes in composites morphology and volume of obtained material.

FE-SEM imaging of the composites confirmed that nHA agglomerates entrapment between fibers its a result of bacterial cells Brownian motions during the synthesis of cellulose. As a side effect of nHA addition to the BC culture faster growth of composite was observed simultaneously with increased particles concentration.

After freeze-drying procedure all samples exhibited porous structure of randomly assembled nanofibers network with nHA particles and agglomerates entangled in between. The present study have shown unique possibilities of new biocomposites fabrication route with great potential in bone tissue regeneration.

Structural and mechanical properties of fly ash-based geopolymers

*Piotr Rożek, Magdalena Król, Włodzimierz Mozgawa
AGH University of Science and Technology, Faculty of Materials Science and Ceramics, Krakow, POLAND
e-mail: prozek@agh.edu.pl

***Keywords**: fly ash; geopolymer; alkali-activation; FTIR; MAS NMR*

The reaction of an aluminosilicate raw material (fly ash, metakaolin) and alkaline activator (sodium hydroxide, sodium silicate) results in hardened materials, called geopolymers. They exhibit thermal, acidic and alkaline resistance as well as relatively high compressive strength, which mainly stem from the structure of geopolymers, i.e. the amorphous to semi-crystalline three-dimensional network built of $[SiO_4]$ and $[AlO_4]$ tetrahedra connected by oxygen bridges. The main product of geopolymerization is amorphous sodium-alumino-silicate-hydrate gel (N–A–S–H). The aim of this work is to assess the effect of different activator contents on the structural and mechanical properties of fly ash-based geopolymers.

Coal fly ash was used as a source of aluminum and silicon. It was activated with sodium hydroxide. Three mixtures, differing in the alkaline activator content, were prepared, with the molar ratios SiO_2:Al_2O_3:Na_2O:H_2O as follows: 2.37:1:0.47:4.67, 2.37:1:0.59:4.67 and 2.37:1:0.79:4.67. Fourier transform infrared spectroscopy (FTIR) and solid-state magic angle spinning nuclear magnetic resonance (MAS NMR) spectroscopy were used to determine the structure of the obtained geopolymers. The phase composition was assessed by means of X-ray diffraction (XRD). The microstructure observations were carried out in a scanning electron microscope (SEM). The apparent density and compressive strength were also measured.

The obtained geopolymers are mainly amorphous due to the presence of disordered aluminosilicate phases. However, hydroxysodalite have been identified as a crystalline product of geopolymerization. The highest NaOH concentration positively influences a dissolution of starting material and therefore formation of the amorphous N–A–S–H gel, which is responsible for mechanical properties of the obtained geopolymers.

Acknowledgements
This work was supported by the Faculty of Materials Science and Ceramics, AGH University of Science and Technology grant no. 15.11.160.210.

Influence of SiO_2/Al_2O_3 ratio on geopolymer properties

*Piotr Rożek, Magdalena Król, Włodzimierz Mozgawa
AGH University of Science and Technology, Faculty of Materials Science and Ceramics, Krakow, POLAND
e-mail: prozek@agh.edu.pl

***Keywords**: metakaolin; fumed silica; geopolymer; compressive strength; FTIR*

The alkali-activation (geopolymerization) of metakaolin or fly ash requires a strongly alkaline medium (Na, K hydroxides or silicates) to dissolve alumina and silica. It results in amorphous geopolymeric gel, composed of repeating units of Si–O–Al–O, Si–O–Al–O–Si–O, Si–O–Al–O–Si–O–Si–O in various forms. The presence of alkaline ions provides electrical charge balance of the geopolymeric framework. Geopolymers exhibit thermal, acidic and alkaline resistance as well as relatively high compressive strength. The aim of this work is to assess the effect of different SiO_2/Al_2O_3 molar ratios on the structure, microstructure and compressive strength of metakaolin-based geopolymers.

The initial SiO_2/Al_2O_3 molar ratio of the metakaolin was 3.5. Aerosil® fumed silica was used as a regulator of SiO_2/Al_2O_3 molar ratio. Therefore, samples with the ratios of 3.5 (reference geopolymer), 4.5, 5.5 and 6.5 were prepared. At first, the fumed silica was dissolved in sodium hydroxide solution and then metakaolin was added. These mixtures were molded, sealed and kept in 80°C for 24 hours. The obtained materials were structurally characterized (Fourier transform infrared spectroscopy – FTIR). The phase composition (X-ray diffraction – XRD) was also determined. The influence of SiO_2/Al_2O_3 molar ratio on compressive strength and apparent density was assessed as well. A scanning electron microscope (SEM) was used for microstructure observations.

The modification of SiO_2/Al_2O_3 molar ratio thanks to the addition of fumed silica has changed the properties of the obtained materials, both structural and mechanical.

Acknowledgements
This work was supported by the Faculty of Materials Science and Ceramics, AGH University of Science and Technology grant no. 15.11.160.210.

Endothelial cells methabolism analysis in contact with steel biomaterial

*Ewa Rybak[1], Paulina Trzaskowska[1], Tomasz Ciach[1]
[1]Warsaw University of Technology, Faculty of Chemical and Process Engineering, Warsaw, POLAND
e-mail: ewaonewi@gmail.com

***Keywords**: stainless steel, endothelial cells, HMEC-1*

Endothelial cells are commonly used in modern laboratory research. Scientists are constantly working on the way of using them to support polymeric and metal implants. The cells could improve the biocompatibility and ability of application of synthetic biomaterials in vascular disease therapy.

Presented work investigatesthe use of modified metal materials to culture HMEC-1 cell line in order to find the most appropriate parameters of modification of the surface and the culture duration. Metal materials – flat discs made from stainless steel 316L - used in this research were electrochemically covered with a polymer coating and then peptide molecules with REDV sequence were covalently attached. Endothelial cells recognize REDV sequence as a surface suitable to proliferate and grow. The materials were sterilized and modified by covering them with 1% and 3% of carboxyl groups using 5 and 30 minutes of electropolimerization and later the REDV layer was prepared using the concentrations of REDV at 0.5 and 5mM.

Firstly, endothelial cells after 3 passages werecultured on materials for 24 and 72 hours. Then they were fixed and dyed with DAPI to visualize nuclei and with anti-Vinculin and anti-vWFantibodies with fluorophore to visualize vinculin and von Willebrand factor. Imagingof visualized structures was carried out using a scanning confocal microscope. Finally it was possible to assess the best conditions in which HMEC-1 line could anchor, develop and functionalize.

The protocole of preparing the cells allowed to see the difference betweencells cultureon modified and unmodified steel and the presence of a peptide layer encouraged endothelial cells growth what can be observed by the presence of vinculin and von Willebrandfactor. The best results of the analysis were observed when steel discs with a layer of REDV peptide with a concentration of 5mM and higher parameters of carboxylation was applied. Good growth of endothelial cells on non-coated steel can be a confirmation that an irregular and rough surface encourages cells to adhere and proliferate.

Acknowledgements
This work was supported by the National Science Centre, Poland (grant number 2013/11/N/ST8/00636 and 2015/19/B/ST8/02015)

Influence of cation in glycerophosphate salts on viscoelastic properties of chitosan solutions

*Anna Rył, Piotr Owczarz, Marek Dziubiński
Department of Chemical Engineering, Faculty of Process and Environmental Engineering, Lodz University of Technology, Lodz, POLAND
e-mail: anna.ryl@dokt.p.lodz.pl

***Keywords**: glycerophosphate salts, chitosan hydrogels, sol-gel phase transition, rheology*

The interest of chitosan thermosensitive hydrogels arises from the possibility of their application in tissue engineering and controlled drug delivery systems. Solutions prepared by dissolving chitosan in acetic condition exhibit a sol-gel phase transition at temperatures significantly above 37°C. The presence of the β-glycerophosphate (GP) salt leads to a decrease in temperature and neutralization of the solution to a physiological pH. This allows the formation of a porous 3D structure (polymer matrix) in vivo. Till now, described in detail in the literature, the GP salt used for the preparation of chitosan hydrogels is disodium β-glycerophosphate. There are no literature reports on the possibility of using other GP salts, e.g magnesium or calcium. The use of these ions would be particularly important in the treatment of cardiac diseases or bone tissue engineering.

The research presents the influence of the GP salt type on the phase transition of chitosan solutions in acids. Colloidal chitosan solutions containing sodium, magnesium and calcium GP were tested. The samples were prepared each time, providing constant ratio of phosphate residues to amino groups. The viscoelastic properties and the sol-gel phase transition conditions were determined in a cone-plate measurement system of a rotational rheometer in oscillatory mode. Mechanical properties were determined by performing measurements at constant and variable strains under both non- and isothermal conditions.

The results of this studies indicate that the use of identical concentrations of GP ions dramatically changes the mechanical properties of the tested solutions. It also significantly influences on the temperature and sol-gel phase transition kinetics of the tested hydrogels.

Acknowledgements
This work was supported by the National Science Center of Poland – Grant NCN UMO – 2014/15/B/ST8/02512

Investigation of the chitosan solutions flow behavior using rotational and oscillatory measurements

*Anna Rył, Piotr Owczarz, Marek Dziubiński
Department of Chemical Engineering, Faculty of Process and Environmental Engineering, Lodz University of Technology, Lodz, POLAND
e-mail: anna.ryl@dokt.p.lodz.pl

***Keywords**: sol-gel phase transition, chitosan hydrogels, rheometry measurements*

In the case of thermosensitive chitosan hydrogels, which have the ability to form a porous structure in vivo, it is extremely important to precisely determine the conditions of the sol-gel phase transition. The most commonly used, described in the literature, method of determining temperature of gelation point is conducting non-isothermal rheometric oscillation measurements at a constant heating rate. The advantages of these measurements are their low invasiveness and simplicity of interpretation of the obtained results. The point of intersection curves of storage and loss modules is considered as the gelation point. At this point, the change from viscous dominance to elastic ones is observed. Due to the fact that chitosan is a long-chain polysaccharide whose molecules occur most often in the form of entangled coil with a solvation shell, it seems important to determine the influence of shear on the gelation process.Conducting non-isothermal rotational measurements, with very small shear strains, can leads to disentangling of polymer chains and easier interaction between functional groups - thus accelerating gelation of the solution.

In order to determine the impact of the type of applied deformation, rotational and oscillatory measurements were carried out.The value of shear stress was determined to correspond to the value of strain applied in oscillatory measurements. The values of the angular frequency and the amplitude strain as well as the geometry of the applied measurement system were taken in the calculation of shear rate values used in rotational measurements.The material was a 2% (w / v) colloidal solution of chitosan with the addition of disodium β-glycerophosphate.

The research allowed to determine the effect of shear on the gelation process. The obtained results from rotational measurements were compared with results from oscillatory mode and with known, from the literature, mechanisms of gelation of colloidal chitosan solutions.

Acknowledgements
This work was supported bythe National Science Center of Poland – Grant NCN UMO – 2014/15/B/ST8/02512.

Synthesis and purification of quinine-based quaternary ammonium halides

*Tomasz Rzemieniecki, Michał Niemczak, Daria Czuryszkiewicz, Anna Turguła, Kamil Czerniak, Agnieszka Biedziak, Damian Kaczmarek
Faculty of Chemical Technology, Poznan University of Technology, Poznan, POLAND
e-mail: tomasz.m.rzemieniecki@doctorate.put.poznan.pl

Keywords: *cinchona alkaloids, quinine, quaternary ammonium salts, alkylation, purification*

Quinine is an alkaloid that may be found mainly in the bark of *Cinchona* genus. It is usually obtained *via* extraction from the bark, along with several other alkaloids. The route of quinine derivatisation with 1-halogenoalkanes is presented in Figure 1. Quaternary derivatives of quinine, as well as quinine itself, were also applied in organic synthesis as efficient stereoselective catalysts.

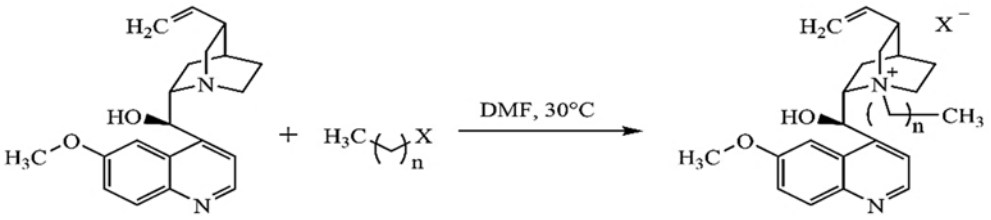

Synthesis of quaternary derivatives of quinine

The crude product of the process is heavily contaminated by the by-products formed in the parallel reaction. In order to obtain products characterized by high purity we have developed a facile and cost-effective method of isolating 1-alkylquinine halides by washing the impurities with non-polar solvents. Additionally, reliable method of their recrystallization in popular organic solvents has been formulated. However, the total yield of process decreased while utilizing 1-halogenoalkaneswith longer alkyl chains. The synthesized quinine derivatives possessed temperatures of decomposition exceeding 160 °C and strong affinity to protic organic solvents, such as methanol or 2-propanol. Additionally, the quaternary structure was confirmed by the deshielding of α-hydrogen atoms observed in the collected ^{1}H NMR spectra at 3.5–4.5 ppm.

Due to the similarity in the chemical structures of 1-alkylquinine halides and the impurities, the purification of the post-reaction mixture required a thoughtful approach in order to obtain pure products without utilizing chromatographic techniques. The simplicity of the adopted methods also facilitates scaling the process up in order to obtain greater quantities of the product.

Herbicidal ionic liquids with bicyclic cation

Tomasz Rzemieniecki[1], Damian Kaczmarek[1], Agnieszka Biedziak[1], Daria Czuryszkiewicz[1], Michał Niemczak[1], Kamil Czerniak[1], Katarzyna Marcinkowska[2], *Anna Turguła[1]

[1]Faculty of Chemical Technology, PoznanUniversity of Technology, Poznan, POLAND

[2]Institute of Plant Protection – National Research Institute, Poznan, POLAND.

e-mail: anna.s.turgula@doctorate.put.poznan.pl

Keywords*:DABCO, quaternary ammonium salts, herbicidal ionic liquids, organic technology, organic synthesis*

Ionic liquids (ILs) are characterized by various properties, which allows them to be widely used in numerous fields of science as well as in the industry. ILs may be divided into three generations, depending on the physicochemical properties and biological activity of the cation or anion. In 2011, ionic liquids with herbicidal activity (herbicidal ionic liquids, HILs) have been described for the first time. Ionic compounds containing bicyclic cation with a long alkyl substituent should exhibit enhanced surface activity, thus providing bactericidal and fungicidal properties as well as improved herbicidal activity.

The primary objective of the study was to develop an effective method for the synthesis of new herbicidal ionic liquids with ammonium bicyclic cation and anion derived from herbicidal acid. Ionic liquids with 1-alkyl-1-azonia-4-azabicyclo[2.2.2]octanecation and 4-chloro-2-methylphenoxyacetate (MCPA) anion were obtained *via* three-step synthesis. HILs' structures were confirmed by proton and carbon nuclear magnetic resonance (^{1}H NMR and ^{13}C NMR).The signals originating from the hydrogen atoms in the heterocyclic structure occurred at values of σ [ppm] = 3.1–3.2 (m, 6H) and 3.3–3.4 (m, 6H), which confirms the presence of quaternary nitrogen atom. According to the analysis of solubility determined in 10 representative solvents characterized by a diverse range of polarity, the obtained HILs were readily soluble in polar aprotic organic solvents: ethyl acetate, acetone or DMSO, and in polarprotic solvents: water, methanol or isopropanol.The biological activity of the obtained compounds was tested under greenhouse conditions.

New herbicidal ionic liquids were obtained in high yield and were characterized by high affinity to many organic diluents. The herbicidal activity of the prepared HILs was found to be significantly higher in comparison to commercially available herbicide for winter oilseed rape and cornflower. The best results were obtained with the use of ionic liquids comprising an alkyl substituent with 18 carbon atoms in the bicyclic cation structure.

Ionic liquids of natural origin with abietate anions

Tomasz Rzemieniecki[1], Michał Niemczak[1], Agnieszka Biedziak[1], Anna Turguła[1], Damian Kaczmarek[1], Kamil Czerniak[1], Tomasz Klejdysz[2], *Daria Czuryszkiewicz[1]

[1]Department of Chemical Technology, Poznan University of Technology, Poznan, POLAND

[2]Institute of Plant Protection – National Research Institute, Poznan, POLAND

e-mail: daria.m.czuryszkiewicz@doctorate.put.poznan.pl

Keywords*: ionic liquids, abietic acid, deterrent, antifeedant, quaternary ammonium salts*

The occurrence of pests in cereal warehouses or granaries is a crucial problem which significantly contributes to the loss of quality and commercial value of the products. Among the numerous groups of described antifeedants, ionic liquids (ILs) occupy a special position due to their designability.

In our study we developed a new methodology of synthesis of bio-based ionic liquids with abietate anion. The products were subsequently characterised in terms of physicochemical properties of the obtained compounds as well as antifeedant activity with particular consideration of the length of alkyl chain attached to the quaternary nitrogen atom. The synthesis of ILs derived from abietic acid was conducted using ion-exchange or neutralization methods and the products were obtained with high yields exceeding 85%. Figure 1 illustrates the antifeedant activity of ionic liquids with abietate anion.

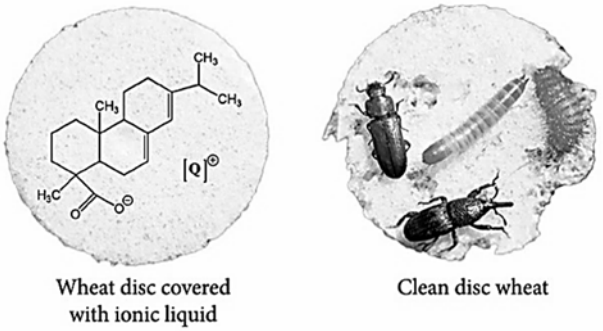

Ionic liquids with abietate anions as effective deterrent compounds

The study confirmed strong influence of the chemical structure on the solubility, thermal stability and phase transitions. The results also revealed excellent deterrent properties of ILs with abietate anion, reaching or exceeding the values obtained for azadirachtin. Cations with the longest alkyl substituents were characterized by the highest antifeedant activity.

Application of porogenes in the process of production of porous polymers by supercritical foaming

*Katarzyna Sawicka, Katarzyna Kosowska, Marek Henczka
Faculty of Chemical and Process Engineering, Warsaw University of Technology, Warsaw, POLAND
e-mail: saw.kasia@gmail.com

***Keywords**: tissue engineering, supercritical fluids, foaming, poly(ε-caprolactone), porogenes*

The development of chemical engineering is directly related to tissue engineering, an emerging interdisciplinary field aiming to produce biodegradable scaffolds that restore, maintain and improve damaged organs or tissues. Foaming of polymers using supercritical fluids is commonly applied to preparation functionalized, highly porous structures useful for biomedical applications.

The effects of treatment with supercritical carbon dioxide of poly(ε-caprolactone) (PCL) and its composites were investigated. In performed experiments composites from graphene-oxide (GO), nano-hydroxyapatite (nHA) and nano-cellulose (nC) were prepared. In order to explore the utility of the porogenes, a number of tests were performed. The porous structures with $scCO_2$, at two various foaming pressures (9 MPa and 18 MPa), at three different temperatures (50°C, 70°C and 100°C) for different saturation times (0.5 h, 1 h and 4 h) were treated.

The morphology of cross-section and side surface of the porous foams was characterized by Phenom scanning electron microscope (SEM). The mechanical properties of these biomedical scaffolds, such as Young's module and maximum compressive strength were measured using static compression test. The differential scanning calorimetry (DSC) was used to assess the effect of used porogen and foaming conditions on the melting properties of PCL and its composites.

Effect of porogen concentration and foaming process parameters on mechanical properties of the three-dimensional porous structure, was identified. By analyzing the results of carried out research, the most appropriate foam for biomedical application, was selected. No negative changes in foams structure and properties, that would limit the usability of the porogens in polymer foaming process, were observed.

Atomic force microscope as a study tool for surface structuring mechanisms of polymeric membranes based on chitosan

*Tatyana Sazanova, Kseniia Otvagina, Ilya Vorotyntsev
Nanotechnology and Biotechnology Department, Nizhny Novgorod State Technical University n.a. R.E. Alekseev, Nizhny Novgorod, RUSSIA
e-mail: yarymova.tatyana@yandex.ru

***Keywords**: atomic force microscopy, material characterization, surface structuring mechanisms, chitosan, polymeric membrane*

Biodegradable polymers represent a basic component of a large range of various application including membrane technologies for gas separation. Since one of the first stages in gas separation is a contact of gas mixture with a membrane surface, there is an important task to study its surface structuring features and their correlation with physicomechanical and physicochemical properties. In this context, microscopy techniques such as atomic force microscopy (AFM) are emerging as fundamental tools to study deeply morphology and structural properties at micro- and nanoscale.

In the present work, AFM was used for study of surface structuring features of chitosan (CS) graft and block copolymers with polyacrylonitrile (PAN) and polystyrene (PSt) modified with ionic liquids (ILs) based on a cation of 1-butyl-3-methylimidazolium (bmim) with various anions ($[BF_4]$, $[PF_6]$ and $[Tf_2N]$) at each stage of modification.

Mathematical statistics methods were used for stability study of surface structure of the CS copolymers. There was shown that the block copolymers were better in comparison with the graft ones.

Also special impact of the original and modified copolymers surface structure on their mechanical properties were studied. It was shown that ILs immobilization caused the decrease of the surface packing density of the copolymers, and by this resulted in the deterioration of their mechanical properties. At that, the block copolymers were more resistant to this effect than the graft ones. However, the strength and elastic properties of the CS copolymers with PAN showed better than of ones with PSt.

This approach to study surface structuring is important to develop a technique for formation of modified membranes (for gas separation processes) and other functional materials based on polymers with controlled structure and properties.

Acknowledgements
This work was supported by the Russian Science Foundation, project 15-19-10057.

Multiparametric mathematical algorithm for describing unsteady-state membrane gas separation with pulsed retentate mode

*Tatyana Sazanova, Maxim Trubyanov, Stanislav Battalov, Egor Puzanov, Vladimir Vorotyntsev, Pavel Drozdov, Ilya Vorotyntsev
Nanotechnology and Biotechnology Department, Nizhny Novgorod State Technical University n.a. R.E. Alekseev, Nizhny Novgorod, RUSSIA
e-mail: yarymova.tatyana@yandex.ru

Keywords*: unsteady-state membrane gas separation, membrane module, pulsed retentate operation, mathematical modeling, separation kinetics*

Membrane-based separation processes for gas separation have received considerable attention throughout the past time owing to several advantages, such as ease of operation and scale-up, low cost of operation, energy requirements and high selectivity factors. The key issues for improvement of membrane separation are synthesis of new membrane materials with high permeability and selectivity, development of new process designs and their configurations, and optimization of operating conditions for the existing separation processes. There is a variety of engineering approaches for improving selectivity and productivity of gas separation processes by optimization of their unsteady operating conditions, which allows to separate even hardly separable gas mixtures.

In this research, the kinetics of novel unsteady-state membrane gas separation with a pulsed retentate flow operation was simulated and studied by the example of separating a mixture consisting of a slow-permeant basic component and a fast-permeant impurity. The novel process implies cyclic alternation of a “closed” operating mode of a separation module with a short-term retentate withdrawal. It provides significantly higher separation performances in the small-productivity domain due to the driving force increase as compared to a steady-state operation at the same given value of the product recovery (same productivity) which was verified experimentally. The mathematical algorithm developed using the MathCad software package is multiparametric and considers the basic operational parameters of the pulsed retentate flow operation (stripping time and withdrawal time, total cycle time, withdrawal amount, withdrawal flowrate etc.) influencing the kinetics of the separation process.

The mathematical modeling results correlate well with the experimental data. Based on the results, a strategy for optimization of the unsteady-state process was developed.

Acknowledgements
This work was supported by the Russian Science Foundation, Project № 17-79-10464.

Xenon recovery from natural gas by gas hydrate crystallisation

*Maria Sergeeva, Anton Petukhov, Vladimir Malyshev, Vladimir Vorotyntsev
Nanotechnology and Biotechnology Department, Nizhny Novgorod State Technical University n.a. R.E. Alekseev, Nizhny Novgorod, RUSSIA
e-mail: sergeeva.m.s@rambler.ru

***Keywords**: gas hydrate crystallisation, xenon, separation, natural gas*

Xenon occurs in slight traces in the atmosphere of Earth about 0.087 ppm. Thereby, xenon is manufactured on a small scale by the fractional distillation of liquid air. Because of its low abundance, xenon is much more expensive than the other noble gases. The natural gas contains four orders of magnitude more xenon than the atmosphere. Therefore, the extraction from it is the priority direction. Xenon is extracted from the natural gas in the process of cryogenic separation and low-temperature sorption. Disadvantages of these methods are the low efficiency of gas separation and complexity of hardware design.

In the process of directional gas hydrate crystallisation the dissociation pressure of xenon gas hydrate is lower than the dissociation pressure of the main component (methane), so xenon will be concentrating in the hydrate phase and methane will be concentrating in the gas phase. Therefore, the method of directional gas hydrate crystallisation can be used for the recovery of xenon from natural gas. For the optimise hydrate formation conditions a mathematical modeling method was chosen. Different gas mixtures approximating composition of natural gas (CH_4=94.85%; H_2S=2.5%; CO_2=2.5%; Xe=0.15%) were chosen for modeling. Xenon is a good hydrate-forming gas with a low dissociation pressure, which will contribute to its concentration.

The linear dependence of the absolute distribution coefficient of xenon on its fraction in the gas phase was obtained. It was found that the absolute distribution coefficient depends significantly on the composition of the gas mixture and weakly on the hydrate formation conditions (changes in the mixture pressure and concentration of the gases). Optimum conditions for hydrate formation was obtained. Advantages of gas hydrate crystallisation: low power consumption, the process of gas hydrate crystallisation at 0 °C, high separation coefficient, high gas capture due to the structure of gas hydrates.

Acknowledgements
This work was supported by the Russian Science Foundation (grant no. 17-79-20286).

The application of carbon–based electrodes modified with MWCNTs and GNPs for the sensitive voltammetric determination of selected pesticides

*Karolina Sipa, Mariola Brycht, Andrzej Leniart, Sławomira Skrzypek
Department of Inorganic and Analytical Chemistry, University of Lodz, Łódź, POLAND
e-mail: karolina.sipa@gmail.com

***Keywords**: graphene nanoplatelets, multi-walled carbon nanotubes, pesticides, metobromuron, dichlorophen*

In order to increase the sensitivity of voltammetric methods for the determination of biologically active substances, modifications of the surfaces of working electrodes are applied. Electroanalytical applications of β–cyclodextrins (β–CDs) are based on the formation of an inclusion complex, biomolecular recognition and selective preconcentration of analyte at the electrode surface. Additionally, nanomaterials, such as graphene nanoplatelets (GNPs) and multi-walled carbon nanotubes (MWCNTs), have proved to be excellent modifiers due to their extremely good conducting properties. These materials have been successfully incorporated into electrochemical sensors.

The detection of pesticides with high precision is extremely important in order to monitor and analyse the permissible level. Dichlorophen (Dcp) is a veterinary fungicide classified as a chemical group of chlorinated phenols. Furthermore, this pesticide is utilized as an ingredient in shampoos and soaps agents. Metobromuron (Mbn) is a herbicide belongs to the urea derivatives group. Mbn is used in cultivation of potatoes, tobacco, maize and sugar beet.

In this work, glassy carbon electrode modified with β–cyclodextrins and multi–walled carbon nanotubes (β–CDs–MWCNTs–GCE) was used as a working electrode for the determination of Dcp, while ultra trace graphite electrode modified with graphene nanoplatelets (GNPs–UTGE) was applied as a working electrode for the determination of Mbn. Both modified electrodes were analysed using atomic force microscopy (AFM) and cyclic voltammetry (CV). The voltammetric procedures for the determination of Dcp and Mbn were developed using square–wave adsorptive stripping voltammetry (SWAdSV) and square–wave voltammetry (SWV), respectively.

The proposed methods exhibited acceptable analytical performance in terms of the linearity and the detection limits.

Acknowledgements
This work was supported by University of Lodz, Poland (Grant No. B1611100001291.02 and B1711100001602.02).

B-Cyclodextrins and multiwalled carbon nanotubes modified boron-doped diamond electrode for voltammetric analysis of carbendazim

*Karolina Sipa[1], Mariola Brycht[1], Valéria Guzsvány[2], Sławomira Skrzypek[1]
[1]Department of Inorganic and Analytical Chemistry, University of Lodz, Łódź, POLAND
[2]Department of Chemistry, Biochemistry and Environmental Protection, University of Novi Sad, Novi Sad, REPUBLIC OF SERBIA
e-mail: karolina.sipa@gmail.com

***Keywords**: β–cyclodextrins, multi-walled carbon nanotubes, NAFION®, boron–doped diamond electrode, carbendazim*

Nowadays, the application of various nanomaterials in the preparation of modified working electrodes is getting more and more popular. Surface modification of the electrodes allows to increase the sensitivity and reduce the limits of detection and quantification in determination of biologically active compounds. Carbon nanotubes (CNT) are often used for this purpose due to the fact that they are characterized by increased electrode surface area, fast electron transfer rate, significant mechanical strength and good chemical stability. Nafion is a sulfonated cation–exchange polymer which is used as dispersant and stabilizer. β–cyclodextrins (β–CDs) are oligosaccharides which can form an inclusion complex with analyte and increase the sensitivity of the determination method.

In this work, boron–doped diamond electrode (BDDE) modified with MWCNTs, NAFION®, and β–CDs as easy to use, simple to prepare, environmentally friendly, inexpensive, sensitive, and reliable promising working electrode with rapid response time was applied for the voltammetric determination of Carbendazim (Cbz). Cbz is a pesticide which belongs to the group of fungicides, and it acts against broad spectrum of diseases on crops (cereals, cotton, tobacco, fruits, vegetables, and ornamentals).

The square–wave adsorptive voltammetric (SWAdSV) peak current of Cbz oxidation response on β–CD–MWCNTs–BDDE was linear in the range of 6.72×10^{-7}–1.12×10^{-5} mol L^{-1} with a detection limit (LOD) of 1.96×10^{-7} mol L^{-1}.

Acknowledgements
This work was supported by the Ministry of Science and Technological Development of the Republic of Serbia (Project Nos. 172012 and 172059), CEEPUSIII (CZ–0212–09–1516) network and University of Lodz, Poland (Grant No. B1611100001291.02).

Square-wave voltammetric determination of pesticide bixafen using graphene paste electrode

Mariola Brycht[1], *Karolina Sipa[1], Sławomira Skrzypek[1], Kurt Kalcher[2]
[1]Department of Inorganic and Analytical Chemistry, University of Lodz, Łódź, POLAND
[2]Institute of Chemistry – Analytical Chemistry, Karl-Franzens University Graz, Graz, AUSTRIA
e-mail: karolina.sipa@gmail.com

Keywords*: graphene nanoplatelets, paste electrode, electrochemical sensor, bixafen, square–wave voltammetry.*

Nowadays, graphene is considered important nanotechnology achievement. Graphene and its derivatives are receiving great attention in the area of electrochemistry as a tool for enhancing voltammetric response.

In this work, novel and sensitive graphene nanoplatelets (GNP) paste electrode (GNPPE) was prepared and characterized by atomic force microscopy (AFM), electrochemical impedance spectroscopy (EIS), and cyclic voltammetry (CV). The advantages of carbon–based paste electrodes are mainly easy and rapid preparation, low cost, simple surface renewal, low residual current in a wide potential window, and ease of modification with even labile compounds.

Further, as-prepared GNPPE was applied as a working electrode for the analytical purposes. The square–wave voltammetric (SWV) procedure for the determination of pesticide bixafen was developed. Bixafen is a pyrazole–carboxamide fungicide which belongs to a new generation of succinate dehydrogenase (SDH) inhibitors. It was developed specifically for foliar application to control important cereal diseases, such as septoria leaf blotch (*Septoria tritici*) in intensive cereal growing regions. The linear relationship between peak current vs. increasing concentrations of bixafen was defined using GNPPE, and the limits of detection and quantification were calculated. For the comparison, the classical carbon paste electrode (CPE) was also prepared and investigated in analogous way.

The obtained results showed that GNPPE possess advantages in terms of linearity, sensitivity and detectability when compared to the traditional CPE.

Acknowledgements
This work was supported by the National Center for Science (NCN) in Cracow, Poland (Grant no. UMO–2014/15/N/ST4/02285).

Multilayer composites as coatings for neural devices: PEDOT/gold films

*Małgorzata Skorupa[1], Daria Więcławska[1], Katarzyna Krukiewicz[1,2], Manus Biggs[2]

[1]Department of Physical Chemistry and Technology of Polymers, Silesian University of Technology, Gliwice, POLAND

[2]Centre for Research in Medical Devices, National University of Ireland, Galway, IRELAND

e-mail: gosia.skorupa1@gmail.com

***Keywords**: conducting polymers, gold particles, neural devices, PEDOT*

Neural prosthetic devices are used as brain-computer interfaces enabling stimulation and recording of signals from neural tissue. They pose a tool for better understanding of nervous system functions, as well as diagnosis and treatment of related degenerative conditions, such as Parkinson's or Alzheimer's diseases. Materials used in neural engineering should exhibit great biocompatibility and significant conductivity. Low impedance values are conducive to high signal-to-noise ratio.

In the new design, composites consisting of gold particles and a biocompatible conductive polymer - poly (3, 4 - ethylenedioxythiophene) polystyrene sulfonate (PEDOT:PSS) have been prepared by sputter coating and spin coating techniques. Electrochemical performance of multilayer composites was investigated by cyclic voltammetry and impedance measurements. By comparison of the results, the optimal number of layers was determined. After electrochemical modification, gold particles formed fractal-like structures on the film surface, which was proved by SEM and EDS analysis. In vitro cytotoxicity has been investigated by culturing of SH-SY5Y cells on the surface of composites and performing the live/dead assay.

Eventually, the advantageous charge storage capacity, low impedance and unique topography facilitating neurite growth, proved that the material is a promising candidate for application as neural interfaces.

Acknowledgements

This research is supported in part by a research grant from Science Foundation Ireland (SFI) and is co-funded under the European Regional Development Fund under Grant Number 13/RC/2073. MB is an SFI Starting Investigator SIRG COFUND fellow, grant no. 11/SIRG/B2135. KK is grateful to the National Science Centre in Poland for financing the research in the framework of SONATA program (2016/23/D/ST5/01306).

Removal of Rhodamine B from aqueous solutions: new reaction system for synthesis of magnetic macroporous sorbents from waste PMMA

*Małgorzata Skorupa, Dominik Zdybał and Andrzej Milewski
Department of Inorganic, Analytical and Electrochemistry, Silesian University of Technology, Gliwice, POLAND
e-mail: gosia.skorupa1@gmail.com

***Keywords**: Rhodamine B, PMMA, wastewater treatment, waste management, adsorption*

In this work two environmental issues have been addressed: poly(methyl methacrylate) – PMMA waste management and removal of dyes from industrial wastewaters. The currently applied processes for PMMA recycling are usually slow and highly energy consuming; therefore new methods need to be investigated.

In the novel approach for PMMA modification, simultaneous hydrolysis and cross-linking processes take place in a one-pot DMSO-diethylene glycol diethyl ether solvent system. Due to homogeneous and highly basic environment, the reaction occurs rapidly and effectively, leading to cross-linked poly(methyl methacrylate)-*co*-poly(methacrylic acid). By introduction of nanomagnetite into the reaction system, the obtained hydrogels, capable of adsorbing cationic dyes, have also magnetic properties. Their highly porous structure was proved by SEM imaging. Adsorption studies have been performed in model Rhodamine B solutions, with various concentrations. Adsorption isotherms and kinetics have been investigated, as well as desorption of dye with use of a green solvent – water/ethanol.

Due to high porosity of the materials, the sorbents obtained from waste PMMA were proved to be efficient in dye removal – fast adsorption rate and high capacity. They can be also easily separated by magnetic sedimentation and regenerated, enabling the sorbent reuse.

Voltammetric analysis of active substances content in oral contraceptive pills

*Joanna Smajdor
Faculty of Materials Science and Ceramics, AGH University of Science and Technology, Kraków, POLAND
e-mail: smajdorj@agh.edu.pl

***Keywords**: Voltammetry, hormone, mercury film electrode, carbon black.*

Due to increasing number of endocrine system diseases, an analogous growth in the sales of hormonal drugs used in the therapy is observed. One of the most common group of hormones used in medicine includes sex hormones and their synthetic derivatives. Drugs containing hormones such as estradiol, ethinyl estradiol or drospirenone are used mostly in the form of tablets, less frequently as patches, rings or gels. They are commonly encountered in gynaecological applications as contraceptive drugs, in hormonal replacement therapy and during treatment of selected dermatological conditions.

Estradiol is an estrogenic hormone produced by the body of both women and men. Its concentration in the woman's body is subjected to cyclical fluctuations associated with the phase of the menstrual cycle. The most commonly used estrogen in medicine is the synthetic estradiol derivative - ethinyl estradiol. It is the main component of most contraceptive preparations, both in the form of tablets (two-phase and three-phase), as well as patches and contraceptive rings. Drospirenon, however, belongs to the group of synthetic progestagens, which have both antiandrogenic and anti-mineralscortoid effects. It is used in combination with ethinyl estradiol, mainly for contraception and hormone replacement therapy, but also in treatment of some dermatological illnesses.

In this work, voltammetric determination methods of selected hormones in oral contraceptive pills are presented. In order to achieve low limits of detection, different working electrodes were used. Optimal conditions of measurements were selected, potential interferents were tested, the linear range and limit of detection was calculated for drospirenone, estradiol and ethinyl estradiol.

Acknowledgment
The work was supported by Ministry of Education and Science (AGH University Project No. 11.11.160.799).

Voltammetric determination of betamethasone on mercury film silver based electrode (Hg(Ag)FE)

*Joanna Smajdor, Robert Piech, Beata Paczosa-Bator
Faculty of Materials Science and Ceramics, AGH University of Science and Technology, Kraków, POLAND
e-mail: smajdorj@agh.edu.pl

***Keywords**: Voltammetry, hormone, mercury film electrode, carbon black.*

Betamethasone is one of the synthetic glucocorticoid representative. Due to its anti-inflammatory effects, it is widely used for a treatment of numerous conditions, such as rheumatic disorders, skin diseases, allergic conditions, Crohn's disease or different types of cancer. It is available as oral pills, injections and creams. Betamethasone is on the World Health Organization's List of Essential Medicines, the most effective and safe medicines needed in a health system.

In this work electrochemical behavior of betamethasone at a mercury film electrode (Hg(Ag)FE) was presented and a differential pulse adsorptive stripping voltammetric method (DPAdSV) was developed for determination of this steroid. A multipurpose Electrochemical Analyzer M161 with the electrode stand M164 (both MTM-ANKO, Poland) were used for all voltammetric measurements. Homemade silver based mercury film electrode (Hg(Ag)FE) was used for sensitive betamethasone determination. Instrumental parameters of proposed method, such as pulse of amplitude, potential step, preconcentration time and composition of supporting electrolyte were optimized. Repeatability of measurements was determined as RSD (%).

Linear range of method, recovery and limit of detection has been calculated. Suggested mechanism of betamethasone reduction mechanism has been proposed. According to the obtained results, the proposed method allows to measure nanomolar amounts of betamethasone in different drug samples, such as injections and ointments. The proposed method was validated using recovery parameter. New procedure was successfully applied for betamethasone sensitive determination in different pharmaceutical products.

Acknowledgment
The work was supported by Ministry of Education and Science (AGH University Project No. 11.11.160.799).

Synthesis and characterization of nanostructured anodic TiO_2 modified/doped with transition metal ions

*Monika Sołtys[1], Grzegorz D. Sulka[1]
[1]Department of Physical Chemistry and Electrochemistry, Jagiellonian University, Krakow, POLAND
e-mail: soltys@chemia.uj.edu.pl

***Keywords**: titanium dioxide, anodization, modifications of anodic TiO_2, transition metal ions*

Among several methods used to obtain nanoporous titanium dioxide (TiO_2) layers, anodization of titanium is becoming more and more popular. TiO_2 is one of the semiconductors widely used in various applications, including photocatalysis and medicine due to its good chemical stability, biocompatibility and non-toxicity. However, the main disadvantage of TiO_2 as a semiconductor for photoelectrochemical applications is absorption of the light from the UV range, which significantly limits its use as e.g., catalysts. Therefore, it is possible to increase the range of absorbed radiation by applying different modifications of this semiconductor such as electrochemical deposition and impregnation with the solution containing transition metal ions.

In this study we applied a three-step anodization in an ethylene glycol based electrolyte containing 0.38% wt. NH_4F and 1.79% wt. H_2O at a constant potential of 40 V. The samples were annealed at various temperatures (400-1000°C). Under different conditions several strategies mentioned before were used to synthesize nanostructured TiO_2 modified/doped with cobalt, copper and iron ions. The morphology and chemical composition of synthesized materials were investigated by using a field emission scanning electron microscope (FE-SEM/EDS), and their structure was determined by X-ray diffraction (XRD). The photoelectrochemical properties were characterized by UV-Vis spectroscopy.

The data showed that the annealing temperature from the range of 400-700°C does not change the morphology of anodic TiO_2 layers, but at higher annealing temperatures the nanoporous structure disappears. The modified TiO_2 samples exhibited photoelectrochemical properties. In conclusion, obtained material can be a promising nanomaterial with improved photoelectrochemical performance.

Acknowledgements
This work was supported by National Science Centre, Poland (Project No. 2016/23/B/ST5/00790).

Influence cleaning works on the swimming pool on microbial contamination

*Emilia Stańkowska[1]
[1]Faculty of Mining Surveying and Environmental Engineering, AGH University of Science and Technology, Cracow, POLAND
e-mail: stankowska@agh.edu.pl

***Keywords**: microbial purity, swimming pools, bacterial contamination, swimming pool floor*

Keeping proper microbiological purity of swimming pools is important for the health of users. The problem of microbial contamination in the swimming pool is the object of research all over the world. High temperature and humidity, which constantly prevailing in this objects, is an ideal environment for growing and development of pathogens. One of the operations against microbial contamination is to carry out daily cleaning activities around swimming pools. Proper selection of cleaning preparations and methods is important for sanitary and hygienic conditions of swimming pools.

The objective of this work is investigations of influence cleaning works on the microbiological purity of surfaces around swimming pools. Microbiological purity tests have been selected fragments of the surfaces around the pool basin. The samples were examined the total number of microorganisms, fungi and staphylococci pathogens.

The obtained results show the high degree of contamination of the tested surfaces. The analysis shows that the cleaning works carried out on have a positive impact on the microbiological purity of the floors.

Furthermore, attention is drawn to the size of a problem, which results from the lack of applicable standards and regulations. This information may be useful for further research in this area.

Alternatives to bottled waters

*Emilia Stańkowska[1]
[1]Faculty of Mining Surveying and Environmental Engineering, AGH University of Science and Technology, Cracow, POLAND
e-mail: stankowska@agh.edu.pl

***Keywords**: bottled water, drinking water, environment protection, water quality*

Water is a basic component of the human body. It is necessary for the proper functioning. Are said that people have to drinking about two liters water a day. When we drinking bottled water, we contribute to the creation of a huge number of garbage. That's why researchers are looking for alternatives to bottled water. It is a very important impact to our environment. One of them are drinking tab water, using water filters jug or drinking from urban sources.

The aim of this work iscomparison of alternatives for bottled water. Examined the quality of tap water, filtered water in filter jugs and water from the municipal source. It has done analysis of selected water quality parameters such as: total hardness, carbonate, determination of calcium ions, pH, conductivity, chemical oxygen demand, determination of microbial contamination. The results were related to the standards and producer's declaration.

The study has showed some advantages and disadvantages analyzed methods. Each consumer should individually choose the right alternatives for bottled waters. Minimizing the purchase of bottled water can give real benefits to environmental protection. Its essence is the reduction of garbage by limiting the consumption of products that excessively generate waste, according to the idea: reduce, reuse, recycle.

Staining techniques as a tool for assessing surface hydrophobicity

*Sylwia Stiler, Sylwia Golba
Faculty of Materials Science, University of Silesia in Katowice, POLAND
e-mail: stiler.sylwia@wp.pl

***Keywords**: contact lenses, staining techniques, Sudan IV*

Nearly half of those using contact lenses are experiencing discomfort and dryness in the eyeball. One of the reasons for these sensations is changes in the lens surface resulting from the deposition of proteins and lipids on the surface of the lens during its use.

Dyeing is an important biochemical technique that enables visual detection of interesting investigator sites on the material without isolating them. One of the dyes used in the study is Sudan IV, which is a lipophilic pigment (fat soluble). It has the form of red-brown crystals and has a melting temperature of 199°C. Its presence on the examined material after the staining is a clear marker of its hydrophobic nature.

The performed investigations included the assessment of the surface hyrdophilicity in one-day (hydrogel) and also biweekly and monthly (silicone-hydrogel) lenses. The analysis of the results allowed to determine the percentage share of hydrophobic domains that are potential sites for the deposition of lipids, proteins and other organic contaminants on the surfaces of contact materials.

The examined lenses before the staining procedure were stored in the following environments: commercial liquid for lens storage, saline solution, artificial tears and distilled water. Based on the procedures proposed in the literature, the lenses were held in liquids for 30 minutes or 24 hours. After removing from the solution, a photo of the lenses was taken, and then the obtained image was analyzed using the ImageJ software.

The monthly lens has become the largest color. This indicates the most hydrophobic nature of its surface.

Contact lenses as controlled release drug systems on the example of Tymolol

*Sylwia Stiler, Sylwia Golba
Faculty of Materials Science, University of Silesia in Katowice, POLAND
e-mail: stiler.sylwia@wp.pl

***Keywords**: contact lenses, controlled release drug systems, tymolol*

The first attempts to use contact lenses as drug release dies took place as early as in the 1960s. Initially, the main method of applying the drug in a hydrogel lens was dipping it in the drug solution, and then immediately applying it to the patient. This method was more effective than eye drops, however, it lengthened the possibility of drug application by several hours compared to the original method.

The results scientists have obtained so far, the relevant applications of silicone hydrogel lenses, which were dipped in drug solutions, have already allowed their initial use as drug carriers. Due to the enormous potential of contact materials, several methods have been developed that allow to increase the saturation of the material with the drug, as well as extend its release to several or even several dozen days.

The aim of the research was to study the sorption and desorption of timolol in polymer matrices. The newly opened lens was thoroughly rinsed with distilled water and its absorption spectrum was recorded. The material was then placed in a vessel filled with a solution of timolol and held for a given time (1 day, 3 days or 7 days) to allow diffusion of the substance molecules in the polymer matrix. The lenses were then removed, rinsed to clean the surface adsorbed molecules and placed in a measuring cuvette in order to register the spectrum.

Absorptive spectra for solutions and for lenses after their retention in solutions were recorded. Subsequently, the timolol release curves were recorded from polymer matrices. Determination of timolol desorption was carried out using a UV VIS spectrophotometer. The lens was placed on the bottom of a quartz cuvette and flooded with 2 ml of distilled water, then the spectra were recorded at 30 seconds intervals until the identical solution spectrum was stabilized for 5 consecutive measurements.

The drug substance used for the study gives promising results in terms of its use in contact materials as controlled drug release systems, because during the use of the drug directly into the eyeball it remains in it only a few minutes, while from the lens is released for several dozen minutes.

Thermogravimetric studies of hydrogel contact lenses

*Sylwia Stiler, Sylwia Golba
Faculty of Materials Science, University of Silesia in Katowice, POLAND
e-mail: stiler.sylwia@wp.pl

***Keywords**: contact lenses, thermogravimetric studies, hydrogel*

In recent years, Hy lenses have been replaced more and more by Sil-Hy lenses. Thanks to better parameters, silicone hydrogel lenses disrupt the corneal physiology to a lower extent, which is very beneficial from the point of view of the user. They are characterized by better oxygen permeability, which allows avoiding complications and the possibility of a longer uninterrupted time of wearing them. The permeability of the material of which the lens is made is different to the permeability of the finished product.

An important parameter characterizing these systems is the equilibrium water content (EWC). It determines the degree of material hydration, it is related to the material's ability to bind water under given environmental conditions. It is extremely important from a clinical point of view, because it directly affects many usable parameters of the lens.

First, desorption tests were carried out (distilled water, artificial tears, lens storage liquid and saline solution), which consisted in measuring changes in the mass of the tested material during desorption after storage in a given environment. The tests were carried out at 37°C to simulate the body conditions.

Before the test, the samples were placed in individual solutions for a period of 24 hours. They were then put into a laboratory dryer and the analytical balance determined their mass at intervals of 5 minutes until it stabilized, which meant the end of desorption. Two samples were tested for each of the solutions. From the data obtained in the measurements, the desorption curves of solutions from contact lenses and the desorption coefficient were determined.

After desorption, the lenses were re-sorbed in analogous solutions to determine if the lens returned to its original mass (before desorption). The resorption was carried out analogously at 37°C.

From the obtained data, the resorption curves of the solutions were determined, as well as the resorption coefficient for each of the lenses.

Thermogravimetric analysis showed great variation in the course of the dynamics of the drainage process, indicating the interaction of the polymer matrix with each of the environments in a specific way. For individual samples, changes in the DR coefficient indicate at least two dehydration areas for each of the environments, with the indication that the individual steps are differently distributed over time.

Examination of the kinetics of adsorption and desorption of water by HAP nanoparticles

*Urszula Szałaj[1], Anna Świderska-Środa[1], Agnieszka Chodara[1,2], Witold Łojkowski[1]
[1]Laboratory of Nanostructures, Institute of High Pressure Physics, Polish Academy of Sciences, Warsaw, POLAND
[2]Faculty of Materials Engineering, Warsaw University of Technology, Warsaw, POLAND
e-mail: u.szalaj@labnano.pl

***Keywords**: hydroxyapatite, adsorption, desorption, kinetics, BET isotherm*

Nanotechnology has became one of the key directions of public interest, with the special respect to nanomedicine applications. One of the most popular biomaterial is Hydroxyapatite (HAP). Composites consisting of HAP nano-crystals and biocompatible polymers have been widely used in orthopedic and dental application. These composites can provide both ease of use and superior mechanical properties of polymers, osteoconductivity and bioactivity of HAP.

It is well known, that water adsorbed on nanoparticle's surface can strongly influence the production process and final properties of complex nanomaterials. Hydroxyapatite presents hydrophilic properties. Therefore kinetics of water adsorption/desorption is an important factor in preparation and application of HAP-nanocomposites.

The aim of the work is to examine the speed and efficiency of water adsorption and desorption from the surface of different types of hydroxyapatite nanoparticles. The mass change caused by water adsorption/desorption on the surface of nanopowders exposed to various humidity level of around: 26%, 38% and 60% were detected. Experiments were performed with use of HAP nanopowders produced in the Laboratory of Nanostructures at the Institute of High Pressure Physics, Polish Academy of Sciences in Warsaw, signed with trade mark GoHAP™. Two types of GoHAP™ were used: type 1 and 6, with Specific Surface Area of 50 and 250 m2/g, respectively.

The results clearly indicate that the air humidity can have outstanding influence on the nanopowder mass and, consequently, on the material properties. The mass increase depends on the humidity of the air: higher the humidity, the faster and more efficient adsorption of water from the air is; eg. at 38% air humidity, the mass of nanopowder has increased by 6%. The highest weight gain was observed in the first minutes of exposure of the sample to ambient conditions. The BET isotherm model was determined, which allowed to determine the optimal working conditions with nanohydroxyapatite.

Folin-Ciocalteu method in determination of polyphenols in tea extracts

*Magdalena Szaniawska, Anna Taraba, Katarzyna Szymczyk
Department of Interfacial Phenomena, Maria Curie-Sklodowska University, Lublin, POLAND
e-mail: magdalena.szaniawska@poczta.umcs.lublin.pl

***Keywords**: polyphenols, tea, Folin-Ciocalteu method, secondary plant metabolites*

Polyphenols are one of the group of the secondary plant metabolites. Polyphenols are compounds of vegetable origin, soluble in water, which, with the exception of oxygen atoms, do not contain heteroatoms and have at least two hydroxyl groups. These compounds have a number of health-promoting properties, such as: antioxidant, anti-inflammatory, antiallergic, anti-sclerotic and antimutagenic. Polyphenols contained in the leaves protect both photosynthetic apparatus against the negative influence of visible light and plants against UV radiation.

The aim of the this research was to determine the content of polyphenols in various types of teas, including black, red, yellow and green, using the Folin-Ciocalteu method.

The total polyphenols content of tea extracts was assessed accoriding to Folin-Ciocalteu method. Briefly, 0,2 mL extract, 0,4 mL of Folin-Ciocalteu's reagent and 4 mL of distilled water were mixed together. Then, 2 mL of 15% Na_2CO_3 was added. The solution was mixed and incubated for 1 h at the room temperature. The absorbance of tea extracts sample was measured at 765 nm against a blank (corresponding extraction mixture was used instead of algal extract) on UV/VIS spectrometer. Gallic acid was used as a standard to construct the calibration curve. The total polyphenols content of tea extracts samples was expressed in mg/g of gallic acid equivalent.

The total amount of polyphenols in the tea extracts was calculated based on the absorbance value at 765 nm and on calibration curve of the gallic acid.

The amount of polyphenols, which was calculated in extract from green tea is 11,94 mg/g, from red tea 7,86 mg/g, from black tea 9,74 mg/g and from yellow tea is 12, 96 mg/g. The main conclusion from this research is that the most polyphenols are contained in green and yellow tea.

Determination of antioxidant activity of coffee and tea extracts by DPPH method

*Magdalena Szaniawska, Anna Taraba, Katarzyna Szymczyk
Department of Interfacial Phenomena, Maria Curie-Sklodowska University, Lublin, POLAND
e-mail: magdalena.szaniawska@poczta.umcs.lublin.pl

***Keywords**: free radicals, antioxidant, polyphenols, DPPH*

Knowledge about the dangers of free radicals leads to the search for natural substances to support the body's antioxidant defense. A direction of particular interest is the study of secondary metabolites obtained from plants with recognized dietary or curative effects. So far, a number of research methods have been developed that allow to determine the antioxidant potential of plant extracts. One the method with the DPPH reagent (1,1-diphenyl-2-picrylhydrazyl) is used more often, which is a stable free radical. It has an unpaired electron on the valence shell on one of the nitrogen atoms that form the nitrogen bridge. Due to the delocalisation of the electron, DPPH molecules do not form dimmers.

The aim of presented study was to determine the total antioxidant activity in coffee and tea extracts by the DPPH method.

The weighed amount of coffee and tea was placed in beakers, 100 cm^3 of distilled water at 90 was poured. After 10 minutes, the solutions are filtered and cooled to the room temperature. The extracts were diluted with water in a 1: 1 ratio. Absorbance at 513 nm will be determined after 60 min at room temperature in the dark. The percentage inhibition activity will be calculated from $[(A_0 - A_1)/A_0] \times 100$. A_0 is the absorbance of the control, and A_1 is the absorbance of the extract.

The most important conclusion of the measurements is that the coffee extract showed greater antioxidant activity and it was equal 86,05%. The tea extract showed a smaller percentage of inhibition, which means that the antioxidant activity of tea is lower.

Determination of critical micelle concentration of Kolliphor surfactants from the absorption and emission spectra of pyrene

*Magdalena Szaniawska, Anna Taraba, Katarzyna Szymczyk
Department of Interfacial Phenomena, Maria Curie-Sklodowska University, Lublin, POLAND
e-mail: magdalena.szaniawska@poczta.umcs.lublin.pl

***Keywords**: Kolliphor surfactants, pyrene, absorption, emission spectra, critical micelle concentration*

Kolliphor ELP is synthesized by reacting castor oil (glycerol triricinoleate) with ethylene oxide. Kolliphor ELP is used as an solubilizer fat-soluble vitamins A, D, E and K in aqueous solutions. Kolliphor RH40 is a nonionic surfactant obtained by reacting hydrogenated castor oil and ethylene oxide. It is also used as a solubilizer fat-soluble vitamins.

The fluorescence emission spectra of pyrene monomer in solution have a fine structure with five apices. The intensity of five apices is closely correlated with the surrounding polarity of pyrene monomers in solution and it is very useful in the investigations of solutions of different substances, especially surface active agents (surfactants). The ratio of the first and the third peaks intensity (I_1/I_3 parameter) in the function of concentration of the surfactant allows to determine of the critical micelle concentration (CMC). In the absorption spectra of pyrene occurs eight peaks. On the base this locations of the pyrene peaks, actually from the difference between second and seventh peak intensity, CMC also can be calculated.

The aim of presented study was to determine the critical micelle concentration of Kolliphor ELP and Kolliphor RH40 at different temperatures from the emission and absorption spectra of pyrene.

The aqueous solutions of surfactants, Kolliphor ELP and Kolliphor RH40 ($C=10^{-8}$-10^{-2} M) with the pyrene ($C_{pyrene}=4\cdot10^{-6}$M) were prepared. The emission spectra of pyrene were recorded on Hitachi FL-2700 spectrofluorimeter and the absorption spectra were recorded on Hitachi U-2900 spectrophotometer at the temperature range 293, 303 and 313K. By determining the parameter I_1/I_3 and P2-P7 parameter critical micelle concentration of Kolliphor surfactants in aqueous solutions was designated in the presented range of temperature.

The most important conclusion of the measurements is that the temperature has an impact on values of the critical micelle concentration of the surfactants.

Influence of particles swelling on viscosity of water suspensions of vegetal particles

*Adriana Szydłowska, Jerzy Hapanowicz
Department of Process Engineering, Opole University of Technology, Opole, POLAND
e-mail: a.szydlowska@doktorant.po.edu.pl

***Keywords**: organic particles, suspension, viscosity*

Water suspensions of organic particles are often met e.g. in processes of food industry or wastewater treatment processes. The fraction of solid and its properties can have key impact on the viscosity of the suspension. As a result of swelling, physical properties (sizes and weight) of the vegetal particles change, that results in change of suspension viscosity, according to the mentioned above. In turn, the viscosity influences basically on pattern of flow of the suspensions, their resistances of flow, convection heat transfer and also velocity of settling of solid particles or lifting of gas bubbles. Value of viscosity may also result in time and shear rate, that is connecting with flow velocity in a pipe or mixing intensity in a tank. Changes of suspensions viscosity can be verified basing on the results of rheometeric measurements of these fluids.

Water suspensions of dry grass were examined. This material indubitable occurs in sewage sludge. Three size fractions of the solid were used in the experiments, whereby the biggest size fraction did not exceed 212μm. Also three solid volume fractions corresponding diluted suspensions were used in the experiments. The viscosity measurements were done with the rotating rheometer with coaxial cylinders. The measurements were carried out after passing of twenty four hours from the samples preparation. It was aiming at taking into consideration phenomena that occur in the mixture whose processing, due to the specificity of certain processes, may last even several dozen hours.

Before carrying out the rheometeric measurements, growth of particles sizes and partially decline of liquid phase were observed. In turn, fluidity loosing of examined substances came forward during the rheometeric studies. This result was a consequence of the effect of swelling of vegetal particles. It was found out that the effect of swelling has essential impact on the viscosity of water suspensions of vegetal particles.

At current state of knowledge, determination influence of the effect of swelling of vegetal particles on the growth of suspension viscosity on the analytical way is impossible. Hence, in order to improve an efficiency of long-standing processes systems involving a water suspension of vegetal particles, earlier carrying out of experiment under conditions of actual process is necessary.

Composite layer fabricated in situ in steel castings

*Łukasz Szymański[1,2], Ewa Olejnik[1,2], Sylwia Żymankowska-Kumon[2], Dariusz Drożyński[2], Tomasz Tokarski[3]
[1]Innerco Ltd., Cracow, POLAND
[2]AGH University of Science and Technology, Faculty of Foundry Engineering, Cracow, POLAND
[3]AGH University of Science and Technology, Academic Centre of Materials and Nanotechnology, Cracow, POLAND
email:lsz@agh.edu.pl

***Keywords**: composite, in situ, TiC, hardness, MMCs*

Wear abrasive is one of the main processes of destruction construction elements that occurs primarily on the working surfaces of details. Therefore ones seeks to design materials reinforced surface or zonal reinforcement using techniques such as laser cladding, thermal spraying, and welding (TIG). A separate group consists of foundry methods, which allows the generation in situ ceramic phases as results of reactions between the substrates carbides and liquid alloy.

The aim of this study was to produce layers of composite type TiC-Fe. In this order aqueous foundry coating with the addition of substrates TiC and carboxymethylcellulose (CMC) acting as a binding material was prepared. In the first stage of the research structures analyze of CMC using spectroscopic techniques (FTIR) was conducted. Further a coating on the basis of a 2% aqueous solution of CMC containing a powder of titanium and graphite was prepared. The coating was characterized in terms of physicochemical and technological properties such as thermal decomposition, viscosity and contact angle. The technological process of producing the composite layer type TiC-Fe based on cover cavity mold prepared coat and pouring liquid alloy.

As a result the composite layer having a thickness from 5 to 1.5 mm was obtained. Composite layer characterized by a heterogeneous structure which was related to reactive infiltration manifested separation area by base alloy. Research of structures made by X-ray analysis (XRD) and the microstructure using scanning electron microscopy (SEM) revealed the presence of TiC ceramic phase. This proves for the reaction of synthesis we recess in the mould cavity. Conducted hardness measurement by Vickers method in the area of the composite layer showed a hardness of 700 HV1 cooperation accounted for more than two-fold increase compared to the base alloy.

The developed technological process enables obtaining composite castings with the work surface reinforced by TiC particles.

The influence of particle size of porogenes on the process of supercritical foaming of poly(ε–caprolactone)

*Joanna Środa[1], Katarzyna Kosowska[1], Marek Henczka[1]
[1]Faculty of Chemical and Process Engineering, Warsaw University of Technology, Warsaw, POLAND
e-mail: joannasroda.4@gmail.com

***Keywords**: tissue engineering, porous materials, supercritical carbon dioxide, heterogeneous nucleation*

Tissue engineering has made lately significant progress on the field of research by merging new techniques from material chemistry and life sciences to prepare biodegradable 3D scaffolds applicable for regeneration of damaged tissue. From among all of the methods of production of porous polymers the use of supercritical fluids as blowing agent has gained significant interest. In particular, polymer porous structures can be produced using gas foaming technique with supercritical fluid as blowing agent from poly(ε – caprolactone) enriched with porogenes such as hydroxyapatite, cellulose and graphene oxide in the form of nano – and microparticles.

In the performed experiments the polymer composites were manufactured using supercritical CO_2 at two different foaming pressures (9 MPa and 18 MPa) and at three various temperatures (50°C, 70°C and 100°C) for different process times (0 h, 1 h and 4 h).

The morphology and mechanical properties of foams were investigated using analytical methods such as scanning electrone microscopy, the differential scanning calorimetry. The Young's module and maximum compressive strength were investigated using the static compression test.

The obtained results showed that porogene particles size has a major effect on the nucleation of gas bubbles in the polymer structure. Increase of the concentration of nanohydroxyapatite in composite lead to increase of maximum compressive strength, decrease of melting temperature and increase of degree of crystallinity. No side effects of using supercritical fluid as blowing agent in foaming process of polycaprolactone composites were observed.

The influence of the surfactant on the properties of quercetin solutions

*Anna Taraba[1], Magdalena Szaniawska[1], Katarzyna Szymczyk[1]
[1]Faculty of Chemistry, Department of Interfacial Phenomena, Maria Curie-Skłodowska University, Lublin, POLAND
e-mail: anna.taraba@poczta.umcs.lublin.pl

***Keywords**: surfactant, quercetin, flavonoids*

Quercetin belongs to a group of plant pigments called flavonoids. They give many fruits, flowers, and vegetables their colors. Flavonoids, such as quercetin, are antioxidants. They can scavenge particles in the body, free radicals, which damage cell membranes, tamper with DNA, and cause cell death. The antioxidant properties of quercetin can help in neutralization of free radicals. They may reduce or even help prevent some of the damage free radicals cause. In test tubes, quercetin has strong antioxidant properties.

One of the newest way of obtaining flavonoids is micellar extraction. In this process the solutions of surfactants are used. So the aim of presented studies was to determine the influence of the non-ionic surfactant, Triton X-114, on the quercetin solutions at different temperatures.

The solutions of quercetin (C_{qe} =10^{-5} M) with different contain of Triton X-114 (10^{-6} – 5x10^{-3}M) were prepared in 100ml flask. Next the analysis of these solutions was made on the basis of pH and conductivity measurements at 293, 303 and 313K.

The main conclusions are that the conductivity increases with the increase of the temperature in examined system, pH changes with the temperature and the pH oscillates around similar values at all temperatures.

Acknowledgements
This work was supported by the Ministry of Science and Higher Education, Poland, Project no. BS-M-03-002-17-D-01.

Temperature studies of rutin-surfactant systems

*Anna Taraba[1], Magdalena Szaniawska[1], Katarzyna Szymczyk[1]
[1]Faculty of Chemistry, Department of Interfacial Phenomena, Maria Curie-Skłodowska University, Lublin, POLAND
e-mail: anna.taraba@poczta.umcs.lublin.pl

***Keywords**: surfactant, rutin, flavonoids*

Flavonoids consist of a large group of polyphenolic compounds, which have a benzo-γ-pyrone structure and are ubiquitously present in plants. They are synthesized by phenylpropanoid pathway. Secondary metabolites of phenolic nature including flavonoids are responsible for the variety of pharmacological activities. Flavonoids are known to be synthesized by plants in response to microbial infection. Their activities are structure dependent. The chemical nature of flavonoids depends on their degree of hydroxylation, structural class, other substitutions and conjugations, and degree of polymerization. Flavonoids have potential health benefits for example antioxidant properties.

Rutin is a bioflavonoid, or plant pigment, that can be found in certain vegetables and fruits. It has powerful antioxidant properties. It also helps your body produce collagen and use vitamin C.

The aim of presented studies was to determine the influence of temperature on the rutin-Tween 80 systems.

The solutions of rutin ($C_{ru} = 10^{-5}$ M) with different contain of Tween 80 (10^{-6} – $5x10^{-3M)}$ were prepared in 100ml flask.

Next the analysis of these solutions was made on the basis of the UV-vis and fluorescence emission spectra measurements in 293, 303 and 313K.

The main conclusion is that with the increase of the temperature the signal from rutin decreases in both spectra (absorption and emission).

Acknowledgements
This work was supported by the Ministry of Science and Higher Education, Poland, Project no. BS-M-03-002-17-D-01.

The temperature influence on the conductivity in the rutin-surfactant systems

*Anna Taraba[1], Magdalena Szaniawska[1], Katarzyna Szymczyk[1]
[1]Faculty of Chemistry, Department of Interfacial Phenomena, Maria Curie-Skłodowska University, Lublin, POLAND
e-mail: anna.taraba@poczta.umcs.lublin.pl

***Keywords**: surfactant, rutin, flavonoids, conductivity*

Conductivity is the ability of a solution, a metal or a gas - in brief all materials - to pass an electric current. In solutions the current is carried by cations and anions whereas in metals it is carried by electrons. Conductivity is typically measured in aqueous solutions of electrolytes. Electrolytes are substances containing ions, i.e. solutions of ionic salts or of compounds that ionise in solution. The ions formed in solution are responsible for carrying the electric current. Electrolytes include acids, bases and salts and can be either strong or weak. Most conductive solutions measured are aqueous solutions, as water has the capability of stabilising the ions formed by a process called solvation.

Rutin is biologically compound, which can be found in fruit and vegetables. It has pro-health properties such as: anticancer, anti-inflammatory and anti-scavenging.

The aim of presented studies was to determine the influence of temperature on conductivity in the rutin-Tween 80 systems and rutin-Triton X-114 systems.

The solutions of rutin (C_{ru} =10^{-5} M) with different contain of Tween 80 (10^{-6} – 5x10^{-3}M) and Triton X-114 (10^{-6} – 5x10^{-3}M) were prepared in 100ml flask. Next the analysis of these solutions was made on the basis of conductivity measurements at 293, 303 and 313K.

Conclusion is that the conductivity increases with the increase of the temperature in both examined systems.

Acknowledgements
This work was supported by the Ministry of Science and Higher Education, Poland, Project no. BS-M-03-002-17-D-01.

Polyphenolic compounds in the juice of citrus fruits-components of the voltammetric analysis

*Justyna Ubysz[1], Katarzyna Jedlińska[1]
[1] Faculty of Materials Science and Ceramics, AGH University of Science and Technology, Kraków, POLAND
e-mail: justyna.ubysz@gmail.com

***Keywords**: polyphenolic compounds, naringenin, coumarin, voltammetric determination, citrus fruits*

Nowadays, the excessive use of medications without proper knowledge of the possible interactions of therapeutic substances from food supplementation, is a serious problem. Some of polyphenolic compounds, which are occurring in citrus fruits, can interfere with the effect of drugs.

This paper deals with the development of a voltammetric procedure for the determination of selected polyphenolic compounds in citrus fruit juices. The tests were carried out in two measuring systems, depending on the compound which was tested. In order to determine naringenin, a system with a glassy carbon electrode was used (GCE), while in the case of coumarin determination a Controlled Grow Mercury Drop Electrode (CGMDE) was used.

In both cases, the experiments were split into two stages. At the first stage, the composition and concentration of the supporting electrolyte and the instrumental parameters of DPV voltammograms were optimized. With those parameters set, the calibration curves for both analytes were determined. Second step was attempts of determinating naringenin and coumarin in real samples. Quantitative analysis of tested compounds was realized using standard addition method.

Determination of biologically active compounds with using Glassy Carbon Electrode

*Justyna Ubysz[1], Katarzyna Jedlińska[1]
[1] Faculty of Materials Science and Ceramics, AGH University of Science and Technology, Kraków, POLAND
e-mail: justyna.ubysz@gmail.com

***Keywords**: glassy carbon electrode, naringenin, vitamin K2, voltammetric detection*

This paper take up the development of a voltammetric procedure for the determination of biologically active compounds. We focused on marking naringenin and vitamin K2 with use of Glassy Carbon Electrode (GCE).

Vitamin K2 is a group of essential liposoluble micronutrients, which plays an important role in human health. To detect vitamin K2 with use GCE, different factors such as composition of supporting electrolyte and instrumental parameters were tested with differential pulse adsorptive stripping voltammetry (DP AdSV). The best result were recorded in supporting electrolyte containing 40 % of ethanol and 0,04M Britton-Robinson buffer with the scanning performed in the range from -0,2 V to -0,8 V, in both cathodic and anodic directions. Using parameters, which were considered optimal, attempts were made to determinate vitamin K2 in selected food supplements.

Naringenin occurs in citrus fruits and can interact with some medicine. To detect naringenin with use GCE, experiments were carried out in two stages. The first stage concerned optimization of supporting electrolyte and instrumental parameters. Second stage was attempts of determinating naringenin in citrus fruit juices.

Developed methods allowed determination of test substances in real samples. In citrus fruit juices we marked naringenin and vitamin K2 in dietary supplements.

Influence of liquid flow rate on size of nanobubbles generated by porous-membrane modules

*Karol Ulatowski[1], Paweł Sobieszuk[1]
[1]Faculty of Chemical and Process Engineering, Warsaw University of Technology, Warsaw, POLAND
e-mail: Karol.Ulatowski.dokt@pw.edu.pl

***Keywords**: nanobubbles, porous membranes, size distribution*

Nanobubbles are spherical gas objects in continuous liquid phase. They are smaller than 1 μm. In case of such fine bubbles, some extraordinary characteristics are observed. The inside pressure of bubble of size 100 nm in water is equal to around 27 atm, what leads to significant increase of gas density. As a result, nanobubbles have nearly non-existent rising velocity and are moving mostly by Brownian motion. Surprisingly, bubbles of this size are also very stable in liquid, both coalescence and dissolution are not appearing. Nanobubbles are used widely in various branches of industry (such as flotation, surface cleaning, hydroponics) but literature lacks fundamental research of their properties and generation methods.

The aim of this work is to investigate the influence of distilled water flow rate in two different porous-membrane modules on size of generated nitrogen nanobubbles. Modules had different diameter and number of tubular membranes inside the module. Bubbles were cut off from the membrane surface by the sheer stress induced by the liquid velocity. Changing the liquid flow rate should change the size of bubbles as they will be cut off after different residence time on the surface. Size distribution of generated bubbles were measured using Dynamic Light Scattering (DLS) technique.

For both modules, higher liquid velocity induced generation of smaller bubbles, what was consistent with expectations. What is more, the effect occurred for modules both with single and with multiple membrane tubes. This effect can help us in generation of bubbles of desired size.

This research are the first, but very important, step to describe the phenomena occurring during generation of bubbles on porous membranes. This work validated the hypothesis of possibility of controlling nanobubble generation in membrane modules by changing the flow rate of liquid.

Acknowledgements
This work was supported by Andrzej Mróz, Ph.D. Eng., from Net Water Technologies, who constructed and shared with us the membrane modules.

Cultures of HL-60 cells in a wave-type agitated single-use bioreactor

*Kamil Wierzchowski[1], Maciej Pilarek[1], Iwona Grabowska[2]
[1]Faculty of Chemical and Process Engineering, Warsaw University of Technology, Warsaw, POLAND
[2]Faculty of Biology, University of Warsaw, Warsaw, POLAND
e-mail: kamil.wierzchowski.dokt@pw.edu.pl
***Keywords**: wave-type agitation, single-use bioreactor, non-adherent cell culture, HL-60 human cell line*

Single-use bioreactor are commonly applied for scaling-up of *in vitro* cell cultures. Substituting of typical culture vessels made of stainless steel or glass by disposable polymer-based bags is very useful and flexible in the case of mammalian cells and tissues cultures. Application of the oscillating movement to bioreactor's tray results in wave-type mixing of liquid and gas phases filling culture bag. During the wave-induced agitation, the interfacial area between gas phase and culture medium is continuously renewed, and therefore the bubble-free surface aeration of the culture broth is accomplished. Simultaneously, such gentle wave-type agitation significantly limits the level of shear forces, as well as inhibit the shear stress effects which negatively influence on the fragile biomass.

The ReadyToProcess WAVE^{TM}25 bioreactor (WAVE 25; GE Healthcare, Sweden), equipped with 2 dm^3 polymer-based culture bag, has been applied to perform *in vitro* culture of non-adherent HL-60 (promyeloctic leukemia) cells. The influence of the oscillation angle of bioreactor's tray on (i) the growth rate and (ii) the viability of cells, as well as on (iii) the dissolved oxygen level and (iv) the specific glucose consumption rate were investigated during 7-days of the culture. All results were referenced to the typical non-mixed (i.e. static) cultures of HL-60 cells.

The highest value of the growth rate of HL-60 cells have been noted for the oscillation angle equaled to 6º. The viability of cells was independent from the oscillation angle in the studied range of this parameter. Increase of the oscillation angle resulted in higher values of the dissolved oxygen concentration and lower values of the specific glucose consumption rate.

The results of the study clearly confirmed the applicability of WAVE 25 bioreactor supported with wave-induced agitation as the right platform for submerged culture of non-adherent animal cells.

Acknowledgement
This work has been supported by the budget sources for The National Centre for Science, Poland, Grant no. DEC-2015/17/B/ST8/00631.

Comparative study of sol – gel and hydrothermal synthesis of MWCNTs-TiO_2 composite nanoparticles

*Patrycja Wilczewska[1], Agnieszka Fiszka Borzyszkowska[1], Aleksandra Bielicka–Giełdoń[1], Ewa Maria Siedlecka[1]

[1]Department of Environmental Technology, University of Gdańsk, Gdańsk, POLAND

e-mail: patrycja.wilczewska@phdstud.ug.edu.pl

***Keywords**: cytostatic drugs, photocatalysis, multi-walled carbon nanotubes, MWCNTs, TiO_2*

Multi-walled carbon nanotubes (MWCNTs) are widely reported to synergistically enhance the photocatalytic activity of TiO_2 through high-surface area and high quality active sites, retardation of electron–hole recombination and absorption under visible light by modification of band-gap and/or sensitization. Cytostatics have been reported to have low biodegradability so their concentration in environment is gradually increased. These kinds of drugs are showed high toxicity and they can potentially exert adverse effects on the ecosystem and aquatic environment even at trace levels.

The aim of this work was developing an effective way to synthetize TiO_2 modified MWCNTs photocatalyst for the removal of two cytostatic drugs from water. The kinetics and efficiency of the photocatalytic decay and mineralization of cyclophosphamide (CF) and imatinib (IMA) in solar, visible and UV light was investigated. MWCNTs – TiO_2 nanocomposite was prepared by sol – gel and hydrothermal methods. Photocatalysts samples were synthesized with the loading 2,5% wt. amount of MWCNT and precursor of *titanium dioxide was titanium tetrabutoxide*.

The prepared hybrid materials were characterized analyzing spectra of UV-VIS/DRS and PL and discussed the results. Both MWCNTs – TiO_2 nanocomposites have great adsorption in the ultraviolet region. Photocatalyst made by hydrothermal method has much higher light adsorption below 420 nm. No significant differences have been found in the photoluminescence spectra between samples. However, the MWCNT – TiO_2 composite prepared by the sol – gel method showed a better degradation rate than the other nanocomposite in UV and solar light. In the presence of MWCNTs/TiO_2 both cytostatic drugs have been completely removed in the UV light.

The results show that method of synthesis has an impact on the nanocomposites ability to absorb radiation in the visible and solar light and the photocatality activity. According to the UV-Vis/DRS analysis and using the Kubelka – Munk equation, the band gap was calculated and discussed.

BiOXY modified by multi-walled carbon nanotubes – synthesis, characterization and environmental applications

*Patrycja Wilczewska[1], Agnieszka Fiszka Borzyszkowska[1], Aleksandra Bielicka–Giełdoń[1], Ewa Maria Siedlecka[1]

[1]Department of Environmental Technology, University of Gdańsk, Gdańsk, POLAND

e-mail: patrycja.wilczewska@phdstud.ug.edu.pl

***Keywords**: BiOXY, bismuth oxyhalides, photocatalysis, multi-walled carbon nanotubes, MWCNTs*

Environmental pollution and energy shortage are the two main problems humans are facing now. Traditional pollutant treatment techniques cannot completely remove low biodegradable organic compounds. Semiconductor photocatalytic technology is regarded as an efficient, green and promising solution to solve environmental problems and energy crises. Bismuth oxyhalides (BiOX) are of lower valence band energy, so they have strong oxidation ability. Furthermore, BiOX dependently of type of X can be a high or low energy gap (Eg) semiconductor. For example, a doping BiOCl by Br allows to tune the band gap, which may result in an increase of photocatalytic activity in solar or visible light. Modified by multi-walled carbon nanotubes (MWCNTs) this type of semiconductors increases photocatalytic activity and gives an innovative approach, still undergoing research.

In this study, doped bismuth oxyhalide (BiOXY (X,Y = Cl, Br)) semiconductors were prepared by a simple solvothermal method, with glycerol serving as solvent and KCl, KBr and $Bi(NO_3)_3 \cdot 5H_2O$ respectively as halogen and a bismuth source. MWCNTs were dispersed in the mixture before solvothermal treatment by sonification. The photocatalytic properties of the materials were studied by monitoring the degradation of rhodamine B (RhB) and reduction of Cr (VI), under visible light absorption. The characteristics of prepared materials were analyzed by means of scanning electron microscopy, UV–visible diffuse reflectance spectra and photoluminescence spectra.

The addition of MWCNTs had a positive effect on the ability to absorb light in the visible range by photocatalysts. PL spectra showed the decrease in irradiation emission for photocatalysts containing surface modification in MWCNTs. Reducing emissions while increasing photocatalytic activity is explained by the phenomenon of effective absorption of irradiation, thus inhibiting the recombination process of generated charges in the electron-hole. MWCNTs/BiOClBr showed largest photocatalytic activity compared with the others photocatalysts.

Application of zirconium nanopowders for chromium sorption

*Katarzyna Wilkosz, Ewa Niewiara, Łukasz Magda, Władysław W. Kubiak
AGH University of Science and Technology, Faculty of Material Science and Ceramics, Department of Analytical Chemistry, Cracow, POLAND
e-mail: katwilkosz@gmail.com

***Keywords**: adsorption, chromium, zirconium dioxide, nanopowders*

Chromium occurs in inorganic systems in several forms but only Cr(III) and Cr(VI) are significant in biological systems. Hexavalent chromium is known as a toxic and genotoxic form in contrast to trivalent form which is considered as an important bioelement. Therefore, there is a need to find a selective method which will be able to remove only toxic forms of chromium. Adsorption method using nanopowders based on zirconium dioxide gives successful results for this purpose.

Nanopowders based on zirconium dioxide synthesized by ammonia method with hydrothermal crystallization were used as a sorbent for testing sorption effectiveness of trivalent and hexavalent chromium. Sorption processes were carried out depending on the time sorption and pH of nanopowder suspension.

Sorption efficiency of Cr(III) for unmodified nanopowders based on zirconium dioxide 3YSZ is between 31.9% and 66.5% and better results are obtained for pH 6.7 which is a value for isoelectric point for this nanpowder. Sorption efficiency of Cr(VI) also for unmodified nanopowders based on zirconium dioxide is between 31.2% and 99.0% and better results are received in acidic environmental at pH 3.5. Sorption efficiency of Cr(VI) for modified zirconium nanopowders by addition of neodymium in amount of 0.5 %mol is between 53.2% and 99.1% and better results are obtained also for pH 3.5 which is a value for isoelectric point for this nanopowder. Sorption efficiency of Cr(III) for modified nanopowders based on zirconium dioxide is between 47,0% and 63.4% and better results are received for pH 6.5. Sorption time research helped to assess whether chromium retention on nanopowders is stable or not due to possible desorption process in time.

Based on received results there is a possibility to apply tested nanopowders based on zirconium dioxide as selective sorbent for toxic forms of chromium.

Acknowledgements
This study was carried out within the AGH – University of Science and Technology (Cracow) - grant number 15.11.160.017

Removal of organic impurities using nanopowders based on zirconium dioxide

*Katarzyna Wilkosz, Ewa Niewiara, Łukasz Magda, Władysław W. Kubiak
AGH University of Science and Technology, Faculty of Material Science and Ceramics, Department of Analytical Chemistry, Cracow, POLAND
e-mail: katwilkosz@gmail.com

***Keywords**: sorption, humic acids, zirconium dioxide, nanomaterials*

Humic compounds are natural component of groundwater. The presence of humic acids in groundwater for human consumption is unfavorable because they decline organoleptic properties such as taste, odor and color. Humic substances as pure forms are not harmful for humans' health however, due to their sorption properties they may adsorb some toxic compounds e.g. heavy metals. This research shows sorption efficiency of humic acids using nanopowders based on zirconium dioxide as a sorbent.

Modified by lanthanides nanopowders based on zirconium dioxide synthesized by ammonia method with hydrothermal crystallization were used as a sorbent for testing sorption effeciency of humic acids. Sorption processes were carried out depending on pH value of nanopowder suspension and time sorption.

Sorption efficiency of humic acids for all tested nanopowders has the greatest value in acidic environmental. Addition of modifier - neodymium cause improvement of adsorption efficiency in basic environment. The optimal time of sorption for all tested nanopowders is about 30 minutes. Sorption process of humic acids for unmodified nanopowder based on zirconium dioxide is more stable in time than for modified nanopowders. Increasing in amount of modifier for zirconium nanopowder has no beneficial impact on removal humic acids from the water.

Based on above results there is a possibility to apply nanopowders based on zirconium dioxide as sorbent for natural components of water such as humic acids.

Acknowledgements
This study was carried out within the AGH – University of Science and Technology (Cracow) - grant number 15.11.160.017

Effect of microwave radiation power on the size of aggregates of ZnO NPs prepared using microwave solvothermal synthesis

*Jacek Wojnarowicz[1], Tadeusz Chudoba[1], Witold Lojkowski[1]
[1] Laboratory of Nanostructures, Institute of High Pressure Physics, Polish Academy of Sciences, Warsaw, POLAND
e-mail: jacek.wojnarowicz@tlen.pl

***Keywords**: zinc oxide nanoparticles (ZnO NPs), Microwave Solvothermal Synthesis (MSS), microwave reactors, agglomerates and aggregates, ZnO NPs water suspension*

The effect of the changed power of microwave heating on the properties of ZnO nanoparticles (NPs) obtained by the microwave solvothermal synthesis from zinc acetate dissolved in ethylene glycol was tested for the first time. The following properties of ZnO NPs were determined: phase purity (XRD), skeleton density, specific surface area (BET), morphology, average particle size and crystallite size distribution. The obtained ZnO NPs were characterised by hexagonal wurtzite structure without presence of a foreign phase. The increase in the microwave radiation power resulted in the reduction of the total synthesis time with simultaneous preservation of the constant size and shape of single ZnO NPs, which were synthesised at the pressure of 4 bar (~230˚C). All the obtained ZnO NPs samples were composed of homogeneous spherical particles being single crystals with the average size of 27±3 nm with a developed specific surface area of 40 m^2/g and the skeleton density of 5.18±0.03 g/cm^3.

The effect of the changed power of microwave heating on the average size of particles (particles, agglomerates, aggregates) in water suspensions was observed, which were tested using the dynamic light scattering (DLS) technique. Water suspensions of ZnO NPs were obtained using ultrasonic homogenisation. The average size of ZnO particles in the suspensions ranged from 60 to 120nm depending on the power of microwave radiation used in the synthesis of ZnO NPs. SEM images revealed an impact of the change of microwave radiation power on the morphology of the obtained agglomerates/aggregates of NPs.

Acknowledgements
The work was prepared as part of the execution of the research project no. UMO-2015/19/N/ST5/0366 financed from the funds of the National Science Centre Poland.

MSS2 - A novel microwave reactor for hydro- and solvothermal scale-up nanomaterials synthesis

*Jacek Wojnarowicz[1], Sylwia Dąbrowska[1], Tadeusz Chudoba[1], Andrzej Majcher[2], Witold Lojkowski[1]

[1]Laboratory of Nanostructures, Institute of High Pressure Physics, Polish Academy of Sciences, Warsaw, POLAND

[2]Institute for Sustainable Technologies – NRI – Control Systems Department, Radom, POLAND

e-mail: jacek.wojnarowicz@tlen.pl

***Keywords**: microwave reactors, nanoparticles (ZnO NPs), Microwave Solvothermal Synthesis (MSS), Microwave Hydrothermal Synthesis*

Microwave solvothermal synthesis consists in using microwaves for heating a liquid reaction mixture closed in a high-pressure chamber. This technology is environmentally friendly. The process solutions applied by us are ahead of the world level and enable synthesising highest quality nanopowders: ultrapure, homogeneous in terms of phase, with an assumed morphology and particle size.

The specialised high-temperature pressure seals developed by us in the MSS2 reactor model enable introduction of substrates, performance of processes and discharge of products in tracks formed in chemically inert materials. The use of microwave radiation and the unique design of the reactor enable precise pressure control during rapid synthesis processes, controlled with an accuracy of 1 second. In the MSS2 reactor model, the reactor chamber is emptied exactly immediately after finishing the heating, as a result of which the course of reaction is rapidly cooled down and frozen.

The obtained process chamber volume (470 ml) and the process automation in the "stopped flow" operation mode ensure achieving such an efficiency of nanopowder production that is unavailable in other solutions. The equipment control system is consistent with PN-EN 61512 standard (ANSI/ISA-S88.01 Batch Control) and enables, among others: monitoring the equipment status, monitoring and recording the process parameters, performing processes in the manual, semi-automatic and automatic control mode (procedural control).

Acknowledgements

The MSS2 reactor was constructed as part of the CePT project, reference: POIG.02.02.00-14-024/08, financed by the European Regional Development Fund within the Operational Programme "Innovative Economy" for 2007–2013.

Microwave solvothermal synthesis and characterization of nanocrystalline ZnO doped with Mn^{2+} and Co^{2+}

*Jacek Wojnarowicz[1], Tadeusz Chudoba[1], Witold Lojkowski[1]
[1]Laboratory of Nanostructures, Institute of High Pressure Physics, Polish Academy of Sciences, Warsaw, POLAND
e-mail: jacek.wojnarowicz@tlen.pl

***Keywords**: microwave reactors, nanoparticles (ZnO NPs), Microwave Solvothermal Synthesis (MSS), Microwave Hydrothermal Synthesis*

Using the Microwave Solvothermal Synthesis (MSS), we obtained $Zn_{(1-y)}Co_yO$ and $Zn_{(1-x)}Mn_xO$ nanomaterials with varied contents of dopants. The synthesis of $Zn_{(1-y)}Co_yO$ and $Zn_{(1-x)}Mn_xO$ NPs in ethylene glycol can be expressed with the following equations:

$$(CH_3CO_2)_2Zn + (CH_3CO_2)_2Co \xrightarrow{C_2H_4(OH)_2,.T,.P} Zn_{(1-y)}Co_yO_{\downarrow} + \text{other products (liquid)}$$
$$(CH_3CO_2)_2Zn + (CH_3CO_2)_2Mn \xrightarrow{C_2H_4(OH)_2,.T,.P} Zn_{(1-x)}Mn_xO_{\downarrow} + \text{other products (liquid)}$$

The syntheses of NPs were carried out for 25 minutes in the Ertec 02-02 microwave reactor.

The MSS allows the preparation of a uniform nanocrystalline $Zn_{1-x}Co_xO$ with high concentration, up to 15 mol%. The $Zn_{1-x}Co_xO$ NPs have a fully pure single phase wurtzite crystalline structure corresponding to zinc oxide. No other secondary phase such as $Co(OH)_2$, CoO, Co_3O_4 or Co metal was found at $x \leq 0.15$, which shows the doped Co ions are substituted at the Zn ions sites. The obtained $Zn_{1-x}Co_xO$ NPs were composed of spherical particles with monocrystalline structure and average particle size ≈30 nm. SEM images did not show an impact of an increase in dopant on the morphology of NPs.

The content of Mn^{2+} in $Zn_{1-x}Mn_xO$ ranged from 1 to 25 mol%. The average particle size of $Zn_{1-x}Mn_xO$ was determined using the Scherrer's formula, the Nanopowder XRD Processor Demo web application and by converting the specific surface area results. X-ray diffraction of synthesized samples shows a single phase wurtzite crystal structure of ZnO without indication of additional phases. The obtained $Zn_{1-x}Mn_xO$ were composed of spherical particles with monocrystalline structure and average particle size from 17 nm to 30 nm depending on the content of dopant. SEM images showed an impact of an increase in dopant on the morphology of NPs.

Mechanism of formation and growth of nanohydroxyapatite layers deposited by ultrasonic method

*Bartosz Woźniak[1],Agnieszka Chodara[1], Maciej Łojkowski[2], Jan Mizeradzki[1], Dawid Myszka[3], Witold Łojkowski[1]

[1]Laboratory of Nanostructures, Institute of High Pressure Physics, PAS, Warsaw, POLAND

[2]Warsaw University of Technology, Faculty of Materials Engineering, Warsaw, POLAND

[3]Warsaw University of Technology, Faculty of Production Engineering, Warsaw, POLAND

e-mail: b.wozniak@labnano.pl

Keywords*:nanotechnology, nanohydroxyapatite, thin layers, ultrasonics*

Ultrasonic coating technology is a method for surface modification of material for different applications, mainly related to medicine. It is based on cavitation phenomenon where bubbles formation and implosion in liquid medium cause water jet formation with velocity up to 280 m/s. The jetting in the presence of solution with nanoparticles, enable to deposit thin layers on materials surface like textiles, porous structures, solid objects etc. One of most promising application is coating materials with hydroxyapatite nanoparticles (nHAp) for bone regeneration applications. However, it is not exactly known how nanoparticles form a layer and how it grows in time.

The aim of the study was to determine the mechanisms occurring during ultrasonic coating of PCL substrates with nHAp under variable process parameters. Two types of nHAp (15±1 nm, 43±4 nm) and thin PCL pellets were used as a substrates. The scope of work covered developing research procedures, measurement of samples including SEM analysis (determining degree of coverage, specific features of the layers) and water angle wettability.

During the process of ultrasonic coating, specific dendritic-shape structures of nHAp are formed which tend to grow within a time of deposition. Formation of suchstructures is possible due to mechanism of nanoparticles deposition and embedding in the surface of material. Dynamic water jets and shock waves from cavitation implosions are speeding up nanoparticles towards anchor points on a surface, thus causing an island-shape objects expansion.

Explanation of processes occurring during ultrasonic coating allows to obtain new knowledge for better process control and use new modifications. It was also demonstrated that ultrasonic method is effective by mean of process time (<10 minutes), temperature (below 30^0C) and very efficient use of hydroxyapatite (low w/v aqueous particles concentration).

Adsorption equilibrium of carbon dioxide on Zeolite 13X at high-pressures

*Kamila Zabielska, Tomasz Aleksandrzak, Elżbieta Gabruś
Faculty of Chemical Technology and Engineering, West Pomeranian University of Technology, Szczecin, POLAND
e-mail: kamila.zabielska@zut.edu.pl

Keywords: *carbon dioxide, Zeolite 13X, adsorption equilibrium, adsorption isotherm*

Carbon dioxide (CO_2) is a compound responsible for the greenhouse effect, so it is looking for technologies that are designed to limit the emission of this gas to the atmosphere. One of the methods of CO_2 capture from the gas stream is adsorption process. For proper design of adsorption processes equilibrium data in a wide range of temperature and pressure are necessary.

The adsorption equilibrium isotherms of CO_2 on Zeolite 13X were measured in different temperatures (293.15 K, 303.15 K, 313.15 K, 323.15 K) and under pressures up to 2 MPa. Measured adsorption isotherms have been conducted on an IGA-002 apparatus (Hiden Isochema, UK). It is intelligent gravimetric analyser which uses static gravimetric method. As a result of the research, adsorption isotherms for the system carbon dioxide–Zeolite 13X were obtained for wide range of pressures. The measurements were performed for 136 pressure points.

All isotherms are type I according to the Brunauer, Deming, Deming and Teller classification (BDDT). For mathematical modelling of adsorption equilibrium the multitemperature models of Toth, Langmuir–Freundlich, and Langmuir were selected. Values of parameters of the models were calculated by nonlinear regression using Statistica 13.1 (Statsoft) by fitting them to experimental data. In the article, the relative average error δ and coefficient of determination R^2 were calculated. The multitemperature adsorption isotherms Toth, Langmuir−Freundlich, Langmuir were fitted to the experimental data with relative average errors of 2.45%, 16.47%, 22.18%, respectively.

Zeolite 13X is characterized by high adsorption capacity and can be used in the process of carbon dioxide removal. At 293.15 K and 2 MPa, the highest adsorption capacity of 6.04 mol/kg was obtained. From selected models, the best fit to the experimental data have Toth model with relative average error 2.45% and coefficient of determination 0.9996. The experimental and simulation results can be used for modeling of cyclic adsorption processes.

A new cerium doped bioglasses for bone tissue engineering

*Barbara Zagrajczuk[1], Michal Dziadek[1], Agnieszka Sobol[1], Katarzyna Cholewa-Kowalska[1], Maria Laczka[1]
[1]Dept. of Glass Technology and Amorphous Coatings, Fac. of Mat. Sci. and Ceramics, AGH University of Science and Technology, Krakow, POLAND;
e-mail: b.zagrajczuk@gmail.com

***Keywords**: bioglasses, anti-inflammatory performance, sol-gel method, cerium, bone tissue engineering*

Bioglasses are materials that can create a permanent bond with bone tissue and stimulate it to faster regeneration. Cerium oxide can act as antioxidant in biological systems due to their low reduction potential and the coexistence of mixed valence state (both Ce^{3+}/Ce^{4+}).

The aim of the study was structural characteristics and bioactivity evaluation of the gel-derived bioglasses doped with cerium. Glasses from the SiO_2-CaO-P_2O_5-CeO_2 system were obtained by the sol-gel route. They differed in the CaO/SiO_2 ratio and the concentration of the CeO_2, varying between 0-5 % mol. The XRD patterns were measured in order to investigate phase composition of obtained powders. There was the beginning of crystallization in the materials observed, rising along with the cerium content. In order to characterize the structure of materials, FTIR analysis has been performed. The FTIR spectra showed changes in the materials structure depending on the CaO/SiO_2 ratio and the cerium oxide content. Glass powders morphologies and compositions were tested with the SEM microscopy coupled with EDS spectroscopy, and revealed phase separation in the materials, caused by the presence of cerium in the concentrations higher than 3%mol. Bioactive properties of the powders were tested, through their immersion in simulated body fluid solution (SBF) for 7 and 14 days.

Changes in the powders structure after incubation were characterized with FTIR spectroscopy and XRD analysis. Moreover, morphological differences were examined with the SEM/EDS methods. Considerable changes in the structure and morphology of the powders, confirming the appearance of apatite after immersion in SBF have been indicated.

Acknowledgements
This work was supported by the National Science Centre Poland Grant nos. 2014/13/B/ST8/02973 (ML) and PRO-2017/25/N/ST8/01593 (BZ).

Dual-resonance long-period grating in fiber loop mirror structure for liquid refractive index measurement

*Renata Zawisza[1], Leszek R. Jaroszewicz[1]
[1]Institute of Applied Physic, Military University of Technology, Warsaw, POLAND
e-mail: renata.wonko@wat.edu.pl

***Keywords**: Optical engineering, Polarization-maintaining fiber, Dual-resonance long-period grating, Fiber optics sensors, Fiber loop mirror*

Long Period Gratings (LPGs) have become very popular as base for chemical, biological and physical sensors because of their high sensitivity, low cost, compact size and insensitivity to external electro-magnetic fields. An interferometric structure based on a Dual-Resonance Long-Period Grating (DRLPG) inside a Fiber Loop Mirror (FLM) is presented in this paper. Its purpose is to measure the refractive index (RI) of liquid samples.

In this experiment the grating acts as a the RI sensing probe, while the FLM serves as a band-pass filter. Proposed sensor structure consists of the wide-band source 1520-1620 nm, the DRLPG, the 3-dB coupler, insulator, a part of polarization maintaining fiber, the polarization controller and optical spectrum analyzer (OSA). Due to the high extinction ratio of the FLM, amplitude measurements can be obtained, allowing implementation of the differential interrogation method to establish the sensitivity of the device. The use of a polarization controller makes it possible to fine-tune the interferometric peaks with respect to the two notches of the DRLPG.

By changing the state of polarization (SOP) of the propagating beam we were able to move the interference peaks up to 9 nm and the amplitude about 11.25 dBm. Precisely aligned configuration produces a maximum sensitivity of 3871.5 dB/RIU within the RI range of 1.3333 up to 1.3419 with linear sensor response. The maximum change was observed for approximately 30 dB.

The monitoring of the amplitude changes enabled us to apply a differential interrogation method to obtain a signal expressed in dB as a computational tool for sensitivity enhancement. Such structure can be applied as a passive refractometer or as a optical sensor for biological or chemical samples monitoring.

Acknowledgements:
Our investigation was partially supported by the internal Military University of Technology project no. RMN 08/690.

Study of initial substrate concentration on MoS_2 nanoparticles size produced in turbulent micromixers

*Katarzyna Zubańska, Michał Wojtalik, Łukasz Makowski,
Faculty of Chemical and Process Engineering, Warsaw University of Technology, Warsaw, POLAND
e-mail: kzubanska@gmail.com

***Keywords**: MoS_2, nanoparticles, DLS, turbulent micromixers, precipitation*

MoS_2 nanoparticles are widely used as a lubricant and catalyst in the petrochemical industry. It is also potentially used as semiconductor. Research on the properties of molybdenum disulphide is important because this substance has no alternatives in its lubricating properties. The course of precipitation and kinetics of MoS_2 synthesis are not well understood. Currently, the main source of obtaining this substance are molybdenum ores containing various difficult to separate chemical compounds. In this work authors were focused on improving the wet method of MoS_2 synthesis. The team investigated the effect of reagent concentration on the size of the MoS_2 nanoparticles produced in turbulent micromixers and performed studies to determine the kinetics of the precipitation process.

It has been proven that presence of citric acid causes MoS_2 nanoparticles to aggregate, which falsifies the results of their size measurement. Also the efficient sample preparation procedure has been developed to eliminate the influence of citric acid viscosity on the particles size results. The prepared MoS_2 nanoparticle were measured using DLS (Dynamic Light Scattering) and laser diffraction with: Beckman Coulter LS 13 320 with ULM module and Zetasizer Nano – ZS Malvern Instruments Ltd. As a result of the research it was found that with higher concentration of reagents larger MoS_2 nanoparticles are formed.

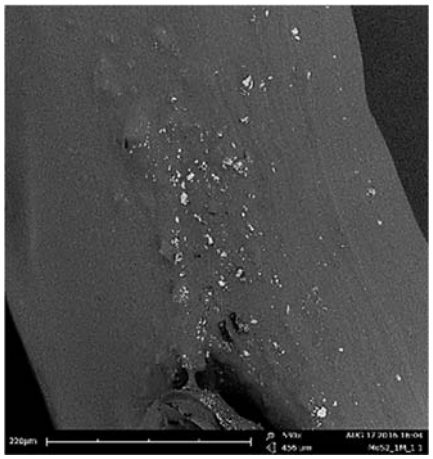

SEM image of the sample.

Influence of MTMS aerogel modification of fibrous filters on the effectiveness of oil mist separation

*Maria Zuzga[1], Bartosz Nowak[1], Łukasz Werner[1], Anna Jackiewicz-Zagórska[1], Marta Bojarska[1,2],
[1]Faculty of Chemical and Process Engineering, Warsaw University of Technology, Warsaw, POLAND
[2]GVS Filter Technology, Zola Predosa (Bologna), ITALY
e-mail: Maria.Zuzga.dokt@pw.edu.pl

***Keywords**: fibrous filters, aerogel, surface modification, oil mist separation*

Oil mist separation is a problem that occurs in many branches of industry: e.g. chemical, petrochemical or mechanical. One of the way to separate oil/gas dispersion is filtration on fibrous filters. In this research in order to increase separation properties of fibrous filters, the modification of the surface of the polymer fibers with a porous material - called aerogel, was applied. The aerogel based on the methyltrimethoxysilane (MTMS) has hydrophobic, oleophilic and oil-sorptive properties which can help to remove oil droplets from air.

Fibrous filters used in modification were made of polypropylene via melt-blown technique. The aerogel was synthesized in two-step sol-gel process, using different precursor (MTMS) to solvent (methanol) ratios from 1:10 to 1:20. The efficiency of oil mist separation (in respect to droplets with diameter 0.02-2 μm) and pressure drop on modified filters was examined.

Modification of filters with aerogel was successful, as a result aerogel coated the surface of the fibers in the whole volume of the filter. Different MTMS:methanol ratio had an effect on the amount of deposited aerogel and its distribution in the filter volume. For lower MTMS:methanol ratios (1:10, 1:13) higher aerogel deposition was observed on the filter surface while for higher MTMS:mathanol ratios (1:20, 1:18, 1:15) most of the aerogel was deposited in the filter volume and the thin foil was observed on the filter surface. The mass fraction of aerogel in the top layers and in the filter volume was determined. Almost all modified filters improve the fractional efficiency of oil mist separation. The pressure drop on modified filters has been higher than on unmodified ones. The influence of aerogel deposition in top layers of the filter on the efficiency of oil mist separation and pressure drop was examined.

Acknowledgements
This work was supported by NCBiR project “Oil removal from gas and liquid streams thanks to filter media modified by aerogel” LIDER/011/L-6/14/NCBR/2015.

Classification of tea infusions based on voltammetric signals

*Justyna Zuziak, Małgorzata Jakubowska
AGH University of Science and Technology, Faculty of Materials Science and Ceramics, Department of Analytical Chemistry, Cracow, POLAND
e-mail: zuziak@agh.edu.pl

***Keywords**: voltammetry, Chinese and Vietnamese tea infusions, partial least squares discriminant analysis (PLS-DA), support vector machine (SVM), cross validation*

Tea is the most consumed beverage throughout the world, right after the water. The reasons is good taste, healthy, dietetic and therapeutic benefits. Tea quality is very important issue. Also the origin is usually displayed on the label and it plays an important role in the consumers' choice. As a global trend, more and more food manufacturers tend to offer pure origin products. These products require a reliable confirmation of origin and quality. A modern strategy to solve this problem consists in defining classification models for samples of known origin and their use for new, unknown objects. A problem presented in this work is distinction of teas types and origin based on voltammetric signals.

Electrochemical experiments were carried out in a three electrode quartz cell with a multipurpose electrochemical analyzer 8KCA. Voltammetric signals were registered from black, green, red and white tea infusions of China and Vietnam origin. The composition of the supporting electrolyte was 0.03 M sodium hydroxide. All experiments were carried out using 3 independent samples (without special preparation) of 8 tea species and for each sample recording was done in triplicate. Classification models were defined using two algorithms, i.e. Partial Least Squares Discriminant Analysis (PLS-DA) and Support Vector Machine (SVM) with linear and radial kernel, and next validated using leave-one-out cross validation (CV). As a preprocessing procedure autoscaling was applied. Smoothing and baseline correction, typical for voltammetry, was not necessary. In the effect obtained models enabled classification of 8 various tea types. In PLS-DA selectivity CV and specificity CV was greater than 89%, while in the case of SVM it was 100%. In PLS-DA the number of optimal latent variables was six.

In this way it was proved, that voltammetric signals combined with advances classification algorithms, which are optimal in the case when the number of variables is many times greater than number of objects, are useful in distinction of tea infusions.

Acknowledgements
This work was supported by AGH University of Science and Technology, Poland (Project No. 18.18.160.766).

DP and LAP voltammograms as a data source in food profiling

*Justyna Zuziak, Małgorzata Jakubowska
AGH University of Science and Technology, Faculty of Materials Science and Ceramics, Department of Analytical Chemistry,Cracow, POLAND
e-mail: zuziak@agh.edu.pl

Keywords*: differential pulse voltammetry (DPV), large amplitude pulse voltammetry (LAPV), Chinese and Vietnamese tea infusions, multivariate data visualization and analysis*

Various researchers have made a number of efforts to correlate food quality with its chemical composition. This problem can be solved using various instrumental methods combined with multivariate data analysis. Mentioned strategy may provide important qualitative conclusions that allow the assessment of food origin and authenticity.

In this study a review of multivariate data visualization and unsupervised modeling methods was presented, applied to differential pulse (DP) and large amplitude pulse (LAP) voltammetric signals of black, green, red and white tea infusions of China and Vietnam origin. Electrochemical experiments were carried out in a three electrode quartz cell (Hg(Ag)FE as a working electrode) with a multipurpose electrochemical analyzer 8KCA (mtm-anko, Poland). It was proved that graphical presentation by diagrams and charts has a number of advantages in comparison to analysis of the measured signals or numerical datasheets. The same data presented and modelled by different methods may deliver various, complementary conclusions and also the strategy verifies the quality of the experiments. Insight to the experimental data and extraction of the useful information were done applying Chernoff faces, star plots, radar plot and matrix scatterplot.

Using self - organizing maps (SOMs) and Principal Component Analysis (PCA) it was demonstrated that DP voltammograms enabled distinction of the tea species with some problems with separation of the green and white ones, while LAP voltammetry signals distinguished the origin of the infusions. Successful separation of the 8 different types of objects was done by polar dendrogram, first time applied in voltammetry.

Acknowledgements
This work was supported by AGH University of Science and Technology, Poland (Project No. 18.18.160.766).

Optimization of the thermal treatment conditions of modified anodic WO_3 with enhanced photoelectrochemical properties

*Marta Zych, Karolina Syrek, Grzegorz D. Sulka
Department of Physical Chemistry and Electrochemistry, Jagiellonian University, Kraków, POLAND
e-mail: marta.zych@doctoral.uj.edu.pl

***Keywords**: anodization, anodic tungsten trioxide, in situ modification of WO_3*

Recently, semiconductor metal oxides (such as nanostructured TiO_2 and WO_3) have been extensively studied due to their very interesting chemical, physical and catalytic properties. It is known, that doping with transition metal ions have a significant impact on enhancement of their photoelectrochemical properties. Doped semiconductor nanomaterials can find promising applications.

WO_3 samples were prepared by electrochemical anodization of tungsten foil in an aqueous electrolyte containing F^- ions at 50 V. In order to transform amorphous oxide into a photoactive phase and obtain the best photoelectrochemical response samples were annealed at 500°C for 2 h. Furthermore, *in situ* modification of tungsten trioxide was performed by anodization in an electrolyte containing Cu ions, which incorporate in the structure of WO_3 during the process. These materials were annealed at previously optimized conditions (500°C, 2 h).

Received materials were characterized by SEM, EDS and XRD analyses. The photoelectrochemical measurements were carried out in a three-electrode system, where Pt was used as a counter electrode, saturated calomel electrode in a Luggin capillary filled with 1 M KNO_3 as a reference electrode, and nanoporous WO_3 as a working electrode. The generated photocurrents were measured using a photoelectric spectrometer equipped with the 150 W xenon arc lamp and combined with a potentiostat.

In conclusion, the best photoelectrochemical performance of the anodic tungsten oxide was observed for the sample annealed for 2 h at the optimized annealing temperature (500°C). It can be attributed to a higher degree of crystallization of WO_3 and decrease in surface defects. What is more, the photoelectrochemical properties of photoanode were improved via *in situ* modification of WO_3 by incorporating metals into the anodic layers.

Acknowledgements
This work was supported by National Science Centre, Poland (Project No. 2016/23/B/ST5/00790).